

DOE/PC/91008-24
Distribution Category UC-122

Using Microstructure Observations to Quantify Fracture Properties and
Improve Reservoir Simulations

By

S.E. Laubach, R. Marrett, W. Rossen, J. Olson,
L. Lake, O. Ortega, Y. Gu, R. Reed

January 1999

Work Performed Under Subcontract No. G4S51732 Contract DE-AC22-94PC91008

Prepared for
U.S. Department of Energy
Assistant Secretary for Fossil Energy

Robert E. Lemmon, Technology Manager
National Petroleum Technology Office
P.O. Box 3628
Tulsa, OK 74101

Prepared by:
Bureau of Economic Geology
The University of Texas at Austin
University Station, Box X
Austin, TX 78713-8924

MASTER

DISTRIBUTION OF THIS DOCUMENT IS UNLIMITED

DISCLAIMER

This report was prepared as an account of work sponsored by an agency of the United States Government. Neither the United States Government nor any agency thereof, nor any of their employees, make any warranty, express or implied, or assumes any legal liability or responsibility for the accuracy, completeness, or usefulness of any information, apparatus, product, or process disclosed, or represents that its use would not infringe privately owned rights. Reference herein to any specific commercial product, process, or service by trade name, trademark, manufacturer, or otherwise does not necessarily constitute or imply its endorsement, recommendation, or favoring by the United States Government or any agency thereof. The views and opinions of authors expressed herein do not necessarily state or reflect those of the United States Government or any agency thereof.

DISCLAIMER

Portions of this document may be illegible in electronic image products. Images are produced from the best available original document.

CONTENTS

PART 1: INTRODUCTION AND PROJECT DESCRIPTION	1
SUMMARY	1
STRUCTURE OF THE REPORT	2
THE CHALLENGE OF RESERVOIR FRACTURE ANALYSIS.....	3
PROJECT IMPLEMENTATION.....	4
ACCOMPLISHMENTS	5
Summary of New Methods.....	6
Example: Identifying Fracture Production.....	8
Fracture Documentation Methods.....	9
Fracture Observation, Scaling Analysis, and Geomechanical Modeling.....	12
Numerical Simulation	13
INFORMATION TRANSFER INITIATIVES.....	14
FOLLOW-UP WORK	18
REFERENCES.....	21
APPENDIX A: PERMEABILITY, POROSITY, AND SHEAR-WAVE ANISOTROPY FROM SCALING OF OPEN FRACTURE POPULATIONS	45
APPENDIX B: APPLICATION OF SCANNED CL TO RESERVOIR ISSUES	65
APPENDIX C: CLASSIFICATION OF MICROFRACTURES	69
APPENDIX D: SYNKINEMATIC CEMENT AND FRACTURE ATTRIBUTES.....	71
APPENDIX E: ADDITIONAL BACKGROUND MATERIAL.....	77
APPENDIX F: FRACTURE ORIGINS	87
REFERENCES.....	92
PART II. CHARACTERIZATION AND SCALING.....	107
INTRODUCTION	107
Hypotheses to be Tested and Approach Taken.....	109
Implications and Importance.....	109

REGIONAL SETTING.....	111
San Juan Basin	111
Fracture Systems in the San Juan Basin.....	112
Mesaverde Group.....	112
Blanco-Mesaverde Gas Field.....	113
Mesaverde Outcrops in Northwestern New Mexico.....	113
OBSERVATION METHODS.....	114
Macroscopic Data from Cores	114
Macroscopic Data from Outcrops.....	116
Microscopic Data	118
Measurement of Fracture Orientation.....	119
Measurement of Fracture Length.....	119
Measurement of Fracture Apertures	122
Other Data Collected.....	123
FRACTURE DIAGENESIS	124
Rock Texture and Mineralogy	124
Paragenetic Sequence.....	125
Fracture Cement Characterization	126
FRACTURE MORPHOLOGY AND CONNECTIVITY	130
Macrofracture morphology	130
Microfracture morphology.....	131
Fracture Connectivity.....	133
FRACTURE ORIENTATION.....	138
Macrofracture Orientation.....	138
Analysis of Microfractures for Prediction of Macrofracture Orientation.....	139
Comparisons of Microfracture and Macrofracture Orientations.....	142
Riddle D LS 4A Microfracture and Macrofracture Orientations.....	142

Effects of Amount of Data Collected on Macrofracture Orientation Prediction	143
Other Cases	145
FRACTURE SIZE DISTRIBUTIONS AND FRACTURE FREQUENCY.....	148
Fracture Size Population Analysis	148
Error Analysis of the Distribution and Selection of Limits for Least Squares Regression ...	151
Use of Microfracture Frequency to Predict Macrofracture Frequency	152
Prediction of Macrofracture Length.....	153
Fracture Height Distributions.....	154
Aperture-Length Relationships	154
Scanline Data: 2D-1D Conversions	155
Test of Potential Microfracture Sampling Bias.....	156
Effect of Important Mechanical Boundaries on Size Distributions of Fractures.....	156
CONCLUSIONS.....	160
REFERENCES.....	163
APPENDIX A. CORE MACROFRACTURE DATA.....	227
APPENDIX B. OUTCROP MACROFRACTURE DATA.....	237
APPENDIX C. TEXTURAL AND PETROGRAPHIC ANALYSIS OF SAMPLES	269
APPENDIX D. MICROFRACTURE DATA.....	273
PART III. ENGINEERING APPLICATION OF RESULTS	361
INTRODUCTION TO PART III: INCORPORATING GEOLOGIC INFORMATION IN DUAL-POROSITY SIMULATORS	361
Geomechanical Modeling	364
Modeling Concepts	364
The Model.....	364
Model Results	366
Implications for Fracture Geometry.....	368
CHAPTER 1: INTRODUCTION	369
1.1 Characterization of Naturally Fractured Reservoirs	370

1.1.1 Basic Properties of Fractures	370
1.1.2 Outcrop Study	370
1.1.3 Detection and Evaluation of Fractures.....	371
1.1.4 Core Analysis.....	372
1.1.5 Definition of Dual Porosity.....	372
1.2 Simulation of Naturally Fractured Reservoirs	373
1.3 Advances in Characterization of Fracture Systems	374
1.3.1 Correlation between Microfractures and Macrofractures	374
1.3.2 An Outcrop Study	376
1.4 Delineation of Research Motivations and Objectives.....	377
1.4.1 Research Motivations.....	377
1.4.2 Research Objectives.....	378
CHAPTER 2: A SIMPLIFIED MONTE CARLO STUDY OF FRACTURE APERTURE AND PERMEABILITY DISTRIBUTIONS	385
2.1 Fracture Aperture Distribution.....	385
2.2 A Simplified Fractured Reservoir Model.....	386
2.2.1 Model Assumptions	386
2.2.2 Effective Permeability and Porosity	388
2.3 Monte Carlo Study of Fracture Aperture Sampling.....	389
2.3.1 Computational Approach.....	389
2.3.2 Results and Analysis	390
2.4 Monte Carlo Study of Fractured-Reservoir Permeability.....	392
2.4.1 Computational Approach.....	392
2.4.2 Results and Analysis	393
2.5 Conclusions.....	395
CHAPTER 3: 3-D FRACTURE NETWORK INTERCONNECTIVITY.....	415
3.1 Generation of 3-D Fracture Network.....	415
3.1.1 FracMan™ Program and Conceptual Geometry Models.....	415

3.1.2 Constraints on Modeling.....	416
3.2 Simulation Study of Fracture Interconnectivity.....	420
3.2.1 Input Parameters for FracMan™	420
3.2.2 Simulation Results	423
3.2.2.1 Realizations Using The Original Westwater Data and The Enhanced Baecher Model	423
3.2.2.2 Realizations Using The Original Westwater Data and Other Models	423
3.2.2.3 Effect of Pre-Exponential Factor	424
3.2.2.4 Effect of Fracture Orientation.....	427
3.3 Conclusions.....	428
CHAPTER 4: CONCLUDING REMARKS AND FUTURE WORK.....	451
4.1 Conclusions.....	451
4.2 Future Work.....	453
REFERENCES.....	455
APPENDIX A. PROBABILITY ANALYSIS OF PROPERTIES OF A SIMPLIFIED FRACTURED RESERVOIR.....	457
APPENDIX B. FRACTURE FREQUENCY IN OUTCROPS AND SCALING OF FRACTURE FREQUENCY WITH VOLUME OF OBSERVATION.....	465
APPENDIX C. NOMENCLATURE	479
PART IV: TECHNOLOGY TRANSFER	483
INDUSTRY GROUP.....	483
Publications and Presentations.....	484
Published Papers	484
Published Abstracts.....	485
Completed Thesis.....	488
Papers in Press	488
Lectures.....	488
Awards	492
ACKNOWLEDGMENTS	493

PART 1: INTRODUCTION AND PROJECT DESCRIPTION

SUMMARY

The research for this project, funded by the U.S. Department of Energy, provides new technology to understand and successfully characterize, predict, and simulate reservoir-scale fractures. Such fractures have worldwide importance because of their influence on successful extraction of resources. For example, many conventional U.S. reservoirs yield about one-third of the oil originally in place, but some estimates suggest that reservoirs with naturally occurring fractures yield only about 10 percent of their reserves. This is a serious technical and financial challenge for producers of reservoirs containing natural fractures.

Most fractures are below the limits of seismic resolution or detection and are difficult or impossible to characterize adequately using currently available well test, full-diameter core, or geophysical well log technology; this is because large fractures are intrinsically difficult to sample with conventional wellbore sampling methods owing to their wide spacing. Consequently, fractured reservoirs have been intractable to describe and interpret effectively, impeding accurate reservoir description and simulation. Accurate characterization of reservoir fractures, however, still holds great potential for improving production by increasing the efficiency of exploration and recovery processes.

The scope of this project includes creation and testing of new methods to measure, interpret, and simulate reservoir fractures that overcome the challenge of inadequate sampling. The key to these methods is the use of microstructures as guides to the attributes of the large fractures that control reservoir behavior. One accomplishment of the project research is a demonstration that these microstructures can be reliably and inexpensively sampled. Great potential exists, therefore, for increasing the quality and quantity of fracture data acquired as well as reducing the cost.

Specific goals of this project were to

- create and test new methods of measuring attributes of reservoir-scale fractures, particularly as fluid conduits, and test the methods on samples from reservoirs;
- extrapolate structural attributes to the reservoir scale through rigorous mathematical techniques and help build accurate and useful 3-D models of the interwell region; and
- design new ways to incorporate geological and geophysical information into reservoir simulation and verify the accuracy by comparison with production data.

The goals of this study are practical; they aim to improve diagnosis of natural fracture attributes in hydrocarbon reservoirs and accurately simulate their influence on production. Emphasis is on reaching the goal of increased domestic production by improving tools for exploring and developing reservoirs that contain fractures. New analytical methods developed in the project are leading to a more realistic characterization of fractured reservoir rocks. Testing diagnostic and predictive approaches was an integral part of the research, and several tests were successfully completed.

STRUCTURE OF THE REPORT

This report summarizes research accomplishments during this study and describes technology transfer. The report is in four major parts. Part I summarizes the issues the research addressed and describes some of the key findings. Part II is an in depth description of research focused on the key issue of fracture scaling. Part III recounts our research on incorporation of geological information into reservoir simulators, which emphasis on incorporation of scaling data. The material in this section of the report has not previously been described in our earlier accounts or in papers published or submitted during the course of the project. Parts II and III are thus complementary reports on a central issue of the study: scaling. Part IV documents technology transfer and lists publications resulting from the study. Some important aspects of

project research that are not described in detail in this report are described in these other accounts. Some issues covered in these other reports are briefly summarized in the appendices.

This project has created significant new technologies, some of which have already been introduced to domestic operators through our technology transfer efforts. Research has also revealed promising directions for further inquiry; additional efforts in the general field of applying microanalytical methods to rock sample analysis hold the promise of significant breakthroughs in meeting the challenge of exploring and developing hydrocarbon reservoirs that contain fractures.

This report summarizes the justification for this research approach. There is a strong need for accurate, site-specific data on natural fractures in the subsurface and for new ways to use such information in reservoir simulators; the report also includes the specific project objectives and project implementation. Owing to outstanding industry cooperation, we have been able to test aspects of our technology in a spectrum of hydrocarbon reservoir settings; some of our key findings with examples drawn from the tests are illustrated in the report.

The accomplishments of the research are revealed by examining the key hurdles to overcome in fracture characterization and simulation, and key accomplishments are listed. The final section of the report describes technology transfer accomplishments. We also look ahead to areas of valuable follow-up research.

THE CHALLENGE OF RESERVOIR FRACTURE ANALYSIS

Although reservoir modeling and development technology are rapidly advancing as a result of improved computer capabilities and increased knowledge of reservoir complexity, knowledge of one of the most important geological variables affecting reservoir performance is nevertheless inadequate. Natural fractures play a large role in effective permeability in many reservoirs, including those that do not display the production characteristics of a classic “fractured reservoir.” Because they are nearly impossible to characterize effectively with existing

technology, however, fracture networks are an almost unknown factor in reservoir models. The enormous heterogeneity that is intrinsic to fracture networks cannot be predicted adequately on a site-specific basis without site-specific data. Conventional technology at best provides site-specific data on only a small number of fractures because these methods address only large fractures, ones that are sparse and commonly oriented nearly parallel to wellbores. Consequently, there is a serious problem of undersampling. We have documented aspects of this situation in several publications (for example, Laubach and others, 1997; Marrett, 1997).

Understanding geologic control of reservoir heterogeneity is fundamental to modeling subsurface fluid flow and to predicting the efficiency of different recovery processes. Accordingly, improved diagnosis and predictions of natural fracture attributes in reservoirs are vital for projections of asset value and can lead to drastic modifications in exploration and production decisions. To be most useful to reservoir engineers, information on natural fractures must not only be far more complete and accurate than at present but must also be in a quantitative form suitable for flow simulation.

Because of the worldwide importance of resources in fractured reservoirs, improved reservoir models are required not only to quantify fracture occurrence and fracture attributes but also to accurately predict their spatial variation and simulate their effects on fluid flow. In order to even begin constructing such models, however, improvements must be made in how subsurface fracture attributes are measured. This research project was initiated to investigate the above problems by using subsurface data as well as outcropping rocks that are analogs to those in fractured reservoirs.

PROJECT IMPLEMENTATION

The project was carried out by a team of petroleum engineers and geologists at The University of Texas at Austin working closely with scientists from a group of nine companies from the petroleum and scientific instruments industries. Collaboration was facilitated by a

specially designed project Web site (Burns and Laubach, 1997) and by periodic review meetings. The integration of geologic and petroleum engineering approaches was crucial to this project.

The disciplines brought to bear on the problem include microstructural and structural diagenetic analysis, geomechanical modeling, scaling, and flow modeling. We used samples, production records, and other data supplied by the sponsor as the starting point for our analysis. Access to wells and production data were used to test the accuracy of our results. We completed two major integrated studies that involve subsurface data analysis and analysis of outcropping rocks that serve as analogs for subsurface reservoirs. Owing to the cooperation of industry, we have also been able to test aspects of our methods in numerous other rock units (Reed and Laubach, 1998; Laubach and Reed, in preparation). Now that we have observed the requisite microstructural indicators that our method depends on in more than 50 formations, we are confident that our approach is widely applicable.

ACCOMPLISHMENTS

We will now discuss the general accomplishments of the project in the context of the multifaceted challenges for reservoir fracture characterization and simulation. As illustrated in figure 1, our aim was to obtain site-specific information that can help make decisions such as how to specify target zones for completion or horizontal drilling. Figure 3 illustrates measurements of fracture quality (left side of diagram) and fracture orientation (right side of diagram). A key issue addressed in parts II and III of this reports describes efforts to measure and simulate another key variable, fracture scaling (Marrett, 1997).

The research program was designed to accomplish project goals that include (1) establishing geologically realistic descriptions of fractured reservoir rocks whose acquisition is cost effective, (2) developing techniques that permit more accurate diagnosis of fracture and fault attributes in the subsurface (including methods that enhance well-test and seismic interpretations), and (3) finding better methods of exploiting the fracture descriptions through improved prediction

and simulation. Testing of diagnostic and predictive approaches developed from outcrop, core, and well-test studies was an integral part of the study.

Summary of New Methods

Our new methods are summarized in figures 1 through 22, which graphically depict how our approach works from sample acquisition to reservoir simulation. Figure 1 illustrates one innovative way we collect data from rock samples: the use of sidewall cores for systematic fracture analysis. We have devised a technique that allows oriented sidewall core samples to be reliably obtained. Figure 2 shows typical basic fracture data that we collect using new imaging techniques: a plan view scanning electron microscope-based scanned cathodoluminescence (scanned CL) image of a microfracture, quartz cement, and clastic grains. Note the 100 micron bar scale. The rapid collection and interpretation of such small features is key to collecting the large amount of microstructure data necessary to make reliable inferences about the large fracture that are of primary interest in reservoirs.

Figure 3 is a diagram that shows how various parameters, such as permeability anisotropy, fracture size distributions, and fracture fluid conduction capacity, should be incorporated into a concept of reservoir fracture heterogeneity. Although the diagram is schematic, the patterns of shifting fracture strike and fracture quality (openness) depicted in this diagram are from wells and outcrops studied in this research project. The nuanced view of reservoir natural fractures shown here requires systematic collection of site-specific information that can only be achieved with the methods we developed in this project.

Figures 4 and 5 illustrate a 'blind' test of our fracture orientation analysis method. In this test in the Spraberry oil play of West Texas, we determined fracture orientations from microstructure observations from samples collected by a third party. The true geographic orientation of the samples was withheld from analysts until the microanalysis was complete.

These results are described elsewhere in the report. They illustrate that macrofracture orientations can be obtained reliably from microfracture observations.

Fracture size distributions can also be measured from microfracture information, as shown in figure 6. Figure 7 illustrates the concept that the size of the fractures and the scale of the measurement are important for predicting fracture behavior in reservoirs. The data exemplified by figure 6 illustrate how we can now address this issue. As discussed at length elsewhere in this report, these results point toward techniques that will give accurate estimates of the role of fractures in reservoir behavior. Incorporating such results in reservoir simulators was a major task in this project, and is described in detail in parts II and III of this report.

Figures 8 through 13 illustrate how fracture 'quality' can be measured, and how this can relate directly to producibility. This concept is examined in more detail in the next section of the report. This innovative method allows identification of areas where productive fractures exist in reservoirs without the necessity to directly sample the fractures. These illustrations include tests where this procedure was used to identify productive and non-productive wells. This aspect of the project has identified several fundamental controls on reservoir behavior that were not evident before. Follow-up work should be undertaken to understand the basic geologic processes that cause this phenomenon so that production can be better predicted ahead of drilling.

One way to predict fracture attributes in advance of drilling that can be applied now is to use existing and new rock material and our methods to map fracture attributes. Since our methods can use samples that do not contain macroscopically visible fractures, a far greater data density can be achieved than was hitherto possible. Figure 14 shows how measured fracture attributes can be combined to map fracture heterogeneity in an example from the East Texas Basin and thus predict fracture attributes in potential infill drilling locations.

Figures 15 through 21 show the conceptual steps involved in putting these observations into reservoir simulators. This material is discussed at greater length in part III of this report. The illustrations show conventional dual-porosity simulator grid blocks and how we can now use site-specific information and outcrop analogs (as well as geomechanical modeling, which is not

shown) to scale up to assign grid block attributes, select grid block sizes, and scale up to effective properties.

Example: Identifying Fracture Production

Figures 9–14 show examples of how one aspect of our research can be useful in practical exploration and production evaluation. The objective of this test is to identify where conductive fractures are located in reservoirs in situations where the well has not encountered a fracture. In the example in figure 10, we accurately predicted which of the two wells was an economically successful hydrocarbon producer (Clift and others, 1997). Conventional approaches were unsuccessful in finding a significant geological or engineering distinction between the two wells, which are in the same field and are completed in the same sandstone interval using identical methods, and which have statistically identical conventional porosity values (Laubach, in preparation). Conventional core-analysis and borehole-image-log data from both wells correctly indicated that natural fractures were present in both wells but inaccurately diagnosed fractures in both wells as open and potential fluid conduits. In fact, only one of the wells contains open, conductive fractures. The technique we illustrate here, however, has been shown to work even in situations where conventional methods discover no reliable information about natural fractures.

The parameter we used to determine that the well has conductive fractures (postkinematic cement volume) was readily obtained from small core samples (such as sidewall cores) that do not contain macroscopically visible fractures. This parameter, known as postkinematic cement volume, predicts the location of closed (mineral-filled) fractures that will not act as fluid conduits and therefore can discriminate between nonproductive wells and production “sweet spots” in areas where natural fractures are the key to producibility. A report defining this and related parameters and the evidence for their widespread applicability has been reported and a fuller account is in press (Clift and others, 1997; and in press). The illustrations shown here show this parameter (displayed in different ways) for a wide range of structural settings and rock types.

The Larsen and Emerald well examples are from the prolific Rangely oil field (Weber Formation) and illustrate that this method can detect fracture system heterogeneity that was accurately diagnosed using conventional geological or well analysis methods.

Because samples used to obtain data such as those illustrated in this example can be targeted in intervals or areas of exploration or development interest, this approach for the first time permits key natural fracture attributes to be systematically mapped. This greatly improved data density on natural fracture attributes can vastly improve the input for reservoir simulators, as well as aid decision-making.

The widespread occurrence of this phenomenon is documented in an appendix to this report, which shows pre-, syn, and postkinematic cement in a wide range of formations. Postkinematic cement is the key predictor of fracture occlusion (Laubach, 1997, and in preparation).

Fracture Documentation Methods

To meet the challenge of fracture characterization and prediction, we quantified interrelationships among fractures, diagenesis, rock properties, and facies architecture by using both core and outcrop reservoir analogs. We discovered that many of the critical attributes of fracture networks that are difficult or impossible to measure directly in the subsurface can be deduced from microstructural and diagenetic relations by appropriately applying advanced detection tools, scaling methods, and geomechanical modeling. Such deduction is possible because fractures evolve in, and are strongly influenced by, the stratigraphic and diagenetic context in which they form and interact.

The new fracture characterization approaches described above are widely applicable (Milliken and Laubach, in press; Reed and Laubach, 1998, and in preparation; Marrett and others, 1998); they provide data that are critically useful to development and exploration planning. Although much remains to be learned and important tests of these methods are still in

progress, we have presented results to the industry through papers and lectures. Several key steps needed to incorporate new observations in simulators have been derived because of our research.

We have found it possible to make observations at the scale of structures in available samples (including samples as small as conventional cuttings) and to rigorously extrapolate results to the critical scales that affect reservoir behavior. In other words, we use structures (microfractures) with length scales of microns to millimeters to diagnose the attributes of structures (macrofractures) with length scales of meters to decimeters. At this time, we can acquire qualitative or semiquantitative information about large fractures from some microscopic observations. From others, we have been able to make accurate quantitative predictions of the attributes of large fractures. We have also identified attributes that are scale dependent or that have nonlinear changes in attributes with changes in size. An example of using microscopic data qualitatively is by predicting fracture occlusion as shown in figure 9. Quantitative measures of fracture attributes are illustrated by measurements of fracture-size and fracture-strike distribution (figures 5 and 6). These results are great advances over what can be achieved using conventional techniques.

These methods address the central challenge of successful reservoir fracture analysis: inadequate and unrepresentative sampling of the fracture network. The lack of adequate sampling results from the wide (>1 m) spacing and steep dips of large fractures, which make large fractures elusive targets for conventional wells (that is, excluding expensive horizontal wellbores). Despite improvements in detection and characterization of fractures and faults by geophysical logging tools, subsurface fracture and fault properties are commonly conjectural because large fractures rarely intersect wellbores where they can be observed. It is not unusual therefore, for many fracture attributes that critically affect hydraulic and mechanical properties of subsurface rocks to remain unknown, even after extensive coring and logging efforts. Seismic detection or resolution of fractures is limited, moreover, and improvement in seismic methods is greatly hindered by an absence of fracture data with which to calibrate and verify seismic response.

Inadequate fracture sampling is a problem in virtually all reservoirs. The key advantage of our method is that it provides site-specific fracture information reliably and at any user-specified level of completeness. Our approach can therefore work even without measuring elusive, difficult-to-sample, large fractures.

As our unpublished results and a few preliminary published reports show, initial results of applying this fracture characterization approach are highly encouraging (Laubach, 1997; Marrett and Laubach, 1997; Marrett and others, 1998; Olson and others, 1998). The results offer a tantalizing glimpse of the major advances possible through our research. Our approach is beneficial because of reduced costs, as data can in many cases be acquired by wireline sampling (sidewall cores) or, in some analyses, cuttings. This year we performed successful tests of our method to obtain oriented sidewall cores. This approach makes use of commercially available, relatively inexpensive wireline-conveyed coring devices to collect samples that are then oriented by a combination of analysis of the core itself and geophysical well logs that run subsequent to core collection to image sample locations on the borehole wall (Doherty and Laubach, in preparation). Our research has demonstrated how the orientation of these cores can be measured with a high degree of accuracy. We have tested our methods on cuttings supplied by one of our industry research partners. It may be possible to use cuttings for some fracture diagnostics applications.

The critical steps in applying these results to numerical reservoir simulation include understanding how to extrapolate results to scales relevant to reservoir behavior, predicting properties between data points (wellbores), and formatting results so that they can be incorporated into reservoir simulators. These issues were central to the last phase of the research on this project. Measures of the speed, accuracy, and value of these new approaches have been gathered in our laboratory and in tests with industry partners. These measures and our field tests show that the impact of this research can be substantial.

Fracture Observation, Scaling Analysis, and Geomechanical Modeling

Our approach to solving the fundamental sampling problem is to diagnose fracture attributes by analyzing proxies: microscale structures and their relationships to diagenesis. We have demonstrated that in many rocks, microfractures, which have lengths of microns to millimeters, are thousands of times more common than large fractures and can be sampled effectively even in small volumes of rock by using modern microimaging technology, as shown in figure 2.

We have made significant progress in developing imaging techniques, particularly in the area of digital color scanned CL imaging, as illustrated on our project Web site. We have also made advances in image-interpretation procedures. Imaging microfractures is one step in the process of diagnosing properties of large fractures. Advancements have also been made in diagenetic analysis, mathematical scaling methods, and geomechanical models for deriving information from fracture observations and obtaining high-resolution (bed-by-bed) information on fracture orientation, size distribution, clustering, conductivity, and other fracture properties. Among the most striking accomplishments are the rigorous demonstrations of fracture scaling in several reservoirs and reservoir analogs. Results of some of this work are being prepared for publication (Ortega, 1997). Figure 4 shows a typical scaling data set from an ongoing reservoir study.

This approach to characterization presents new opportunities for fracture prediction. Predictive models are enhanced because through diagenetic modeling we analyze the mechanical development of the entire rock, not just the fractures within it. Model predictions are, moreover, designed to be testable by means of microstructural information. With limited samples, the accuracy of model predictions can thus be rigorously evaluated before expensive additional drilling is carried out; this will be a promising area for follow-up research.

For example, predictive geomechanical models that are coupled with basin history and diagenetic models in order to specify the location, size, orientation, and connectedness of fracture swarms may soon be attainable. We have explored this possibility as part of the

modeling work mandated in this project by combining geomechanical models that we developed with our diagenesis models and commercial predictive models of diagenesis that have recently become available (in particular, the program EXEMPLAR). Although such predictions cannot be accomplished at this time, our preliminary studies suggest that this may be possible in the future.

Our model predictions are inherently testable because they predict the attributes of both large fractures that control production behavior and small fractures that can be readily sampled and examined for verification of predictions. Methods that identify zones that have conductive fractures (thief zones or sweet spots) can be used, for example, to design vertical or horizontal wells to intersect or avoid fractured areas. This is one example of how project results have direct applications to exploration, development, and reservoir management.

Numerical Simulation

Numerical simulation of fluid flow in hydrocarbon reservoirs forms the basis for choices that industry makes among various reservoir production strategies. Without accurate prediction of these flow properties, hydrocarbon reservoirs cannot be efficiently exploited. The basis for our approach was described in last year's annual report, and technical publications on this work are in preparation.

The goal of our simulation work is to measure directly the properties that will define the simulator cell attributes. Fracture orientation information has been used to predict permeability anisotropy and production interference directions. Fracture "conduit quality" has been used to predict areas where a single-porosity simulation is appropriate because fractures are blocked by authigenic cement. We developed and tested a method of collecting field data, such as distribution of fracture apertures, lengths, orientations, and other attributes, and deriving a probability distribution for effective permeability. This probability distribution forms the basis for assigning cell properties in dual-porosity simulation.

Our approach has great potential for enhanced, yet practical, simulation of fractured reservoirs. It permits improvement in widely used dual-porosity approaches to flow modeling. Figure 17 illustrates our approach to deriving probability density functions for fracture reservoir simulation that are based on site-specific well data or maps of fracture attributes that have well control on attributes derived from our observational methods.

Some of the technical accomplishments of this aspect of our study are enumerated in a later section of this report. Specific accomplishments are listed in the following section; we will mention several general conclusions that can be drawn.

INFORMATION TRANSFER INITIATIVES

Innovation in technology transfer was accomplished through two related initiatives in this project. We formed a group of industry scientists who participated in aspects of the research in addition to periodically reviewing our progress. Second, to aid integration of the diverse disciplines represented in our research group and to facilitate collaboration and rapid technology transfer with industry partners, the project created and currently uses a unique Web-based virtual laboratory (Burns and Laubach, 1997).

Having now observed the requisite microstructural indicators that our method depends on in more than 50 formations, we are confident that our approach is widely applicable.

- Fracture orientation procedures were successfully tested in a “blind” test from a major oil reservoir (Spraberry Formation), and additional tests were completed that test the reliability and accuracy of results.

- Drilled sidewall cores were successfully oriented in three wells using our procedure. Additional tests were carried out in various formations under different coring scenarios to identify bottlenecks and limitations of the procedure.

- Fracture “conduit quality” indices have been measured in many reservoir rocks and have been used to accurately predict reservoir behavior. Indices were tested in five formations where

suitable well-pair comparisons could be performed. These tests demonstrate that this new parameter is a powerful predictor of natural fracture attributes and well performance. We also showed that this index can be successfully incorporated into a conventional dual-porosity simulator.

- A key requirement is that new methods must ultimately be cost effective. We determined that samples can be collected using wireline devices and that results can be obtained rapidly. These demonstrations suggest that deployment of these methods will be cost effective.

We have made several major discoveries regarding the scaling of natural fractures in petroleum reservoir rocks:

- We have developed new techniques for measuring the mechanical apertures of fractures in core and outcrop. Through a combination of portable magnifiers (for example, hand lens) and comparators that we developed specifically for this purpose, we can now systematically measure fracture apertures down to the scale of ~50 microns in the field (presuming rock exposure permits).

- We have collected several data sets that consist of uniformly accurate mechanical aperture measurements covering four to five orders of magnitude. This is twice the range of the best data sets in the world prior to this project. The most important result of these data sets is the direct confirmation that, at least in the cases investigated, microfractures and macrofractures follow the same fractal distributions. This provides a solid basis for using microfracture observations to predict the spatial frequencies of macrofracture apertures, a key to reservoir simulation.

- Through numerous examples, we have demonstrated the feasibility of measuring statistically significant numbers of microfracture lengths and mechanical apertures from small borehole samples. By combining this information with the results above, we can now use locally acquired data to predict the critical attributes of subsurface macrofractures on a layer-by-layer basis, and in the time frame of a few days after sample collection and sample preparation.

- We have found that the finite thickness of sedimentary layers in a fractured reservoir has a significant effect on the observed scaling of fractures. As observed in two-dimensional rock surfaces, fracture lengths apparently follow different scaling depending on whether they are longer or shorter than the layer thickness. However, once sampling effects are accounted for, we find that long and short fractures follow the same fractal distribution in a three-dimensional volume. This is a significant result because, although fracture observation is almost always limited to one- and two-dimensional sampling, fluid flow should be modeled in three dimensions.

- Our research has repeatedly found that fracture attributes follow power-law fractal scaling. This conclusion holds for both fracture length and mechanical aperture, microfractures and macrofractures, and dozens of data sets from different rock units. An understanding of this scaling provides the quantitative link between microscopic observations and a wide array of valuable predictions about associated macrofractures, which have the most significant effect on reservoir performance.

- Questions to which we can now provide quantitative answers, based on local fracture observation, include the following: What values should be used for fracture porosity and permeability in a reservoir simulation? What is the appropriate size of reservoir blocks in a fractured reservoir simulation? How much variability of reservoir performance should be expected from location to location? How long should a horizontal borehole be drilled to optimize fracture permeability encountered versus the drilling cost?

In the key area of developing accurate reservoir simulation methods that use these data, important progress has been made. Some of the steps that have been taken are outlined here.

- The effect of wide fracture aperture distribution has been studied. We analyzed the influence of the type of power-law distributions we observed on effective permeability in the simplified case where all fractures extend through an entire grid block, and showed that in this case the widest single fracture in a block dominates flow through the entire block. As a result, probability distribution can be derived for the widest single fracture in a block and for the

effective permeability of the block. This probability distribution is extremely wide—that is, permeability can vary by large factors from block to block.

- We dropped the assumption that fractures extend throughout a grid block and considered sets of fractures with location, length, aperture, and orientation selected randomly from statistics determined from field data. We determined implications of power-law scaling of fracture length on effective permeability of the fracture pore space. For certain ranges of exponents in the power law, the large population of short fractures link up on the microscopic scale; for other ranges, the largest fractures link up on the megascopic scale. For power-law exponents between two and three, like those in one of our case study areas (Westwater pavement, Mesaverde sandstone of the San Juan Basin), and with fractures confined within a single layer of finite thickness, neither short nor long fractures are guaranteed to link up; one must determine connectivity from Monte Carlo studies for each given case.

- We showed the relationship between fracture statistics derived from two-dimensional (2-D) (outcrop) data and frequency statistics in three dimensions (3-D). We confirmed that different power-law scaling is observed in outcrops for fractures shorter and longer than layer thickness, as reported for Westwater pavement, and that both are consistent with a single power-law frequency in 3-D. Frequency function in 3-D is related to, but not identical to, power laws for either small or large fractures.

- Currently, we are studying intensively the implications of the fracture statistics determined for the Westwater pavement, Mesaverde sandstone of the San Juan Basin, on effective permeability. It appears that clustering fractures may be essential to obtaining connectivity between fractures and long-range effective permeability.

- Geomechanical modeling work is also in progress to understand the conditions that lead to fracture clustering and to determine how this fracture pattern can be quantified using microstructural data. We have studied the clustering of fractures on the micron scale that is qualitatively similar to that which we have observed among large fractures in horizontal wells and in outcrop reservoir analogs.

We have studied probability distributions for effective fracture permeabilities based on fracture statistics from field studies, starting with the most widely studied outcrop reservoir analog and extending to other fields. A key challenge was understanding how to model connectivity using the raw statistical data from fracture observations. Introduction of clustering in some form to get connectivity is only a partial solution. Flow in reservoir intergranular porosity between fracture strands is important to fracture fluid flow. In this regard, geomechanical modeling can help guide how fracture connectivity is visualized.

FOLLOW-UP WORK

We foresee some areas where profitable follow-up work will be beneficial. Extrapolation to carbonate rocks of the methods we are devising and testing in siliciclastic rocks has great potential value. Many of the methods and procedures we have devised could be automated. Studying this area further could multiply the impact of our research on the domestic petroleum industry. Microimage acquisition and processing is one area where many of the needed components for an automated system already exist for other uses. These technologies could be readily recruited for an automated natural fracture analysis system based on the approach outlined in our research. Among the technologies that could be incorporated into such a system are automated digital color image capture and tiling, automated mechanical scanning electron microscope/cathodoluminescence microscope stages, image analysis software, and neural network technology.

A key next step should be a thorough study of fracture-occluding postkinematic cements (Laubach, in preparation). Such a study provide critical guidance to successful well placement and drilling strategy in many reservoirs.

Our research also indicates that industry can gain much more information from fluid-inclusion analysis than has been accomplished. Our image analysis shows that many of the fluid inclusions in rocks that are currently discounted probably contain valuable data about the thermal

and fluid-content evolution of rocks. Such information can be used in exploration and development, and additional work could demonstrate the value of using these data.

Our research highlights many valuable opportunities for researching scaling studies and the link between scaling studies and reservoir simulation; a few examples of future work in this area are described below.

The smallest fractures observed in a population, regardless of the scale of observation, typically show evidence of truncation bias. Our preliminary work has found that the data affected by this sampling problem follow exponential distributions that contrast with the power-law distributions of larger fractures. A better understanding of the behavior of truncation bias would facilitate isolating its effects in data sets and significantly reduce the uncertainties of predicting macrofractures from microfractures.

Our work has shown that fracture lengths follow a single fractal distribution across the length scale of sedimentary layering. It is still uncertain, however, how fracture apertures behave across this threshold. Fracture-network permeabilities depend heavily on the apertures of the largest fractures, so accurate macrofracture-aperture prediction from microfracture observation requires an understanding of this problem.

The spatial distribution of fractures as a function of fracture size is still poorly known, and this is one of the critical parameters for generating virtual fracture networks for reservoir simulation. Fortunately, we now have numerous data sets that would be ideal for analyzing spatial distributions.

Preliminary compilations of data suggest that fracture length and mechanical aperture are not linearly related. Understanding this relationship may provide important constraints on fracture growth, but it is also important for pragmatic reasons such as predicting both macrofracture lengths and apertures from limited microfracture data.

Although we have not yet pursued the issue, it would be feasible to study how mechanical aperture varies along individual fractures. This would illuminate how fractures grow and interconnect.

We have made preliminary studies of how to quantify the connectivity of a fracture network. Although the idea of connectivity is intuitively obvious, it is conceptually difficult to quantify, even apart from the practical challenges it may present. Nevertheless, connectivity could be the single most significant parameter governing fluid flow through a fracture network. Developing a protocol for measuring connectivity and controlling it in models should be a high priority for future reservoir modeling studies. This is an area where progress could come from studying both the petrology governing evolving rock properties and the mechanics of growing fractures as simulated by numerical models.

Preliminary observations suggest that the degree of mineral fill in natural reservoir fractures varies according to the size of fractures. Microfractures are typically completely or almost completely mineralized even where macrofractures are mostly open. Understanding why this occurs and how to predict the scale of fractures at the transition is important because intermediate-size fractures can be required to provide a connection between large fractures, and whether or not the intermediate fractures are open may govern fluid flow through a fracture network. A related concern is whether the degree of synkinematic mineral fill also scales with the identity of the phase involved (for example, does ankerite tend to be more effective in filling fractures than quartz?).

Numerous indirect techniques for observing fractures such as production logs and surface/borehole seismic are now widely utilized. Little work has yet been done, however, to calibrate these tools to actual measurements of fracture attributes; the application of our approach would permit such calibration.

REFERENCES

- Clift, S. J., Abegg, F. E., Aslesen, K. S., Laroche, T. M., Stanley, R. G., and Laubach, S. E., 1997, Predicting fracture cementation in Permian sandstone, Pakenham (Wolfcamp) Field, Terrell County, Texas (abs.): W. D. DeMis, ed., Permian Basin Oil and Gas Fields: Turning Ideas into Production, West Texas Geological Society Publication No. 97-102.
- Burns, S. L., and Laubach, S. E., 1997, Virtual collaboratory *Frac City* facilitates geoscientific collaboration and technology transfer: GIS paper, invited.
- Laubach, S. E., 1997, New core analysis methods for fractured siliciclastic reservoirs (abs.): American Association of Petroleum Geologists Annual Convention Official Program, v. 6, A67.
- Laubach, S. E., Marrett, R., and Lake, L., 1997, Progress report on new methods of natural fracture characterization and simulation: The University of Texas at Austin, Bureau of Economic Geology, research progress report prepared for industry sponsors of Natural Fracture project and the Department of Energy, 22 p. + attachments.
- Marrett, R., and Laubach, S. E., 1997, Diagenetic controls on fracture permeability and sealing: *Int. J. Rock Mech. & Min. Sci.*, v. 34, no. 3-4.
- Marrett, R., Laubach, S. E., Rossen, W., Olson, J., Lake, L., 1998, Integration of new fracture observation, characterization, and fluid-flow modeling technology (abs.): American Association of Petroleum Geologists Annual Convention Official Program, v. 7.
- Marrett, R., 1997, Permeability, porosity, and shear wave anisotropy from scaling of open fracture populations: *in* Fractured Reservoirs: Characterization and Modeling, Rocky Mountain Association of Geologists Guidebook, p. 217-226.

Milliken, K. L., and Laubach, S. E., in press, Brittle deformation in sandstone diagenesis as revealed by scanned cathodoluminescence imaging with application to characterization of fractured reservoirs: Springer-Verlag.

Olson, J. E., Hennings, P. H., and Laubach, S. E., 1998, Integrating wellbore data and geomechanical modeling for effective characterization of naturally fractured reservoirs: EUROCK 98.

Ortega, O. J., 1997, Prediction of macrofracture properties using microfracture information, Mesaverde Group sandstones, San Juan Basin, New Mexico, The University of Texas at Austin, thesis, 278 p.

Reed, R., and Laubach, S. E., 1998, Density and distribution of microfractures in sandstone: importance to diagenesis (extended abs.): American Association of Petroleum Geologists Annual Convention Official Program, v. 7.

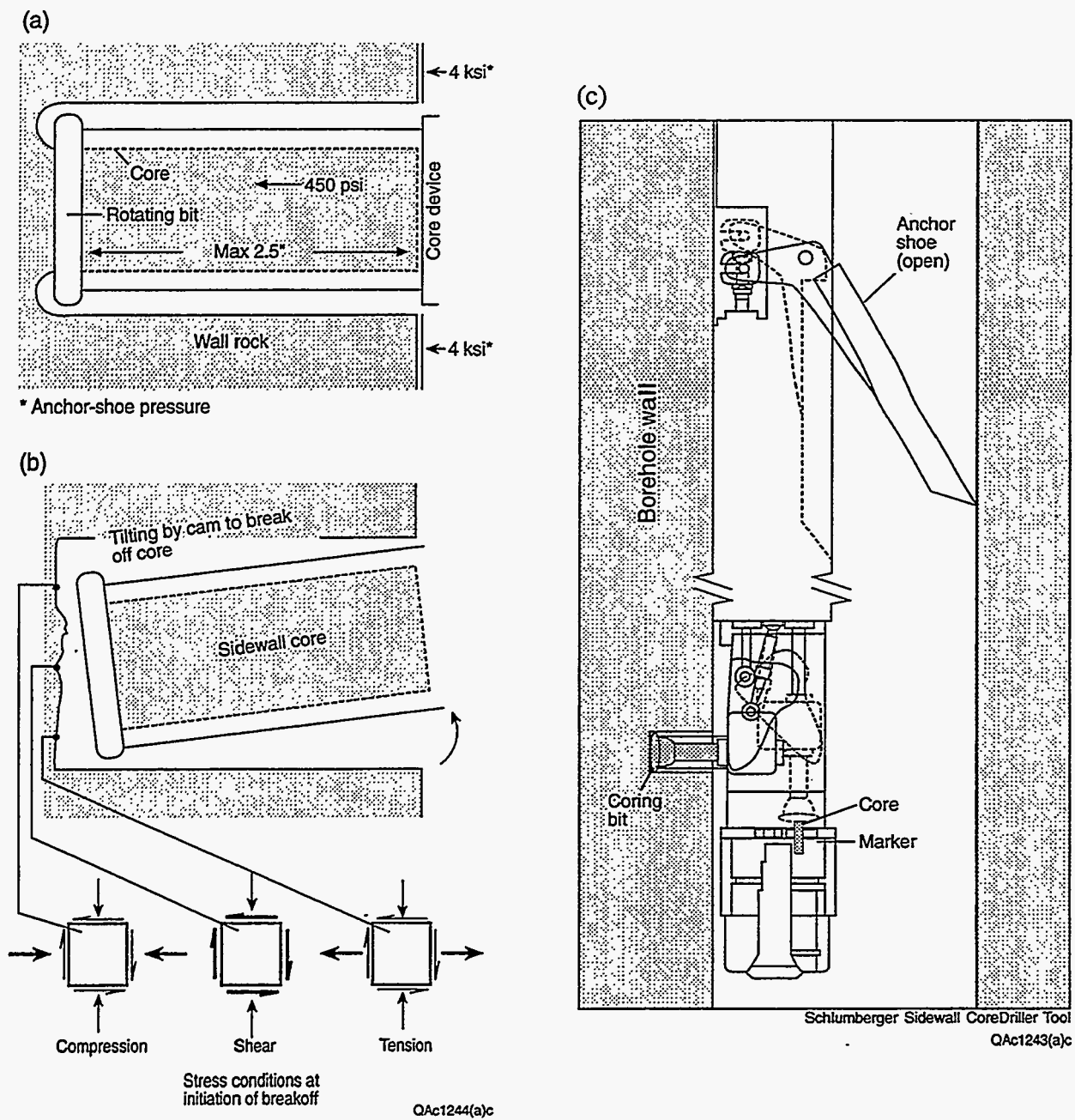
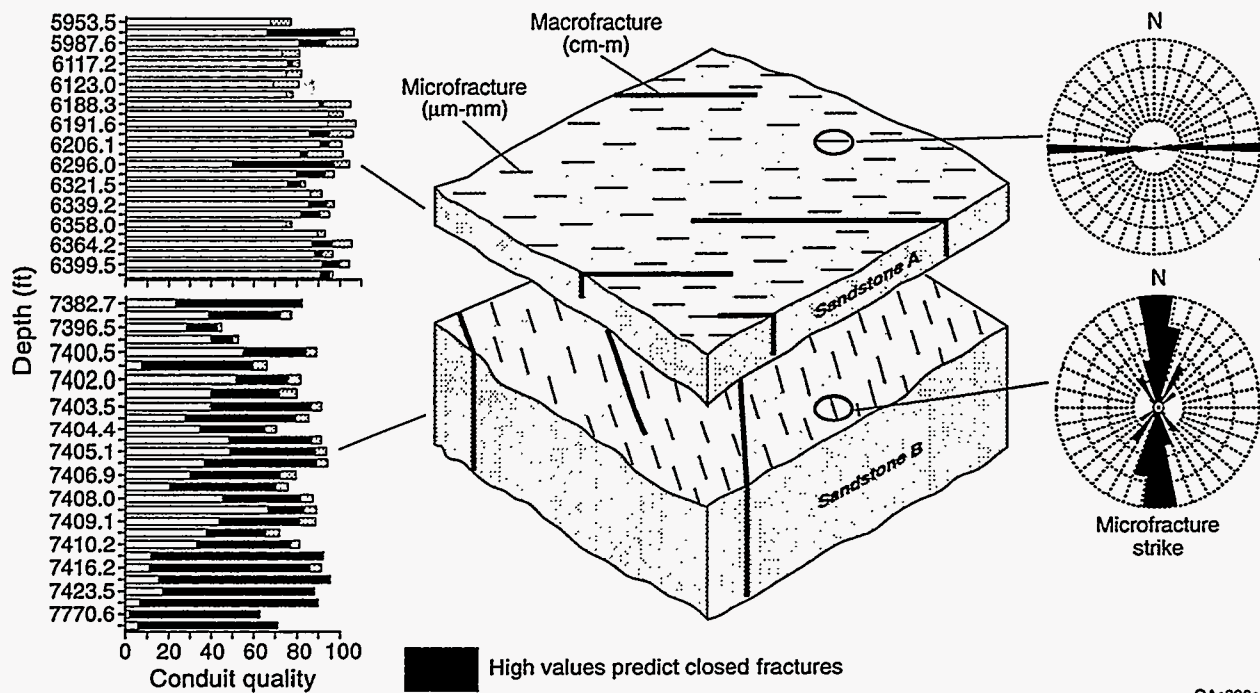


Figure 1. Collection of drilled sidewall core. (a) and (b) show local stresses during drilling and initiation of breakoff. (c) shows a schematic diagram of a typical wireline core drilling tool, showing its deployment in the wellbore, position of the drill during coring, and collection of the core and marker in the receiving cylinder.



QAc1226c

Figure 2. Scanned CL image of a quartz lined microfracture in the Davis Sandstone, Fort Worth basin. Bar scale is 100 microns. Light grey areas are grains, dark grey is quartz cement and fracture fill, and black areas are porosity. Thin section is cut parallel to bedding in sandstone, so this is a plan view. North is to top of image, so fracture strikes eastnortheast. New imaging technology helps reveal microfractures that were previously invisible. These small fractures can be used as proxies for large fractures that are difficult or impossible to sample. These fractures from gas reservoirs in Texas are invisible when using conventional observation methods. Their orientation matches those of large fractures in the well, and their size-distribution patterns provide evidence of the patterns of larger fractures.



QA920c

Figure 3. Concept diagram of fracture heterogeneity in a reservoir. Central block diagram is based on outcrops of the Frontier Formation in the Green River basin; right hand rose diagrams of microfracture strikes are from core data. Diagrams on the left show syn- and postkinematic cement values and porosity as a proportion of cement volume. High values of postkinematic cement (black) predict closed fractures.

Site-specific information about fracture attributes is critical information that is difficult or impossible to acquire. This is one of the chief stumbling blocks to effective simulation of reservoir fractures. This diagram depicts the objective of our studies: accurate site-specific information about key fracture attributes on a scale appropriate for drilling decisions and simulation. Illustrated here: fracture quality and orientation. Reservoir-analog studies show that fracture attributes can be highly variable. For characterization and simulation of reservoirs that contain such features, site-specific fracture information is required. Abrupt shifts in fracture size and variation in degree of fracture mineral fill and intensity have been observed in outcrop and in core.

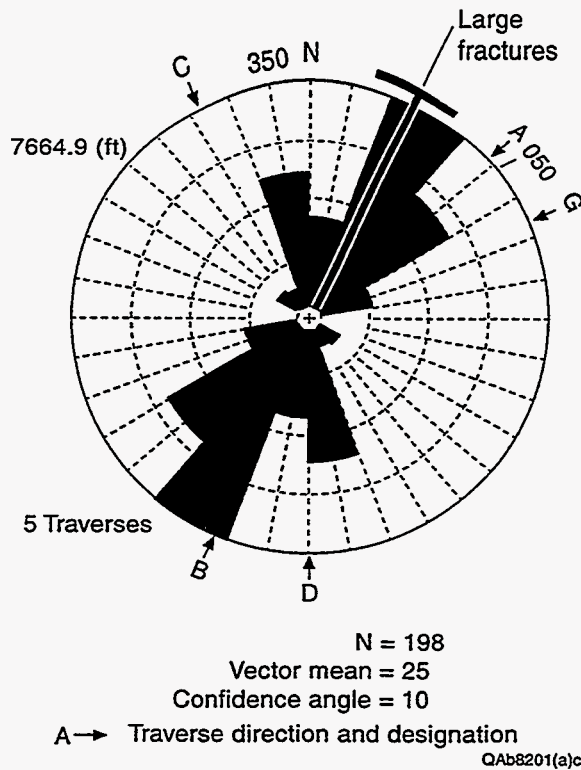


Figure 4. Rose diagram of microfracture strike in Spraberry oil reservoir samples, compared to the strike of large fractures in the same horizontal well. Microfractures accurately predict the orientation of the large fractures. This example is from the Spraberry Formation, a major oil play in West Texas. In this “blind test” samples were collected by a third party and supplied without any indication of their orientation (samples were taken from a horizontal core where macrofracture strikes had been measured). Subsequent comparison shows that the mean strike determined by our method and that of the macrofractures is identical. Rose diagram and mean and 95 percent confidence angle for macrofractures is shown in comparison to mean and 95 percent confidence for microfracture strikes.

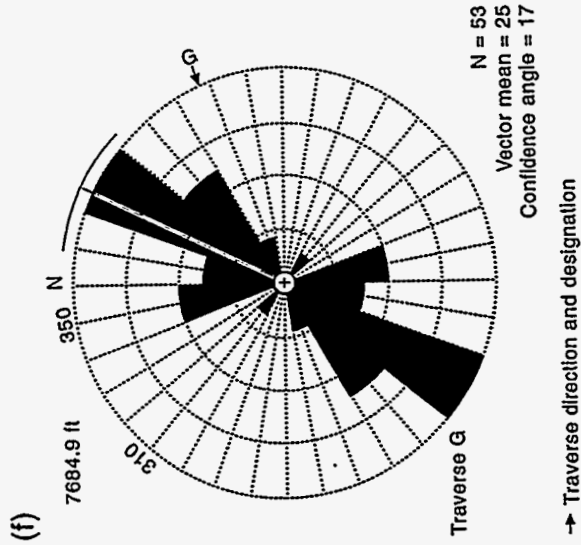
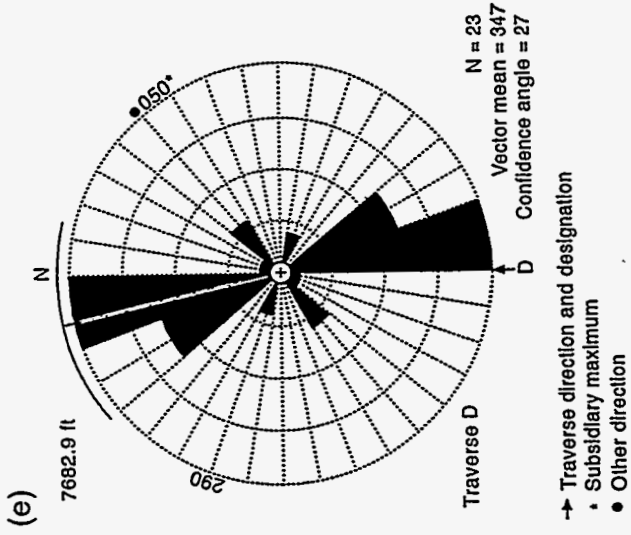
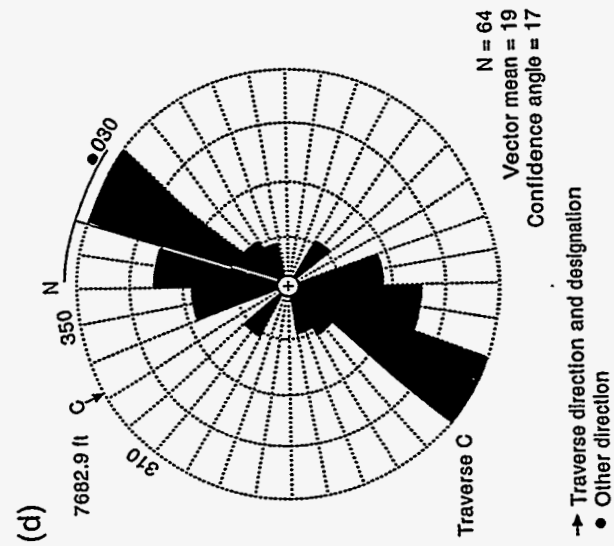
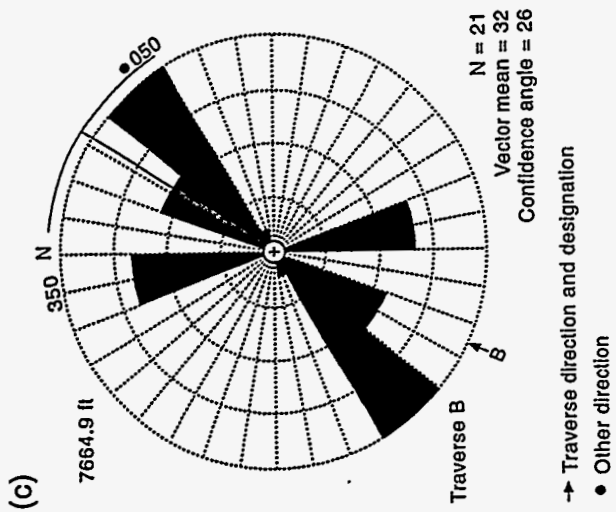
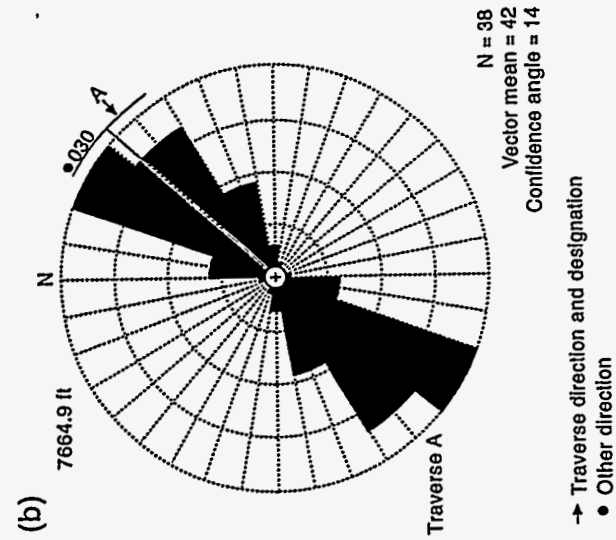
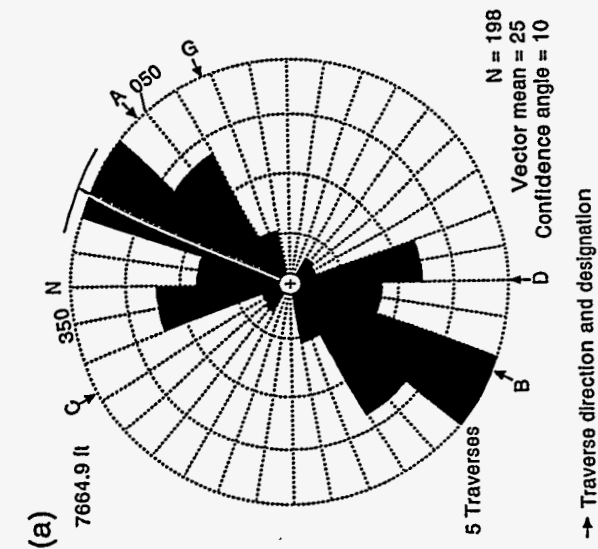


Figure 5. Rose diagrams of microfracture strike in Spraberry oil reservoir samples, subdivided by analysis area. Results show consistency of the method for smaller sample areas.

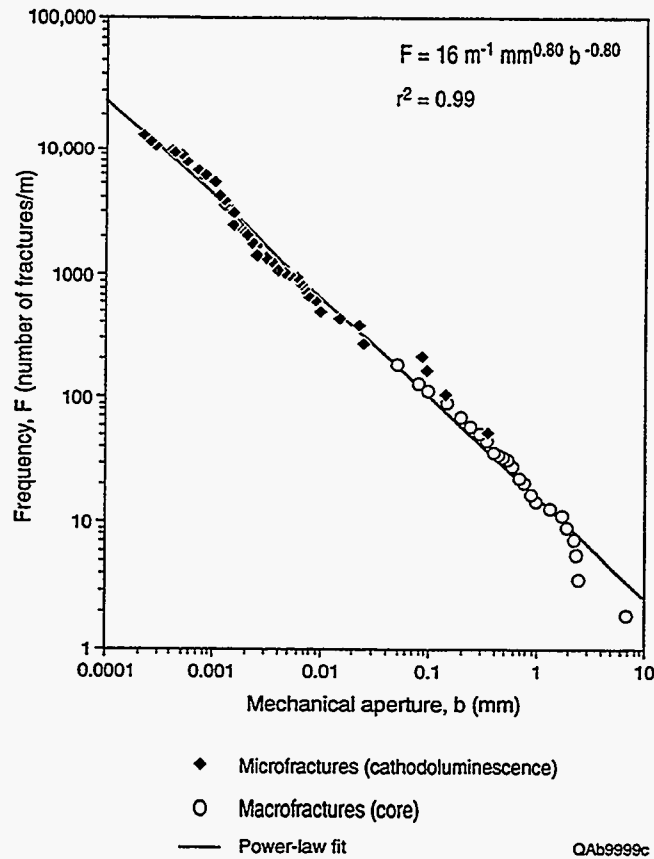


Figure 6. Large open fractures and interconnected fracture networks have the greatest effect on reservoir flow quality of fractured reservoirs. Consistent scaling patterns of fracture apertures suggest that large and small fractures are commonly merely different size fractions of the same fracture population, giving confidence that small fractures can be used to infer the properties of large. Although fraught with interpretation pitfalls, rigorous scaling analysis is a potentially powerful tool for fracture analysis and a link to fractured reservoir simulation. Our studies of open-fracture populations can be used to infer fracture permeability, porosity, and shear-wave anisotropy. In this example from Texas, because the spatial frequency of fractures having apertures smaller than 1 micron to nearly 1 centimeter follows a single relation, the microfractures provide an accurate means of predicting the abundance of large fractures. Such data can be a key input to reservoir simulators.

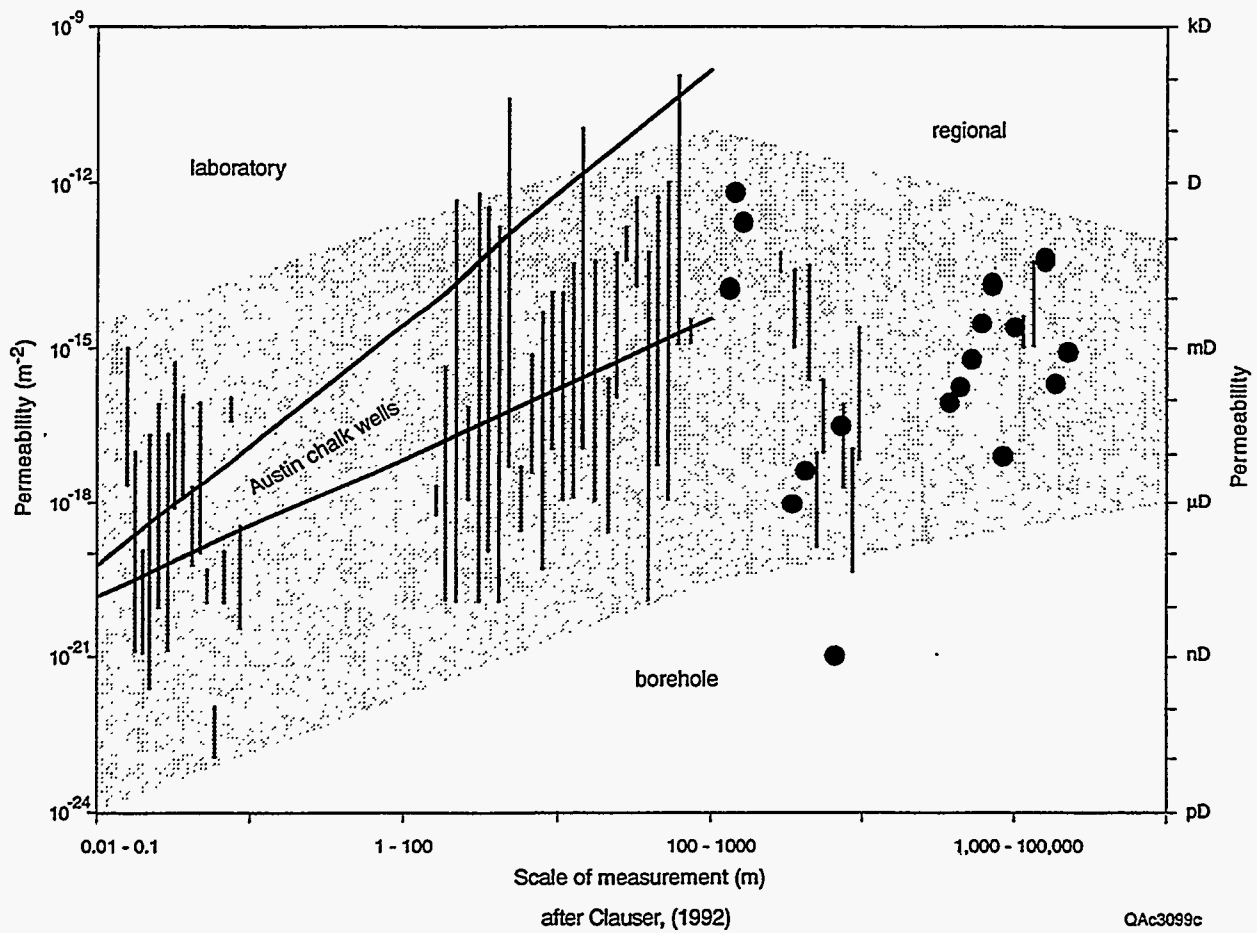
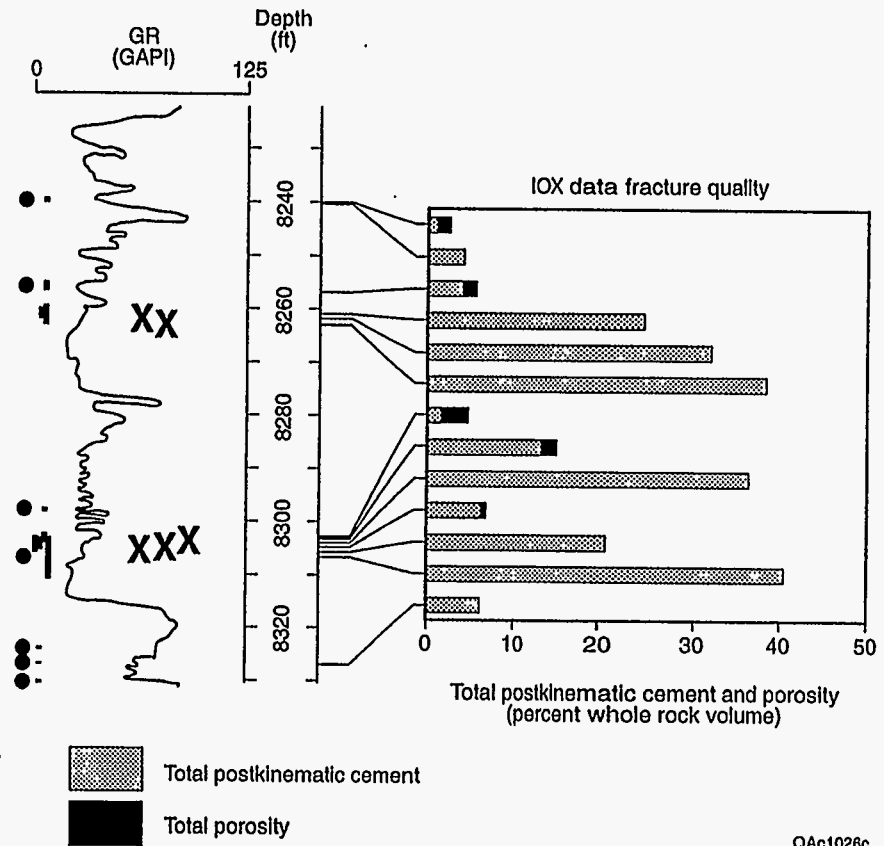
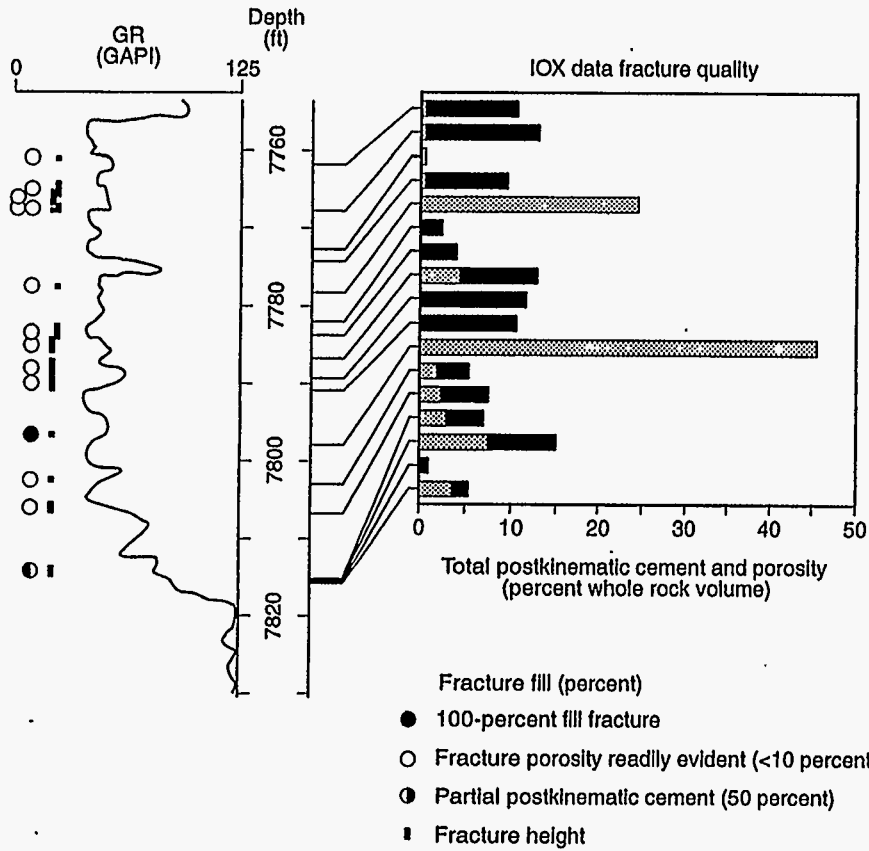


Figure 7. Measured permeability versus the scale of measurement (from Marrett, R. unpublished).

Chevron Mitchell: IP 2.5 MMcfpd

Chevron University: plugged and abandoned



QA1026c

Figure 8. How do we distinguish fractures that contribute to production from those that do not, without directly sampling the fractures? Predicting or diagnosing variations in degree of mineral infill is critical to predicting how fractures will affect reservoir performance and to targeting areas having fracture attributes favorable to exploration and development wells. In this example from West Texas, techniques created in this study identified open fractures as the prime control on high production. Productive and nonproductive areas were successfully identified on a bed-by-bed basis. The technique does not require visible fractures to be present in the sample, and samples the size of conventional cuttings can be used.

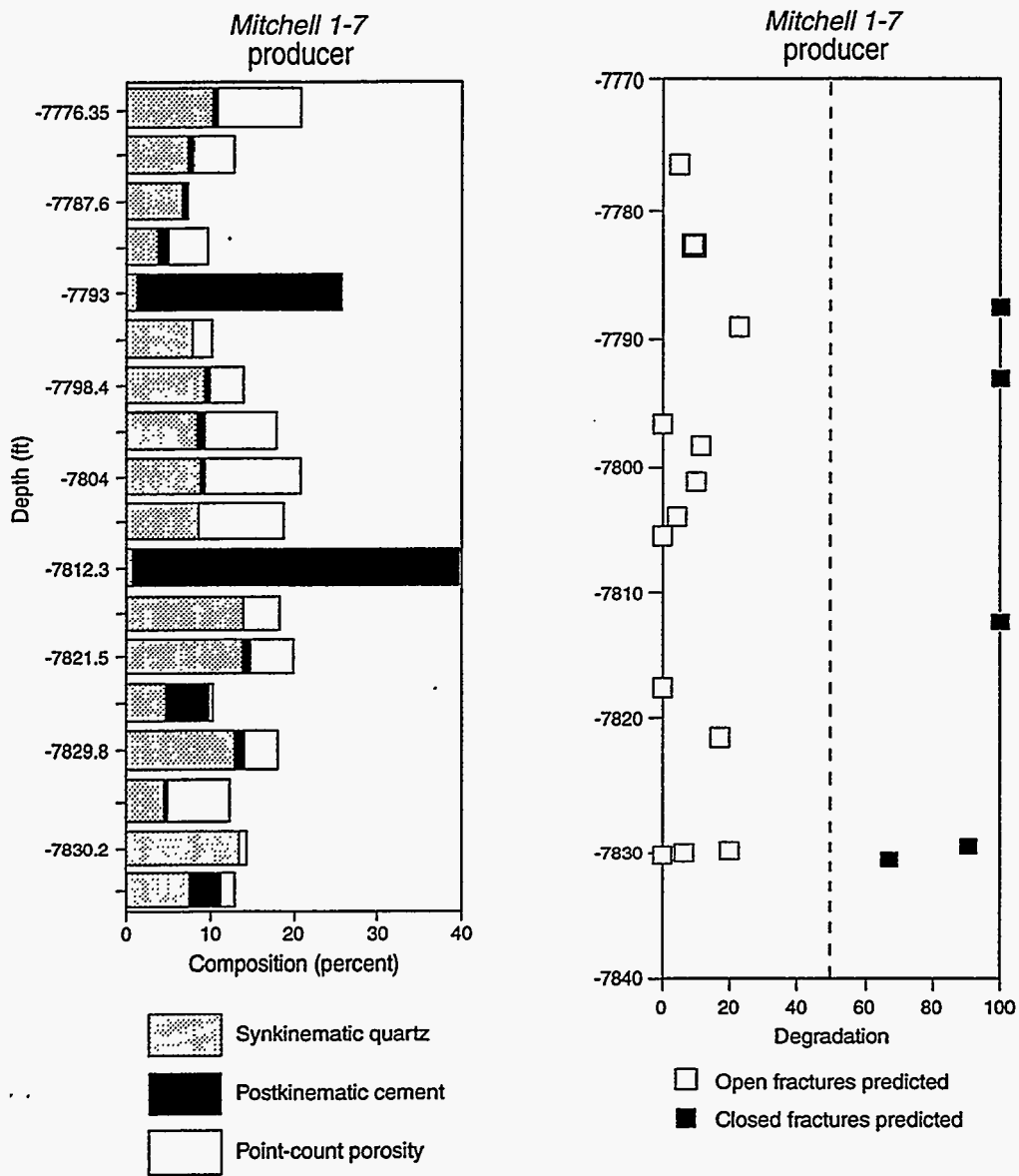


Figure 9. Postkinematic cement values shown as percent of rock and as 'degradation index.' Degradation index is the ratio of postkinematic cement to post fracture opening porosity, as determined by microstructural criteria. Areas having high values of postkinematic cement (in either representation) will tend to have closed fractures.

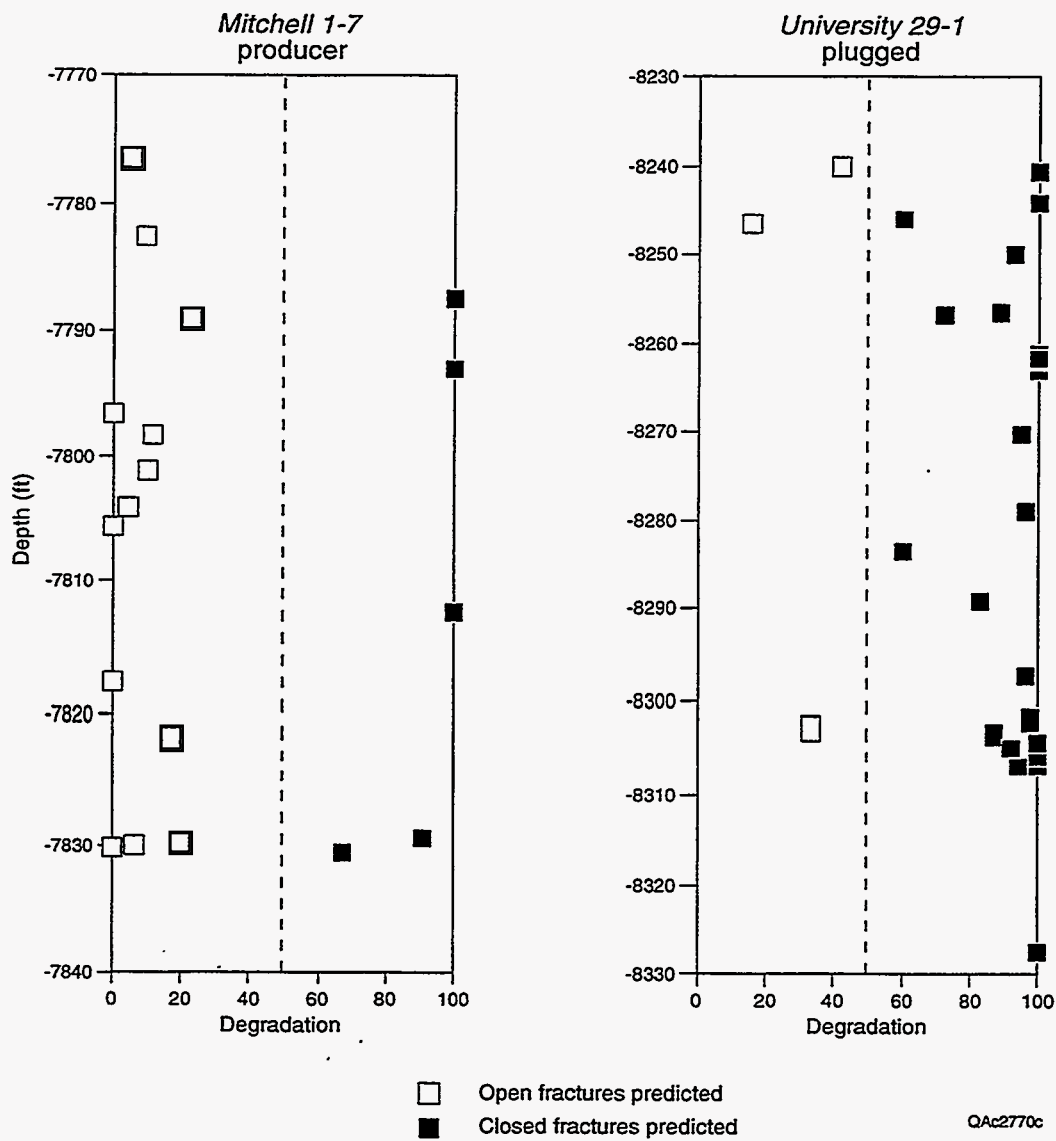


Figure 10. Wolfcamp sandstone well pair compared using degradation index.

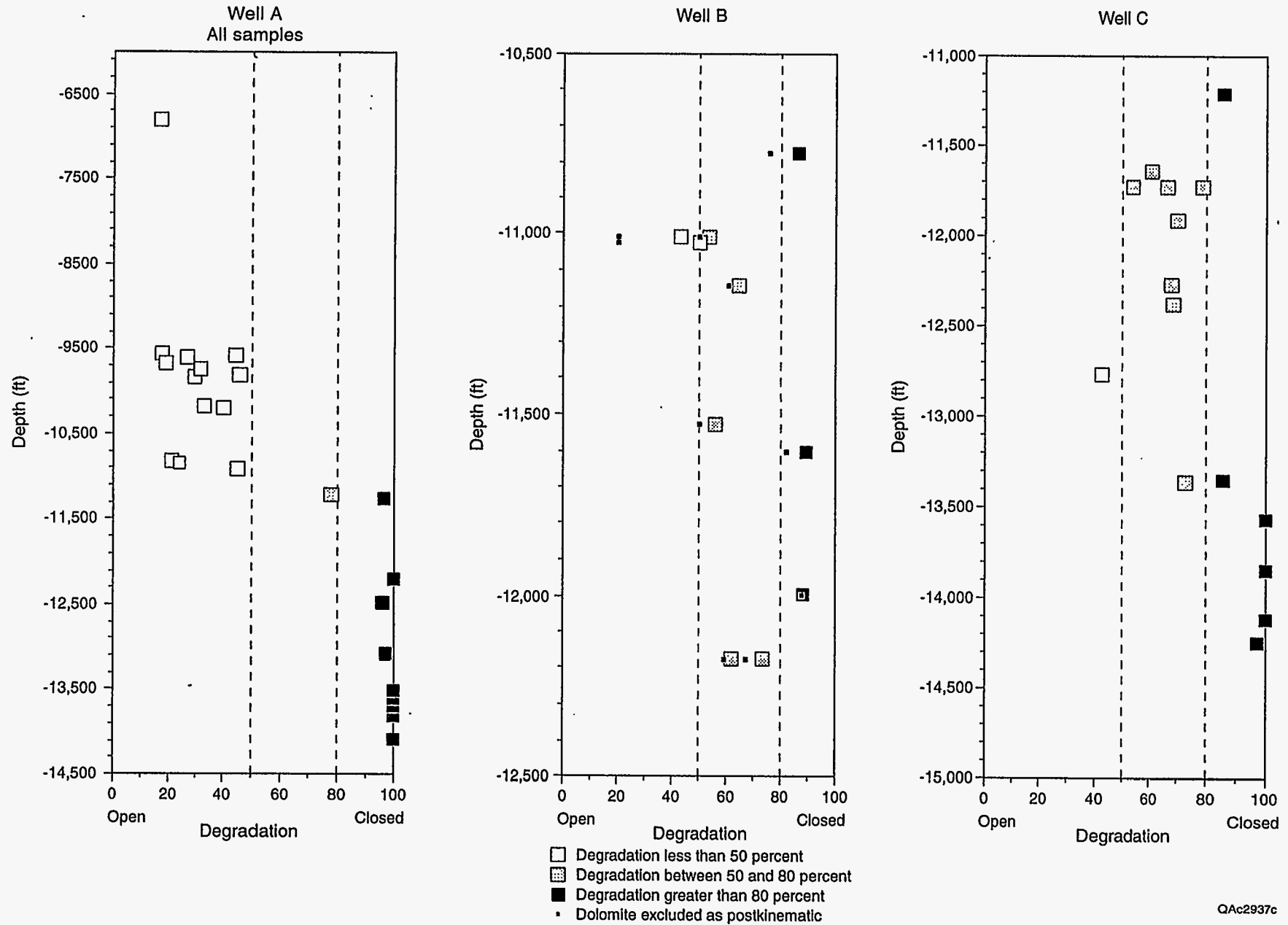


Figure 12. Degradation index for three Wyoming wells, showing heterogeneity in fracture quality.

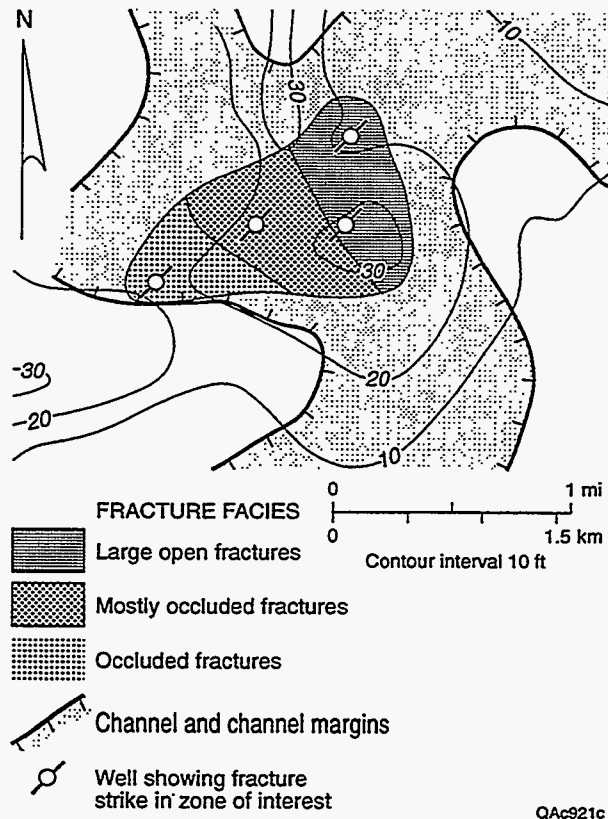


Figure 14. Map of fracture attributes derived from microanalysis, Waskom field, East Texas basin. Fracture quality, size, and orientation are shown.

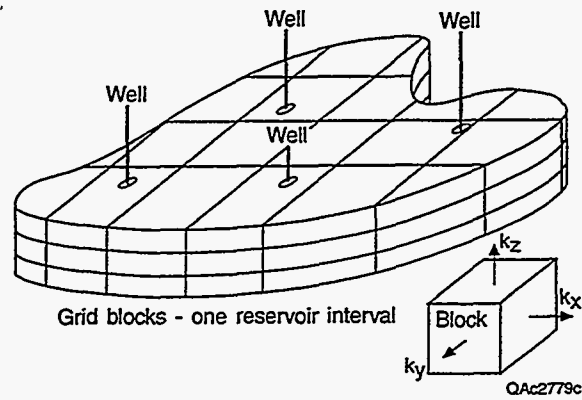


Figure 15. How geology enters a reservoir simulator. A focus of the project was gaining the capability to acquire data that can easily be used in existing and advanced reservoir simulators. We can obtain fracture information in all wells that penetrate a horizon of interest, and have gained insights into how to extrapolate between data points. Future research should address the latter issue more fully.

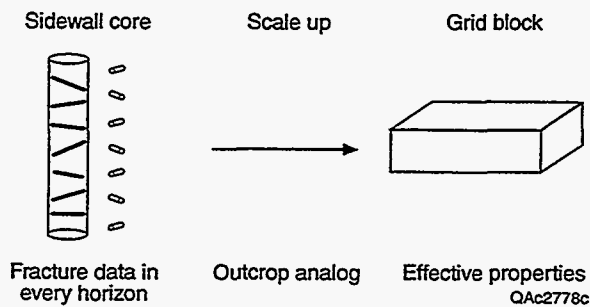


Figure 16. Illustration of the link between observations and effective grid block properties. To accomplish scale up, we used scaling criteria (Part II), from cores and outcrop analogs. We also investigated use of geomechanical modeling for this application (Part III). More research on this aspect of the problem is warranted.

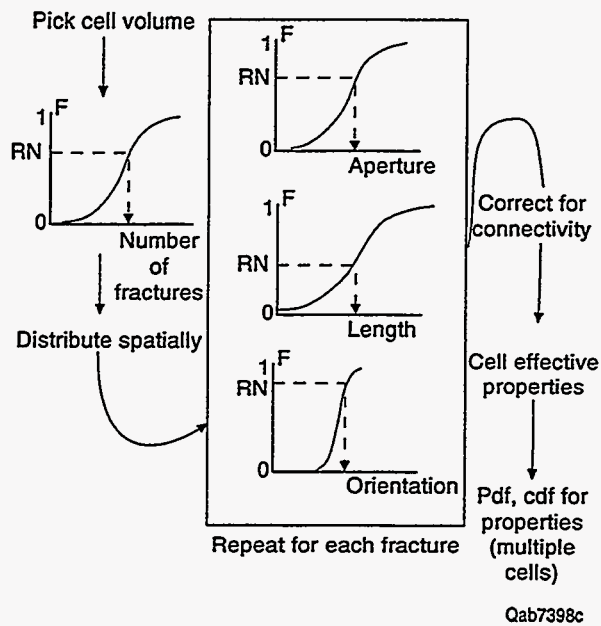


Figure 17. Diagram illustrating conversion of measured fracture attributes to probability density functions that can be used in reservoir simulators. We have made progress in the use of microfracture scaling patterns to determine orientation, porosity and permeability inputs.

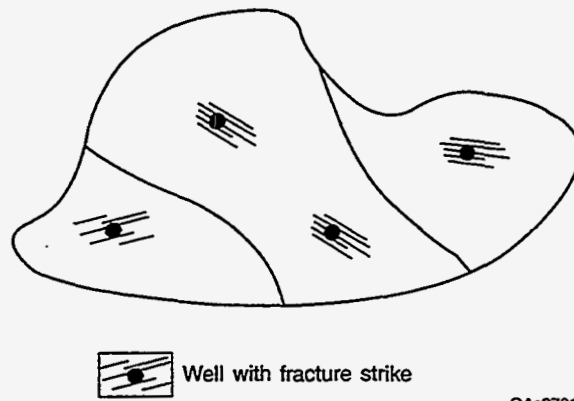
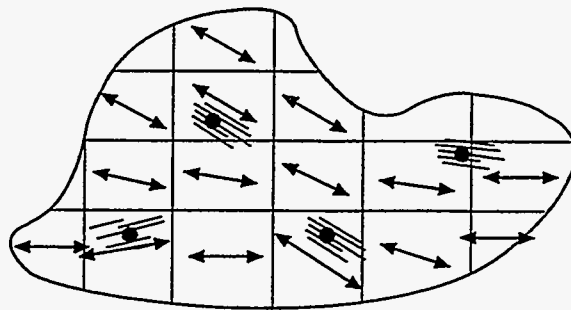


Figure 18. Map of reservoir shown in figure 15, with fracture strikes determined at each well locations (Laubach, 1997) and structural domains (strike domains) delineated.



←→ Directions of maximum permeability

QAc2782c

Figure 19. Map of reservoir shown in figures 15 and 18, which permeability anisotropy delineated and grid blocks assigned.

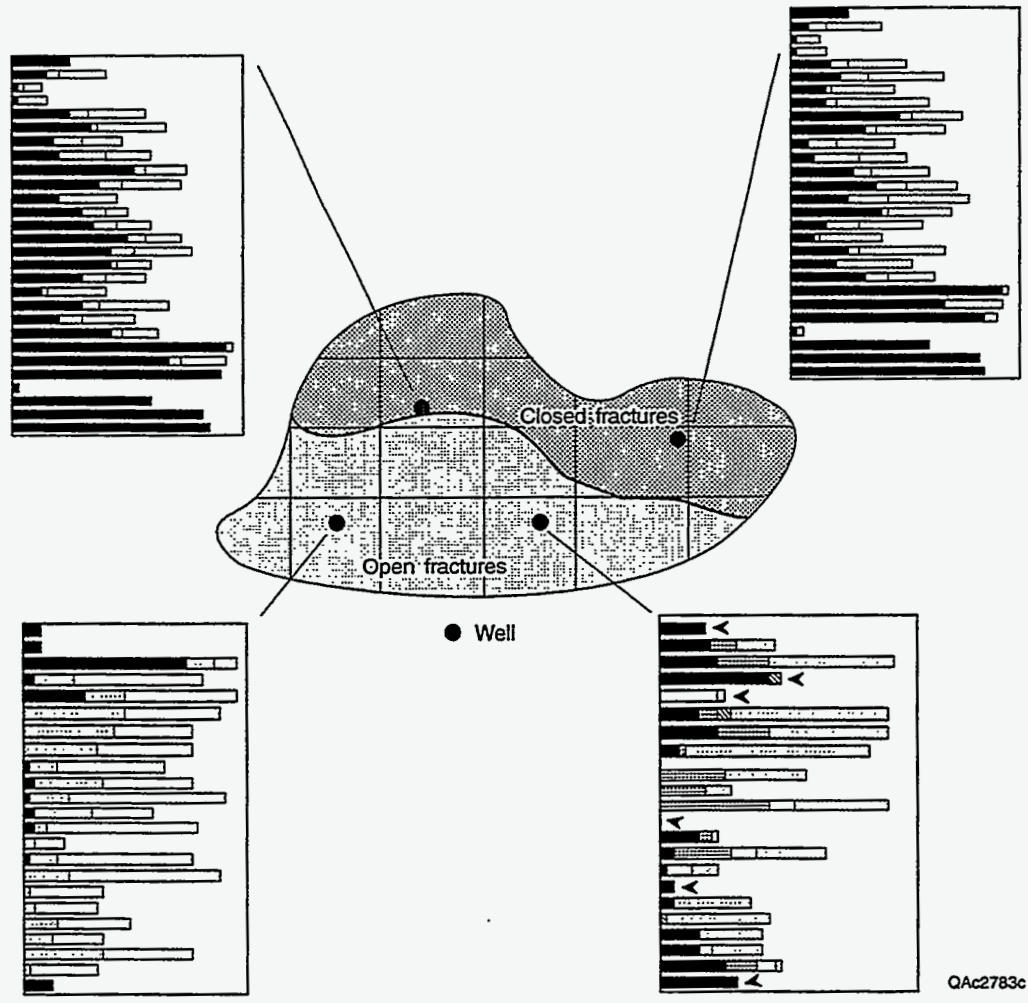


Figure 20. Fracture quality data from each well in reservoir shown in figure 15. For each well, a representative depth profile of postkinematic cement (black) and primary and secondary porosity (grey and no pattern) are shown. Wells with little postkinematic cement are interpreted to have open fractures. The depth profiles are from Texas reservoirs.

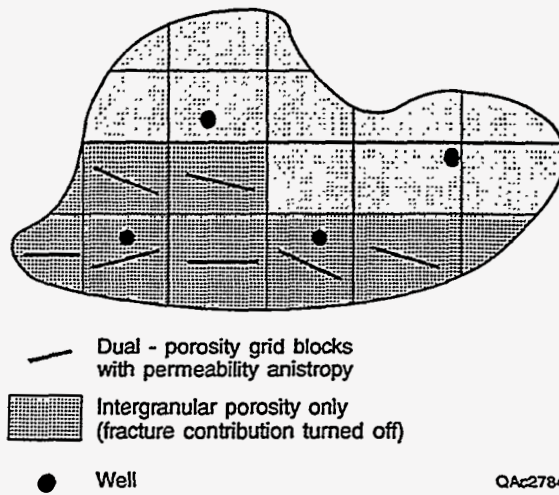
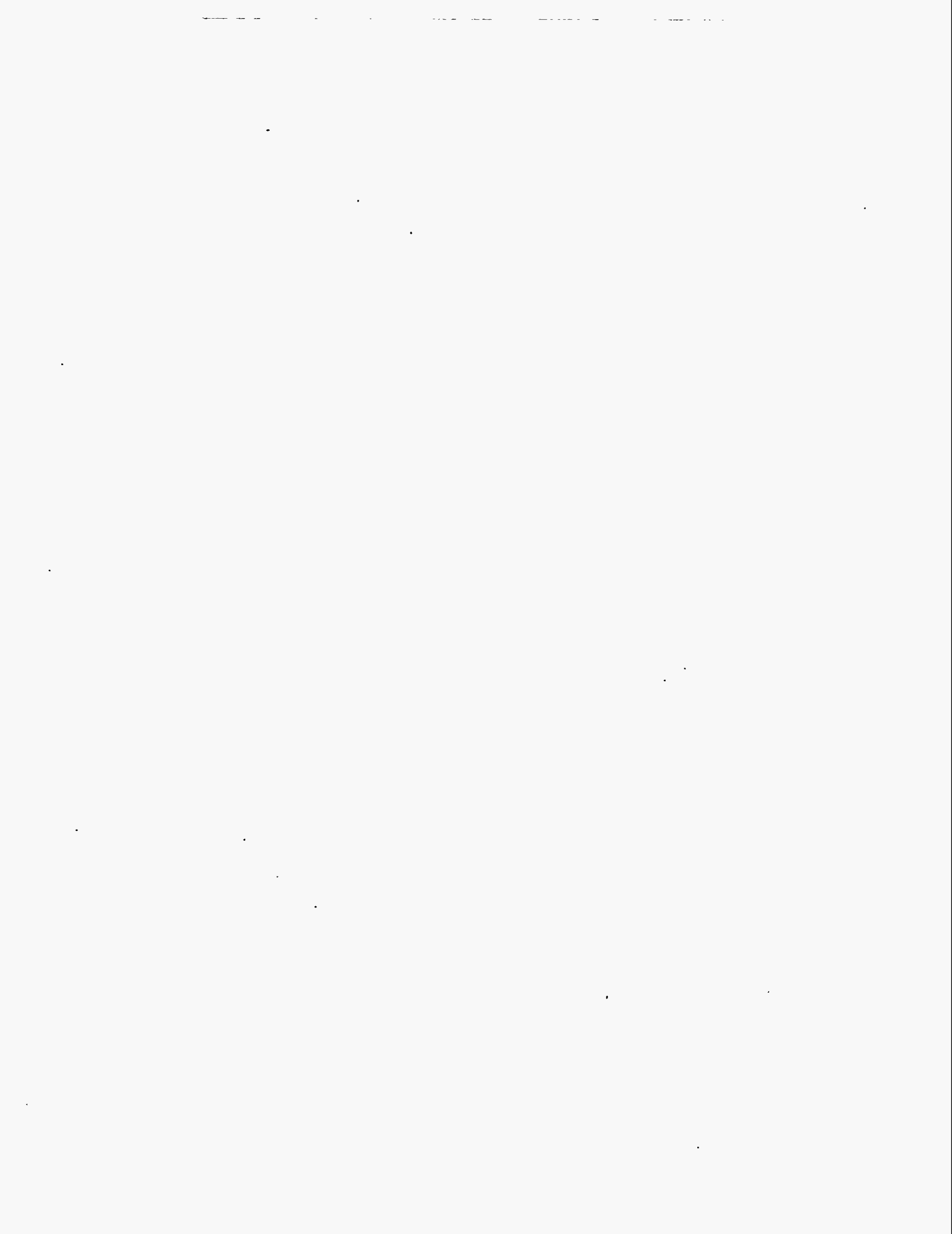


Figure 21. Example of simulator conditioned by observations in every well. Where fractures are indicated to be closed (light grey), fractures are 'turned off.' Where fractures are 'on', fracture anisotropy (or isotropy) is indicated by microfracture orientation patterns. A key step not shown here is collection and incorporation of fracture size and connectivity information in simulators. These critical issues are discussed in depth in parts II and III of this report.



APPENDIX A: PERMEABILITY, POROSITY, AND SHEAR-WAVE ANISOTROPY FROM SCALING OF OPEN FRACTURE POPULATIONS

Summary

Open fractures have a profound impact on fluid flow and shear-wave propagation in rock. Previous models have specified the permeability, porosity, and shear-wave anisotropy caused by a fracture system in terms of average geometric attributes of extension fractures. However, new and published data indicate that the apertures and lengths of extension fractures follow power-law scaling, which implies that average geometric attributes are not meaningful. The fluid flow and seismic models are recast in forms consistent with the scaling of extension fractures so that fracture-associated permeability, porosity, and shear-wave anisotropy are related to the scaling variables of extension fracture populations. Combination of the results offers the possibility of remote quantification of fracture permeability and porosity via shear-wave seismic methods.

Some of the salient characteristics of fluid flow through fractured rock may be understood as consequences of the scaling of extension fractures. The significant spatial heterogeneity of fluid flow in a sample of fractured rock results from virtually all fracture permeability in a given sample being derived from only the few largest-aperture fractures. Anomalous pressure-transient curves are consequences of most matrix-fracture cross flow and fluid storage occurring in fractures that contribute minimal permeability. Finally, the observed scale-dependence of fracture permeability results from the tendency to encounter larger-aperture fractures in longer samples.

Technical Challenge

Fluid flow in the upper crust is dramatically affected by the presence of fractures. Fractures commonly differ from host rock in terms of permeability, and consequently introduce heterogeneity and anisotropy to flow. Shear fractures (i.e., faults) in many cases produce barriers to fluid flow by locally decreasing permeability. Extension fractures (i.e., joints, veins, microcracks) that are open in the subsurface produce fluid conduits that locally enhance permeability. Fracture-enhanced permeability is important in a wide array of problems, including hydrocarbon reservoirs (Nelson, 1985), aquifers (Sharp, 1993), waste repositories (Barton and Hsieh, 1989), and hydrothermal mineralization (Sanderson et al., 1994). Despite the importance of fracture-enhanced fluid flow, major problems remain in terms of the characterization of fracture systems, the relations between fracture system and fluid flow, and effective means for evaluation without direct observations of fluid flow.

The permeability, porosity, and shear-wave anisotropy induced by open fracture systems may be addressed by referring to the geometrical attributes of the fractures. For convenience assume that fractures are vertical, and refer to the horizontal fracture-parallel dimension as the length and the vertical fracture-parallel dimension as the height. The aperture of an extension fracture at a specific location is the fracture-perpendicular distance between the fracture walls. The aperture of an open fracture may be related to permeability using the 'cubic law' for flow between parallel plates (Lamb, 1932; Snow, 1969). Open fracture length may be related to the velocity anisotropy of elastic shear-waves propagating vertically through fractured rock (Thomsen, 1995).

A basic problem for theories of fluid flow and seismic propagation in fractured rock has been that fracture systems comprise many individual fractures collectively ranging over many orders of magnitude in aperture and length. Previous fluid flow and seismic propagation models for fractured rock have been defined in terms of the average apertures, spacings, and lengths of extension fractures. However, meaningful averages cannot be defined for phenomena that follow

power laws, and recent analyses show that the apertures and lengths of extension fractures in many systems define populations that follow power-law scaling (Gudmundsson, 1987a; Barton and Hsieh, 1989; Wong et al., 1989; Heffer and Bevan, 1990; Barton and Zoback, 1992; Hatton et al., 1993; McCaffrey et al., 1993; McCaffrey et al., 1994; Sanderson et al., 1994; Belfield and Sovich, 1995; Clark et al., 1995; Gross and Engelder, 1995; this paper). The objective of this paper is to incorporate explicitly the scaling of extension fracture populations into simple theories of fluid flow and seismic propagation in fractured rock, to relate the fluid and seismic properties, and to elucidate some of the typical fluid flow characteristics of fractured rock.

Fracture Scaling Relations

The apertures and lengths of extension fractures defining a fracture system commonly range over many orders of magnitude. However, a variety of sampling biases affect collection of fracture aperture and length data (e.g., Baecher and Lanney, 1978; Barton and Zoback, 1992). Censoring bias results from inadequate characterization of the largest fractures in a population, for example when fractures are longer than the exposed sampling surface or when apertures are large enough to produce disruption in a borehole. Truncation bias results from inadequate characterization of the smallest fractures in a population, for example when the threshold for detection of small fractures is inconsistent over the study domain due to variable exposure in outcrop. Size bias results if the topologic dimension of a sampling domain is lower than the topologic dimension occupied by a fracture population, for example when fractures in a volume are sampled along a scanline or over an exposed surface. The effects of truncation bias may explain why early studies of extension fracture aperture and length populations (e.g., Snow, 1970; Baecher et al., 1977) concluded that data follow negative exponential or log-normal size distributions.

Several recent analyses have suggested that extension fracture aperture and length populations follow power-law scaling (Gudmundsson, 1987a; Barton and Hsieh, 1989; Wong et

al., 1989; Heffer and Bevan, 1990; Barton and Zoback, 1992; Hatton et al., 1993; McCaffrey et al., 1993; McCaffrey et al., 1994; Sanderson et al., 1994; Belfield and Sovich, 1995; Clark et al., 1995; Gross and Engelder, 1995), analogous to fault displacement and length populations (e.g., Shaw and Gartner, 1986; Gudmundsson, 1987b; Childs et al., 1990; Scholz and Cowie, 1990; Marrett and Allmendinger, 1992). In a specific region of size S (length of sample line, area of sample surface, or volume of sample solid) the cumulative number (N) of extension fractures having aperture $\geq b_N$ or length $\geq l_N$ may be expressed as $N = S a b_N^{-c}$ or $N = S d l_N^{-e}$, and the cumulative frequency (f) may be expressed as $f = a b_N^{-c}$ or $f = d l_N^{-e}$, where a and d are measures of fracture intensity and c and e are constants for a specific population. If aperture and length scale linearly with each other according to $l = g b$, as expected from linear elastic fracture mechanics (e.g., Pollard and Aydin, 1988), then $c = e$ and $a = d g^{-e}$. Some observations are consistent with a linear relation between aperture and length (Vermilye and Scholz, 1995), however other results (Johnston, 1992; Hatton et al., 1994) indicate a nonlinear relation of the form $l = g b^z$, in which case $c = e z$ and $a = d g^{-e}$. Because fracture data typically are collected along one-dimensional (scanline, borehole) or two-dimensional (map, cross section) samples taken at high angle to fractures in three-dimensional volumes, a size bias is introduced. To convert exponents from 1D to 2D or from 2D to 3D, the number one must be added to measured values of e and $1/z$ must be added to measured values of c (Marrett and Allmendinger, 1991; Marrett, 1996). This follows from recognizing that the probability of sampling a randomly located fracture on a map (or scanline) taken at an arbitrary position through a volume depends linearly on the height (or area) of the fracture, which is assumed to be proportional to the fracture length (or length squared).

Values of c determined from 1D samples of extension fracture apertures commonly range from 0.75 to 0.85 (Fig. A.1). Most of the fractures represented by these data are partially or completely mineralized. While this drastically reduces the fluid flow and seismic propagation effects of the fractures in their current states, the mineralization preserves the apertures that existed in the subsurface if the fractures did not develop via a progressive crack-seal process.

Values of e determined from 2D samples of extension fracture lengths commonly range from 1.6 to 1.9 (Fig. A.2). The smallest members in some of the fracture aperture and length populations deviate from the power laws fit to the data sets, probably reflecting the effects of truncation. Censoring effects on the largest members of the populations generally appear negligible, however combining data from serial scanlines (i.e., Fig. A.1: Monterey Fm., Rutland quartzite, Westerly granite) has produced steep trends for the largest members in some of the populations (e.g., Childs et al., 1990). It is interesting that, despite the distinct rock types represented by the data, only limited variation of c and e are required to model data from fracture apertures collectively spanning seven orders of magnitude, and from fracture lengths spanning five orders of magnitude. This might indicate that the exponents are largely insensitive to the mechanical properties of rock and the physical conditions during fracture. Converting the exponents determined from 2D sampling of fracture lengths to 1D exponents (i.e., subtracting the number one) yields values of e between 0.6 and 0.9. This range of values overlaps with the observed range of c , consistent with $z = 1$ and linear proportionality between fracture aperture and length.

Parallel-Plate Model of Fracture Permeability and Porosity

The simplest model relating the geometrical attributes of fractures to their fluid flow characteristics is the parallel-plate model (e.g., Lamb, 1932; Snow, 1969). The parallel-plate model assumes single-phase laminar flow through a set of aligned fractures having smooth walls, constant apertures, and heights equal to the thickness of the fractured layer under consideration. The parallel-plate model is fundamentally one-dimensional because the fractures are assumed to be infinitely long, a seemingly unrealistic simplification of natural fractures in rock. However, even essentially parallel fractures have a tendency to be linked with other fractures along strike (e.g., Laubach, 1992), a tendency that is strongest for the longest fractures in a population. Due to linkages with adjacent fractures, the longest fractures can provide fluid flow conduits that are

effectively infinite in length although more tortuous than depicted by the parallel-plate model. To a significant degree, the connectivity of a fracture system will be increased by the presence of multiple fracture sets, which are ignored in the present analysis. Consequently, the parallel-plate model may be useful for describing the first-order characteristics of fluid flow through fractured rock.

Previous treatments of the parallel-plate model additionally assume that a set of fractures may be represented adequately by an average fracture aperture and an average fracture spacing (e.g., Nelson, 1985). The power-law scaling of fracture apertures suggests that the use of average fracture attributes is not meaningful. The one-dimensional parallel-plate model is generalized here (Derivation A.I) by application to each fracture of a fracture set that is sampled one-dimensionally along a scanline of length L , taken perpendicular to the fractures. In this case, the apertures of the individual fractures may be honored and there is no need to specify fracture spacings (Fig. A.3). The fracture set has porosity (ϕ_{total}) and permeability (k_{total}) of:

$$\phi_{\text{total}} = \zeta \left(\frac{1}{c} \right) \frac{b_1}{L} = \zeta \left(\frac{1}{c} \right) \phi_1 \quad (\text{A.1})$$

$$k_{\text{total}} = \zeta \left(\frac{3}{c} \right) \frac{b_1^3}{12 L} = \zeta \left(\frac{3}{c} \right) k_1, \quad (\text{A.2})$$

and by equating the fracture-aperture terms of equations A.1 and A.2:

$$k_{\text{total}} = \frac{\zeta \left(\frac{3}{c} \right)}{\zeta^3 \left(\frac{1}{c} \right)} \frac{L^2}{12} \phi_{\text{total}}^3, \quad (\text{A.3})$$

where the subscript 1 refers to the largest-aperture fracture and ζ is the Riemann zeta function (see Derivation A.I for definition). The Riemann zeta function converges for arguments > 1

(Apostal, 1957), and a good approximation (accurate to 3 significant figures) is given by summing the first three terms of the Riemann series and taking the first two terms of the Euler-Maclauren summation formula (Dahlquist and Björck, 1974) to express the remainder, yielding $\zeta(x) \cong 1 + 2^{-x} + 3^{-x} + \frac{x+7}{2(x-1)} 4^{-x}$ (Marrett, 1996). Consequently, the total fracture permeability converges for $c < 3$ but the total fracture porosity converges only for $c < 1$, where c is determined from 1D sampling. Thus, if the total fracture porosity converges, then the total fracture permeability will converge very rapidly ($k_{\text{total}} \leq 1.20 k_1$). Because natural fracture-aperture populations typically show scatter about a power law, the most accurate estimates of fracture porosity and permeability may be made by using actual fracture data for the range of data unaffected by sampling truncation and by using analytical expressions (e.g., Riemann zeta function or integration; Marrett and Allmendinger, 1992; Marrett, 1996) for extrapolation over the range of truncated data. Note that a 1D-sampling power-law distribution of fracture apertures requires $a = \frac{b_1^c}{L}$, so $b_1 = (aL)^{1/c}$ may be substituted into equations A.1 and A.2 to give:

$$\phi_{\text{total}} = \zeta\left(\frac{1}{c}\right) \frac{b_1}{L} = \zeta\left(\frac{1}{c}\right) a^{1/c} L^{(1-c)/c} \quad (\text{A.4})$$

$$k_{\text{total}} = \zeta\left(\frac{3}{c}\right) \frac{b_1^3}{12L} = \frac{1}{12} \zeta\left(\frac{3}{c}\right) a^{3/c} L^{(3-c)/c} \quad (\text{A.5})$$

Several important characteristics of fracture-enhanced fluid flow may be inferred from these relations. Taking $c = 0.8$ as a representative value for fracture aperture populations, we see from equations A.1 and A.2 that $\phi_{\text{total}} \cong 4.59 \phi_1$ and $k_{\text{total}} \cong 1.10 k_1$. This implies that the single largest-aperture fracture in a sample accounts for most of the total fracture permeability (91%), but the other fractures account for most of the total fracture porosity (78%). In addition, fracture surface area, where cross flow from matrix porosity into fracture porosity must occur, is strongly partitioned into the smallest fractures (Marrett, 1996). A corollary to these statements is the

inference (Nelson, 1987) that the largest fractures control short-term flow rates and smaller fractures control long-term flow rates during reservoir depletion, producing pressure-transient curves that are anomalous by comparison with those from homogeneous rocks in which fluids flow through intergranular pores (Aguilera, 1980). The result that the single largest-aperture fracture in a sample dominates fracture permeability explains the large spatial heterogeneity typical of fracture-enhanced fluid flow (e.g., Nelson, 1985), because the aperture of the largest fracture in a specific sample depends greatly on the location in which the sample is taken.

Again taking $c = 0.8$, we see from equations A.4 and A.5 that $\phi_{\text{total}} \sim L^{0.25}$ and $k_{\text{total}} \sim L^{2.75}$. This implies that fracture porosity and permeability in a specific region depend on the size of the sampling domain considered, at least over the range of sample scales that contain a fracture aperture population following a single power law (i.e., constant a and c). The sample-length dependence of fracture porosity and permeability results from the tendency to encounter larger-aperture fractures in longer samples. In particular, the aperture of the largest fracture (and therefore fracture porosity) and the aperture cubed of the largest fracture (and therefore fracture permeability) increases faster than the length of a scanline as progressively longer scanlines are addressed. The dependence of fracture porosity on sample length is relatively weak, however fracture permeability should increase rapidly with increases in sample length. The predicted dependence of fracture permeability on sample length is consistent with observations in fractured crystalline rocks up to sample lengths on the order of 100 m (Clauser, 1992; Neuman, 1994), which might represent the maximum sample scale at which fracture aperture populations follow a single power law in the crystalline rocks that were studied.

Penny-Shaped Crack Model of Shear-Wave Anisotropy and Porosity

Although fracture apertures hold fundamental importance to fluid flow in fractured rock, it is commonly impractical to quantify apertures directly. Analysis of many problems would benefit from remote detection and characterization of extension fracture systems. Previous

seismic studies (e.g., Mueller, 1991) have shown that both fracture orientations and spatial distributions may be remotely quantified because a set of open, aligned fractures produces velocity anisotropy of elastic shear-waves propagating in a direction at a low angle to the fractures. The magnitude of the velocity anisotropy can be quantified in terms of fracture geometry and size using a penny-shaped crack model.

The penny-shaped crack model (e.g., Thomsen, 1995) assumes that fractures are fluid-filled ellipsoids embedded in rock, and is fundamentally a three-dimensional model. The ellipsoids are assumed to have two equal long dimensions (fracture length and height) and a much smaller short dimension (fracture aperture), and the short dimensions of the ellipsoids are assumed to be aligned. Consequently the fractures are treated as isolated features, which is a poor generalization of natural fractures in rock. However, to the extent that connected fractures behave as fractures having lengths exceeding their heights, connectivity will have negligible effects on observed shear-wave anisotropy (Skjærstein et al., 1995). Provided that fracture heights are small by comparison with the wavelength of vertically propagating seismic energy, the penny-shaped crack model should provide reasonable first-order estimates of the shear-wave anisotropy produced by fractures even if they are linked along strike.

A volume of rock containing aligned vertical fractures will polarize vertically propagating shear waves into components having particle motion parallel to (velocity = v_{fast}) and transverse to (velocity = v_{slow}) the fractures (Thomsen, 1995). The velocities are related by the shear-wave anisotropy (γ) such that $v_{fast} = (1 + \gamma) v_{slow}$, and γ may be expressed in terms of the lengths of fractures distributed in a sample volume (Thomsen, 1995). Based on the power-law scaling of fracture lengths in a volume, we find (Derivation A.II):

$$\gamma = \zeta \left(\frac{3}{e+1} \right) \frac{1-\nu}{3(2-\nu)} \frac{l_1^3}{V} = \zeta \left(\frac{3}{e+1} \right) \gamma_1, \quad (\text{A.6})$$

where ν is Poisson's ratio of the intact rock, V is the volume of rock containing the fractures, and e is the 2D-sampling exponent of the fracture-length distribution. Shear-wave anisotropy depends on sampling scale for the same reason that fracture porosity and permeability do. Because seismic waves of different frequency effectively sample different size volumes of rock, we may anticipate that shear-wave anisotropy will be somewhat frequency dependent.

Using the penny-shaped crack model and volumetric sampling, we also can calculate the total fracture porosity (Derivation A.II) in a similar manner to that of the previous section. Assuming that fracture apertures are linearly related to lengths ($l = g b$) we determine:

$$\phi_{\text{total}} = \zeta \left(\frac{3}{e+1} \right) \frac{\pi}{6} \frac{l_1^3}{g V} = \zeta \left(\frac{3}{e+1} \right) \phi_1 \quad (\text{A.7})$$

By equating the fracture-length terms of equations A.6 and A.7, we find that the shear-wave anisotropy and the fracture porosity are linearly proportional:

$$\phi_{\text{total}} = \frac{\pi}{2} \frac{2-\nu}{g(1-\nu)} \gamma, \quad (\text{A.8})$$

as found by Thomsen (1995). Taking $\nu = 0.33$ and $g = 1000$, for example, we get the approximate result of $\phi_{\text{total}} = (0.0039) \gamma$. Note that, although both shear-wave anisotropy and the fracture porosity are scale dependent and functions of the size distribution of the fractures, they depend on scale and the fracture size distribution in exactly the same way. Thus, the relationship *between* shear-wave anisotropy and the fracture porosity is independent of the size distribution of the fractures and the sampling scale.

Fracture Permeability/Shear-Wave Anisotropy Relation

The parallel-plate and penny-shaped crack models summarized above make fundamentally different assumptions regarding the geometries of natural fractures in rock. The two models represent end-members in terms of their implications about the connectivity among essentially parallel fractures. The penny-shaped crack model assumes that fractures are completely unconnected, whereas the parallel-plate model implies that fractures are ideally well connected. Natural fractures are somewhere in between. Nevertheless, for the reasons outlined above, the models may be accurate enough for the first-order analyses presented.

Fracture porosity was analyzed using both the parallel-plate and penny-shaped crack models. Both models are adequate for fracture porosity calculations, because porosity is insensitive to the connectivity of fractures. As one extension fracture decreases in aperture along strike, an overlapping fracture typically increases in aperture such that the sum of apertures varies little (e.g., Peacock, 1991). However, another difference between the two fracture porosity analyses is the three-dimensional (penny-shaped crack model) versus one-dimensional (parallel-plate model) configuration. Stereological arguments guarantee that the two approaches are exactly equivalent, regardless of the shapes, sizes, or orientations of fractures (Underwood, 1970, p. 25-30). Point counting of two-dimensional rock samples provides valid three-dimensional estimates of porosity for the same reasons. Therefore, we may substitute equation A.8 into equation A.3 to yield a relation between shear-wave anisotropy and the total fracture permeability:

$$k_{\text{total}} = \frac{\pi^3}{96} \left(\frac{2-\nu}{1-\nu} \right)^3 \frac{\zeta \left(\frac{3}{c} \right)}{\zeta^3 \left(\frac{1}{c} \right)} \frac{L^2}{g^3} \gamma^3 \quad (\text{A.9})$$

Similar to the fracture porosity-permeability relation, the cube of shear-wave anisotropy is proportional to fracture permeability. Taking $c = 0.8$, $\nu = 0.33$, and $g = 1000$, for example, we get the approximate result of $k_{\text{total}} = (17 \text{ darcy m}^{-2}) L^2 \gamma^3$ where L is the lesser of the seismic resolution or the sampling-length scale at which the apertures cease following a single power law.

The significance of equation A.9 is that it provides a basis for using remote detection methods for before-the-bit prediction of fracture permeability. In principle, this relationship combined with shear-wave anisotropy measurements should provide minimum estimates of fracture permeability, because the presence of multiple fracture sets will decrease shear-wave anisotropy but increase fracture permeability. However, the parallel-plate model probably yields over-estimates fracture permeability and the penny-shaped crack model probably yields under-estimates shear-wave anisotropy. Additional degrees of uncertainty derive from the potentially significant variation of the parameters c , ν , and g . Consequently, an empirical approach to evaluating the coefficient (F) of equation A.9 is desirable:

$$k_{\text{total}} = F \gamma^3 \quad (\text{A.10})$$

For example, in local areas where both fracture permeability and shear-wave anisotropy measurements are available, F can be determined empirically. Equation A.10 may then be used to map fracture permeability using seismic data in adjacent areas. Because fracture permeability is scale-dependent, the permeability predictions made from seismic data will represent permeability at the length scale of the seismic resolution.

Discussion

Some important aspects of fracture systems have been ignored in this paper. The parallel-plate model for fluid flow is limited by the assumption that natural fractures are connected.

Because long fractures have greater probabilities of being connected than do short fractures, on average long fractures will more closely approach the permeabilities predicted by the parallel-plate model. The scale-dependence of connectivity will reinforce the cubic relation of the parallel-plate model, so that the combined effect in the permeability-aperture relation will be an exponent statistically greater than 3. Another limitation of the parallel-plate model stems from the assumption of smooth fracture surfaces. The rough surfaces typical of natural fractures reduce the effective aperture for fluid flow, however recent studies offer the possibility of accounting for fracture surface roughness in a modified parallel-plate model (Brown et al., 1995).

Important uncertainties regarding the limits of fracture scaling remain. If microfractures generally follow the same scaling law as macrofractures in the same population, then microfracture observations may prove useful for characterizing the macroscopic properties of fractured reservoirs. For example, microfractures observed in core plugs might be used to infer (via empirically defined scaling laws) the frequency and aperture of macrofractures, and consequently the associated fracture permeability. An upper limit to extension fracture scaling might be anticipated based on the observed change in scaling for earthquakes that span the seismogenic zone (e.g., Pacheco et al., 1992). In layered sedimentary rocks, extension fractures often are limited in height by the thickness of individual beds, so the scaling of extension fractures that span a mechanically significant bed might differ from the scaling of smaller fractures in the same bed. An understanding of such a change in scaling (or lack thereof) is necessary before microfracture observations can be used to make useful reservoir-scale predictions.

Conclusions

The geometric attributes of individual extension fractures, which collectively form a fracture system, follow power-law scaling. The implications of extension fracture scaling reach

beyond the geometry of fracture systems, and encompass fluid flow and seismic propagation characteristics. In particular, knowledge of the scaling relations of an extension fracture population enables specification of fracture permeability, fracture porosity, and shear-wave anisotropy due to the entire fracture system in terms of a few variables. Perhaps more importantly, the fluid flow and seismic propagation characteristics may be related to one another. This offers the prospect of remote quantification of fracture permeability and porosity.

Some of the salient characteristics of fluid flow through fractured rock may be recognized as consequences of the scaling of extension fractures. The significant spatial heterogeneity of fluid flow in fractured rock results from almost all fracture permeability in a given sample deriving from only the few largest-aperture fractures. Anomalous pressure-transient curves are consequences of most matrix-fracture cross flow and fluid storage occurring in fractures that contribute minimal permeability. The observed variation of permeability with the length scale of sampling results from the tendency to encounter larger-aperture fractures in longer samples, at least over a wide range of length scales.

Derivation I

The total porosity of a set of aligned fractures in the parallel-plate model can be determined by one-dimensionally summing the porosity contributions of all fractures in the set:

$$\phi_{\text{total}} = \sum_{N=1}^{\infty} \phi_N, \quad (\text{A.II})$$

where subscripts are the fracture numbers defined by the power-law distribution of apertures.

The porosity contribution of each individual fracture in the set, as measured along a scanline of length L oriented perpendicular to the fracture set, is the ratio of the fracture aperture and L .

Substituting this relation into equation A.II yields:

$$\phi_{\text{total}} = \sum_{N=1}^{\infty} \frac{b_N}{L} \quad (\text{A.I2})$$

Using the 1D power-law distribution of the fracture apertures and setting $N = 1$ (i.e., largest-aperture fracture in the population) we find:

$$N = L a b_N^{-c} \Rightarrow L a = b_1^c \quad (\text{A.I3})$$

Substituting the result of equation A.I3 into the 1D aperture distribution and solving for the aperture of the N th fracture gives:

$$N = b_1^c b_N^{-c} \Rightarrow b_N = \frac{b_1}{N^{1/c}} \quad (\text{A.I4})$$

Equation A.I4 can now be substituted into equation A.I2 to yield the total porosity of the fracture set as the product of the porosity contribution of the largest-aperture fracture and an infinite series:

$$\phi_{\text{total}} = \frac{b_1}{L} \sum_{N=1}^{\infty} N^{-1/c} = \phi_1 \sum_{N=1}^{\infty} N^{-1/c} \quad (\text{A.I5})$$

The infinite series is known as the Riemann zeta function (Marrett, 1996), defined as:

$$\zeta(x) = 1^{-x} + 2^{-x} + 3^{-x} + \dots \quad (\text{A.I6})$$

Finally, the total fracture porosity is the product of the porosity contribution of the largest-aperture fracture and the Riemann zeta function with argument $1/c$:

$$\phi_{\text{total}} = \zeta\left(\frac{1}{c}\right) \phi_1 \quad (\text{A.I7})$$

The total fracture-parallel permeability induced by a set of aligned fractures in the parallel-plate model can be determined by summing the permeability contributions of all fractures in the set:

$$k_{\text{total}} = \sum_{N=1}^{\infty} k_N \quad (\text{A.I8})$$

The permeability contribution of each individual fracture in the set, following the parallel-plate model (e.g., Lamb, 1932; Snow, 1969), is the cube of the fracture aperture divided by 12 L. Substituting this relation into equation A.I8 yields:

$$k_{\text{total}} = \sum_{N=1}^{\infty} \frac{b_N^3}{12 L} \quad (\text{A.I9})$$

Substituting equation A.I4 into equation A.I9 yields the total permeability of the fracture set in terms of the permeability contribution of the largest-aperture fracture multiplied by an infinite series, which we recognize as the Riemann zeta function with argument 3/c:

$$k_{\text{total}} = \frac{b_1^3}{12 L} \sum_{N=1}^{\infty} N^{-3/c} = \zeta\left(\frac{3}{c}\right) \frac{b_1^3}{12 L} = \zeta\left(\frac{3}{c}\right) k_1 \quad (\text{A.I10})$$

Derivation II

The total anisotropy that affects elastic shear-waves propagating parallel to a set of aligned fractures embedded within a solid of volume V can be determined by three-dimensionally summing the anisotropy contributions of all fractures in the set:

$$\gamma = \sum_{N=1}^{\infty} \gamma_N \quad (\text{A.II1})$$

The shear-wave anisotropy contribution of each individual fracture in the set (Thomsen, 1995) depends on the cube of the fracture length:

$$\gamma = \sum_{N=1}^{\infty} \frac{1-\nu}{3(2-\nu)} \frac{l_N^3}{V} \quad (\text{A.II2})$$

Using the 3D power-law distribution of the fracture lengths and setting $N = 1$ (i.e., longest fracture in the population) we find:

$$N = V d l_N^{-(e+1)} \Rightarrow V d = l_1^{e+1}, \quad (\text{A.II3})$$

where e is the exponent of the 2D fracture length distribution. Substituting the result of equation A.II3 into the 3D fracture length distribution and solving for the length of the N th fracture gives:

$$N = l_1^{e+1} l_N^{-(e+1)} \Rightarrow l_N = \frac{l_1}{N^{1/(e+1)}} \quad (\text{A.II4})$$

Substituting equation A.II4 into equation A.II2 yields the total shear-wave anisotropy of the fracture set in terms of the anisotropy contribution of the longest fracture multiplied by an infinite series, which we recognize as the Riemann zeta function with argument $3/(e+1)$:

$$\gamma = \frac{1-\nu}{3(2-\nu)} \frac{l_1^3}{V} \sum_{N=1}^{\infty} N^{-3/(e+1)} = \zeta\left(\frac{3}{e+1}\right) \frac{1-\nu}{3(2-\nu)} \frac{l_1^3}{V} = \zeta\left(\frac{3}{e+1}\right) \gamma_1 \quad (\text{A.II5})$$

The three-dimensional determination of total fracture porosity follows the derivation in Derivation A.I. The fracture porosity is the sum of porosity contributions of all fractures in a set:

$$\phi_{\text{total}} = \sum_{N=1}^{\infty} \phi_N \quad (\text{A.II6})$$

The porosity contribution of each individual fracture is the ratio of the fracture volume and V. Using the ellipsoidal shape of the fractures and linear proportionality between fracture length and aperture, we may write:

$$\phi_N = \frac{4 \pi}{3} \frac{b_N}{2} \left(\frac{l_N}{2}\right)^2 \frac{1}{V} = \frac{\pi l_N^3}{6 g V} \quad (\text{A.II7})$$

Equations A.II7 and A.II4 may be substituted into equation A.II6 to yield the total fracture porosity:

$$\phi_{\text{total}} = \sum_{N=1}^{\infty} \frac{\pi l_N^3}{6 g V} = \frac{\pi l_1^3}{6 g V} \sum_{N=1}^{\infty} \frac{1}{N^{3/(e+1)}}, \quad (\text{A.II8})$$

which we recognize as the porosity contribution of the longest fracture multiplied by the Riemann zeta function with argument $3/(e+1)$:

$$\phi_{\text{total}} = \zeta\left(\frac{3}{e+1}\right) \frac{\pi l_1^3}{6 g V} = \zeta\left(\frac{3}{e+1}\right) \phi_1 \quad (\text{A.II9})$$

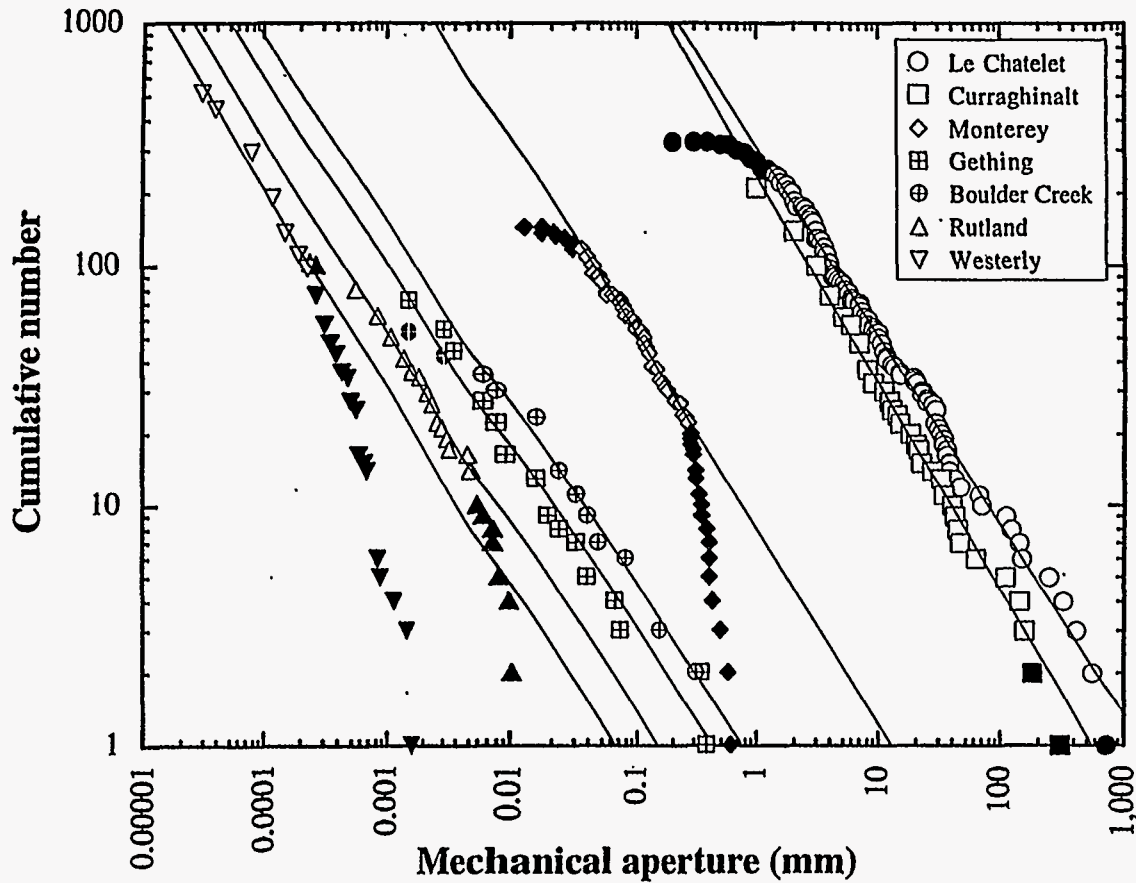


Figure A.1. Cumulative number vs. aperture plots. 1D sampling of extension fractures from Le Châtelet gold deposit, France ($N = (309 \text{ mm}^{0.786}) b^{-0.786}$, $r^2 = 0.993$; McCaffrey et al., 1994); Curraghinalt gold deposit, Ireland ($N = (234 \text{ mm}^{0.859}) b^{-0.859}$, $r^2 = 0.993$; McCaffrey et al., 1994); Monterey Fm. dolostone, California ($N = (7.92 \text{ mm}^{0.811}) b^{-0.811}$, $r^2 = 0.987$; Gross and Engelder, 1995); Gething Fm. sandstone, British Columbia ($N = (0.529 \text{ mm}^{0.764}) b^{-0.764}$, $r^2 = 0.972$; this paper); Boulder Creek Fm. sandstone, British Columbia ($N = (0.808 \text{ mm}^{0.758}) b^{-0.758}$, $r^2 = 0.989$; this paper); Rutland quartzite ($N = (0.216 \text{ mm}^{0.797}) b^{-0.797}$, $r^2 = 0.988$; 25 serial scanlines combined; Wong et al., 1989); and Westerly granite ($N = (0.106 \text{ mm}^{0.823}) b^{-0.823}$, $r^2 = 0.984$; 32 serial scanlines combined; Wong et al., 1989). Open symbols indicate data used to evaluate power-law exponent.

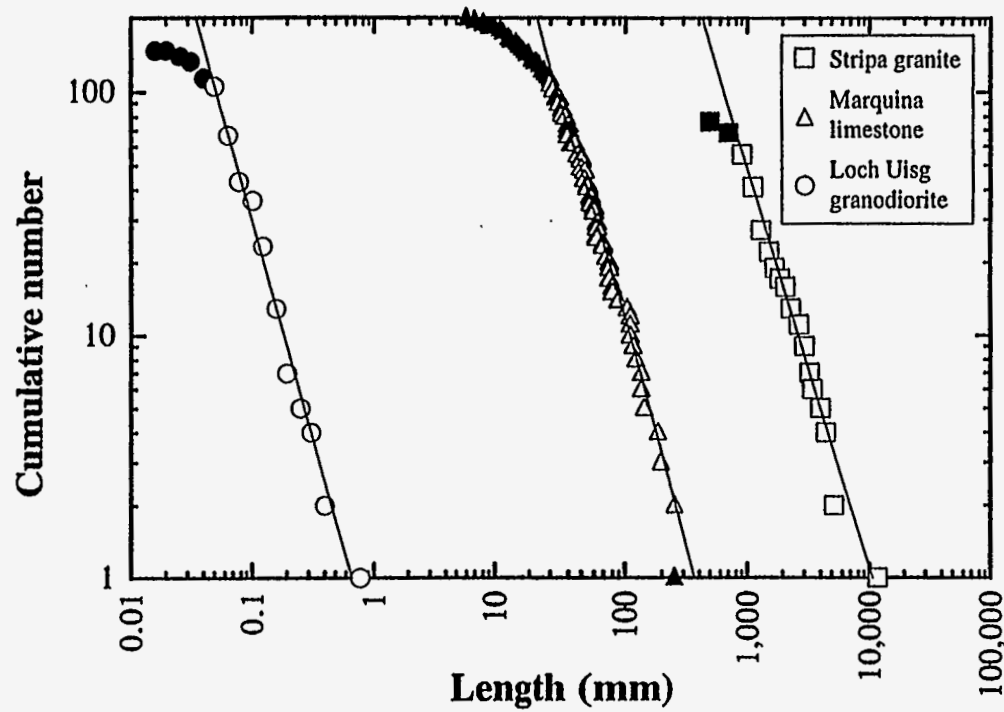


Figure A.2. Cumulative number vs. length plots. 2D sampling of extension fractures from Stripa granite, Sweden ($N = (3.85 \times 10^6 \text{ mm}^{1.64}) l^{-1.64}$, $r^2 = 0.979$; Rouleau and Gale, 1985); Negro Marquina limestone, Spain ($N = (8.51 \times 10^4 \text{ mm}^{1.93}) l^{-1.93}$, $r^2 = 0.994$; this paper); and Loch Uisg granodiorite, Scotland ($N = 0.504 \text{ mm}^{1.77} l^{-1.77}$, $r^2 = 0.988$; Hatton et al., 1993). Open symbols indicate data used to evaluate power-law exponent.

APPENDIX B: APPLICATION OF SCANNED CL TO RESERVOIR ISSUES

Although the degree to which fractures are open and interconnected in the subsurface governs their ability to transmit fluid, information on in situ fracture apertures and connectivity is usually incomplete. Accurate data from areas away from direct observation will clearly be difficult to obtain with foreseeable remote sensing methods. Even for fractures accurately measured in core, there is rarely a sound basis for extrapolating aperture patterns.

Although loading conditions are commonly viewed as the prime cause of fracture closure (or of variations in fracture aperture), core observations from petroleum reservoir rocks show that fracture pore space usually is strongly modified or destroyed by mineral precipitates (authigenic cements). We use this observation to suggest a simple parameter based on the diagenetic character of the host sandstone for estimating fracture conductivity in siliciclastic rocks. Diagenesis comprises the physical and chemical changes in sediment after deposition that converts it to consolidated rock. In sandstones, diagenesis involves compaction, cementation, dissolution, and replacement of grains and cements. Because diagenetic changes occur under circumstances of tectonic and burial loading and fluid flow, fracture on a range of scales can be an integral part of diagenesis. Diagenesis information is potentially a useful indirect guide to subsurface fracture attributes because specific observations about diagenetic relations can be gotten more easily than direct information on fractures.

Though many diagenetic processes, in particular the duration of cementation events, are matters of dispute, it is generally possible to treat discrete authigenic cements as being the result of relatively short (ca. 10 m.y.) precipitation episodes. The relative sequence of cement precipitation events and volumes of cements in a sandstone can generally be determined unambiguously using conventional petrographic methods.

We define three categories of cementation event that can influence the distribution of fractures and fracture attributes in a layered sequence. These categories are distinguished on the basis of the timing of cement precipitation relative to fracture growth. The three categories are:

- (1) prekinematic, where cement precipitates before fractures open,
- (2) synkinematic, where cement is precipitated during fracturing, and
- (3) postkinematic, where cement is precipitated after fractures form.

Sandstones may have several fracture opening events, as well as repetitive sequences of mineral precipitation, so this classification must be referenced to a fracture event. Because large fractures are rarely encountered in core, this would make application of the classification difficult if microfracture observations were not available. Scanned CL observations, however, can be used to define the timing of fracture opening movements within a diagenetic sequence where no large fractures are sampled.

Data on cement types compiled on a bed-by-bed basis show a range of values for individual beds about averages. Proportions of cement types differ for formations and for individual beds.

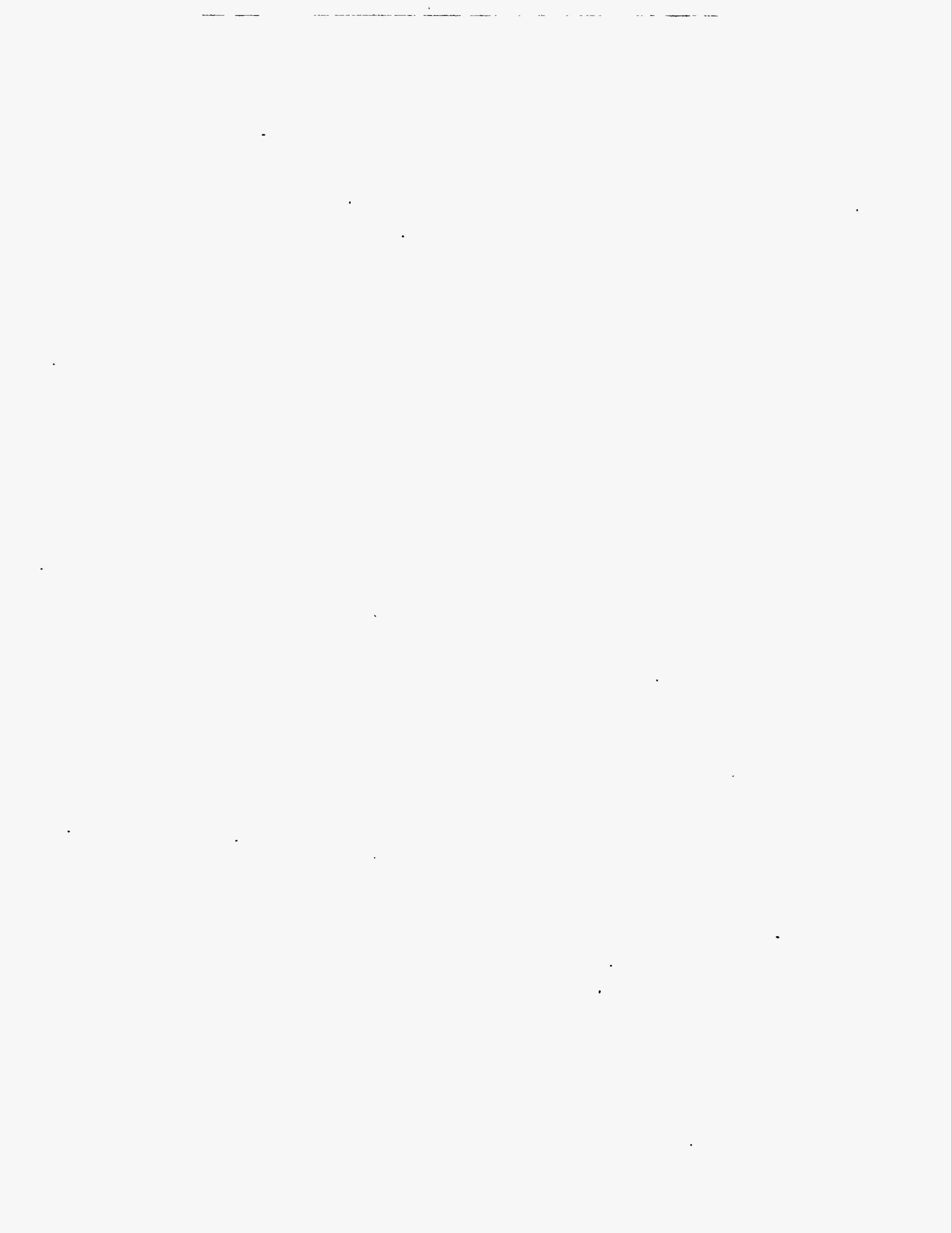
Fractures are a variety of porosity and thus are susceptible to being filled with cement. In sandstone fractures we examined, fractures commonly record sequences of mineral precipitation that closely match those of diagenetic minerals found filling adjacent sandstone pore space. However, fractures form at a specific time (or times) in the rock's burial history, and this governs what cements can be in fractures: syn- and postkinematic cements. Studies in progress show that where numerous macrofractures are available for observation, postkinematic cement occludes intergranular porosity to about the same extent that it fills fracture porosity.

Although large fractures, especially if they are in interconnected networks, likely do not fill in exactly the same way as small pores, these observations suggest that postkinematic cement volume is an easily obtained index of fracture porosity preservation. Microfractures and narrow parts of large fractures are key areas for fracture connectivity (and thus play a key role in overall fracture-network conductivity), and it is these areas that postkinematic cements can be most detrimental to the continuity of overall fracture system plumbing by plugging fracture-network

choke points. In studies of flow and precipitation patterns in pore networks (which might be analogs for fracture networks) Wu (1992) showed that for pores in series, mineral precipitates choke off the smallest pores first.

Fractures in areas of synkinematic cement tend to preserve fracture porosity. For example, in 104 large fractures that are lined and partly bridged with synkinematic quartz in 9 wells from one Gulf Coast Cretaceous sandstone, those that contained only quartz had visible fracture porosity, whereas fractures that contained quartz and later (postkinematic) calcite, ankerite, barite or anhydrite are mostly (>60 percent) sealed. This indicates that substantial (i.e., macroscopically visible) fracture porosity existed in most fractures after quartz precipitation even in fractures that are now filled. Reopening of fractures during cement precipitation (marked by crack-seal microstructures) tends to preserve fracture channelways in these rocks.

Cement compositions have been measured from a wide variety to petroleum reservoirs (S. Laubach, manuscript in preparation 1998). These key cement types are widespread and can readily be recognized and measured.



APPENDIX C: CLASSIFICATION OF MICROFRACTURES

Microfracture identification and classification is key to appropriate use of microfractures to determine macrofracture strike, for use in identification of the timing of cement precipitation, and for scaling studies. Our classification approach is briefly outlined here. More information is presented in Laubach (1997).

Tables C-1 and C-2 classify microfractures into three categories and five degrees of reliability as guides to macrofracture strike. Shape and arrangement are used to rank fractures into style categories I, II, and III, as described. Reliability is highest for postdepositional opening-mode microfractures that have straight traces and steep dips (category I). Fracture-type designations “a+” through “d” index the certainty with which fractures can be classified as postdepositional. This is evident in crosscutting relations among fractures and cement that are readily determined for microfractures that are large relative to grain size (type a+).

For small intergranular and intracement fractures, positive identification of a crosscutting relationship with cement is progressively more challenging as fracture size decreases, but also depends on image resolution. Where crosscutting relationships are certain but fractures cut only one grain, they are rated as moderately reliable (type a), where probable crosscutting relations are found, they are rated marginally reliable (type b). Reliability is lowest—fractures are questionably postdepositional—where fractures are intragranular or where ambiguous intersecting relations with cement are found. Many small and indistinct fractures fall into this marginally unreliable (type c) classification. Unreliable (type d) fractures have indeterminate relation to cement, and many may be inherited. Laubach (1997) summarizes the basis for this fracture classification.

Table C-1. Microfracture categories and their interpreted origins.

Category	Habit	Length (range)	Shape	Distribution	Interpretation (Application ⁴)
I Straight ¹	Isolated; locally parallel sets	µm to mm; gradational to macroscopic	Lens; aspect ratios 10 ⁻³ , 10 ⁻⁴	All formations & depths	Equivalent to macrofractures (regional)
II Web ^{1,2}	Curved, intersecting; crisscrossing & radiating arrays	= grain size & smaller	Lens to irregular & angular	All formations & depths	Primarily due to grain-grain interaction (local)
III Truncated ^{1,3}	Isolated within grains; end within grains or at grain margins	= grain size & smaller	Simple tabular	All formations	Inherited (none ⁵)

¹All categories consist mainly of opening-mode fractures.

²Intersecting arrays of contemporaneous fractures.

³May end within grains and have crisscrossing patterns that resemble category II.

⁴Appropriate scale for use as a post-depositional structural indicator.

⁵Inherited fractures may have application as provenance indicators.

Table C-2. Microfracture data-quality index for assessing reliability of macrofracture strike determination.

Microfracture Category		Microfracture Type					Decreasing size and/or resolution of relation to cement ¹ →	
		I. Fractures having straight traces	Large transgranular	Trans-cement, intra-cement	Probable trans-cement	Ambiguous relation to cement	Indistinct	
Reliability based on style	Reliable	I. Fractures having straight traces	^{a+} Highly reliable	^a Reliable	^b Marginally reliable	^c Marginally unreliable	^d Unreliable	
	Unreliable	II. Fractures in crisscrossing arrays	n.a.	Present (rare) ²	Present ²	Present ²	Present	
		III. Inherited fractures	n.a.	n.a.	n.a.	Possibly inherited ³	Probably Inherited ⁴	

Footnotes

¹Based on crosscutting and abutting relation of vein fill to cement

²Unreliable based on fracture style

³Category III fractures may be mistaken for category I or II, type c

⁴Many type d fractures are also category III

APPENDIX D: SYNKINEMATIC CEMENT AND FRACTURE ATTRIBUTES

Fractured sandstone cores from ten sedimentary basins have identical microstructures that indicate authigenic quartz precipitated during fracture opening. Evidence for repeated fracture opening and sealing includes quartz that spans fractures in pillar-shaped bridges containing crack-seal structure, and arrays of quartz-filled microfractures disseminated throughout the rock mass that preserve crosscutting relations with cement. Degree of occlusion by synkinematic quartz depends on fracture size, with large fractures (mechanical apertures greater than 0.5 mm) preserving extensive porosity. The probable cause of fracturing is episodic increases in pore fluid pressure caused by influx of quartz-precipitating fluids and porosity reduction due to quartz deposition. For sandstones, mechanical and diagenetic models suggest that fractures can form when burial and diagenetic processes elevate pore pressure to only about 0.5 times overburden, with or without a reduction in minimum stress due to tectonics or other processes. Thus, regional fractures may not result from shortening or extension associated with specific tectonic events.

A key petroleum geology problem is the effective use of natural fracture models to infer properties of subsurface regional fracture arrays between observation points. Establishment of relationships between regional fractures and their causes can help guide these inferences. Because elevated pore-fluid pressure can promote fracture development (Secor, 1965) one approach to this problem is to relate fracture formation to other evidence for elevated pore pressure, such as is provided by observations of fractures and their relations to microstructure and diagenesis. Our core fracture data set of more than 50 wells and about 20 stratigraphic units, primarily from oil and gas reservoirs in well-indurated sandstone, contains what we interpret to be examples of 'regional fractures' (Nelson, 1985).

Structures within minerals precipitated in the fractures permits us to relate fracture opening to diagenesis. Sample burial depths extend from several hundred feet to more than 6,000 m for rocks deposited in fluvial and shallow marine to deep marine environments, and in structural

settings that include platforms and foreland and passive margin basins mainly distant from large faults and folds.

A recurrent relationship between fracture formation and certain diagenetic events is evident. Most notably, crack-seal structure in fracture-filling quartz shows that fracture opening is typically coincident with quartz cement precipitation. Review of recent studies of quartz cement suggest that episodic increases in pore pressure could be associated with precipitation of this mineral, linking diagenesis and fracturing.

This section focuses on core observations for the following reason. The advent of wellbore-imaging geophysical logs and horizontal drilling has expanded our knowledge of subsurface fracture attributes. Nevertheless, most subsurface data sets are incomplete. Measurement of the attributes of large fractures is challenging because such fractures rarely intersect wellbores where they can be observed. Consequently, our perception of subsurface fractures tends to be biased by the fractures geologists are most familiar with: those in outcrop.

Although valuable because they provide the only way to measure certain aspects of fracture patterns (for example, mechanical connectivity), such outcrop observations can be misleading if, on average, they differ in significant ways from those typical of the subsurface. Core observations are inherently limited but remain the best way to check the usefulness of our perceptions of reservoir-scale deformation as guided by outcrop data.

We measured natural fracture and microfracture attributes in sandstone cores from more than 20 formations as part of a larger study of fracture and microfracture attributes (Laubach and others, 1995; Marrett and others, 1998; Reed and Laubach, 1998, and unpublished). Cores are generally from areas distant from recognizable folds or faults. Fractures are opening-mode fractures (joints). Some are open or locally mineral bridged, whereas others are filled by a variety of authigenic cements, including quartz. These fractures form regionally extensive arrays in otherwise undeformed rock. They are typically near vertical or normal to bedding. Where fracture orientation patterns are known, fracture strikes are apparently uniform over wide (~km²)

areas. In other words, these structures are regional fractures (Nelson, 1985). Note that figure and appendix descriptions are ranked independently within parts 1-3.

In our data set, where reliable fracture attitudes have been measured, fractures show preferred orientations that may reflect uniform regional patterns (Laubach, 1988; Laubach, 1992). However, a wide range of fracture strikes is evident in most of these data sets, and the presumed trends are based on small numbers of reliably oriented fractures from widely separated wells, as is typical for data sets of this type. For example, in one of our largest data sets, from the Travis Peak Formation in the East Texas basin, only 61 reliably oriented macrofractures were recovered from about 600 m of core in 10 study wells scattered over an area of about 5400 km². Although fractures from these wells generally strike east-northeast, they have a range of strikes of more than 100 degrees. Regional fracture orientation patterns could be more diverse than can be readily discerned with such sparse samples. Probably mainly because of sampling limitations, abutting and crosscutting fractures are rarely observed in these sample sets.

Fractures have a wide range of apertures and, presumably, lengths and heights. Apertures range from microscopic to more than 5 mm. Fractures visible only with magnification (microfractures) are described in the following section. The upper size limit may reflect incomplete sampling and the tendency for core having large fractures to become disaggregated so that core recovery is impaired. Many fractures end within sandstone beds by gradually tapering to imperceptible width. Fractures also terminate at shaly interbeds or other slight changes in lithology within sandstones, reflecting the well-known outcrop observation that mechanical layer thickness influences fracture properties such as size and spacing (Pollard and Aydin, 1988; Narr, 1991; Ortega and Marrett, 1997).

Fractures visible to the unaided eye are typically lens-shaped in plan view and cross section, although some fractures that are truncated by or terminate against stylolites or bedding surfaces have roughly triangular or, locally, rectangular shapes. Stylolites are most commonly subparallel to bedding, but vertical stylolites are present in core from below 4,000 m in the Green River basin and elsewhere. Fracture height/width and length/width ratios generally show fractures that

are much taller and longer than they are wide, but fracture-trace mapping of cores shows that these ratios can be highly variable even within a given core for fractures that are likely members of the same set. As discussed in the next section, this can be accounted for in some instances by differences in growth history among fractures in a set.

Height is the fracture length dimension most readily measured in vertical core. Among macroscopic fractures, a spectrum of fracture heights (and thus fracture sizes) is present in all units. The tallest fractures completely sampled in core are more than 5 m high, but the local presence of taller fractures at the wellbore is suggested by fracture traces on borehole image logs. Some tall fractures are composed of coplanar segments, ranging in length from centimeters to tens of centimeters, which are locally arranged in an echelon and relay patterns. Segments may be separated by intact rock or by short curved or straight subsidiary fractures or microfractures.

Information on the intensity of fracture development is sparse and challenging to interpret or to compare from bed to bed or well to well. The number of fractures per length of core is generally small but highly variable, ranging from absent or rare to more than 1:1 (Laubach and others, 1995). Although direct measurements of fracture separation (spacing) and size distribution are rare because generally restricted to horizontal or slant core or fortuitous circumstances (e.g., Ortega and others, 1998), available evidence suggests that some fracture arrays show clustering (fracture swarms), whereas others do not (cf. NRC, 1996). Measuring the length distribution, saturation, or connectivity of subsurface fractures is highly problematic because of obvious sampling limitations. Inferring these attributes based on core measurements is an area of ongoing research that we do not review here (Marrett, 1997).

In summary, the fractures we sampled are mainly simple opening-mode fractures that could be accounted for by a wide variety of regional (or local) fracture models. Although orientations, dimensions, separations, and patterns likely vary from unit to unit in ways that are challenging to measure using conventional methods, these fractures also share a great many attributes. The simple morphology and uninformative style of these fractures are reasons these features commonly cannot be explained by a unique basin history or structural model, even where these

models are guided by appropriate mechanical principles and careful outcrop studies of subsurface analogs. For example, fractures formed in response to bending-related stretching and those caused by uplifted-related rock contraction could have identical shapes and orientation patterns.

In cores we sampled in units listed in Table 1, all of the fractures visible to the unaided eye are lined, bridged, or filled by quartz. Although other phases locally accompany quartz in these fractures, quartz evidently precipitated first after (or while) fractures opened. For some fractures, repeated fracture opening and quartz precipitation indicate these processes operated concurrently. This is a startling observation since these rocks all have diverse diagenetic mineral assemblages that evolved over millions or hundreds of millions of years. Moreover, all of these units have experienced burial and tectonic histories that might have caused fracturing at various times during the course of diagenesis. At least for the cores we sampled, the histories of fracturing and diagenesis are more similar and systematic than would be suggested by inspection of burial history curves. Why has such a unique fracture and diagenesis relationship developed so consistently in such a wide range of settings?

Evidence for the timing of quartz precipitation comes from petrographic and other microstructural observations of the fractures. The most direct evidence is crack-seal structure revealed by transmitted light microscopy and scanning electron microscope-based cathodoluminescence (scanned CL). Locally, particles of broken grain are visible, in particular where feldspar or lithic grains are incorporated in the fracture (Figure Madden example). Although some pillars have numerous planes of fluid inclusions parallel to fracture walls that may be symmetric about the fracture centerline, many pillars show no obvious structure in transmitted light.

The sequence in which minerals precipitated in fractures has been established using crosscutting relations, where a younger phase grows across and covers a crystal face of an older mineral. This evidence shows that synkinematic quartz predates various other phases. Typical late phases in fractures include ankerite, dolomite, chlorite, other clay minerals including dickite,

anhydrite, barite, and solid hydrocarbons (dead oil). The sequence in which minerals precipitated in the intergranular pore space was established using the same criteria, and these sequences match those in associated fractures. Congruence of diagenetic patterns in fractures and intergranular pore space is further evidence that the quartz in fractures and in pore space is contemporaneous.

Fractures have preferred orientations over wide regions, but no plausible tectonic 'event' to account for their orientation in passive margin basins (Travis Peak Formation; Laubach, 1988) and in foreland basins (Frontier Formation; Laubach, 1992).

Crack-seal structure in fracture-filling quartz shows that quartz precipitated during episodic fracture opening. Rocks can fracture at different times, but still have their orientation influenced by uniform regional stress orientations. magnitude of load could vary (hooking, clustering); much will depend on individual rock diagenetic history. Could account for observed shifts in strike (Laubach, 1992), clustering, and saturation (Olson and others, 1998).

APPENDIX E: ADDITIONAL BACKGROUND MATERIAL

Natural fractures, diagenesis, and simulation

Little has been published on the relationship between deformation and diagenesis; it is a subject on the border of two disciplines. A genetic and temporal relation between fracture and diagenesis was demonstrated for opening-mode fractures in the Cretaceous Travis Peak sandstone of East Texas (Laubach, 1988), and similar relations are evident in Pennsylvanian Sonora and Ozona Canyon sandstone of the Val Verde Basin, Texas (Laubach and others, 1994). Planes of fluid inclusions interpreted to be microfractures were shown to parallel macrofractures in the Travis Peak Formation (Laubach, 1989). Our subsequent scanned CL analysis demonstrates that these fluid-inclusion planes are quartz-sealed microfractures that contain primary fluid inclusions. Explicit documentation of the relationship of diagenesis, changing rocks properties, stress, and fracture is rare.

A complete description of the attributes of natural fracture systems that can affect fluid flow requires information on many different variables, including fracture-size distributions, spacing, porosity, orientation patterns, connectivity, compliance, *in situ* stress conditions, etc. (National Research Council, 1995; Nelson, 1985). In contrast, fractured-reservoir simulators in the oil industry currently only use a continuum representation of effective fracture transport and storage properties, along with an exchange coefficient for flow between fractures and matrix blocks (Aguilera, 1980; van Golf-Racht, 1982; Dershowitz and LaPointe, 1994). Present simulators typically are dual continuum (dual porosity or dual permeability) with matrix blocks divided into regular patterns by grids of fractures (Kazemi and others, 1976; van Golf-Racht, 1982). In such simulators matrix and fractures are represented by separate continua with distinct properties. The extreme geometrical simplification of flow pathways is required to allow numerical solution of the complex differential equations that are used to simulate such effects as imbibition, residual saturation, and multiphase flow.

Conventional continuum simulators cannot explicitly represent many fractures without creating a model too large for solution. Simulation regions are large (on the order of mi^2), and fractures smaller than the simulation region, if important individually to flow, may be too numerous to explicitly incorporate.

Recognizing the disparity between real fracture networks and dual-continuum models, industry and academic researchers in this field have responded by developing reservoir simulators with ever-increasing capabilities for taking into account the complexities of real fracture systems. Thus, discontinuum approaches including discrete fracture modeling (i.e., Long, 1984; Dershowitz and LaPointe, 1994), and hybrid discrete fracture dual-porosity models (Miller, 1992) increasingly use geostatistics and fractal descriptions of fractures to represent complex, heterogeneous fracture systems (Dershowitz and LaPointe, 1994). Yet this approach has a fundamental limitation that has not been widely appreciated. In most cases the requisite description of the attributes of natural fracture systems *in the reservoir* is unobtainable.

Fracture Characterization

Subsurface fracture attributes can only be measured imperfectly or not at all with current technology, despite dramatic improvements in technology for imaging fractures in the subsurface with wireline logging devices. This situation is not likely to improve in the foreseeable future. The reason is sampling bias. In cases where one fracture set is present, fracture spacing is regular, and fractures extend vertically across the interval of interest, the probability of encountering a vertical fracture with a vertical core is the ratio of core diameter to the fracture spacing. Where the fractures of interest may have irregular spacing on the order of tens to hundreds of feet (Laubach, 1992), and wellbores have diameters on the order of 10 inches, fractures will be rarely encountered in the wellbore. Fracture spacing (except in horizontal wells) and connectivity cannot be obtained, and fracture porosity (i.e., are the fractures open?) and orientation are commonly inadequately sampled and characterized, even where costly whole core

is obtained and borehole-imaging logs have been employed. Yet in a typical producing field, there may be many intervals of interest, each with its own characteristic fracture patterns.

Inadequate characterization of subsurface fractures limits the applicability of both discrete fracture methods and conventional dual-continuum fractured reservoir approaches. Basic observations identifying beds that contain open fractures and the strike of those fractures are typically lacking. Detection of other attributes that are important in outcrop fracture-pattern characterization, such as fracture length distributions and connectivity patterns, is beyond the scope of any conventional technology currently envisioned, although it can be derived from the measurements pioneered in this study.

Thus, to effectively apply any fractured-reservoir simulator to a reservoir, seemingly insurmountable sampling problems apparently require either an unjustified statistical extrapolation from limited core or well-log fracture observations, or the use of statistics derived from situations where fractures can be fully characterized: outcrops or models. Both of these latter approaches have serious drawbacks. Modeling of fracture formation generally leads to nonunique predictions of even the most basic fracture attributes. The burial, tectonic, fluid-flow, and rock-property history of most reservoir rocks is too complex and poorly known to yield more than a range of possibilities (Engelder, 1985; Laubach and others, 1998).

Stress-history models have been used for fracture analysis in several basins (e.g., Engelder, 1985; Laubach, 1989; Warpinski, 1989; Apotria and others, 1994). During burial history, lithifying sediments undergo variations in burial load, pore pressure, and temperature, and rock properties that change as a result of episodic diagenetic events. Yet typically stress-history models assume that rocks are elastic, homogeneous, and isotropic and that their properties vary linearly with depth during burial until they attain final values at maximum burial. For a number of reasons, these assumptions are rarely met.

Outcrops offer the best opportunity for characterizing the types of fractures that may exist in the subsurface. Most of the important attributes of fracture systems can be documented in outcrop. Moreover, it is possible to identify fractures in outcrop that are representative of the

subsurface and to obtain statistical attributes of fracture populations from outcrops of reservoir-facies rocks (Laubach, 1992; Marrett, 1997). Yet this does not imply that statistical data from outcrops can be directly applied in simulators without the necessity of mapping subsurface fracture attributes.

Aside from the fact that only a few reservoir rocks are exposed in outcrops in which representative subsurface fracture patterns can be identified, extrapolation of fracture statistical data from outcrop to a particular volume of the subsurface is fraught with potential pitfalls. Inasmuch as many important reservoir-rock diagenetic and natural fracture properties vary with burial history (e.g., Dutton, in preparation) it is no surprise that fracture statistical attributes obtained from outcrops also differ from those obtained from the subsurface. This has been demonstrated for the Austin Chalk, where outcrops (Collins and others, 1992), large excavations and tunnels (Laubach and others, 1995), and core and well logs from industry oil wells (Belfield, 1994) have highly contrasting fracture-system characteristics. Direct extrapolation of fracture statistics from outcrop to subsurface—and even from one subsurface location to another—would be difficult to justify.

Outcrop studies can serve as valuable guides to patterns that may occur in the subsurface, but clearly methods are needed that allow attributes of subsurface fractures to be identified and mapped. To accomplish this the sampling limitation that has so far hindered subsurface fracture characterization must be overcome—implying the apparent paradox that fracture information must be obtained from wells in which fractures have not been intersected. This is why indirect methods such as those are developing are important.

The importance of mineral precipitation as a cause of fracture occlusion is widely recognized (Nelson, 1985), and such minerals can govern fracture response to changes in effective stress during petroleum production (Dyke, 1991). Precipitation reactions can have surprising effects on the distribution of effective permeability in fractures. In studies of flow and precipitation patterns in pore networks (which might be analogs for fracture networks) Wu (1992) showed that for pores in series, mineral precipitates choke off the smallest pores first, yet

for pores in parallel high flow rates can cause the widest pore to fill first. From this, it might seem that extending this work to fracture networks is essential to untangling the relations among cementation patterns, the resulting distribution of fracture apertures, and the effective permeability of the fracture network, but this is not the case. Addressing such questions is an aspect of our study, but the success of our approach does not depend on unraveling the infilling pattern of static fractures. Although data collected in our study has implications for the nature of diagenetic processes, the success of is not dependent on solving basic problems in diagenesis.

We seek to distinguish average differences in fracture properties between rocks where cement was precipitated prior to and during fracture opening from rock where dominant cements precipitated after fractures were open. Preliminary evidence, partly reported in Laubach and others (1994) and Laubach and Milliken (1996), Marrett and Laubach (1997), indicates that this distinction can be made and that it corresponds to differences in degree of fracture occlusion.

With indirect evidence of key fracture attributes from subsurface samples, and with direct observations of microscopic features that scale, appropriate properties and strategies for simulating the fractured reservoir can be applied. The effective physical properties of a grid block can be approximated by scaling up sub-grid heterogeneities for field-scale simulation (Kasap and Lake, 1989).

Simulation Issues and Scaling

One of the principal objectives of the proposed research is to quantify distributions of key fracture attributes (e.g., aperture, length, spacing) and to implement this information in fractured reservoir simulators. Of particular importance are the fracture contributions to reservoir permeability and porosity. Estimates of fracture permeability and porosity may be determined directly from geometric information on open fracture apertures and spatial distribution (e.g., Nelson, 1985). Often such estimates are based on simplistic assumptions of regular fracture spacing and constant aperture, or on average spacings and apertures. Because work to date

suggests that fracture apertures follow power-law distributions, simplistic approaches to permeability and porosity calculations are bound to fail. Nevertheless, it is possible to analytically determine more accurate estimates of fracture permeability and porosity if the scaling parameters of the fracture attributes are known.

The simplest model relating the geometrical attributes of fractures to their fluid flow characteristics is the parallel-plate model (e.g., Lamb, 1932; Snow, 1969). The parallel-plate model is ordinarily applied to average fracture aperture and spacing (e.g., Nelson, 1985); however, it is not limited to this case. A generalization of the model (Marrett, in review) admits fracture populations characterized by power-law scaling and expresses the total fracture permeability and porosity of a fracture set as the product of a factor depending on the exponent of the appropriate power-law and the permeability/porosity contribution of the largest fracture in the population.

Fracture aperture populations (apertures ranging from 0.03 μm to 0.5 m) commonly are consistent with power-law exponents of about -0.8, which implies that the total fracture permeability is about 1.1 times the permeability contribution of the largest fracture and the total fracture porosity is about 4.6 times the porosity contribution of the largest fracture (Marrett, in review). Consequently, almost all fracture permeability derives from the largest fracture in a sampled interval, but most fracture porosity derives from smaller fractures. This is consistent with the inference of Nelson (1987) that the largest-aperture fractures intersected by a well control short-term flow rates and that smaller-aperture fractures control long-term flow rates. A corollary to the model described above is that fracture permeability will show a significant positive correlation with the size of a sample (i.e., fracture-perpendicular length of a well bore). This is consistent with permeability observations in fractured crystalline rocks up to sample lengths on the order of 100 m (Clauser, 1992).

There are two fundamental considerations required to understand the scaling of a fracture population: the effect of sampling biases and the limits of scaling. A variety of sampling biases affect the collection and analysis of fracture population data (e.g., Baecher and Lanney, 1978),

and their effects are now well understood (e.g., Marrett, in review). The limits of opening-mode fracture scaling are not yet known. At the smallest scales, power-law scaling must break down because the smallest fractures will have finite sizes. However, fracture apertures less than 0.1 μm show scaling indistinguishable from that of larger fractures, so the lower limit of scaling is as yet uncertain. At the largest scales, it is widely recognized that fractures in sandstone are commonly limited to single sedimentary beds. Consequently, we expect that bedding thickness will impose an upper limit to the scaling of fractures. Our working hypothesis is that the fractures spanning a bed will follow scaling distinct from but systematically related to the scaling of smaller fractures. Data bearing on this idea are summarized in the discussion of the Mesaverde case study, and will also be addressed in the Spraberry, Tensleep, Wolfcamp, and Frontier cases studies. Testing the hypothesis will be important to the success of the scaling aspects of our approach, inasmuch as the fractures accounting for most permeability will generally span a sandstone bed but subsurface observations are often limited to smaller fractures.

Scanned CL Imaging

The stable observing conditions, high magnifications, and sensitive light detection that are characteristic of scanning electron microscope-based cathodoluminescence (scanned CL) imaging overcome several of the disadvantages of conventional light-microscope-based CL systems, allowing more routine application of this petrographic method for description of micron-scale textural relationships between detrital grains, cements, and fractures in sandstones. Scanned-CL imaging has great utility for documenting the interrelation between deformation and diagenesis at the micrometer scale in siliciclastic rocks. A survey of sandstone units of widely varying age, location, and burial history suggests that quartz-sealed microfractures are nearly ubiquitous in lithified quartzose sandstones (Laubach, 1997 and work in progress). Because fractures formed in association with quartz precipitation are prevalent in quartz-cemented

siliciclastic reservoir rocks, scanned CL imaging of microfractures can yield important information on subsurface fracture populations that have engineering and economic significance.

Images in our study were produced using Oxford Instrument's photomultiplier CL detector CL302 installed on a JEOL T330A SEM and using a P2 CL detector on a JEOL T300 SEM. Light is collected with the parabolic mirror inserted about 1 mm above an epoxy-impregnated carbon-coated polished thin section. Panchromatic images are observed on the CRT of the SEM and recorded on Polaroid film. An accelerating voltage of 10 kV with sample current set near 90% of the maximum for the SEM provides adequate photon emission for examining the luminescence variations in authigenic (relatively dark-luminescing) and detrital quartz (relatively bright luminescence).

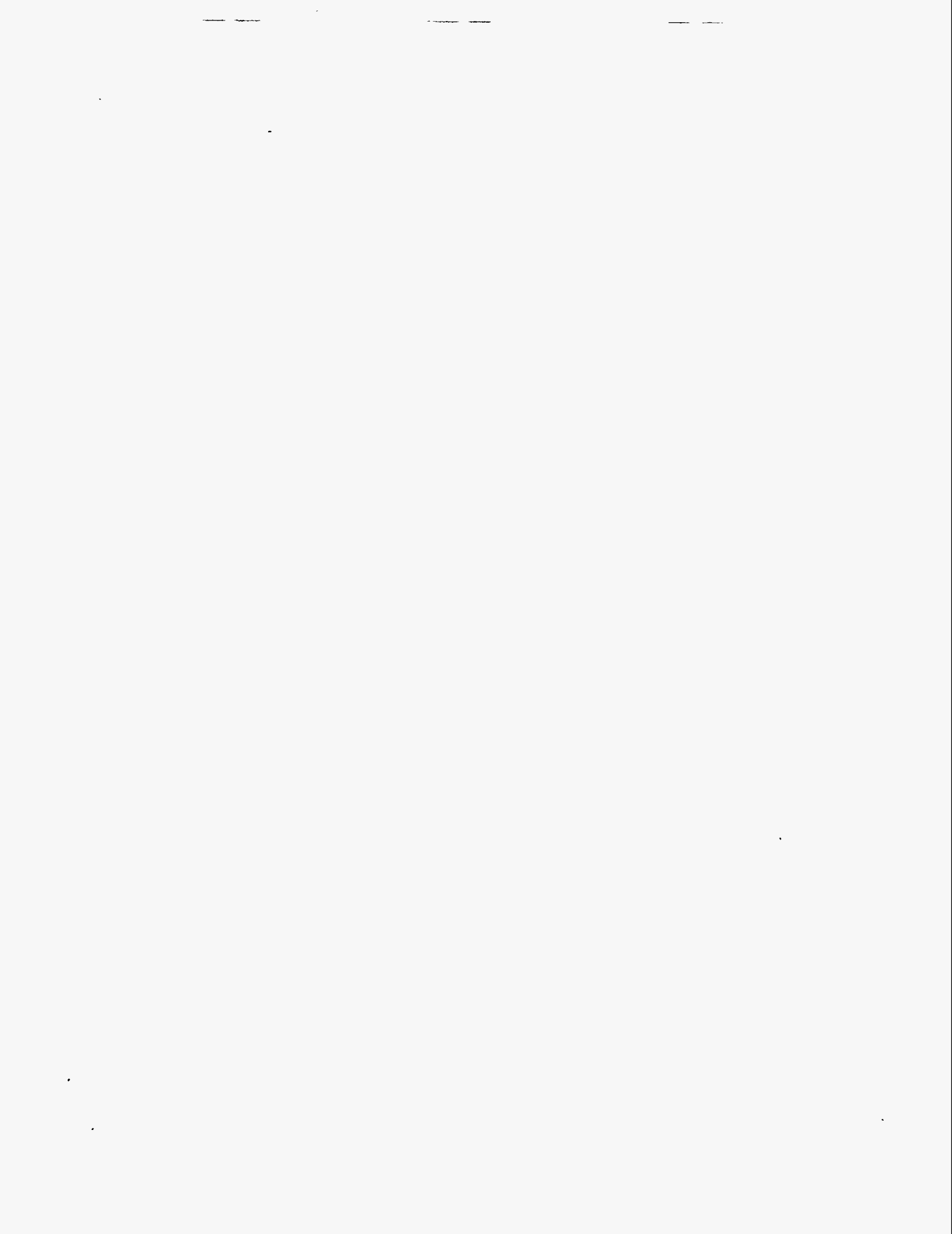
Since the late 1970s, CL microscopy has been used to address issues in sandstone petrology. CL has particular utility for examining features in detrital and authigenic quartz. Quartz lacks the major compositional and textural variability that makes other major sandstone components, such as feldspars and lithic fragments, amenable to application of petrographic and chemical methods that depend on large degrees of chemical and textural variation (e.g., back-scattered electron imaging).

Large variations in cathodoluminescence intensity however arise from the relatively slight variations in trace element content or defect structure that characterize quartz of various origins (Sipple, 1968 and numerous subsequent publications). In the realm of chemical diagenesis, CL imaging clearly yields superior quantification of quartz cement volumes (e.g., Evans and others, 1994) and CL zoning in quartz cements has been used to study cement timing and paragenesis, in a manner analogous to CL studies of carbonate cementation (e.g., Hogg and others, 1992). As recognized by Sipple, CL images are an important key to deciphering the role of local pressure solution versus silica import as a cause for quartz cementation (Houseknecht, 1984, 1987, 1991).

It has also been suggested that CL colors (Matter and Ramseyer, 1985; Owen, 1991; Kennedy and Arikian, 1990) and CL textures (Milliken, 1994a) in detrital quartz grains might be useful as provenance indicators in siliciclastic rocks. With this goal in mind, a number of studies

have focused on characterization of CL properties of quartz, especially in crystalline rocks that represent potentially significant sources of sediment (e.g., Zinkernagel, 1978; Sprunt and others, 1978; Ramseyer and others, 1988; Owen and Garson, 1990). Practical applications of this approach to provenance determination (e.g., Owen and Anders, 1988) have been few, however, and additional basic studies on the systematics of quartz CL character in various igneous and metamorphic rocks and in modern sediments are clearly warranted.

Certain analysis methods in sandstone petrology can be used in combination with scanned CL to overcome the uncertainties that result from the small-scale and sometimes cryptic mixing of authigenic and detrital quartz that occurs through cementation and brittle deformation (Milliken and Laubach, in preparation). For example, laser-extraction isotope analysis (Hervig and others, 1995), and fluid inclusion analysis (e.g., Burley and others, 1989) take advantage of scanned CL to characterize with greater certainty the nature of the material analyzed.



APPENDIX F: FRACTURE ORIGINS

Fractures without any observable shear offset are opening-mode fractures. The orientation of such fractures can be related to past stress fields. Yet mechanisms responsible for fracture formation can rarely be specified uniquely. For accurate predictions of fracture patterns away from the wellbore, the relevant (or typical) loading conditions that produce them need to be better known. Do fractures form mainly during burial, at depth after lithification, or during uplift? Fracture mechanics and diagenesis arguments can shed light on this issue.

Fractures primarily accommodating opening displacement propagate along a plane of zero shear stress, specifically the plane perpendicular to the least compressive principal stress (Lawn and Wilshaw, 1975). This makes such fractures indicators of past stress orientations, where vertical fractures include the maximum horizontal stress direction at the time of their formation. Secor (1965) helped resolve the controversy over how joints form by showing that the concept of effective stress (Hubbert and Rubey, 1959) could account for opening-mode fracture development in a compressive stress state if the pore pressure was sufficiently high.

Conditions under which fractures (or other opening-mode fractures) form can best be described using fracture mechanics. K_I , the opening mode (or mode I) stress intensity factor, measures the magnitude of the stress concentration at the crack tip. For a vertical, uniformly loaded, planar fracture whose length is much greater than its height, $K_I = \Delta\sigma(\pi \cdot h/2)^{1/2}$, where $\Delta\sigma$ is the driving stress and h is fracture height (Lawn and Wilshaw, 1975). When K_I exceeds a critical value, K_{Ic} , the fracture will propagate. For stress concentration to occur, there must be fracture-opening displacement, which requires a positive driving stress.

Driving stress is defined as $\Delta\sigma = (p - \sigma_{Hmin})$, where σ_{Hmin} is the minimum in situ stress (compression is positive) and p is magnitude of pore pressure acting inside the fracture. Driving stress can be positive under two conditions—the local minimum stress acting on the fracture is tensile or the pore pressure in the fracture exceeds the minimum stress. Absolute tension may be

possible at or near the surface, but for fracturing at depth, where even the minimum stress is compressive, there must be some contribution from pore pressure.

Most subsurface rocks experience a negative driving stress most of the time. The special situation of a positive driving stress at depth can come about under three conditions—pore pressure increases to exceed minimum stress, minimum stress decreases to fall below the magnitude of the pore pressure, or a combination of both. Numerous processes active during basin evolution can lead to such conditions. For example, mechanisms that cause a decrease in minimum stress are uplift, cooling, gentle folding, and regional extension. All of these factors could potentially induce regional vertical fractures in subhorizontal beds. One diagenetic process that could contribute to pore pressure increase in sandstone is quartz cementation (Laubach, 1988; Lander, 1998).

The process by which fractures propagate under the influence of pore pressure is natural hydraulic fracturing. Pore pressure and in situ stress are not independent variables due to poroelastic effects in rock. So care must be taken in determining stress and pore pressure conditions under which opening-mode fracture propagation occurs. However, by properly combining the driving stress equation with an expression for minimum in situ stress, we can generalize about conditions necessary for fracture propagation, and this leads to the conclusion that natural hydraulic fracturing is possible for low pore pressure relative to overburden stress.

Recognizing that the critical stress intensity factor can be small under geologic conditions for saturated rocks (Atkinson and Meredith, 1987; Olson, 1993), for illustration we assume a positive driving stress is sufficient for crack growth (Engelder and Lacazette, 1990). For a positive driving stress, the following condition is necessary: $p > \sigma_{\min}$. The expression for minimum stress due to gravitational loading only is: $\sigma_{\min} = \nu/(1-\nu) (\sigma_{\text{overburden}} - \alpha p) + \alpha p$, where ν is Poisson's Ratio, α is Biot's poroelastic constant, and $\sigma_{\text{overburden}}$ is vertical stress from overburden. Combining these two equations gives the pore pressure required for fracturing in terms of material properties and overburden stress required for positive driving stress, $P > (\nu\sigma_{\text{overburden}})/(1-\nu+2\nu\alpha-\alpha)$.

Inspection of this relation shows that fracturing may require pore pressure from as small as 0.1 times the overburden for $\nu=0.1$ and $\alpha=0$ to equal the overburden stress for any Poisson's Ratio and $\alpha=1$. Typical numbers for rock are $\nu=0.2$ and $\alpha=0.6$, which predicts a pore pressure of 0.5 times overburden for fracturing to occur, without reducing minimum stress due to tectonics or other processes. This value is just slightly over hydrostatic in most basins. If we include the other effects that can reduce minimum stress, fracture mechanics relations predict that fracturing can take place at sub-hydrostatic pore pressures.

Aspects of quartz cementation are consistent with transient elevated pore fluid pressure. In the commonly encountered situation where scanned CL observations rule out local sources of silica via pressure solution, the low solubility of SiO_2 in water and observed large volumes of quartz cement imply large influxes of extraformational fluid. Yet cement precipitation decreases intergranular porosity and permeability, creating an increasingly efficient barrier to fluid movement as cementation proceeds (for example, Gal and others, 1998).

Cement modeling shows that rates of porosity loss due to quartz cementation can approach or surpass rates due to compaction, and unlike mechanical compaction, quartz cementation rates under conditions in sedimentary basins are not sensitive to changes in effective stress (Lander, 1998). Quartz diagenesis modeling based on assumptions of temperature-dependent quartz precipitation predicts fluid overpressure under a range of typical burial histories (Lander, 1998). Experimental diagenesis also supports elevated pore fluid pressure due to porosity reduction by cementation (Scholtz and others, 1995). If episodic, abrupt movements of pore fluid also occur in sedimentary basins, they will tend to intensify these effects. This interpretation is compatible with observed regional fracture timing relations and fracture orientations. In the formations we surveyed, crack-seal structures show that fracturing is typically contemporaneous with quartz precipitation (Laubach, 1988, 1997; Milliken, 1994; Reed and Laubach, 1998).

For sandstones, favorable conditions for fracturing occur when diagenetic processes combine to elevate pore pressure, perhaps to about 0.5 times overburden, with or without a reduction in minimum stress due to tectonics or other processes. Under these circumstances,

fracture strike is governed by anisotropic regional stress fields, which are persistent but do not necessarily imply specific tectonic events or significant shortening or extension to account for uniform patterns of fracture strike over large (~10 km²) areas.

Our results imply that in many—perhaps most—moderately to deeply buried sandstones, episodic increases in pore fluid pressure are the most important factor leading to creation of regional fracture sets. We conclude that fracturing is episodic because crosscutting relations of fractures with diagenetic phases show that sets of fractures typically cease opening at some time after fracturing initiates. Subsequently, fractures may be passively filled with cements that can be linked to later parts of the rock's burial history. The duration of fracturing and concomitant diagenetic episodes is unknown, although diagenetic models suggest that the coinciding diagenetic episodes could be on the order of tens of millions of years (Lander, 1998).

In the future, it may be feasible to combine tectonic, burial history, and quantitative diagenesis models to predict pore pressure and rock property changes and the timing of fracture formation. Geomechanical models that predict fracture patterns for given loading and rock property conditions (Olson, 1993), together with diagenesis models, may lead to progress in predicting regional fracture attributes. Key to refining such approaches will be more reliable methods to characterize subsurface fractures and thus test predictions.

Finally, these observations point to a need for caution in the use of outcrops as analogs for subsurface fracture patterns in some applications. Although many outcrop studies of fractures are aimed at understanding mechanical principles of fracture growth, and their objectives are not to match fracture patterns in a specific subsurface locality, in some studies outcrop observations are used to augment subsurface fracture observations. An example is conditioning fractured reservoir simulations. In these situations it is important to assess how closely patterns in outcrop are likely to match those in the subsurface. Our results suggest that a key ingredient in such an assessment must be comparison of the diagenetic history of subsurface and outcrop rocks. These observations point to criteria for evaluating outcrops as exact analogs for subsurface fracture patterns. The diagenetic history of the outcrop analog must be evaluated and modeled along with

the fracture attributes if the aim of the study is accurate extrapolation of subsurface fracture patterns.

Regional fractures (opening-mode fractures or joints) are commonly said to be ubiquitous structures in the Earth's crust, yet the basinal conditions that lead to their formation in the subsurface is imperfectly understood. A key ingredient in understanding creation of such fractures is an appreciation of how progressive diagenesis can interact with fracturing, evolving rock properties and paleo pore-fluid pressure.

Core observations in a variety of settings show an unexpected but repeated association between precipitation of quartz cement and opening of regional fractures in sandstone. This association is marked by crack-seal structure and the preservation of fracture porosity in opening-mode fractures having apertures greater than about 0.5 mm, and by arrays of quartz-filled microfractures disseminated throughout the rock mass. These observations, in the context of recent diagenesis modeling results, suggest that for many moderately to deeply buried sandstones having quartz cement, episodic increases in pore fluid pressure was the key factor leading to fracture creation. Contrary to some recent models, this conclusion implies that regional fractures do not necessarily reflect specific tectonic events.

REFERENCES

- Aguilera, R., 1980, Naturally fractured reservoirs: Tulsa, PennWell Publishing, 703 p.
- Apostol, T.M., 1957, Mathematical Analysis: Reading, Massachusetts, Addison-Wesley Publishing, 559 p.
- Apotria, T., Kaiser, C. J., and Cain, B. A., 1994, Fracturing and stress history of the Devonian Antrim Shale, Michigan Basin, *in* Nelson, P. P., and Laubach, S. E., eds., Proceedings, North American Rock Mechanics Symposium, v. 1: Rotterdam, Balkema, p. 809–816.
- Atkinson, B. K. and Meredith, P. G., 1987, The theory of subcritical crack growth with applications to minerals and rocks. Atkinson, B. K., ed., Fracture Mechanics of Rock, Academic Press, Orlando, p. 111–116.
- Baecher, G. B., and Lanney, N. A., 1978, Trace length biases in joint surveys: 19th U.S. Symposium on Rock Mechanics, p. 56–65.
- Baecher, G.B., N.A. Lanney, and H.H. Einstein, 1977, Statistical description of rock properties and sampling: 18th US Symposium on Rock Mechanics, p. 5C1.1 - 5C1.8.
- Barton, C.A., and M.D. Zoback, 1992, Self-similar distribution and properties of macroscopic fractures at depth in crystalline rock in the Cajon Pass scientific drill hole: Journal of Geophysical Research, v. 97, p. 5181-5200.
- Barton, C.C., and P.A. Hsieh, 1989, Physical and hydrologic-flow properties of fractures: Washington, D.C., American Geophysical Union, 28th International Geological Congress Field Trip Guidebook T385, 36 p.

- Belfield, W., 1994, Multifractal characteristics of natural fracture apertures: *Geophysical Research Letters*, v. 21, no. 24, p. 2641–2644.
- Belfield, W.C., and J.P. Sovich, 1995, Fracture statistics from horizontal wellbores: *Journal of Canadian Petroleum Technology*, v. 34, no. 6, p. 47-50.
- Bird, R. B., Stewart, W. E., and Lightfoot, E. N., 1960, *Transport Phenomena*, John Wiley & Sons, New York.
- Brown, S.R., H.W. Stockman, and S.J. Reeves, 1995, Applicability of the Reynolds equation for modeling fluid flow between rough surfaces: *Geophysical Research Letters*, v. 22, p. 2537-2540.
- Chen, J., Miller, M. A., and Sepehrnoori, K., 1991, Comparisons of counter-current imbibition transfer functions in dual-porosity models of naturally fractured reservoirs: *In Situ*, v. 15, no. 2.
- Chen, J., Miller, M. A., and Sepehrnoori, K., 1995, Investigations of matrix-fracture transfer flows in dual-porosity modeling of naturally fractured reservoirs: SPE 29562, to be presented at 1995 Society of Petroleum Engineers Rocky Mountain Section Regional Low Permeability Reservoirs Symposium and Exhibition.
- Childs, C., J.J. Walsh, and J. Watterson, 1990, A method for estimation of the density of fault displacements below the limit of seismic resolution in reservoir formations, *in* A.T. Buller, E. Berg, O. Hjelmeland, J. Kleppe, O. Torsaeter, J.O. Aasen, eds., *North Sea Oil and Gas Reservoirs II*: London, Graham and Trotman, p. 309-318.
- Cladouhos, T.T., and Marrett, R., 1996, Are fault growth and linkage models consistent with power-law distributions of fault lengths?: *Journal of Structural Geology*, v. 18, p. 281-293.

- Clark, M.B., Brantley, S.L., and Fisher, D.M., 1995, Power-law vein-thickness distributions and positive feedback in vein growth: *Geology*, v. 23, p. 975-978.
- Clauser, C., 1992, Permeability of crystalline rock: *Eos*, v. 73, p. 233 and 237-238.
- Collins, E. W., Hovorka, S. D., and Laubach, S. E., 1992, Fracture systems in Austin Chalk, North-Central Texas, *in* Schmoker, J. W., Coalson, E. B., and Brown, C. A., eds., Geological studies relevant to horizontal drilling, Rocky Mountain Association of Geologists, p. 75-88.
- CORELAB, 1995, Fracture Analysis Report for Amoco Production Co. Riddle D LS No. 4A. San Juan County Field. San Juan County, New Mexico. Midland, TX, 8 p.
- CORELAB, 1996, Petrographic Study for AMOCO ATTC. RIDDLE D LS #4 well. San Juan County, New Mexico. File 196005. Corrollton, TX, 8 p.
- Crouch, S. L. and Starfield, A. M. (1983). *Boundary Element Methods in Solid Mechanics*. George Allen and Unwin, London, U. K.
- Dahlquist, G., and Å . Bjö rck, 1974, *Numerical Methods*: Englewood Cliffs, N.J., Prentice-Hall, 573 p.
- Dershowitz, W. S. and Einstein, H. H., 1988. Characterizing rock joint geometry with joint system models. *Rock Mech. Rock Eng.*, 21, 21-51.
- Dershowitz, W., and LaPointe, P., 1994, Discrete fracture approaches for oil and gas applications, *in* Nelson, P. P., and Laubach, S. E., eds., *Rock Mechanics, Models and Measurements: Proceedings, North American Rock Mechanics Symposium*, v. 1, Rotterdam, Balkema, p. 19-30.

- Dershowitz, W., Lee, G., Geier, J., Hitchcock, S., and LaPointe, P., 1993, User documentation: FracMan Interactive Discrete Feature Data Analysis, Geometric Modeling, and Exploration Simulation: Seattle, WA, Golder Associates, variously paginated.
- Dutton, S. P., and Land, L., 1988, Cementation and burial history of a low-permeability quartzarenite, Lower Cretaceous Travis Peak Formation, East Texas: Geological Society of America Bulletin, v. 100, no. 8, p. 1271–1282.
- Dvorkin, J., and Nur, A., 1992, Filtration fronts in pressure compliant reservoirs: Geophysics, v. 57, p. 1089–1092.
- Dyke, C. C., 1991, How sensitive is natural fracture permeability at depth to variation in effective stress? Conference preprints, Fractured and Jointed Rock Masses, LBL-32379, p. 88–95.
- Engelder, T., 1985, Loading paths to joint propagation during a tectonic cycle: an example from the Appalachian Plateau, U.S.A.: Journal of Structural Geology, v. 7, p. 459–476.
- Engelder, T., and Lacazette, A., 1990, Natural hydraulic fracturing, in Barton, C., Stephansson, O., eds., Rock Joints: Balkema, Rotterdam, p. 35–43.
- Erdogan, F. and Sih, G. C. (1963). On the crack extension in plates under plane loading and transverse shear. ASME Transactions, 85, 519-527.
- Folk, R. L., 1980, Petrology of Sedimentary Rocks. Hemphill Publishing Company, Austin, TX, 184 p.
- Gal, D., Dvorkin, J., and Nur, A. M., 1998, A physical model for porosity reduction in sandstones: Geophysics, v. 63, no. 2, p. 454–459.

- Gross, M.R., and T. Engelder, 1995, Strain accommodated by brittle failure in adjacent units of the Monterey Formation, U.S.A.: scale effects and evidence for uniform displacement boundary conditions: *Journal of Structural Geology*, v. 17, p. 1303-1318.
- Gudmundsson, A., 1987a, Tectonics of the Thingvellir fissure swarm, SW Iceland: *Journal of Structural Geology*, v. 9, p. 61-69.
- Gudmundsson, A., 1987b, Geometry, formation and development of tectonic fractures on the Reykjanes Peninsula, southwest Iceland: *Tectonophysics*, v. 139, p. 295-308.
- HALLIBURTON, 1995, EMI. San Juan 32-9 well, San Juan County, New Mexico. Service logging report for Meridian Oil Company. Confidential.
- Hatton, C.G., I.G. Main, and P.G. Meredith, 1993, A comparison of seismic and structural measurements of scaling exponents during tensile subcritical crack growth: *Journal of Structural Geology*, v. 15, p. 1485-1495.
- Hatton, C.G., I.G. Main, and P.G. Meredith, 1994, Non-universal scaling of fracture length and opening displacement: *Nature*, v. 367, p. 160-162.
- Hatton, C.G., Main, I.G., and Meredith, P.G., 1994, Non-universal scaling of fracture length and opening displacement: *Nature*, v. 367, p. 160-162.
- Heffer, K.J., and T.G. Bevan, 1990, Scaling relationships in natural fractures—data, theory and applications, *in* Proceedings of the Second European Petroleum Conference: SPE paper 20981, p. 367-376.
- Hubbert, M. K., and Rubey, W. W., 1959, Mechanics of fluid-filled porous solids and its application to overthrust faulting: *Geol. Soc. Am. Bull.*, v. 70, p. 115-166.

- Jensen, J. L., Lake, L. W., Corbett, P. M. W., and Goggin, D. J., 1997, *Statistics for Petroleum Engineers and Geoscientists*, Prentice Hall, Englewood Cliffs, NJ.
- Johnston, J.D., 1992, The fractal geometry of vein systems: the potential for ore reserve calculation, *in* A.A. Bowden, G. Earls, P.G. O'Connor, and J. Pyne, eds., *The Irish Minerals Industry 1980-1990*: Dublin, Association for Economic Geology, p. 105-117.
- Johnston, J.D., and McCaffrey, K.J.W., 1996, Fractal geometries of vein systems and the variation of scaling relationships with mechanism: *Journal of Structural Geology*, v. 18, p. 349-358.
- Kasap, E., and Lake, L. W., 1989, An analytical method to calculate the effective permeability tensor of a grid block and its application in an outcrop study: *Proceedings, Tenth SPE Symposium on reservoir simulation*, SPE 18434.
- Kazemi, H., Merrill, L. S., Porterfield, K. L., and Zeman, P. R., 1976, Numerical simulation of water-oil flow in naturally fractured reservoirs: *SPE*, p. 317-326.
- Kulander, B. R., Dean, S. L., and Ward, B. J. Jr., 1990. *Fractured Core Analysis. Interpretation, Logging, and Use of Natural and Induced Fractures in Core*. A.A.P.G. *Methods in Exploration Series*, No 8., Tulsa, OK., 88 p.
- Kulatilake, P. H. S. W., Wathugala, D. N., and Stephasson, O., 1993, Joint network modeling with a validation exercise in Stripa mine, Sweden. *Int. J. Rock Mech. Min. Sci. & Geomech Abstr.*, 30-5, 503-526.
- Lake, L., 1989, *Enhanced Oil Recovery*, Prentice Hall, Englewood Cliffs, NJ.
- Lamb, H., 1932, *Hydrodynamics*: New York, Dover Publications, 738 p.

- Lander, R. H., 1998, Effect of sandstone diagenesis on fluid overpressure development (abs.): AAPG Annual Convention Abstracts.
- LaPointe, P., 1981, Analysis of the spatial variation in rock mass properties through geostatistics: Proceedings, 21st U.S. Symposium on Rock Mechanics, p. 570–580.
- Laubach, S. E., 1988, Subsurface fractures and their relationship to stress history in East Texas Basin sandstone: *Tectonophysics*, v. 156, p. 37–49.
- Laubach, S. E., 1989, Paleostress directions from the preferred orientation of closed microfractures (fluid-inclusion planes) in sandstone, East Texas Basin, U.S.A.: *Journal of Structural Geology*, v. 11, p. 603–611.
- Laubach, S. E., 1992, Fracture networks in selected Cretaceous sandstones of the Green River and San Juan basins, Wyoming, New Mexico, and Colorado, *in* Schmoker, J. W., Coalson, E. B., and Brown, C. A., eds., *Geological studies relevant to horizontal drilling*: Rocky Mountain Association of Geologists, p. 61–74.
- Laubach, S. E., 1997, A method to detect natural fracture strike in sandstones: *AAPG Bulletin*, v. 81, no. 4.
- Laubach, S. E., Clift, S. J., Hamlin, H. S., Dutton, S. P., Hentz, T. F., Baek, Hwanjo, and Marin, B.A., 1994, Geology of a stratigraphically complex natural gas play: Canyon Sandstones, Val Verde Basin, Texas: The University of Texas at Austin, Bureau of Economic Geology topical report prepared for Gas Research Institute, 135 p.
- Laubach, S. E., Hentz, T. F., Johns, M. K., Baek, H., and Clift, S. J., 1995, Using diagenesis information to augment fracture analysis. The University of Texas at Austin Bureau of Economic Geology, GRI Report no.94/0455., Austin, TX, 189 p.

- Laubach, S. E., Mace, R. E., and Nance, H. S., 1995, Fault and fracture swarms in a normal fault zone: Proceedings, 2nd International Conference on Mechanics of Jointed and Faulted Rock.
- Laubach, S. E., Marrett, R., Olson, J., and Scott, A. R., 1998, Characteristics and origins of coal cleat: a review: *International Journal of Coal Geology*, v. 35, p. 175–207.
- Laubach, S. E., Milliken, K. L., Clift, S. J., Burns, S. J., and R. Reed, 1996. New subsurface characterization methods for fractured siliciclastic rocks: GSA 30th Annual South Central Section, Austin, March 11-12.
- Laubach, S.E., 1992, Fracture networks in selected Cretaceous sandstones of the Green River and San Juan basins, Wyoming , New Mexico, and Colorado, *in* J.W. Schmoker, E.B. Coalson, and C.A. Brown, eds., *Geological Studies Relevant to Horizontal Drilling: Examples from Western North America*: Denver, Rocky Mountain Association of Geologists, p. 115-127.
- Lawn, B. R., and Wilshaw, T. T., 1975, *Fracture of Brittle Solids*: Cambridge Univ. Press, Cambridge, 204 p.
- Long, J., 1984, Investigation of equivalent porous medium permeability in networks of discontinuous fractures: University of California, Berkeley, Ph.D. dissertation.
- Marret, R. and Laubach, S. E., 1997, Diagenetic controls on fracture permeability and scaling: *Int. J. Rock Mech. & Min. Sci.* v. 34, no. 3-4.
- Marrett, R., 1996, Aggregate properties of fracture populations: *Journal of Structural Geology*, v. 18, p. 169-178.
- Marrett, R., 1997, Permeability, porosity, and shear wave anisotropy from scaling of open fracture populations, *in* Hoak, T.E., Blomquist, P.K., and Klawitter, A. (Editors), *Fractured*

Reservoirs: Descriptions, Predictions and Applications: Rocky Mountain Association of Geologists Guidebook.

Marrett, R., and Allmendinger, R. W., 1992, Amount of extension on "small" faults: an example from the Viking graben: *Geology*, v. 20, p. 47-50.

Marrett, R., and R.W. Allmendinger, 1991, Estimates of strain due to brittle faulting: sampling of fault populations: *Journal of Structural Geology*, v. 13, p. 735-738.

Marrett, R., in review, Permeability, porosity, and seismic anisotropy from scaling of open fracture populations: *Geology*.

Marrett, R., 1996. Aggregate properties of fracture populations: *Journal of Structural Geology*, 18, 2/3, p. 169-178

McCaffrey, K.J.W., J.D. Johnston, and M. Feely, 1993, Use of fractal statistics in the analysis of Mo-Cu mineralisation at Mace Head, County Galway: *Irish Journal of Earth Sciences*, v. 12, p. 139-148.

McCaffrey, K.J.W., J.D. Johnston, and M.A. Loriga, 1994, Variation of fractal dimension in vein systems, in P.A. Cowie, I.G. Main, and R. Knipe, eds., *Fault populations: Edinburgh, Tectonic Studies Group Special Meeting*, p. 103-105.

McNaughton, D., and Garb, F., 1975, Finding and evaluating petroleum accumulations in fractured reservoir rock: Matthew Bender & Co., *Exploration and Economics in the Petroleum Industry*, v. 13.

Miller, R., 1992, User documentation, MAFIC Matrix/Fracture Hydraulic Interaction Code with Solute Transport: Seattle, WA, Golder Associates, variously paginated.

- Milliken, K. L., 1994, The widespread occurrence of healed microfractures in siliciclastic rocks: evidence from scanned cathodoluminescence imaging, *in* Nelson, P. P., and Laubach, S. E., eds., *Rock Mechanics, Models and Measurements: Proceedings, North American Rock Mechanics Symposium*, v. 1: Rotterdam, Balkema, p. 825–832.
- Milliken, K. L., and Land, L. S., 1994, Evidence of fluid flow in microfractures in geopressed shales: discussion: *American Association of Petroleum Geologists Bulletin*, v. 78, p. 1637–1640.
- Molenaar, C. M. and Blair J. K., 1990, Stratigraphic cross section of Upper Cretaceous rocks across the San Juan Basin, northwestern New Mexico and southwestern Colorado. *In*: Carter, L. M. H (Editor), *USGS research on energy resources, 1990, programs and abstracts*. USGS Circular, Reston VA, p.55-56
- Mueller, M.C., 1991, Prediction of lateral variability in fracture intensity using multicomponent shear-wave surface seismic as a precursor to horizontal drilling in the Austin Chalk: *Geophysical Journal International*, v. 107, p. 409-415.
- Narr, W., 1991, Fracture density in the deep subsurface; techniques with application to Point Arguello oil field: *AAPG Bulletin*, v. 75, no. 8, p. 1300–1048.
- National Research Council, 1996, *Rock Fractures and Fluid Flow*: National Academy Press, Washington, 551 p.
- Nelson, R. A., 1985, *Geological analysis of naturally fractured reservoirs*: Gulf Pub. Co., Houston, 320 p.
- Nelson, R. A., 1987, Fractured reservoirs: turning knowledge into practice: *Journal of Petroleum Technology*, p. 407–414.

- Nelson, R.A., 1985, Geologic analysis of naturally fractured reservoirs: Houston, Gulf Publishing, 320 p.
- Neuman, S.P., 1994, Generalized scaling of permeabilities: validation and effect of support scale: *Geophysical Research Letters*, v. 21, p. 349-352.
- Olson, J. E. and Pollard, D. D., 1989, Inferring paleostresses from natural fracture patterns: A new method. *Geology*, 17, 345-348.
- Olson, J. E., 1993, Joint pattern development: Effects of subcritical crack growth and mechanical crack interaction. *Journal of Geophysical Research*, 98-B7, 12251-12265.
- Ortega, O. J., and Marrett, R., 1997, Significance of finite layer thickness on scaling of fractures (abs.): *Geological Society of America Abstracts with programs*, v. 28, no. 7.
- Ortega, O. J., Marrett, R., Hamlin, S., Clift, S., and Reed, R., 1998, Quantitative macrofracture prediction using microfracture observations: a successful case study in the Ozona gas Field, West Texas (abs.): *AAPG Annual Convention Abstracts*, v. 7.
- Pacheco, J.F., C.H. Scholz, and L.R. Sykes, 1992, Changes in frequency-size relationship from small to large earthquakes: *Nature*, v. 355, p. 71-73.
- Peacock, D.C.P., 1991, A comparison between the displacement geometries of veins and normal faults at Kilve, Somerset: *Proceedings of the Ussher Society*, v. 7, p. 363-367.
- Pollard, D. D., Segall, P., and Delaney, P. T., 1982, Formation and interpretation of dilatant echelon cracks. *Geological Society of America Bulletin*, 93, 1291-1303.
- Pollard, D.D., and A. Aydin, 1988, Progress in understanding jointing over the past century: *Geological Society of America Bulletin*, v. 100, p. 1181-1204.

- Reed, R. M., and Laubach, S. E., 1996, The role of microfractures in the development of quartz overgrowth cements in sandstones: New evidence from cathodoluminescence studies: GSA, Abstracts with Programs, 1996 Annual Meeting, Denver Colorado. October 28-31, p. A-280.
- Reed, R. M., and Laubach, S. E., 1998, Density and distribution of microfractures in sandstones: importance to diagenesis (abs.): AAPG Annual Convention Abstracts, v. 7.
- Renshaw, C. E. and Pollard, D. D., 1994, Numerical simulation of fracture set formation: A fracture mechanics model consistent with experimental observations. *Journal of Geophysical Research*, 99-B5, 9359-9372
- Rouleau, A., and J.E. Gale, 1985, Statistical characterization of the fracture system in the Stripa granite, Sweden: *International Journal of Rock Mechanics and Mining Science*, v. 22, p. 353-367.
- Sabins, F. F. Jr., 1962, Grains of detrital, secondary, and primary dolomite from Cretaceous strata of the western interior: *GSA Bull.*, 73, p. 1183-1196.
- Sanderson, D.J., S. Roberts, and P. Gumiel, 1994, A fractal relationship between vein thickness and gold grade in drill core from La Codosera, Spain: *Economic Geology*, v. 89, p. 168-173.
- Scholz, C.H., and P.A. Cowie, 1990, Determination of total strain from faulting using slip measurements: *Nature*, v. 346, p. 837-839.
- Scholtz, C.H., Leger, A., Karner, S.L., 1995, Experimental diagenesis: exploratory results: *Geophys. Res. Lett.*, v. 22, p. 719-722.

- Schultz-Ela, D. D., and Yeh, J., 1992, Predicting fracture permeability from bed curvature, *in* Tillerson, J. R., and Wawersik, W. R., eds., Rock mechanics: Proceedings, 33rd U.S. Symposium on Rock Mechanics: Rotterdam, Balkema, p. 579–589.
- Schultz-Ela, D. D., Jackson, M. P. A., and Vendeville, B. C., 1993, Mechanics of active diapirism: Tectonophysics, v. 228, p. 275–312.
- Secor, D. T., 1965, Role of fluid pressure in jointing: Am. J. Sci., v. 263, p. 633–646.
- Segall, P. and Pollard, D. D., 1983, Joint formation in granitic rock of the Sierra Nevada. Geological Society of America Bulletin, 94, 563-575.
- Segall, P., 1984, Formation and growth of extensional fracture sets. Geological Society of America Bulletin, 95, 454-462.
- Segall, P., 1984a, Rate-dependent extensional deformation resulting from crack growth in rock. Journal of Geophysical Research, 89-B6, 4185-4195.
- Sharp, J.M. Jr., 1993, Fractured aquifers/reservoirs: approaches, problems and opportunities, *in* S.B. Banks, and D. Banks, eds., Hydrogeology of hard rocks: Oslo, Memoires of the 24th Congress of the International Association of Hydrogeology, p. 23-38.
- Skjærstein, A., E. Fjær, and J.S. Rathore, 1995, Acoustic anisotropy of rocks with non-circular cracks: 57th European Association of Geoscientists and Engineers meeting, Paper P021.
- Snow, D.T., 1969, Anisotropic permeability of fractured media: Water Resources Research, v. 5, p. 1273-1289.
- Snow, D.T., 1970, The frequency and apertures of fractures in rock: International Journal of Rock Mechanics and Mining Science, v. 7, p. 23-40.
- Stauffer, D., 1985, Introduction to Percolation Theory, Taylor and Francis, London.

- Thomsen, L., 1995, Elastic anisotropy due to aligned cracks in porous rock: *Geophysical Prospecting*, v. 43, p. 805-829.
- Underwood, E.E., 1970, *Quantitative stereology*: Reading, Massachusetts, Addison-Wesley Publishing, 274 p.
- Vermilye, J.M., and C.H. Scholz, 1995, Relation between vein length and aperture: *Journal of Structural Geology*, v. 17, p. 423-434.
- Walsh, J.J., and Watterson, J., 1993, Fractal analysis of fracture patterns using the standard box-counting technique: valid and invalid methodologies: *Journal of Structural Geology*, v. 15, p. 1509-1512.
- Warpinski, N., 1989, Elastic and viscoelastic calculations of stresses in sedimentary basins: *SPE Formation Evaluation*, June 1992, p. 123-131.
- Wolff, M., Miller, M. A., and Lake, L. W., 1990, Oil recovery from geologically-based fracture networks: *In Situ*, v. 14, no. 4, p. 407-427.
- Wolff, M., Oney, B., Lake, L. W., and Miller, M. A., 1991, On the imbibition of oil from fractured reservoir matrix blocks: *In Situ*, v. 15, no. 1, p. 1-33.
- Wong, T.-F., J.T. Fredrich, and G.D. Gwanmesia, 1989, Crack aperture statistics and pore space fractal geometry of Westerly Granite and Rutland Quartzite: implications for an elastic contact model of rock compressibility: *Journal of Geophysical Research*, v. 94, p. 10267-10278.
- Wu, Gang, 1992, Pore-network evolution induced by interaction between minerals and migrating fluids: implications for rock diagenesis: The University of Texas at Austin, Ph.D. dissertation, 340 p.

Wu, H. and Pollard, D. D., 1993, Effect of strain rate on a set of fractures. *Int. J. Rock Mech. Min. Sci. & Geomech Abstr.*, 30-7, 869-872.

Wulf, A. G., 1996, Magnetic Orientation of Core Samples from Sunray H Com #6 for AMOCO. Department of Geological Sciences. University of Texas at Austin. Internal Report.

Yacobi, B. G., and Holt, D. B., 1990, Cathodoluminescence microscopy of inorganic solids: Plenum, New York, 292 p.

PART II. CHARACTERIZATION AND SCALING

INTRODUCTION

Fractures are present in all rock masses. The study of fracture systems in rocks has a variety of applications in human activities. Fractures are major fluid flow conduits in the subsurface and they are also important depositories of mineral resources of economic value. The study of fractures is essential in civil engineering studies and for quality control of man-made artifacts.

Open-mode fracture size distributions have been studied by a few authors (Gudmundsson, 1987; Heffer and Bevan, 1990; Barton and Zoback, 1992; Gillespie et al., 1993; Hatton et al., 1994; Sanderson et al., 1994; Johnston and McCaffrey, 1996, Marrett, 1997). These authors show that open-mode fracture systems are organized such that their size distributions follow power-laws (i.e. fractal relationships). A common characteristic of fractal systems is that they are governed by the interaction of individuals in a population. In the case of fracture systems, the growth of individual fractures is affected by their interaction with other growing fractures in the system (Olson, 1993; 1997).

Deviations from a simple power-law relationship by the smallest and largest observed fractures have been recognized in fracture populations. Sampling biases have been used to explain these deviations (Baecher and Lanney, 1978; Laslett, 1982; Barton and Zoback, 1992; Hatton et al., 1994, Pickering et al., 1995). On the other hand, Marrett (1996) shows how sampling topology affects observed fracture-attribute scaling giving an alternative explanation for these deviations.

The influence of rock heterogeneities on fault scaling has been studied by Wojtal (1994, 1996) and could explain some of the "anomalies" observed in open-mode fracture size distributions. Rock masses are complex materials showing a high degree of heterogeneity at certain scales. For example, clastic sedimentary sequences are most obviously heterogeneous at

the scale of the beds (macroscopic scale) and also at the grain scale (microscopic scale). This report focuses on the influence of these heterogeneities on size distributions of fractures and explores the possibilities of using microfracture data to characterize the macrofractures.

By definition, microfractures are only visible using magnification devices (Laubach, 1997), in contrast to macrofractures, which are visible to the unaided eye. Yet within these categories, fractures may have a wide range in size. In this study, microfractures range from 1 micron to 1 mm. Macrofractures range from 1 mm to more than 10 meters.

Structural intuition suggests that accurate extrapolation of fracture characteristics over many orders of magnitude in size from the microscale to the macroscale is fraught with potential danger. For example, many different types of mechanical discontinuities, such as grain boundaries and bed boundaries, are known to exist in sedimentary rocks. It is widely recognized that such boundaries can affect the propagation of fractures. Yet the orientation of micron-scale fractures is consistent with the orientation of meter-scale fractures in some sandstones (Laubach, 1997), suggesting that under some circumstances the extrapolation of some fracture attributes is justified. Thus this study attempts the first systematic, rigorous investigation of extrapolation of microscopic data to predict macroscopic scale fracture-size distributions in hydrocarbon reservoir rocks and their outcrop analogs.

Gas-producing sandstones of the Mesaverde Group in the San Juan Basin, New Mexico, were selected for the study. These rocks were chosen based on the large amount of high quality subsurface information available and the high quality of the outcrops. Microfractures in these sandstones can be revealed in an unprecedented manner using the cathodoluminescence detector attached to a Scanning Electron Microscope (SEM-CL). Quartz-filled microfractures in sandstones are almost invisible using optical microscopy but slight differences of the luminescence of quartz grains and quartz fill in fractures can be detected under the SEM-CL, allowing the collection of microfracture data in these rocks (Laubach and Milliken, 1996).

Hypotheses to be Tested and Approach Taken

The present study tests the following hypotheses:

1. Can microfracture information be used to predict some aspects of macrofracture characteristics such as: orientation, size and frequency?
2. Are fracture geometrical parameters, like fracture length and fracture aperture, fractal systems that follow power laws of the form: $N=Sa^c$; where, N is the cumulative number of fractures, S is the size of the sampled space, b is the fracture size (fracture aperture in this case), and a and c are scaling constants?
3. Are the boundaries of the mechanical layer in which fractures develop important limits on fracture growth and do they have an effect on the scaling relationships of fractures and fluid flow through them?

A strategy was established to test the above hypotheses:

1. Macrofractures were described from large outcrops and from core.
2. Microfractures were described in core and outcrop samples using petrographic microscope and SEM-CL.
3. Statistical analysis and comparison of microscopic scale and macroscopic scale data were carried out.

Implications and Importance

The use of microfracture data to predict macrofracture characteristics may have a major impact on fractured systems characterization with applications to the exploration and exploitation of oil, gas, minerals and water resources. In the subsurface, cores are the only direct source of geological macrofracture data and cores are usually scarce, not oriented and represent a very limited volume of the fractured rock.

Geophysical logs are at present the best way to indirectly detect macrofractures in the subsurface. Image logs provide information on the fractures intersecting the walls of the borehole

but only macrofractures can be detected with this tool and there is potential for misinterpretation. Extrapolations from the well bore to the rest of the rock volume are limited by incomplete sampling. Additionally, the scarcity of macrofractures in the subsurface puts severe limitations to the use of image logs in vertical boreholes for the characterization of fracture systems. If size-distributions vary vertically, the limited sampling that can be achieved in vertical wells is inadequate for assessing fracture-size distributions.

As this study helps demonstrate, abundant microfracture data can be collected from small areas (few mm²) of a thin section under the SEM-CL in many siliciclastic rocks. If reliable predictions of macrofracture characteristics are possible based on microscopic data collected rapidly from small areas, small oriented samples will augment the information about the macrofractures in terms of orientation, size distribution and frequency. Beds with different composition, diagenesis or thickness often show different fracture frequencies and even different fracture orientations. The prediction of which beds are more likely to have large fractures and what orientations and spatial frequencies those fractures have, carries important economic implications and adds profound insight on the basic physic and mechanic principles of how fractures develop in buried rocks.

REGIONAL SETTING

The objectives of this study require the selection of fractured sedimentary units that provide high quality microfracture and macrofracture data from surface and subsurface. Sandstones of the Mesaverde Group can be found in the subsurface and in a rim of outcrops around the San Juan basin of New Mexico and Colorado (Fig. 1). Surface data were collected from sandstone pavements in the Ute Mountain Reservation to the northwest of Farmington, New Mexico. In this study a "pavement" is defined as a bedding-plane parallel exposure that is largely devoid of vegetation and other surface cover. Subsurface data were obtained from oriented cores of three wells in the Blanco-Mesaverde gas field, approximately 50 kilometers away from the outcrops, in the northern part of the basin.

San Juan Basin

The San Juan basin is a structural basin in the Four Corners area of the Colorado Plateau containing more than 5000 m of sedimentary rocks. The area may have been a depocenter as early as Early Paleozoic and experienced significant paleogeographic changes which have been recorded in the strata filling the basin. The deepest part of the basin is located towards its northern and northeastern margin. The structural contours of the basin at Cretaceous and younger levels indicate that strata uniformly dip toward the deepest part of the basin and are remarkably unaffected by folds or faults. The borders of the basin show more complex structural features like the Hogback monocline, Nacimiento uplift and Archuleta uplift. Triassic and Jurassic continental sediments were the first sediments to fill the basin. A major Cretaceous transgressive cycle composed of several minor advances and retreats of the coast line across the basin followed the continental deposition. During this time the Mesaverde Group, a thick clastic wedge, was deposited (Reynolds, 1994).

The end of subsidence and sedimentation of this second stage in the evolution of the San Juan basin is associated with the Laramide orogeny that affected the western part of North America from the Late Cretaceous to the Eocene (several authors in Schmidt et al., 1993). Finally, continental deposits were deposited during the Tertiary (Baltz, 1962; Peterson et al., 1965).

Fracture Systems in the San Juan Basin

The fracture systems of the San Juan basin have been studied by a number of authors (Kelley and Clinton, 1960; Gorham et al., 1979; Condon, 1988, 1989; Laubach and Tremain, 1991; Dart, 1992; Huffman and Condon, 1993). These studies primarily focused on description of the fracture systems in parts of the basin and in a variety of stratigraphic units. Several hypotheses have been proposed to explain these fracture systems in the context of the evolution of the Colorado Plateau (Gorham et al., 1972).

Mesaverde Group

According to Molenaar and Baird (1991), the Mesaverde Group can be subdivided in three units which, from bottom to top, are: The Point Lookout Formation (40-100 m), the Menefee Formation (50-650 m) and the Cliff House Formation (15-75 m). The Mesaverde Group is Late Cretaceous in age and it is underlain by the Mancos Shale and overlain by the Lewis Shale, also Cretaceous in age and laterally equivalent with the Mesaverde Group in part (Baltz, 1962; Molenaar and Baird, 1991). The Mesaverde Group represents a major regressive-transgressive cycle in the filling history of the basin from a sediment source located to the south (Fig. 2). In general terms, the Point Lookout Formation is a seaward-stepping set of nearshore sandstones, the Menefee Formation is a coastal plain assemblage and the Cliff House Formation is a set of landward-stepping nearshore sandstones (Reynolds, 1994; Pasternack, 1995).

Blanco-Mesaverde Gas Field

The Blanco-Mesaverde Gas Field is a giant hydrodynamically and stratigraphically controlled hydrocarbon trap (Berry, 1959; Rice, 1983). The production of gas comes from different sandstone units of the Mesaverde Group. The accumulation is controlled by the presence of nearshore sandstones in a belt that runs in northwest-southeast direction for about 120 km and with a width of about 55 km (Pasternack, 1995).

The sandstones of the Mesaverde Group are characterized in the subsurface by low porosity, on the order of 0 to 5% (Weir, 1996). The reservoirs have long been recognized as fractured reservoirs (Hollenshead and Pritchard, 1961). Fractures represent a minor contribution to the storage capacity of the system but they provide the dominant flow conduits to economically produce the reservoir (Weir, 1996). Maps comparing sandstone thickness with the locations of the most productive wells indicate that these wells do not necessarily occur in areas of thick sandstones as would be expected if matrix permeability were dominant (Pasternack, 1995). Most of the production is attributed to less than two percent of all wells. Operators speculate that these wells intercepted areas of localized permeability enhancement due to the presence of important fractures (“cracks”). “Crack” wells can produce at rates more than an order of magnitude above an average well (Pasternack, 1995).

Mesaverde Outcrops in Northwestern New Mexico

A significant geomorphic feature delineating the border of the San Juan basin is the Hogback monocline, an alignment of cuestas controlled by Cretaceous sandstones of the Mesaverde Group and adjacent units. The mesas and flat-irons of the Hogback in northwestern New Mexico develop large pavements of sandstone that allow the study of steeply dipping macrofractures in cross section and plan view. Westwater pavement and Cottonwood pavement (Fig. 1) were identified for analyses of the macro- and microscopic fracture systems in these sandstone pavements because of their large size and exceptional clean exposure.

OBSERVATION METHODS

Fracture systems of Mesaverde Group sandstones were characterized both macroscopically and microscopically. The source of subsurface fracture data was three oriented cores taken in producing intervals within the Mesaverde Group in the Blanco-Mesaverde gas field. Surface fracture data were collected on outcrops of the same units that were analyzed in the subsurface. The description of the fracture systems included measurement of geometrical and cement characteristics of the fractures as well as observation of cross-cutting relationships between different fracture sets. Fracture-size distributions and fracture orientations obtained from microfractures were compared with those obtained from macrofractures.

Macroscopic Data from Cores

The three cores used in this study (Tables 1 and 2) were each oriented using different techniques. The core from the Riddle D LS 4A well was the only one oriented before this study was initiated. The method used to orient this core was unconventional. The borehole was drilled at approximately 45° relative to bedding along an azimuth of 90°. The elliptical section of the stratification in the core was used to orient the core, considering that seismic reflection data show that the stratification is nearly horizontal.

The Sunray H Com #6 core was oriented using the so called "paleomagnetic" method. Three core segments containing natural macrofractures were selected for magnetic orientation (Table 3). To orient these cores, core plugs were subjected to progressive alternating field demagnetization in 10 steps from 10 to 400 Oersteds (1 to 40 millitesla). The magnetic remanence was measured with a superconducting magnetometer and the results were analyzed by the principal component method (Gose, 1996). The magnetic field detected is presumed to be recent and then the core can be referred to magnetic north.

Core segments containing macrofractures from the San Juan 32-9 well were oriented using image logs (Electric Micro Imager, EMI, Halliburton, 1995) Image logs are high-resolution microresistivity tools that provide an image of the walls of the wellbore from which features like bedding planes, sedimentary structures and fractures can be interpreted. These logs and the cores of the San Juan 32-9 well were correlated using sedimentary and structural features recognizable both in the core and on the image logs. The mismatch in depth was corrected for the core and true north was marked in the oriented core segments.

Well	Core Length (m)	Number of Thin Sections	Method of Orientation
Riddle D LS 4A	17.5	35	Inclined Well
Sunray H Com #6	13.1	16	Magnetic
San Juan 32-9	56.8	14	Image Log

Table 1. Summary of subsurface data sources used in the study.

Well	Formation	Depths of cored interval (m)
Riddle D LS 4A	Cliff House	1502-1537
Sunray H Comp 6	Cliff House	1472-1480
		1496-1527
San Juan 32-9	Cliff House	1692-1716
	Menefee	1783-1815
	Point Lookout	1814-1840

Table 2. Depth intervals and formations analyzed in wells.

Sample Group #	Sample number	Orientation of predefined line in core plug
1	5000.3	1.5°±13.7° W
	5000.4	
	5000.6	
	5000.7	
2	4986.7	30.9°±19.7° E
	4986.8	
	4986.9	
3	4984.0	Not reliable (Possible drilling induced remagnetization)
	4984.5	
	4984.7	

Table 3. Summary of magnetic analyses for the Sunray H Com #6 well.

Once the cores were oriented, a thorough description of the macrofractures present in them was made. The description included: depth of the upper tip of the fractures, height, aperture, strike, dip, and type of mineral fill in the fracture, if any. Natural and drilling induced fractures were distinguished based on the presence of cement in the fracture or distinctive drilling-induced fracture shapes (e.g. petal-centerline configurations, Kulander et al., 1990). The depth of lithologic contacts and the depth and type of samples taken from the core were also recorded. Appendix A includes tables with the fracture data collected from the cores.

Macroscopic Data from Outcrops

The exposure of fracture systems in sandstone pavements of the Mesaverde Group allowed the collection of three-dimensional data on the fracture shapes. Scattered lichen patches cover the top of the exposed sandstone surface and limit the visibility of macrofractures shorter than approximately 10 cm long. On the other hand, weathering helps in the identification of the fractures due to the difference in weathered color and resistance to erosion between the fracture fill and the host rock.

The selection of pavements for the study was a two-step process:

1. A study of 1:30000 scale aerial photographs provided a short list of potential study areas. Some of these areas were initially visited to determine the potential of the pavements for a macroscopic fracture study. Sandstone pavements appear in the air photos as clear patches with little vegetation.
2. An aircraft survey allowed the selection of the best places for study. Even though numerous pavements exist in the region, many of them are not very extensive, are partially covered by vegetation or have limited accessibility. Two fracture pavements were selected for study: Westwater pavement (Fig. 3) and Cottonwood pavement (Fig. 4).

Areas within the pavements with particularly well exposed swarms of open-mode fractures were selected for studies of macrofracture properties. Surveys along these areas were carried out to calculate the surface area of observation (Table 4). The selection of different size observation areas allowed the comparison of macrofractures larger and shorter than the thickness of the mechanical layer (Corbett et al., 1987).

Pavements	Formation	Bedding Dip ($^{\circ}$)	Area (m^2)		Samples
			Small	Large	
Westwater	Point Lookout	5	2000	13400	17
Cottonwood	Cliff House	10	200	2050	18

Table 4. Summary of outcrop pavements used in the study.

After highlighting and numbering the fractures using chalk, schematic maps of the fracture swarms were prepared and descriptions of the fracture properties were made (Fig. 5). Appendix B contains the data collected in the field, organized in tables.

Microscopic Data

Microfracture data were collected from both subsurface and surface samples. Based on observations in other formations (Laubach, 1997), I assumed that most microfractures related to macrofractures are oriented at high angles with the stratification. Thus, thin sections were cut from the samples in an orientation parallel to the stratification to speed collection of microfracture strike data. Standard petrographic analysis of the sandstones was carried out to determine texture, composition and paragenetic sequence of cements (Appendix C).

The thin sections were polished with aluminum and covered with a carbon coating (dark blue degree) for their study under the SEM-CL. The methodology to image microfractures included random shots throughout the thin section, systematic transects in predefined orientations or mosaics covering certain areas. Standard operating procedures are described by Milliken (1994). Magnification values were set on the order of 200x for general microfracture detection and 500x for close-ups.

Fracture length, maximum mechanical aperture and fracture strike were determined for each microfracture in the photographs (Appendix D). The Energy Dispersive x-ray Spectrum device (EDS) allowed the determination of the composition of microfracture fill.

Microfractures were classified using Laubach's (1997) microfracture classification, which distinguishes two categories of postdepositional fractures and transported fractures inherited from the sediment source area (categories I, II and II). A grading scheme derived from Laubach's (1997) classification assigned a ranking of microfractures based on the relationships of microfractures with grains, cement, and other microfractures. This ranking refers to the likelihood (suitability) that a microfracture is a product of the same processes that generated the macrofractures (see chapter on fracture orientation). Microfracture suitability is a genetic alternative to the term "reliability" in Laubach's (1997) purely descriptive classification, where "reliability" merely refers to the certainty with which microfractures can be documented to post-

date deposition of grains based on observed crosscutting relationships between fractures and cement.

Measurement of Fracture Orientation

The attitude of most macrofractures is nearly vertical, so only macrofracture strike was recorded in most cases. Occasionally, individual fractures change in orientation along strike; in these cases, the visually estimated average orientation of the trace was recorded. Rose diagrams of fracture strike were made to analyze the macrofracture orientation (see chapter on fracture orientation).

Microfracture orientations were measured directly from the photomicrographs using a protractor. Similarly, only the strike of the microfractures were recorded based on U-stage measurements in other formations which show that microfractures are also nearly vertical in most cases (Laubach, 1997). Rose diagrams for the microfractures were also prepared. Diagrams weighted microfracture data based on microfracture's suitability to predict macrofracture strike.

Measurement of Fracture Length

From core, macrofracture lengths in plan view cannot be obtained in most cases due to fracture lengths exceeding the diameter of the core. Fracture height (at least a minimum value) can be obtained in most cases. For the Riddle D LS 4A well, all the height values obtained are minimums because the core is inclined with respect to the stratification and the fractures are perpendicular to the stratification.

In outcrop, fracture length measurement is complicated by the challenge of defining what constitutes an individual fracture where multiple fracture strands are present. Some apparently long fractures are likely composed of shorter fractures that have become interconnected through fracture growth. Rock mechanics theory and experiments predict the way fractures can interconnect under different driving stress regimes (Olson, 1993), but no specific criteria have

been proposed to uniquely determine the lengths of individual fracture segments where they have become interconnected. Fractures frequently grow through the linkage of small fractures. Mechanics predicts that in the linkage process some segments of the original fractures are abandoned or they grow at slower rates than the interconnected segments.

Figure 6 shows the different types of fracture termination observed on the pavements. These different morphologies can be separated in three basic groups: isolated fractures (not connected), fractures connected to another fracture and having one isolated tip, and fractures connected with other fractures in more than one place.

- I. Isolated fracture tips are separate from any other fracture.
- II. Abrupt connections indicate that branch b terminates against or branches from throughgoing segment a.
- III. Hooked connections indicate that segment b has propagated towards segment a and terminated against it (Olson, 1993).
- IV. Bridge connections indicate that segment b has propagated towards segments a and c and terminated against both.
- V. Double-hooked terminations indicate the propagation and termination of en echelon fractures toward each other (Olson, 1993).

Although linkage is a significant mechanism of fracture growth, distinguishing between linked and unlinked fractures is commonly difficult. One important reason for this is that in many cases the recognition of a fracture connection depends on the observation scale. This is evident in fracture linkage classifications such as Laubach (1992) where "constricted" connections shift to either "connected" or "dead end" as the connection is viewed at greater magnification. Ideally, detailed observations would reveal the variation of fracture aperture in the vicinity of possible fracture connections and provide a basis for detecting the linkage of fractures. However, in most cases the apertures of macrofractures, especially at connection points, cannot be readily discerned in the field. None of these approaches addresses the problem

of mineral fill, which may preferentially clog the narrow connections between fracture segments. In such cases geometric linkage is not equivalent to linkage of fracture porosity.

The best approach to measuring the length of a fracture is to use criteria that uniquely identify fracture tips. That is, meaningful determination of fracture length hinges on the distinction between linked and unlinked fractures. Once the tips of a fracture are identified, depending on the evaluation of their linkage with other fractures, measuring its length is trivial. Below are the set of criteria used in this study, in descending order of applicability:

1. At the branch point of three connected fracture segments, the two segments having the most similar apertures are a throughgoing fracture and the third segment represents a different fracture.
2. If the material filling two interconnected fracture segments is continuous, then they are a single fracture.
3. If a connection between fracture segments is not discernible with the naked eye at a distance of approximately 1.5 m above a pavement surface, then the fracture segments are considered to be elements of a single fracture.

These criteria for defining macrofracture tips were also applied to microfractures, although significantly less fracture connectivity was observed at the microscopic scale. The recognition of microfracture linkage characteristics is influenced by the difficulties imaging the complete length of the microfractures. For example, some microfractures may be the same as grain boundaries, they can terminate against pores or they can simply be difficult to identify within the cement.

Rigorous fracture-length data analysis evaluated the type of distribution that best fits the observed population. The possible causes of artifacts in the fracture size distributions were also analyzed (see chapter on fracture size distributions). For example, Microfractures that continue past the borders of the microphotographs were also measured and their lengths correspond to the portions present inside the photographs. This procedure introduces an error that most strongly affects the longest microfractures, and consequently produces a systematic effect in the fracture length distribution.

In addition to two-dimensional sampling of fracture lengths, two-dimensional fracture heights were collected along Westwater Springs canyon to analyze fracture-height distribution and compare it with the fracture length data obtained from the pavements. This procedure allows to study the geometry of the fracture surfaces and the influence of fracture geometry on fracture-size distributions. Fracture length data were also collected along scanlines on Westwater pavement. The purpose of the one-dimensional data set was to test the approach of estimating two-dimensional fracture distributions using one-dimensional data (Marrett, 1996).

In order to study the effect of the mechanical layer thickness on fracture size distributions, fracture lengths smaller and larger than the thickness of the mechanical layer were studied on the Westwater and Cottonwood pavements. These fracture populations were analyzed separately using statistical methods. Error analysis allowed the selection of the best mathematical model for the fracture-size distributions observed allowing to compare the parameters of the fracture-size distributions of fractures larger and smaller than the mechanical-bed thickness.

Measurement of Fracture Apertures

The measurement of macrofracture apertures was done using feeler gauges, rulers and magnifiers and includes the width of any cementing material filling the fractures. Fracture aperture measurements correspond to the maximum mechanical aperture of the fracture. This value is assumed to be recorded by the material filling the space created during fracture formation and growth. The mechanical aperture is assumed to be a paleohydraulic aperture, which is the space in the fracture that allowed fluid flow at a certain time in the past. In cases where synkinematic fill occurs in fractures, marked by crack-seal texture, the hydraulic aperture at any point in time will be smaller than the final mechanical aperture.

Broken fractures, ones with walls no longer face to face in their original configuration and physically separated in non-continuous pieces, are abundant in cores. In these cases no reliable estimate of the fracture aperture can be obtained. Only a minimum fracture aperture can be estimated from the thickness of the remaining cement on the broken surfaces of such a fracture.

For these cores, the possibilities for obtaining meaningful fracture aperture distributions are limited.

Fracture apertures were also difficult to measure in the field because the fracture aperture, filled with quartz and carbonate, is usually surrounded by a fracture skin of carbonate-cemented sand grains in which the exact location of the walls of the original fracture is unclear even under magnification. In order to obtain better values for this fracture property, macrofracture apertures were measured in thin section using the petrographic microscope.

Microfracture aperture data were measured using optical or SEM-CL photomicrographs. These aperture values correspond to the maximum distinguishable apertures measured perpendicular to the fracture walls. Widths are exaggerated if fractures are not truly perpendicular to the stratification as assumed.

Other Data Collected

The type of connection for every fracture termination was recorded in the field, and where the termination was a branch point, the acute angle of connection was measured. The thickness of the mechanical layer in which the fractures are developed was also recorded. The definition of this layer depends on the stratigraphic consistency of upper and lower fracture tips within a bed or group of beds (Corbett et al., 1987; Helgeson and Aydin, 1991; Gross, 1993). The differences in mechanical properties of adjacent materials in a stratified sequence at the time when fractures formed controlled the vertical extent of the mechanical layer (Laubach et al., 1995). An estimate of the thickness of the mechanical layer for both pavements was determined by studying the fracture system in cross section along the canyons (Figs. 7 and 8). Often, significant changes in fracture frequency help determine the limits of the mechanical layer. These differences in fracture frequency can be controlled by compositional or depositional facies variations, authigenic cement distribution, porosity or a combination of these and other factors. In some cases the mechanical differences of the layers also correlate with differences in their resistance to weathering.

FRACTURE DIAGENESIS

Rock Texture and Mineralogy

Appendix C and Figure 9 show the grain size, sorting and predominant grain contacts for subsurface and outcrop samples used in this study. The textural characterization of the sandstones is based on 100 counts of grains per sample. The petrographic analysis is based on 400 point counts per sample. The sandstones analyzed are medium to very fine. Sandstones from the Cliff House Formation show larger average grain sizes in outcrop and in the Sunray H Com #6 well than in the Riddle well. This result agrees with previous interpretations (Molenaar and Baird, 1991) of environments of deposition in terms of the relative position of these areas and the direction of transport of sediments at the time of deposition. Similarly, the average grain size of the Point Lookout Formation sandstones in outcrop is larger than in the San Juan 32-9 well, located basinward of the outcrops. The degree of sorting of the sandstones also diminishes towards the paleodepocenter of the basin.

The degree of compaction is low, as indicated by the predominance of point contacts between the grains, except in the Sunray H Com #6 well where the effects of early compaction and grain-to-grain interpenetration are more significant (Fig. 9). Furthermore, the core from this well shows macroscopic bed-parallel stylolites that also indicate a greater degree of compaction.

According to Folk's (1980) classification, the sandstones are sublitharenites and litharenites (Appendix C, Fig. 10). Dissolution of feldspar grains and/or their replacement by carbonate cement suggests that the original rock was more feldspathic, but probably still within the litharenite-sublitharenite clans. The rock fragments present include chert, argillaceous rock, detrital carbonates and siltstones.

The subsurface rocks have low permeability, in general less than 1 mDarcy, Weir (1996) and porosities are in the order of 0 to 5% (Appendix C, Fig. 11, Weir, 1996). The samples from

outcrops of the same formations are more porous (3-15%, Appendix C, Fig. 11). The porosity is mainly primary intergranular porosity (2-10%, Fig. 12) and secondary porosity due to dissolution of feldspar grains (0-2%, Fig. 13).

The volume of cement is greater in the sandstone samples from the subsurface than in samples from the outcrops (Appendix C, Fig. 11). In both outcrop and subsurface samples, quartz is the dominant cement, but in some samples carbonate cement is volumetrically more important (Appendix C, Fig. 14). Vertical and lateral variations in the volume of cements from subsurface and surface samples are complex and require further research. In subsurface samples from the Point Lookout Formation (San Juan 32-9 well), carbonate cements are volumetrically more important (24 to 54 percent of the total volume of cement in the sandstones) than quartz cements (8 to 40 percent) whereas in samples from outcrops of the same formation (Westwater pavement) quartz cement dominates (28 to 86 percent of the total volume of cement). Carbonate cement dominates over quartz cement in outcrop sandstones of the Cliff House Formation (Cottonwood pavement, 38 to 62 percent of the total volume of cement) whereas in the Sunray H Com #6 well, carbonate cement is less abundant (0 to 48 percent) than quartz (18 to 70 percent) but in the Riddle D LS 4A well, carbonate cement dominates over quartz in some samples.

Paragenetic Sequence

Figure 15 shows the paragenetic sequence. Diagenetic phases shown in this figure have a greater or lesser volume in samples from the different units analyzed. Variations also exist between surface and subsurface samples of the same units, but the sequence of events is the same in both. Recent dissolution is most pervasive in outcrop samples.

Carbonate cement, probably ferroan-dolomite (CORELAB, 1996), occurs around carbonate fragments, including reworked dolomite grains. This cement also surrounds some quartz grains that do not show quartz overgrowths, suggesting that this cement precipitated before quartz (Fig. 16A). Loose grain packing in areas with ferroan-dolomite cement also suggests early

precipitation of this cement (Fig 16B). Sabins (1962) interpreted Mesaverde Group sandstones having similar ferroan-dolomite cement to have been cemented, in the near surface environment. The lack of evidence for significant grain-to-grain interpenetration suggests that authigenic quartz also precipitated relatively early in the diagenetic history of these rocks. Shallow-depth quartz cements are discussed in McBride (1989). SEM-CL images show that the cements forming quartz overgrowths and the cement filling post-depositional fractures have the same luminescence behavior indicating that microfracturing was partially synchronous with quartz overgrowths when there still was significant porosity in the sandstones (Fig. 17). Additionally, crack-seal quartz cement in macrofractures of the Riddle D LS 4A confirm this observation (see chapter on fracture morphology and connectivity). This timing relationship may explain in part the scarcity of transgranular fractures observed under the SEM-CL device.

Carbonate cement fills remnant primary porosity left by quartz overgrowths, suggesting it precipitated later. Fractures also show this timing relationship, with carbonate filling spaces between quartz overgrowth lined fracture walls (Fig. 18). Carbonate cementation was accompanied by replacement of feldspar grains. Carbonate cement also filled the space left by dissolved feldspars. Feldspar dissolution was therefore probably earlier and partially contemporaneous with carbonate cement and replacement. Early migration of gas to the fractures could have prevented carbonate cement in fractures of the Riddle D LS 4A and Sunray H Com #6 wells. Gas generation and migration probably occurred during and after the maximum burial of these rocks (Bond, 1984). Clay cements precipitated in remaining pore spaces indicating their more recent occurrence (Fig. 19).

Fracture Cement Characterization

The cores from the three wells studied show differences in macrofracture cement volume and mineralogy. In the Riddle D LS #4 and Sunray H COM #6 cores the surfaces of most macrofractures lack cement visible to the naked eye. The natural origin of these fractures was confirmed using the petrographic microscope by the recognition of euhedral quartz overgrowths

in some areas of the fracture space (Fig. 20). In the San Juan 32-9 well the cement filling the natural macrofractures is mostly sparry carbonate (Fig. 21).

The samples from macrofractures in outcrops of the Mesaverde Group sandstones show fractures partially lined with quartz and subsequently sealed by carbonate cement (Fig. 22). Carbonate cement filling the fractures forms a halo around the fracture which fills adjacent remnant primary porosity in the matrix of these rocks. This timing relationship contrasts with subsurface conditions in the surroundings of the wells Riddle D LS 4A and Sunray H Com #6, where carbonate cement could have been inhibited by the presence of gas in the fracture system. Virtually all of the microfractures detected under the SEM-CL are filled with quartz. The quartz filling the fractures is generally continuous with the cement surrounding grains. SEM-CL high magnification photomicrographs of fracture tips (500x, 750x) at grain borders (Reed and Laubach, 1996) show evidence of quartz cement nucleation on microfracture surfaces and subsequent growth into the intergranular porosity. This supports the idea that, at least in part, quartz overgrowths start at narrow constrictions between or within grains (McBride, 1989).

From a structural perspective, all cements can be categorized according to when they precipitated relative to fracture opening (Laubach, 1988; Laubach, 1997). Prekinematic cements are formed before fracturing occurs, filling matrix porosity but not fracture space (which does not exist yet). Synkinematic cements are synchronous with fracture formation and propagation. They usually show crack-seal features within fractures and fibrous crystals rooted in both fracture walls. Crack-seal structure results from repeated cracking and mineral precipitation in veins (Ramsay and Huber, 1983). Finally, postkinematic cements fill fractures after propagation ceased; they usually show spatially continuous and homogeneous fracture cements.

Prekinematic cements cannot occlude fractures, but result in reduced storage capacity in the reservoir. Postkinematic cements reduce fracture permeability and occlude matrix porosity, decreasing the potential of the reservoir (Laubach et al., 1995). Synkinematic cements can give the same results as postkinematic cements if the cement is pervasive, but frequently this type of cement yields only partially filled fracture space. The presence of mineral bridges in partially

filled fractures also prevents fracture closure and preserves fracture permeability during the production history of fractured reservoirs (Marrett and Laubach, 1997).

Differences in fracture opening and fracture cement timing can be recognized in samples from surface and subsurface in this study (Fig. 23). Since the thin sections were not systematically stained for carbonate identification, the classification of the samples according to Laubach et al. (1995) for cement precipitation/fracture formation timing was approached in a qualitative way. Subsurface fracture cements from the Riddle D LS #4A and Sunray H COM #6 wells are predominantly prekinematic. The percentage of the macrofracture space occupied by synkinematic or postkinematic cements in these wells is minimal. Hydrocarbon migration to these fractures soon after their formation possibly prevented further cement precipitation. The San Juan 32-9 well also shows prekinematic cement, but synkinematic quartz overgrowths and postkinematic carbonate cement are present in important volumes in this well. These observations indicate that fracture/cement timing relationships in the Riddle D LS #4A and Sunray H Com #6 wells were more conducive to preservation of fracture permeability than in the San Juan 32-9 well, resulting in open macrofractures in the Riddle D LS #4A and Sunray H Com #6 wells and mostly sealed macrofractures in the San Juan 32-9 well.

The macrofractures in samples from outcrops are dominantly filled by postkinematic cements. Most of the fracturing in these rocks occurred prior to porosity occlusion by cements. This timing relationship did not favor the preservation of fracture porosity and permeability in these rocks. A second possibility is that the cement filling these fractures is associated to surface processes. In this case, the cement filling these fractures is not a proxy of the cement filling the fractures in the subsurface of the same area.

Most of the microfractures in all samples are sealed by synkinematic cement. Most microfracture cements were contemporaneous with the quartz overgrowth (95 percent) and fewer (5 percent) are contemporaneous with the later carbonate precipitation. Large transgranular fractures show quartz and carbonate cements. Quartz cement forms bridges sealing the space between split quartz grains and carbonate cement fills the remnant space (Fig. 24). The

differences in the degree of occlusion of the microfractures and macrofractures in the samples analyzed in this study suggests that microfracture cement volume is not a simple proxy of the degree of occlusion of the macrofractures in the same units. These results also suggest that microfractures tend to be more readily filled by cement than macrofractures, probably because of their reduced size, impurity-free fracture walls and greater surface area to volume ratios.

FRACTURE MORPHOLOGY AND CONNECTIVITY

Macrofracture morphology

Three distinct natural fracture systems were identified in outcrops of the Mesaverde Group: shear-mode conjugate fractures (faults, Fig. 25), open-mode sealed fractures (veins, Fig. 26) and surface-related fractures (joints and polygonal cracks, Fig. 27). These fracture systems can be separated in relative time of formation and they probably occurred under distinct tectonic conditions related to the evolution of the San Juan basin (Fig. 28).

Shear-mode fractures are commonly rectilinear and crosscut each other showing offsets, both sinistral and dextral, and forming acute angles of 70 to 25 degrees in conjugate patterns. The conjugate shear-mode fracture system is also characterized by the presence of gouge. The degree of mechanical connectivity is highest in this fracture system. Shear fractures were recognized only in outcrops and not in cores.

Open-mode quartz-carbonate sealed fractures are typically grouped in swarms. They show more sinuous traces than the shear-mode fractures. This set crosscuts and is younger than the shear-mode fractures. No shear offsets were identified in plan or cross-sectional view of this fracture set in the field. Hooked connections between fractures suggest open-mode propagation under nearly isotropic remote stresses (Olson, 1993).

Long straight joints, probably resulting from surface processes, are also present (Fig. 27A). They are most abundant near canyons cut through the outcrops, suggesting an association with unconfinement and gravitational effects due to topographic breaks. These fractures are typically rectilinear, do not contain minerals, and cross-cut the open-mode sealed fractures without offsetting them laterally. Polygonal fractures are also present, especially in the slopes of gullies (Fig 27B). Their formation might be related to weathering, possibly to repeated seasonal or diurnal changes in temperature helped by the action of ice and water.

Natural macrofractures in core were more difficult to identify, in part due to the lack of obvious mineralization on the surfaces of most fractures, but also due to the limited amount of material available for study. Natural fractures in the Riddle D LS 4A well typically show smooth surfaces, usually covered with dust from the drilling process. These fractures intersect the laminations or bedding surfaces at high angle (Fig. 29). On the other hand, induced fracture surfaces are generally rougher and commonly are parallel or inclined to bedding planes.

In the core of the Sunray H COM #6 well, natural fractures are subvertical and show an echelon arrangement (Fig 30). The cores from the San Juan 32-9 well show natural mineral lined fractures and common drilling-induced fractures (Fig. 31) as described by Kulander et al. (1990).

Microfracture morphology

The morphologic characteristics of the open-mode macrofractures and shear-mode macrofractures under the petrographic microscope are distinctive (Fig. 32). Open-mode fractures walls are covered by euhedral quartz overgrowths and/or carbonate cements. Partially filled fractures of the San Juan 32-9, Riddle D LS 4A and Sunray H COM #6 wells contain synkinematic cements showing crack-seal features (Fig. 33). The shear-mode fractures exhibit cataclastic textures with grain-size reduction and concentration of clay and opaque minerals. Porosity is frequently reduced along these fractures. If present in the reservoir rock these fractures could act as barriers to fluid flow (e.g. Antonellini and Aydin, 1995) but additional data would be required to test this hypothesis.

The analysis of microfracture morphology in sandstones has improved due to the capability of imaging quartz-filled microfractures under the SEM-CL (Laubach and Milliken, 1996). Figure 34 shows a comparison of a fractured quartz grain observed under the petrographic microscope and under the SEM-CL. In the petrographic image the mineralized fractures present in the grain are barely suggested by the presence of fluid-inclusion planes. In the SEM-CL image, the fractures are clearly displayed showing details of their morphology, orientation, connection and relationships with the surrounding cement. Additionally, induced fractures

produced during the making of the thin section, which dominate in the petrographic image, can be identified by comparison with the SEM-CL image.

Under the SEM-CL the microfracture morphologies show a high degree of variability (Fig. 35). Microfracture walls can be rectilinear, curved, wavy, diffuse or crooked. They can be contained within the limits of a single grain (intragranular), cut the cement or grains and cement (transcement) or cut several grains (transgranular). They can also be arranged in geometric patterns like: orthogonal, en echelon, parallel, anastomosing, conjugate, radial. Fracture apertures can be relatively constant or variable along the fractures, showing elliptical, sigmoidal or wedge geometry.

Several geologic processes can explain the presence of microfractures in sandstones but only some of these processes produce macrofractures. Laubach (1997) provides a comprehensive discussion on microfracture morphology and origin. Some microfractures are present in grains previous to deposition (inherited). Other microfractures are generated during compaction and do not have macroscopic equivalents. Another group of microfractures are associated with postdepositional tectonic processes that also produce macrofractures. This last group of microfractures (tectonic microfractures) are the most significant in this study since they most probably represent the microscopic expression of the macrofractures.

Morphology and cross-cutting relationships can be used to classify microfractures. Inherited microfractures usually show wavy and diffuse traces that suggest formation at high temperatures such as in igneous, metamorphic or hydrothermal environments. These microfractures show abrupt terminations against the surrounding cement and can be filled with a type of cement absent elsewhere in the rock. These fractures are of no use for macrofracture prediction.

Some particularly brittle grains show a multitude of microfractures in crisscrossing or radial arrays. These microfractures have been most probably generated by stress concentration at grain boundaries (crushed grains). The crushing of these grains might be due to either tectonic or compaction processes. In areas distant from faults, these microfractures usually end near the

margin of the crushed grains but they can also cut the surrounding cement. They are rarely transgranular.

The local stress field applied at grain contacts can also promote fracture propagation at the same time that rotation of one fracture-bounded fragment occurs. These microfractures usually show curved traces with variable apertures, most commonly wedge shaped. Such microfractures are not adequate for macrofracture prediction because point-loading processes do not generate macrofractures.

Orthogonal, conjugate, en echelon and parallel fracture patterns develop under the influence of long-term remote stress (Olson, 1993, 1997), probably associated with tectonic events or the ambient within plate-tectonic stress field. These fractures are characterized by relatively constant, elliptical or sigmoidal apertures. In quartz-cemented rocks the orientation of most transgranular and transcement microfractures reflects long-term stress field that also govern the strike of macrofractures. The timing of fracture formation in such rocks is episodic, and appears to be most closely linked to a combination of decreased porosity and increased pore fluid pressure associated with burial and quartz precipitation (Laubach, 1988).

Transgranular and transcement microfractures can show significant variations in orientation along their traces due to the heterogeneity of sandstones at the microscopic scale but, as they grow longer, they tend to maintain a regular average propagation direction which reproduces the orientation of macrofractures. The identification of tectonic-related microfractures is the goal of the microfracture ranking scheme adopted in this work (see chapter on fracture orientation).

Fracture Connectivity

Connectivity, or its lack, is a fundamental property of fracture systems. The quantification of this parameter would allow comparison of the connectivity of different fracture networks and modelling of fluid flow through fracture systems in ways that are more realistic than currently used. The relationships between geometric fracture parameters and connectivity will help to

quantitatively predict the degree of connectivity of fracture networks using more readily measurable fracture parameters.

The connectivity of a fracture system has different meanings in mechanical and hydrodynamical contexts. The mechanical connectivity of fractures focuses on the degree of physical connection among the fractures in a network. On the other hand, in fluid flow applications, some fractures can be physically connected to the network but isolated in the sense that they do not contribute to the flow (e.g. mineral filled fractures).

The hydrodynamic connectivity of fractures is affected by physical and chemical factors. Physical factors include: fracture density, number of fracture sets in the network, variability of orientation shown by fractures in a set, and fracture size (especially fracture length). Chemical factors include cementation and dissolution.

Most previous work on fracture connectivity and fluid flow derives from percolation theory (e.g. Long and Whitherspoon, 1985). In percolation theory the objective is to determine if a fracture network allows fluid to flow between two points. It has been proposed that natural fracture networks attain their final geometrical configuration once the network has interconnected such that it surpasses the percolation threshold. This hypothetical phenomenon is explained as "stress relief" of the fracture networks (Gueguen et al., 1991; Renshaw, 1996). However, some fracture networks have been identified that are connected beyond the percolation threshold (Wilke et al., 1985; de Marsily, 1985), strongly suggesting that a fracture system can continue growing and connecting after the hydrodynamic conductivity threshold has been reached. In any case, percolation theory yields a positive or negative answer to the question: Is the network connected?, but no quantification of the connectivity is obtained with this technique (Lee and Farmer, 1993).

Some mathematical models have been proposed to evaluate the degree of connectivity of fracture networks. Robinson (1983) proposed a parameter to quantitatively characterize the connectivity of fracture networks:

$$\text{Connectivity} = \frac{\text{Number of intersections}}{\text{Number of fractures}}$$

This parameter does not give information about the spatial arrangement of the fracture network and does not uniquely characterize fracture systems. Figure 36 shows the connectivity of the open-mode fracture swarms studied in the field. This diagram suggests that fractures are better connected in fracture swarms of Westwater pavement and more poorly connected in Cottonwood pavement. Although no indication of the geometry of the fracture connections can be derived from these diagrams, they suggest that 20 to 30 percent of the fractures have at least one connection.

Robinson's (1983) approach was followed by Rouleau and Gale (1985) who proposed a connectivity index that takes into account the orientation, size, spacing and density of the discontinuity sets. The connectivity index can be used in randomly generated fracture networks to perform backbone analysis using the percolation theory. Randomly generated fracture patterns greatly differ from natural fracture systems and this approach is inadequate to model fluid flow in real fracture systems (Berkowitz, 1995).

La Pointe (1988) studied the effect of the fracture density on the fractal dimension of fracture systems and used it as an empirical indicator of the degree of connectivity. This method uses box counting as a basis to obtain the fractal dimension and it is independent of the geometry of the fracture network. However, the box counting method is inadequate to characterize the fractal dimension of fracture-size distributions (Walsh and Watterson, 1993) and the geometry of fracture systems obviously influences the probability of connection of fractures in the network.

Zhang et al. (1992) proposed a methodology to practically quantify the connectivity of fracture networks based on their geometrical properties. This method characterizes the connectivity using a connectivity ratio, similar to Robinson's (1983), and a parameter called the network extent. The network extent is a measure of the extent of the largest connected network

in a fracture system. This method adds uniqueness to the calculation of connectivity but no attention is paid to the geometry of the individual connecting fractures or their terminations.

All the calculations proposed above ignore the effects that cementation and dissolution can have on fracture connectivity. At present, no studies of these effects on the connectivity of fracture networks have been carried out.

In this work, an additional approach was taken to characterize connectivity. This approach takes into account the amount of connections of individual fractures with other fractures and the amount of fractures in the entire system as in Robinson's (1983) approach, but it also takes into account the number of fractures with two or more connections, one connection or no connections in the system.

A single fracture can be isolated, partially connected (i.e. connected with only one other fracture along its length) or totally connected (i.e. connected in two or more places along its length). The proportion of connection (null, partial or total) is given by the ratio of the number of fractures in the population that are isolated, partially connected or totally connected with respect to the total number of fractures. In this way, a particular fracture swarm or fracture network can be characterized by the proportion that an individual fracture in the system is isolated, partially or totally connected. This approach is similar to Laubach's (1992) approach but substitutes the "Constricted" fractures by fractures with only one connection to another fracture. Fractures with only one connection do not significantly contribute to fluid flow through the network and should be separated from totally connected fractures. As Laubach (1992) pointed out, the interconnectivity of fracture networks is a scale dependent parameter. This scale effect is particularly important if we consider that small "invisible" fractures could be connecting large fractures.

The proportion of connection calculated for the open-mode fracture swarms studied in the field are shown in Figure 37. These diagrams characterize the fracture swarms by their locations within the ternary diagram and allow the comparison of their degrees of connectivity at the macroscopic scale. Isolated fractures and partially connected fractures are the most common in

the swarms. As a result, the total connectivity of the open-mode fractures observed in the field is low. Geometrical information is also embedded in the graph since an indication of the way fractures are connected complements the characterization of the connectivity.

Map traces of microfractures from samples analyzed under the SEM-CL show that most of the microfractures are isolated. This implies that their physical connectivity is smaller than that of the macrofractures in the same rock volume. However, some grain boundaries are almost certainly "fractures" that we cannot readily identify.

Samples from the Cliff House Formation show that most of the microfractures are completely filled with quartz cement also indicating that their effective hydrodynamic connectivity is low. The macrofractures instead show a greater degree of effective hydrodynamic connectivity and proportionally lower volume of cement. For example, samples from the Point Lookout Formation show macrofractures lined with quartz cement and subsequently filled with carbonate cement. Almost all the microfractures in these samples are filled with quartz cement only. These observations suggest that the hydrodynamic connectivity and the proportions of cements filling the fractures varies with fracture size in these rocks.

An understanding of the dependence of connectivity with scale might be useful to estimate an adequate representative elementary volume to model fluid flow through fractured rock. Most of the flow would be controlled by the degree of connection and effective apertures of large fluid-flow conducting fractures. Smaller fractures and pores would control fluid flow in the rock matrix.

FRACTURE ORIENTATION

Macrofracture information from oil and gas reservoirs is frequently scarce. Cores represent the best source of direct geological fracture data from the subsurface. Cores provide a limited sample of the macrofractures but microfractures are present in great abundance even in the smallest pieces of rock (Ortega and Marrett, 1996; Marrett et al., 1997; Ortega et al., 1997, unpublished). In this chapter we explore the possibilities of using SEM-CL observations to record microfracture orientation in sandstones samples and predict macrofracture orientation from them. If the microfractures were formed under the same conditions as the macrofractures, they should show similar orientations. Tests of this hypothesis were conducted in the three oriented cores and two outcrop locations.

If this technique produces accurate data rapidly, we can count on a relatively inexpensive tool to predict macrofracture orientations in the subsurface without requiring direct observation of the macrofractures themselves (Laubach, 1997). Only small samples of rock are necessary. Oriented side wall samples have been used successfully for this purpose (Laubach and Doherty, 1997, unpublished).

Macrofracture Orientation

Macrofracture orientations for the wells in this study were obtained from oriented core and from image logs. Macrofracture strike is preferentially north to north-northeast in the Riddle D LS 4A and San Juan 32-9 wells. The Sunray H Com #6 has a preferential fracture strike of 60-90° (Fig. 38). The orientation of induced fractures in the Riddle D LS 4A and San Juan 32-9 wells suggests that the current maximum horizontal stress trends north-south (Fig. 38).

Conjugate shear fractures (faults) are present in both Westwater and Cottonwood pavements. Conjugate faults strike east and northwest suggesting that the maximum shortening axis was oriented WNW during faulting (Fig. 38). The open-mode sealed fractures show

constant N10-30°E strike in both pavements. This orientation is consistent with a WNW trending maximum principal extension orientation and inconsistent with the orientation of the shortening axis of the conjugate faults, indicating that the shear and extension fractures formed at different times. Crosscutting relationships observed in the field confirm that open-mode fractures formed after the faults.

Analysis of Microfractures for Prediction of Macrofracture Orientation

Microfracture orientations were obtained from SEM-CL photomicro-graphs taken from oriented thin sections cut parallel to the stratification in the cores and the outcrops. The varied morphology and possible origins of the microfractures visible with the SEM-CL were discussed previously (see chapter on fracture morphology and Fig. 35). I developed a scheme derived from Laubach's (1997) classification to rank microfractures by inferred generative processes and suitability for predicting macrofracture characteristics. The ranking assesses the likelihood that a microfracture is a proxy for macrofractures in the same volume (Table 5).

This rank scheme assigns higher suitability to those microfractures most probably formed after deposition of grains and most probably related to the macrofractures. This scheme is applicable to Mesaverde Group sandstones only. Ranking of Laubach's (1997) descriptive microfracture types could vary for other sandstone units.

High suitability microfractures are preferred for orientation prediction because we can assume that they formed under the same remote stress conditions as the macrofractures. In the rank scheme of Table 5 microfractures with high suitability (1) are partially equivalent to microfracture types Ia+ and Ia in Laubach's (1997) classification. Medium suitability microfractures (2) are microfractures in which the material cementing the microfractures is indistinguishable from the cement surrounding the grains. The cement of these microfractures is contemporaneous and physically continuous with the cement surrounding the grain. As a result

no cross-cutting relationships exist between the microfracture and the cement filling the pores. These microfractures are abundant in Mesaverde Group sandstones.

Low suitability microfractures are identified by their morphologic characteristics and include microfractures most probably generated by processes that do not generate macrofractures. Microfractures filled with cement not in physical continuity with the surrounding cement, microfractures cutting only a portion of the grain and open microfractures are also included in this group.

Microfractures possibly generated by local point loads at grain contacts (Category II, Laubach's (1997) classification) are included in suitability 3 group and were avoided for orientation analyses. The orientation of microfractures generated at grain-grain contacts might differ from the orientation of the macrofractures, reflecting local concentration of stress. In addition to that, point-load generated fractures do not have a representation at the macroscopic scale. Their inclusion in orientation analysis introduces a degree of dispersion that can obscure the signal of the microfractures most probably related to the macrofractures.

Microfractures at the tips, borders or corners of angular grains can form by stress concentration around corners of angular fragments. These fractures can show no morphologic difference with microfractures formed by a remote stress field, although microfractures affecting the tips of the grains are usually smaller and grain restricted. These microfractures are also included in suitability 3 group.

Fractures restricted to grain boundaries and with no distinguishable relationship with cement have also low suitability. These microfractures partially include Id microfractures of Laubach's (1997) classification. Open micro-fractures with no distinguishable cementing material are also considered suitability 3 microfractures. The natural origin of these fractures is questionable. Open microfractures can be artificially generated during the making of the thin section or manipulation of the sample.

Inherited microfractures are restricted to the grains and formed before the grains were deposited. The cement in these microfractures can differ from the cement surrounding grains and

filling pores in the rock. The presence of a different cement filling these fractures can be considered diagnostic but the characteristics of the cement filling the microfractures are commonly difficult to determine if the cementing material is quartz. Inherited fractures usually show odd traces, aperture size variations and/or diffuse walls. New-formed fractures (post-depositional) usually cut inherited fractures facilitating their recognition, but inherited microfractures can also be reactivated under new stress conditions. Their orientation should only have fortuitous relationship with the orientation of macrofractures.

Appendix D contains a summary of the microfracture orientations measured, their classification according to Laubach's (1997) descriptive classification and their ranking according to the suitability scheme in Table 5. Comments about the morphology, cross cutting relationships, fracture cement characteristics, etc., have also been included in Appendix D.

In some instances, the SEM-CL cannot illuminate the details of the microfracture morphology necessary to classify the microfractures. The presence of highly luminescent minerals in the rock greatly affects image quality. In particular, sandstones from the Mesaverde Group contain important amounts of carbonate grains and cement which reduce the resolution of the SEM-CL device by producing blurry photomicrographs. These limitations added uncertainty to the classification of some microfractures in the samples.

The highest suitability microfractures according to the classification scheme used in this study are transgranular, usually the largest ones visible at the microscopic scale. These fractures are the least common in the thin sections studied. In samples from the Mesaverde Group, after taking about 20 SEM-CL photomicrographs of a thin section (approximately 8 mm² at 200x magnification), at most 30 rank 3 or higher microfractures could be identified. Of these fractures, usually less than ten percent (i.e. three microfractures) can be classified as transgranular or transcement (suitability 1). This small number of microfractures is insufficient to determine the macrofracture orientation with high confidence. The minimum amount of high suitability microfractures necessary to obtain the orientation of the macrofractures can vary with the sample and can be related to the mechanical properties, diagenetic and tectonic history of the rock. It is

not within the scope of this study to investigate the full extent of this problem, but preliminary results of collecting increasing amount of microfracture orientation data for macrofracture orientation prediction are discussed in the next section.

Comparisons of Microfracture and Macrofracture Orientations

Several different approaches were taken to analyze the microfracture orientation data and compare them with the macrofracture data. All microfracture orientations obtained from the photomicrographs taken from each sample were initially plotted and compared with the associated macrofracture orientation. In some cases the preferential orientation of all the microfractures in a sample (i.e. without discriminating among the microfractures in different categories) corresponds with the orientation of the macrofractures developed in the same bed. In cases in which the orientation of all the microfractures did not match the macrofracture orientation, comparisons were made between the macrofracture orientation and the orientation of increasing suitability microfractures. In order to avoid subjective interpretations introduced by the rank scheme, the microfracture orientations were weighted according to lengths. In this way the longest fractures, i.e. the ones that are most likely to be transgranular or transcement, have the most influence on the microfracture orientation.

Riddle D LS 4A Microfracture and Macrofracture Orientations

In the cores of the Riddle D LS 4A well this analysis was carried out in several beds because most of the core was oriented. In this well, the macrofractures have a consistent N-S strike, with a secondary fracture set striking E-W (4996' and 5003').

Some interesting observations derive from the comparison of micro- and macrofracture orientations (Fig. 39):

1. Some samples show microfracture orientations similar to the macrofracture orientations (samples 2-7, 3-3, 3-8, 3-14, 3-18, 4-10 and 4-21). Among them, microfracture strike in samples 3-3, 3-18 and 4-21 match macrofracture orientation.
2. Sample 3-20 appears to have been inverted. In this particular case, the macrofracture and microfracture orientation would match well if the sample were rotated 180° around the N-S axis. Problems with the orientation of samples are to be expected because of the various manipulation needed to acquire oriented samples (including core handling). Flipping the orientation of the samples is easy if care is not taken during the process of cutting, notching, labeling and attaching the samples to the glass.
3. Microfracture orientation is more complex in the lower part of the Cliff House Formation (samples 4-12, 4-16 and 4-23). In these sandstones an additional set of microfractures with a NE strike is apparent. Similarly, the relative importance of the N-S striking microfracture set diminishes.
4. Most of the microfractures measured in the samples are intragranular microfractures. The origin of these fractures is difficult to establish, as I discussed above. In retrospect, a better approach to address macrofracture orientation prediction from microscopic observations would be to measure only microfractures that are considerably longer than the average grain size.

Effects of Amount of Data Collected on Macrofracture Orientation Prediction

A test carried out with sample 2-7 explored the effects that the amount of data collected has on the prediction of macrofracture orientation. This test was also used to study the effect of the classification scheme on the determination of the microfracture orientation (Fig. 40). The first set of rose diagrams were obtained after collecting the orientation of 17 microfractures (approximately 3 mm^2). The diagram for all the fractures indicates a preferential northwest strike and a secondary east-northeast strike. The dispersion in the data is relatively small with these two

preferential orientations well differentiated from the background orientation noise. The diagram considering fractures with suitability 3 or better also indicates a northwest preferential strike with an equally important east-northeast strike. The dispersion in this group of data has increased with respect to the rose diagram including all the microfractures. The rose diagram considering only high suitability fractures (1 and 2) shows high dispersion but maintains the north-northwest preferential strike. Only six fractures have this degree of suitability and the west-northwest preferential strike is indicated by the presence of only two fractures in this orientation.

The second row of rose diagrams in Figure 40 shows the orientation of similar groups of microfractures but in this case the orientation of 51 microfractures, including 34 microfractures observed on additional SEM-CL pictures taken from sample 2-7, were used (approximately 8.5 mm^2). The rose diagram for all the microfractures measured in the sample indicates a preferential east-west strike not present in the rose diagram of the original set of 17 microfractures. The preferential northwest microfracture strike indicated by the original rose diagram does not show clearly in the rose diagram for 51 microfractures. In this case, the northwest strike cannot be clearly differentiated from the orientation noise in the rose diagram. The rose diagram for the microfractures with suitability 3 or better shows a high degree of dispersion but the northwest strike is slightly preferential over the background orientation noise, which indicates fractures in almost all orientations. The signal of the east-west striking microfractures cannot be differentiated from the background orientation noise. The rose diagram for the high suitability microfractures of the increased data set shows a preferential northwest orientation similar to the most reliable fractures of the original data set. The dispersion in this rose diagram is also very high and the amount of suitable fractures has only increased by two. In this case there is only one more high suitability microfracture which adds to the northwest preferential orientation.

The last row of rose diagrams (Fig. 40) shows the results of length weighting the group of 51 microfracture orientation data. The rose diagram for all microfractures shows two preferential strikes: north-south and east-west. These are also the preferential orientations obtained for the

macrofractures in the cores of this well. In this particular bed, from which sample 2-7 was taken, the four macrofractures measured show a single preferential north-south orientation. This rose diagram shows a considerable amount of orientation noise but the north-south and east-west preferential strikes significantly stand out from the background noise. The rose diagram for length-weighted microfractures of suitability 3 or better confirms the results of the rose diagram for all the microfractures but shows a considerably higher dispersion, whereas the rose diagram for the length-weighted microfractures with highest suitability indicates a preferential north-south microfracture strike with a secondary preferential northwest strike similar to the rose diagrams obtained for the higher suitability microfractures described above. Notice that the north-south and east-west striking microfractures that indicate the macrofracture orientation in this example were not present in the original data set of 17 fractures. These fractures were measured from the additional SEM-CL pictures taken from sample 2-7.

According to this test, additional data collected from the other samples analyzed might also increase the agreement between macrofracture and microfracture orientation. Additionally, these results suggest that a classification scheme for the microfractures might not be necessary to obtain the orientation signal of the macrofractures when a “sufficiently large” amount of data is collected.

Other Cases

The results of microfracture orientation analysis for samples from the other two wells in the study and samples from outcrops are shown in Figure 41. In each of these samples between 70 and 160 microfractures were measured. A larger population than in any one sample from the Riddle D LS 4A well. Working with larger microfracture populations allows better assessment of the applicability of the technique. The Point Lookout Formation sample from the San Juan 32-9 well shows microfracture orientations in excellent agreement with the macrofracture orientation. In contrast, in the same well but about 14 ft higher, the orientation of the macrofractures only appears clearly in the high suitability microfractures. In this case, two important microfracture

sets are recognized, each having its own signature in the sample. Many intragranular fractures are also present in this sample, adding to the diversity of the orientations of the less reliable microfractures. The presence of east-west striking macrofractures is possible in this well if the conditions that formed the macrofractures were similar to those at the Riddle D LS 4A well, but these macrofracture orientations were not recognized by correlation of the natural fractures identified in the cores with the image log.

The sample analyzed from the Sunray H Com #6 well exemplifies another kind of microfracture orientation behavior (Fig. 41). In this well the macrofracture strike is clearly E-W. A swarm of four fractures is located where this sample was taken from the core. However, the rose diagrams of microfracture orientation indicates a N-S strike. In this case it is possible that most of the microfractures are aligned with the regional macrofracture orientation system as seen in other wells.

Outcrop samples also show interesting microfracture orientations when compared with the macrofractures. In the Cottonwood sample (Fig. 41) a strong northwest microfracture strike is produced by a few long microfractures. This orientation is parallel to the shortening direction associated with the shear-mode fractures. The rest of the microfractures show a preferred NNE strike, aligned with the open-mode macrofracture system.

Westwater sample WS-13 was intensively studied from a mosaic of SEM-CL photographs. Microfracture strikes in this sample (Fig. 41) corresponds very well with the strike of the open-mode macrofractures.

Microfracture orientations are characterized by a high level of complexity. This complexity in part reflects the material heterogeneity of sandstones at the microscopic scale. Particularly, the sandstones from the Mesaverde Group have a complex composition, texture and diagenetic history that created a heterogeneous medium for fracture propagation.

In order to further test the hypothesis that microfracture orientation can be used to predict the orientation of the macrofractures, some questions will need to be answered:

1. What is the minimum amount of observations required to accurately predict macrofracture orientation and how does this vary with rock type and burial history?
2. Where multiple macrofracture strikes are present, can the technique accurately identify each of these orientations or would these strikes become indistinguishable from the “orientation noise”? If differentiation of these multiple macrofracture strikes is possible (for example via cross-cutting relationships), what is the minimum amount of observations required to accurately predict their orientations using microfracture data?
3. How do the diagenetic history, matrix composition and texture affect the predictive capability of the technique? Is it possible to use these characteristics of the rock as an indication of the amount of microfracture data required for macrofracture prediction purposes?
4. Image processing software and automation can potentially greatly increase the amount of data collected. Can scaling analysis specify the minimum analysis area required to guarantee representative sampling?

FRACTURE SIZE DISTRIBUTIONS AND FRACTURE FREQUENCY

Geometric fracture attributes span several orders of magnitude in nature from the microscopic scale to the macroscopic scale. Fracture size data can be obtained at different scales using various tools. Microscopes and other high magnification devices can be used to measure microfractures. Macrofracture data can be obtained from cores, outcrops and aerial or radar photos. In this section, I illustrate how size information was obtained from Mesaverde Group sandstones at micro- and macroscales and how I interpreted the results.

Fracture Size Population Analysis

For individual fracture sets, the fracture-size distributions recorded at macroscopic scale usually show internal consistency (Baecher and Lanney, 1978; Gudmundson, 1987; Heffer and Bevan, 1990; Barton and Zoback, 1992; Gillespie et al., 1993; Hatton et al., 1994; Sanderson et al., 1994; Vermilye and Scholz, 1995; Johnston and McCaffrey, 1996). Given such internal organization, it might be possible to extrapolate geometrical characteristics of fractures from small to large sizes using the physical laws that regulate their size distributions. The scaled organization of fracture sizes also suggests that simple averages of geometrical properties for fracture systems are not adequate to model fracture system properties. Aggregate properties that depend on the geometrical parameters of fractures, such as porosity, permeability and shear-wave propagation, would also be controlled by this organization (Marrett, 1996).

Not all fracture systems are expected to show scaling distributions. Basalt columnar joints, surface-related joints and desiccation cracks are examples of fracture populations and processes that probably do not follow this type of organization because these fractures commonly show limited variation of fracture sizes.

To obtain the size distribution function of a population of fractures we can construct a histogram of the frequency of sizes in the population. Histograms of fracture sizes usually show

a high frequency of small fractures and frequencies that progressively decrease with increasing fracture size. A more useful representation of a fracture size distribution is the cumulative size distribution plot. To obtain this graph we plot the cumulative number of individuals in the population that are larger than or equal to a particular size against the geometrical property that we measure. A simple way to do this is to sort the fracture sizes from largest to smallest and to number them accordingly.

Cumulative fracture size distributions are best illustrated using log-linear and log-log graphs. Linear segments can be fit to the data points plot in both types of graphs suggesting that either exponential or power (fractal) laws, respectively, can be used to model fracture size distributions. Extrapolations of the linear segments past the scale of observation are different for exponential and power laws, so it is important to determine which distribution best characterizes fracture sizes. Different authors have supported one or the other type of distribution with particular data sets (negative exponential: Snow, 1970; Baecher et al., 1977, power-law: Gudmundsson, 1987; Wong et al., 1989; Heffer and Bevan, 1990; Barton and Zoback, 1992; Hatton et al., 1993; Sanderson et al., 1994; Belfield and Sovich, 1995; Clark et al., 1995; Gross and Engelder, 1995; Marrett, 1997).

We can also plot the fracture size distribution in terms of spatial frequency. This normalization procedure allows us to study the variation of the fracture density of the same fracture population as a function of fracture size. Fracture measurements in this study were made over surface areas, so the fracture frequency is obtained by dividing cumulative number of fractures by surface area in which the observations were made. The observation area for microscopic data corresponds to the area of the photographs (SEM-CL) used to study the microfractures. The observation area for the macrofractures corresponds to the area surveyed in the field.

Figure 42 shows an example of a fracture data set to which exponential and power law fits have been applied. Lines fit to the data in a log-linear plot (i.e., exponential laws) predict either fewer small fractures or fewer large fractures than the numbers observed, depending on which

line we use to fit the data. Although sampling limitations may result in data that inadequately represent a fracture size distribution, the errors will result in data points on plots that fall below the true distributions (i.e., too few fractures observed or measured fracture sizes that are too small). Under the assumption that one of these lines represents the real fracture size distribution, the exponential model under-predicts the number of fractures observed and consequently is an inadequate model for this fracture size distribution.

The power-law model, on the other hand, overestimates the number of fractures observed at the smallest and largest scales. The deficiency of observations at the scale of the smaller fractures could be explained as a consequence of missing small fractures during the collection of data (truncation bias, Barton and Zoback, 1992). As shown in Figure 42 the difference in the number of fractures predicted and observed, for the smaller fractures, increases as the size of the fractures decreases. Smaller fractures would be increasingly more difficult to detect and progressively more of the smaller fractures would be missed in the count. Another possibility to explain why the power law model overestimates the amount of small fractures observed is that the distribution of sizes at this scale is indeed different and it follows another distribution function.

The deficiency of observations at the scale of the largest fractures is more difficult to explain. An explanation of this deviation is that the complete length of the longest fractures was not measured in the observation area (censoring bias, Barton and Zoback, 1992). Some fractures, especially the longest ones, can continue outside the borders of the observation area. As a consequence the sizes of the longest fractures can be underestimated (Baecher and Lanney, 1978; Barton and Zoback, 1992). If this is the case, then the anomaly would disappear when recording data from larger observation areas.

Alternatively, a real change could also explain the deviation. Real changes in power-law scaling could reflect differences in fracture growth at different scales and/or changes in the mechanical properties of the fractured medium at certain scales (Hatton et al., 1994; Wojtal, 1996). In stratified rocks two important mechanical boundaries can be recognized at different

scales: the boundaries of the individual grains at the microscopic scale and the limits of the laminations, beds or sequences at the macroscopic scale.

Marrett (1996) suggests that these changes can be related to sampling topology artifacts. For example, two-dimensional sampling of fractures that span the thickness of a mechanical layer would reveal the complete three-dimensional population of fractures in the layer. These fractures would show the same lengths and frequencies regardless of whether two-dimensional or three-dimensional sampling domains were studied (assuming that the fractures are rectangular in shape, perpendicular to the bed and that the two-dimensional sampling domains selected are bed-parallel surfaces)

An understanding of fracture size distributions at large scales is an important objective of this study. In addition, a method to objectively choose between exponential and power-law models for fracture size distributions is presented.

Error Analysis of the Distribution and Selection of Limits for Least Squares Regression

In order to avoid subjective treatment of data sets, selection of the model that best describes a fracture size distribution is based on application of error analysis. This is the first application of error analysis to the study of fracture size distributions in the literature. This procedure also helps to determine which part of the data set should be used to obtain the parameters of the least squares regression that best describes the distribution.

The lines shown on Figure 42 have been visually estimated and served the purpose of the previous discussion about the “anomalies” found in observed fracture-size distributions. A better approach to fit lines to the fracture-size distributions in these graphs is to evaluate the error that derives from fitting exponential and power-law models to the observed fracture size distribution. A parameter that measures this error is the correlation coefficient of the line fitting the data (r^2). This parameter has been calculated for the exponential and power-law fits to the distributions in the following way:

1. The correlation coefficient (r^2) is calculated for the three smallest fracture sizes in the cumulative or frequency size distribution considering both the exponential model and the power-law models. This parameter (r^2) is recalculated including the next largest fracture size in the distribution. The procedure is repeated adding larger fracture sizes until the largest fracture size of the distribution has been included in the calculation. Similarly, this procedure is applied starting with the three largest fracture sizes and continuing by adding smaller fracture sizes and recalculating the correlation coefficient.
2. The results of the calculation of r^2 can be analyzed in a graph showing the variation of r^2 along the range of fracture sizes for different starting points and models. The results of the error analysis for the data set in Figure 42 are shown in Figure 43. The model that best explains the observations shows the highest r^2 values for the corresponding range of fracture sizes. Significant inflection points in the r^2 curves indicate fracture sizes where a particular model starts to depart significantly from the observations. These points determine the limits of the distribution to be used for the least squares regression, from which the parameters that describe the distribution are obtained.

Use of Microfracture Frequency to Predict Macrofracture Frequency

In previous chapters I discussed the limitations inherent in sampling macrofractures in the subsurface. Characterization of macrofracture size distribution and frequency in fractured reservoirs is even more difficult than sampling orientation because a large and complete sample inventory of the fractures is necessary. For economically important large fractures such an inventory is not possible using current technology.

If fracture-size distributions follow simple cumulative distribution functions from the microscopic scale to the macroscopic scale, then we could use microfracture frequency observations to predict the frequency of macrofractures. This possibility opens new opportunities to characterize fractured systems without directly sampling the macrofractures.

In the next two sections I test the hypothesis that microfracture frequency- size distributions can be used to predict macrofracture frequency-size distributions. Outcrop data on macrofractures and microfractures are sufficient to test the hypothesis. In the subsurface, on the other hand, severe limitations of collecting macrofracture data arise from working with cores and image logs. Only macrofracture height data can be reliably obtained from vertical cores and these data are scarce. Macrofracture aperture can be collected from partially or totally mineralized fractures but this information can also be very limited.

Prediction of Macrofracture Length

Tip-to-tip measurements of macrofracture length in selected areas of bedding-parallel pavements were collected. Microfracture lengths were collected from SEM-CL microphotographs. Micro- and macrofracture length distributions for the Westwater and Cottonwood pavements were normalized by the area of observation and plotted in the same log-log graph (Fig. 44). Lines fitting the linear segments of the microfracture length distributions and extrapolated to the macroscale reasonably predict the frequencies of the macrofractures in these pavements. This result suggests that a prediction of macrofracture frequency might be possible using microfracture frequency data. Additionally, this result also suggests that there are no major changes in the fracture length distributions from the microscale to the macroscale, and that these two scales of fractures are only two different subsets of the same fracture systems.

In contrast, exponential models for the microfracture length distributions do not accurately predict the observations at the macroscopic scale (Fig. 44), suggesting that either the exponential model is an invalid mathematical description of the fracture system, or that the micro- and macrofracture populations are not expressions of the same fracture system.

Fracture Height Distributions

Fracture height data were collected along Westwater Springs canyon by treating the canyon walls as a two-dimensional sampling space. The size distribution obtained (Fig. 45) can be adequately represented by a power-law of exponent -1.34. The model reproduces the intermediate fracture heights up to the scale of the thickness of the mechanical layer. Sampling truncation appears to have occurred at the smallest fracture heights.

A comparison of the microfracture length distribution with fracture height is possible if we assume that the fractures are penny shaped, namely that fracture lengths are comparable in directions parallel and perpendicular to the mechanical layer. The power-law relationship obtained from the microfracture length population predicts the fracture height distribution reasonably well in this case (Fig. 46), up to the scale of the thickness of the bed in which the fractures are developed.

Aperture-Length Relationships

Only high suitability microfracture data and apertures of partially or completely cemented macrofractures were taken into account in Figure 47. Even though the data are very sparse in this graph, aperture-length scaling of the form $b=gl^m$ (Marrett, 1996) can be used as a model for the observed distribution through nearly six orders of magnitude of length variation. The aperture data are not sufficiently abundant as to determine if changes of aperture-length relationships occur at certain scales for each data set studied as reported by Hatton et al. (1994) for volcanic rocks. Marrett and Laubach (1997) analyzed aperture/length data from different sources and speculate about the interplay of fracture propagation and diagenesis as a possible explanation for the dispersion of these types of data. Figure 47 suggests that the macrofracture aperture/length data collected from cores and outcrops of Mesaverde Group sandstones follow different patterns. Fractures from cores have a larger aspect ratio than fractures from outcrops. Core and outcrop fractures also show significantly different diagenetic histories.

Another explanation for the differences in aspect ratio of subsurface and surface fractures is that fractures in core generally have a single segment whereas outcrop fractures in many cases are composed of multi-segments. Differences in the aspect ratio of single- and multi-segment fractures have been documented by Vermilye and Scholz (1995). Limitations of macrofracture sampling make it difficult to test this second hypothesis. On the other hand, Johnston and McCaffrey (1996) showed differences in the aspect ratio for small and large veins that they explained as a consequence of differences in vein growth mechanisms. Small fractures from subsurface samples would show large aspect ratios (inflation mechanism) whereas outcrop samples would be characterized by small aspect ratios (elongation mechanism).

Scanline Data: 2D-1D Conversions

Fracture data in this study were collected from two-dimensional sampling domains. The fractal dimension, represented by the exponent of a power-law distribution, depends on the topological dimension of the observational sampling domain. Marrett (1996) derived expressions to convert fracture size distributions from one topological dimension to another. To test this topological conversion the lengths of fractures intercepted along 16 scanlines were collected from the Westwater pavement. Figure 48 shows the cumulative size distributions obtained from scanline and two-dimensional observation sampling domains. A least-squares power-law fit was made to fracture lengths observed in two-dimensions, and this empirical two-dimensional model was used to calculate predicted one-dimensional length distributions using Marrett's (1996) approach. Predictions match with the fracture size distribution of small fractures. Long fractures are expected to have a distribution with a power-law exponent similar to the two-dimensional distribution of the same size fractures because long fractures are likely to be sampled regardless of the sampling topology.

Test of Potential Microfracture Sampling Bias

Measurement of microfractures from SEM-CL photographs was potentially biased by the selection of regions within the thin sections that showed more intense development of fractures. The effect of such a bias would be to inflate the microfracture frequencies obtained for a sample. To assess this potential bias, a mosaic of pictures of a continuous area was obtained from sample 2-7 in the Riddle D LS 4A well and its microfracture frequencies determined. The microfracture frequency of a continuous area of the thin section is not affected by the selection of interesting fractured places identified while navigating on the thin section with the SEM-CL device. The microfracture frequency distribution obtained was compared to the one obtained using the potentially biased procedure. The fracture frequencies determined using the potentially biased procedure are not systematically higher. It may be that pictures are taken where fractures are easiest to see (e.g., highly luminescent grains) and not where fractures are most concentrated. The microfracture intensity affecting highly luminescent grains is similar to the microfracture intensity of less luminescent grains. There are differences in frequencies for small and large microfractures for each procedure. When isolated pictures are taken the tendency is to photograph large microfractures which are also best recognized whenever they cut highly luminescent grains. The construction of mosaics allows the determination of more realistic microfracture frequencies for the smallest fractures (usually intragranular).

Effect of Important Mechanical Boundaries on Size Distributions of Fractures

Changes of mechanical properties across boundaries could produce differences in the fracture size distributions of the fractures that encountered these limits. For example, size distributions of microfractures in sandstones could be affected by changes in mechanical properties across grain boundaries. Then, the extrapolation of fracture frequencies from microscale to macroscale across the scale of grain diameters might be invalid. Other important mechanical surfaces in sedimentary rocks are the boundaries of lithologic beds or mechanical

units. These surfaces commonly restrict the propagation of fractures across them. Gross (1993) provides a recent definition of mechanical units for fracture studies.

In order to study the effect of mechanical layering on fracture length scaling, two sets of data were collected on Westwater pavement and one data set on Cottonwood pavement. All visible fractures in an area of 2069 m² at Westwater pavement were recorded to obtain the size distribution of macrofracture lengths smaller than the mechanical layer thickness (2.9 m). The criteria used to determine the mechanical layer thickness was explained in the methodology chapter. A larger area (13000 m²) on the Westwater pavement was selected to measure a large number of fractures longer than the thickness of the mechanical layer (Fig. 50).

The fracture frequency size distribution was obtained for both large and small observation areas and compared in the same log-log graph (Fig. 51). The fracture size distribution of the large observation area, representing fractures longer than the layer thickness, can be adequately modeled by a power-law. In this case, all fractures longer than the thickness of the bed were used to calculate the power-law regression line. To select the best model for the fracture frequency size distribution of fractures shorter than the layer thickness, an analysis of the least-squares regression errors for the small observation area was carried out. The smallest fractures of this population are best modeled by an exponential curve. Longer fractures are best modeled using a power-law. The starting point to calculate the power-law regression was obtained by the error analysis shown in the lower part of Figure 51. The ending point of the power-law regression corresponds to fractures equal to the thickness of the mechanical layer (2.9 m).

The fracture length distributions show a change in the slope of the power-law regressions at the scale of the thickness of the bed in which the fractures developed. This change is also suggested by the longest fractures in the small area but the number of fractures longer than 2.9 m observed does not allow satisfactory definition of a power law for this segment of the distribution. Previous interpretations of analogous changes observed in the distributions of the longest fractures related the changes to a bias in the sampling procedure (Baecher and Lanney,

1978; Barton and Zobach, 1992). The censoring bias is produced by incomplete length measurements of the longest fractures, because they extend beyond the limits of the map. Censoring bias has been reduced in this experiment by collecting more than 300 large fractures from an area more than six times larger than the small observation area. These data are sufficient to obtain the fracture-size distribution of the large fractures. The exponent of the power-law fit to the large fractures is greater than predictions of sampling three-dimensional populations of fractures from a two-dimensional sampling domain (Marrett, 1996), suggesting that other factors are affecting the size distribution of large fractures in Westwater pavement. Furthermore, the consistency in the power-law slope of long fractures from the small and large areas suggests that a real change in the fracture size distribution might happen where the fractures reach the limits of a mechanical layer. These results indicate that when fractures propagate to the boundaries of a mechanical layer, the fractures grow differently and produce changes in the power-law exponent of the fracture distribution. Indications of this type of change have been documented for aperture-length data in columnar basalt (Hatton et al., 1994) and faults (Wojtal, 1996).

In order to confirm these results, a second set of data was recorded from Cottonwood pavement. In this case the thickness of the mechanical layer is smaller (1.5 m) and the collection of macrofracture data in two different size observation areas was not necessary. A single area of about 2000 m² was selected to measure all the fractures visible without magnification. A significant change in the fracture size distribution occurs in this case as well (Fig. 52). Again, the change occurs at the scale of the thickness of the mechanical layer and the exponent of the power-law fit to the large fracture sizes is greater than predictions from topological conversions.

Intragranular microfractures might also show a fracture size distribution that differs from that of transgranular microfractures if grain boundaries are mechanically significant. Plots of microfracture frequency show changes of the fracture size distribution for fractures longer than the average grain size of the samples (Fig. 53). These changes might be an artifact produced by limitations of the observation device (SEM-CL) to illuminate the dimensions of microfractures where they cross cement (similar to censoring bias of Barton and Zobach, 1992). Another

explanation for this change is that most microfracture cements are synkinematic and formed when there was still significant porosity in the rock. Many microfractures probably terminate against pores that were subsequently filled with cement. The effect of censoring bias and fracture/cement timing is to diminish the number of fractures longer than the average diameter of the grains. One way to test if this change really occurs would be to record only the microfractures longer than the average grain size in a large and continuous observation area. This approach has not been taken yet due to technological restrictions with the SEM-CL imaging device.

In spite of observed deviations from a power-law fit for fracture sizes larger than the average diameter of the grains, the validity of extrapolating fracture frequencies from the microscopic scale to the macroscopic scale holds as demonstrated in Figure 44. Power-laws obtained using the linear segment of the microfracture population can adequately predict the frequency distribution of macrofractures within the mechanical layer in which the fractures propagated.

CONCLUSIONS

This study evaluated the use of microfracture data to predict macrofracture properties and found that useful information can be reliably derived using this approach. Systematic analysis of the abundance of microfractures in small pieces of rock overcomes the almost complete lack of subsurface macrofracture data. Fractal models are useful to characterize fractured systems. As illustrated here, some geometrical characteristics of fractures, such as aperture and length, can be best modeled using power-law distributions within the range of scales at which observations are less affected by sampling biases.

This study contributes to understanding the relationships between the characteristics of microfractures and macrofractures in sandstones and opens new areas of research on fracture characterization. These areas of research include: improvement of methods for fracture observation, improvement of methods to measure micro- and macrofracture properties, better understanding of the effects of mechanical boundaries on fracture-size distributions, better understanding of the nature and origin of microfractures in sandstones, methods to quantitatively evaluate the connectivity of fracture networks and methods to quantify and predict the volume of cement filling the fractures.

Tests carried out on samples from intervals where macrofracture orientation and frequency are known showed that in some cases the predictive capability of the microfractures is high (i.e. microfractures are an expression of the macrofracture system at the microscopic scale). Fracture orientation remains constant through different scales in many cases. Classification of microfracture data in terms of their relationship with macrofractures, weighting with respect to fracture length and the collection of statistically significant amount of data are important to successfully predict macrofracture orientation.

Outcrop data analysis indicates that extrapolations of fracture frequencies from the microscopic scale to the macroscopic scale are possible and reliable at least up to the scale of

mechanical layers. The size-distributions of fractures that span the mechanical layer follow power-laws of greater exponent than followed by smaller fractures. At least three aspects can contribute to this change in fracture size distributions: 1) censoring bias, 2) sampling of three-dimensional populations in two-dimensional sampling domains and 3) real differences of fracture-size organization above and below the scale of the mechanical layer.

Experiments carried out on large fractured pavements in which fractures larger and smaller than the scale of the mechanical thickness were measured, demonstrate that the presence of mechanical boundaries affects the fracture-size distribution. Namely, the parameters of the power-law for fractures that span the mechanical layer thickness differ from predictions of three-dimensional sampling (Marrett, 1996) when censoring bias are avoided. An indirect support for this conclusion is the common observation that fractures terminate at the boundaries of mechanical layers, suggesting that fracture propagation is modified once fractures reach the boundaries of the layer in which they grow.

Fractures longer than the thickness of the bed show less size heterogeneity than smaller fractures. An increase in the homogeneity of the fracture sizes at large scales helps to constrain the maximum fracture size in a sampling domain. Once the dimensions of the mechanical layer are determined a theoretical approach to calculate fracture permeability can be addressed, knowing that the permeability is fundamentally controlled by the largest fractures in the reservoir (Marrett, 1996).

Structural intuition suggests that grain boundaries can modify microfracture size distributions. In this study, fractures longer than the average grain size of the samples show an increase in the slope of their power law distributions. Censoring bias related to limitations of the observation device (SEM-CL), the synkinematic character of the cement filling the microfractures, high porosity present at the time of microfracturing and complex diagenetic history involving dissolution of framework components and precipitation of late cements in the pore space are some of the factors that could explain these changes at the scale of the average diameter of the grains, but a systematic study of sampling bias is required to test this hypothesis.

The quantification of fracture connectivity and cement kinematics can help to evaluate the capacity of a particular fracture system to allow fluid flow and adequately drain fluids stored in the rock matrix. In this study, the characterization of fracture connectivity was approached using new concepts. The proportion of connections of individual fractures in the fracture network, as a function of the number of fractures, number and type of connections, can be obtained for any fracture system. This parameter takes into account the geometrical characteristics of the fracture network and complements previous approaches to quantify fracture connectivity (Robinson, 1983).

Subsurface sandstones of the Mesaverde Group show important volumes of prekinematic cements and small volumes of postkinematic cements indicating that fractures in the sampled intervals should be open, as inferred from production data. The volume of postkinematic cement in outcrop samples is greater than in subsurface samples possibly due to regional variations in diagenetic history and fracture timing. Microfractures are mostly filled with cement and do not contribute to porosity and permeability in the reservoir.

REFERENCES

- Antonellini, M., and A. Aydin, 1995. Effect of Faulting on Fluid Flow in Porous Sandstones; Geometry and Spatial Distribution. *American Association of Petroleum Geologists, Bulletin*, 79, 5, pp. 642-671.
- Baecher, G. B., N. A. Lanney, and H. H. Einstein, 1977. Statistical Description of Rock Properties and Sampling: 18th US *Symposium on Rock Mechanics*, pp. 5C1.1-5C1.8.
- Baecher, G. B., and N. Lanney, 1978. Trace Length Biases in Joint Surveys. *Proceedings, Symposium on Rock Mechanics*, 19, 1, pp. 56-65.
- Baltz, H. E., 1962. Stratigraphy and Geologic Structure of Uppermost Cretaceous and Tertiary Rocks of the East-Central Part of the San Juan Basin, New Mexico. The University of New Mexico. Dissertation. *University Microfilms, Inc.*, Ann Arbor, Michigan, 294 p.
- Barton, C. A., and M. D. Zoback, 1992. Self-similar Distribution and Properties of Macroscopic Fractures at Depth in Crystalline Rock in the Cajon Pass Scientific Drill Hole. *Journal of Geophysical Research*, B, 97, 4, pp. 5181-5200.
- Belfield, W. C., and J. P. Sovich, 1995. Fracture Statistics from Horizontal Wellbores: *Journal of Canadian Petroleum Technology*, 34, 6, pp. 47-50.
- Berkowitz, B., 1995. Analysis of Fracture Network Connectivity Using Percolation Theory. *Mathematical Geology*, 27, 4, pp. 467-483.
- Berry, F. A. F., 1959. Hydrodynamics and Geochemistry of the Jurassic and Cretaceous Systems in the San Juan basin, Northwestern New Mexico and Southwestern Colorado: PhD dissertation, *Stanford University*, 192 p.

- Bond, W. A., 1984. Application of Lopatin's Method to Determine Burial History, Evolution of the Geothermal Gradient, and Timing of Hydrocarbon Generation in Cretaceous Source Rocks in the San Juan Basin, Northwestern New Mexico and Southwestern Colorado. In: Hydrocarbon Source Rocks of the Greater Rocky Mountain Region. J. Woodward, F. F. Meissner and J. L. Clayton (eds.). *Rocky Mountain Association of Geologists.*, pp. 433-448.
- Clark, M. B., S. L. Brantley, and D. M. Fisher, 1995. Power-law Vein Thickness Distributions and Positive Feedback in Vein Growth. *Geology*, 23, 11, pp. 975-978.
- Condon, S. M., 1988. Joint Patterns on the Northwest Side of the San Juan Basin (Southern Ute Indian Reservation), Southwest Colorado. In: Coal-Bed Methane in San Juan Basin, Colorado and New Mexico. J. E. Fassett (ed.) *Rocky Mountain Association of Geologists*, pp. 61-68.
- Condon, S. M., 1989. Fracture Studies on the Eastern Side of the Southern Ute Indian Reservation. *USGS Administrative Report*, BIA-19-II-E, 34 p.
- Corbett, K, M. Friedman, and J. Spang, 1987. Fracture Development and Mechanical Stratigraphy of Austin Chalk, Texas. *American Association of Petroleum Geologists*. Bull. 71, 1, pp. 17-28.
- CORELAB, 1996. Petrographic Study for Amoco ATTC. Riddle D LS #4 well. San Juan County, New Mexico. File 196005. Corrollton, Texas, 8 p.
- Dart, S. W., 1992. Evaluation of San Juan Basin Fractured Reservoirs from Surface Data. In: Geological Studies Relevant to Horizontal Drilling: Examples from Western North America. Schmoker, J. K., E. B. Coalson and C. A. Brown (eds). *Rocky Mountain Association of Geologists*, pp. 95-114.

- de Marsily, G., 1985. Flow and Transport in Fractured Rocks: Connectivity and Scale Effect: IAH International Symposium: Hydrogeology of Rocks of Low Permeability, *International Association of Hydrogeologists*, 17, II, pp. 267-277.
- Folk, R. L., 1980. Petrology of Sedimentary Rocks. *Hemphill Publishing Company*, Austin, Texas, 184 p.
- Gillespie, P. A., C. B. Howard, J. J. Walsh, and J. Watterson, 1993. Measurement and Characterization of Spatial Distributions of Fractures. *Tectonophysics*, 226,1-4, pp. 113-141.
- Gorham, F. D., L. A. Woodward, J. F. Callender, and A. R. Greer (1979). Fractures in Cretaceous Rocks from Selected Areas of San Juan Basin, New Mexico Exploration implications. *American Association of Petroleum Geologists, Bull.*, 63, 4, pp. 598-607.
- Gose, W. A., 1996. Paleomagnetic Orientation of Core Samples from Sunray H Com #6 for AMOCO. Department of Geological Sciences. *University of Texas at Austin*. Report, 12 p.
- Gross, M. R., 1993. The Origin and Spacing of Cross Joints: Examples from the Monterey Formation, Santa Barbara Coastline, California. *Journal of Structural Geology*, 15, 6, pp. 737-751.
- Gross, M. R., and T. Engelder, 1995. Strain Accomodated by Brittle Failure in Adjacent Units of the Monterey Formation, U.S.A.: Scale Effects and Evidence for Uniform Displacement Boundary Conditions. *Journal of Structural Geology*, 17, 9, pp. 1303-1318.
- Gueguen, Y., D. Christian, and P. Gavrilenko, 1991. Percolation networks and fluid transport in the crust. In: Crustal-scale fluid transport; magnitude and mechanisms. T. Torgersen (prefacer). *Geophysical Reserarch Letters, American Geophysical Union*, 18, 5, pp. 931-934.

- Gudmundsson, A., 1987. Geometry, Formation and Development of Tectonic Fractures on the Reykjanes Peninsula, Southwest Iceland. *Tectonophysics*, 139, 3/4, pp. 295-308.
- Halliburton, 1995. EMI. San Juan 32-9 well, San Juan County, New Mexico. Service logging report for Meridian Oil Company. *Halliburton Confidential*.
- Hatton, C. G., I. G. Main, and P. G. Meredith, 1994. Non Universal Scaling of Fracture Length and Opening Displacement. *Nature*, 367, 6459, pp. 160-162.
- Heffer, K. J., and T. G. Bevan, 1990. Scaling Relationships and Natural Fractures: Data, Theory and Applications. *Society of Petroleum Engineers*. Paper No 20981. Europec 90, The Hague, Oct 22-24, pp. 367-376.
- Helgeson, D., and A. Aydin, 1991. Characteristics of Joint Propagation Across Layer Interfaces in Sedimentary Rocks. *Journal of Structural Geology*, 13, 8, pp. 897-911.
- Hollenshead, C. T., and R. L. Pritchard. 1961. Geometry of Producing Mesaverde Sandstones, San Juan Basin. In: *Geometry of Sandstone Bodies - A symposium*. J. A. Peterson and J. C. Osmond (eds.). *American Association of Petroleum Geologists*, 45th Annual Meeting, Atlantic City, NJ, April 25-28, pp. 98-118.
- Huffman, A. C. Jr., and S. M. Condon, 1993. Stratigraphy, Structure and Paleogeography of Pennsylvanian and Permian Rocks, San Juan Basin and adjacent areas, Utah, Colorado, Arizona, and New Mexico; *U.S.G.S. Bulletin*, pp. 1-44.
- Johnston, J. D., and K. J. W. McCaffrey, 1996. Fractal Geometries of Vein Systems and the Variation of Scaling Relationships with Mechanism. *Journal of Structural Geology*, 18; 2/3, pp. 349-358.

- Kelley, V. C., and N. J. Clinton, 1960. Fracture Systems and Tectonic Elements of the Colorado Plateau. New Mexico University Publications Publications in Geology 6, *New Mexico University Press*, 104 p.
- Kulander, B. R., S. L. Dean, and B. J. Ward, Jr., 1990. Fractured Core Analysis. Interpretation, Logging, and Use of Natural and Induced Fractures in Core. *American Association of Petroleum Geologists. Methods in Exploration Series, No 8.*, Tulsa, Ok., 88 p.
- La Pointe, P. R., 1988. A Method to Characterize Fracture Density and Connectivity Through Fractal Geometry. *International Journal of Rock Mechanics, Mining Sciences & Geomechanics, Abstracts*, 25, 6, pp. 421-429.
- Laslett, G. M., 1982. Censoring and Edge Effects in Areal and Line Transects Sampling of Rock Joint Traces. *Mathematical Geology*, 14, 2, pp. 125-140.
- Laubach, S. E., 1988. Subsurface Fractures and their Relationship to Stress History in East Texas Basin Sandstone. *Tectonophysics*, 156, 4, pp. 495-503.
- Laubach, S. E., and C. M. Tremain, 1991. Regional Coal Fracture Patterns and Coalbed Methane Development. In: *Rock Mechanics as a Multidisciplinary Science*. J. C. Roegiers (ed). Proceedings of the 32nd U. S. Symposium on Rock Mechanics 32. *Balkema*. pp. 851-859.
- Laubach, S. E., 1992. Fracture Networks in Selected Cretaceous Sandstones of the Green River and San Juan Basins, Wyoming, New Mexico and Colorado. In: *Geological Studies Relevant to Horizontal Drilling: Examples from Western North America*. J. W. Schmoker, E. B. Coalson, C. A. Brown (eds.). Rocky Mountain Association of Geologists. pp. 115-127.

- Laubach, S. E., T. F. Hentz, M. K. Johns, H. Baek, and S. J. Clift, 1995. Using Diagenesis Information to Augment Fracture Analysis. Bureau of Economic Geology. *The University of Texas at Austin*. Topical Report #GRI-94/0455, Austin, Texas, 189 p.
- Laubach, S. E., and K. L. Milliken, 1996. New fracture characterization methods for Siliciclastic Rocks. In: Proceedings 2nd North American Rock Mechanics Symposium, M. Aubertin, F. Hassani, and H. Mitri (eds.). *Balkema*, Rotterdam, pp. 1209-1213.
- Laubach, S. E., 1997. A Method to Detect Natural Fracture Strike in Sandstones. *American Association of Petroleum Geologists*, Bulletin, 81, 4, Tulsa, OK, pp. 604-623.
- Laubach, S. E. and E. Doherty, 1997. Side wall samples orientation for microfracture studies. Bureau of Economic Geology. University of Texas at Austin. Unpublished.
- Lee, C. and I. Farmer, 1993. Fluid Flow in Discontinuous Rocks. *Chapman & Hall*, London, 68 p.
- Long, J. C. S. and P. A. Whitherspoon, 1985. The Relationship of the Degree of Interconnection to Permeability in Fracture Networks. *Journal of Geophysical Research*, 90, B, 4, pp. 3087-3098.
- Marrett, R., 1996. Aggregate Properties of Fracture Populations. *Journal of Structural Geology*, 18, 2/3, pp. 169-178.
- Marrett, R., O. Ortega, R. Reed and S. Laubach, 1997. Predicting Macrofracture Permeability from Microfractures. *American Association of Petroleum Geologists*. Abstracts with Programs. Annual Meeting, Dallas, 1997. p. A76.
- Marrett, R., 1997. Permeability, Porosity, and Shear-wave Anisotropy from Scaling of Open Fracture Populations. In: *Fractured Reservoirs: Characterization and Modeling Guidebook*,

T.E. Hoak, A. L. Klawitter, P. K. Blomquist (eds.). *Rocky Mountain Association of Geologists*, pp. 217-226.

Marrett, R., and S. E. Laubach, 1997. Diagenetic Controls on Fracture Permeability and Sealing. *International Journal of Rock Mechanics and Mining Sciences*, 34, 3/4, Paper No. 204.

McBride, E. F., 1989. Quartz Cement in Sandstones: A Review. *Earth-Science Reviews*, 26, pp. 69-112.

Milliken, K. L., 1994. Cathodoluminescent Textures and the Origin of Quartz Silt in Oligocene Mudrocks, South Texas. *Journal of Sedimentary Research*, A64, 3, pp. 567-571.

Molenaar, C. M. and J. K. Baird, 1991. Stratigraphic Cross Sections of the Upper Cretaceous Rocks in the Northern San Juan Basin, Southern Ute Indian Reservation, Southwestern Colorado. In: *Geologic Framework and Stratigraphy of Cretaceous and Tertiary Rocks of the Southern Ute Indian Reservation, Southwestern Colorado*. W. M. Aubrey, C. M. Molenaar, J. K. Baird, and R. S. Zech (eds.). *U.S.G.S. Professional Paper*, pp. C1-C12.

Olson, J. E., 1993. Joint Pattern Development, Effects of Subcritical Crack Growth and Mechanical Crack Interaction. *Journal of Geophysical Research*, B, 98, 7, pp. 12251-12265.

Olson, J. E. 1997. Natural Fracture Pattern Characterization Using a Mechanically-based Model Constrained by Geologic Data - Moving Closer to a Predictive Tool. *International Journal of Rock Mechanics and Mining Sciences*, 34, 3/4, Paper No. 237.

Ortega, O. and R. Marrett, 1996. Significance of Finite Layer Thickness on Scaling of Fractures. *Geological Society of America. Abstracts with Programs. Annual Meeting, Denver, 1996*. p. A-135.

- Ortega, O., R. Marrett, S. Hamlin, S. Clift and R. Reed, 1997. Quantitative Macrofracture Prediction Using Microfracture Observations: A Successful Case Study in the Ozona Sandstone, West Texas. Abstract submitted to the *American Association of Petroleum Geologists*. Annual Meeting, Salt Lake City, 1998. Unpublished.
- Pasternack, I. (1995). Fracture Controls on Mesaverde Gas Production, San Juan Basin, New Mexico and Colorado. Southern Rockies Business Unit, Report, *Amoco*, Denver, 18 p.
- Peterson, J., A. J. Loleit, Ch. W. Spencer, and R. A. Ullrich, 1965. Sedimentary History and Economic Geology of San Juan Basin. *American Association of Petroleum Geologists, Bulletin.*, 49, 11, pp. 2076-2119.
- Pickering, G., J. M. Bull, and D. J. Sanderson, 1995. Sampling Power-law Distributions. *Tectonophysics*, 248, 1/2, pp. 1-20.
- Ramsay, J., and M. Huber, 1983. Modern Structural Geology. Volume 1: Strain Analysis. *Academic Press*, New York, 307 p.
- Reed, R. M., and S. E. Laubach, 1996. The Role of Microfractures in the Development of Quartz Overgrowth Cements in Sandstones: New Evidence From Cathodoluminescence Studies. *Geological Society of America*. Abstracts with Programs, Annual Meeting, p. A-280.
- Renshaw, C., 1996. Influence of Subcritical Fracture Growth on the Connectivity of Fracture Networks. *Water Resources Research*, 32, 6, pp. 1519-1530.
- Reynolds, R. A., 1994. Field Guide Notes-Mancos Canyon Mesaverde Stratigraphy, Southern Rockies Business Unit, field trip June 1994, *Amoco*, Denver, 20 p.
- Rice, D. D., 1983. Relation of Natural Gas Composition to Thermal Maturity and Source Rock Type in San Juan Basin, Northwestern New Mexico and Southwestern Colorado. *American Association of Petroleum Geologists.*, *Bulletin*, 67, 8, pp.1199-1218.

- Robinson, P. C., 1983. Connectivity of Fractured Systems -A Percolation Theory Approach: *Journal of Physics. A: Mathematical and General*, 17, 14, pp. 605-614.
- Rouleau, A. and J. E. Gale, 1985. Statistical Characterization of the Fracture System in the Stripa Granite, Sweden. *International Journal of Rock Mechanics, Mining Sciences and Geomechanics. Abstracts*, 22, pp. 353-367.
- Sabins, F. F. Jr., 1962. Grains of Detrital, Secondary, and Primary Dolomite from Cretaceous Strata of the Western Interior. *Geological Society of America, Bulletin.*, 73, 10, pp. 1183-1196.
- Sanderson, D. J., S. Roberts, and P. Gumiel, 1994. A Fractal Relationship Between Vein Thickness and Gold Grade in Drill Core from La Codosera, Spain. *Economic Geology*, 89, 1, pp. 168-173.
- Schmidt C. J., R. B. Chase, and E. A. Erslev, 1993. Laramide Basement Deformation in the Rocky Mountain Foreland of the Western United States. *Geological Society of America. Special paper 280*. Boulder, 365 p.
- Snow, D. T., 1970. The Frequency and Apertures of Fractures in Rock: *International Journal of Rock Mechanics and Mining Sciences*, 7, 1, pp. 23-40.
- Vermilye, J. M., and C. H. Scholz, 1995. Relation Between Vein Length and Aperture. *Journal of Structural Geology*, 17, 3, pp. 423-434.
- Walsh, J. J., and J. Watterson, 1993. Fractal Analysis of Fracture Patterns Using the Standard Box-counting Technique: Valid and Invalid Methodologies. *Journal of Structural Geology*, 15, 12, pp. 1509-1512.

- Weir, G., 1996. Petrophysical Characterization of the Tight Gas Production in the Mesaverde Group of the San Juan Basin. Petrophysics Project Report No.: S96-G-13. Amoco. Tulsa, OK. 110 p.
- Wilke, S., E. Guyon, and G. de Marsily, 1985. Water Penetration Through Fractured Rocks: Test of Three-dimensional Percolation Description: *Mathematical Geology*, 17, 1, pp. 17-27.
- Wong, T. F., J.T. Fredrich, and G. D. Gwanmesia, 1989. Crack Aperture Statistics and Pore Space Fractal Geometry of Westerly Granite and Rutland Quartzite: Implications for an Elastic Contact Model of Rock Compressibility. *Journal of Geophysical Research*, B, 94, 8, pp. 10267-10278.
- Wojtal, S. F., 1994. Fault Scaling Laws and the Temporal Evolution of Fault Systems. In: Applications of Strain; from Microstructures to Orogenic Belts. M. T. Brandon, J. R. Henderson, W. D. Means, S. R. Peterson (eds.). *Journal of Structural Geology*, 16, 4, pp. 603-612.
- Wojtal, S. F., 1996. Changes in Fault Displacement Populations Correlated to Linkage Between Faults. *Journal of Structural Geology*, 18; 2/3, pp. 265-280.
- Zhang, X., R. M. Harkness, and N. C. Last, 1992. Evaluation of Connectivity Characteristics of Naturally Jointed Rock Masses. *Engineering Geology*, 33, 1, pp. 11-30.

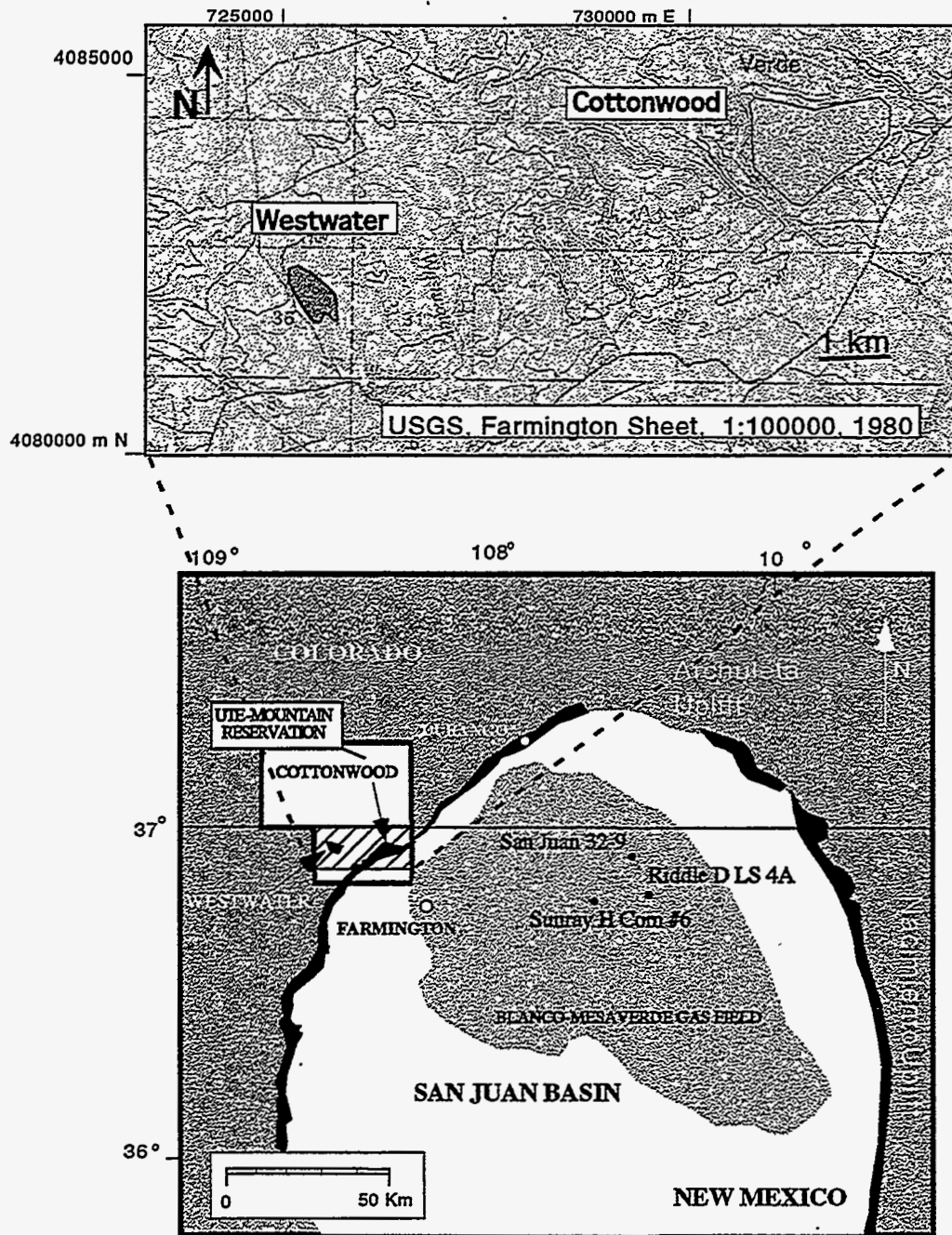


Figure 1. Location map of study areas. White area represents the area of the basin surrounded by the hogback, a topographic feature around the basin containing outcrops of weather resistant units of Cretaceous and Tertiary age (Black). Light gray area represents gas fields included in the Blanco-Mesaverde giant gas accumulation. The enlarged area in the upper figure shows the detailed locations of the pavements studied in the Ute Mountain Reservation.

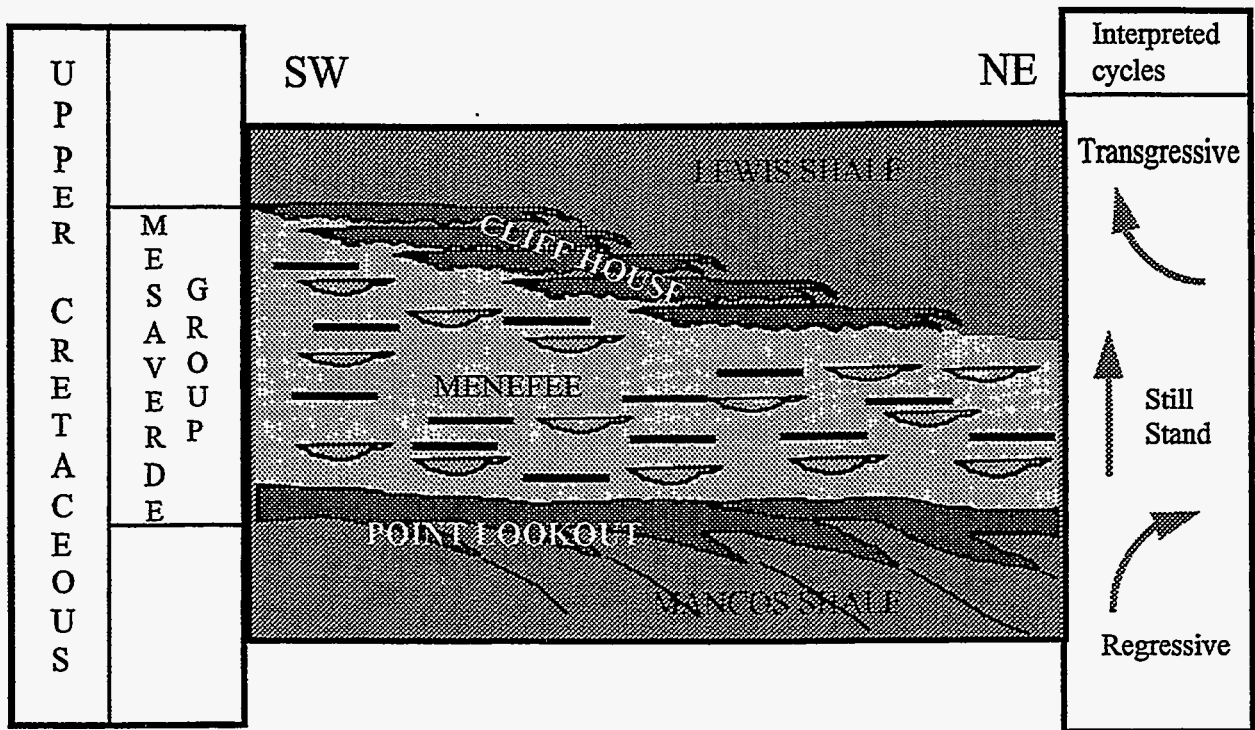


Figure 2. Schematic stratigraphic diagram of the Mesaverde Group and the depositional architecture of the sandstone units studied. Modified from Reynolds(1994).

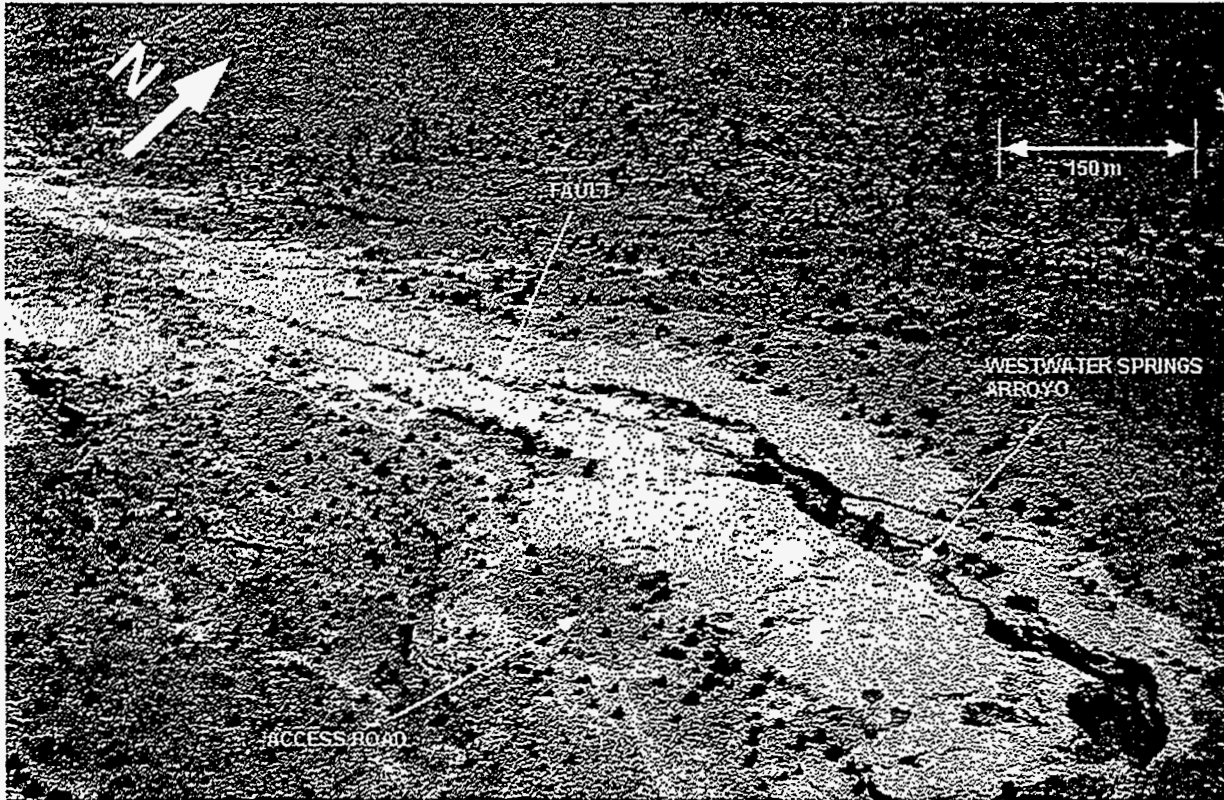


Figure 3. Oblique aerial view of Westwater pavement. Westwater Springs arroyo cuts the pavement allowing study of the fractures in cross section. A strike-slip fault is present in the northern part of the pavement. Bushes and small trees grow along the fault trace.

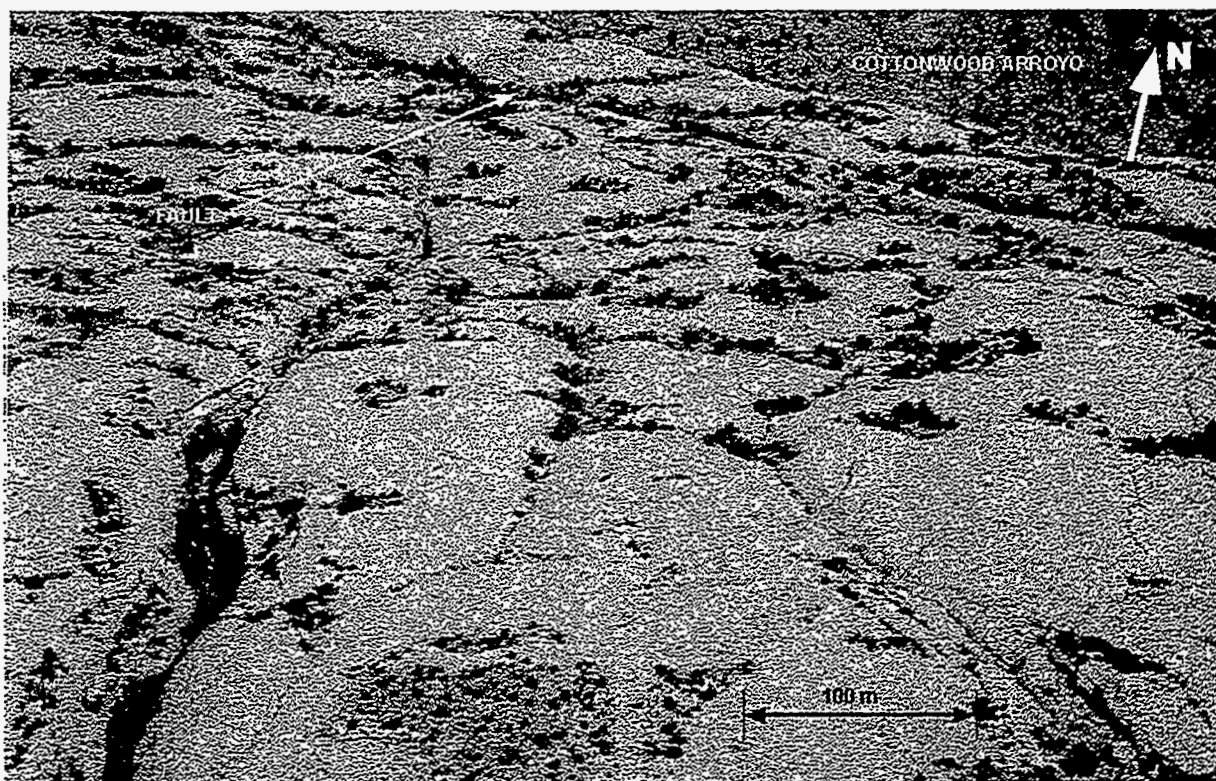


Figure 4. Oblique aerial view of Cottonwood pavement. This pavement is one of a set of flat-irons on the forelimb of a regional-scale monocline called the Hogback. A strike-slip fault is also present in the northern part of this pavement.

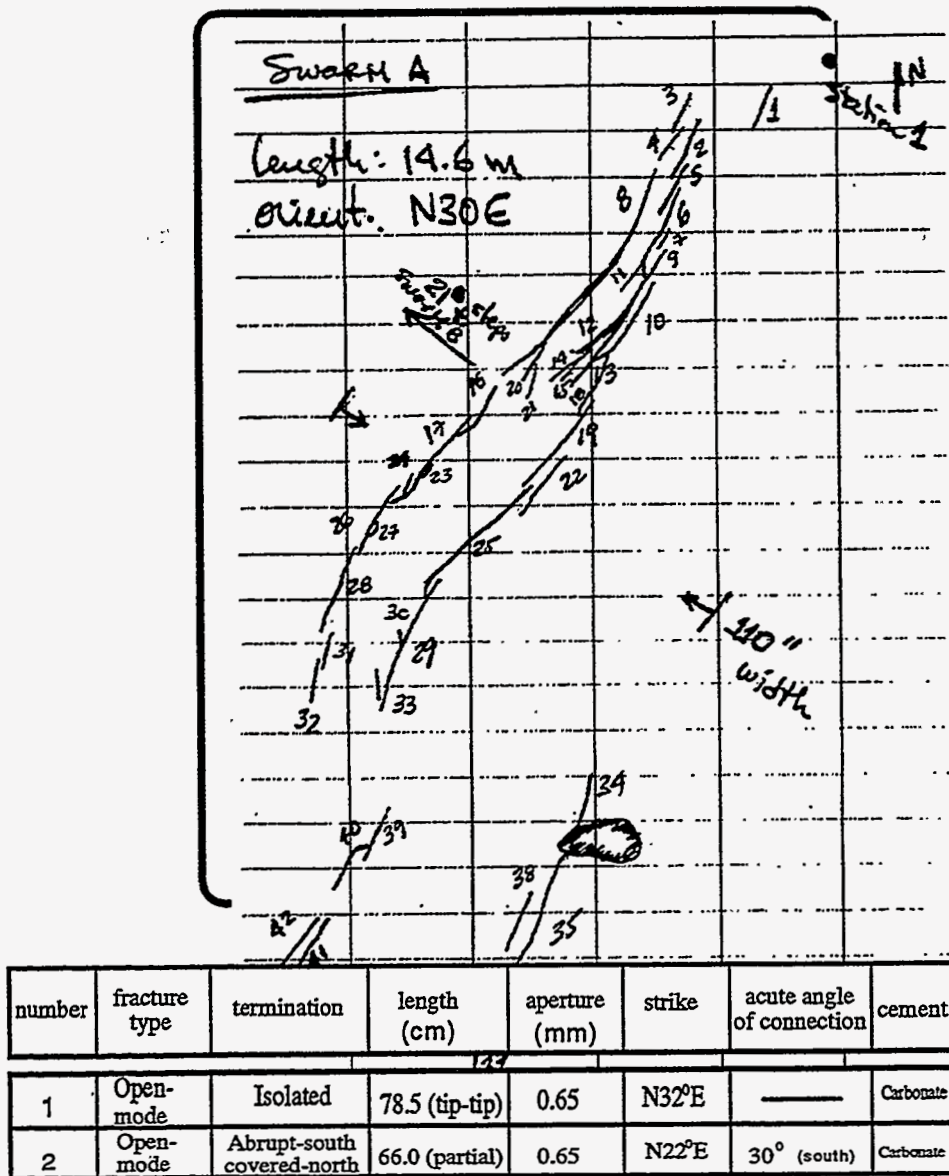


Figure 5. Sketch map of fracture swarm A, Cottonwood pavement. The table in the lower part of the figure shows an example of the parameters collected from the macrofractures in the field.

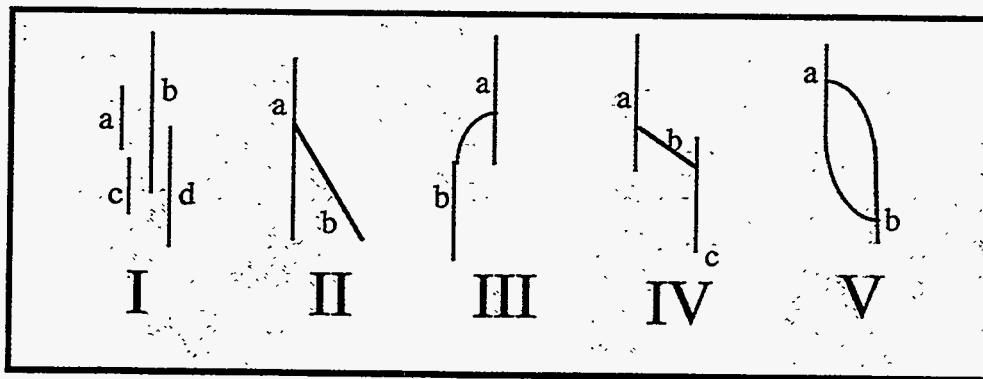


Figure 6. Fracture termination types observed in the field. The identification of fracture termination is the basis for the selection of fracture tips. Fracture length is the distance between the tips of the fracture measured along the trace of the fracture.

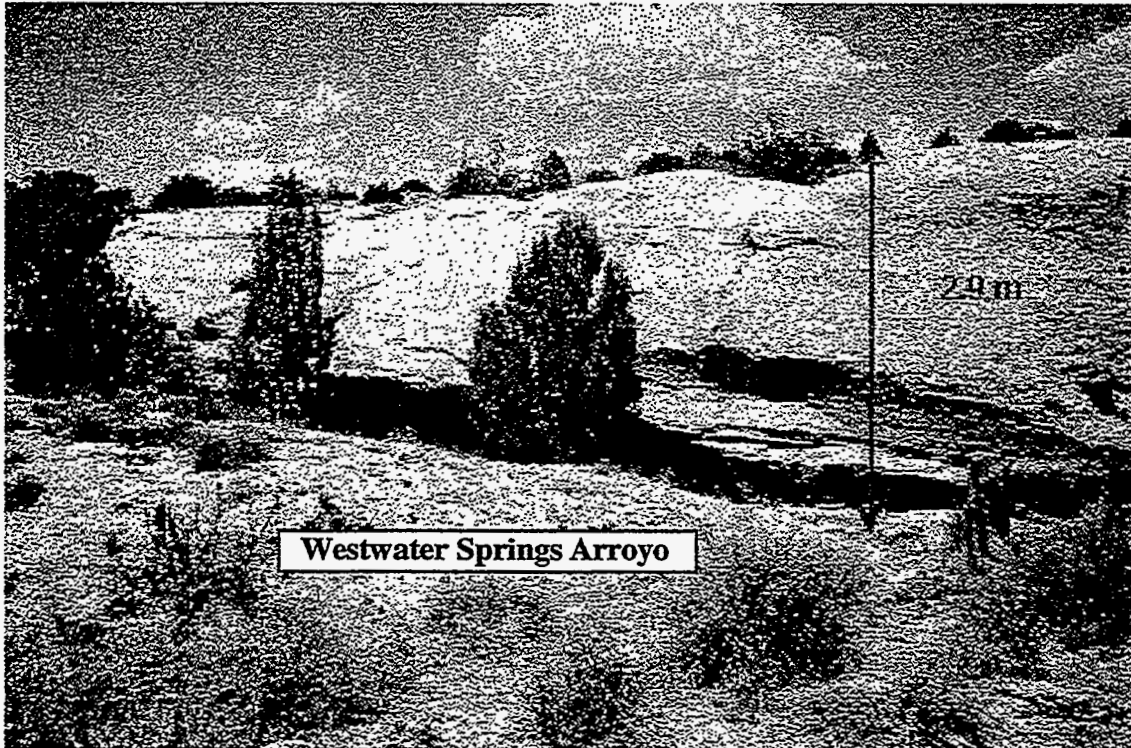


Figure 7. Mechanical layer in Westwater pavement.

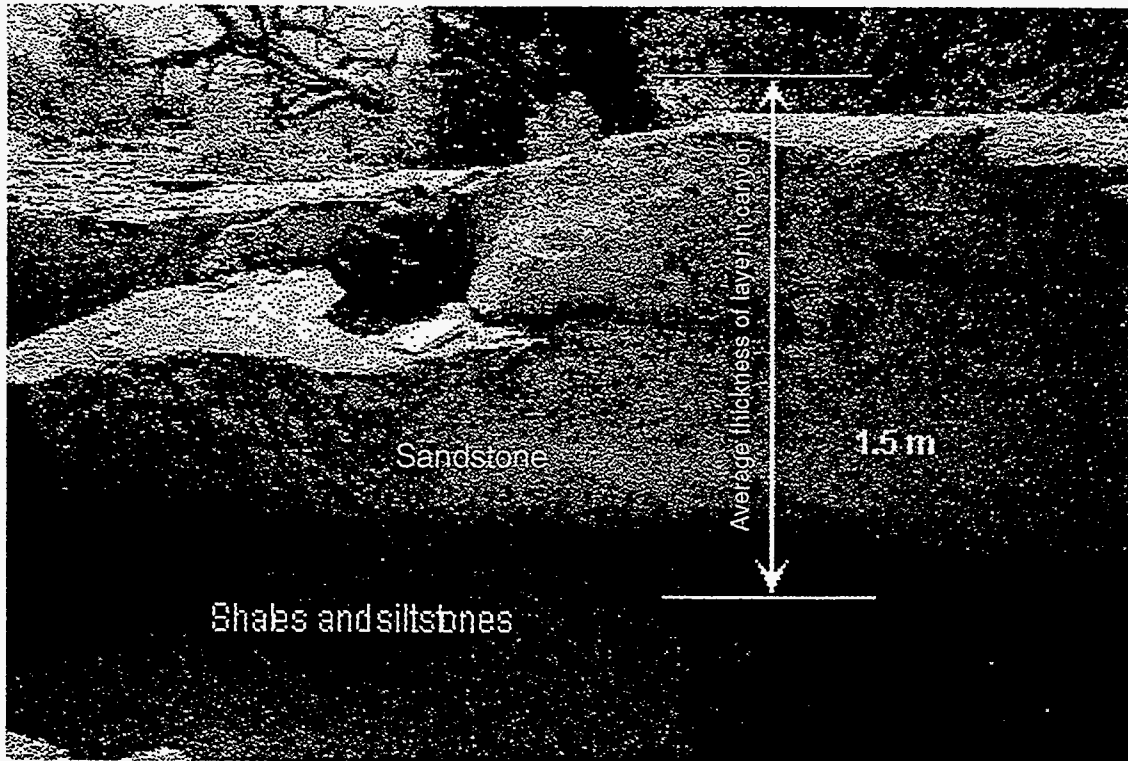


Figure 8. Mechanical layer in Cottonwood pavement.

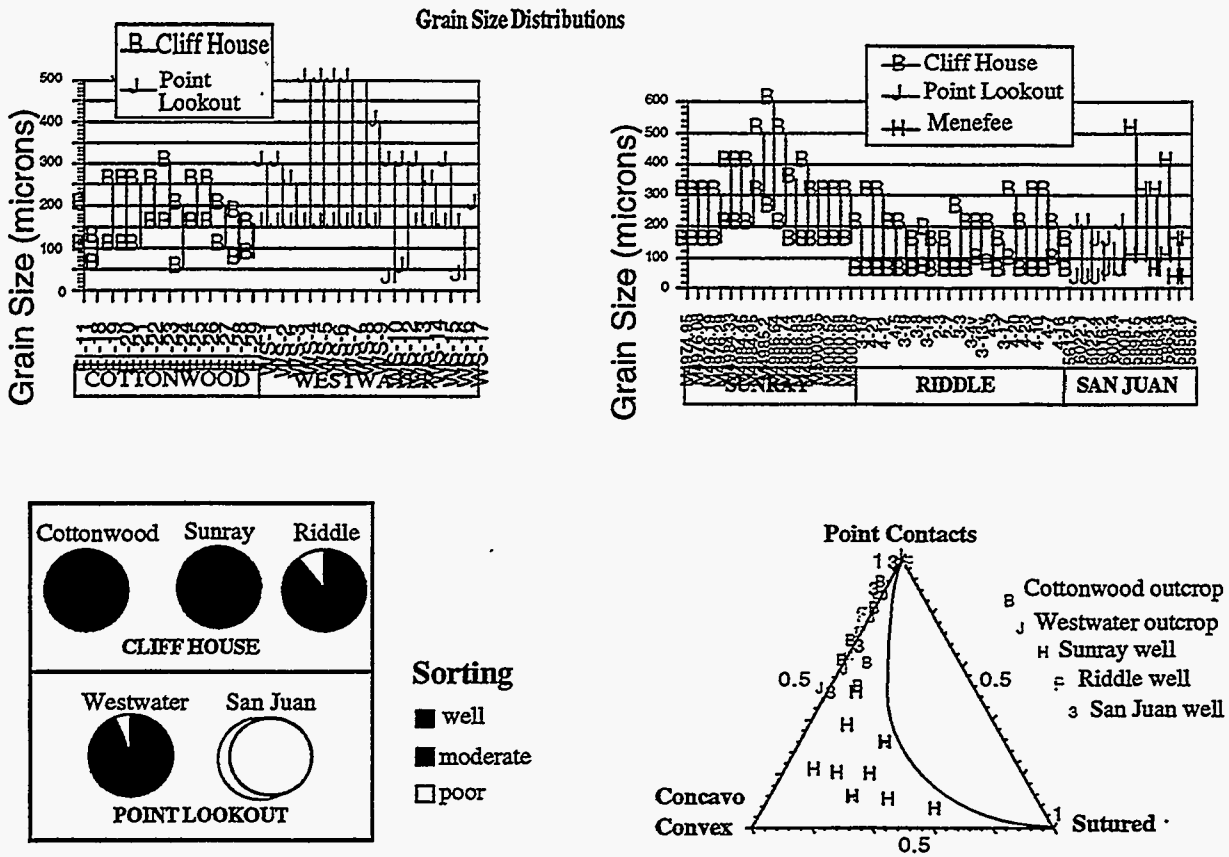


Figure 9. Textural characterization of samples analyzed (based on 100 counts per sample).

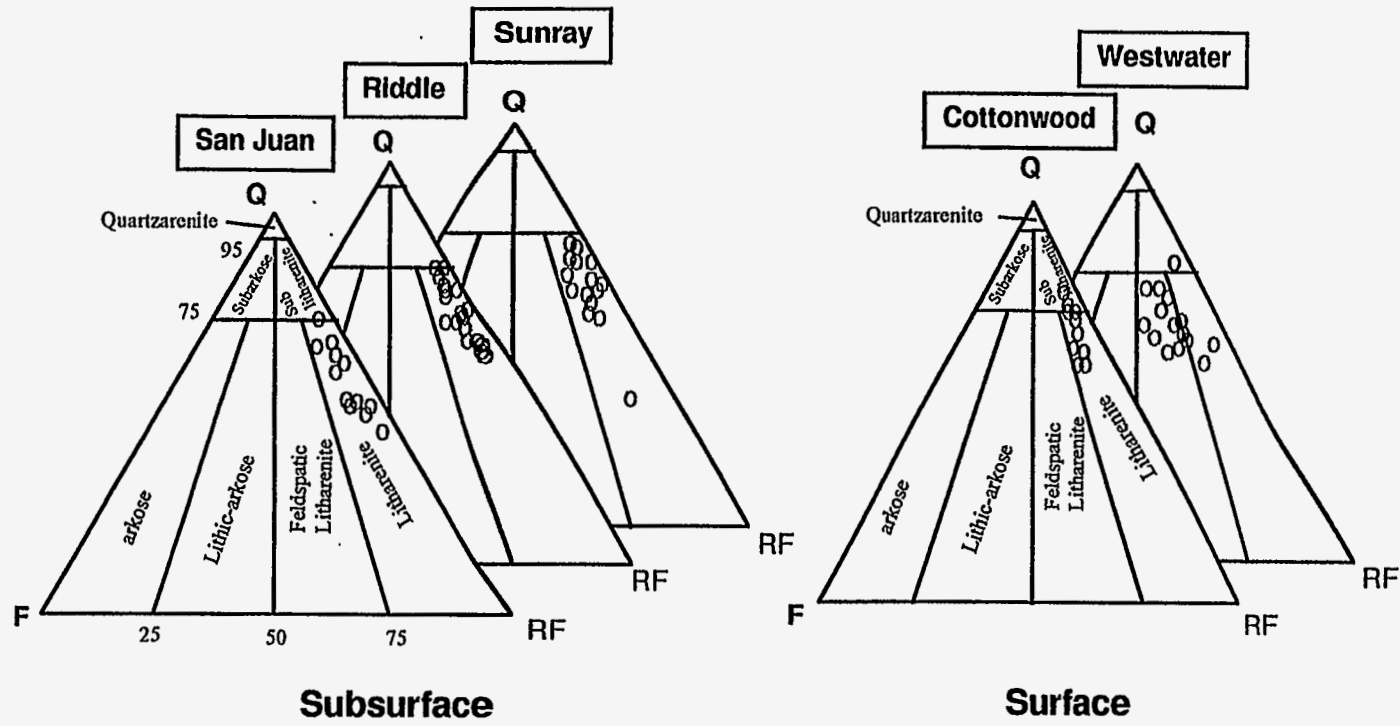
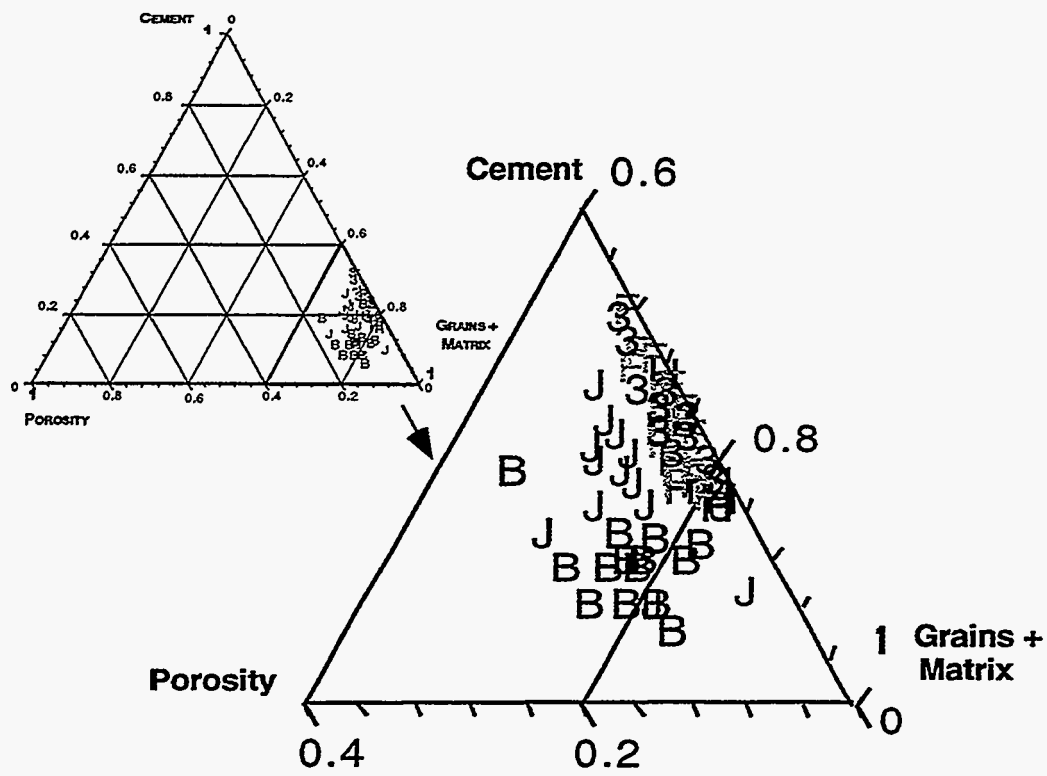


Figure 10. Compositional classification of samples analyzed. Folk's (1980) classification scheme for sandstones. Q: quartz, F: feldspars, RF: rock fragments.



B Westwater J Cottonwood H Sunray F Riddle 3 San Juan

Figure 11. Grains+matrix-cement-porosity ternary diagram for samples analyzed.

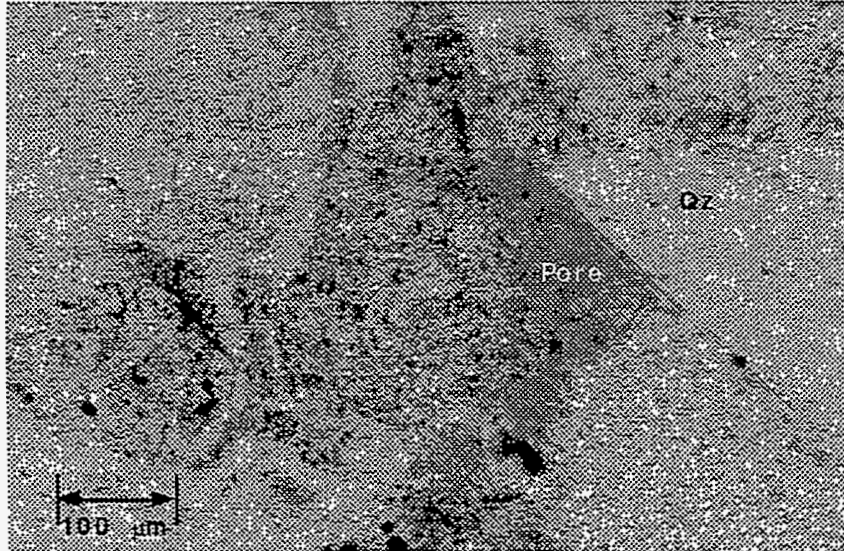


Figure 12. Photomicrograph of primary intergranular porosity. Sample 3-20, plane light, Riddle D LS 4A.

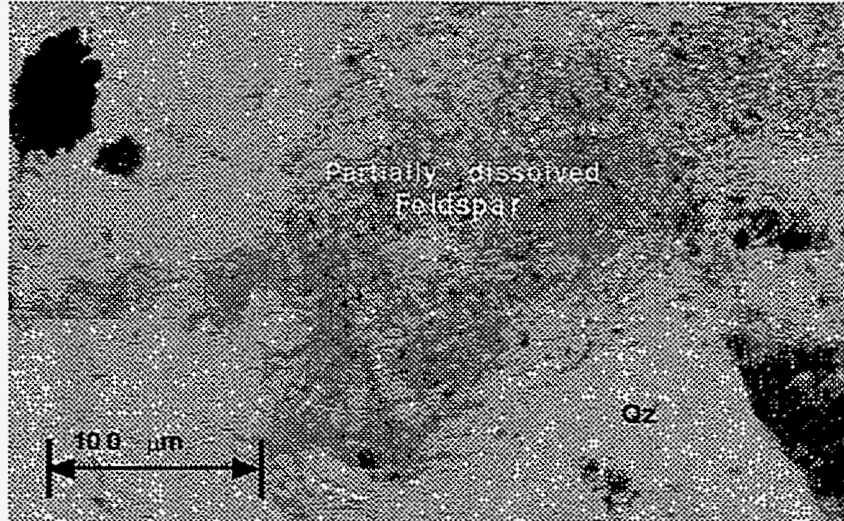


Figure 13. Photomicrograph of secondary porosity associated to partial dissolution of feldspar grain. Sample 3-20, plane light, Riddle D LS 4A.

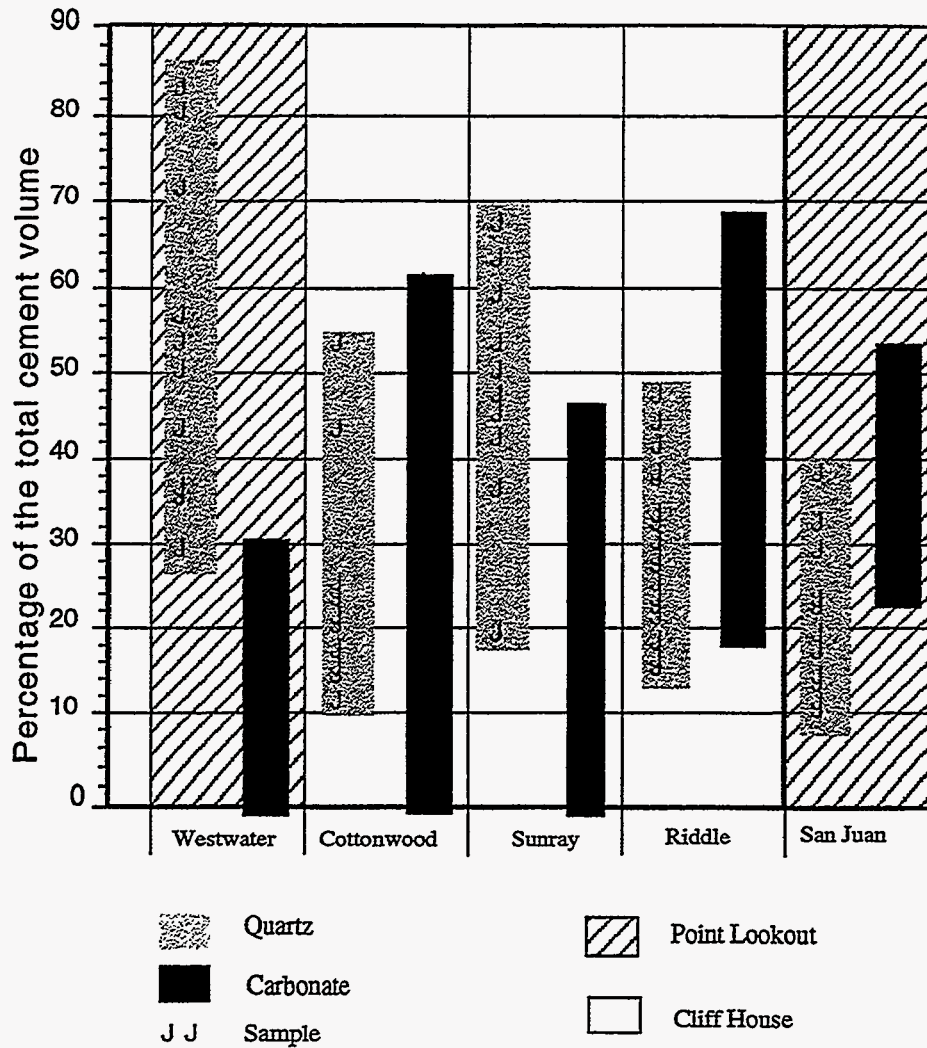


Figure 14. Contribution of quartz and carbonate cements to the total volume of cement in the sandstones analyzed.

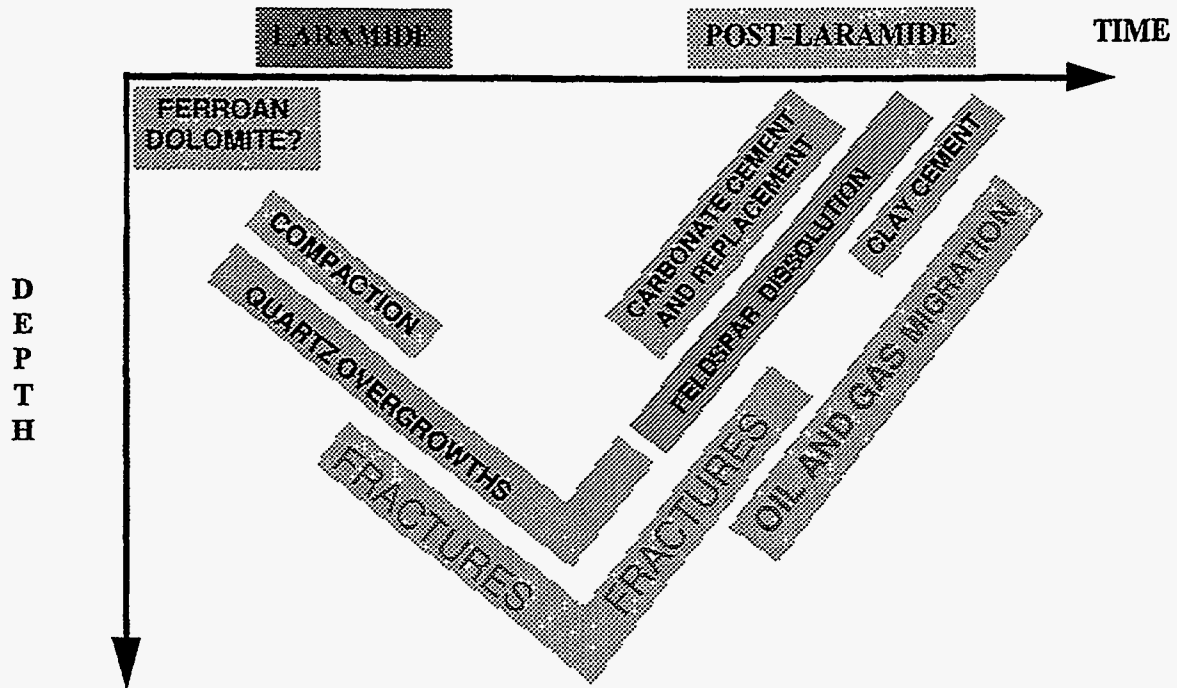


Figure 15. Speculative paragenetic sequence for Mesaverde Group sandstones based on the samples analyzed. Fractures probably formed during burial and subsequent uplifting. Timing is based on crosscutting relationships between fractures, cement and dissolution/replacement events. Gas migration and schematic burial history are interpreted from Bond (1984).

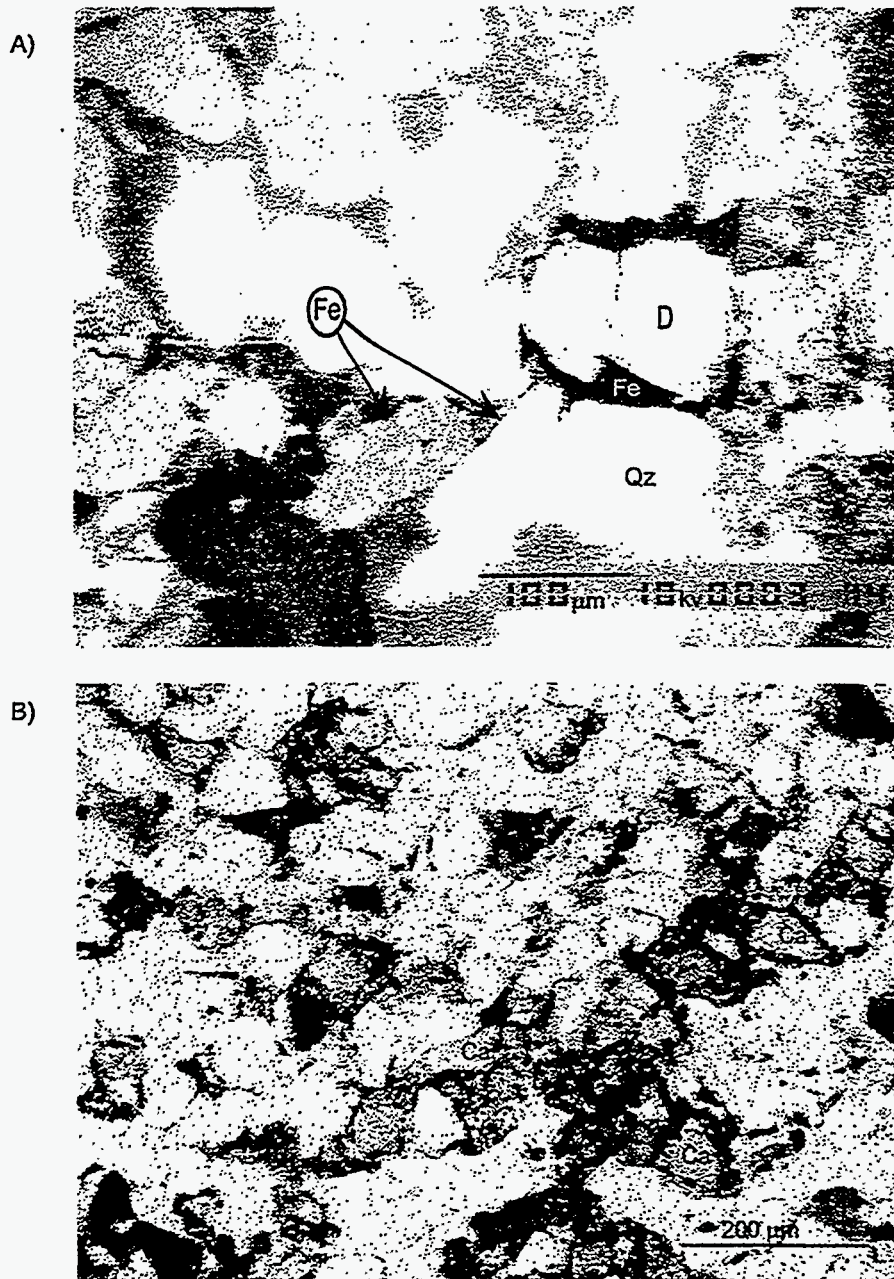


Figure 16. Scanned CL (a) and transmitted light (b) images of rock microstructure. Fe, iron-rich carbonate mineral; Qz, quartz; D, detrital grain; Ca, detrital carbonate material.

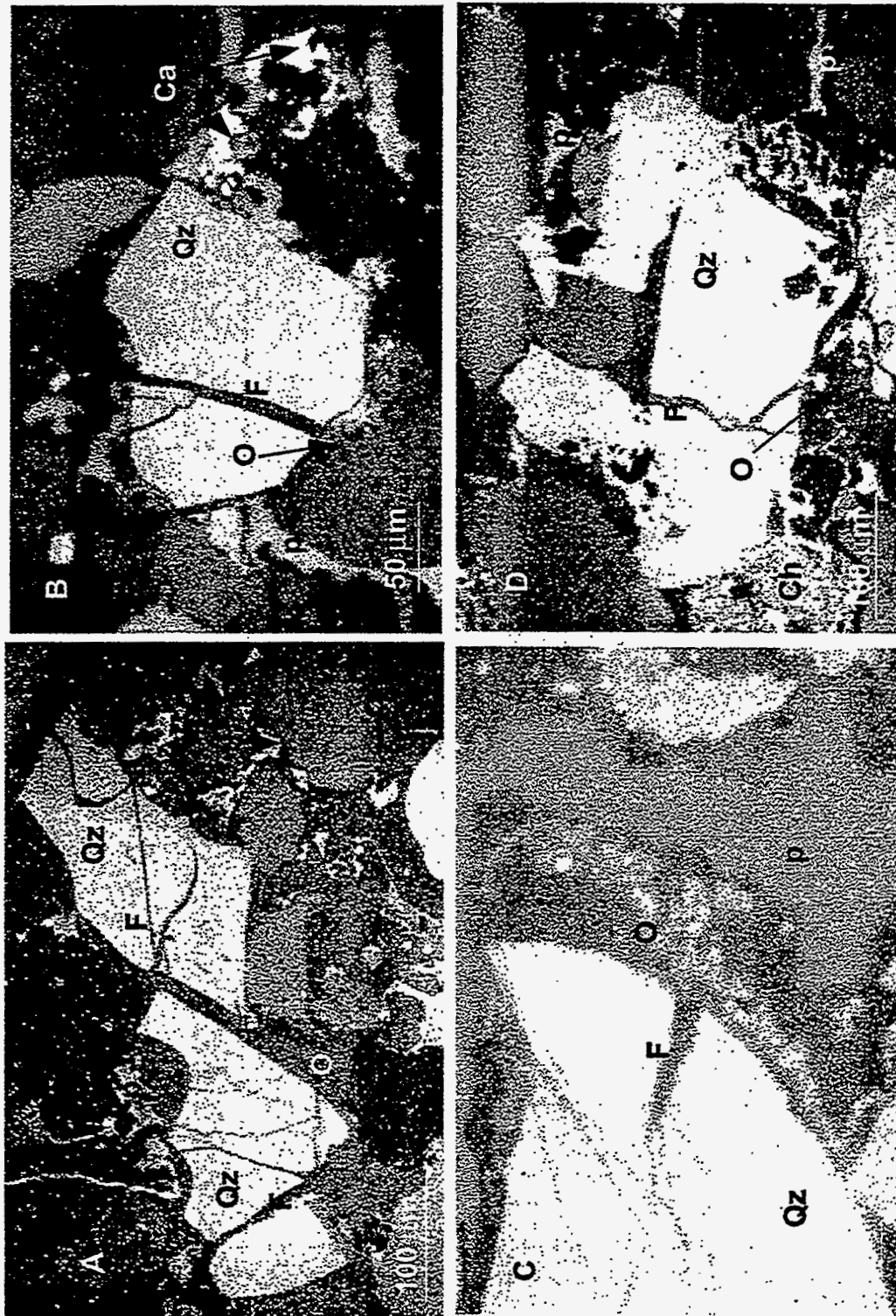


Figure 17. Scanned CL images of microfractures. Qz, quartz; Ch, chlorite; O, overgrowth quartz cement; Ca, calcite; P, porosity; F, fracture.

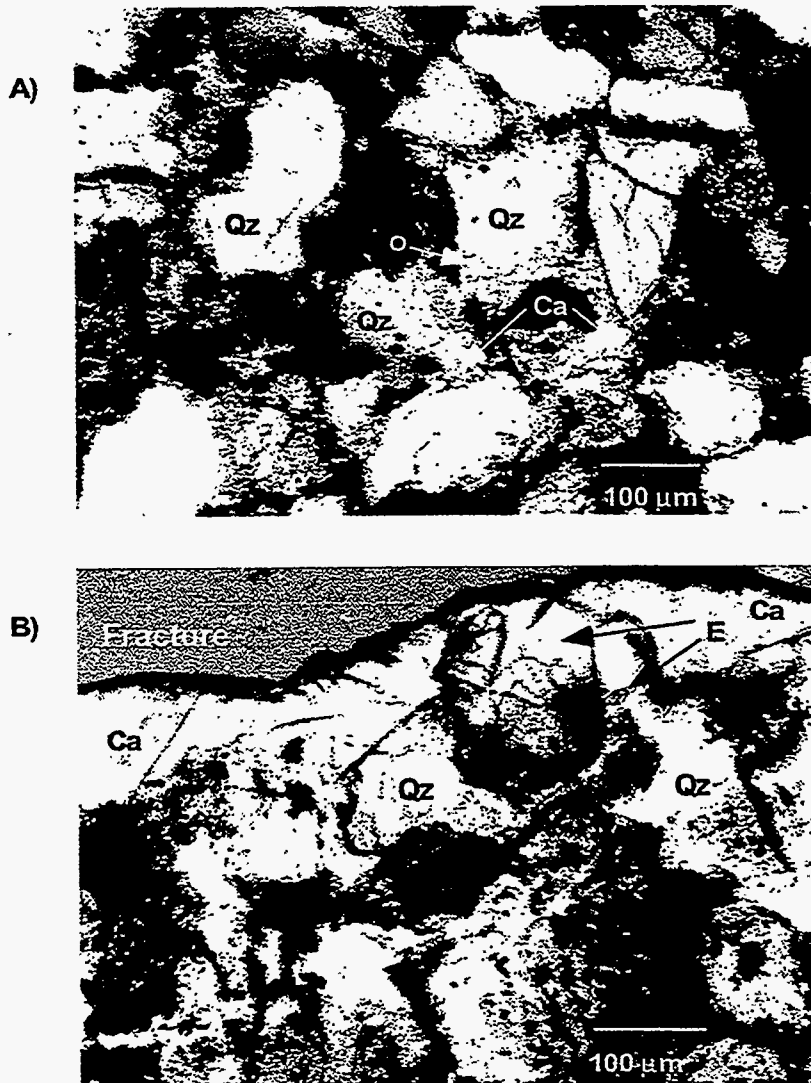


Figure 18. Late carbonate cement in sandstones of the Mesaverde Group. A) Carbonate cement (Ca) surrounding quartz overgrowths (O). Sample FI-29, Cottonwood pavement, crossed polars. B) Late carbonate cement (Ca) lining fracture wall. Notice euhedral quartz (E) rooted in matrix quartz grains and surrounded by carbonate cement. Sample 6008, San Juan 32-9 well, plane light.

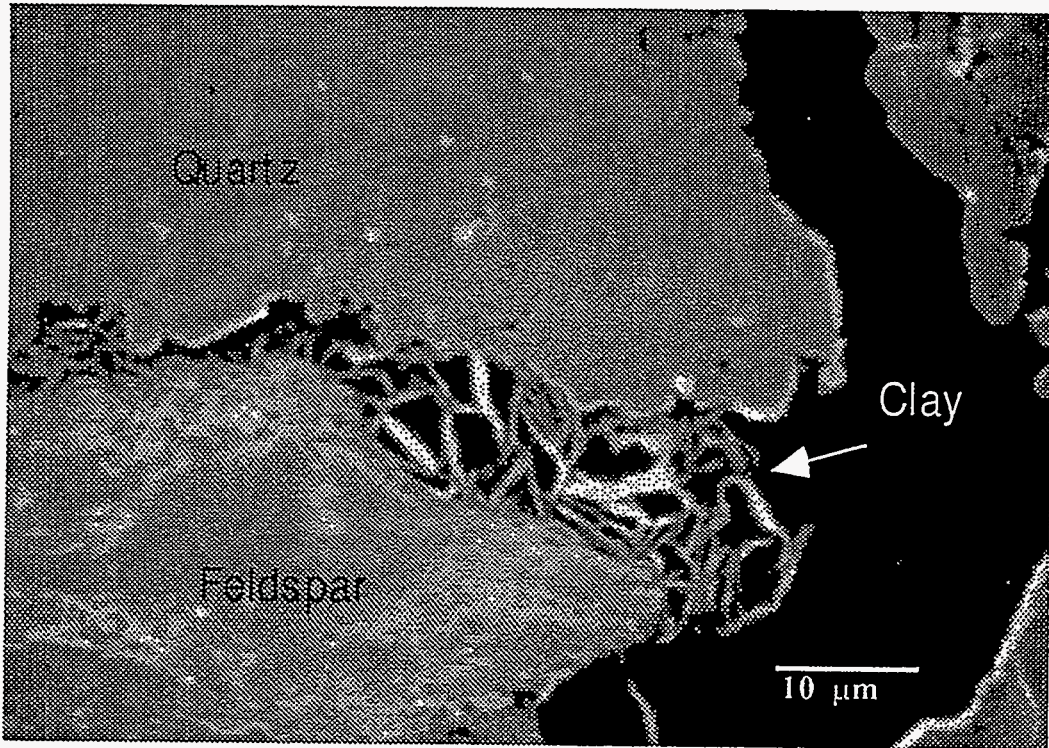


Figure 19. Late clay cement. Sample 3-8, SEM photomicrograph. Riddle D LS 4A. This cement is usually found in association with partially dissolved feldspar grains clogging remnant porosity left by late carbonate cement.

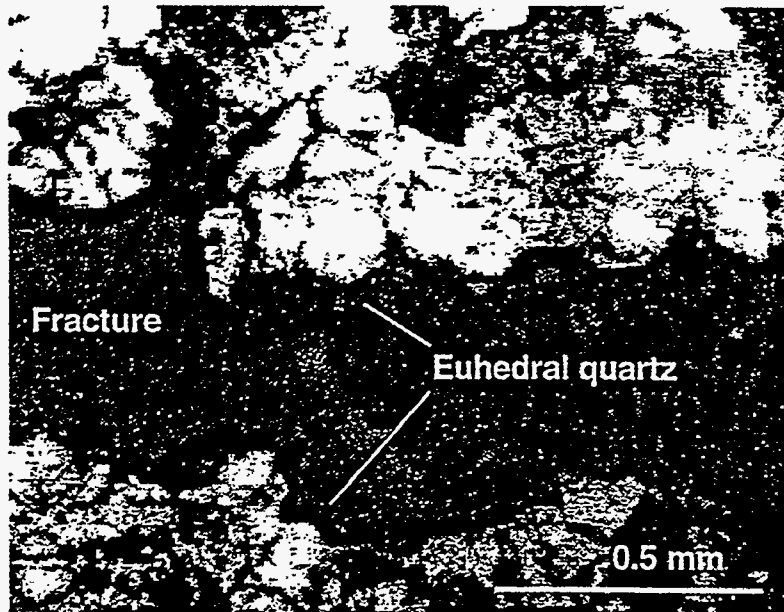


Figure 20. Euhedral quartz in fracture that appears no mineralized at macroscopic scale. Sample 5009.3, plane light, Riddle D LS 4A.

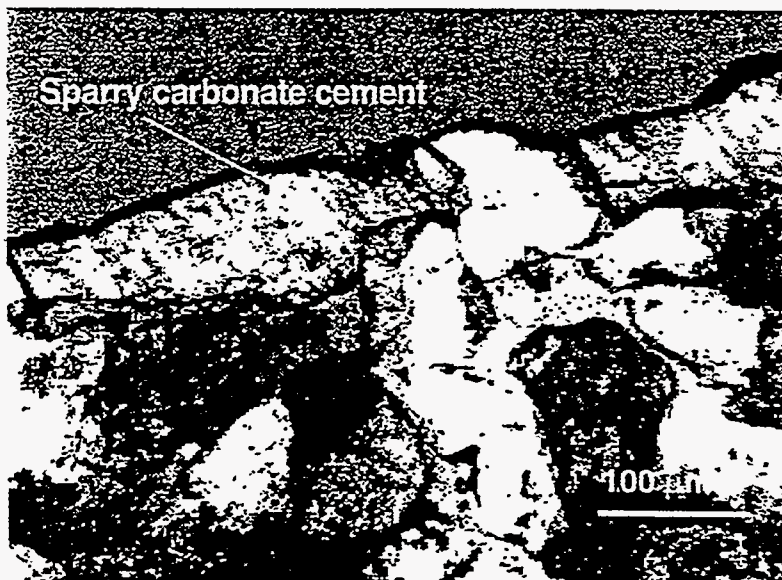


Figure 21. Sparry carbonate cement on fracture wall. Sample 6008, plane light, San Juan 32-9.

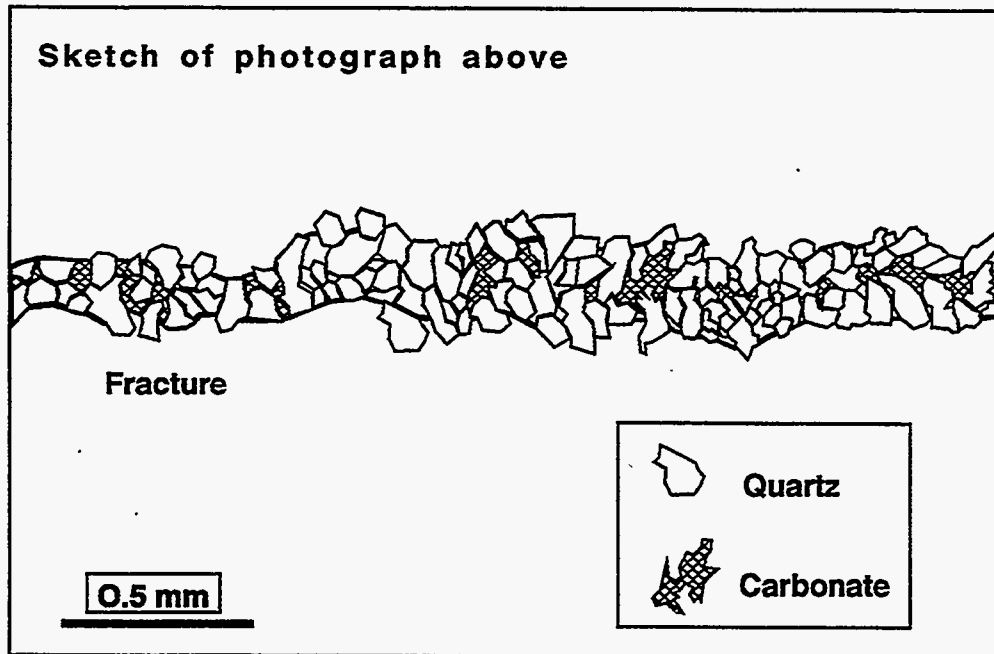
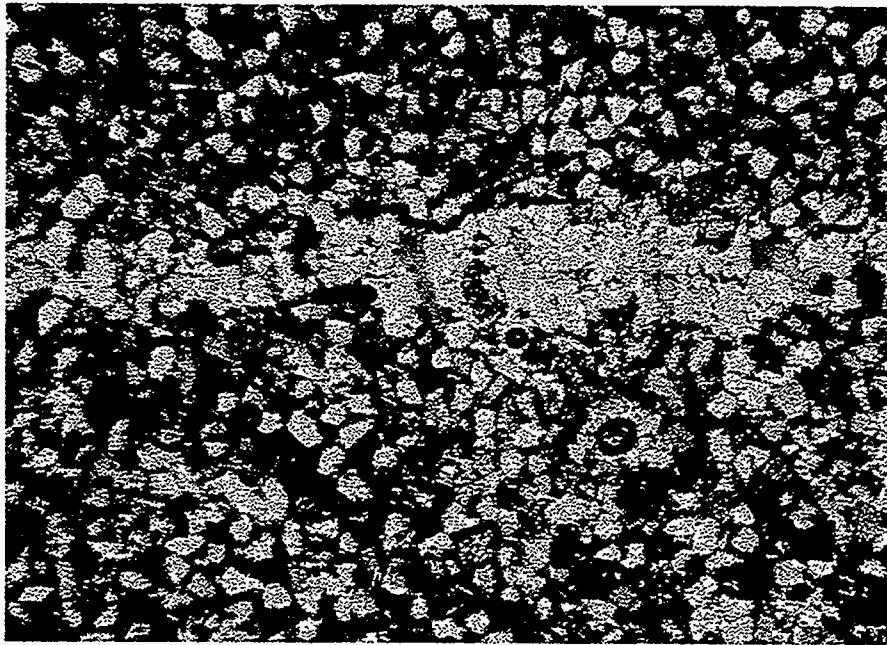


Figure 22. Quartz- and carbonate-filled open-mode fracture. Sample FI-18, cross-polarized light, Cottonwood pavement.

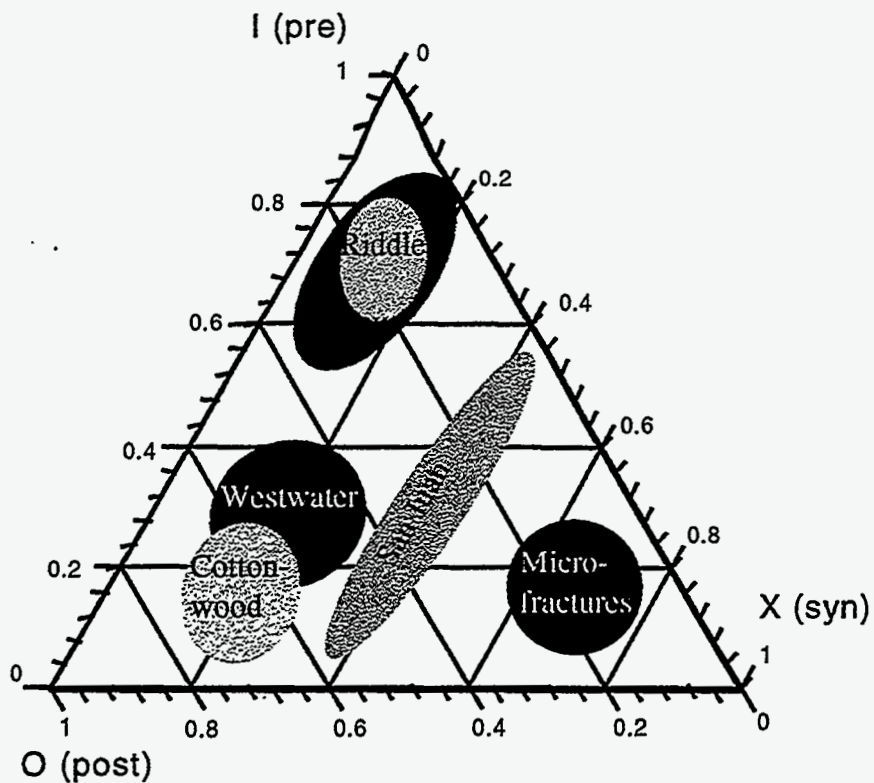


Figure 23. Cement classification of samples analyzed according to macrofracture formation/cement precipitation timing. Riddle D LS 4A and Sunray H Com #6 wells macrofractures are lined with small volumes of synkinematic and postkinematic euhedral quartz but most of the cement is prekinematic. San Juan 32-9 well macrofractures are filled with synkinematic euhedral quartz and variable amounts of postkinematic carbonate cement. Outcrop samples show important volumes of postkinematic carbonate cement. Most microfractures in the samples analyzed are filled with synkinematic quartz cement

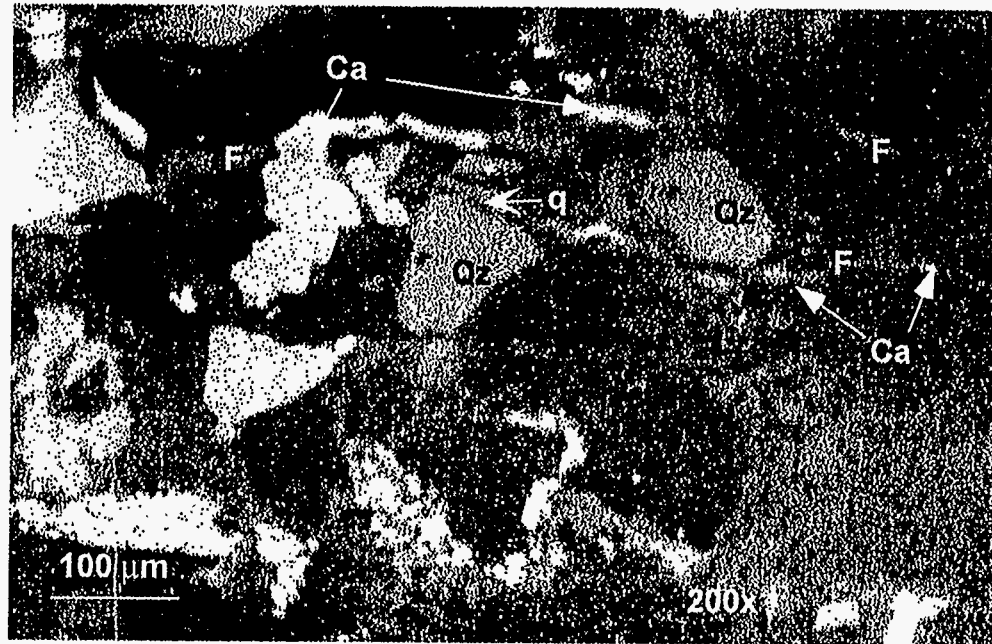


Figure 24. SEM-CL photomicrograph showing transgranular (category I) fractures (F) in sample 6008.1, San Juan 32-9 well. Notice that quartz cement (q) fills segments of the fractures where quartz grains were cut, other segments contain highly luminescent carbonate cement (Ca) or they are open.

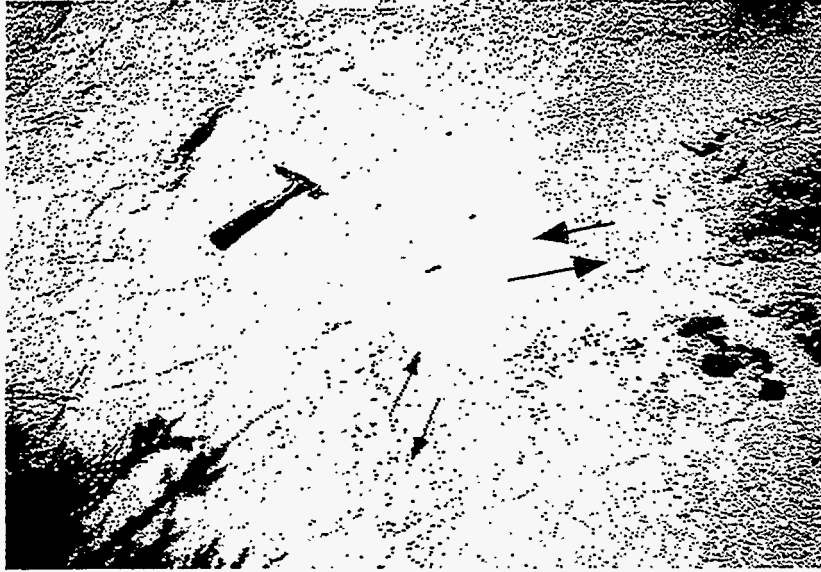


Figure 25. Shear-mode fractures (faults, marked in white) showing interpreted kinematics. Westwater pavement.

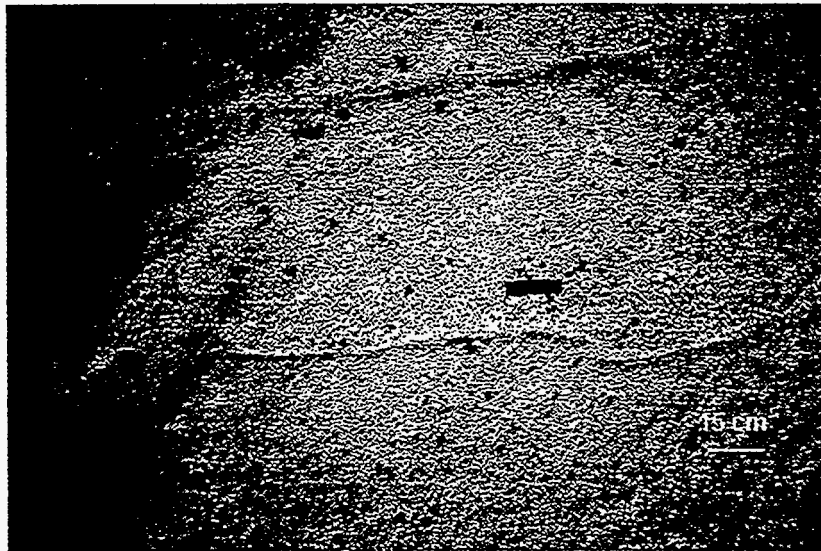


Figure 26. Open-mode fractures. Westwater pavement. Ruler (rectangle) indicates location of double hook fracture terminations (type V in Fig. 6). Another fracture, showing a hook termination (type III) appears in the upper right side of the photo.



Figure 27. Joints at the border of a canyon in Westwater pavement (A) and polygonal cracks next to a creek, Cottonwood pavement (B).

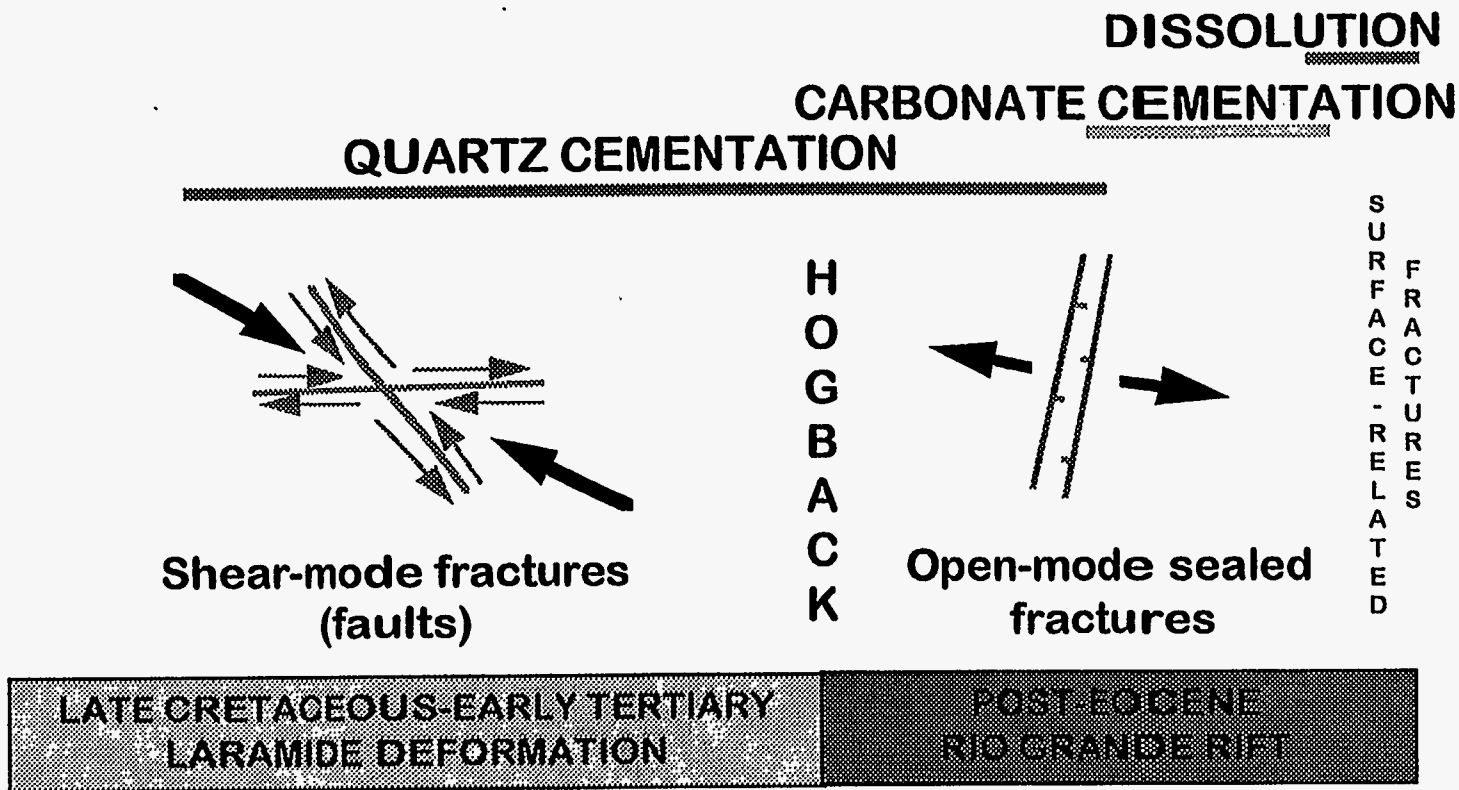


Figure 28. Proposed fracture history of the Mesaverde Group derived from outcrop observations and interpreted diagenetic history. Only open-mode fractures were identified in the subsurface.

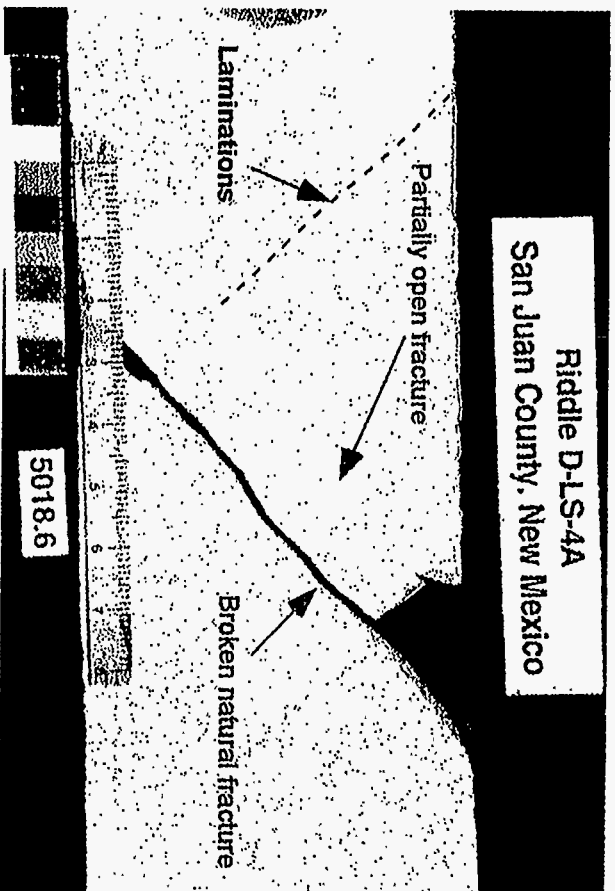


Figure 29. Open-mode natural fractures. Laminations are dark and light bands at high angle with the fractures. Riddle D LS 4A. Ruler is graduated in centimeters.

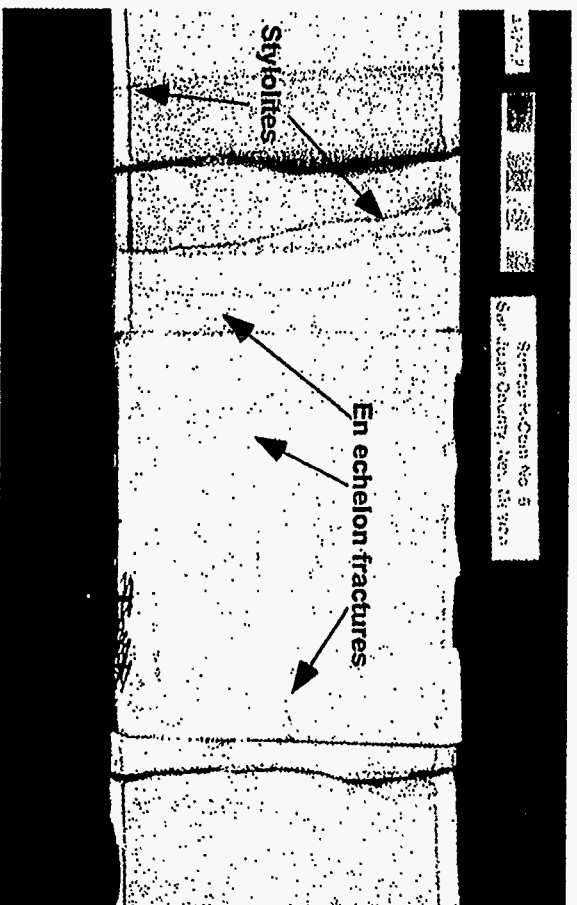


Figure 30. En echelon natural fractures and stylolites. Stylolites are dark, irregular and serrate surfaces at high angle with the axis of the core. Sunray H Com #6. Ruler is 8 centimeters long.

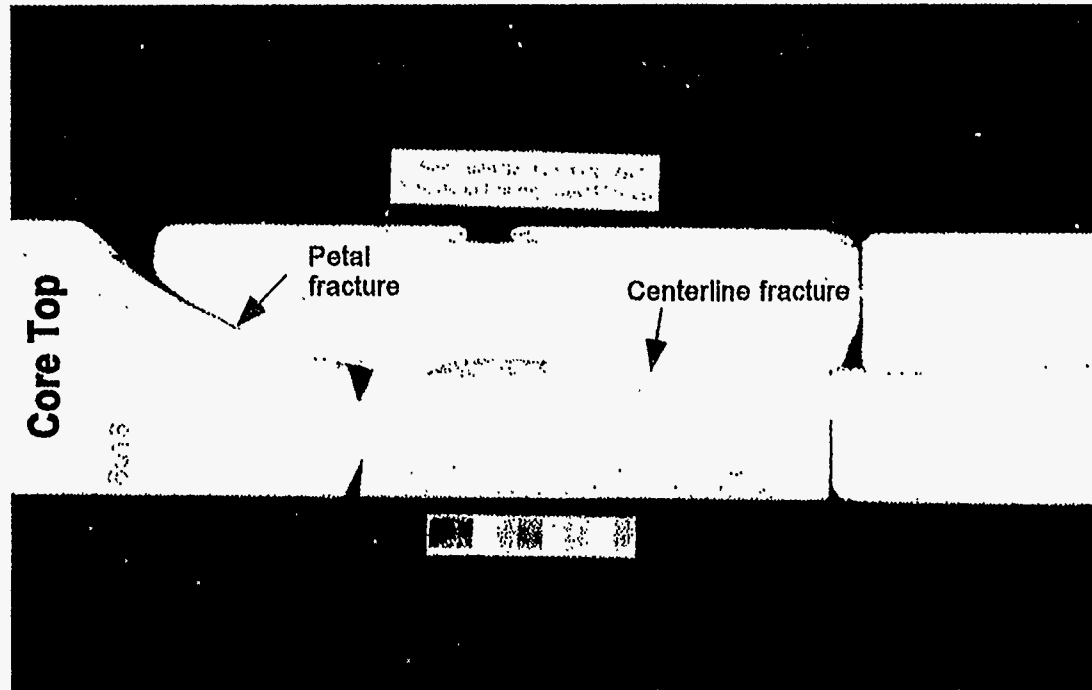


Figure 31. Drilling induced petal-centerline fracture (Kulander et al., 1990). San Juan 32-9. Ruler is 8 centimeters long.

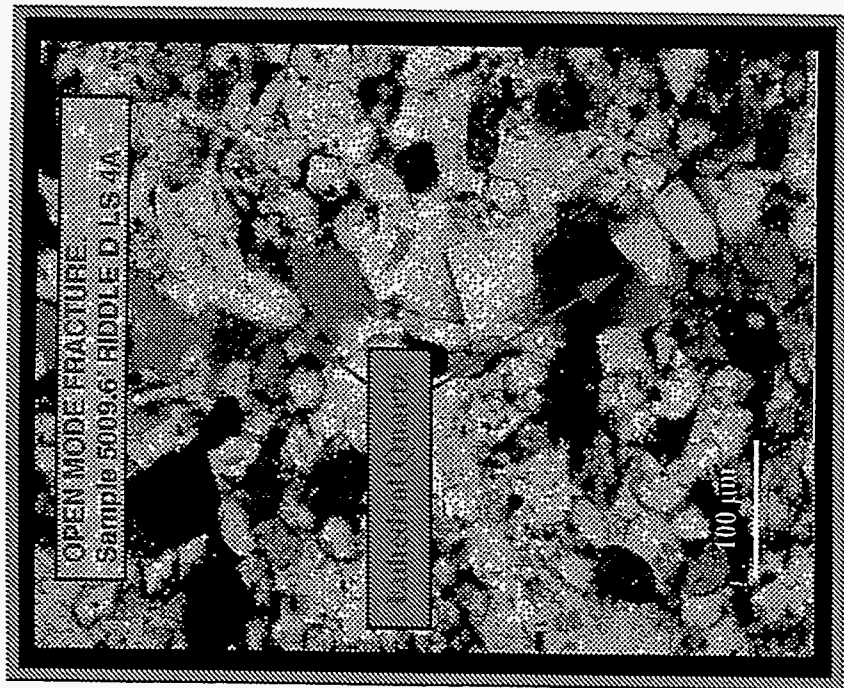
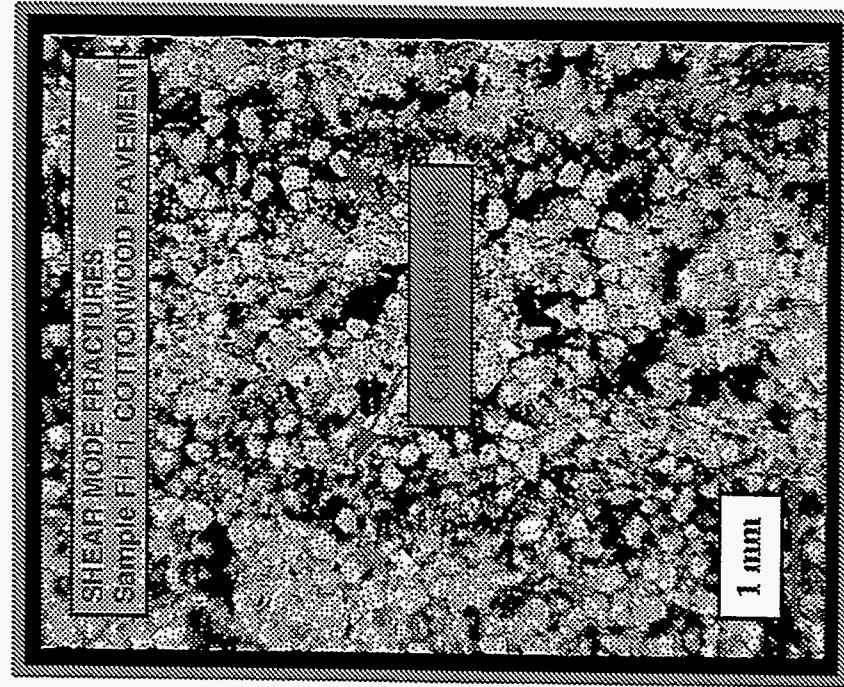


Figure 32. Microscopic morphology of open-mode and shear-mode macrofractures.

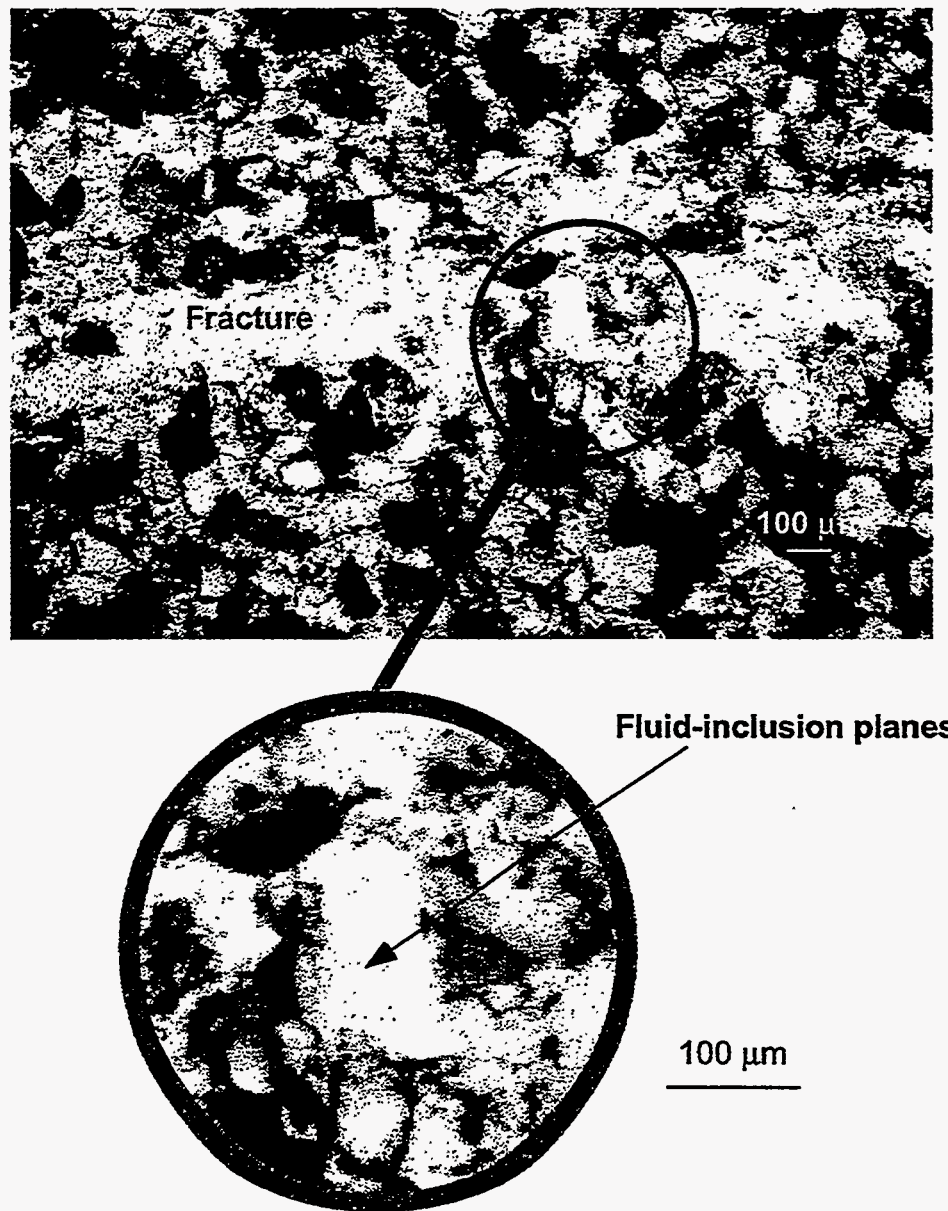
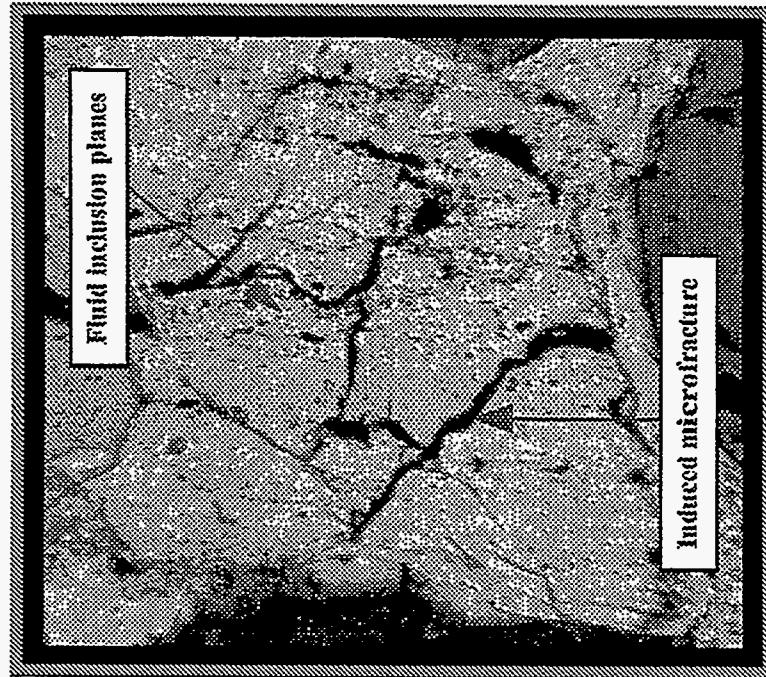


Figure 33. Definitive evidence for synkinematic crack-seal texture in quartz crystal. Partially filled fracture. Light gray patches next to euhedral quartz are fracture-porosity remnants. Sample 5009.6, plane light, Riddle D LS 4A.

A) PETROGRAPHIC IMAGE



B) CL-DETECTOR IMAGE

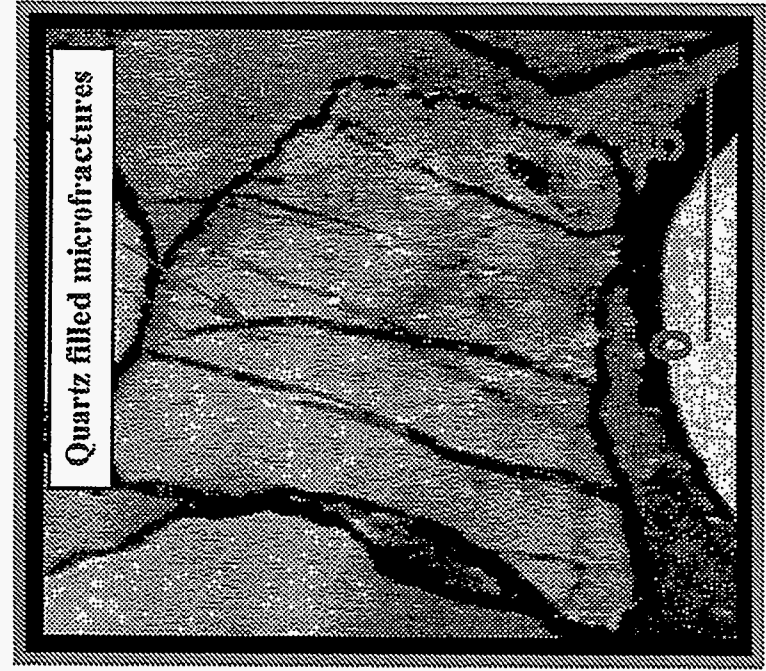
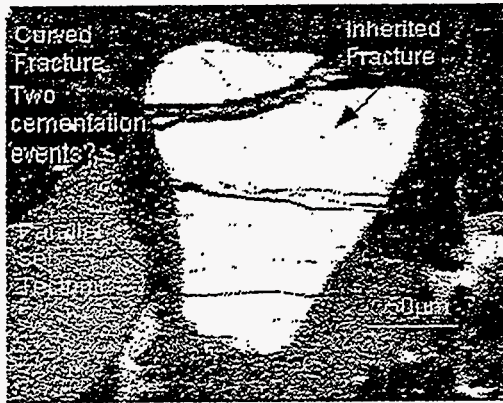
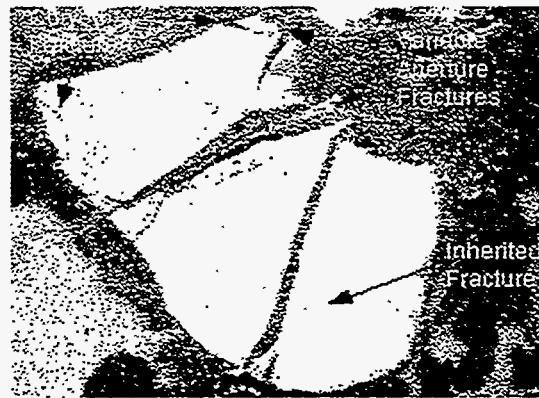


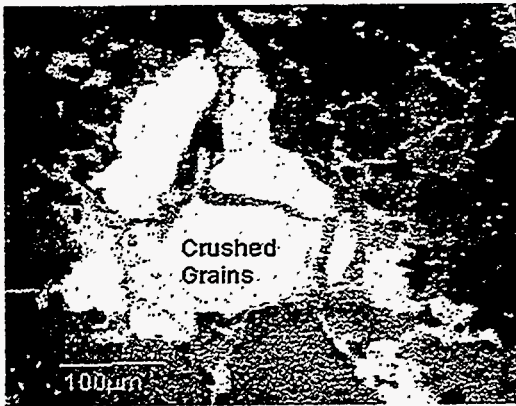
Figure 34. Petrographic (A) and SEM-CL image (B) of a fractured quartz grain. Sample FI-20. Cottonwood pavement.



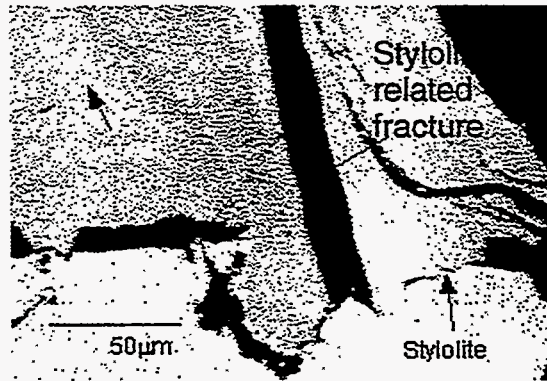
A. Riddle D LS 4A. Sample 3-20. 5013.15'.



B. Riddle D LS 4A. Sample 3-3. 4995.15'.



C. Riddle D LS 4A. Sample 4-12. 5027.1'.

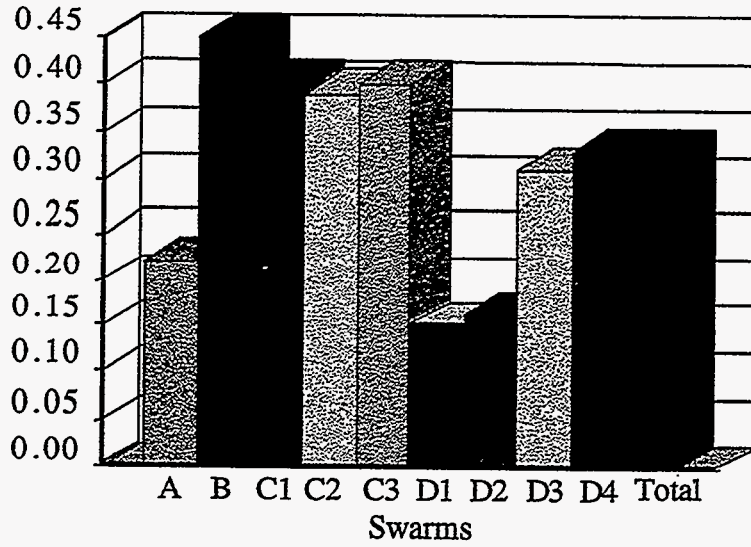


D. Sunray H Com #6. Sample M4974. 4974.95'.

Figure 35. Microfracture morphologies under the SEM-CL. Fractures show varied morphologies at this observational scale. Microfracture generation processes are also diverse.

C
o
n
n
e
c
t
i
v
i
t
y

Westwater Pavement



C
o
n
n
e
c
t
i
v
i
t
y

Cottonwood Pavement

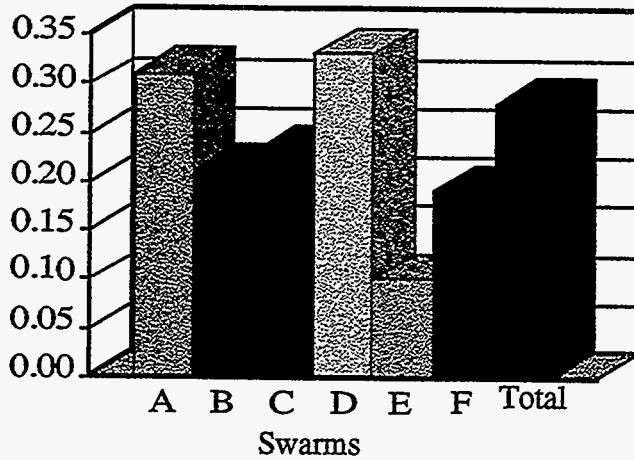


Figure 36. Degree of connectivity in fracture swarms, following Robinson (1983). The degree of connection of fracture swarms in Westwater pavement is higher than in Cottonwood pavement.

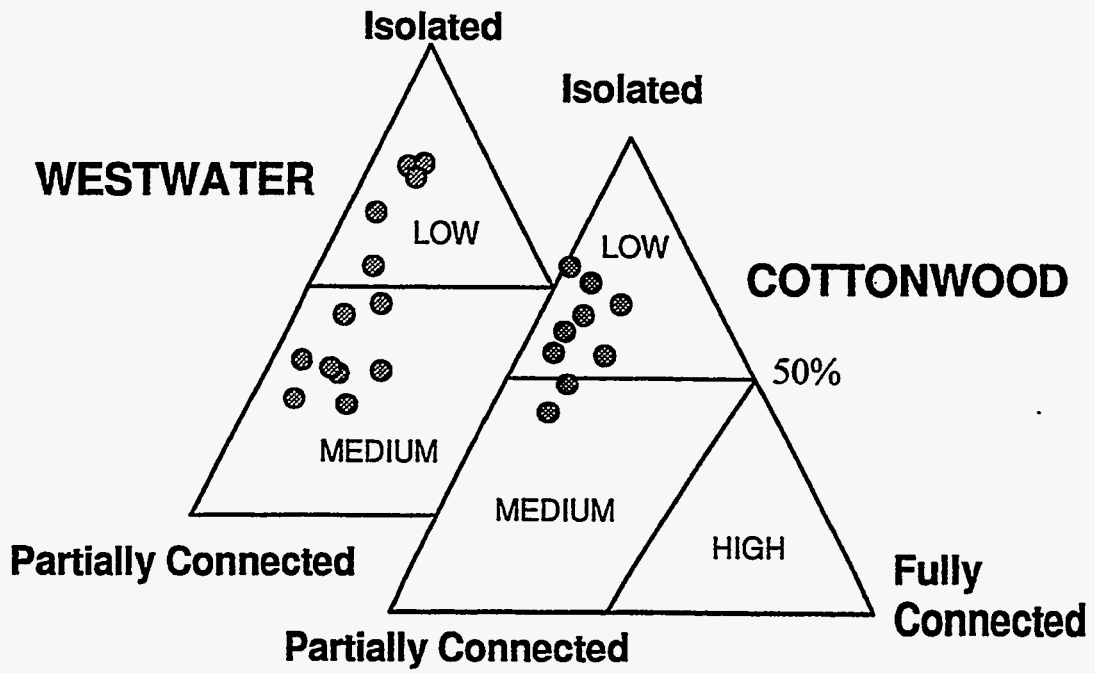


Figure 37. Proportion of connection of fracture swarms in pavements studied. (Modified from Laubach, 1992)

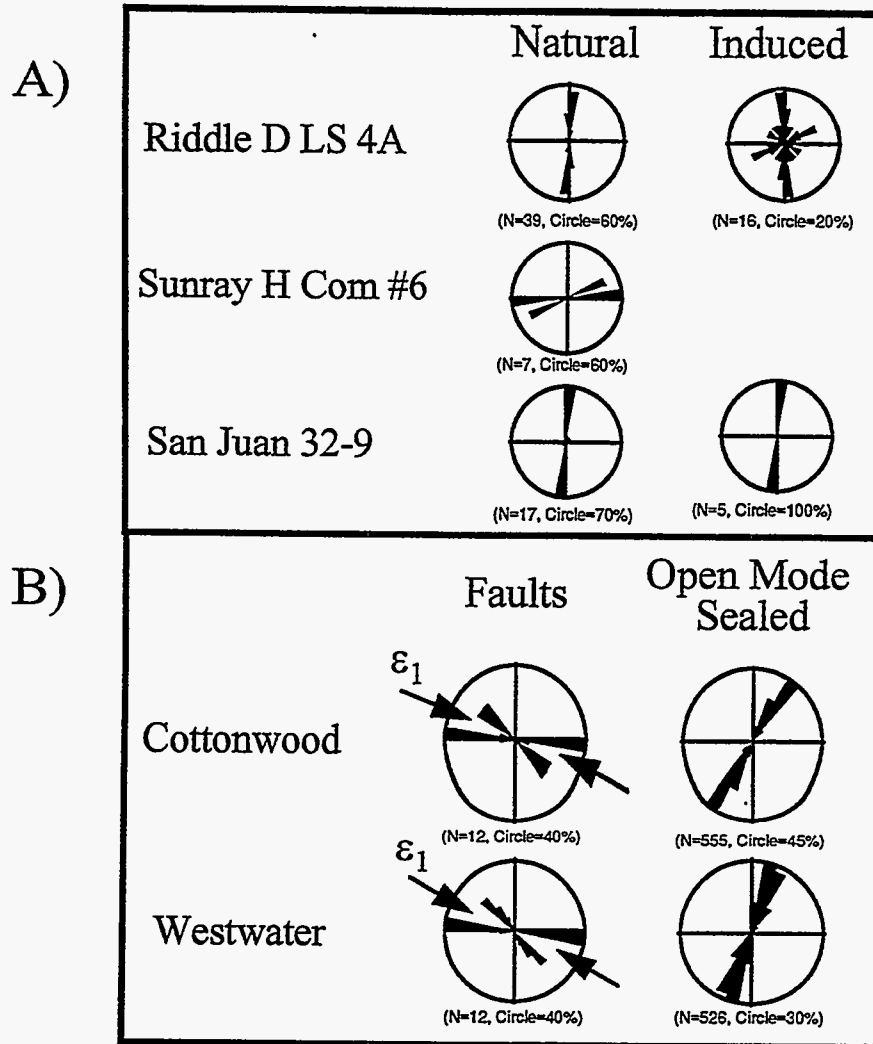


Figure 38. Macrofracture strikes from cores (A) and outcrops (B) of Mesaverde Group sandstones. N is the number of macrofractures measured; Circle indicates approximate size (as a percentage of the total population of fractures) of largest petal in rose diagrams; ϵ_1 , is the interpreted horizontal projection of the maximum principal shortening direction for the conjugate fault systems.

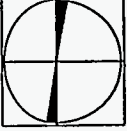
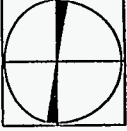

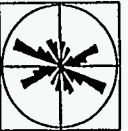
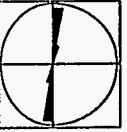
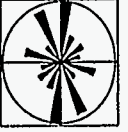


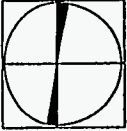
UNIT	BEDS	FRACTURE TIP DEPTH (feet)	MACROFRACTURE ORIENTATION	SAMPLE	DEPTH (feet)	WEIGHTED ORIENTATION	WEIGHTED ORIENTATION	WEIGHTED ORIENTATION	OBSERVATIONS
						1+2	1+2+3	ALL	
CLIFF	NO DATA								
	1	4936.5 4936.6	 N=2, CIRCLE=100%						
HOUSE	NO DATA								
	2	4939.4	 N=1, CIRCLE=100%	2-3	4939.2	 N=10, CIRCLE=20%	 N=19, CIRCLE=20%		NO MATCH
	NO DATA								
	3	4940.7 4941 4942.1 4942.5	 N=4, CIRCLE=80%	2-7	4943.5	 N=8, CIRCLE=12%	 N=38, CIRCLE=12%	 N=51, CIRCLE=16%	TESTED IF SUFFICIENT SAMPLES GIVE MACROFRACTURE ORIENTATION
	4	4944.7	 N=1, CIRCLE 100%	4946.1	4946.1				

Figure 39. Microfracture vs. macrofracture orientations. Riddle D LS 4A .


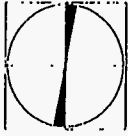
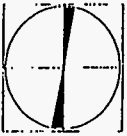
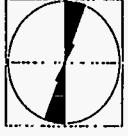
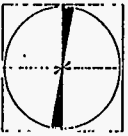
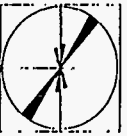
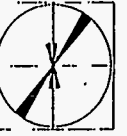

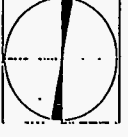
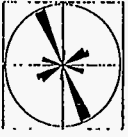

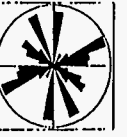
UNIT	BEDS	FRACTURE TIP DEPTH (feet)	MACROFRACTURE ORIENTATION	SAMPLE	DEPTH (feet)	WEIGHTED ORIENTATION	WEIGHTED ORIENTATION	WEIGHTED ORIENTATION	OBSERVATIONS
						I+2	I+2+3	ALL	
CLIFF HOUSE	NO DATA								
	5	4996 4996 4996.1 4996.1 4996.1	 N=5, CIRCLE=40%	3-3 3-4V	4995.15 4996.3	 N=17, CIRCLE=88%	 N=27, CIRCLE=92%		VERY GOOD MATCH
	6	5000 5000.1 5000.1 5000.2 5000.4 5000.4 5001.1	 N=7, CIRCLE=40%	3-8	5000.45	 N=4, CIRCLE=78%	 N=6, CIRCLE=46%	 N=25, CIRCLE=46%	GOOD RESULTS. NORTHEAST ORIENTATION CORRESPONDS TO INDUCED MICROFRACTURES
	NO DATA								
7	5003.9 5003.9 5004	 N=3, CIRCLE=66%	3-13 V	5005					
8	5005.7 5005.8 5006 5006.3 5006.3 5006.6	 N=6, CIRCLE=100%	3-14	5006.3	 N=6, CIRCLE=40%	 N=14, CIRCLE=22%	 N=23, CIRCLE=32%	FAIR RESULTS	

Figure 39 (Continued). Microfracture vs. macrofracture orientations. Riddle D LS 4A .

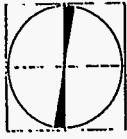
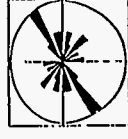


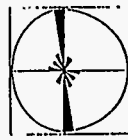
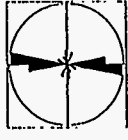

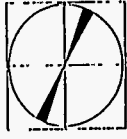
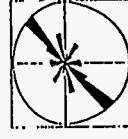
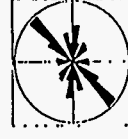
UNIT	BEDS	FRACTURE TIP DEPTH (feet)	MACROFRACTURE ORIENTATION	SAMPLE	DEPTH (feet)	WEIGHTED ORIENTATION 1+2	WEIGHTED ORIENTATION 1+2+3	WEIGHTED ORIENTATION ALL	OBSERVATIONS
CLIFF	NO DATA								
	9	5009.3 5009.6	 N=2, CIRCLE=100%	3-17	5009.54	 N=13, CIRCLE=22%	 N=21, CIRCLE=16%	 N=27, CIRCLE=14%	FAIR RESULTS
	NO DATA								
HOUSE				3-18	5011.4	 N=7, CIRCLE=44%	 N=17, CIRCLE=36%	 N=29, CIRCLE=34%	NO MACRO DATA. 1+2 CONSISTENT WITH MACROFRACTURE ORIENTATION AT OTHER DEPTHS
	10			3-19	5012.1				
		5013.5	 N=1, CIRCLE=100%	3-20	5013.15	 N=11, CIRCLE=30%	 N=24, CIRCLE=22%		POSSIBLE SAMPLE ORIENTATION PROBLEM
NO DATA									

Figure 39 (Continued). Microfracture vs. macrofracture orientations. Riddle D LS 4A .

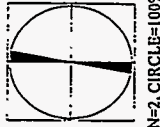

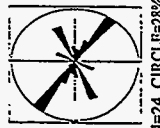
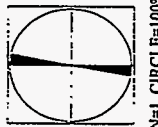
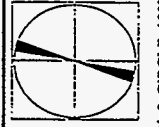


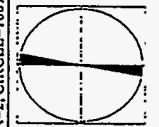
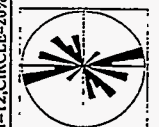
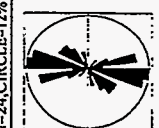
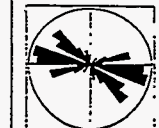
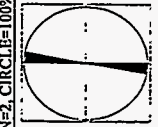

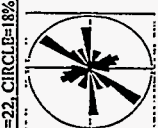

UNIT	BEDS	FRACTURE TIP DEPTH (feet)	MACROFRACTURE ORIENTATION	SAMPLE	DEPTH (feet)	WEIGHTED ORIENTATION I+2	WEIGHTED ORIENTATION I+2+3	WEIGHTED ORIENTATION ALL	OBSERVATIONS	
CLIFF HOUSE	11	5018.5018.5	 N=2, CIRCLE=100%	4-3	5018.25	 N=11, CIRCLE=30%	 N=24, CIRCLE=28%	ALL	POOR RESULTS	
		5020.4	 N=1, CIRCLE=100%	4-5	5020.1					
		5023.1 5023.3	 N=2, CIRCLE=100%	4-7	5022.45	 N=12, CIRCLE=20%	 N=24, CIRCLE=12%			FAIR RESULTS
	12	5025.8 5026	 N=2, CIRCLE=100%	4-10	5025.1	 N=10, CIRCLE=22%	 N=22, CIRCLE=18%	 N=29, CIRCLE=18%		GOOD RESULTS
		5028.5	 N=1, CIRCLE=100%	4-12	5027.1	 N=21, CIRCLE=18%	 N=27, CIRCLE=18%	 N=33, CIRCLE=14%		AMBIGUOUS RESULTS

Figure 39 (Continued). Microfracture vs. macrofracture orientations. Riddle D LS 4A .

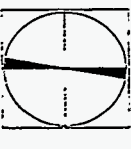

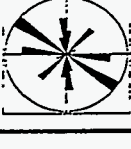
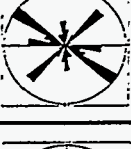



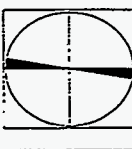
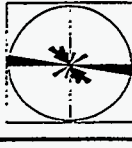
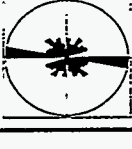

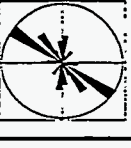


UNIT	BEDS	FRACTURE TIP DEPTH (feet)	MACROFRACTURE ORIENTATION	SAMPLE	DEPTH (feet)	WEIGHTED ORIENTATION 1+2	WEIGHTED ORIENTATION 1+2+3	WEIGHTED ORIENTATION ALL	OBSERVATIONS
CLIFF	13	5031.4	 N=1, CIRCLE=100%	4-16	5031.15	 N=5, CIRCLE=50%	 N=12, CIRCLE=26%	 N=20, CIRCLE=22%	FAIR RESULTS
	NO DATA								
HOUSE				4-20	5035.2	 N=5, CIRCLE=38%	 N=18, CIRCLE=20%	 N=27, CIRCLE=12%	NO MACRO-FRACTURE DATA
	14	5036.2	 N=2, CIRCLE=100%	4-21	5036.1	 N=11, CIRCLE=30%	 N=18, CIRCLE=18%	 N=19, CIRCLE=16%	VERY GOOD RESULTS
				4-23	5038.1	 N=10, CIRCLE=30%	 N=13, CIRCLE=26%	 N=24, CIRCLE=16%	NO MACRO-FRACTURE DATA

Figure 39 (Continued). Microfracture vs. macrofracture orientations. Riddle D LS 4A .

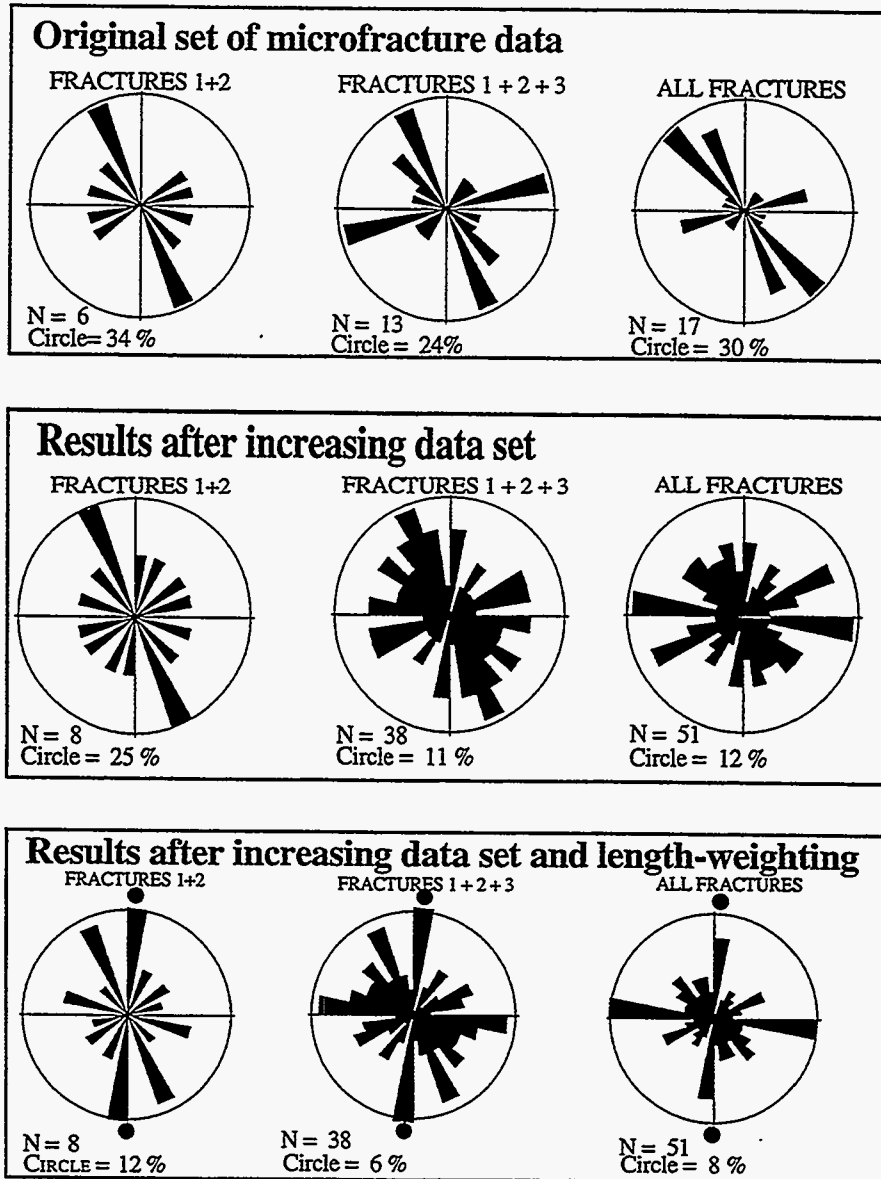






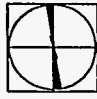
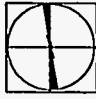
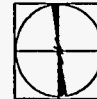
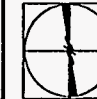

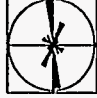





Figure 40. Microfracture orientation abundance data test. Sample 2-7, Riddle D LS 4A. Black circles outside the rose diagrams in lowest row indicate the strike of the macrofractures at the depth of sample 2-7.

San Juan 32-9

UNIT	BED	FRACTURE TIP DEPTH (feet)	MACROFRACTURE ORIENTATION	SAMPLE	DEPTH (feet)	WEIGHTED ORIENTATION 1	WEIGHTED ORIENTATION 1+2	WEIGHTED ORIENTATION 1+2+3	WEIGHTED ORIENTATION ALL	OBSERVATIONS
MENEFER	1	5887.0 5893.5		32-9 5894.4H	5894.4					RECORDS TWO SETS OF OPEN MODE MACRO-FRACTURES (NS/EW)
			N=2, CIRCLE=100%			N=20, CIRCLE=18%	N=93, CIRCLE=12%	N=135, CIRCLE=10%	N=157, CIRCLE=10%	
LOOKNOTUT	2	6007.4"		32-9 6008.1H	6008.1					VERY GOOD RESULTS
			N=1, CIRCLE=100%			N=21, CIRCLE=70%	N=43, CIRCLE=38%	N=85, CIRCLE=42%	N=100, CIRCLE=38%	

Sunray H Com #6

UNIT	BED	FRACTURE TIP DEPTH (feet)	MACROFRACTURE ORIENTATION	SAMPLE	DEPTH (feet)	WEIGHTED ORIENTATION 1	WEIGHTED ORIENTATION 1+2	WEIGHTED ORIENTATION 1+2+3	WEIGHTED ORIENTATION ALL	OBSERVATIONS
CHOUFSF	1	4986.58' 4986.62' 4986.64' 4986.73'		M4986.74	4986.64					GOOD MATCH WITH N-S FRACTURE SET BUT NOT E-W LOCAL MACRO-FRACTURES
			N=4, CIRCLE=100%			N=9, CIRCLE=36%	N=43, CIRCLE=16%	N=93, CIRCLE=10%	N=107, CIRCLE=12%	

Outcrops









UNIT	BED	PAVEMENT	MACROFRACTURE ORIENTATION	SAMPLE	WEIGHTED ORIENTATION 1+2	WEIGHTED ORIENTATION 1+2+3	WEIGHTED ORIENTATION ALL	OBSERVATIONS
CHOUFSF	1	COTTON-WOOD		FI-19				POSSIBLE SAMPLE ORIENTATION PROBLEM
			N=555, CIRCLE=4%		N=35, CIRCLE=22%	N=79, CIRCLE=16%	N=95, CIRCLE=14%	
LOOKNOTUT	2	WEST-WATER		WS-13				GOOD RESULTS
			N=1, CIRCLE=100%		N=75, CIRCLE=16%	N=89, CIRCLE=14%	N=151, CIRCLE=10%	

Figure 41. Microfractures vs. macrofracture orientations. San Juan 32-9, Sunray H Com #6 wells and outcrops.

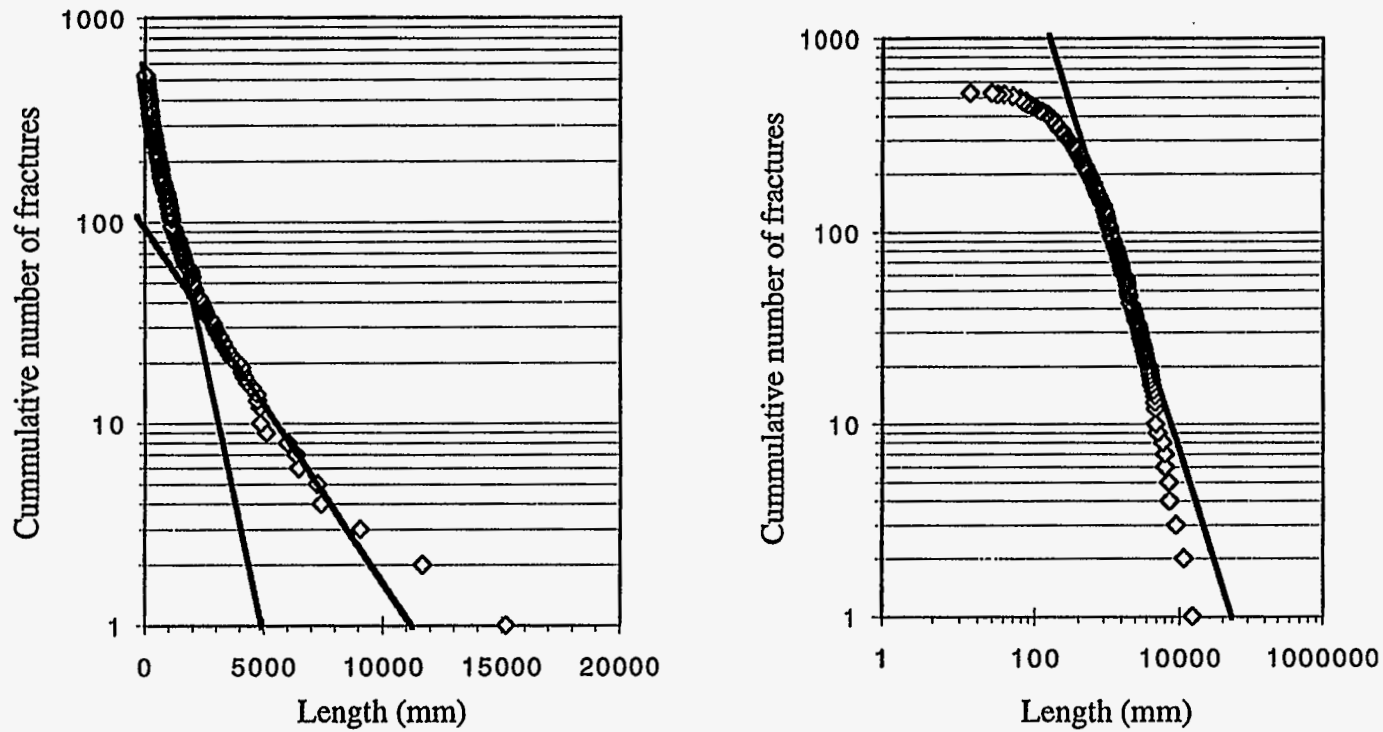


Figure 42. Log-linear and log-log graphs for one fracture size population in the study. Notice that exponential function underestimates number of observed fractures regardless of whether small or large fractures are used to generate a regression fit. Power-law model best fits observations but overpredicts number of fractures, which is possible if sampling is inadequate at extreme ends of size distribution.

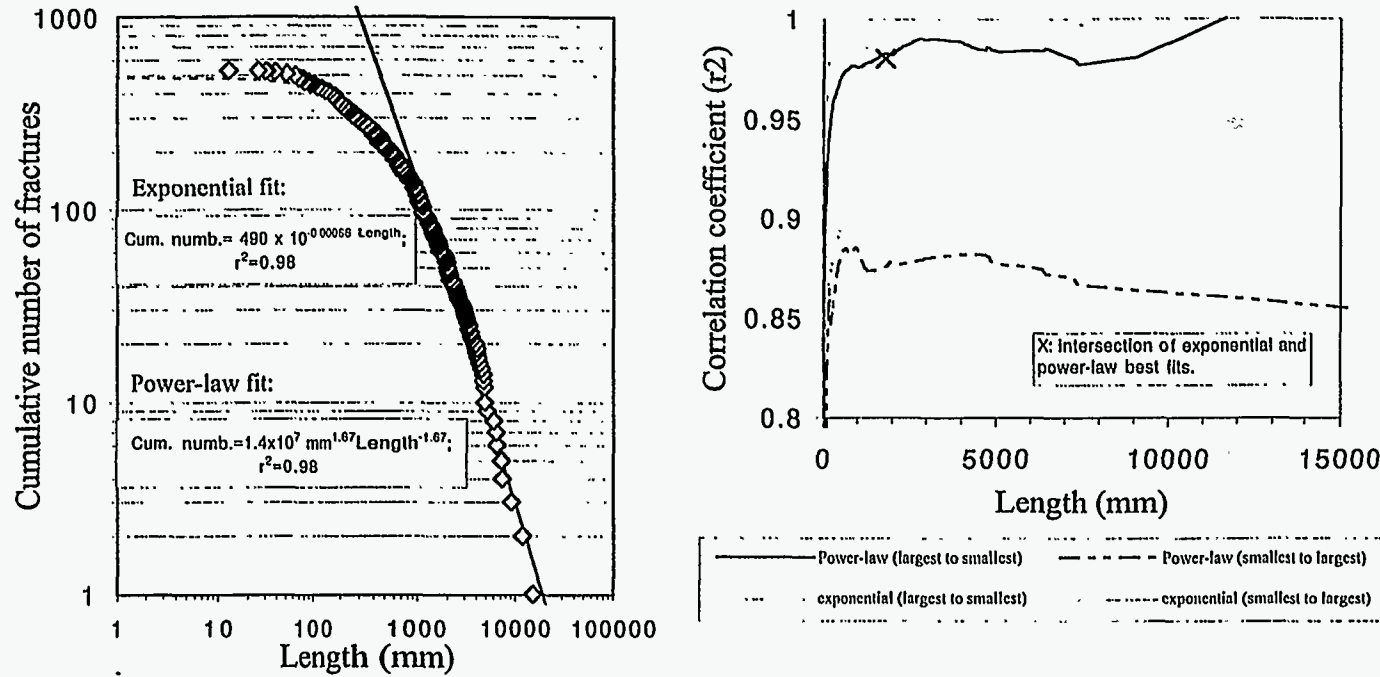


Figure 43. Multiple regression correlation-coefficient analysis for the fracture size distribution in Figure 42. The exponential model best explains the smallest fracture sizes but the power-law model best explains the middle part of the distribution. The correlation coefficient (r^2) is maximum for this selection of models as indicated by the graph to the right. The power-law model parameters are considered the ones characteristic for this fracture size distribution because they better explain the part of the distribution with best control in this observation scale. The exponential distribution for the smallest fractures is probably an artifact produced by sampling truncation.

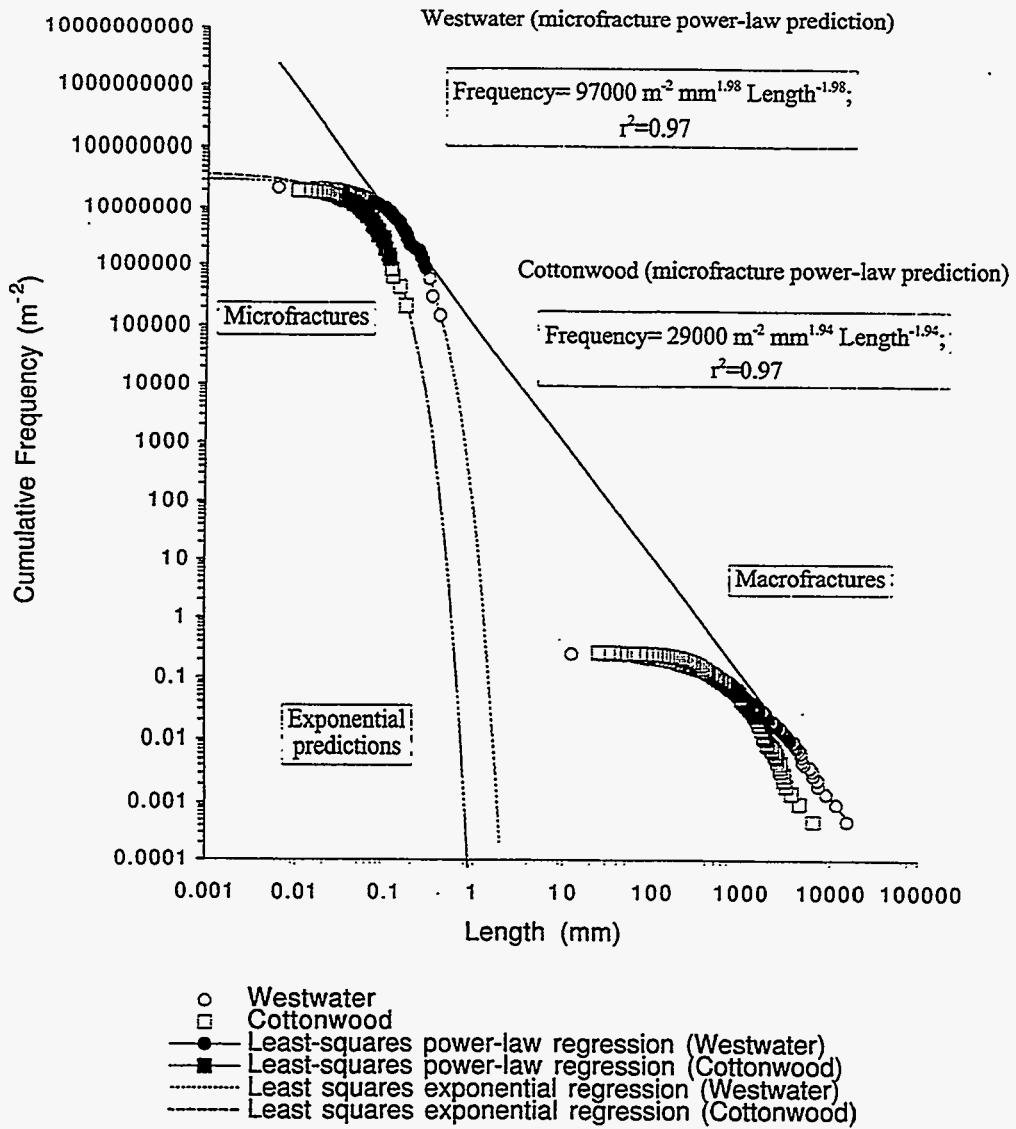


Figure 44. Fracture size distribution, Westwater Canyon pavement.

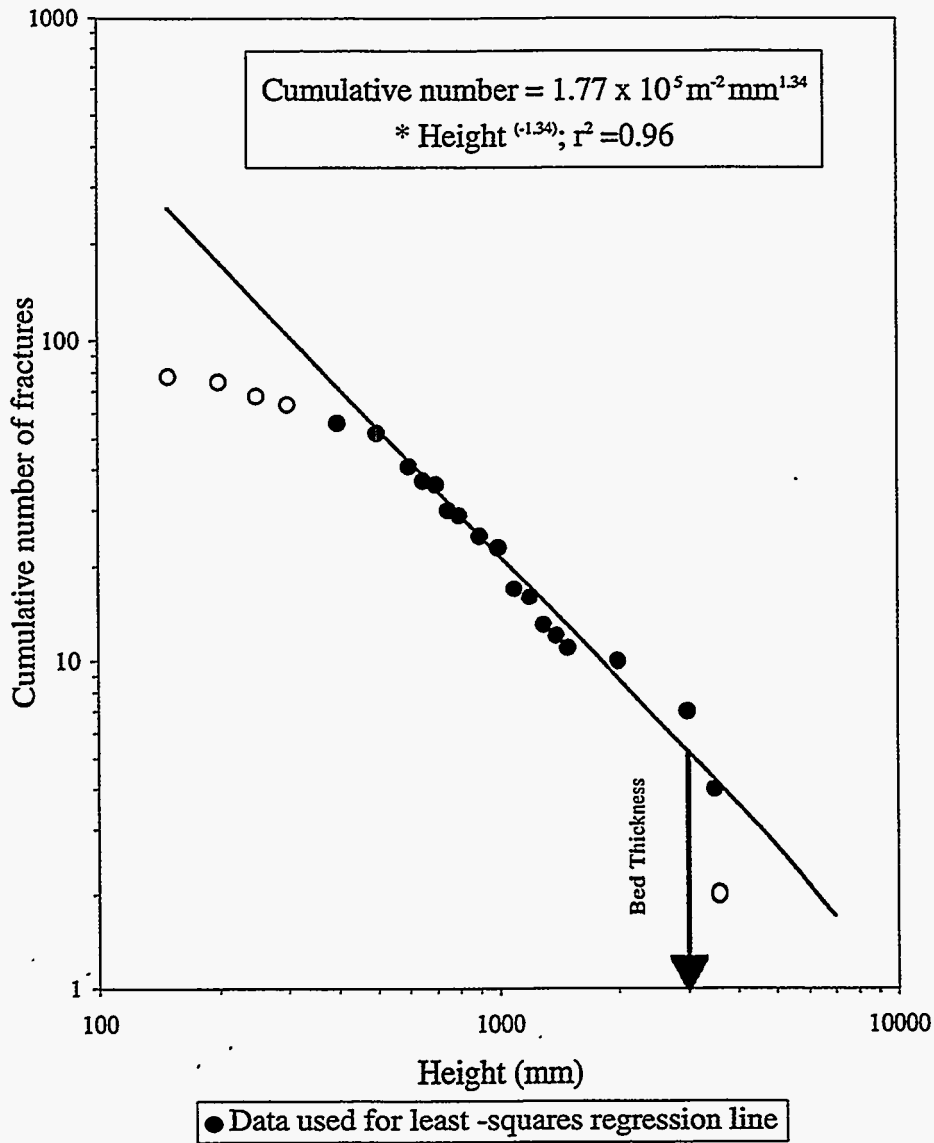


Figure 45. Fracture height distribution. Westwater Springs Canyon. Fracture height distribution data can be adequately modeled using a power-law up to the scale of the bed thickness.

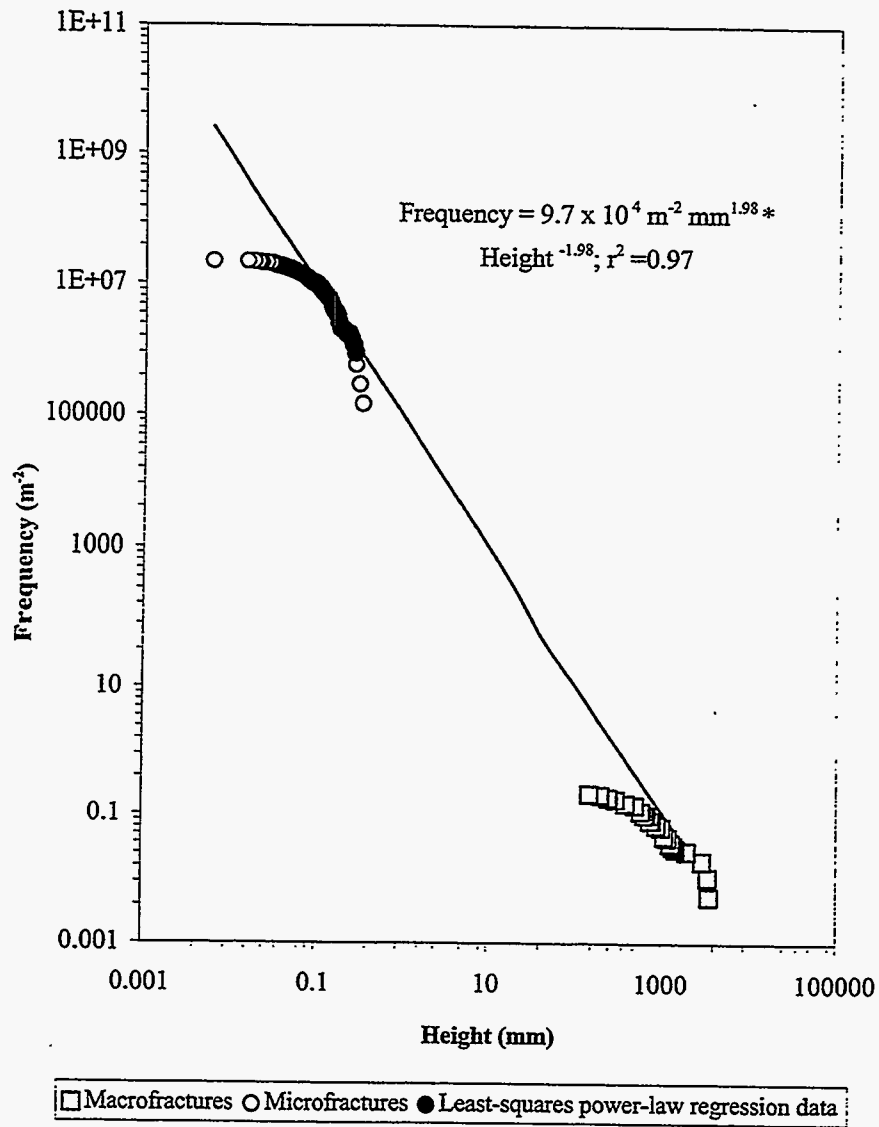


Figure 46. Fracture height frequency prediction. Westwater Springs Canyon. The parameters of the power-law fit to the microfracture size distribution in Figure 44 also give a reasonable prediction of the macrofracture height distribution at least up to the scale of the bed thickness.

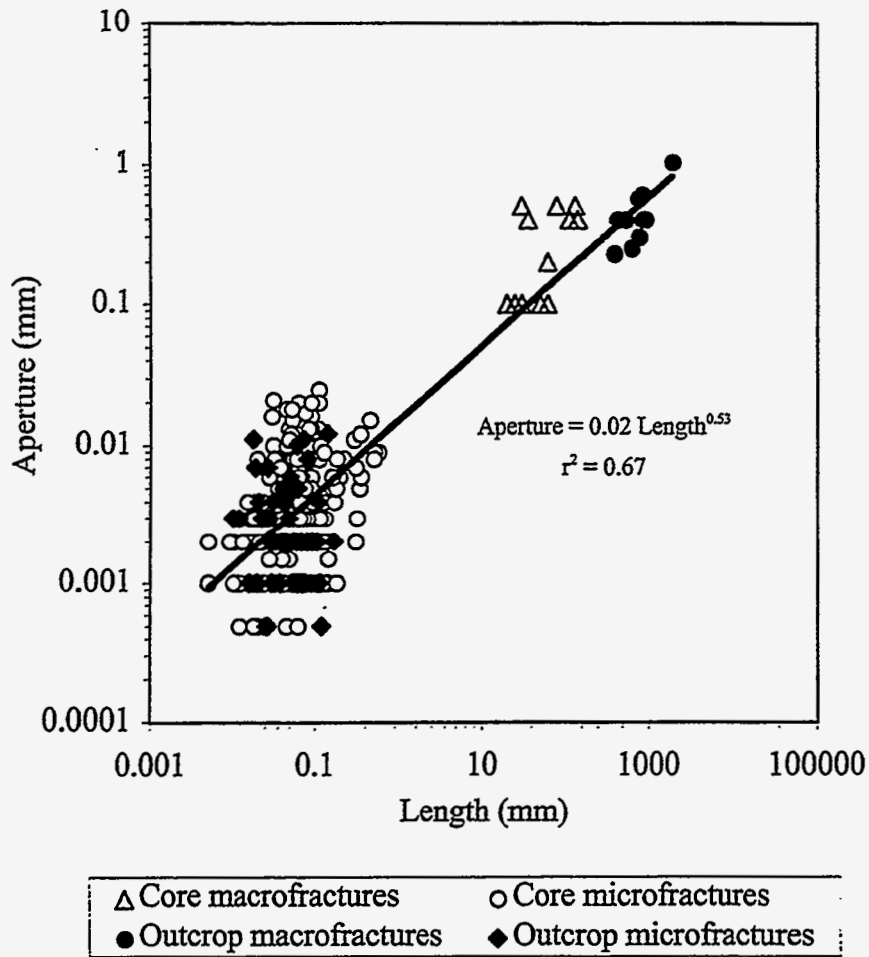


Figure 47. Aperture vs. length. Core and outcrop data. Only transgranular and transcement microfractures are considered. Only mechanical apertures of filled macrofractures (veins) are shown. A least squares regression line to all data points yields a low-confidence correlation coefficient of 0.67. Core and outcrop macrofracture data plot in slightly different places.

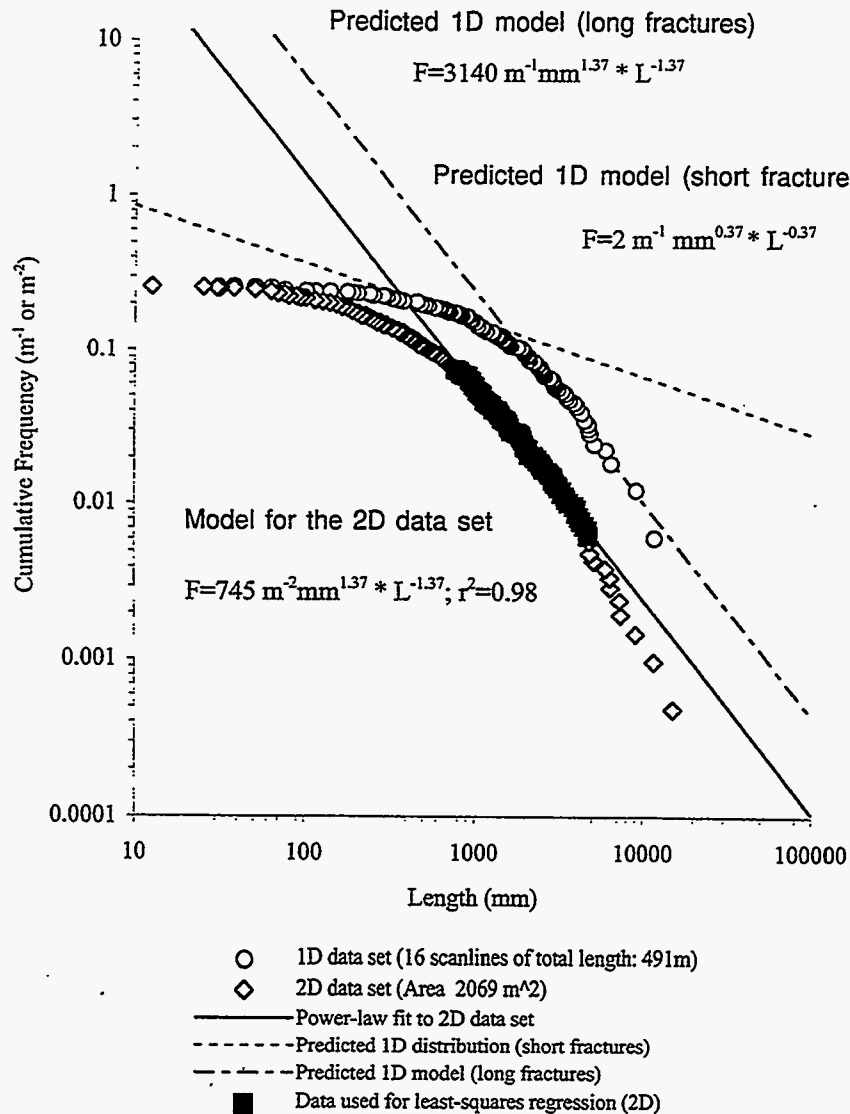


Figure 48. Test of 2D-1D sampling domain conversion, Westwater pavement. The predicted 1D distribution using formulas in Marrett (1996) adequately predict the smallest fracture sizes from scanlines. The slope of the size distribution for relatively long fractures is similar to the slope of the 2D distribution because the probability of sampling relatively long fractures with fracture-perpendicular scanlines repeatedly crossing the study area is similar to sampling the fractures in the 2D observation area.

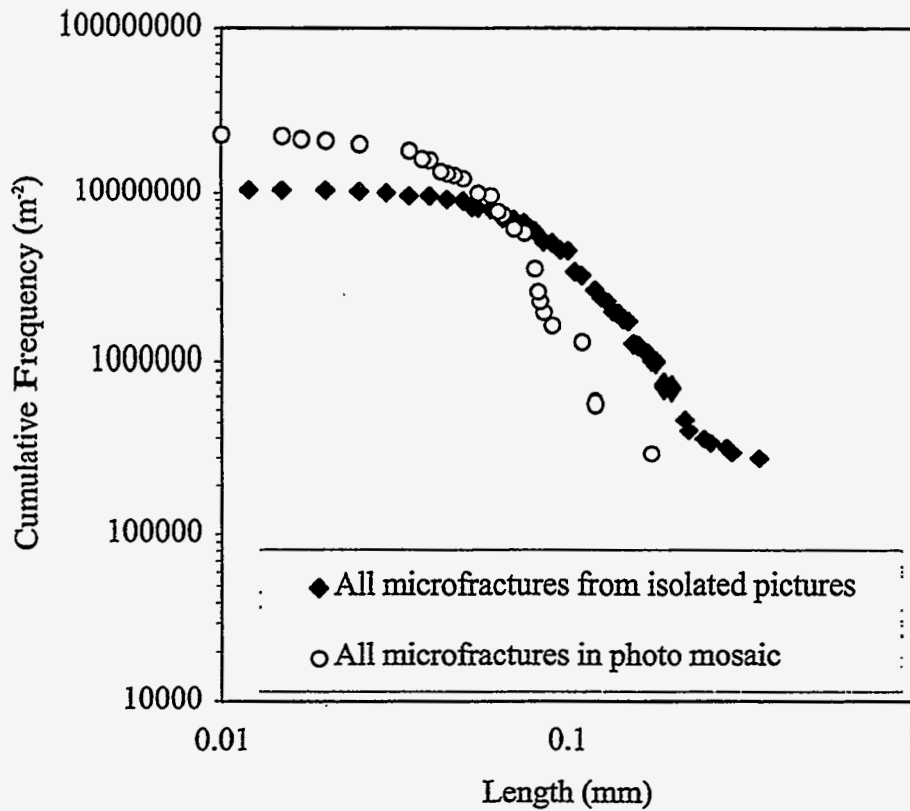


Figure 49. Test of bias in microfracture frequency calculations. Microfracture frequencies of systematicaly (mosaic) versus non systematicaly (isolated) microphotographs do not show significant variations. This result suggests that there is no bias in the procedure used in photographing the sample. More luminescent grains are frequently selected for isolated pictures because they show better contrast with the cement. This also facilitates microfracture measurement and classification.

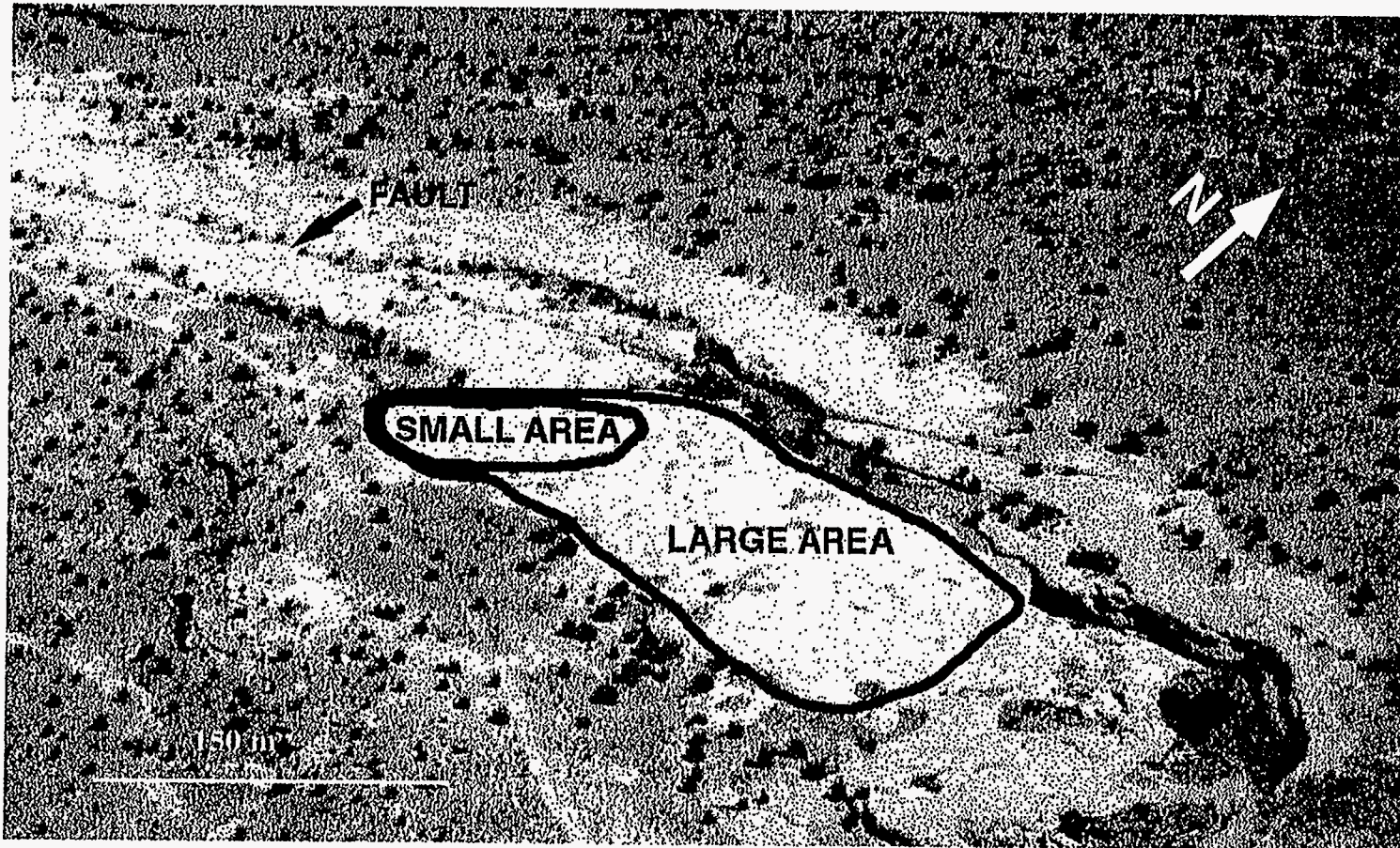


Figure 50. Areas selected to study the effects of the mechanical layer on fracture size distributions. Westwater Pavement. Only fractures larger than the thickness of the bed were measured in the large area (gray border). All fractures visible with a naked eye were measured in the small area (black border). The thickness of the mechanical bed was determined in the canyon nearby.

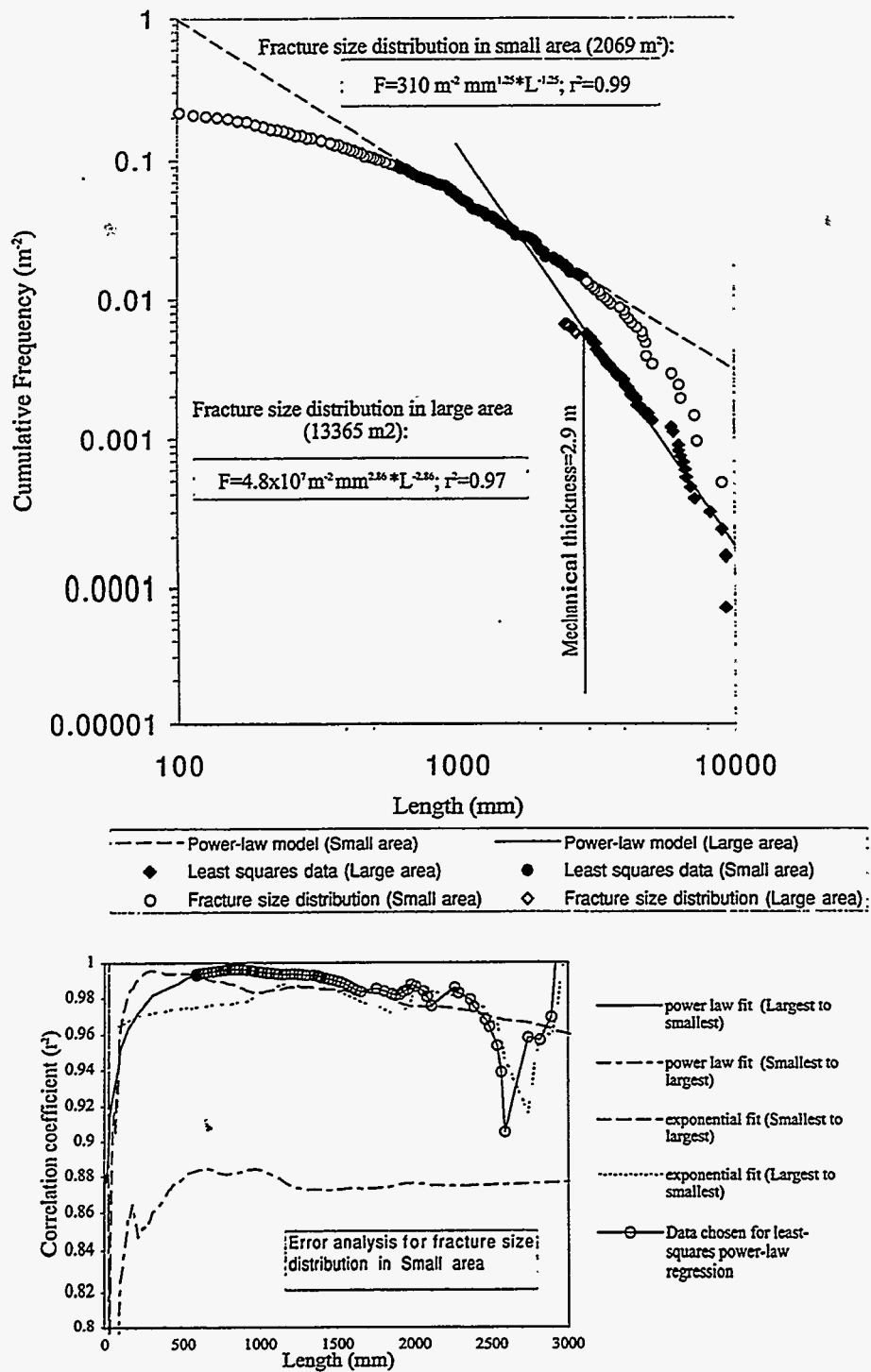


Figure 51. Fracture size attributes for part of study area ("small" area).

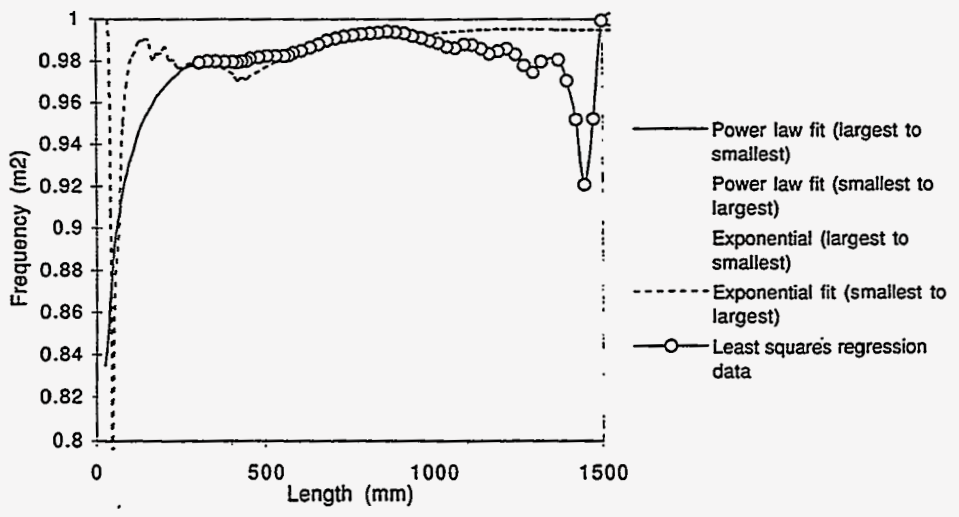
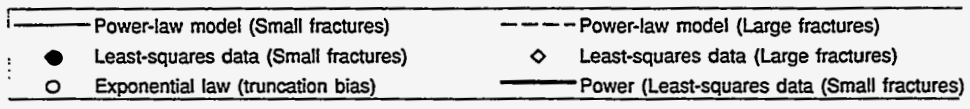
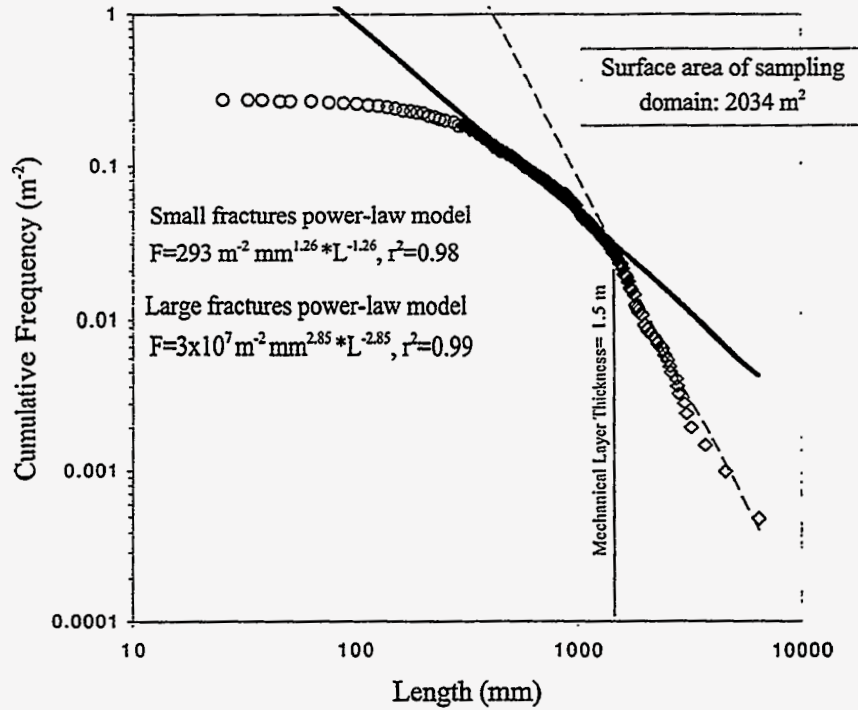


Figure 52. Fracture size attributes for large area domain of study area.

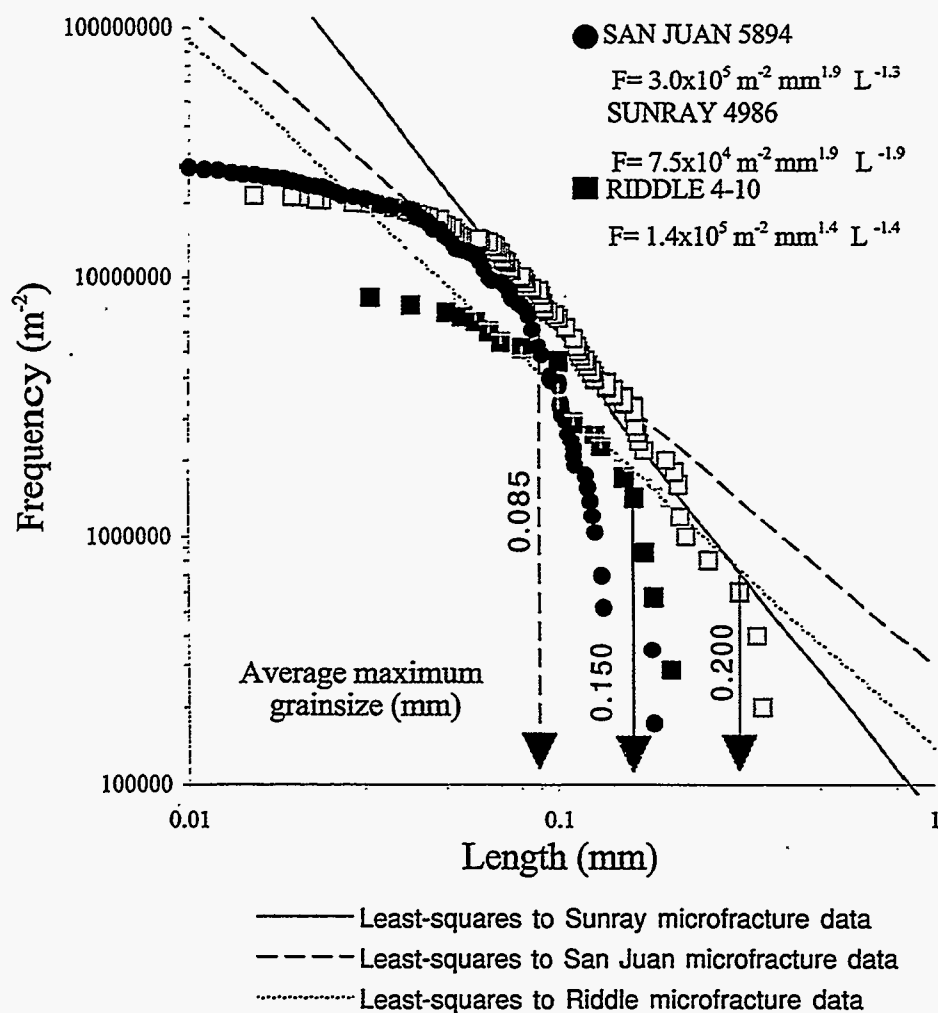


Figure 53. Microfracture-size distributions showing large-size-microfracture anomalies. Notice that in these examples there is a significant change in the slope of the fracture size distribution once the microfractures pass the scale of the average maximum grain size of the sample. Maximum average grain size is given by an average of the largest diameters measured in quartz grains without taking into account quartz overgrowths.

APPENDIX A. CORE MACROFRACTURE DATA

This appendix contains data from cores, including operational data, top of stratigraphic units, cored intervals, lost and unmeasurable zones, orientable pieces, samples for magnetic analysis, bed plane depths, samples for petrographic analysis and macrofracture data in general.

Core acquisition data. Riddle D LS 4A

	Top core (')	Bottom core (')	Cut (')	Recovered (')	Horizontal Projection (')
	4936	4957	21	12	8.49
	4993	5016	23	21	14.85
	5016	5040	24	24	16.97
Total			68	57	

Core acquisition data. Sunray H Com #6

	Start core (')	Finish core (')	Cut (')	Recovered (')
	4964.2	4978	13.8	12.3
	4978	5008.8	30.8	30.8
Total			44.6	43.1

Core acquisition data. San Juan 32-9

	Start core (')	Finish core (')	Cut (')	Recovered (')
	5551	5569	18	16.5
	5569	5580	11	9
	5580	5603.5	23.5	20
	5603.5	5628.8	25.3	25.3
	5850	5877	27	16.8
	5877	5899	22	21.5
	5955	6013	58	55.7
	6013	6034.5	21.5	21.5
Total			206.3	186.3

The following table explains the meaning of abbreviations used to describe different aspects of the fractures in the cores.

EXPLANATION
B: Broken. Separate walls
DI: Difficult to recognize. Diffuse
I: Induced
C: Closed
PO: Partially open
PI: Possibly induced
M: Mineralized
NM: Not mineralized

Core description and sample inventory. Riddle D LS 4A (*: CORELAB aperture assumption)

CORE #	UNIT	CORE INTERVAL (feet)	OBSERVATIONS	BED TOP (feet)	FRACTURE TIP DEPTH (feet)	FRACTURE ORIENTATION	Fracture Height, Aperture (mm)	OBSERVATIONS	SAMPLE NUMBER	DEPTH (feet)	OBSERVATIONS	
1	C L I F F H O U S E	4929.0-4936.0	NOT ANALYZED									
2		4936.0-4937.8	ORIENTABLE	4936.0	4936.5	N06E87S	35.00, 0.01(*)	B,NM,N				
						4936.6	N07E83N	26.39, 0.01(*)	B,NM,N			
			4937.6-4938.8	RUBBLEZONE								
			4938.8-4940.0	ORIENTABLE	4938.8					2-3	4939.2	HORIZONTAL PLUG
						4939.4	N08E86S	24.61, 0.01(*)	B,NM,N			
			4940.0-4940.7	RUBBLEZONE								
			4940.7-4947.4	ORIENTABLE	4940.0	4940.7	N05E85N	29.79, 0.01(*)	B,NM,N			
						4941	N11E85S	26.70, 0.01(*)	B,NM,N			
						4941.7	N23E49S	86.89, 0.01(*)	DI,PI			
						4941.7	N51E43S	114.40, 0.4	DI,O,PI			
						4942.1	N03E83N	29.79, 0.01(*)	B,NM,N			
						4942.5	N-S90		PO,PM			
						4942.8	N80E30N		I			
					4943.5	4944.7	N08E85S	36.50, 0.4	B,NM,N	2-7	4943.5	HORIZONTAL PLUG
										4946.1	4946.1	CORELAB SAMPLE
			4947.4-4993.0	RUBBLEZONE								
3			4993.0-5001.4	ORIENTABLE	4993.0					3-3	4995.15	HORIZONTAL PLUG
						4996	N18E83S	38.10, 0.01(*)	DI,C,NM,N			
						4996	N05W89S	62.71, 0.01(*)	B,M,N			
					4996.1	N05W86S	49.00, 0.01(*)	B,M,N				
					4996.1	N84E82S	91.29, 0.01(*)	DI,C,NM,N				
					4996.1	N88E86S	48.79, 0.01(*)	B,NM,N				
					4996.1	N74E16S	21.49, 0.01(*)	B,PI				
									3-4 V	4996.3	VERTICAL PLUG	

CORE #	UNIT	CORE INTERVAL (feet)	OBSERVATIONS	BED TOP (feet)	FRACTURE TIP DEPTH (feet)	FRACTURE ORIENTATION	Fracture Height, Aperture (mm)	OBSERVATIONS	SAMPLE NUMBER	DEPTH (feet)	OBSERVATIONS		
3	C L I F F	4993.0-5001.4	ORIENTABLE	4997.2	5000	N07E88S	74.91, 0.01(*)	B,NM,N				TOP OF BED	
					5000.1	N28E87S	46.99, 0.01(*)	B,NM,N					
					5000.1	N08W89S	65.41, 0.01(*)	B,NM,N					
					5000.2	N08W89S	67.01, 0.01(*)	B,NM,N					
					5000.2	N18E89S	39.70, 0.01(*)	DI,B,PI					
					5000.4	N12E89S	34.90, 0.01(*)	B,NM,N					
					5000.4	N12E88S	80.01, 0.01(*)	B,NM,N					
					5000.8	N84E45N	65.41, 0.01(*)	DI,B,I			3-8	5000.45	HORIZONTAL PLUG
					5000.8	N08E47S	32.69, 0.01(*)	DI,B,PI					
					5000.8	N01E39S	46.99, 0.01(*)	DI,B,PI					
					5001.1	N13E75N	26.49, 0.01(*)	B,NM,N					
5001.4-5002.4			RUBBLE ZONE										
	H O U S E	5002.4-5007.8	ORIENTABLE	5002.4	5003.9	N08E90	61.49, 0.01(*)	B,NM,N					
					5003.9	N07E89N	57.40, 0.01(*)	B,NM,N					
					5004	N86E77S	29.11, 0.01(*)	DI,C,NM,N					
											5005	VERTICAL PLUG	
				5005.5	5005.7	N08E89S	54.41, 0.01(*)	B,NM,N				5005.5	
					5005.8	N08E86N	32.69, 0.01(*)	B,NM,N					
					5006	N08E84S	85.29, 0.01(*)	B,NM,N			5006	HORIZONTAL PLUG OVERSIZED	
					5006.3	N01E86N	55.40, 0.01(*)	B,NM,N	3-14	5006.3	HORIZONTAL PLUG		
					5006.3	N01E86N	48.31, 0.01(*)	B,NM,N					
					5006.4	N10W72S	26.59, 0.01(*)	DI,PI					
					5006.6	N03E79S	10.11, 0.01(*)	B,NM,N					
5007.8-5007.9			RUBBLE ZONE										
		5007.8-5009.9	ORIENTABLE	5007.9	5009.3	N04E90	68.81, 0.01(*)	B,M,N	5009.3	5009.3	HORIZONTAL PLUG OVERSIZED		
									3-17	5009.54	HORIZONTAL PLUG		

CORE #	UNIT	CORE INTERVAL (feet)	OBSERVATIONS	BED TOP (feet)	FRACTURE TIP DEPTH (feet)	FRACTURE ORIENTATION	Fracture Height, Aperture (mm)	OBSERVATIONS	SAMPLE NUMBER	DEPTH (feet)	OBSERVATIONS	
3	C L I F	5007.8-5009.9	ORIENTABLE	5007.9	5009.6	N09E90	69.39, 0.01(*)	C,M,N	5009.6	5009.6	HORIZONTAL PLUG OVERSIZED	
		5009.9-5011.1	RUBBLE ZONE	-----								
		5011.1-5013.7	ORIENTABLE	5011.1						3-18	5011.4	HORIZONTAL PLUG
										3-19	5012.1	HORIZONTAL PLUG
					5013.3	N09W85S	39.29, 0.01(*)	DI,B,PI				
					5013.3	N68E64S	85.09, 0.01(*)	DI,B,PI				
		5013.5	N21W90	15.80, 0.01(*)	B,M,N							
5013.7-5016.0	LOST CORE	-----										
4	F H O U S E	5016.0-5033.4	ORIENTABLE	5016.0								
					5018	N04E86N	58.60, 0.01(*)	B,M,N				
					5018.5	NS-89W	50.60, 0.01(*)	B,M,N	4-3	5018.25	HORIZONTAL PLUG	
					5020.4	N08W87N	61.11, 0.01(*)	B,M,N	4-5	5020.1	HORIZONTAL PLUG	
				5022.1							TOP OF BED	
									4-7	5022.45	HORIZONTAL PLUG	
				5023.1	N13W76N	66.69, 0.01(*)	B,NM,N					
				5023.3	N10W83N	81.61, 0.01(*)	B,NM,N					
									4-10	5025.1	HORIZONTAL PLUG	
				5025.3	N56W49N	66.80, 0.01(*)	B,I					
				5025.8	N04W89N	48.59, 0.01(*)	B,NM,N					
				5026	N04W81N	56.11, 0.01(*)	B,NM,N					
									4-12	5027.1	HORIZONTAL PLUG	
				5028.5	N02W81N	49.71, 0.01(*)	B,NM,N					
				5030.0							TOP OF BED	
					4-16	5031.15	HORIZONTAL PLUG					

CORE #	UNIT	CORE INTERVAL (feet)	OBSERVATIONS	BED TOP (feet)	FRACTURE TIP DEPTH (feet)	FRACTURE ORIENTATION	Fracture Height, Aperture (mm)	OBSERVATIONS	SAMPLE NUMBER	DEPTH (feet)	OBSERVATIONS	
4	CLIFF HOUSE	5016.0-5033.4	ORIENTABLE	5030.0	5031.4	N04W85N	33.20, 0.01(*)	B,NM,N				
					5031.8	N09W39S	205.74,0.2	PI				
					5032.7	N17W47S	18.29,0.2	PI				
		5033.4-5033.7		UNMEASURABLE		-----						
		5033.7-5040.2	ORIENTABLE	5033.7	5034.8	N22W86N	88.11, 0.01(*)	B,I				
									4-20	5036.2	HORIZONTAL PLUG	
									4-21	5036.1	HORIZONTAL PLUG	
					5036.2	N03E82S	19.61, 0.01(*)	C,NM(?),N				
					5036.2	N01W80N	52.10, 0.01(*)	B,NM,N				
									4-23	5038.1	HORIZONTAL PLUG	
			5039.5	N65W46N	78.11, 0.01(*)	DI,B,PI						

Core description and sample inventory. Sunray H Com #6

CORE #	UNIT	CORE INTERVAL (feet)	OBSERVATIONS	TOP BED (feet)	FRACTURE TIP DEPTH (feet)	ORIENTATION	HEIGHT, APERTURE (mm)	OBSERVATIONS	SAMPLE NUMBER	DEPTH (feet)	OBSERVATIONS	
1	C L I F F	4964.2-4976.5	NOT ORIENTABLE	4964.2	4966' 5"		25.4+, ?	POMN				
					4968' 6"		38.1+, ?	CMN				
					4970' 1"		50.8+, ?	POMN				
					4970' 4"		25.4+, ?	CMN				
				4970.8	4971' 1"	38.1, ?	CMN					
					4971' 2"	25.4, ?	CMN					
				4973.7			M4974.95	4974.95	HORIZONTAL PLUG			
					4976' 0"	101.6, ?	POMN					
					4076' 0"	63.5, ?	POMN	SUNRAY 4976	4976	HORIZONTAL PLUG OVERSIZED		
								M4976.08	4976.08	HORIZONTAL PLUG		
								M4976.19	4976.19	HORIZONTAL PLUG		
								M4976.29	4976.29	HORIZONTAL PLUG		
						4978' 3"	76.2+	POMN				
						4978' 4"	38.1+	POMN				
4976.5-4978.0			NOT RECOVERED									
2	H O U S E	4978.0-5008.8	NOT ORIENTED	4978.0								
			PALEOMAG (NOT RELIABLE)	4984.0	4984' 0"		355.6+	O,I				
									M4984.33	4984.33	HORIZONTAL PLUG	
									M4984.45	4984.45	HORIZONTAL PLUG	
									M4984.85	4984.85	HORIZONTAL PLUG	
									M4985.2	4985.2	HORIZONTAL PLUG	
			PALEOMAG (N30E, RELIABLE)	4986.7	4986' 7"	N83E90	30.5, 0.5	O,NM,N				
					4986' 7"	N84E90	81.3, 0.5	O,NM,N				
					4986' 8"	N85E90	134.6, 0.5	O,NM,N	M4986.84	4986.84	HORIZONTAL PLUG ORIENTED	
					4986' 9"	N88E90	144.8, 0.4	O,NM,N				
									M4986.74	4986.74	HORIZONTAL PLUG ORIENTED	
					4986' 8"		50.8	O,NM,N				
									M4986.83	4986.83	HORIZONTAL PLUG ORIENTED	
									M4986.95	4986.95	HORIZONTAL PLUG ORIENTED	
			NOT ORIENTED		4987' 0"		152.4+	O,NM,N				
					4987' 7"		25.4+	CMN				
					4987' 8"		152.4+	CMN				
			4988.3	4988' 7"			12.7+	PO,MN				
4988' 8"				25.4+	PO,MN							
4988' 8"				38.1+	PO,MN							
4988' 8"				50.8	PO,MN							
4988' 7"				139.7+	O,NM,N							

CORE #	UNIT	CORE INTERVAL (feet)	OBSERVATIONS	TOP BED (feet)	FRACTURE TIP DEPTH (feet)	ORIENTATION	HEIGHT, WIDTH (mm)	OBSERVATIONS	SAMPLE NUMBER	DEPTH (feet)	OBSERVATIONS		
2	CLIFF	4978.0-5008.8	NOT ORIENTED	4980.0	4980' 11"		25.4+	O,NM,N					
					4984' 8"		38.1+	PO,NM,N					
					4985.0	4988' 9"		50.8+	O,B,I				
	HOUSE		PALEOMAG (N-S, RELIABLE)	4989.9	5000' 3"	N60E90	50.8,0.1	O,NM,N					
					5000' 4"	N83E90	30.5,0.1	O,NM,N	M5000.35	5000.35	HORIZONTAL PLUG ORIENTED		
					5000' 6"	N85E90	83.8+,0.3	O,NM,N					
										SUNRAY 5000.8	5000.8	HORIZONTAL PLUG OVERSIZED	

Core description and sample inventory, San Juan 32-9

CORE #	UNIT	CORE INTERVAL	OBSERVATIONS	TOP BED (feet)	FRACTURE TIP DEPTH (feet)	ORIENTATION	HEIGHT, APERTURE (. mm)	OBSERVATIONS	SAMPLE NUMBER	DEPTH (feet)	OBSERVATIONS		
1	CLIFF HOUSE	5551.0'-5567.5'	ORIENTABLE	5551.0	5554'11"	N30E45N	38.1+,0.2	PO,M,N					
					5565'0"	N-S90	165.1,?	B,NM,N(?)					
5567.5'-5569.0' LOST CORE													
2		5569.0'-5578.0'	ORIENTABLE	5569.0	5572'5"	N40E80S	25.4+,0.1	PO,M,N					
					5574'2"	N-S85W	25.4+,?	B,NM,I					
					5576'6"	N-S80W	50.8,?	O,NM,N(?)					
5578.0'-5580' LOST CORE													
3		5580.0'-5600.0'	ORIENTABLE	5580.0	5580'0"	N-S90	83.5,0.1	C,M,N					
					5595.5	5596'11"	N60E70S	25.4,0.1	PO,M,N				
					5599'0"	N-S85E	83.5,0.2	PO,NM,N(?)					
5600.0'-5603.5' LOST CORE													
4	5603.5'-5628.8'	ORIENTABLE	5603.5	5612'1"	N-S90	279.4,?	B,NM,I						
				5617.2	5619'0"	N-S90	165.1,?	B,NM,N(?)	32-9 5612.5H	5612.5	HORIZONTAL PLUG PETAL CENTERLINE		
				5625.8	5627'9"	N-S80W	20.32,0.1	PO,M,N					
					5627'10"	N-S80W	25.4+,0.1	PO,M,N					
					5627'10"	N-S80W	25.4+,0.1	PO,M,N					
5628.8'-5650.0' DRILLED INTERVAL													
5	MENEFE	5650.0'-5666.8'	ORIENTABLE	5650.0	5655'0"	N-S90	635+,?	B,NM,I					
									32-9 5656.7H	5656.7	HORIZONTAL PLUG PETAL CENTERLINE		
									32-9 5656.8H	5656.8	HORIZONTAL PLUG PETAL CENTERLINE		
					5660.5	5663'0"		152.4+,0.1	C,M,N	32-9 5663.5H	5663.5	HORIZONTAL PLUG	
						5664'1"		50.8+,0.2	PO,M,N				
5668.0'-5677.0' LOST CORE													
6		5677.0'-5699.0'	ORIENTABLE	5677.0	5687'0"	N-S80E	228.0+,?	D,NM,N					
					5693'0"	N-S85E	885.0+,?	B,M,N					
									32-9 5694.4H	5694.4	HORIZONTAL PLUG		
									32-9 5695.5H	5695.5	HORIZONTAL PLUG		
5699-5955 UNAVAILABLE													

CORE #	UNIT	CORE INTERVAL	OBSERVATIONS	TOP BED (feet)	FRACTURE TIP DEPTH (feet)	ORIENTATION	LENGTH, APERTURE (mm)	OBSERVATIONS	SAMPLE NUMBER	DEPTH (feet)	OBSERVATIONS	
7	P O I N T	6055.0-6010.7	ORIENTABLE	5955.0	6007'4"	N16E80S	431.8,?	B,M,N				
									32-9 6008.1H	6008.1	HORIZONTAL PLUG	
									32-0 6008.4H	6008.4	HORIZONTAL PLUG	
		6010.7'-6013.0'	LOST CORE	-----								
8	L O O K O U T	6013.0-6034.6	ORIENTABLE	6013.0	6013'0"	N-S90	25.4,?	B,NM,N(?)				
					6014'0"	N-S90	38.1,?	B,NM,N(?)				
					6016'0"	N-S90	330.2+,?	B,NM,I				
										32-9 6016.2H	6016.2	HORIZONTAL PLUG PETAL CENTERLINE
										32-0 6022.1H	6022.1	HORIZONTAL PLUG PETAL CENTERLINE
										32-9 6022.4H	6022.4	HORIZONTAL PLUG PETAL CENTERLINE
					6027'4"		76.2+,0.1	C,M,N				
					6027'9"		63.5,?	B,NM,I				
					6029'5"	N80W70S	50.8,?	B,NM,N				
					6030'0"	E-W75S	50.8+,?	PO,M,N				
					6030'5"	N-S90	50.8,?	B,NM,I				
6030'5"	N-S90	50.8,?	B,NM,I									

APPENDIX B: OUTCROP MACROFRACTURE DATA

This appendix contains fracture data collected in the field. The following table explains the meaning of abbreviations used to describe the fractures.

EXPLANATION

Type

c: closed

o: open

po: partially open

ts: tip termination south

tn: tip termination north

hts: hooked termination south

htn: hooked termination north

tas: abrupt termination south

tan: abrupt termination north

xs: covered to the south

xn: covered to the north

Observations

Di: Diffuse trace

I: Irregular trace

An: Anastomosed trace

ee: en echelon

Fractures are assumed to be near vertical.

Angles are the acute angle in the respective termination relative to the orientation of the intersected fracture. Angle ($^{\circ}$ N) is the angle in the northern termination and Angle ($^{\circ}$ S) is the angle in the southern termination of the fracture, in degrees.

Connectivity parameters are calculated based on complete fractures (no xs or xn fractures counted).

Westwater Springs

Southern pavement. All fractures in small area
Swarm A

Frac. #	Type	Length (mm)	Orientation	Angle(°N)	Angle(°S)	Observations
1	c.ts,htn	965.2	30 90 E	50		
2	c.hts,tn	1066.8	20 90 E		25	
3	c.hts,tn	406.4	22 90 E		40	Di
4	c.ts,tn	609.6	34 90 E			
5	c.ts,tn	355.6	10 90 E			Di
6	c.ts,tn	139.7	16 90 E			Di
7	c.ts,tn	774.7	22 90 E			Di
8	c.xs,tn	508	28 90 E			Di
9	c.xs,htn	1270	24 90 E	45		ee
10	c.tas,tan	76.2	6 90 E	25	45	
11	c.hts,tn	965.2	14 90 E		45	
12	c.ts,xn	355.6	24 90 E			
13	c.hts,xn	1371.6	24 90 E		30	same as 9?
14	c.hts,xn	177.8	46 90 E		45	
15	c.tas,tn	609.6	10 90 E		20	
16	c.xs,tan	1422.4	18 90 E	15		
17	c.ts,tn	1397	12 90 E			
18	c.hts,tn	558.8	10 90 E		35	l
19	c.ts,htn	685.8	24 90 E	40		
20	c.tas,tn	127	346 90 E		25	
21	c.tas,tan	50.8	335 90 E	45	45	
22	c.ts,htn	1574.8	8 90 E	30		
23	c.ts,tn	355.6	8 90 E			
24	c.ts,tan	1600.2	12 90 E	15		An
25	c.ts,htn	5994.4	20 90 E			An
26	c.tas,tn	330.2	344 90 E		50	
27	c.tn,hts	660.4	8 90 E		60	
28	c.ts,tn	304.8	4 90 E			
29	c.ts,tan	660.4	18 90 E	15		
30	c.hts,xn	1371.6	16 90 E		45	
31	c.ts,tn	63.5	2 90 E			
32	c.tas,htn	152.4	354 90 E	40	15	
33	c.ts,tn	152.4	35 90 E			
34	c.ts,tn	152.4	8 90 E			
35	c.ts,tn	114.3	6 90 E			
36	c.xs,tn	939.8	356 90 E			
37	c.tas,tn	203.2	0 90 E		35	
38	c.ts,tn	584.2	0 90 E			
39	c.tas,tan	76.2	40 90 E	35	35	
40	c.hts,tn	482.6	0 90 E			
41	c.ts,tn	381	358 90 E			
42	c.ts,tn	152.4	16 90 E			
43	c.ts,tn	254	25 90 E			
44	c.ts,tn	177.8	12 90 E			
45	c.ts,tn	101.6	12 90 E			
46	c.tas,tn	304.8	14 90 E		15	
47	c.hts,tn	152.4	22 90 E		40	
48	c.ts,htn	355.6	14 90 E			
49	c.ts,xn	863.6	18 90 E			
50	c.tas,tan	139.7	26 90 E	30	45	
51	c.tas,tn	304.8	14 90 E			
52	c.ts,tn	101.6	12 90 E			
53	c.ts,xn	330.2	26 90 E			

Frac. #	Type	Length (mm)	Orientation	Angle(°N)	Angle(°S)	Observations
54	c.xs,tn	279.4	20 90 E			
55	c.ts,tan	406.4	30 90 E	40		
56	c.ts,tan	76.2	8 90 E	40		
57	c.ts,htn	1905	356 90 E			
58	c.ts,tan	165.1	0 90 E	40		
59	c.ts,tn	76.2	8 90 E			
60	c.ts,tn	25.4	8 90 E			
61	c.ts,tn	38.1	358 90 E			
62	c.ts,tn	63.5	340 90 E			
63	c.ts,tn	762	350 90E			
64	c.ts,tn	838.2	16 90 E			
65	c.tas,tan	203.2	354 90 E	50	30	
66	c.ts,tn	2921	10 90 E			
67	c.ts,tn	152.4	20 90 E			
68	c.ts,htn	215.9	6 90 E			
69	c.ts,htn	558.8	4 90 E			
70	c.ts,tn	457.2	2 90 E			
71	c.ts,tn	76.2	330 90 E			
72	c.hts,tn	381	14 90 E			
73	c.ts,htn	381	8 90 E			
74	c.ts,tn	660.4	20 90 E			
75	c.ts,tn	660.4	8 90 E			
76	c.ts,tn	114.3	358 90 E			
77	c.ts,tn	431.8	0 90 E			
78	c.ts,tn	431.8	0 90 E			
79	c.ts,tn	101.6	12 90 E			
80	c.xs,tn	431.8	348 90 E			
81	c.ts,tan	76.2	30 90 E	45		
82	c.ts,tn	177.8	28 90 E			
83	c.xs,tn	381	22 90 E			
84	c.ts,tn	2463.8	354 90 E			
85	c.tas,tan	330.2	350 90 E	30	45	
86	c.tas,tn	50.8	12 90 E		35	
87	c.tas,tn	63.5	12 90 E		30	
88	c.tas,tn	203.2	12 90 E	15		
89	c.ts,tan	203.2	14 90 E	35		
90	c.ts,tn	381	10 90 E			
91	c.tas,tan	203.2	12 90 E	30	30	
92	c.ts,tan	101.6	25 90 E	45		
93	c.ts,tan	63.5	20 90 E	35		
94	c.ts,tan	152.4	10 90 E			
95	c.ts,tn	914.4	345 90 E			
96	c.ts,tan	101.6	8 90 E	35		
97	c.ts,tn	914.4	358 90 E			
98	c.ts,tn	1295.4	10 90 E			
99	c.ts,tn	1803.4	6 90 E			
100	c.ts,tn	1041.4	12 90 E			
101	c.hts,tn	1625.6	16 90 E		40	
102	c.ts,xn	1422.4	15 90 E			
103	c.ts,tn	533.4	20 90 E			
104	c.tas,tan	101.6	35 90 E	35	35	
105	c.ts,xn	660.4	18 90 E			
106	c.xs,tan	304.8	14 90 E	30		
107	c.tas,tn	81.28	46 90 E		50	
108	c.xs,tn	152.4	30 90 E			
109	c.tas,tn	76.2	356 90 E		40	
110	c.ts,tn	63.5	10 90 E			
111	c.ts,tan	93.98	26 90 E	30		
112	c.ts,tn	304.8	8 90 E			Di
113	c.ts,tn	330.2	14 90 E			Di
114	c.ts,tn	457.2	16 90 E			Di
115	c.ts,tn	609.6	10 90 E			

Frac. #	Type	Length (mm)	Orientation	Angle(°N)	Angle(°S)	Observations
116	c,tas,tan	127	8 90 E	15	30	
117	c,tas,tan	50.8	6 90 E	30	30	
118	c.ts.tn	787.4	14 90 E			

Connectivity Parameters		
Number of connection points		
	#	%
≥2	11	11%
1	37	37%
0	52	52%
Type of termination		
	#	%
Tip	136	68%
Hooks	20	10%
Abrupt	44	22%

Westwater Springs

Southern pavement. All fractures in a selected area
Swarm B

Frac. #	Type	Length (mm)	Orientation	Angle(°N)	Angle(°S)	Observations
1	po,tn,xs	1955.8	30 90 E			
2	po,tn,hts	914.4	10 90 E		45	
3	po,ts,tn	2082.8	32 90 E			
4	po,ts,xn	279.4	50 90 E			
5	c,xn,tas	127	30 90 E		45	
6	c,xs,xn	482.6	16 90 E			
7	c,ts,tan	635	22 90 E	30		same as 8?
8	c,ts,tn	4699	25 90 E			
9	c,ts,tn	838.2	32 90 E			
10	c,ts,tan	63.5	14 90 E	25		
11	c,ts,tan	1244.6	52 90 E	45		Di
12	c,tas,tan	254	320 90 E	60	60	Di
13	c,ts,tn	228.6	8 90 E			cement around
14	c,ts,tn	1498.6	10 90 E			cement around
15	c,tas,tn	38.1	32 90 E		15	
16	c,tas,tn	38.1	342 90 E		15	
17	po,ts,tn	584.2	42 90 E			Di
18	c,ts,tn	355.6	22 90 E			Di
19	c,tas,tn	965.2	30 90 E		50	Di
20	po,ts,tn	330.2	350 90 E			
21	c,ts,tn	355.6	322 90 E			Di
22	c,tas,tn	1524	346 90 E		50	Di
23	c,xs,tn	3327.4	24 90 E			
24	c,tas,tn	889	72 90 E		45	Di
24A	c,tas,tn	304.8	10 90 E		20	Di
25	c,tn,tas	609.6	78 90 E		50	
26	c,ts,tn	254	30 90 E			Di
27	c,ts,tn	431.8	32 90 E			Di
28	c,ts,tn	1117.6	18 90 E			same as 29?
29	c,hts,tn	787.4	22 90 E		40	same as 30?
30	c,hts,tn	1016	14 90 E		35	
31	c,tas,tan	25.4	340 90 E	15	15	
32	c,tn,ts	4826	18 90 E			An
33	c,tas,tan	63.5	340 90 E	35	35	
34	c,tn,tas	69.85	330 90 E		35	
35	c,ts,tan	63.5	18 90 E	15		
36	c,tas,tan	31.75	12 90 E	30	30	
37	c,tas,tn	50.8	0 90 E	30		
38	c,tas,tn	152.4	30 90 E		20	
39	c,tas,tn	101.6	20 90 E		15	
40	c,tn,ts	838.2	0 90 E			
41	c,htn,ts	254	10 90 E	50		
42	c,tn,hts	711.2	10 90 E		50	
43	c,tn,ts	292.1	12 90 E			
44	c,ts,tn	101.6	14 90 E			
45	c,hts,tn	1041.4	6 90 E		35	ee
46	c,hts,tn	711.2	24 90 E		50	
47	c,hts,tn	685.8	10 90 E		10	
48	po,ts,tn	3632.2	28 90 E			
49	c,tas,tn	190.5	18 90 E		15	Di
50	c,tan,ts	190.5	34 90 E	20		
51	c,tan,ts	139.7	32 90 E	15		

Frac. #	Type	Length (mm)	Orientation	Angle(°N)	Angle(°S)	Observations
52	po,ts,tn	5105.4	25 90 E			
53	c,tan,ts	457.2	10 90 E	15		
54	c,tn,tas	177.8	28 90 E		40	
55	c,tas,tan	254	20 90 E	45	15	
56	c,ts,tn	1384.3	10 90 E			
57	c,tan,ts	50.8	0 90 E	30		Di
58	c,tan,ts	50.8	352 90 E	30		
59	c,tas,tan	63.5	40 90 E	15	15	
60	c,tan,ts	457.2	18 90 E	15		
61	c,tan,ts	88.9	12 90 E	20		Di
62	c,hts,tn	1270	6 90 E		35	
63	c,hts,tn	279.4	18 90 E		35	
64	c,tas,tn	101.6	0 90 E		10	
65	po,ts,tn	3911.6	30 90 E			
66	c,tas,tn	203.2	12 90 E		15	
67	c,tas,tan	304.8	0 90 E	40	40	
68	c,tas,tn	114.3	50 90 E		40	
69	c,tan,tas	38.1	14 90 E	35	35	
70	c,tn,ts	2971.8	10 90 E			cement around
70A	c,tas,tan	381	20 90 E	30	45	
71	c,ts,tn	304.8	20 90 E			
72	c,tas,tn	482.6	16 90 E		45	
73	c,tas,tn	241.3	10 90 E		45	Di
74	c,ts,tn	101.6	350 90 E			Di
75	c,ts,tn	88.9	10 90 E			Di
76	c,ts,tan	152.4	0 90 E	45		Di
77	po,tn,ts	4292.6	25 90 E			
78	c,tas,tan	190.5	18 90 E	35	35	
79	c,tas,tn	177.8	15 90 E		20	
80	c,ts,tn	279.4	358 90 E			Di
81	po,ts,htn	4064	30 90 E	40		
82	c,tas,tn	355.6	26 90 E		10	
83	c,ts,tan	203.2	35 90 E	35		
84	c,tn,hts	279.4	24 90 E		60	Di
85	po,hts,tn	2006.6	20 90 E		15	
86	c,tas,tn	177.8	20 90 E	45		
87	po,tas,tan	812.8	30 90 E	55	55	
88	po,ts,tan	50.8	45 90 E	25		
89	po,ts,tn	203.2	20 90 E			
90	po,tn,hts	1117.6	28 90 E		35	
91	po,tas,tan	177.8	36 90 E	15	30	
91A	po,ts,htn	1625.6	14 90 E	35		
92	c,ts,tn	190.5	10 90 E			Di
93	c,ts,tn	30.48	0 90 E			Di
93A	c,hts,tn	241.3	15 90 E		60	
94	c,ts,tn	152.4	18 90 E			Di
95	c,tn,tas	101.6	20 90 E		30	
96	c,tn,hts	1193.8	20 90 E		30	
97	c,tas,tan	279.4	20 90 E	15	15	
98	c,tan,tas	508	12 90 E	55	30	
99	po,hts,xn	2082.8	30 90 E		35	
100	po,tas,tn	127	20 90 E		20	
101	po,tas,tn	38.1	25 90 E		20	
102	po,ts,tn	241.3	25 90 E			
103	c,ts,xn	101.6	20 90 E			
104	po,xs,tn	1651	16 90 E			Di
105 A	c,tas,tn	381	28 90 E		30	Di
105	po,ts,xn	15189.2	56 90 E			
106	po,ts,t	812.8	0 90 E			Di
107	c,ts,tn	685.8	20 90 E			Di
108	c,ts,tn	1219.2	18 90 E			
109	c,ts,tan	76.2	12 90 E	15		

Frac. #	Type	Length (mm)	Orientation	Angle(°N)	Angle(°S)	Observations
110	c,tas,tn	228.6	20 90 E		35	
111	c,ts,tn	990.6	16 90 E			
112	c,tas,tn	76.2	35 90 E		10	
113	c,ts,tn	990.6	16 90 E			Di
114	c,ts,tn	1397	20 90 E			
115	c,tas,tan	279.4	14 90 E	15	15	
116	c,ts,xn	762	24 90 E			
117	c,xn,hts	228.6	35 90 E		35	
118	c,xs,htn	939.8	10 90 E	60		
119	c,ts,tan	101.6	4 90 E	30		
120	c,ts,tn	4826	18 90 E			
121	c,tas,tan	241.3	18 90 E	15	15	
122	c,tas,tan	152.4	26 90 E	45	35	
123	c,tas,tn	12.7	12 90 E		15	
124A	c,tas,tn	38.1	10 90 E		15	
124	c,tas,tn	1193.8	12 90 E		35	Di
125	c,ts,tan	254	12 90 E	35		
126	c,ts,tan	127	20 90 E	30		

Connectivity Parameters		
Number of connection points		
	#	%
≥2	18	15
1	68	56
0	35	29
Type of termination		
	#	%
Tip	141	58
Hooks	19	8
Abrupt	82	34

Westwater Springs

Southern pavement. All fractures in a selected area
Swarm C1

Frac. #	Type	Length (mm)	Orientation	Angle(°N)	Angle(°S)	Observations
1	c,xs,tn	4495.8	20 90 E			
2	c,tas,tan	88.9	20 90 E	35	20	
3	c,hts,tn	177.8	18 90 E		30	
4	c,ts,tn	266.7	14 90 E			
5	c,tan,tas	88.9	26 90 E	15	30	
6	c,tn,tas	76.2	10 90 E		30	
7	c,tas,tn	76.2	14 90 E		20	
8	c,tas,tn	177.8	20 90 E		35	
9	c,tas,tn	127	16 90 E		30	
10	c,tas,tn	101.6	14 90 E		30	
11	c,tas,tan	50.8	8 90 E	30	30	
12	c,tas,tan	50.8	8 90 E	15	15	
13	c,tas,tan	95.25	4 90 E	10	10	
14	c,tan,ts	69.85	2 90 E	45		
15	c,tas,tn	25.4	14 90 E		30	
16	c,ts,tn	711.2	12 90 E			
17	c,tas,tan	177.8	25 90 E	15	30	
18	c,tas,tan	31.75	358 90 E	30	30	
19	c,ts,tn	177.8	8 90 E			Di
20	c,ts,tn	279.4	4 90 E			
21	c,xn,ts	584.2	4 90 E			
22	po,ts,tn	609.6	32 90 E			
23	po,ts,tan	177.8	85 90 E	80		
24	po,ts,tn	330.2	40 90 E			
25	po,ts,tn	609.6	32 90 E			
26	po,ts,tn	1168.4	18 90 E			
27	c,ts,tn	965.2	24 90 E			Di
28	po,tn,xs	1016	14 90 E			
29	po,xn,ts	457.2	24 90 E			
30	po,xn,xs	4724.4	0 90 E			
31	po,tn,xs	660.4	8 90 E			
32	po,ts,tn	3530.6	16 90 E			
33	c,ts,tn	2565.4	20 90 E			Di
34	c,xs,tn	304.8	34 90 E			
35	c,xs,htn	9067.8	22 90 E	35		An
36	c,tan,ts	139.7	26 90 E	10		
37	c,tan,ts	254	30 90 E	15		
38	c,tan,ts	177.8	22 90 E	20		
39	c,tan,ts	241.3	28 90 E	15		
40	c,tas,tn	520.7	10 90 E		20	
41	c,tan,ts	1092.2	14 90 E	15		
42	c,tas,tn	1016	348 90 E		35	
43	c,tas,tn	558.8	24 90 E		15	
44	c,hts,tn	558.8	18 90 E		45	
45	c,tas,tan	431.8	12 90 E	35	35	
46	c,ts,tan	254	20 90 E	35		
47	c,ts,tan	241.3	20 90 E	15		
48	c,hts,tn	685.8	30 90 E		25	
49	c,hts,tn	4038.6	26 90 E		35	
50	c,tas,tan	127	16 90 E	15	15	
51	c,tas,tn	1244.6	26 90 E		25	
52	c,tas,tn	812.8	28 90 E		25	
53	c,tas,tn	254	20 90 E		15	

Frac. #	Type	Length (mm)	Orientation	Angle(°N)	Angle(°S)	Observations
54	c.ts,tn	533.4	30 90 E			
55	po.ts,tn	7391.4	4 90 E			
56	c,xn,hts	6350	22 90 E		45	An
57	c,tan.ts	254	32 90 E	25		
58	c,tas,tan	457.2	22 90 E	30	30	
59	c,tas,tn	444.5	34 90 E		20	
60	c,tas,tan	76.2	18 90 E	10	25	
61	c,tas,tn	393.7	24 90 E		45	
62	c,tas,tn	279.4	20 90 E		30	
63	c.ts,tan	558.8	30 90 E	30		
64	c.ts,tn	660.4	24 90 E			
65	po.ts,tn	1549.4	30 90 E			
66	c.ts,tn	368.3	22 90 E			Di
67	c.ts,xn	1041.4	28 90 E			
68	c.ts,tn	215.9	18 90 E			Di
69	c.ts,xn	508	20 90 E			
70	c,xs,tn	7239	30 90 E			
71	c,tas,tn	330.2	35 90 E		15	
72	c,tan,tas	101.6	4 90 E	35	35	
73	c,tas,tn	508	25 90 E		15	
74	c,tas,tn	457.2	25 90 E		30	
75	po,tas,tn	4851.4	320 90 E		70	Di
75	po,tas,tn	4851.4	320 90 E		70	Di

Connectivity Parameters		
Number of connection points		
	#	%
≥2	12	28
1	35	54
0	18	18
Type of termination		
	#	%
Tip	72	55
Hooks	5	4
Abrupt	53	41

Westwater Springs

Southern pavement. All fractures in a selected area
Swarm C2

Frac. #	Type	Length (mm)	Orientation	Angle(°N)	Angle(°S)	Observations
1	c,ts,tn	6451.6	20 90 E			
2	c,tas,tn	38.1	45 90 E		15	
3	c,tas,tn	139.7	25 90 E		30	Di
4	c,tas,tn	152.4	28 90 E		45	Di
5	c,tas,tn	190.5	14 90 E		30	
6	c,tas,tn	25.4	350 90 E		30	
7	po,tan,ts	63.5	30 90 E	30		
8	c,tan,ts	241.3	35 90 E	15		
9	po,tan,ts	114.3	16 90 E	10		
10	po,tan,ts	12.7	30 90 E	40		
11	c,tan,tas	76.2	12 90 E	30	30	
12	c,ts,tn	3022.6	12 90 E			Di
13	po,ts,xn	635	12 90 E			
14	po,ts,xn	1092.2	28 90 E			

Connectivity Parameters		
Number of connection points		
	#	%
≥2	1	8%
1	9	75%
0	2	17%
Type of termination		
	#	%
Tip	13	54
Hooks	0	0
Abrupt	11	46

Westwater Springs

Southern pavement. All fractures in a selected area
Swarm C3

Frac. #	Type	Length (mm)	Orientation	Angle(°N)	Angle(°S)	Observations
1	po,ts,tn	2819.4	12 90 E			
2	c, tas,tn	38.1	32 90 E		30	
3	c,tas,tn	114.3	38 90 E		45	
4	c,tas,tan	88.9	12 90 E	15	15	
5	c,tas,tan	76.2	14 90 E	40	40	
6	c,ts,tn	685.8	2 90 E			
7	c,ts,tan	63.5	352 90 E	40		
8	c,tn,tas	101.6	12 90 E		20	
9	c,ts,tn	2260.6	10 90 E			
10	c,tn,tas	279.4	12 90 E		35	
11	c,ts,tan	457.2	18 90 E	30		
12	c,ts,tan	304.8	18 90 E	20		
13	c,ts,tan	152.4	8 90 E	35		
14	c,ts,tn	2489.2	8 90 E			
15	c,ts,tan	50.8	348 90 E	30		
16	c,ts,tn	215.9	348 90 E			
17	c,ts,tn	3454.4	18 90 E			
18	c,tas,tan	50.8	10 90 E	40	40	
19	c,tas,tan	355.6	18 90 E	15	35	
20	c,tas,tan	50.8	14 90 E	20	20	
21	c,tas,tan	63.5	10 90 E	15	15	
22	c,tas,tan	101.6	10 90 E	30	30	
23	c,ts,tan	203.2	28 90 E	30		
24	c,ts,tn	812.8	4 90 E			
25	c,ts,tn	330.2	18 90 E			
26	c,ts,xn	203.2	0 90 E			
27	c,ts,xn	177.8	0 90 E			Di
28	po,ts,tan	11684	45 90 E	45		
28A	po,ts,tn	3302	55 90 E			
29	po,tn,xs	1574.8	14 90 E			Di
30	c,xs,tn	4191	25 90 E			
31	c,tas,ts	63.5	10 90 E	35		
32	c,ts,xn	1981.2	18 90 E			
33	c,tan,ts	63.5	20 90 E	45		
34	c,tan,tas	139.7	18 90 E	15	15	
35	po,xs,tn	660.4	15 90 E			

Connectivity Parameters		
Number of connection points		
	#	%
>2	7	23
1	14	47
0	9	30
Type of termination		
	#	%
Tip	43	72
Hooks	0	0
Abrupt	17	28

Westwater Springs

Southern pavement. All fractures in a selected area
Swarm D1

Frac. #	Type	Length (mm)	Orientation	Angle(°N)	Angle(°S)	Observations
1	c.ts,tn	2057.4	30 90 E			
2	c.ts,tn	990.6	45 90 E			
3	c.tan,ts	152.4	24 90 E	30		Di
4	c.hts,tn	393.7	55 90 E		15	
5	c.tan,ts	88.9	18 90 E	60		Di
6	c.ts,tn	1117.6	28 90 E			
7	c.ts,tn	2286	34 90 E			
8	c.tan,ts	228.6	56 90 E	30		
9	c.ts,tn	711.2	22 90 E			
10	c.ts,tn	533.4	20 90 E			Di
11	c.ts,tn	203.2	14 90 E			Di
12	c.ts,tn	533.4	6 90 E			Di
13	c.ts,tn	914.4	45 90 E			Di
14	c.ts,tn	1955.8	34 90 E			
15	c.ts,tn	406.4	40 90 E			
16	c.ts,tn	3124.2	35 90 E			
17	c.ts,tan	3175	35 90 E	45		

Connectivity Parameters		
Number of connection points		
	#	%
≥2	0	0
1	5	29
0	12	71
Type of termination		
	#	%
Tip	29	85
Hooks	1	3
Abrupt	4	12

Westwater Springs

Southern pavement. All fractures in a selected area
Swarm D2

Frac. #	Type	Length (mm)	Orientation	Angle(°N)	Angle(°S)	Observations
1	c,xs,tn	190.5	22 90 E			
2	c,tas,tn	38.1	36 90 E		10	
3	c,ts,tn	88.9	14 90 E			Di
4	c,ts,tn	419.1	35 90 E			Di
5	c,tan,ts	76.2	22 90 E	30		Di
6	c,ts,tn	1905	24 90 E			Di
7	c,tas,tan	50.8	24 90 E		35	
8	c,tas,tan	25.4	26 90 E	10	10	
9	c,ts,tn	863.6	26 90 E			
10	c,ts,tn	1143	30 90 E			
11	c,ts,tn	660.4	10 90 E			Di
12	c,ts,tn	1422.4	14 90 E			
13	po,ts,tn	457.2	0 90 E			
14	po,ts,tn	533.4	22 90 E			Di
15	c,ts,tn	635	350 90 E			Di
16	c,ts,tn	406.4	352 90 E			Di
17	c,tas,tn	177.8	0 90 E			Di
18	c,ts,tn	2895.6	352 90 E			
19	po,tas,tn	965.2	22 90 E		40	Di

Connectivity Parameters		
Number of connection points		
	#	%
>2	1	6
1	4	22
0	13	72
Type of termination		
	#	%
Tip	28	78
Hooks	0	0
Abrupt	8	22

Westwater Springs

Southern pavement. All fractures in a selected area
Swarm D3

Frac. #	Type	Length (mm)	Orientation	Angle(°N)	Angle(°S)	Observations
1	po,xs,tn	533.4	28 90 E			
2	c,ts,tn	330.2	22 90 E			Di
3	c,ts,tn	241.3	24 90 E			
4	c,hts,htn	1270	38 90 E	15	35	
5	c,tas,tn	165.1	24 90 E		20	
6	c,htn,ts	457.2	20 90 E	15		
7	c,hts,tn	2590.8	22 90 E		10	Di
8	c,tan,ts	76.2	45 90 E	10		Di
9	c,tan,ts	177.8	42 90 E	10		Di
10	c,ts,tn	508	0 90 E			Di
11	c,tn,ts	939.8	28 90 E			Di

Connectivity Parameters		
Number of connection points		
	#	%
>2	1	11
1	5	56
0	3	33
Type of termination		
	#	%
Tip	11	61
Hooks	4	22
Abrupt	3	17

Westwater Springs

Southern pavement. All fractures in a selected area
Swarm D4

Frac. #	Type	Length (mm)	Orientation	Angle(°N)	Angle(°S)	Observations
1	c,xs,xn	190.5	12 90 E			Di
2	po,xs,xn	228.6	340 90 E			
3	po,xs,tan	1117.6	28 90 E	35		
4	c,tn,tas	114.3	45 90 E		40	
5	po,ts,tn	381	45 90 E			
6	po,tn,ts	2743.2	35 90 E			
7	po,tn,hts	584.2	24 90 E		60	
8	po,ts,tn	1066.8	20 90 E			
9	po,ts,tn	914.4	24 90 E			
10	po,tas,tn	1473.2	30 90 E		10	
11	po,ts,tn	609.6	12 90 E			
12	po,ts,tn	1143	20 90 E			ee
13	c,ts,tn	279.4	24 90 E			ee
14	c,ts,tn	1600.2	24 90 E			ee
15	c,ts,tn	1549.4	0 90 E			
16	c,ts,tn	177.8	4 90 E			Di
17	c,ts,tn	609.6	18 90 E			Di
18	c,tas,tan	381	10 90 E	35	35	
19	c,tan,ts	1930.4	20 90 E	35		
20	c,tan,tas	152.4	20 90 E	15	15	
21	c,htn,ts	762	34 90 E	15		
22	c,hts,tn	1955.8	28 90 E		15	
23	c,ts,tn	533.4	20 90 E			
24	c,tas,tn	812.8	20 90 E		35	
25	c,tan,ts	330.2	12 90 E	15		
26	c,tn,ts	241.3	18 90 E			
27	c,htn,ts	1447.8	22 90 E	10		
28	c,tas,tan	76.2	18 90 E	15	15	
29	c,ts,tn	190.5	26 90 E			
30	c,htn,ts	177.8	26 90 E	35		
31	c,hts,tn	1270	22 90 E		15	
32	c,htn,ts	1016	24 90 E	20		
33	c,tn,tas	50.8	20 90 E	10	10	
34	c,tas,tn	63.5	40 90 E		35	
35	c,hts,tn	1981.2	16 90 E		20	
36	c,tas,tn	431.8	12 90 E		15	
37	c,tas,tn	406.4	20 90 E		50	
38	c,ts,tn	431.8	20 90 E			Di
39	c,ts,tn	1117.6	2 90 E		15	
40	c,tas,tn	304.8	36 90 E		30	
41	po,ts,tn	2540	6 90 E			
42	c,ts,tn	177.8	350 90 E			
42 A	c,tn,ts	508	18 90 E			
43	c,htn,ts	177.8	10 90 E	20		
43 A	c,htn,ts	952.5	22 90 E	15		
43 B	c,htn,ts	711.2	14 90 E	45		
44	c,hts,htn	685.8	24 90 E	15	15	
44 A	c,tan,ts	406.4	12 90 E	15		
45	c,tas,tan	1854.2	32 90 E	30	30	
46	c,tas,tan	241.3	42 90 E	30	30	
47	c,ts,tn	406.4	32 90 E			Di
48	c,ts,tn	406.4	30 90 E			Di
49	c,tn,ts	711.2	24 90 E			

Frac. #	Type	Length (mm)	Orientation	Angle(°N)	Angle(°S)	Observations
50	c.tas,tn	1016	22 90 E		35	
51	c.tn,ts	914.4	16 90 E			
52	c.ts,tn	228.6	15 90 E			Di
53	c.ts,tn	711.2	10 90 E			Di
54	c.htn,ts	1117.6	15 90 E	30		
55	c.tas,tan	127	8 90 E	15	15	
56	c.ts,tn	152.4	8 90 E			Di
57	c.tas,tn	50.8	28 90 E		30	
58	c.htn,ts	914.4	8 90 E	35		
59	c.ts,tn	1625.6	16 90 E			
60	c.hts,tn	254	22 90 E		35	
61	c.xn,hts	533.4	20 90 E			
62	c.tn,xs	304.8	14 90 E			
63	c.tn,xs	965.2	358 90 E			An
64	c.tan,ts	114.3	16 90 E	15		
65	c.htn,ts	241.3	4 90 E	15		
66	c.htn,xs	990.6	22 90 E	30		
67	c.tas,tan	76.2	16 90 E	15	15	Di
67 A	c.ts,tn	469.9	20 90 E			
68	c.ts,tn	203.2	28 90 E			
69	c.ts,tn	1092.2	38 90 E			

Connectivity Parameters		
Number of connection points		
	#	%
>2	7	10
1	32	48
0	28	42
Type of termination		
	#	%
Tip	84	63
Hooks	20	15
Abrupt	30	22

Westwater Springs

Southern pavement. All fractures in a selected area
Infilling fractures between Swarms A and B

Frac. #	Type	Length (mm)	Orientation	Angle(°N)	Angle(°S)	Observations
1	po,xs,tn	2108.2	35 90 E			
2	po,xs,tan	2082.8	15 90 E	45		
3	c,tas,tn	177.8	18 90 E		35	
4	c,tas,tn	457.2	36 90 E		30	
5	po,ts,tan	88.9	30 90 E	35		
6	c,ts,tn	228.6	32 90 E			
7	po,tas,xn	2387.6	338 90 E		45	
8	c,tas,tn	457.2	55 90 E	40		
9	po,xn,tas	736.6	314 90 E		90	Di
10	po,ts,tn	406.4	60 90 E			
11	po,ts,tn	1346.2	54 90 E			
12	c,tas,tn	127	4 90 E		45	Di
13	c,ts,tn	584.2	10 90 E			Di
14	c,tas,tn	190.5	32 90 E		45	
15	c,tas,tn	495.3	24 90 E		45	
16	c,ts,tn	203.2	26 90 E			
17	c,ts,tn	127	26 90 E			
18	c,tas,tn	203.2	352 90 E		35	
19	c,ts,xn	381	20 90 E			
20	po,ts,tn	1117.6	55 90 E			
21	c,tas,tn	736.6	26 90 E		35	
22	c,tan,ts	190.5	32 90 E	20		
23	c,ts,tn	1016	6 90 E			
24	c,ts,tn	495.3	26 90 E			
25	c,ts,tn	2362.2	28 90 E			

Connectivity Parameters		
Number of connection points		
	#	%
>2	0	0
1	13	68
0	6	32
Type of termination		
	#	%
Tip	22	79
Hooks	0	0
Abrupt	8	21

Southern pavement. All fractures in a selected area
Infilling fractures between Swarms C1 and D1/D2

Frac. #	Type	Length (mm)	Orientation	Angle(°N)	Angle(°S)	Observations
1	c,xs,tn	1879.6	18 90 E			
2	o,ts,xn	431.8	14 90 E			
3	o,tas,tan	304.8	80 90 E	90	35	
4	o,xs,xn	508	24 90 E			
5	po,xs,tn	1752.6	16 90 E			
6	po,ts,tn	787.4	12 90 E			

Cottonwood Flat Iron

Large area. All fractures
Swarm A

Frac. #	Type	Length (mm)	Orientation	Angle(°N)	Angle(°S)	Observations
1	c.in.ts	787.4	32 90 E			
2	c.xn.tas	660.4	22 90 E		30	
3	c.xn.ts	457.2	24 90 E			
4	c.in.ts	330.2	32 90 E			
5	c.ts.tn	444.5	35 90 E			
6	c.in.tas	571.5	30 90 E		35	
7	c.tan.ts	101.6	26 90 E	15		
8	c.in.ts	1574.8	52 90 E			same as #4?
9	c.in.ts	584.2	32 90 E			
10	c.tan.htn	787.4	20 90 E	35	40	
11	c.tan.ts	165.1	42 90 E	60		
12	c.tn.ts	279.4	34 90 E			
13	c.tan.ts	355.6	24 90 E	30		
14	c.tan.ts	254	28 90 E	20		
15	c.tan.ts	114.3	20 90 E	30		
16	c.tn.hts	304.8	26 90 E		40	
17	c.tn.hts	965.2	20 90 E		30	
18	c.hts.htn	304.8	18 90 E	50	35	
19	c.tn.ts	1041.4	28 90 E			
20	c.tan.ts	330.2	22 90 E	35		
21	c.tan.ts	114.3	26 90 E	20		
22	c.tn.ts	1574.8	30 90 E			
23	c.tan.tas	33.02	28 90 E	40	40	
24	c.tn.tas	88.9	28 90 E		35	
25	c.tn.hts	1397	30 90 E		15	
26	c.ts.tn	1168.4	30 90 E			
27	c.tas.tan	38.1	32 90 E	15	45	
28	c.tn.ts	355.6	25 90 E			
29	c.tn.ts	1676.4	32 90 E			
30	c.tn.tas	139.7	22 90 E		35	
31	c.tn.ts	228.6	22 90 E			
32	c.tn.ts	228.6	20 90 E			
33	c.tn.ts	152.4	12 90 E			
34	c.tn.xs	736.6	0 90 E			
35	c.xn.hts	2794	34 90 E		40	
36	c.htn.hts	381	32 90 E	45	45	
37	c.htn.ts	762	34 90 E	35		
38	c.tn.ts	660.4	18 90 E			
39	c.tn.ts	355.6	28 90 E			
40	c.htn.ts	558.8	38 90 E	30		
41	c.tn.ts	635	30 90 E			
42	c.tn.ts	660.4	34 90 E			
43	c.tn.ts	838.2	18 90 E			

Connectivity Parameters		
Number of connection points		
	#	%
≥2	5	12
1	17	41
0	19	47
Type of termination		
	#	%
Tip	58	71
Hooks	9	11
Abrupt	15	18

Cottonwood Flat Iron

Large area. All fractures
Swarm B

Frac. #	Type	Length (mm)	Orientation	Angle(°N)	Angle(°S)	Observations
1	c.xn,xs	1803.4	32 90 E			
2	c.xn,ts	1701.8	32 90 E			
3	c.tan,tas	38.1	80 90 E	45	45	
4	c.tn,ts	1574.8	32 90 E			
5	c.htn,ts	508	34 90 E	35		
6	c.tn,ts	939.8	28 90 E			
7	c.tn,ts	1371.6	28 90 E			
8	c.htn,ts	1524	32 90 E	35		
9	c.tn,ts	1600.2	26 90 E			
10	c.tn,ts	2159	22 90 E			
11	c.tn,ts	1422.4	28 90 E			
12	c.tn,ts	1143	34 90 E			
13	c.tan,tas	914.4	30 90 E	15		
14	c.tn,ts	711.2	28 90 E			
15	c.tn,ts	1168.4	30 90 E			
16	c.tn,ts	482.6	38 90 E			
17	c.tan,tas	190.5	52 90 E	35		
18	c.tan,tas	254	32 90 E	15	30	
19	c.tn,ts	584.2	18 90 E			
20	c.htn,tas	558.8	20 90 E	35	40	
21	c.tn,ts	482.6	20 90 E			

Connectivity Parameters		
Number of connection points		
	#	%
≥2	3	16
1	3	16
0	13	68
Type of termination		
	#	%
Tip	28	74
Hooks	3	8
Abrupt	7	18

Cottonwood Flat Iron

Large area. All fractures
Swarm C

Frac. #	Type	Length (mm)	Orientation	Angle(°N)	Angle(°S)	Observations
1	c,xn,xs	3022.6	24 90 E			
2	c,xn,ts	1955.8	36 90 E			
3	c,xn,xs	1244.6	38 90 E			
4	c,tn,xs	330.2	32 90 E			
5	c,tn,ts	279.4	34 90 E			
6	c,tn,ts	685.8	24 90 E			
7	c,xn,xs	381	38 90 E			
8	po,xn,ts	381	34 90 E			
9	c,xn,ts	965.2	38 90 E			
10	c,htn,ts	762	20 90 E	25		
11	c,htn,ts	406.4	22 90 E	35		
12	c,tn,ts	558.8	34 90 E			
13	c,tan,ts	190.5	30 90 E	35		
14	c,tn,ts	355.6	30 90 E			
15	c,htn,ts	355.6	30 90 E	15		
16	c,tn,tas	228.6	35 90 E		15	
17	c,tn,ts	685.8	26 90 E			
18	c,tn,ts	584.2	32 90 E			
19	c,htn,ts	1143	46 90 E	35		
20	c,tan,ts	711.2	38 90 E	10		
21	c,tn,ts	685.8	42 90 E			
22	c,tn,ts	406.4	38 90 E			
23	c,tn,ts	241.3	38 90 E			
24	c,tn,hts	508	42 90 E		40	
25	c,tn,ts	381	40 90 E			
26	c,tn,ts	965.2	45 90 E			
27	c,tn,hts	2057.4	28 90 E		35	
28	c,tn,ts	431.8	40 90 E			Di
29	c,tn,ts	381	38 90 E			Di
30	c,tn,tas	381	28 90 E		25	
31	c,tn,ts	3708.4	25 90 E			
32	c,tn,ts	635	40 90 E			
33	c,tn,ts	2616.2	22 90 E			
34	c,tn,ts	2286	32 90 E			
35	c,tn,tas	152.4	42 90 E		20	
36	c,tn,tas	381	14 90 E		35	
37	c,tn,ts	990.6	30 90 E			
38	c,tn,ts	533.4	30 90 E			
39	c,tan,tas	190.5	28 90 E	20	15	
40	c,tan,ts	355.6	40 90 E	20		
41	c,tn,hts	1803.4	40 90 E		30	
42	c,tn,hts	330.2	26 90 E		30	Di
43	c,htn,tas	1651	24 90 E	20	10	Di
44	c,tan,tas	63.5	290 90 E	60	60	
45	c,tn,ts	2463.8	34 90 E			
46	c,tn,hts	1752.6	26 90 E		35	
47	c,tn,hts	1117.6	34 90 E		35	
48	c,tn,ts	889	32 90 E			
49	c,tn,ts	889	28 90 E			
50	c,tn,ts	914.4	32 90 E			Di
51	c,tn,hts	330.2	30 90 E		40	
52	c,htn,ts	355.6	32 90 E	40		
53	c,htn,ts	685.8	28 90 E	35		Di

Frac. #	Type	Length (mm)	Orientation	Angle(°N)	Angle(°S)	Observations
54	c.tn.ts	533.4	22 90 E			
55	c.tn.ts	406.4	24 90 E	10		
56	c.tn.ts	736.6	32 90 E			
57	c.tn.ts	939.8	32 90 E			
58	c.tn.ts	812.8	24 90 E			
59	c.hfn.ts	406.4	18 90 E	60		
60	c.tn.ts	1600.2	25 90 E			
61	c.tn.ts	228.6	34 90 E			

Connectivity Parameters		
Number of connection points		
	#	%
≥2	3	6
1	22	41
0	29	53
Type of termination		
	#	%
Tip	80	74
Hooks	15	14
Abrupt	13	12

Cottonwood Flat Iron

Large area. All fractures
Swarm D

Frac. #	Type	Length (mm)	Orientation	Angle(°N)	Angle(°S)	Observations
1	c,xn,ts	508	42 90 E			
2	c,htn,ts	457.2	42 90 E	35		
3	ctn,ts	381	10 90 E			
4	c,tn,ts	63.5	52 90 E			
5	po,tn,ts	88.9	52 90 E			
6	po,tn,ts	38.1	38 90 E			
7	c,tn,ts	76.2	58 90 E			
8	c,tn,ts	76.2	54 90 E			
9	po,tn,ts	127	24 90 E			
10	po,tn,ts	127	24 90 E			
11	c,tn,ts	304.8	24 90 E			
12	c,tn,hts	177.8	28 90 E		40	
13	c,tan,ts	304.8	22 90 E	10		
14	c,xn,ts	635	32 90 E			
15	c,tn,xs	609.6	28 90 E			
16	c,tn,hts	330.2	38 90 E		35	
17	c,tn,xs	508	28 90 E			
18	c,xn,xs	660.4	28 90 E			
19	c,tn,xs	355.6	24 90 E			
20	c,tan,ts	165.1	34 90 E	30		
21	c,tn,ts	990.6	32 90 E			
22	c,tn,ts	279.4	28 90 E			
23	c,tan,xs	1143	26 90 E	45		
24	c,tn,xs	355.6	28 90 E			
25	c,xn,ts	279.4	45 90 E			
26	c,tn,ts	304.8	30 90 E			
27	c,tn,tas	228.6	65 90 E		40	
28	c,xn,xs	990.6	32 90 E			same as #18?
29	po,tn,xs	482.6	26 90 E			
30	c,xn,ts	2590.8	34 90 E			
31	c,xn,ts	1955.8	30 90 E			
32	c,xn,ts	1320.8	32 90 E			
33	c,xn,tas	2006.6	32 90 E		20	
34	c,tn,tas	1752.6	34 90 E		10	
35	c,tn,tas	330.2	34 90 E		20	
36	c,tn,ts	1244.6	28 90 E			
37	c,tan,tas	38.1	346 90 E	35	35	
38	c,tan,ts	139.7	52 90 E	40		
39	c,tn,ts	457.2	28 90 E			
40	c,tn,hts	431.8	50 90 E		45	
41	c,tan,ts	279.4	34 90 E	30		
42	c,tan,ts	330.2	28 90 E	15		
43	c,tn,tas	241.3	35 90 E		30	
44	c,htn,ts	1016	34 90 E	35		
45	c,tn,tas	203.2	26 90 E		30	
46	c,tn,tas	50.8	36 90 E		20	
47	c,tn,tas	101.6	294 90 E		80	
48	c,tas,tn	38.1	24 90 E		30	
49	c,ts,tan	228.6	34 90 E	80		
50	c,tn,ts	482.6	30 90 E			
51	c,tn,ts	228.6	45 90 E			
52	c,tn,ts	101.6	30 90 E			
53	c,tan,ts	381	26 90 E	30		

Frac. #	Type	Length (mm)	Orientation	Angle(°N)	Angle(°S)	Observations
54	c.ts,tan	76.2	32 90 E	20		
55	c.tn,ts	177.8	35 90 E			
56	c.tan,ts	203.2	38 90 E	40		
57	c.tn,ts	241.3	28 90 E			
58	c.tan,ts	457.2	32 90 E	15		
59	c.tn,ts	139.7	28 90 E			
60	c.ts,tn	330.2	30 90 E			
61	c.tn,tas	279.4	35 90 E		80	
62	c.tan,ts	139.7	280 90 E	80		
63	c.tan,ts	203.2	35 90 E	80		
64	c.tn,hts	1041.4	33 90 E		35	
65	c.ts,tan	1016	30 90 E	45		
66	c.tn,ts	304.8	26 90 E			
67	c.tn,hts	685.8	28 90 E		30	
68	c.tas,htn	1016	38 90 E	40	15	
69	c.tas,tn	63.5	358 90 E		50	
70	c.tan,tas	50.8	357 90 E	45	45	
71	c.tn,tas	1524	32 90 E		20	
72	c.tn,tas	215.9	40 90 E		20	
73	c.htn,tas	939.8	30 90 E	20	50	
74	c.tan,tas	152.4	352 90 E	45	45	
75	c.htn,tas	254	35 90 E	40	20	
76	c.htn,ts	1371.6	32 90 E	15		
77	c.htn,hts	1092.2	36 90 E	35	45	
78	c.tn,hts	203.2	45 90 E		20	
79	c.tn,hts	152.4	38 90 E		15	
80	c.tn,ts	63.5	10 90 E			
81	c.hts,tan	406.4	48 90 E	20	45	
82	c.tan,tas	609.6	24 90 E	15	15	
83	c.tn,tas	787.4	36 90 E		45	
84	c.tan,ts	304.8	30 90 E	60		
85	c.ts,tan	558.8	34 90 E	35		
86	c.tas,tan	304.8	84 90 E	60	45	
87	c.tn,ts	177.8	30 90 E			
88	c.tn,ts	431.8	16 90 E			
89	c.tn,ts	1143	32 90 E			
90	c.tn,ts	406.4	32 90 E			
91	c.hts,tn	215.9	28 90 E		35	
92	c.tn,ts	304.8	42 90 E			
93	c.tan,tas	45.72	295 90 E	90	90	
94	c.tn,ts	635	34 90 E			
95	c.htn,ts	939.8	20 90 E	20		
96	c.tn,ts	635	26 90 E			
97	c.htn,tas	889	12 90 E	45	40	
98	c.hts,tn	330.2	52 90 E		60	
99	c.hts,tan	1143	42 90 E	35	45	
100	c.tan,ts	203.2	358 90 E	45		
101	c.tas,tn	152.4	30 90 E		45	
102	c.tas,tn	88.9	270 90 E		60	
103	c.tas,tn	330.2	24 90 E		30	
104	c.tas,tan	177.8	22 90 E	35	50	
105	c.tas,tn	584.2	31 90 E		40	
106	c.ts,tan	3073.4	30 90 E	35		
107	c.tn,tas	203.2	254 90 E		35	
108	c.tan,ts	330.2	52 90 E	35		
109	c.tn,ts	736.6	26 90 E			
110	c.tan,ts	4572	28 90 E	50		
111	c.ts,tan	482.6	54 90 E	45		
112	c.ts,tan	254	44 90 E	35		
113	c.ts,tan	177.8	14 90 E	45		
114	c.tan,tas	215.9	63 90 E	35	45	
115	c.tan,ts	76.2	55 90 E	60		

Frac. #	Type	Length (mm)	Orientation	Angle(°N)	Angle(°S)	Observations
116	c,tn,ts	889	33 90 E			
117	c,tn,ts	1447.8	34 90 E			
118	c,ts,htn	889	22 90 E	45		
119	c,tn,hts	203.2	30 90 E		45	
120	c,tan,ts	431.8	24 90 E	30		
121	c,tn,ts	304.8	32 90 E			
122	c,tn,ts	355.6	27 90 E			
123	c,tan,hts	482.6	30 90 E	45	15	
124	c,htn,ts	939.8	35 90 E	45		
125	c,tn,ts	241.3	20 90 E			
126	c,tan,ts	203.2	14 90 E	45		
127	c,htn,ts	431.8	40 90 E	45		
128	c,tn,ts	203.2	18 90 E			Di
129	c,tn,tas	1473.2	30 90 E		30	
130	c,hts,tn	2768.6	33 90 E		35	
131	c,tn,ts	457.2	31 90 E			
132	c,htn,hts	406.4	31 90 E	45	45	
133	c,tan,tas	203.2	58 90 E	35	35	
134	c,tn,tas	990.6	20 90 E		15	
135	c,tan,ts	762	33 90 E	10		
136	c,tn,ts	1549.4	34 90 E			
137	c,tan,ts	127	36 90 E	30		
138	c,tn,ts	152.4	32 90 E			
139	c,tan,ts	812.8	38 90 E	15		
140	c,tn,ts	1498.6	33 90 E			
141	c,htn,ts	635	34 90 E	45		
142	c,tn,ts	508	36 90 E			
143	c,hts,tn	508	34 90 E		45	
144	c,tn,ts	279.4	31 90 E			
145	c,tn,ts	304.8	34 90 E			
146	c,tn,ts	1701.8	28 90 E			
147	c,hts,tn	1828.8	30 90 E		45	
148	c,tan,tas	177.8	30 90 E	45	30	
149	c,tas,tn	381	29 90 E		30	
150	c,tn,ts	1854.2	32 90 E			
151	c,tn,ts	533.4	26 90 E			
152	c,ts,tan	457.2	32 90 E	30		
153	c,tn,ts	406.4	38 90 E			
154	c,tn,ts	330.2	24 90 E			
155	c,tn,ts	711.2	42 90 E			
156	c,tan,tas	127	22 90 E	35	35	
157	c,tn,ts	609.6	40 90 E			
158	c,tn,ts	228.6	41 90 E			
159	c,tn,ts	127	36 90 E			
160	c,tas,tn	101.6	40 90 E		20	
161	c,tas,tn	279.4	42 90 E		40	
162	c,ts,tan	88.9	27 90 E	15		
163	c,tas,tan	38.1	18 90 E	30	35	
164	c,ts,tan	838.2	15 90 E	45		
165	c,tn,ts	990.6	35 90 E			
166	c,tas,tan	152.4	41 90 E	10	10	
167	c,tan,ts	101.6	342 90 E	60		
168	c,tan,ts	139.7	30 90 E	60		
169	c,tn,ts	203.2	34 90 E			
170	c,tan,ts	6426.2	32 90 E	30		
171	c,tn,ts	152.4	18 90 E			
172	c,tn,ts	139.7	28 90 E			
173	c,tn,ts	215.9	20 90 E			
174	c,tan,ts	419.1	30 90 E	40		
175	c,tn,ts	1727.2	26 90 E			
176	c,tn,t	787.4	37 90 E			
177	c,tn,ts	355.6	36 90 E			

Frac. #	Type	Length (mm)	Orientation	Angle(°N)	Angle(°S)	Observations
178	c.tan.ts	584.2	28 90 E	15		
179	c.tas.tn	127	30 90 E		30	
180	c.tas.tan	254	36 90 E	30	45	
181	c.tn.tas	254	33 90 E		25	
182	c.tan.tas	304.8	32 90 E	10	10	
183	c.tan.ts	1803.4	33 90 E	25		
184	c.tn.tas	25.4	52 90 E		35	
185	c.tn.ts	431.8	38 90 E			
186	c.tn.ts	254	34 90 E			
187	c.tn.ts	152.4	32 90 E			
188	c.tan.ts	101.6	36 90 E	70		
189	c.tn.ts	584.2	44 90 E			
190	c.tan.ts	152.4	37 90 E	45		
191	c.tn.tas	406.4	32 90 E		15	
192	c.tn.s	228.6	38 90 E			
193	c.tan.ts	279.4	39 90 E	30		
194	c.tn.ts	584.2	40 90 E			
195	c.tan.tas	38.1	10 90 E	45	45	
196	c.ts.tn	889	37 90 E			
197	c.ts.tn	63.5	37 90 E			
198	c.ts.tn	508	33 90 E			
199	c.ts.tn	76.2	35 90 E			
200	c.htn.ts	114.3	40 90 E	30		
201	c.tn.ts	304.8	44 90 E			
202	c.tn.ts	431.8	41 90 E			
203	c.tn.ts	304.8	39 90 E			
204	c.tn.ts	1803.4	30 90 E			
205	c.tan.ts	76.2	39 90 E	30		
206	c.tn.s	1524	32 90 E			Di
207	c.hts.tn	1397	29 90 E		45	
208	c.xn.ts	406.4	30 90 E			
209	c.ts.xn	1219.2	35 90 E			
210	c.tan.ts	355.6	39 90 E	30		
211	c.tn.ts	203.2	38 90 E			
212	c.tn.ts	63.5	26 90 E			
213	c.tn.ts	177.8	36 90 E			
214	c.tn.ts	254	24 90 E			
215	c.tn.tas	508	37 90 E		10	
216	c.tn.ts	279.4	30 90 E			
217	c.tan.ts	304.8	22 90 E	30		
218	c.tan.ts	254	10 90 E	10		
219	c.tan.ts	38.1	38 90 E	10		
220	c.tn.ts	558.8	34 90 E			
221	c.htn.ts	812.8	34 90 E	45		
222	c.tan.ts	762	38 90 E	30		
223	c.tan.ts	101.6	0 90 E	10		
224	c.tas.tn	127	10 90 E		15	
225	c.hts.tn	736.6	32 90 E		35	
226	c.tn.ts	812.8	26 90 E			
227	c.tan.ts	203.2	28 90 E	30		
228	c.tan.ts	1016	32 90 E	35		
229	c.tn.tas	177.8	20 90 E		30	
230	c.tn.ts	457.2	29 90 E			
231	c.tan.tas	88.9	46 90 E	25	25	
232	c.tn.ts	431.8	26 90 E			
233	c.hts.tan	381	36 90 E	15	15	
234	c.htn.ts	1117.6	34 90 E	20		
235	c.tn.ts	228.6	31 90 E			
236	c.tn.ts	127	38 90 E			
237	c.tn.ts	279.4	22 90 E			
238	c.tn.ts	152.4	24 90 E			
239	c.tn.ts	609.6	20 90 E			

Frac. #	Type	Length (mm)	Orientation	Angle(°N)	Angle(°S)	Observations
240	c.tn,ts	76.2	28 90 E			
241	c.tn,ts	355.6	18 90 E			
242	c.tn,tas	203.2	32 90 E		35	
243	c.tan,tas	114.3	32 90 E	20	30	
244	c.tn,tas	88.9	29 90 E		25	
245	c.tn,ts	1625.6	28 90 E			
246	c.tan,ts	609.6	22 90 E	35		
247	c.tn,ts	304.8	2 90 E			
248	c.tn,ts	1498.6	26 90 E			
249	c.tan,ts	228.6	34 90 E	35		
250	c.tn,tas	457.2	42 90 E		35	
251	c.tn,ts	406.4	25 90 E			
252	c.tn,ts	355.6	6 90 E			
253	c.tn,ts	558.8	24 90 E			
254	c.tn,ts	1295.4	20 90 E			
255	c.tas,tn	355.6	18 90 E		35	
256	c.tas,tn	1016	10 90 E		15	
257	c.tas,tn	152.4	12 90 E		20	
258	c.tn,ts	50.8	19 90 E			
259	c.tn,ts	736.6	20 90 E			
260	c.tan,ts	127	18 90 E	15		
261	c.tan,ts	381	19 90 E	15		
262	c.tas,tn	330.2	24 90 E		15	
263	c.tas,tn	203.2	22 90 E		15	
264	c.tan,ts	482.6	20 90 E	15		
265	c.htn,ts	533.4	19 90 E	35		
266	c.tn,ts	711.2	18 90 E			
267	c.htn,ts	508	16 90 E	30		
268	c.tas,tn	76.2	10 90 E		40	
269	c.tn,ts	558.8	36 90 E			
270	c.tn,ts	381	20 90 E			
271	c.htn,ts	1270	22 90 E	60		
272	c.tn,ts	736.6	24 90 E			
273	c.tn,ts	533.4	20 90 E			
274	c.tas,tn	558.8	20 90 E		15	
275	c.tan,ts	330.2	46 90 E	40		
276	c.tn,ts	381	24 90 E			
277	c.tn,ts	381	18 90 ER			
278	c.tan,tas	431.8	18 90 E	60	60	
279	c.htn,ts	431.8	19 90 E	45		
280	c.tas,tn	584.2	26 90 E		20	
281	c.tan,tas	101.6	78 90 E	60	70	
282	c.tan,ts	889	20 90 E	60		
283	c.tan,tas	38.1	76 90 E	60	60	
284	c.tas,tn	736.6	35 90 E		35	
285	c.tas,tan	127	38 90 E	15	15	
286	c.tas,tan	406.4	22 90 E	45	45	
287	c.tn,hts	406.4	24 90 E		25	
288	c.htn,ts	863.6	24 90 E	25		
289	c.th,ts	279.4	18 90 E			
290	c.tn,ts	304.8	18 90 E			
291	c.tas,tn	63.5	65 90 E		70	
292	c.tn,ts	254	30 90 E			
293	c.ts,htn	203.2	18 90 E	40		
294	c.tn,ts	787.4	18 90 E			
295	c.tn,ts	533.4	18 90 E			
296	c.tn,ts	609.6	27 90 E			
297	c.tan,xs	431.8	30 90 E	15		Di
298	c.tn,ts	254	30 90 E			
299	c.tn,ts	228.6	20 90 E			
300	c.tn,ts	254	18 90 E			
301	c.tas,tn	812.8	18 90 E		15	

Frac. #	Type	Length (mm)	Orientation	Angle(°N)	Angle(°S)	Observations
302	c.tn.ts	431.8	16 90 E			
303	c.tan.ts	381	14 90 E	25		
304	c.htn.ts	584.2	16 90 E	35		
305	c.tan.ts	139.7	54 90 E	40		
306	c.tan.tas	1117.6	14 90 E	15	10	
307	c.tn.ts	584.2	22 90 E			
308	c.tn.ts	990.6	24 90 E			
309	c.tn.hts	1955.8	24 90 E		15	
310	c.tn.ts	279.4	22 90 E			
311	c.htn.hts	254	16 90 E	20	15	
312	c.htn.ts	381	18 90 E	20		
313	c.tan.hts	228.6	28 90 E	15	20	
314	c.htn.tas	1244.6	36 90 E	30	40	

Connectivity Parameters		
Number of connection points		
	#	%
≥2	35	12
1	138	47
0	123	41
Type of termination		
	#	%
Tip	384	64
Hooks	51	9
Abrupt	159	27

Cottonwood Flat Iron

Large area. All fractures
Swarm E

Frac. #	Type	Length (mm)	Orientation	Angle(°N)	Angle(°S)	Observations
1	c,xn,ts	330.2	18 90 E			
2	c,tn,ts	279.4	32 90 E			
3	c,tn,ts	508	28 90 E			
4	c,tn,ts	533.4	30 90 E			
5	c,tn,ts	533.4	35 90 E			
6	c,tn,xs	2235.2	29 90 E			
7	c,tn,xs	304.8	26 90 E			
8	c,xn,xs	355.6	32 90 E			
9	po,xn,xs	1320.8	28 90 E			
10	c,tn,ts	279.4	24 90 E			
11	c,xn,xs	431.8	50 90 E			
12	o,xn,xs	406.4	22 90 E			
13	c,tn,xs	457.2	24 90 E			
14	c,tn,xs	990.6	38 90 E			
15	c,xn,hts	1600.2	18 90 E		30	
16	c,xn,ts	406.4	30 90 E			
17	c,tn,ts	177.8	34 90 E			
18	c,tn,hts	241.3	30 90 E		20	
19	c,htn,ts	177.8	27 90 E	20		
20	c,tan,ts	635	26 90 E	10		
21	c,tn,ts	1270	34 90 E			
22	c,tn,ts	965.2	32 90 E			
23	c,tn,ts	609.6	44 90 E			
24	c,tn,ts	431.8	20 90 E			
25	c,tan,ts	1676.4	32 90 E	25		
26	c,tn,ts	3225.8	35 90 E			
27	c,tn,ts	355.6	34 90 E			
28	c,tn,ts	838.2	38 90 E			
29	c,tn,ts	355.6	43 90 E			
30	c,tn,ts	139.7	42 90 E			
31	c,tn,hts	812.8	34 90 E		35	
32	c,tn,ts	1041.4	30 90 E			
33	c,tn,ts	241.3	32 90 E			
34	c,tn,ts	1016	31 90 E			
35	c,tan,ts	330.2	38 90 E	25		
36	c,tn,ts	685.8	31 90 E			

Connectivity Parameters		
Number of connection points		
	#	%
≥2	0	0
1	7	28
0	18	72
Type of termination		
	#	%
Tip	43	86
Hooks	4	8
Abrupt	3	6

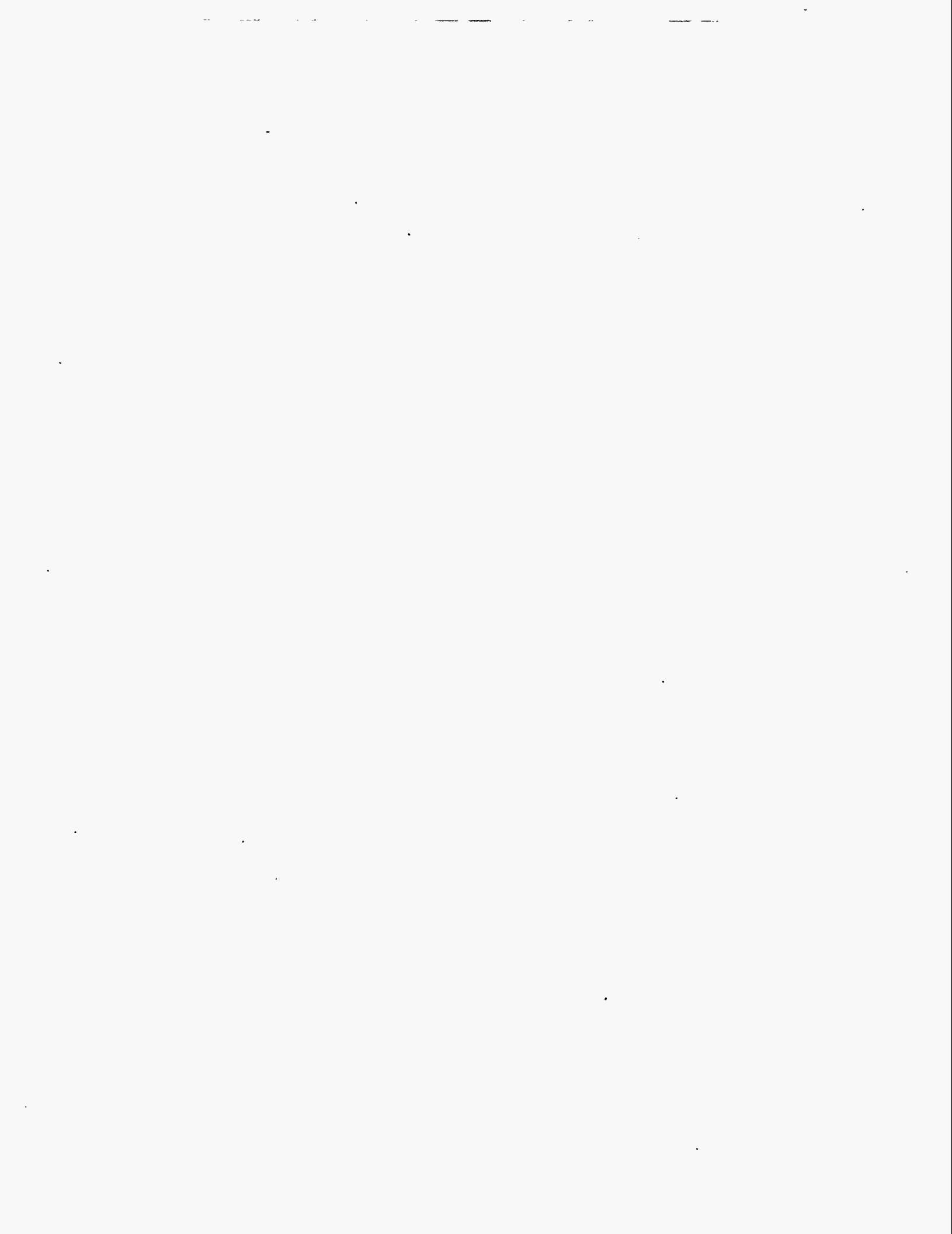
Cottonwood Flat Iron

Large area. All fractures
Swarm F

Frac. #	Type	Length (mm)	Orientation	Angle(°N)	Angle(°S)	Observations
1	c,xn,xs	1193.8	32 90 E			
2	c,tn,xs	330.2	40 90 E			
3	c,xn,ts	1270	52 90 E			
4	c,xn,ts	508	26 90 E			
5	c,tn,t	914.4	29 90 E			
6	c,xn,ts	558.8	34 90 E			
7	c,tan,ts	215.9	49 90 E	35		
8	c,tas,tn	279.4	39 90 E	35		
9	c,tn,ts	355.6	47 90 E			
10	c,tn,xs	533.4	36 90 E			
11	c,xn,xs	1320.8	30 90 E			
12	c,tn,xs	381	25 90 E			
13	c,tn,xs	330.2	28 90 E			
14	c,tn,xs	241.3	30 90 E			
15	c,ts,xn	1041.4	32 90 E			
16	c,xn,ts	152.4	35 90 E			
17	c,xn,ts	152.4	17 90 E			
18	c,tn,ts	355.6	36 90 E			
19	c,tn,ts	482.6	26 90 E			
20	c,htn,ts	355.6	34 90 E	35		
21	c,tn,ts	482.6	30 90 E			
22	c,tn,ts	355.6	36 90 E			
23	c,xn,hts	1498.6	38 90 E		35	
24	c,tn,ts	990.6	33 90 E			
25	c,xn,ts	1371.6	30 90 E			
26	c,tn,ts	1701.8	33 90 E			
27	c,tn,ts	533.4	30 90 E			
28	c,tn,ts	1219.2	32 90 E			
29	c,tn,ts	431.8	38 90 E			
30	c,tan,ts	330.2	36 90 E	40		
31	c,tn,ts	1066.8	37 90 E			
32	c,tn,ts	609.6	41 90 E			
33	c,tan,ts	203.2	37 90 E	25		
34	c,tn,ts	508	30 90 E			
35	c,tan,ts	533.4	42 90 E			
36	c,tn,ts	203.2	45 90 E			
37	c,tn,ts	203.2	48 90 E			
38	c,tn,hts	508	32 90 E		25	
39	c,htn,uts	292.1	26 90 E	25	45	
40	c,tn,tas	228.6	18 90 E		35	
41	c,tn,ts	1092.2	26 90 E			
42	c,tn,hts	1397	32 90 E		35	
43	c,tn,hts	635	30 90 E		30	
44	c,tn,ts	330.2	16 90 E			
45	c,tn,ts	215.9	15 90 E			
46	c,tn,ts	787.4	28 90 E			
47	c,tn,ts	1879.6	30 90 E			
48	c,tn,ts	914.4	18 90 E			
49	c,tn,ts	355.6	42 90 E			
50	c,tn,ts	304.8	30 90 E			
51	c,tn,ts	381	36 90 E			
52	c,tn,ts	1422.4	36 90 E			
53	c,tn,ts	965.2	36 90 E			

Frac. #	Type	Length (mm)	Orientation	Angle(°N)	Angle(°S)	Observations
54	c,tn,hts	990.6	24 90 E		45	
55	c,xn,ts	304.8	28 90 E			
56	c,tn,ts	406.4	24 90 E			
57	c,htrn,ts	1041.4	31 90 E	30		
58	c,tan,ts	279.4	42 90 E	30		
59	c,htrn,ts	304.8	25 90 E	35		
60	c,tn,ts	711.2	33 90 E			
61	c,tn,ts	228.6	12 90 E			
62	c,tn,hts	1422.4	28 90 E		40	
63	c,tn,hts	457.2	26 90 E		30	
64	c,tn,ts	457.2	36 90 E			
65	c,tn,ts	762	34 90 E			
66	c,tan,tas	101.6	34 90 E	30	30	
67	c,tn,ts	177.8	22 90 E			
68	c,tn,hts	2540	32 90 E		35	
69	c,tn,tas	203.2	35 90 E		10	
70	c,tn,hts	304.8	36 90 E		25	
71	c,htrn,ts	2844.8	40 90 E	30		
72	c,tan,tas	355.6	38 90 E	25	15	
73	c,tan,ts	165.1	34 90 E	20		
74	c,tn,tas	482.6	34 90 E		15	
75	c,tn,ts	2413	24 90 E			
76	c,tn,tas	152.4	32 90 E		30	
77	c,tn,ts	533.4	35 90 E			
78	c,tn,ts	838.2	35 90 E			
79	c,tn,ts	431.8	32 90 E			
80	c,tn,ts	1244.6	30 90 E			

Connectivity Parameters		
Number of connection points		
	#	%
≥2	3	5
1	24	37
0	38	58
Type of termination		
	#	%
Tip	100	76
Hooks	15	12
Abrupt	15	12



APPENDIX C. TEXTURAL AND PETROGRAPHIC ANALYSIS OF SAMPLES

This appendix contains tables that summarize textural characteristics and point-counted compositional data of the sandstones studied. The average grain size values are the average minimum and maximum diameters of framework components without measuring overgrowths from 100 grains in SEM-CL photomicrographs. Sorting and proportion of grain contacts were estimated visually using a petrographic microscope. Percentages in petrographic tables are based on 400 points per sample.

Petrographic summary of surface samples.
 (All the values are percentages of the total rock volume)

S A M P L E N U M B E R	Rock fragments					Authigenic minerals					P o r o s i t y				
	Q u a r t z	F e l d s p a r	C a r b o n a t e s	A r g i l l a c e o u s	S i l t s t o n e s	C h e r t	T o t a l R F s	A c c e s s o r i e s	M a t r i x	C l a y s		Q u a r t z	C a r b o n a t e s	O x i d e s	T o t a l A M s
WESTWATER PAVEMENT															
WS-1	45	8			2	25	27	Bio.	3	1	5		1	7	10
WS-2	55	2				15	15	Chlo., Zr.	3	2	8				10
WS-3	50	7		1		23	24	Musc.		1	5		1	7	12
WS-4	40	12				15	15	Glauc., Bio.	3		1		1	2	15
WS-5	40	12		3	5	15	23	Glauc.	3		5			2	7
WS-6	40	10		5	5	15	25	Bio.	3		3	2	2	7	15
WS-7	53	10	3	2	5	10	20				5	1		6	10
WS-8	55	10	2	3	5	10	20	Glauc.				4	1		5
WS-9	53	10	2		2	10	14	Glauc.	2	2	5		3	10	10
WS-10	54	7	2	2		15	19	Bio.	3	3	5		6	14	3
WS-12	48	7		5		10	15		10	10	5		2	17	10
WS-13	45	8		2	5	15	22	Glauc., Musc.	3	3	5		2	10	10
WS-14	45	13			2	18	20	Bio.	2	2	8			10	12
WS-15	40	7	2	2	3	25	32	Musc., Bio.	3	3	5		1	9	9
WS-16	40	3	5	3	2	20	30	Pir.	10	2	8		5	15	3
WS-17	40	7	2	5	5	10	22	Chlo.	10	10	8		5	23	6
COTTONWOOD PAVEMENT															
FI-11	49	3	5	5		10	20		5	5	5	10	5	25	5
FI-18	55	2	3			10	13	Zr., Bio., Glauc.	5	5	5	10		20	7
FI-19	40	4	6	2		15	23	Musc.	6	3	5	8	5	21	6
FI-20	40	5	10	3		8	21	Gar.	6	2	3	5	3	13	15
FI-21	60	2	10	3		8	21	Zr., Apat.	6	2	3	6	3	14	3
FI-22	50	2		6		12	18	Glauc., Gar.	5	5	8		2	15	10
FI-23	52	3	8	3		5	16	Musc.	6	2	3	10	3	18	5
FI-24	63	2	5			10	15	Chlo., Zr.	3	2	3		2	7	10
FI-25	52	2	3	5	2	3	13	Phos	5	5	5	8	2	20	8
FI-26	48	2	6	3		5	14		8	6	3	10	3	22	6
FI-27	40	3	8	2		10	20		10	5	2	10	2	19	8
FI-28	45	2		5		8	13	Zr.	10	5	5	10	5	25	5
FI-29	45	5		10		10	20	Zr., Bio.	5	2	3	12	3	20	5

EXPLANATION

RFs: Rock fragments
 AMs: Authigenic minerals

Accessories:
 Bio.: Biotite
 Chlo.: Chlorite
 Zr.: Zircon
 Musc.: Muscovite
 Glauc.: Glauconite
 Pir.: Piroxene
 Gar.: Garnet
 Phos.: Phosphate
 Apat.: Apatite
 Anf.: Anfibol

TEXTURAL PARAMETERS. SURFACE SAMPLES

Formation	Study area	Sample Number	Grain size (um)	Sorting	% of grain contacts		
					Sutured	Concavo convex	Point
CLIFFHOUSE	COTTONWOOD	FI-11	100-200	moderate		10	90
		FI-18	60-120	well		30	70
		FI-19	100-250	moderate		20	80
		FI-20	100-250	moderate		30	70
		FI-21	100-250	well	10	30	60
		FI-22	150-250	moderate	10	40	50
		FI-23	150-300	well		30	70
		FI-24	50-200	moderate		40	60
		FI-25	150-250	well		40	60
		FI-26	150-250	moderate		40	60
POINTLOKOUT	WESTWATER	WS-1	150-300	well		30	70
		WS-2	150-300	well		20	80
		WS-3	150-250	well		30	70
		WS-4	150-500	well		10	90
		WS-5	150-500	well			100
		WS-6	150-500	well			100
		WS-7	150-500	well		30	70
		WS-8	150-500	well		30	70
		WS-9	150-400	well		40	60
		WS-10	20-300	poor		10	90
WS-12	50-300	moderate		20	80		
WS-13	150-300	moderate		40	60		
WS-14	150-250	well		30	70		
WS-15	150-300	moderate		50	50		
WS-16	30-150	poor		10	90		
WS-17	200-500	well	10	40	50		

APPENDIX D. MICROFRACTURE DATA

This appendix contains the description of individual microfractures in petrographic and SEM-CL photomicrographs from outcrop and core samples. Microfractures were numbered consecutively and classified using Laubach's (1977) descriptive classification scheme. A degree of suitability for macrofracture properties prediction is also assigned to each microfracture. Microfracture length and microfracture aperture are indicated, as well as the microfracture strike. Comments complement or emphasize the characteristics of microfractures.

WELL: RIDDLE D LS 4A

SAMPLE: 2-3

DEPTH: 4939.2'

NOTCH AZIMUTH: 100

FRACTURE INVENTORY

FRACTURE NUMBER	DETECTION METHOD	Classification		PICTURE NUMBER	LENGTH (um)	APERTURE (um)	AZIMUTH (°)	OBSERVATIONS
		Laubach's (1997)	PREDICTIVE SUITABILITY					
1	PETR. MIC.	la+	4	11			0	FLUID INCLUSION PLANES
2	SEM-CL	lb	3	1	100	5	290	VARIABLE APERTURE. ENDS WITHIN GRAIN
3	SEM-CL	lb	3	1	70	5	63	AMBIGUOUS RELATION TO CEMENT. DIFFUSE WALLS
4	SEM-CL	la	2	3	125	5	300	ODD SHAPE. CUTS INHERITED FRACTURES
5	SEM-CL	lb	3	3	60	7	82	SMALL. TIP OF GRAIN. CURVED TRACE
6	SEM-CL	lb	3	3	90	3	24	VARIABLE APERTURE. ENDS WITHIN GRAIN
7	SEM-CL	la	2	5	100	5	295	STRAIGHT TRACE.
8	SEM-CL	la	2	5	90	5	315	STRAIGHT TRACE. CUTS INHERITED FRACTURES
9	SEM-CL	lb	3	5	45	2	0	AMBIGUOUS RELATION TO CEMENT
10	SEM-CL	la	2	7	60	5	0	TIP OF GRAIN
11	SEM-CL	lb	3	7	40	2	295	VARIABLE APERTURE. ENDS WITHIN GRAIN
12	SEM-CL	la	2	8	80	10	330	CUTS INHERITED FRACTURES. TWO APPARENT CEMENTATION EVENTS
13	SEM-CL	la	2	8	50	8	330	STRAIGHT TRACE. CUTS INHERITED FRACTURES.
14	SEM-CL	la	2	9	110	6	348	STRAIGHT TRACE. ODD SHAPE
15	SEM-CL	lb	3	9	60	5	70	CURVED TRACE. ODD SHAPE. TIP OF GRAIN
16	SEM-CL	la	2	10	80	8	68	STRAIGHT TRACE. DIFFUSE WALLS. TRANSCEMENT
17	SEM-CL	la	2	10	50	8	65	STRAIGHT TRACE. DIFFUSE WALLS. TRANSCEMENT

18	SEM-CL	lb	3	10	40	4	84	VARIABLE APERTURE. AMBIGUOUS RELATION TO CEMENT.
19	SEM-CL	la	2	12	65	7	50	STRAIGHT TRACE. TRANSCEMENT
20	SEM-CL	lb	3	13,14	70	3	76	VARIABLE APERTURE. ENDS AT GRAIN BORDER

WELL: RIDDLE D LS 4A

SAMPLE: 2-7

DEPTH: 4943.5'

NOTCH AZIMUTH: 355

FRACTURE INVENTORY

276

FRACTURE NUMBER	DETECTION METHOD	Classification		PICTURE NUMBER	LENGTH (um)	APERTURE (um)	AZIMUTH (°)	OBSERVATIONS
		Laubach's (1997)	PREDICTIVE SUITABILITY					
1	PETR. MIC.	la+	4	3,2			315	FLUID INCLUSION PLANES
2	PETR. MIC.	la+	4	1			335	FLUID INCLUSION PLANES
3	PETR. MIC.	la+	4	2			315	FLUID INCLUSION PLANES
4	PETR. MIC.	la+	4	3			315	FLUID INCLUSION PLANES
5	SEM-CL	lb	2	1	75	5	330	TRANSCEMENT. STRAIGHT TRACE
6	SEM-CL	lb	3	1	20	3	70	ENDS WITHIN GRAIN. AMBIGUOUS RELATION TO CEMENT
7	SEM-CL	la	3	3	120	3	310	AMBIGUOUS RELATION TO CEMENT
8	SEM-CL	lb	2	3	80	8	55	DIFFUSE WALLS. CUTS INHERITED SYSTEM
9	SEM-CL	lb	3	3	50	5	38	DIFFUSE WALLS. POSSIBLY REOPENED INHERITED SET
10	SEM-CL	lb	3	3	30	5	40	DIFFUSE WALLS. POSSIBLY REOPENED INHERITED SET
11	SEM-CL	lb	3	4	50	8	300	VARIABLE APERTURE. DIFFUSE WALLS
12	SEM-CL	lb	3	4	40	8	335	VARIABLE APERTURE. CURVED SHAPE
13	SEM-CL	la	2	4	60	8	70	TRANSCEMENT. ODD SHAPE
14	SEM-CL	la	2	5	80	3	330	APPARENTLY TWO FRACTURES CONNECTED EN ECHELON
15	SEM-CL	lb	3	5	60	2	70	ENDS WITHIN GRAIN. CURVED TRACE
16	SEM-CL	la	2	7	60	10	312	TWO CEMENTATION EVENTS
17	SEM-CL	la	2	8	110	25	288	LARGE APERTURE. PIECES OF GRAIN FILL THE FRACTURE
1	SEM-CL	lc	4	1	25	1	52	SMALL, INTRAGRANULAR
2	SEM-CL	llb	4	1	20	0.5	35	SMALL, INTRAGRANULAR
3	SEM-CL	llb	4	1	15	0.5	270	SMALL, INTRAGRANULAR
4	SEM-CL	llb	4	1	15	0.5	60	SMALL, INTRAGRANULAR

5	SEM-CL	lb	3	2	60	5	2	PROBABLY TRANSCEMENT
6	SEM-CL	lc	4	3	65	0.5	314	THIN, CURVED TRACE
7	SEM-CL	lc	3	3	85	0.5	35	SMALL, STRAIGHT, CUTS #8
8	SEM-CL	lc	4	3	75	0.5	45	CURVED TRACE, AVERAGE ORIENTATION
9	SEM-CL	lb	3	3	82	7	323	THICK, STRAIGHT, PROBABLY TRANSCEMENT
10	SEM-CL	lc	4	3	55	3	356	THIN, INTRAGRANULAR, CURVED
11	SEM-CL	lc	4	4	40	0.5	275	THIN, INTRAGRANULAR
12	SEM-CL	lc	4	4	40	0.5	316	THIN, INTRAGRANULAR
13	SEM-CL	lc	4	4	25	0.5	70	THIN, INTRAGRANULAR
14	SEM-CL	lc	4	4	90	0.5	270	THIN, INTRAGRANULAR
15	SEM-CL	lc	4	4	30	0.5	35	THIN, INTRAGRANULAR
16	SEM-CL	lb	3	5	60	2.5	292	FILLED WITH OVERGROWTH CEMENT
17	SEM-CL	lc	4	5	25	0.5	301	THIN, INTRAGRANULAR
18	SEM-CL	lc	4	5	38	0.5	68	THIN, INTRAGRANULAR
19	SEM-CL	lc	4	5	35	0.5	295	THIN, INTRAGRANULAR
20	SEM-CL	lc	4	5	40	0.5	43	THIN, INTRAGRANULAR
21	SEM-CL	lb	3	5	50	3	303	FILLED WITH OVERGROWTH CEMENT
22	SEM-CL	lb	3	5	40	2	300	NO CLEAR RELATIONSHIP WITH CEMENT
23	SEM-CL	lb	3	5	47	5	340	CURVED TRACE, FILLED WITH OVERGROWTH CEMENT
24	SEM-CL	lb	3	6	50	5	270	VARIABLE APERTURE, PROBABLY TRANSCEMENT
25	SEM-CL	lc	3	6	63	1.5	270	THIN, PARALLEL TO #24
26	SEM-CL	lb	3	7	75	7	60	STRAIGHT TRACE
27	SEM-CL	lc	3	7	50	1	82	DOUBTFUL
28	SEM-CL	lb	4	8	75	5	5	COULD BE AN ARTIFACT
29	SEM-CL	la+	2	8	175	5	0	COULD BE AN ARTIFACT
30	SEM-CL	lb	3	8	45	1	67	THIN AND CURVE
31	SEM-CL	lb	4	8	83	2.5	303	IRREGULAR SHAPE, UNCLEAR
32	SEM-CL	lc	3	9	47	1.5	9	THIN, FILLED WITH OVERGROWTH
33	SEM-CL	lb	3	9	40	1.5	64	THIN, FILLED WITH OVERGROWTH
34	SEM-CL	lb	4	9	110	8	0	BAD PHOTO. LUMINESCENT CARBONATES, PARALLEL TO
35	SEM-CL	lb	3	9	75	7	295	BAD PHOTO. LUMINESCENT CARBONATES.

36	SEM-CL	lc	4	9	65	0.5	60	THIN AND ODD SHAPE
37	SEM-CL	lc	4	9	30	0.5	315	THIN AND SIG SAG TRACE
38	SEM-CL	lc	4	9	75	0.5	275	THIN AND SIG SAG TRACE
39	SEM-CL	lc	4	9	30	0.5	15	THIN AND SIG SAG TRACE
40	SEM-CL	lb	3	10	17	10	345	THICK AND STRAIGHT
41	SEM-CL	lb	3	10	40	10	273	THICK AND STRAIGHT
42	SEM-CL	lc	4	10	60	1	340	THIN, CURVED
43	SEM-CL	lc	4	10	50	5	320	DOUBTFUL. BAD PICTURE. (DARK)
44	SEM-CL	lc	4	10	25	5	275	DOUBTFUL. BAD PICTURE. (DARK)
45	SEM-CL	lb	3	13	43	1	345	VARIABLE APERTURE, CURVED.
46	SEM-CL	lc	4	13	25	0.5	355	THIN, INTRAGRAIN
47	SEM-CL	lc	4	13	35	0.5	20	THIN, INTRAGRAIN
48	SEM-CL	llb	4	13	65	4	87	POSSIBLY CRUSHED GRAIN
49	SEM-CL	llb	4	13	20	5	60	POSSIBLY CRUSHED GRAIN
50	SEM-CL	llb	4	13	75	7	343	POSSIBLY CRUSHED GRAIN
51	SEM-CL	lb	3	14	65	4	285	THICK, BORDER OF GRAIN, CURVED
52	SEM-CL	lc	3	14	10	0.5	320	THIN PARALLEL TO lb SET
53	SEM-CL	lc	3	14	15	0.5	320	THIN PARALLEL TO lb SET
54	SEM-CL	lb	3	14	70	5	353	THICK, VARIABLE APERTURE, CURVED
55	SEM-CL	lc	3	14	50	0.5	335	THIN PARALLEL TO lb SET
56	SEM-CL	lb	2	15	80	10	20	THICK, STRAIGHT, PROBABLY CUTS CEMENT

WELL: RIDDLE D LS 4A

SAMPLE: 3-14

DEPTH: 5006.3

NOTCH AZIMUTH: 100

FRACTURE INVENTORY

FRACTURE NUMBER	DETECTION METHOD	Classification		PICTURE NUMBER	LENGTH (um)	APERTURE (um)	AZIMUTH (°)	OBSERVATIONS
		Laubach's (1997)	PREDICTIVE SUITABILITY					
1	PETR. MIC	la+	4	0,4			335	FLUID INCLUSIONS PLANE
2	PETR. MIC	la+	4	1			350	FLUID INCLUSIONS PLANE
3	SEM-CL	lc	4	1	50	1	35	POSSIBLY INHERITED. AMBIGUOUS RELATION TO CEMENT
4	SEM-CL	lb	3	4	75	7	85	DIFFUSE WALLS . CUTS INHERITED SYSTEM.
5	SEM-CL	lb	3	4	90	3	0	DIFFUSE WALLS . CUTS INHERITED SYSTEM. CURVED TRACE
6	SEM-CL	la	2	6	70	2	330	POSSIBLE VERTICAL COMPONENT OF DISPLACEMENT. TWO CEMENTATION EVENTS
7	SEM-CL	lb	3	7	70	2	290	POSSIBLY INHERITED. AMBIGUOUS RELATION TO CEMENT
8	SEM-CL	lc	4	8	145	2	77	POSSIBLY INHERITED. AMBIGUOUS RELATION TO CEMENT
9	SEM-CL	lc	4	8	150	3	65	POSSIBLY INHERITED. AMBIGUOUS RELATION TO CEMENT
10	SEM-CL	lc	4	8	60	3	80	POSSIBLY INHERITED. AMBIGUOUS RELATION TO CEMENT
11	SEM-CL	lc	4	9	40	2	310	POSSIBLY INHERITED. AMBIGUOUS RELATION TO CEMENT
12	SEM-CL	lc	4	9	50	2	330	POSSIBLY INHERITED. AMBIGUOUS RELATION TO CEMENT

13	SEM-CL	lc	4	9	53	2	293	POSSIBLY INHERITED. AMBIGUOUS RELATION TO CEMENT
14	SEM-CL	la	2	9	40	6	0	DIFFUSE WALLS. DISSOLUTION EFFECTS. PIECES OF GRAIN WITHIN FRACTURE
15	SEM-CL	lb	3	11	60	2	302	AMBIGUOUS RELATION TO CEMENT
16	SEM-CL	lb	3	11	40	2	315	ENDS WITHIN GRAIN
17	SEM-CL	lb	3	11	30	2	0	ENDS WITHIN GRAIN
18	SEM-CL	lb	3	11	50	2	7	INTRAGRANULAR. POSSIBLY INHERITED
19	SEM-CL	la	2	12	70	7	56	TWO CEMENTATION EVENTS. STRAIGHT TRACE. CUTS INHERITED SYSTEM
20	SEM-CL	la	2	13	60	3	280	STRAIGHT TRACE
21	SEM-CL	lb	3	15	90	3	305	STRAIGHT TRACE. CUTS INHERITED SYSTEM
22	SEM-CL	la	2	18	80	2	60	DIFFUSE WALLS
23	SEM-CL	la	2	19	90	10	335	STRAIGHT TRACE. TWO CEMENTATION EVENTS

WELL: RIDDLE D LS 4A

SAMPLE: 3-17

DEPTH: 5009.54

NOTCH AZIMUTH: 0

FRACTURE INVENTORY

FRACTURE NUMBER	DETECTION METHOD	Classification		PICTURE NUMBER	LENGTH (um)	APERTURE (um)	AZIMUTH (°)	OBSERVATIONS
		Laubach's (1997)	PREDICTIVE SUITABILITY					
1	SEM-CL	la	2	1	45	3	65	STRAIGHT TRACE
2	SEM-CL	la	2	1	50	5	342	VARIABLE APERTURE. PROBABLY TWO CEMENTATION EVENTS
3	SEM-CL	la	2	1	20	3	75	PARALLEL TO FRACTURE #1 BUT SMALLER
4	SEM-CL	lb	3	2	90	3	55	BRANCH IN TWO FRACTURES. IMPRECISE RELATIONSHIP WITH CEMENT
5	SEM-CL	lb	3	2	50	5	37	MAYBE COMPACTION RELATED. VARIABLE APERTURE
6	SEM-CL	lb	3	3	80	3	12	PARALLEL SET CUTS INHERITED FRACTURES
7	SEM-CL	lb	3	3	40	2	25	PARALLEL SET CUTS INHERITED FRACTURES. CURVED TRACE TOUGH
8	SEM-CL	lb	3	4	30	5	295	UNCLEAR RELATIONSHIP WITH CEMENT. TIP OF GRAIN
9	SEM-CL	la (OPEN)	4	5	45	2	60	SMALL, OPEN FRACTURE CUTS CEMENT AND GRAIN
10	SEM-CL	la (OPEN)	4	5	50	2	75	EN ECHELON CONNECTED OPEN FRACTURES. CUTS GRAIN AND CEMENT
11	SEM-CL	lb (OPEN)	4	5	50	2	0	INTRAGRAIN. SMALL. CURVED TRACE
12	SEM-CL	lb	3	5	60	2	310	AMBIGUOUS RELATION TO CEMENT. PARALLEL SET

13	SEM-CL	lb	3	5	55	2	310	AMBIGUOUS RELATION TO CEMENT. PARALLEL SET
14	SEM-CL	la	2	6	75	5	350	STRAIGHT TRACE. CLEARLY CUTS CEMENT AND INHERITED FRACTURES
15	SEM-CL	la	2	6	30	2	345	SEGMENT #1 OF FRACTURE PARALLEL TO #14
16	SEM-CL	la	2	6	50	2	25	SEGMENT #2 OF FRACTURE PARALLEL TO #14
17	SEM-CL	la	2	6	80	2	15	INTEGRATION OF FRACTURES #15 AND #16.
18	SEM-CL	lb	3	6	110	4	23	AMBIGUOUS RELATION TO CEMENT. DIFFUSE WALLS
19	SEM-CL	lb (OPEN)	4	6	150	3	87	PARTIALLY FILLED WITH HIGHLY LUMINESCENT MATERIAL (CALCITE ?)
20	SEM-CL	lb (OPEN)	4	6	50	2	90	SMALL INTRAGRANULAR
21	SEM-CL	lb (OPEN)	4	6	30	2	80	SMALL INTRAGRANULAR
22	SEM-CL	la	2	7	90	3	45	VARIABLE APERTURE. POSSIBLY TWO CEMENT EVENTS
23	SEM-CL	la	2	8	100	20	320	STRAIGHT TRACE. LARGE APERTURE. MULTIPLE FRACTURE EVENTS
24	SEM-CL	la	2	9	60	5	85	TRANSCEMENT. PROBABLY TWO CEMENTATION EVENTS. STRAIGHT TRACE
25	SEM-CL	la	2	9	60	4	320	PROBABLY TWO CEMENTATION
26	SEM-CL	la	2	9	55	3	310	STRAIGHT TRACE. PARALLEL TO #25
27	SEM-CL	lb	3	9	25	2	18	BIFURCATION OF FRACTURE #26
28	SEM-CL	la	2	7			45	VARIABLE APERTURE. POSSIBLY TWO CEMENTATION EVENTS

WELL: RIDDLE D LS 4A

SAMPLE: 3-18

DEPTH: 5011.4

NOTCH AZIMUTH: 350

FRACTURE INVENTORY

FRACTURE NUMBER	DETECTION METHOD	Classification		PICTURE NUMBER	LENGTH (um)	APERTURE (um)	AZIMUTH (°)	OBSERVATIONS
		Laubach's (1997)	PREDICTIVE SUITABILITY					
1	PETR. MIC.	la+	4	4			330	FLUID INCLUSION PLANES
2	PETR. MIC.	la+	4	7			330	FLUID INCLUSION PLANES
3	PETR. MIC.	la+	4	8			325	FLUID INCLUSION PLANES
4	PETR. MIC.	la+	4	8			45	FLUID INCLUSION PLANES
5	SEM-CL	la+ (OPEN)	3	1	250	5	296	SEGMENT #1 OF OPEN FRACTURE (INDUCED ?)
6	SEM-CL	la+ (OPEN)	3	1,2,3,4	1000	5	264	SEGMENT #2 OF OPEN FRACTURE (INDUCED ?)
7	SEM-CL	lc (OPEN)	4	3	115	2	330	BIFURCATION OF PREVIOUS FRACTURE AROUND GRAIN
8	SEM-CL	lc (OPEN)	4	3,4	200	2	60	CONTINUATION OF BIFURCATION AROUND GRAIN
9	SEM-CL	la+ (OPEN)	3	1,2,3,4	1250	5	276	INTEGRATION OF SEGMENTS #1 AND #2
10	SEM-CL	la+	1	6	75	1	30	TRANSGRANULAR. COULD BE INHERITED RE-OPEN
11	SEM-CL	la	2	6	75	15	300	TRANSCEMENT. TWO CEMENTATION EVENTS. SPLIT GRAIN
12	SEM-CL	lb	3	7	75	2	320	BRANCH OF A MORE CLEARLY TRANSCEMENT FRACTURE
13	SEM-CL	lb	4	7	100	3	280	REOPENING OF INHERITED FRACTURE
14	SEM-CL	la (OPEN)	4	8	400	5	283	PROBABLY INDUCED. FOLLOWS GRAIN BORDERS AND CUT CEMENT
15	SEM-CL	la	2	8	75	1	23	CUTS CEMENT. SMALL. VERTICAL COMPONENT OF MOVEMENT

16	SEM-CL	lb	3	8	110	2	272	STOPS AT BORDER OF GRAIN APPARENTLY RELATED TO FRACTURE #15
17	SEM-CL	la (OPEN)	4	9	400	6	275	PROBABLY INDUCED. FOLLOWS GRAIN BORDERS AND CUTS CEMENT
18	SEM-CL	la (OPEN)	4	9	160	5	50	PROBABLY INDUCED. FOLLOWS GRAIN BORDERS AND CUT CEMENT
19	SEM-CL	la+	2	10	200	2	352	DOUBTFUL. DIFFERENT CHARACTER IN DIFFERENT GRAINS.
20	SEM-CL	la	2	11	100	5	278	TRANSCEMENT. DIFFUSE WALLS. CROSSES INHERITED SYSTEM
21	SEM-CL	lb	3	11	40	2	16	PROBABLY TRANSCEMENT. SIMILAR TO #20 BUT STOPS AT GRAIN BORDER.
22	SEM-CL	lb	3	11	110	2	335	PROBABLY TRANSCEMENT. SIMILAR TO #20 BUT STOPS AT GRAIN BORDER.
23	SEM-CL	llc	4	12	100	10	295	PROBABLY CRUSHING RELATED. ODD SHAPES. VARIABLE APERTURE.
24	SEM-CL	llc	4	12	60	10	300	PROBABLY CRUSHING RELATED. ODD SHAPES. VARIABLE APERTURE.
25	SEM-CL	la	2	13,14,15	150	10	350	TRANSCEMENT. TWO CEMENTATION EVENTS. SPLITS GRAIN
26	SEM-CL	la	2	16,17	100	10	330	TRANSCEMENT. VARIABLE APERTURE POSSIBLY PRODUCED BY COMPACTION
27	SEM-CL	lb	3	17	50	1	12	PROBABLY TRANSCEMENT. SIMILAR TO #26 BUT STOPS AT GRAIN BORDER.
28	SEM-CL	lb	3	17	120	1	25	PROBABLY TRANSCEMENT. SIMILAR TO #26 BUT STOPS AT GRAIN BORDER.
29	SEM-CL	lb	3	17	110	1	27	PROBABLY TRANSCEMENT. SIMILAR TO #26 BUT STOPS AT GRAIN BORDER.

WELL: RIDDLE D LS 4A

SAMPLE: 3-20

DEPTH: 5035.2

NOTCH AZIMUTH: 350

FRACTURE INVENTORY

FRACTURE NUMBER	DETECTION METHOD	Classification		PICTURE NUMBER	LENGTH (μm)	APERTURE (μm)	AZIMUTH ($^{\circ}$)	OBSERVATIONS
		Laubach's (1997)	PREDICTIVE SUITABILITY					
1	SEM-CL	la	2	1	125	10	308	STRAIGHT TRACE. CUTS INHERITED FRACTURES
2	SEM-CL	la	2	2	75	8	15	STRAIGHT TRACE.
3	SEM-CL	la	2	2	60	8	282	PARALLEL SET. CUTS INHERITED FRACTURES
4	SEM-CL	la	2	2	90	10	300	PARALLEL SET. CUTS INHERITED FRACTURES
5	SEM-CL	lb	3	2	85	3	49	PARALLEL SET. AMBIGUOUS RELATION TO CEMENT
6	SEM-CL	lb	3	3	50	3	309	PARALLEL SET. AMBIGUOUS RELATION TO CEMENT
7	SEM-CL	la	2	3	140	15	260	STRAIGHT TRACE.
8	SEM-CL	la	2	3	25	8	350	STRAIGHT TRACE.
9	SEM-CL	la	2	4	160	18	340	PROBABLY TWO EVENTS OF CEMENTATION
10	SEM-CL	la	2	5	105	8	35	STRAIGHT TRACE. CUTS INHERITED SYSTEM
11	SEM-CL	la	2	5	80	5	35	CUTS INHERITED SYSTEM. TIP OF GRAIN. PARALLEL SET
12	SEM-CL	la+	1	6	145	10	273	APPARENT TWO CEMENTATION EVENTS. CUTS TWO GRAINS IN CONTACT

13	SEM-CL	la	2	7	100	10	340	CUTS INHERITED SYSTEM. PIECES OF GRAIN FILLING THE FRACTURE
14	SEM-CL	lb	3	7	80	2	0	PARALLEL SYSTEM. CUTS INHERITED ONE.
15	SEM-CL	lb	3	7	80	2	0	PARALLEL SYSTEM. CUTS INHERITED ONE. ENDS WITHIN GRAIN
16	SEM-CL	lb	3	7	100	2	0	PARALLEL SYSTEM. CUTS INHERITED ONE. ENDS WITHIN GRAIN
17	SEM-CL	lb	3	7	75	2	350	PARALLEL SYSTEM. CUTS INHERITED ONE. ENDS WITHIN GRAIN
18	SEM-CL	lb	3	7	60	2	350	PARALLEL SYSTEM. CUTS INHERITED ONE. ENDS WITHIN GRAIN
19	SEM-CL	lb	3	7	55	2	8	TIP OF GRAIN PARALLEL SET
20	SEM-CL	la	2	8	110	20	315	ODD SHAPE. VARIABLE APERTURE. DIFFUSE WALLS
21	SEM-CL	lb	3	8	90	3	17	ENDS WITHIN GRAIN
22	SEM-CL	la	2	9	290	10	310	STRAIGHT TRACE. CUTS INHERITED SYSTEM
23	SEM-CL	la	2	9	120	8	310	STRAIGHT TRACE. CUTS INHERITED SYSTEM
24	SEM-CL	la	2	9	80	8	46	STRAIGHT TRACE. CUTS INHERITED SYSTEM

WELL: RIDDLE D LS 4A

SAMPLE: 3-3

DEPTH: 4995.15

NOTCH AZIMUTH: 5

FRACTURE INVENTORY

FRACTURE NUMBER	DETECTION METHOD	Classification		PICTURE NUMBER	LENGTH (um)	APERTURE (um)	AZIMUTH (°)	OBSERVATIONS
		Laubach's (1997)	PREDICTIVE SUITABILITY					
1	PETR. MIC.	la+	4	1			60	FLUID INCLUSION PLANES
2	SEM-CL	la	2	1	100	15	344	CUTS INHERITED SET OF FRACTURES
3	SEM-CL	la	2	1	115	3	350	CUTS INHERITED SET OF FRACTURES
4	SEM-CL	la	2	1	20	3	60	PIECES OF GRAIN FILL THE FRACTURE
5	SEM-CL	la+	1	2,3,4	200	5	285	TRANSGRANULAR-TRANSCEMENT. PARTIALLY DISSOLVED IN SOME PLACES
6	SEM-CL	la	2	3	50	8	60	REOPENED. VARIABLE APERTURE. PIECES OF GRAIN FILL THE FRACTURE
7	SEM-CL	lb	3	3	60	4	330	VARIABLE APERTURE. ETCHED. SLIGHTLY CURVED.
8	SEM-CL	la	2	5	60	12	300	STRAIGHT TRACE. LARGE APERTURE.
9	SEM-CL	la	2	5	90	2	335	STRAIGHT TRACE. DISPLACES FRACTURE #8
10	SEM-CL	la	2	5	40	1	300	PARALLEL TO #8. CUTS INHERITED FRACTURES
11	SEM-CL	lb	3	6	50	5	300	VARIABLE APERTURE. ENDS INSIDE THE GRAIN
12	SEM-CL	la	2	6	80	8	280	ODD SHAPE. PIECES OF GRAIN FILL THE FRACTURE
13	SEM-CL	lb	3	6	70	3	330	AFFECTS TIP OF GRAIN. STRAIGHT TRACE

14	SEM-CL	lb	3	6	35	3	85	AFFECTS TIP OF GRAIN. STRAIGHT TRACE
15	SEM-CL	lb	3	7	55	8	45	CURVED TRACE. TIP OF GRAIN
16	SEM-CL	la	2	7	100	3	20	STRAIGHT TRACE. TRANSCEMENT
17	SEM-CL	la	2	8,10	90	2	290	STRAIGHT TRACE. CUTS INHERITED SET
18	SEM-CL	la	2	8,10	100	8	335	VARIABLE APERTURE. CLEAR TWO EVENTS OF CEMENTATION.
19	SEM-CL	lb	3	8,10	15	3	290	VARIABLE APERTURE. ENDS INSIDE THE GRAIN
20	SEM-CL	lb	3	8,10	25	3	290	VARIABLE APERTURE. ENDS INSIDE THE GRAIN
21	SEM-CL	lb	3	9,10	75	2	300	VARIABLE APERTURE. ENDS INSIDE THE GRAIN
22	SEM-CL	lb	3	9,10	80	2	293	VARIABLE APERTURE. ENDS INSIDE THE GRAIN
23	SEM-CL	la	2	12	35	1	300	SMALL. TIP OF GRAIN.
24	SEM-CL	la	2	12	55	5	280	SMALL. TIP OF GRAIN. PARTIALLY OPENED
25	SEM-CL	la	2	12	40	3	300	ODD SHAPE. PARALLEL TO #23.
26	SEM-CL	la	2	12	110	6	70	STRAIGHT FACES. TRANSCEMENT
27	SEM-CL	la	2	13,14	90	5	300	TWO CEMENTATION EVENTS.

WELL: RIDDLE D LS 4A

SAMPLE: 3-8

DEPTH: 5000.46

NOTCH AZIMUTH: 100

FRACTURE INVENTORY

FRACTURE NUMBER	DETECTION METHOD	Classification		PICTURE NUMBER	LENGTH (um)	APERTURE (um)	AZIMUTH (°)	OBSERVATIONS
		Laubach's (1997)	PREDICTIVE SUITABILITY					
1	PETR. MIC.	la+	4	21			20	FLUID INCLUSION PLANES
2	PETR. MIC.	la+	4	23			330	FLUID INCLUSION PLANES
3	SEM-CL	la+ (OPEN)	3	1,2,3	2100	15	348	OPEN FRACTURE POSSIBLY INDUCED. EN ECHELON PATTERN
4	SEM-CL	la+ (OPEN)	3	2,3,4	1700	10	0	OPEN FRACTURE POSSIBLY INDUCED
5	SEM-CL	la+ (OPEN)	3	3,4,5,6	3600	20	30	OPEN FRACTURE POSSIBLY INDUCED
6	SEM-CL	la+ (OPEN)	3	7,8	1900	10	30	OPEN FRACTURE POSSIBLY INDUCED
7	SEM-CL	la+ (OPEN)	3	8,9	900	15	335	OPEN FRACTURE POSSIBLY INDUCED. EN ECHELON PATTERN
8	SEM-CL	la+ (OPEN)	3	9,10	850	10	22	OPEN FRACTURE POSSIBLY INDUCED. EN ECHELON PATTERN
9	SEM-CL	la+ (OPEN)	3	9,10	800	15	30	OPEN FRACTURE POSSIBLY INDUCED. EN ECHELON PATTERN
10	SEM-CL	lb (OPEN)	3	13	180	5	0	OPEN FRACTURE. INTRAGRANULAR
11	SEM-CL	lb (OPEN)	3	13	110	5	90	OPEN FRACTURE. INTRAGRANULAR
12	SEM-CL	lb (OPEN)	3	13	100	3	90	OPEN FRACTURE. INTRAGRANULAR
13	SEM-CL	la (OPEN)	3	14,15	200	5	40	OPEN FRACTURE. TRANSCEMENT
14	SEM-CL	la (OPEN)	3	14,15	180	5	21	OPEN FRACTURE. TRANSCEMENT
15	SEM-CL	la+ (OPEN)	3	14,15	120	5	20	OPEN FRACTURE. TRANSGRANULAR
16	SEM-CL	la (OPEN)	3	17	125	5	0	OPEN. ODD SHAPE. MAINLY INTRAGRANULAR
17	SEM-CL	llc	5	18	120	2	348	CRUSHING RELATED. PRESSURE SOLUTION ZONE
18	SEM-CL	llc	5	18	100	2	0	CRUSHING RELATED. PRESSURE SOLUTION ZONE
19	SEM-CL	llc	5	18	100	2	346	CRUSHING RELATED. PRESSURE SOLUTION ZONE
20	SEM-CL	lb	3	18	40	5	90	VARIABLE APERTURE. TIP OF GRAIN

21	SEM-CL	la	2	22	220	5	0	PARALLEL SET. PIECES OF GRAIN WITHIN FRACTURE
22	SEM-CL	la	2	22	220	4	0	PARALLEL SET. PIECES OF GRAIN WITHIN FRACTURE
23	SEM-CL	la	2	22	60	3	90	TIP OF GRAIN. ORTHOGONAL TO PREVIOUS SET
24	SEM-CL	la	2	22	70	15	55	LARGE APERTURE. SMALL SIZE
25	SEM-CL	lb	3	22	30	2	60	SMALL. TIP OF GRAIN. AMBIGUOUS RELATION TO CEMENT

WELL: RIDDLE D LS 4A

SAMPLE: 4-7

DEPTH: 5022.45

NOTCH AZIMUTH: 355

FRACTURE INVENTORY

FRACTURE NUMBER	DETECTION METHOD	Classification		PICTURE NUMBER	LENGTH (um)	APERTURE (um)	AZIMUTH (°)	OBSERVATIONS
		Laubach's (1997)	PREDICTIVE SUITABILITY					
1	SEM-CL	la	2	1	130	8	350	STRAIGHT TRACE. CUTS INHERITED FRACTURES
2	SEM-CL	lb	3	1	90	5	295	VARIABLE APERTURE. ENDS WITHIN GRAIN
3	SEM-CL	lb	3	1	60	5	290	VARIABLE APERTURE. ENDS WITHIN GRAIN
4	SEM-CL	la	2	2	125	20	50	TWO CEMENTATION EVENTS. CUTS INHERITED SYSTEM
5	SEM-CL	la	2	2	50	5	72	TIP OF THE GRAIN. SMALL
6	SEM-CL	la	2	3	140	10	310	STRAIGHT TRACE. PROBABLY TWO CEMENTATION EVENTS
7	SEM-CL	lb	3	3	50	5	308	VARIABLE APERTURE
8	SEM-CL	lb	3	3	90	5	300	EN ECHELON. ODD SHAPE. PROBABLY COMPACTION RELATED
9	SEM-CL	la	2	4	150	10	85	PROBABLY TWO CEMENTATION EVENTS. CUTS INHERITED SYSTEM
10	SEM-CL	la	2	4	140	15	70	PROBABLY TWO CEMENTATION EVENTS. CUTS INHERITED SYSTEM
11	SEM-CL	lb	3	4	100	25	18	CUTS FRACTURES #9 AND #10
12	SEM-CL	lb	3	5	55	5	335	VARIABLE APERTURE. ENDS AT GRAIN BORDER
13	SEM-CL	lb	3	5	70	10	70	VARIABLE APERTURE. POSSIBLY COMPACTION RELATED

14	SEM-CL	lb	3	5	40	8	40	PIECES OF GRAIN WITHIN FRACTURE. VARIABLE APERTURE
15	SEM-CL	la	2	6	175	10	345	TWO EVENTS OF CEMENTATION
16	SEM-CL	la	2	6	110	8	340	DISSOLUTION PROCESS AFFECTING WALLS
17	SEM-CL	la	2	7	70	5	35	STRAIGHT TRACE
18	SEM-CL	lb	3	7	70	1	35	AFFECTED BY DISSOLUTION. INHERITED?
19	SEM-CL	la+	1	8	100	5	63	STRAIGHT TRACE. CUTS TWO GRAINS AND CEMENT
20	SEM-CL	lb	3	8	70	3	290	CURVED TRACE. POSSIBLY INHERITED. ENDS WITHIN GRAIN
21	SEM-CL	la	2	8	50	3	47	SMALL, TIP OF GRAIN
22	SEM-CL	lb	3	8	60	3	337	VARIABLE APERTURE. POSSIBLY COMPACTION RELATED
23	SEM-CL	lb	3	8	115	2	15	IT IS CUT BY FRACTURE #19. DIFFUSE WALLS
24	SEM-CL	la	2	9	150	5	30	POSSIBLY TWO CEMENTATION EVENTS. CUTS INHERITED SYSTEM.

WELL: RIDDLE D LS 4A

SAMPLE: 4-10

DEPTH: 5025.1'

NOTCH AZIMUTH: 90

FRACTURE INVENTORY

FRACTURE NUMBER	DETECTION METHOD	Classification		PICTURE NUMBER	LENGTH (um)	APERTURE (um)	AZIMUTH (°)	OBSERVATIONS
		Laubach's (1997)	PREDICTIVE SUITABILITY					
1	SEM-CL	la	2	1	160	10	40 90 E	STRAIGHT TRACE. CUTS INHERITED
2	SEM-CL	lb	3	1	100	3	30 90 E	VARIABLE APERTURE. ENDS WITHIN
3	SEM-CL	lb	3	2	200	12	0 90 E	VARIABLE APERTURE. SIG-SAG
4	SEM-CL	lb	3	2	170	3	0 90 E	VARIABLE APERTURE. ENDS WITHIN
5	SEM-CL	la	2	2	130	5	70 90 E	STRAIGHT TRACE. AFFECTED BY DISSOLUTION.
6	SEM-CL	lb	3	3	125	5	30 90 E	VARIABLE APERTURE. ENDS AT GRAIN BORDER
7	SEM-CL	lb	3	3	60	3	10 90 E	ENDS WITHIN GRAIN. VARIABLE APERTURE
8	SEM-CL	lb	3	4	65	8	47 90 E	VARIABLE APERTURE. ENDS AT GRAIN BORDER
9	SEM-CL	lb	3	5	150	3	330 90 E	AFFECTED BY DISSOLUTION. PROBABLY INHERITED
10	SEM-CL	lb	3	5	160	8	17 90 E	VARIABLE APERTURE. ENDS AT GRAIN BORDER
11	SEM-CL	la	2	6	100	20	18 90 E	STRAIGHT TRACE. POSSIBLY TWO CEMENTATION EVENTS
12	SEM-CL	lc	4	7	25	8	5 90 E	CRUSHING RELATED
13	SEM-CL	lc	4	7	25	8	80 90 E	CRUSHING RELATED
14	SEM-CL	lc	4	7	40	8	63 90 E	CRUSHING RELATED
15	SEM-CL	lc	4	7	55	5	82 90 E	CRUSHING RELATED
16	SEM-CL	lc	4	7	100	3	13 90 E	CRUSHING RELATED
17	SEM-CL	lc	4	7	100	5	30 90 E	CRUSHING RELATED. VARIABLE APERTURE
18	SEM-CL	lb	3	8	40	3	340 90 E	ODD SHAPE. SIG SAG TRACE

19	SEM-CL	lb	3	8	50	3	0 90 E	DIFFUSE WALLS. AMBIGUOUS RELATION TO CEMENT
20	SEM-CL	lc	4	9	180	8	225 90 E	CURVED TRACE. CRUSHING RELATED
21	SEM-CL	lb	3	9	80	5	57 90 E	VARIABLE APERTURE. ENDS WITHIN GRAIN
22	SEM-CL	la	2	10	70	5	15 90 E	AFFECTED BY DISSOLUTION. CEMENTED BY LATER EVENT
23	SEM-CL	la	2	11	100	5	57 90 E	STRAIGHT TRACE
24	SEM-CL	la	2	11	60	3	68 90 E	STRAIGHT TRACE
25	SEM-CL	la	2	12	130	5	340 90 E	ODD SHAPE. STRAIGHT WALL SEGMENTS
26	SEM-CL	la	2	12	100	10	340 90 E	DIFFUSE WALLS
27	SEM-CL	lb	3	12	65	3	340 90 E	VARIABLE APERTURE. ENDS WITHIN GRAIN
28	SEM-CL	la	2	13	110	10	350 90 E	CUTS INHERITED SYSTEM
29	SEM-CL	la	2	13	80	3	315 90 E	ENDS AGAINST OTHER FRACTURE.

WELL: RIDDLE D LS 4A

SAMPLE: 4-12

DEPTH: 5027.1'

NOTCH AZIMUTH: 80

FRACTURE INVENTORY

295

FRACTURE NUMBER	DETECTION METHOD	Classification		PICTURE NUMBER	LENGTH (um)	APERTURE (um)	AZIMUTH (°)	OBSERVATIONS
		Laubach's (1997)	PREDICTIVE SUITABILITY					
1	PETR. MIC.	la+	4				315 90 E	FLUID INCLUSION PLANE
2	SEM-CL	la	2	1	150	8	335 90 E	TWO EVENTS OF CEMENTATION. COMPACTION EFFECTS
3	SEM-CL	la	2	1	60	10	32 90 E	TWO EVENTS OF CEMENTATION. STRAIGHT TRACE
4	SEM-CL	llc	5	2	60	12	0 90 E	CRUSHING RELATED
5	SEM-CL	llc	5	2	60	2	0 90 E	CRUSHING RELATED
6	SEM-CL	llc	5	2	110	8	275 90 E	CRUSHING RELATED
7	SEM-CL	llc	5	2	120	2	310 90 E	CRUSHING RELATED
8	SEM-CL	llc	5	2	80	2	298 90 E	CRUSHING RELATED
9	SEM-CL	la	2	3	110	10	60 90 E	PIECES OF GRAIN IN FRACTURE FILL. MULTIPLE FRACTURE EVENTS
10	SEM-CL	lb	3	3	100	8	30 90 E	VARIABLE APERTURE. POSSIBLY AFFECTED BY COMPACTION
11	SEM-CL	la+	1	4,5	300	5	276 90 E	TRANSGRANULAR. DIFFUSE WALLS.
12	SEM-CL	la	2	4	115	5	35 90 E	TRANSCEMENT
13	SEM-CL	la	2	4	60	3	335 90 E	PARALLEL SET TO #13
14	SEM-CL	la	2	4	25	3	333 90 E	PARALLEL SET TO #13
15	SEM-CL	la	2	4	110	8	340 90 E	TRANSCEMENT. PIECES OF GRAIN FILL FRACTURE.
16	SEM-CL	la	2	6	80	3	290 90 E	TRANSCEMENT. STRAIGHT TRACE
17	SEM-CL	la	2	6	85	3	295 90 E	TRANSCEMENT. STRAIGHT TRACE

18	SEM-CL	lb	3	6	80	3	65 90 E	TRANSCEMENT. AVERAGE ORIENTATION
19	SEM-CL	lb	3	6	85	2	317 90 E	SAME SET AS FRACTURES #18 AND #19. DOUBTFUL
20	SEM-CL	la	2	6	100	10	340 90 E	POSSIBLY REOPENED DURING COMPACTION
21	SEM-CL	la	2	7	180	10	35 90 E	PARTIALLY OPENED
22	SEM-CL	la	2	8	180	12	85 90 E	APPARENT TWO CEMENTATION EVENTS
23	SEM-CL	lb	3	9	150	5	350 90 E	POSSIBLY TRANSCEMENT
24	SEM-CL	la	2	9	110	5	45 90 E	VARIABLE APERTURE. PARTIALLY OPENED. COMPACTION REOPENING
25	SEM-CL	la	3	9	100	3	45 90 E	VARIABLE APERTURE. COMPACTION RELATED REOPENING
26	SEM-CL	la	2	9	120	5	85 90 E	VARIABLE APERTURE. COMPACTION RELATED REOPENING
27	SEM-CL	la	3	9	75	5	305 90 E	REOPENING RELATED TO COMPACTION. DOES NOT CUT ALL THE GRAIN
28	SEM-CL	la+	1	10	200	5	325 90 E	COMPONENT OF MOVEMENT PERPENDICULAR TO PICTURE.
29	SEM-CL	la	2	10	30	8	80 90 E	SMALL. VARIABLE APERTURE.
30	SEM-CL	la	2	10	45	8	85 90 E	SMALL STRAIGHT TRACE. PERPENDICULAR COMPONENT OF MOVEMENT
31	SEM-CL	la	2	11	150	13	0 90 E	TRANSCEMENT. PIECES OF GRAIN FILL FRACTURE.
32	SEM-CL	la	2	11	80	5	280 90 E	CURVED TRACE
33	SEM-CL	la	2	11	90	5	280 90 E	CURVED TRACE

WELL: RIDDLE D LS 4A

SAMPLE: 4-16

DEPTH: 5031.5'

NOTCH AZIMUTH: 88

FRACTURE INVENTORY

FRACTURE NUMBER	DETECTION METHOD	Classification		PICTURE NUMBER	LENGTH (um)	APERTURE (um)	AZIMUTH (°)	OBSERVATIONS
		Laubach's (1997)	PREDICTIVE SUITABILITY					
1	SEM-CL	1a	2	1	155	5	31	STRAIGHT TRACE. CUTS INHERITED FRACTURES
2	SEM-CL	1a	2	2	140	5	5	STRAIGHT TRACE
3	SEM-CL	1b	3	2	50	2	90	TIP OF GRAIN. POSSIBLY INHERITED
4	SEM-CL	1b	3	2	90	2	310	AMBIGUOUS RELATION TO CEMENT. POSSIBLY INHERITED
5	SEM-CL	1b	3	2	85	2	310	AMBIGUOUS RELATION TO CEMENT. POSSIBLY INHERITED
6	SEM-CL	1b	3	3	60	2	70	ENDS WITHIN GRAIN. POSSIBLY INHERITED
7	SEM-CL	1c	4	3	100	5	310	POSSIBLY CRUSHING RELATED
8	SEM-CL	1c	4	3	50	5	0	POSSIBLY CRUSHING RELATED
9	SEM-CL	1a	2	4	65	5	90	ODD SHAPE. TIP OF GRAIN
10	SEM-CL	1b	3	4	50	5	337	VARIABLE APERTURE. ENDS AT GRAIN BORDER
11	SEM-CL	1c	4	4	80	2	310	POSSIBLY INHERITED
12	SEM-CL	1a	2	6	80	10	0	STRAIGHT TRACE. POSSIBLY TWO CEMENTATION EVENTS
13	SEM-CL	1a	2	6	135	5	34	STRAIGHT TRACE
14	SEM-CL	1b	3	6	190	2	80	CUTS INHERITED FRACTURE. CURVED TRACE
15	SEM-CL	1c	4	7	100	2	300	AMBIGUOUS RELATION TO CEMENT

16	SEM-CL	lb	3	7	30	5	70	VARIABLE APERTURE. TIP OF GRAIN. COMPACTION RELATED?
17	SEM-CL	llb	5	8	90	2	63	VARIABLE APERTURE. PROBABLY CRUSHING RELATED
18	SEM-CL	llb	5	8	160	3	27	VARIABLE APERTURE. PROBABLY CRUSHING RELATED
19	SEM-CL	llb	5	8	150	10	35	VARIABLE APERTURE. PROBABLY CRUSHING RELATED
20	SEM-CL	llb	5	8	120	15	15	VARIABLE APERTURE. PROBABLY CRUSHING RELATED

WELL: RIDDLE D LS 4A

SAMPLE: 4-20

DEPTH: 5035.2

NOTCH AZIMUTH: 90

FRACTURE INVENTORY

FRACTURE NUMBER	DETECTION METHOD	Classification		PICTURE NUMBER	LENGTH (um)	APERTURE (um)	AZIMUTH (°)	OBSERVATIONS
		Laubach's (1997)	PREDICTIVE SUITABILITY					
1	SEM-CL	la+	2	1	225	5	310	DOUBTFUL. DIFFUSE WALLS IN ONE GRAIN BUT STRAIGHT IN THE
2	SEM-CL	lb	3	1	150	5	348	PROBABLE TRANSCEMENT. SIMILAR TO FRACTURE #1
3	SEM-CL	lb	3	2	75	5	60	PROBABLE TRANSCEMENT. DIFFUSE WALLS
4	SEM-CL	lb	3	2	130	8	52	PROBABLE TRANSCEMENT. DIFFUSE WALLS
5	SEM-CL	lc	4	2	180	5	77	AMBIGUOUS RELATION TO CEMENT
6	SEM-CL	llb	5	2	150	5	0	CRUSHING RELATED
7	SEM-CL	llb	5	2	140	5	338	CRUSHING RELATED
8	SEM-CL	llb	5	2	100	2	346	CRUSHING RELATED
9	SEM-CL	llb	5	2	100	8	315	CRUSHING RELATED
10	SEM-CL	llb	5	2	50	5	300	CRUSHING RELATED
11	SEM-CL	llb	5	2	60	2	330	CRUSHING RELATED
12	SEM-CL	llb	5	2	100	2	55	CRUSHING RELATED
13	SEM-CL	lc	4	3	130	5	307	AMBIGUOUS RELATION TO CEMENT. PROBABLY RELATED TO COMPACTION
14	SEM-CL	lb	3	3	30	5	294	PROBABLE TRANSCEMENT. VARIABLE APERTURE.
15	SEM-CL	la	3	4	100	10	283	TRANSCEMENT. DOUBTFUL. PROBABLY CRUSHING RELATED

16	SEM-CL	la	3	4	75	3	280	TRANSCEMENT. DOUBTFUL. PROBABLY CRUSHING RELATED
17	SEM-CL	la	3	4	30	5	70	TRANSCEMENT. DOUBTFUL. PROBABLY CRUSHING RELATED
18	SEM-CL	la	2	5	75	8	30	PIECES OF DE GRAIN IN THE FRACTURE. MULTIPLE FRACTURING EPISODES
19	SEM-CL	la	2	5	75	3	286	PIECES OF DE GRAIN IN THE FRACTURE. MULTIPLE FRACTURING EPISODES
20	SEM-CL	lb	3	5	100	15	306	PROBABLE TRANSCEMENT. STRAIGHT FACES
21	SEM-CL	la	2	6	105	3	80	PIECES OF GRAIN IN THE FRACTURE. MULTIPLE FRACTURING EPISODES
22	SEM-CL	la	2	6	105	3	80	PIECES OF GRAIN IN THE FRACTURE. MULTIPLE FRACTURING EPISODES
23	SEM-CL	lb	3	6	30	8	295	PROBABLE TRANSCEMENT. STRAIGHT TRACE
24	SEM-CL	lb	3	6	20	8	295	PROBABLE TRANSCEMENT. STRAIGHT TRACE
25	SEM-CL	lb	3	6	60	8	70	PROBABLE TRANSCEMENT. STRAIGHT TRACE
26	SEM-CL	lb	3	6	110	8	80	COMPOSED OF FRACTURES #23, #24, #25
27	SEM-CL	lb	3	6	60	3	273	DIFFUSE WALLS. CRUSHING RELATED?

WELL: RIDDLE D LS 4A

SAMPLE: 4-21

DEPTH: 5036.1

NOTCH AZIMUTH: 355

FRACTURE INVENTORY

FRACTURE NUMBER	DETECTION METHOD	Classification		PICTURE NUMBER	LENGTH (um)	APERTURE (um)	AZIMUTH (°)	OBSERVATIONS
		Laubach's (1997)	PREDICTIVE SUITABILITY					
1	SEM-CL	lc	4	1	180	2	346	AMBIGUOUS RELATION TO CEMENT. PROBABLY INHERITED
2	SEM-CL	la	2	1	80	5	76	ODD SHAPE. POSSIBLY CRUSHING RELATED. CUTS INHERITED SYSTEM
3	SEM-CL	lb	3	2	110	5	25	POSSIBLY CRUSHING RELATED. CUTS INHERITED SYSTEM
4	SEM-CL	lb	3	2	85	3	310	POSSIBLY CRUSHING RELATED. ZIGZAG PATTERN
5	SEM-CL	lb	3	4	130	10	305	POSSIBLY CRUSHING RELATED IN PART.
6	SEM-CL	lb	3	4	105	10	90	POSSIBLY CRUSHING RELATED IN PART. CURVED TRACE
7	SEM-CL	la	2	5	80	6	285	STRAIGHT TRACE
8	SEM-CL	la	2	5	12	7	15	STRAIGHT TRACE. TIP OF GRAIN
9	SEM-CL	la	2	6	105	5	55	STRAIGHT TRACE. CUTS INHERITED SYSTEM
10	SEM-CL	lb	3	7	80	5	295	CURVED TRACE
11	SEM-CL	la	2	8	75	10	0	CLEARLY TRANSCEMENT. LARGE APERTURE
12	SEM-CL	la	2	8	110	6	320	TRANSCEMENT. POSSIBLE TWO CEMENTATION EVENTS
13	SEM-CL	la	2	9	150	40	45	PIECES OF GRAIN INSIDE FRACTURE. LARGE APERTURE
14	SEM-CL	la	2	10	120	3	67	STRAIGHT TRACE

15	SEM-CL	la	2	10	75	3	0	TIP OF GRAIN
16	SEM-CL	lb	3	10	115	5	330	ENDS WITHIN GRAIN. VARIABLE APERTURE
17	SEM-CL	la	2	10	180	3	6	DISPLACED BY FRACTURE #16. STRAIGHT TRACE
18	SEM-CL	lb	3	10	110	3	15	CURVED TRACE. TIP OF GRAIN
19	SEM-CL	la	2	11	100	7	32	STRAIGHT TRACE. CUTS INHERITED SYSTEM

WELL: RIDDLE D LS 4A

SAMPLE: 4-23

DEPTH: 5038.1'

NOTCH AZIMUTH: 2

FRACTURE INVENTORY

FRACTURE NUMBER	DETECTION METHOD	Classification		PICTURE NUMBER	LENGTH (um)	APERTURE (um)	AZIMUTH (°)	OBSERVATIONS
		Laubach's (1997)	PREDICTIVE SUITABILITY					
1	PETR.MIC	Ia	4				15	FLUID INCLUSIONS PLANE
2	PETR.MIC	Ia	4				315	FLUID INCLUSIONS PLANE
3	SEM-CL	Ib	3	1	110	5	300	STOPS AT GRAIN BORDERS. STRAIGHT FACES THOUGH.
4	SEM-CL	Ib	3	1	100	10	275	VARIABLE APERTURE. POSSIBLY REOPENED AFTER CRUSHING
5	SEM-CL	Ic	4	1	75	2	300	NOT CLEAR RELATIONSHIP WITH CEMENT. SMALL. CRUSHING?
6	SEM-CL	Ia	2	3	130	10	82	CLEAR TRANSCEMENT FRACTURE. STRAIGHT FACES
7	SEM-CL	IIb	5	5	110	5	80	CRUSHING RELATED
8	SEM-CL	IIb	5	5	100	5	348	CRUSHING RELATED
9	SEM-CL	IIb	5	5	60	5	45	CRUSHING RELATED
10	SEM-CL	IIb	5	5	25	7	53	CRUSHING RELATED
11	SEM-CL	IIb	5	5	30	5	90	CRUSHING RELATED
12	SEM-CL	IIb	5	5	90	3	310	CRUSHING RELATED
13	SEM-CL	IIb	5	5	80	3	90	CRUSHING RELATED
14	SEM-CL	IIb	5	5	80	2	300	CRUSHING RELATED
15	SEM-CL	IIb	5	6	170	10	50	CRUSHING RELATED
16	SEM-CL	IIb	5	6	50	15	275	CRUSHING RELATED. CONTINUATION OF FRACTURE #15
17	SEM-CL	IIb	5	6	220	12	65	FRACTURES #15 AND 16 TOGETHER

18	SEM-CL	IIb	5	6	100	7	300	CRUSHING RELATED
19	SEM-CL	IIb	5	6	200	5	275	CRUSHING RELATED
20	SEM-CL	IIb	5	6	60	5	55	CRUSHING RELATED. CONTINUATION OF FRACTURE #19
21	SEM-CL	IIb	5	6	260	5	85	FRACTURES #19 AND #20 TOGETHER
22	SEM-CL	Ib	3	7	25	5	20	PROBABLE TRANSCEMENT, REOPENED AFTER COMPACTION
23	SEM-CL	Ia	2	7	80	3	60	TRANSCEMENT. PIECES OF GRAIN INSIDE FRACTURE. MULTIPLE FRACTURING EPISODES
24	SEM-CL	Ia	2	7	200	2	30	TRANSCEMENT. PIECES OF GRAIN INSIDE FRACTURE. MULTIPLE FRACTURING EPISODES
25	SEM-CL	Ia	1	9	130	2	38	TRANSGRANULAR DISPLACING TRANSCEMENT OLDER FRACTURE
26	SEM-CL	Ia	2	9	75	8	308	TRANSCEMENT. POSSIBLY TWO EVENTS OF CEMENTATION
27	SEM-CL	IIa	5	10	150	20	325	CRUSHING RELATED
28	SEM-CL	IIa	5	10	75	8	305	CRUSHING RELATED
29	SEM-CL	IIa	5	10	75	5	330	CRUSHING RELATED
30	SEM-CL	IIa	5	10	80	8	32	CRUSHING RELATED
31	SEM-CL	Ia	2	11	200	5	50	TRANSCEMENT. VARIABLE APERTURE DUE TO COMPACTION
32	SEM-CL	Ia	2	11	80	5	270	TRANSCEMENT. VARIABLE APERTURE. TWO CEMENTATION EVENTS.
33	SEM-CL	Ia	2	12	50	10	285	TRANSCEMENT. DOUBTFUL
34	SEM-CL	Ia	2	12	50	10	15	TRANSCEMENT. DOUBTFUL
35	SEM-CL	Ia	2	12	75	5	0	MULTIPLE EPISODES OF OPENING.
36	SEM-CL	IIa	5	12	50	5	60	CRUSHING RELATED
37	SEM-CL	Ic (OPEN)	4	12	100	5	20	OPEN INTRAGRANULAR. PROBABLY INDUCED

38	SEM-CL	lc (OPEN)	4	12	50	5	180	OPEN INTRAGRANULAR. PROBABLY INDUCED
39	SEM-CL	lc (OPEN)	4	12	100	5	18	OPEN INTRAGRANULAR. PROBABLY INDUCED
40	SEM-CL	lla	5	13	100	2	320	CRUSHING RELATED
41	SEM-CL	lla	5	13	50	2	308	CRUSHING RELATED
42	SEM-CL	lla	5	13	40	2	80	CRUSHING RELATED
43	SEM-CL	lc (OPEN)	4	13	125	3	82	OPEN INTRAGRANULAR
44	SEM-CL	lc (OPEN)	4	13	50	3	0	OPEN INTRAGRANULAR
45	SEM-CL	lc (OPEN)	4	13	40	3	0	OPEN INTRAGRANULAR

WELL: RIDDLE D LS 4A

SAMPLE: 4-3

DEPTH: 5018.25

NOTCH AZIMUTH: 352

FRACTURE INVENTORY

FRACTURE NUMBER	DETECTION METHOD	Classification		PICTURE NUMBER	LENGTH (um)	APERTURE (um)	AZIMUTH (°)	OBSERVATIONS
		Laubach's (1997)	PREDICTIVE SUITABILITY					
1	PETR.MIC	la+	4	26			290	FLUID INCLUSION PLANES
2	PETR.MIC	la+	4	27			45	FLUID INCLUSION PLANES
3	PETR.MIC	la+	4	29,30			290	FLUID INCLUSION PLANES
4	PETR.MIC	la+	4	31			60	FLUID INCLUSION PLANES
5	SEM-CL	la	2	1	170	20	80	TWO CEMENTATION EVENTS
6	SEM-CL	la	2	2	150	10	25	TRANSCEMENT. STRAIGHT TRACE
7	SEM-CL	lb	3	2	80	8	315	TRANSCEMENT. CURVED TRACE
8	SEM-CL	lb	3	2	40	5	325	TRANSCEMENT. CURVED TRACE
9	SEM-CL	la	2	3	110	5	307	PARALLEL SET.
10	SEM-CL	la	2	3	80	5	300	PARALLEL SET.
11	SEM-CL	lb	3	3	60	5	307	INTRAGRANULAR. NO CLEAR RELATIONSHIP WITH CEMENT
12	SEM-CL	lb	3	3	90	2	303	INTRAGRANULAR. NO CLEAR RELATIONSHIP WITH CEMENT
13	SEM-CL	lb	3	3	60	2	90	INTRAGRANULAR. CUT BY FRACTURES #9 AND #10
14	SEM-CL	lb	3	3	75	2	90	INTRAGRANULAR. CUT BY SET OF FRACTURES #9 AND #10
15	SEM-CL	la	2	4	150	5	293	TRANSCEMENT. DOUBTFUL. DIFFUSE WALLS
16	SEM-CL	la	2	4	60	8	65	VARIABLE APERTURE. TWO CEMENTATION EVENTS

17	SEM-CL	la	2	5	130	5	285	TRANSCEMENT. DOUBTFUL. DIFFUSE WALLS
18	SEM-CL	lb	3	5	135	2	303	POSSIBLY TRANSCEMENT. DIFFUSE
19	SEM-CL	lb	3	5	120	2	300	POSSIBLY TRANSCEMENT. DIFFUSE
20	SEM-CL	lb	3	5	70	5	70	VARIABLE APERTURE.
21	SEM-CL	la	2	5	95	10	290	PIECES OF GRAIN INSIDE THE FRACTURE. MULTIPLE FRACTURING EPISODES
22	SEM-CL	la	2	5	40	5	25	TRANSCEMENT. STRAIGHT TRACE
23	SEM-CL	la	2	6	30	8	340	VARIABLE APERTURE. TWO CEMENTATION EVENTS
24	SEM-CL	la+	1	6	360	5	60	TRANSGRANULAR (THREE GRAINS AND CEMENT). DOUBTFUL THOUGH

WELL: SUNRAY H COMP #6

SAMPLE: 4986.74

DEPTH:4986.74'

NOTCH AZIMUTH: 30

FRACTURE INVENTORY

FRACTURE NUMBER	DETECTION METHOD	Classification		PICTURE NUMBER	LENGTH (um)	APERTURE (um)	AZIMUTH (°)	OBSERVATIONS
		Laubach's (1997)	PREDICTIVE SUITABILITY					
1	SEM-CL	ld	4	1	115	0.5	308	VERY NARROW, INTRAGRANULAR, AMBIGUOUS RELATIONSHIP TO CEMENT
2	SEM-CL	lc	3	2	100	5	341	AMBIGUOUS RELATIONSHIP TO CEMENT, INTRAGRANULAR, DIFFUSE, STRAIGHT TRACE
3	SEM-CL	lc	3	3	20	2	285	AMBIGUOUS RELATIONSHIP TO CEMENT, CONTINUES OUTSIDE OF PHOTO, DIFFUSE
4	SEM-CL	lc	3	4	62	4	278	DIFFUSE, INTRAGRANULAR, VARIABLE APERTURE, AMBIGUOUS RELATIONSHIP TO CEMENT
5	SEM-CL	lc	3	4	73	3	276	DIFFUSE, INTRAGRANULAR, AMBIGUOUS RELATIONSHIP TO CEMENT
6	SEM-CL	lb	2	4	195	6	80	PROBABLY TRANS-CEMENT, FILLED WITH SURROUNDING QUARTZ CEMENT, STRAIGHT TRACE
7	SEM-CL	lc	3	4	105	3	298	AMBIGUOUS RELATIONSHIP TO CEMENT, INTRAGRANULAR, DIFFUSE
8	SEM-CL	lb	2	4	125	4	343	ZIGZAGGING, PROBABLY TRANS-CEMENT, VARIABLE APERTURE, BORDER OF GRAIN
9	SEM-CL	lb	1	4	340	5	352	PROBABLY TRANS-CEMENT, PIECES OF GRAIN WITHIN FRACTURE, PARALLEL SET

10	SEM-CL	lc	2	4	305	2	323	NARROW, PARALLEL SET, AMBIGUOUS RELATIONSHIP WITH CEMENT
11	SEM-CL	ld	3	4	165	1	305	DIFFUSE, INTRAGRANULAR, PARALLEL SET
12	SEM-CL	lb	2	4	352	6	339	VARIABLE APERTURE, PROBABLY TRANS-CEMENT, PARALLEL SET
13	SEM-CL	lc	2	4	141	1	335	NARROW, DIFFUSE, INTRAGRANULAR, BRANCHES FROM F16, PARALLEL SET
14	SEM-CL	lc	2	4	135	2	0	NARROW, DIFFUSE, INTRAGRANULAR, BRANCHES FROM F16, PARALLEL SET
15	SEM-CL	lc	2	4	120	2	355	BORDER OF GRAIN, CURVED, PARALLEL SET
16	SEM-CL	ld	4	4	90	4	90	DIFFUSE, INTRAGRANULAR, AMBIGUOUS RELATIONSHIP TO CEMENT
17	SEM-CL	lc	4	7,11	210	8	340	LARGE APERTURE, PIECES OF GRAIN IN FRACTURE, INTRAGRANULAR
18	SEM-CL	lc	3	7	32	2	85	DIFFUSE, BRANCHES FROM F17
19	SEM-CL	lc	3	7	50	2	2	DIFFUSE, STRAIGHT TRACE, AMBIGUOUS RELATIONSHIP TO CEMENT
20	SEM-CL	la	2	7,8,12	91	4	45	TRANS-CEMENT, ODDLY SHAPED, DOES NOT CUT THE ENTIRE GRAIN
21	SEM-CL	lc	3	7,8	85	1	347	NARROW, PARALLEL SET, DIFFUSE, CUT BY F20
22	SEM-CL	lc	4	8	19	1	59	DIFFUSE, VERY SMALL, NARROW, BORDER OF GRAIN
23	SEM-CL	la	1	8	49	5	46	TRANS-CEMENT, STRAIGHT TRACE, FILLED WITH SURROUNDING CEMENT
24	SEM-CL	ld	3	9	110	3	12	INTRAGRANULAR, DIFFUSE, PARALLEL SET, AMBIGUOUS RELATIONSHIP TO CEMENT

25	SEM-CL	lc	3	9	160	3	11	DIFFUSE, CONTINUES OUT OF GRAIN, AMBIGUOUS RELATIONSHIP TO CEMENT
26	SEM-CL	lb	2	9	22	3	305	PROBABLY TRANS-CEMENT, SMALL, LARGE APERTURE, INTRAGRANULAR
27	SEM-CL	lb	2	9	75	2	300	PROBABLY TRANS-CEMENT, INTRAGRANULAR, PARALLEL SET
28	SEM-CL	la	1	10,11	90	13	301	LARGE APERTURE, TRANS-CEMENT, FILLED WITH SURROUNDING CEMENT
29	SEM-CL	la	1	10	48	10	61	VARIABLE APERTURE, TRANS-CEMENT, FILLED WITH SURROUNDING CEMENT
30	SEM-CL	la	1	11	89	8	18	TRANS-CEMENT, FILLED WITH SURROUNDING CEMENT, VARIABLE APERTURE
31	SEM-CL	lc	2	11	31	3	280	ZIGZAGGING, PARALLEL SET, AMBIGUOUS RELATIONSHIP TO CEMENT
32	SEM-CL	lc	2	11	72	2	280	ZIGZAGGING, PARALLEL SET, AMBIGUOUS RELATIONSHIP TO CEMENT
33	SEM-CL	lc	3	11	75	4	346	IRREGULAR WALLS (INHERITED?), DIFFUSE
34	SEM-CL	lc	3	11	105	6	39	DIFFUSE, INTRAGRANULAR, AMBIGUOUS RELATIONSHIP TO CEMENT
35	SEM-CL	lc	3	11,15	210	6	296	SERPENTINE, VARIABLE APERTURE, AMBIGUOUS RELATIONSHIP TO CEMENT
36	SEM-CL	lb	2	15	28	6	309	VARIABLE APERTURE, PROBABLY TRANS-CEMENT, ENDS WITHIN GRAIN
37	SEM-CL	lc	2	11,15	160	5	24	STRAIGHT TRACE, IRREGULAR WALLS, CUTS F35, AMBIGUOUS RELATIONSHIP TO CEMENT

38	SEM-CL	lb	2	11,12	220	8	335	CUTS A LITHIC FRAGMENT, PROBABLY TRANS-CEMENT, STRAIGHT TRACE
39	SEM-CL	lc	2	12	71	1	280	NARROW, INTRAGRANULAR, PARALLEL SET
40	SEM-CL	lb	2	12	32	1	279	PROBABLY TRANS-CEMENT, TIP OF GRAIN, PARALLEL SET
41	SEM-CL	lb	2	12	20	0.5	90	PARALLEL SET, TIP OF GRAIN, PROBABLY TRANS-CEMENT, DISPLACED
42	SEM-CL	lc	3	16	43	2	327	TIP OF GRAIN, CURVED, AMBIGUOUS RELATIONSHIP TO CEMENT
43	SEM-CL	lc	3	16	40	2	70	INTRAGRANULAR, STRAIGHT TRACE, AMBIGUOUS RELATIONSHIP TO CEMENT
44	SEM-CL	la	1	13	68	6	22	TRANS-CEMENT, TIP OF GRAIN, VARIABLE APERTURE
45	SEM-CL	la	2	13	36	5	53	PROBABLY CRUSHING RELATED, VARIABLE APERTURE, CURVED, TRANS-CEMENT
46	SEM-CL	lc	2	14	53	1	305	NARROW, PARALLEL SET, AMBIGUOUS RELATIONSHIP TO CEMENT
47	SEM-CL	lc	2	14	80	1	285	NARROW, PARALLEL SET, AMBIGUOUS RELATIONSHIP TO CEMENT
48	SEM-CL	lc	2	14	65	1	320	NARROW, PARALLEL SET, AMBIGUOUS RELATIONSHIP TO CEMENT
49	SEM-CL	lc	2	14	45	0.5	310	NARROW, PARALLEL SET, AMBIGUOUS RELATIONSHIP TO CEMENT, ENDS WITHIN GRAIN
50	SEM-CL	lb	2	14	170	4	280	CURVED, PROBABLY TRANS- CEMENT, ODDLY SHAPED, PARTLY DIFFUSE

51	SEM-CL	lc	3	14	91	1	82	DIFFUSED, INTRAGRANULAR, AMBIGUOUS RELATIONSHIP TO CEMENT
52	SEM-CL	lc	3	14	112	5	65	STRAIGHT TRACE, AMBIGUOUS RELATIONSHIP TO CEMENT
53	SEM-CL	lc	3	14	100	5	282	CURVED TRACE, DIFFERENT FILL THAN SURROUNDINGS, AMBIGUOUS RELATIONSHIP TO CEMENT
54	SEM-CL	lc	3	14	54	3	11	DIFFUSED, INTRAGRANULAR, AMBIGUOUS RELATIONSHIP TO CEMENT
55	SEM-CL	ld	4	14	55	6	33	STRAIGHT TRACE, DOES NOT CUT CEMENT, PROBABLY INHERITED
56	SEM-CL	lc	3	14	52	5	300	STRAIGHT TRACE, AMBIGUOUS RELATIONSHIP TO CEMENT
57	SEM-CL	lc	3	14	48	2	45	STRAIGHT TRACE, VARIABLE APERTURE, AMBIGUOUS RELATIONSHIP TO CEMENT
58	SEM-CL	ld	4	14	105	4	63	POSSIBLY INHERITED, INTRAGRANULAR, ASSOCIATED DISSOLUTION ZONE
59	SEM-CL	la	1	14,15	82	9	326	TRANSCEMENT, ZIGZAGGING, FILLED WITH SURROUNDING CEMENT, VARIABLE APERTURE
60	SEM-CL	lc	3	14,15	98	4	29	STRAIGHT TRACE, AMBIGUOUS RELATIONSHIP TO CEMENT
61	SEM-CL	lc	3	15	81	4	308	POSSIBLY INHERITED, INTRAGRANULAR, ASSOCIATED DISSOLUTION ZONE
62	SEM-CL	lc	3	15	52	5	353	AMBIGUOUS RELATIONSHIP TO CEMENT, TIP OF GRAIN, STRAIGHT TRACE
63	SEM-CL	ld	4	15	67	0.5	304	INDISTINCT, NARROW, DIFFUSE
64	SEM-CL	lc	3	15	48	1	0	AMBIGUOUS RELATIONSHIP TO CEMENT, DIFFUSE, PARALLEL SET
65	SEM-CL	lc	3	15	123	3	6	INTRAGRANULAR, PARALLEL SET, ASSOCIATED DISSOLUTION ZONES

66	SEM-CL	lc	3	15	39	1	307	AMBIGUOUS RELATIONSHIP TO CEMENT, BORDER OF GRAIN, STRAIGHT TRACE
67	SEM-CL	lc	3	16	75	2	302	CURVED, BORDER OF GRAIN, AMBIGUOUS RELATIONSHIP TO CEMENT
68	SEM-CL	lc	3	16	23	1	302	SMALL, WITHIN GRAIN, PARALLEL SET
69	SEM-CL	lc	3	16	70	1	0	WITHIN GRAIN, CURVED, DIFFUSE
70	SEM-CL	lc	3	16	100	2	273	CURVED, BORDER OF GRAIN, AMBIGUOUS RELATIONSHIP TO CEMENT
71	SEM-CL	lc	3	16	61	1	315	DIFFUSE, PARALLEL SET, AMBIGUOUS RELATIONSHIP TO CEMENT
71a	SEM-CL	lb	2	16	68	4	300	PROBABLY CUTS CEMENT, FILLED WITH SURROUNDING CEMENT, STRAIGHT TRACE
71b	SEM-CL	la	1	15,16	92	11	297	VARIABLE APERTURE, TWO CEMENTATION EVENTS, CUTS CEMENT
72	SEM-CL	la	1	15,19	110	20	28	VARIABLE APERTURE, TWO CEMENTATION EVENTS, CUTS CEMENT, TIP OF GRAIN
73	SEM-CL	lc	3	13,17	113	6	50	AMBIGUOUS RELATIONSHIP TO CEMENT, CURVED, TIP OF GRAIN, DIFFUSE
74	SEM-CL	lc	3	13	70	8	292	AMBIGUOUS RELATIONSHIP TO CEMENT, DIFFUSE, LARGE APERTURE,
75	SEM-CL	ld	4	17	32	2	292	AMBIGUOUS RELATIONSHIP TO CEMENT, WITHIN GRAIN, COULD BE INHERITED
76	SEM-CL	ld	4	17	65	3	315	AMBIGUOUS RELATIONSHIP TO CEMENT, WITHIN GRAIN, COULD BE INHERITED

77	SEM-CL	ld	4	17	36	5	51	AMBIGUOUS RELATIONSHIP TO CEMENT, WITHIN GRAIN, COULD BE INHERITED
78	SEM-CL	lc	3	17	69	2	66	AMBIGUOUS RELATIONSHIP TO CEMENT, STRAIGHT TRACE, PARALLEL SET
79	SEM-CL	lc	3	17	150	1	72	AMBIGUOUS RELATIONSHIP TO CEMENT, TIP OF GRAIN, STRAIGHT TRACE, PARALLEL SET
80	SEM-CL	ld	4	17	73	4	31	AMBIGUOUS RELATIONSHIP TO CEMENT, COULD BE INHERITED, ODDLY SHAPED
81	SEM-CL	lb	2	17	15	2	90	PROBABLY CUTS CEMENT, PARALLEL SET, TIP OF GRAIN
82	SEM-CL	lc	2	17	42	1	280	AMBIGUOUS RELATIONSHIP TO CEMENT, DIFFUSE, PARALLEL SET
83	SEM-CL	lc	2	17	90	1	74	AMBIGUOUS RELATIONSHIP TO CEMENT, BORDER OF GRAIN, DIFFUSE
84	SEM-CL	lc	3	18	163	1	74	AMBIGUOUS RELATIONSHIP TO CEMENT, DIFFUSE, PARALLEL SET, BORDER OF GRAIN
85	SEM-CL	lc	3	18	39	3	332	AMBIGUOUS RELATIONSHIP TO CEMENT, DIFFUSE, STRAIGHT TRACE
86	SEM-CL	lc	3	18	45	2	298	AMBIGUOUS RELATIONSHIP TO CEMENT, DIFFUSE, STRAIGHT TRACE
87	SEM-CL	lc	3	18	205	1	278	AMBIGUOUS RELATIONSHIP TO CEMENT, DIFFUSE, PARALLEL SET
88	SEM-CL	lc	3	18	212	1	49	AMBIGUOUS RELATIONSHIP TO CEMENT, DIFFUSE
89	SEM-CL	ld	4	18	53	2	315	AMBIGUOUS RELATIONSHIP TO CEMENT, DIFFUSE,
90	SEM-CL	lc	3	18	52	3	315	AMBIGUOUS RELATIONSHIP TO CEMENT, DIFFUSE

91	SEM-CL	lc	3	18	70	1	274	AMBIGUOUS RELATIONSHIP TO CEMENT, PARALLEL SET
92	SEM-CL	lb	2	18	73	3	310	VARIABLE APERTURE, POSSIBLY TRANSCEMENT, TIP OF GRAIN
93	SEM-CL	lc	3	18	82	2	25	AMBIGUOUS RELATIONSHIP TO CEMENT, DIFFUSE, CURVED, TIP OF GRAIN
94	SEM-CL	lc	3	18	68	1	275	AMBIGUOUS RELATIONSHIP TO CEMENT, NARROW, DIFFUSE
95	SEM-CL	lc	3	18	161	1	349	AMBIGUOUS RELATIONSHIP TO CEMENT, NARROW, DIFFUSE
96	SEM-CL	lb	2	18	89	3	70	PROBABLY TRANS-CEMENT, TIP OF GRAIN, DIFFUSE
97	SEM-CL	lb	3	17	74	1	3	PROBABLY TRANS-CEMENT, TIP OF GRAIN, DIFFUSE
98	SEM-CL	lb	2	19	94	2	286	PROBABLY TRANS-CEMENT, STRAIGHT TRACE, FILLED WITH SURROUNDING CEMENT
99	SEM-CL	ld	4	19,20	118	2	303	AMBIGUOUS RELATIONSHIP TO CEMENT, DIFFUSE, PROBABLY INHERITED
100	SEM-CL	lb	3	20	50	2	322	PROBABLY TRANS-CEMENT, STRAIGHT TRACE
101	SEM-CL	ld	4	20	253	5	80	AMBIGUOUS RELATIONSHIP TO CEMENT, DIFFUSE, PROBABLY INHERITED
102	SEM-CL	lb	2	20	81	3	342	PROBABLY TRANS-CEMENT, STRAIGHT TRACE, BORDER OF GRAIN
103	SEM-CL	lb	2	20	40	3	270	PROBABLY TRANS-CEMENT, BORDER OF GRAIN, INTRAGRANULAR
104	SEM-CL	lb	3	20	48	2	57	PROBABLY TRANS-CEMENT, BORDER OF GRAIN, DIFFUSE
105	SEM-CL	lb	2	20	23	4	56	PROBABLY TRANS-CEMENT, SHORT

WELL: SUNRAY H COMP #6

SAMPLE: 5000.68

NOTCH AZIMUTH: 0

FRACTURE INVENTORY

FRACTURE NUMBER	DETECTION METHOD	Classification		PICTURE NUMBER	LENGTH (um)	APERTURE (um)	AZIMUTH (°)	OBSERVATIONS
		Laubach's (1997)	PREDICTIVE SUITABILITY					
1	SEM-CL	lc	3	1	78	1	60	AMBIGUOUS RELATIONSHIP TO CEMENT, DIFFUSE, IRREGULAR TRACE, TIP OF GRAIN
2	SEM-CL	lc	3	1	80	2	61	CONTINUES BEHIND LABEL OF PHOTO, AMBIGUOUS RELATIONSHIP TO CEMENT, IRREGULAR TRACE, DIFFUSE
3	SEM-CL	lb	2	1	138	2	62	PROBABLY CUTS CEMENT, CONTINUES OUTSIDE PHOTO, DIFFUSE, FILLED WITH SURROUNDING CEMENT
3A	SEM-CL	la	1	1	53	8	63	CUTS CEMENT, TIP OF GRAIN, FILLED WITH SURROUNDING CEMENT, VARIABLE AND LARGE APERTURE
4	SEM-CL	ld	4	1	52	2	64	DIFFUSE, PROBABLY PRESSURE SOLUTION RELATED, CURVED TRACE, AMBIGUOUS RELATIONSHIP TO CEMENT
5	SEM-CL	ld	4	1	60	2	65	DIFFUSE, PROBABLY PRESSURE SOLUTION RELATED, CURVED TRACE, AMBIGUOUS RELATIONSHIP TO CEMENT
6	SEM-CL	ld	4	1	52	2	66	DIFFUSE, PROBABLY PRESSURE SOLUTION RELATED, CURVED TRACE, AMBIGUOUS RELATIONSHIP TO CEMENT
7	SEM-CL	lb	2	2	78	2	67	PROBABLY CUTS CEMENT, FILLED WITH SURROUNDING CEMENT, VARIABLE APERTURE, SLIGHTLY CURVED.
8	SEM-CL	lc	3	2	68	1	68	AMBIGUOUS RELATIONSHIP TO CEMENT, APPARENTLY FILLED WITH SURROUNDING CEMENT, TIP OF GRAIN, STRAIGHT TRACE
9	SEM-CL	ld	4	2	192	2	69	STRAIGHT TRACE, PROBABLY INHERITED, NOT FILLED WITH SURROUNDING CEMENT

10	SEM-CL	ld	4	2	120	4	70	LARGE APERTURE, STRAIGHT TRACE, NOT FILLED WITH SURROUNDING CEMENT, PROBABLY INHERITED
11	SEM-CL	ld	4	2	128	13	71	LARGE APERTURE, STRAIGHT TRACE, NOT FILLED WITH SURROUNDING CEMENT, PROBABLY INHERITED
12	SEM-CL	lc	3	3	110	2	72	AMBIGUOUS RELATIONSHIP TO CEMENT, CURVED TRACE, ENDS WITHIN GRAIN
13	SEM-CL	lb	2	3	143	1.5	45	STRAIGHT TRACE, PROBABLY CUTS CEMENT, FILLED WITH SURROUNDING CEMENT
13A	SEM-CL	lc	3	3	80	0.5	46	CURVED, TIP OF GRAIN, THIN, AMBIGUOUS RELATIONSHIP TO CEMENT
14	SEM-CL	la	1	4	130	4	47	CUTS CEMENT, CURVED TRACE, FILLED WITH SURROUNDING CEMENT
15	SEM-CL	lb	2	4	48	1.5	48	PROBABLY CUTS CEMENT, FILLED WITH SURROUNDING CEMENT, STRAIGHT TRACE, TIP OF GRAIN
16	SEM-CL	lb	2	4	129	2	49	ASSOCIATED TO PRESSURE SOLUTION, CUTS CEMENT, STRAIGHT TRACE, FILLED WITH SURROUNDING CEMENT
17	SEM-CL	lc	3	5	112	1	50	AMBIGUOUS RELATIONSHIP TO CEMENT, DISSOLUTION ZONE ASSOCIATED, VARIABLE APERTURE
18	SEM-CL	lc	4	5	33	3	51	PROBABLY ASSOCIATED TO DISSOLUTION ZONE, SHORT, ENDS WITHIN GRAIN AGAINST F-17
19	SEM-CL	lc	2	5	36	3	52	STRAIGHT TRACE, CONTINUES OUTSIDE PHOTO, PROBABLY FILLED WITH SURROUNDING CEMENT, ENDS AGAINST F-20
20	SEM-CL	lb	2	5	50	9	53	PROBABLY CUTS CEMENT, FILLED WITH SURROUNDING CEMENT, STRAIGHT TRACE, CONTINUES OUTSIDE PHOTO
21	SEM-CL	lb	2	6	48	13	54	LARGE APERTURE, FILLED WITH SURROUNDING CEMENT, SHORT
22	SEM-CL	ld	4	7	64	1	72	PROBABLY INHERITED, THIN, STRAIGHT TRACE
22A	SEM-CL	ld	4	7	42	0.5	73	PROBABLY INHERITED, THIN, ENDS WITHIN GRAIN, STRAIGHT TRACE

23	SEM-CL	ld	4	7	78	1	74	PROBABLY INHERITED, THIN, ENDS WITHIN GRAIN, STRAIGHT TRACE
24	SEM-CL	lb	3	8	48	9	75	CONTINUES BELOW PHOTO LABEL, PROBABLY CUTS CEMENT, APPARENTLY PARALLEL TO INHERITED SYSTEM IN GRAIN
25	SEM-CL	lc	3	8	55	1	76	PARALLEL SET, AMBIGUOUS RELATIONSHIP TO CEMENT, DIFFUSE
26	SEM-CL	lc	3	8	60	1	77	PARALLEL SET, AMBIGUOUS RELATIONSHIP TO CEMENT, DIFFUSE
27	SEM-CL	lb	3	8	73	2	78	PARALLEL SET, PROBABLY CUTS CEMENT, DIFFUSE, SLIGHTLY CURVED TRACE
28	SEM-CL	lb	3	10	41	2	79	PROBABLY CUTS CEMENT, FILLED WITH SURROUNDING CEMENT, PROBABLY PARALLEL TO INHERITED SYSTEM (F-28A)
28A	SEM-CL	ld	4	10	61	1	80	PROBABLY INHERITED, THIN, STRAIGHT TRACE
29	SEM-CL	lb	2	11	52	8	81	FILLED WITH SURROUNDING CEMENT, PROBABLY CUTS CEMENT, STRAIGHT TRACE, TIP OF GRAIN
30	SEM-CL	ld	4	11	58	2	82	IRREGULAR TRACE, CONTINUES OUTSIDE PHOTO, PROBABLY INHERITED
31	SEM-CL	lb	2	12	22	2	83	PROBABLY CUTS CEMENT, FILLED WITH SURROUNDING CEMENT, STRAIGHT TRACE
32	SEM-CL	lc	3	13	49	3	84	AMBIGUOUS RELATIONSHIP TO CEMENT, VARIABLE APERTURE, TIP OF GRAIN
33	SEM-CL	lc	3	13	22	2	85	AMBIGUOUS RELATIONSHIP TO CEMENT, STRAIGHT TRACE, LARGE APERTURE
34	SEM-CL	lc	3	13	75	1	86	AMBIGUOUS RELATIONSHIP TO CEMENT, IRREGULAR APERTURE, STRAIGHT TRACE, ENDS WITHIN GRAIN
35	SEM-CL	lc	3	13	70	1	87	AMBIGUOUS RELATIONSHIP TO CEMENT, VARIABLE APERTURE, ENDS WITHIN GRAIN
36	SEM-CL	la	1	13	81	10	60	CUTS CEMENT, TWO CEMENTATION EVENTS, LARGE VARIABLE APERTURE, SLIGHTLY ZIGZAGGING TRACE
36A	SEM-CL	la	1	13	63	6	61	CUTS CEMENT, BRANCHES FROM F-36, SLIGHTLY CURVED TRACE, FILLED WITH SURROUNDING CEMENT, DISPLACE

37	SEM-CL	lb	2	14	29	3	62	PROBABLE CUTS CEMENT, TIP OF GRAIN, FILLED WITH SURROUNDING CEMENT, STRAIGHT TRACE
38	SEM-CL	la	1	14	31	10	63	CUTS CEMENT, LARGE VARIABLE APERTURE, DISPLACED, SPLITS SMALL GRAIN
39	SEM-CL	lb	2	15	72	3	64	PROBABLY CUTS CEMENT, STRAIGHT TRACE, APPARENTLY FILLED WITH SURROUNDING CEMENT
40	SEM-CL	lb	2	15	73	6	65	PROBABLY CUTS CEMENT, PARALLEL TO BORDER OF GRAIN, FILLED WITH SURROUNDING CEMENT
41	SEM-CL	lb	2	15	25	7	66	PROBABLY CUTS CEMENT, FILLED WITH SURROUNDING CEMENT, SHORT, LARGE VARIABLE APERTURE
42	SEM-CL	lb	2	16	31	3	67	PROBABLY CUTS CEMENT, FILLED WITH SURROUNDING CEMENT, STRAIGHT TRACE, CONTINUES OUTSIDE PHOTO
43	SEM-CL	lb	2	17	90	6	68	CUTS CEMENT, FILLED WITH SURROUNDING CEMENT, IRREGULAR TRACE ASSOCIATED WITH DISSOLUTION ZONE
44	SEM-CL	lc	2	17	52	2	69	AMBIGUOUS RELATIONSHIP TO CEMENT, IRREGULAR TRACE, ENDS WITHIN GRAIN, PARALLEL SET
45	SEM-CL	lb	2	17	73	3	70	PROBABLY CUTS CEMENT, FILLED WITH SURROUNDING CEMENT, STRAIGHT TRACE
46	SEM-CL	la	1	17	90	10	60	PROBABLY CUTS CEMENT, FILLED WITH SURROUNDING CEMENT, STRAIGHT TRACE, CONTINUES OUTSIDE PHOTO
47	SEM-CL	lb	2	17	23	2	61	PROBABLY CUTS CEMENT, FILLED WITH SURROUNDING CEMENT, STRAIGHT TRACE, SHORT, PARALLEL SET
48	SEM-CL	lc	2	17	40	1.5	62	APPARENTLY FILLED WITH SURROUNDING CEMENT, WITHIN GRAIN, BRANCHES FROM F-47
49	SEM-CL	lc	2	17	28	1.5	63	STRAIGHT TRACE, BRANCHES FROM F-48, CONTINUES OUTSIDE PHOTO
50	SEM-CL	lb	2	17	11	3	64	PROBABLY CUTS CEMENT, FILLED WITH SURROUNDING CEMENT, STRAIGHT TRACE, SHORT, PARALLEL SET

51	SEM-CL	lb	2	17	19	2	65	PROBABLY CUTS CEMENT, FILLED WITH SURROUNDING CEMENT, STRAIGHT TRACE, SHORT, PARALLEL SET
52	SEM-CL	lc	2	17	21	1	66	THIN, BRANCHES FROM F-48, STRAIGHT TRACE, PROBABLY FILLED WITH SURROUNDING CEMENT
53	SEM-CL	lb	1	18	28	2	67	PROBABLY CUTS CEMENT, FILLED WITH SURROUNDING CEMENT, STRAIGHT TRACE, BRANCHES FROM F54
54	SEM-CL	la	1	18	65	4	68	CUTS CEMENT, PIECES OF GRAIN WITHIN FRACTURE, LARGE VARIABLE APERTURE, FILLED WITH SURROUNDING CEMENT
55	SEM-CL	la	1	18	106	13	69	CUTS CEMENT, PIECES OF GRAIN IN FRACTURE, LARGE VARIABLE APERTURE, FILLED WITH SURROUNDING CEMENT
56	SEM-CL	la	1	19	57	6	70	CUTS CEMENT, FILLED WITH SURROUNDING CEMENT, TIP OF GRAIN, DISPLACED
57	SEM-CL	lb	3	19	59	2	55	APPARENTLY FILLED WITH SURROUNDING CEMENT, CURVED TRACE, PARALLEL TO BORDER OF GRAIN, VARIABLE APERTURE
58	SEM-CL	lc	3	19	50	3	56	AMBIGUOUS RELATIONSHIP TO CEMENT, STRAIGHT TRACE, CONTINUES OUTSIDE PHOTO, PARALLEL TO BORDER OF GRAIN
59	SEM-CL	lb	2	20	29	3	57	PROBABLY CUTS CEMENT, BRANCHES FROM F 60, IRREGULAR APERTURE, FILLED WITH SURROUNDING CEMENT
60	SEM-CL	la	1	20	30	16	58	CUTS CEMENT, SHORT, LARGE VARIABLE APERTURE, FILLED WITH SURROUNDING CEMENT, DISPLACED
61	SEM-CL	lc	4	20	23	3	59	PROBABLY CEMENT BETWEEN TWO DIFFERENT GRAINS, STRAIGHT TRACE, SHORT
62	SEM-CL	lb	2	20	16	1	60	PROBABLY CUTS CEMENT, SHORT, FILLED WITH SURROUNDING CEMENT, TIP OF GRAIN
63	SEM-CL	lb	2	20	12	1	61	PROBABLY CUTS CEMENT, SHORT, FILLED WITH SURROUNDING CEMENT, TIP OF GRAIN
64	SEM-CL	ld	4	20	90	3	62	ENDS WITHIN GRAIN, IRREGULAR TRACE AND APERTURE, PROBABLY INHERITED

65	SEM-CL	lb	2	20	30	2	63	STRAIGHT TRACE, CONTINUES OUTSIDE PHOTO, PROBABLY CUTS CEMENT, FILLED WITH SURROUNDING CEMENT
66	SEM-CL	lb	2	20	100	4	64	ZIGZAGGING TRACE, PROBABLY CUTS CEMENT, FILLED WITH SURROUNDING CEMENT
67	SEM-CL	lb	2	20	40	1	65	PROBABLY CUTS CEMENT, SHORT, FILLED WITH SURROUNDING CEMENT, ENDS WITHIN GRAIN, VARIABLE APERTURE
68	SEM-CL	lc	3	20	29	0.5	66	BRANCHES FROM F-67, PROBABLY FILLED WITH SURROUNDING CEMENT, STRAIGHT TRACE
69	SEM-CL	lc	3	20	62	0.5	67	BRANCHES FROM F-68, PROBABLY FILLED WITH SURROUNDING CEMENT, CURVED TRACE, ENDS AGAINST DISSOLUTION ZONE
70	SEM-CL	lc	3	20	20	0.5	68	BRANCHES FROM F-69, THIN, STRAIGHT TRACE, PROBABLY FILLED WITH SURROUNDING CEMENT, DIFFUSE

WELL: SAN JUAN 32-9

SAMPLE: 5894.4

NOTCH AZIMUTH:

FRACTURE INVENTORY

FRACTURE NUMBER	DETECTION METHOD	Classification		PICTURE NUMBER	LENGTH (um)	APERTURE (um)	AZIMUTH (°)	OBSERVATIONS
		Laubach's (1997)	PREDICTIVE SUITABILITY					
1	SEM-CL	lb	3	1	48	1	59	PROBABLY CUTS CEMENT, CONTINUES OUTSIDE PHOTO, ZIGZAG PATTERN
2	SEM-CL	ld	4	1	50	0.5	304	PROBABLY INHERITED, DIFFUSE, CURVED
3	SEM-CL	la	1	1	61	7	357	CUTS CEMENT, TWO CEMENTATION EVENTS
4	SEM-CL	lb	2	1	101	2	78	PROBABLY CUTS CEMENT, ZIGZAGGING
5	SEM-CL	lc	2	1	82	1	71	AMBIGUOUS RELATIONSHIP TO CEMENT, VARIABLE APERTURE, PARALLEL SET
6	SEM-CL	ld	3	1	40	1	293	PROBABLY INHERITED, NARROW, ASSOCIATED DISSOLUTION ZONE
7	SEM-CL	la	1	1	85	16	351	CUTS CEMENT, VARIABLE APERTURE, FILLED WITH SURROUNDING CEMENT
8	SEM-CL	lb	2	1	42	4	270	PROBABLY CUTS CEMENT, STRAIGHT TRACE, FILLED WITH SURROUNDING CEMENT
9	SEM-CL	lc	2	1	26	3	70	PROBABLY CUTS CEMENT, FILLED WITH SURROUNDING CEMENT
10	SEM-CL	la	1	1	70	10	331	CUTS CEMENT, LARGE VARIABLE APERTURE, FILLED WITH SURROUNDING CEMENT
11	SEM-CL	lb	2	1	66	4	77	CUTS CEMENT, CURVED, FILLED WITH SURROUNDING CEMENT
12	SEM-CL	lb	2	1	83	3	60	PROBABLY CUTS CEMENT, FILLED WITH SURROUNDING CEMENT, CURVED
13	SEM-CL	lb	2	1	15	2	309	PROBABLY CUTS CEMENT, FILLED WITH SURROUNDING CEMENT, TIP OF GRAIN

14	SEM-CL	lb	2	2	82	1	277	PROBABLY TRANSCEMENT, PARALLEL TO BORDER OF GRAIN, NARROW, STRAIGHT TRACE
15	SEM-CL	lb	4	2	14	3	68	SHORT, PROBABLY TRANS-CEMENT, CURVED, PROBABLY CRUSHING RELATED
16	SEM-CL	lb	4	2	48	3	11	CURVED, PROBABLY TRANS-CEMENT, VARIABLE APERTURE, PROBABLY CRUSHING RELATED, TIP OF GRAIN
17	SEM-CL	ld	4	2	46	1	323	INTRAGANULAR, PROBABLY INHERITED, STRAIGHT TRACE, DIFFUSE
18	SEM-CL	lb	3	2	90	2	309	PROBABLY CUTS CEMENT, STRAIGHT TRACE, PARALLEL SET, PROBABLY CRUSHING RELATED
19	SEM-CL	lb	3	2	42	1	326	PROBABLY CUTS CEMENT, STRAIGHT TRACE, PARALLEL SET, PROBABLY CRUSHING RELATED
20	SEM-CL	lb	2	2	41	2	0	PROBABLY CUTS CEMENT, VARIABLE APERTURE, PARALLEL TO BORDER OF GRAIN
21	SEM-CL	la	1	2	83	9	341	CUTS CEMENT, VARIABLE APERTURE, FILLED WITH SURROUNDING CEMENT
22	SEM-CL	ld	4	2,4	43	1	270	AMBIGUOUS RELATIONSHIP TO CEMENT, PROBABLY INHERITED, STRAIGHT TRACE, ENDS WITHIN GRAIN
23	SEM-CL	lb	2	4	31	3	288	PROBABLY CUTS CEMENT, CONTINUES OUTSIDE PHOTO, STRAIGHT TRACE
24	SEM-CL	lb	2	4	52	5	40	PROBABLY CUTS CEMENT, FILLED WITH SURROUNDING CEMENT, STRAIGHT TRACE
25	SEM-CL	ld	4	4	105	1	77	AMBIGUOUS RELATIONSHIP TO CEMENT, PROBABLY INHERITED, NARROW
26	SEM-CL	la	1	4,5	70	15	11	CUTS CEMENT, VARIABLE APERTURE, FILLED WITH SURROUNDING CEMENT
27	SEM-CL	la	1	5	63	20	354	CUTS CEMENT, LARGE VARIABLE APERTURE, PIECES OF GRAIN WITHIN FRACTURE
28	SEM-CL	lb	2	5	18	3	65	PROBABLY CUTS CEMENTS, PIECES OF GRAIN WITHIN FRACTURE, SHORT, FILLED WITH SURROUNDING CEMENT

29	SEM-CL	lb	4	5	52	0.5	36	PROBABLY INHERITED, NARROW, STRAIGHT TRACE
30	SEM-CL	lc	4	5	88	1	12	VARIABLE APERTURE, ODDLY SHAPED, AMBIGUOUS RELATIONSHIP TO CEMENT
31	SEM-CL	lb	2	5	25	2	60	PROBABLY CUTS CEMENT, DISCONTINUOUS, VARIABLE APERTURE
32	SEM-CL	lb	2	5	17	2	331	PROBABLY CUTS CEMENT, FILLED WITH SURROUNDING CEMENT, STRAIGHT TRACE
33	SEM-CL	lb	2	5	48	2	73	PROBABLY CUTS CEMENT, ODDLY SHAPED, COMPLEX, VARIABLE APERTURE
34	SEM-CL	lb	2	5,7	57	2	308	PROBABLY CUTS CEMENT, CURVED, TIP OF GRAIN
35	SEM-CL	lb	2	7	59	10	360	PROBABLY CUTS CEMENT, VARIABLE APERTURE, FILLED WITH SURROUNDING CEMENT
36	SEM-CL	lc	3	7	30	1	35	AMBIGUOUS RELATIONSHIP TO CEMENT, VARIABLE APERTURE
37	SEM-CL	lc	2	7	62	0.5	21	AMBIGUOUS RELATIONSHIP TO CEMENT, NARROW, PARALLEL SET
38	SEM-CL	lb	2	7	45	3	5	PROBABLY CUTS CEMENT, ODDLY SHAPED, VARIABLE APERTURE, ASSOCIATED DISSOLUTION ZONES
39	SEM-CL	lb	2	7	16	2	3	PROBABLY CUTS CEMENT, STRAIGHT TRACE, SHORT
40	SEM-CL	ld	2	7	23	1	0	AMBIGUOUS RELATIONSHIP TO CEMENT, DIFFUSE, ODDLY SHAPED
41	SEM-CL	lb	2	7	23	1	12	PROBABLY CUTS CEMENT, STRAIGHT TRACE, TIP OF GRAIN
42	SEM-CL	lb	2	7	106	1	86	NARROW, PROBABLY CUTS CEMENT, ASSOCIATED DISSOLUTION ZONES
42A	SEM-CL	lb	4	8	19	9	299	PROBABLY CUTS CEMENT, PIECES OF GRAIN WITHIN FRACTURE, LARGE VARIABLE APERTURE
43	SEM-CL	ld	4	7,8	63	3	85	INTRAGRANULAR, ASSOCIATED DISSOLUTION ZONES, APPARENTLY FILLED WITH SURROUNDING CEMENT

44	SEM-CL	lc	3	9	39	3	349	AMBIGUOUS RELATIONSHIP TO CEMENT, APPARENTLY FILLED WITH SURROUNDING CEMENT, STRAIGHT TRACE, DIFFUSE
45	SEM-CL	lb	2	9	85	3	361	APPARENTLY TRANS-CEMENT, POSSIBLY DISPLACED, APPARENTLY FILLED WITH SURROUNDING CEMENT
46	SEM-CL	la	1	9	73	8	278	CUTS CEMENT, PIECES OF GRAIN WITHIN FRACTURE, STRAIGHT TRACE
47	SEM-CL	lb	2	8,9	62	3	88	APPARENTLY FILLED WITH SURROUNDING CEMENT, PARALLEL TO BORDER OF GRAIN, STRAIGHT TRACE
48	SEM-CL	ld	4	9	20	0.5	303	PROBABLY INHERITED, SHORT, DIFFUSE
49	SEM-CL	ld	4	9	12	0.25	50	PROBABLY INHERITED, SHORT, DIFFUSE
50	SEM-CL	lb	2	10	21	2	18	PROBABLY CUTS CEMENT, PROBABLY TWO CEMENTATION EVENTS, SHORT, ENDS WITHIN GRAIN
51	SEM-CL	lb	2	10	63	6	65	PROBABLY CUTS CEMENT, VARIABLE APERTURE, FILLED WITH SURROUNDING CEMENT
52	SEM-CL	la	1	10	90	16	82	CUTS CEMENT, APPARENTLY TWO CEMENTATION EVENTS, VARIABLE APERTURE
53	SEM-CL	lb	2	10	85	2	358	PROBABLY CUTS CEMENT, STRAIGHT TRACE, FILLED WITH SURROUNDING CEMENT
54	SEM-CL	lc	3	10	36	1	304	CURVED, TIP OF GRAIN, APPARENTLY FILLED WITH SURROUNDING CEMENTS
55	SEM-CL	la	1	10	90	5	305	CUTS CEMENT, FILLED WITH SURROUNDING CEMENT, PIECES OF GRAIN WITHIN FRACTURE
56	SEM-CL	lb	1	10	60	4	313	BRANCHES FROM F55, PIECES OF GRAIN WITHIN FRACTURE, APPARENTLY FILLED WITH SURROUNDING CEMENT
56A	SEM-CL	lb	2	11	18	1	40	PROBABLY CUTS CEMENT, APPARENTLY FILLED WITH SURROUNDING CEMENT, STRAIGHT TRACE

57	SEM-CL	lb	2	11	24	1	67	PROBABLY CUTS CEMENT, APPARENTLY FILLED WITH SURROUNDING CEMENT, STRAIGHT TRACE
58	SEM-CL	lb	2	11	5	1	305	PROBABLY CUTS CEMENT, FILLED WITH SURROUNDING CEMENT, SHORT, TIP OF GRAIN
59	SEM-CL	lb	2	11	10	1	312	STRAIGHT TRACE, SHORT, APPARENTLY FILLED WITH SURROUNDING CEMENT
60	SEM-CL	lb	2	11	25	3	328	APPARENTLY FILLED WITH SURROUNDING CEMENT, PARALLEL SET, VARIABLE APERTURE
61	SEM-CL	la	1	11	31	21	338	LARGE VARIABLE APERTURE, CUTS CEMENT, PIECES OF GRAIN WITHIN FRACTURE
62	SEM-CL	lb	2	11	20	3	23	STRAIGHT TRACE, PROBABLY CUTS CEMENT, FILLED WITH SURROUNDING CEMENT
63	SEM-CL	lb	2	11	16	3	22	STRAIGHT TRACE, PROBABLY CUTS CEMENT, FILLED WITH SURROUNDING CEMENT
64	SEM-CL	la	1	11	100	10	21	ODDLY SHAPED WALLS, CUT CEMENT, STRAIGHT TRACE
65	SEM-CL	lb	2	11	48	2	0	STRAIGHT TRACE, PROBABLY CUTS CEMENT
66	SEM-CL	lb	2	11	19	1	278	PARALLEL SET, PARALLEL TO BORDER OF GRAIN, FILLED WITH SURROUNDING CEMENT
67	SEM-CL	lb	2	11	25	0.5	276	PARALLEL SET, PARALLEL TO BORDER OF GRAIN, FILLED WITH SURROUNDING CEMENT
68	SEM-CL	lb	2	11	32	2	270	PARALLEL SET, PARALLEL TO BORDER OF GRAIN, FILLED WITH SURROUNDING CEMENT, ENDS WITHIN GRAIN
69	SEM-CL	lb	2	11	45	3	280	PARALLEL SET, PARALLEL TO BORDER OF GRAIN, FILLED WITH SURROUNDING CEMENT, ENDS WITHIN GRAIN
69A	SEM-CL	lb	2	11	9	2	6	PROBABLY CUTS CEMENT, SHORT, BORDER OF GRAIN

70	SEM-CL	lc	3	11	12	2	50	ODDLY SHAPED WALLS, AMBIGUOUS RELATIONSHIP TO CEMENT
71	SEM-CL	lc	3	11	11	1	3	ODDLY SHAPED WALLS, AMBIGUOUS RELATIONSHIP TO CEMENT
72	SEM-CL	lc	3	11	18	1	305	ODDLY SHAPED WALLS, AMBIGUOUS RELATIONSHIP TO CEMENT
73	SEM-CL	ld	4	11	88	0.5	316	NARROW, DIFFUSE, PARALLEL SET, PROBABLY INHERITED
74	SEM-CL	lc	3	11	73	1	12	PARALLEL SET, AMBIGUOUS RELATIONSHIP TO CEMENT, NARROW
75	SEM-CL	la	1	11	45	18	88	VARIABLE APERTURE, CUTS CEMENT, TIP OF GRAIN
76	SEM-CL	lb	2	11	13	2	0	STRAIGHT TRACE, FILLED WITH SURROUNDING CEMENT, SHORT
77	SEM-CL	lb	2	11	40	2	47	STRAIGHT TRACE, PROBABLY CUTS CEMENT, FILLED WITH SURROUNDING CEMENT
78	SEM-CL	lc	3	13	50	4	1	AMBIGUOUS RELATIONSHIP TO CEMENT, DIFFUSE, PROBABLY FILLED WITH SURROUNDING CEMENT
79	SEM-CL	lc	3	13	73	1	39	PARALLEL SET, AMBIGUOUS RELATIONSHIP TO CEMENT, PROBABLY FILLED WITH SURROUNDING CEMENT
80	SEM-CL	lb	3	13	62	1	38	NARROW, PARALLEL SET, AMBIGUOUS RELATIONSHIP TO CEMENT
81	SEM-CL	lc	3	13	50	1	38	PARALLEL SET, AMBIGUOUS RELATIONSHIP TO CEMENT
82	SEM-CL	ld	2	14	19	4	302	APPARENTLY FILLED WITH SURROUNDING CEMENT, INTRAGRANULAR, PARALLEL SET, STRAIGHT TRACE
83	SEM-CL	ld	2	14	30	2	283	FILLED WITH SURROUNDING CEMENT, INTRAGRANULAR, PARALLEL SET, ODD SHAPE, ASSOCIATED DISSOLUTION
84	SEM-CL	ld	2	14	42	2	306	FILLED WITH SURROUNDING CEMENT, INTRAGRANULAR, PARALLEL SET, ODD SHAPE, ASSOCIATED DISSOLUTION

85	SEM-CL	ld	2	14	23	3	304	APPARENTLY FILLED WITH SURROUNDING CEMENT, INTRAGRANULAR, PARALLEL SET, STRAIGHT TRACE
86	SEM-CL	lb	2	14	100	2	69	PROBABLY CUTS CEMENT, CURVED, FILLED WITH SURROUNDING CEMENT, PARALLEL SET, ENDS WITHIN GRAIN
87	SEM-CL	lb	2	14	111	3	72	PROBABLY CUTS CEMENT, CURVED, FILLED WITH SURROUNDING CEMENT, PARALLEL SET, ENDS WITHIN GRAIN
88	SEM-CL	lb	2	14	83	3	67	PROBABLY CUTS CEMENT, CURVED, FILLED WITH SURROUNDING CEMENT, PARALLEL SET, ENDS WITHIN GRAIN
89	SEM-CL	ld	2	14	85	2	304	INTRAGRANULAR, VARIABLE APERTURE, PARALLEL TO BORDER OF GRAIN, FILLED WITH SURROUNDING CEMENT
90	SEM-CL	lb	2	14	53	3	48	PROBABLY CUTS CEMENT, TIP OF GRAIN, STRAIGHT TRACE
91	SEM-CL	la	1	15	75	5	53	CUTS CEMENT, VARIABLE APERTURE, FILLED WITH SURROUNDING CEMENT
92	SEM-CL	lc	2	15	52	1	29	PARALLEL SET, TIP OF GRAIN
93	SEM-CL	lc	3	15	44	4	323	CONTINUES OUTSIDE GRAIN, POSSIBLY FILLED WITH SURROUNDING CEMENT, VARIABLE APERTURE
94	SEM-CL	ld	4	15	62	0.5	60	POSSIBLY INHERITED, CONTINUES OUTSIDE GRAIN, NARROW, ENDS WITHIN GRAIN
95	SEM-CL	lc	3	15	28	1	40	CONTINUES OUTSIDE GRAIN, POSSIBLY FILLED WITH SURROUNDING CEMENT, STRAIGHT TRACE
96	SEM-CL	lb	2	15	110	8	2	PROBABLY CUTS CEMENT, CURVED, ENDS WITHIN GRAIN, VARIABLE APERTURE
97	SEM-CL	lb	2	15	65	4	355	PROBABLY CUTS CEMENT, CURVED, ENDS WITHIN GRAIN, VARIABLE APERTURE
98	SEM-CL	lc	2	15	80	1	2	PARALLEL SET, TIP OF GRAIN, PROBABLY FILLED WITH SURROUNDING CEMENT, STRAIGHT TRACE

99	SEM-CL	lc	3	15	44	1	46	NARROW, AMBIGUOUS RELATIONSHIP TO CEMENT, PARALLEL SET, STRAIGHT TRACE
100	SEM-CL	lc	3	15	74	0.5	55	NARROW, AMBIGUOUS RELATIONSHIP TO CEMENT, PARALLEL SET, STRAIGHT TRACE
101	SEM-CL	ld	4	15	74	0.5	300	CURVED, DIFFUSE, PROBABLY INHERITED
102	SEM-CL	ld	4	15	32	2	85	INTRAGRANULAR, VARIABLE APERTURE, ASSOCIATED DISSOLUTION ZONES, PROBABLY INHERITED
103	SEM-CL	lc	3	15	125	1	41	NARROW, AMBIGUOUS RELATIONSHIP TO CEMENT, PARALLEL SET, STRAIGHT TRACE
104	SEM-CL	ld	4	15	58	2	276	CURVED, DIFFUSE, PROBABLY INHERITED
105	SEM-CL	lc	3	15	130	1	41	NARROW, AMBIGUOUS RELATIONSHIP TO CEMENT, PARALLEL SET, STRAIGHT TRACE
106	SEM-CL	lc	3	15	83	1	42	NARROW, AMBIGUOUS RELATIONSHIP TO CEMENT, PARALLEL SET, STRAIGHT TRACE
107	SEM-CL	lb	3	15	44	1	341	PROBABLY CUTS CEMENT, STRAIGHT TRACE, APPARENTLY FILLED WITH SURROUNDING CEMENT
108	SEM-CL	ld	4	16	123	0.5	315	POSSIBLY INHERITED, NARROW, DIFFUSE, AMBIGUOUS RELATIONSHIP TO CEMENT
109	SEM-CL	lb	3	16	80	2	77	POSSIBLY CUTS CEMENT, FILLED WITH SURROUNDING CEMENT, STRAIGHT TRACE
110	SEM-CL	lc	3	16	90	1	298	STRAIGHT TRACE, DIFFUSE, AMBIGUOUS RELATIONSHIP TO CEMENT
111	SEM-CL	lc	3	16	40	1	322	STRAIGHT TRACE, DIFFUSE, AMBIGUOUS RELATIONSHIP TO CEMENT
112	SEM-CL	lb	4	16	12	1	84	STRAIGHT TRACE, DIFFUSE, AMBIGUOUS RELATIONSHIP TO CEMENT, TIP OF GRAIN, SHORT

113	SEM-CL	ld	3	16	95	2	14	INTRAGRANULAR, APPARENTLY FILLED WITH SURROUNDING CEMENT, ODDLY SHAPED WALLS.
114	SEM-CL	lc	3	16	28	1	0	AMBIGUOUS RELATIONSHIP TO CEMENT, DIFFUSE, ZIGZAGGING, ENDS WITHIN GRAIN
115	SEM-CL	lc	3	16	72	1	315	AMBIGUOUS RELATIONSHIP TO CEMENT, PROBABLY INHERITED, TIP OF GRAIN
116	SEM-CL	lb	2	16	15	4	66	LARGE APERTURE, TIP OF GRAIN, PROBABLY CUTS CEMENT, FILLED WITH SURROUNDING CEMENT
117	SEM-CL	lb	2	16,17	125	1	304	PROBABLY CUTS CEMENT, FILLED WITH SURROUNDING CEMENT, STRAIGHT TRACE
118	SEM-CL	lb	2	17	24	3	58	PROBABLY CUTS CEMENT, STRAIGHT TRACE, TIP OF GRAIN, FILLED WITH SURROUNDING CEMENT
119	SEM-CL	lb	2	17	39	3	37	PROBABLY CUTS CEMENT, VARIABLE APERTURE, TIP OF GRAIN, FILLED WITH SURROUNDING CEMENT
120	SEM-CL	la	1	17	75	17	89	LARGE APERTURE, CUTS CEMENT, PIECES OF GRAIN WITHIN FRACTURE, FILLED WITH SURROUNDING CEMENT
121	SEM-CL	lc	3	18	35	5	298	AMBIGUOUS RELATIONSHIP TO CEMENT, STRAIGHT TRACE
122	SEM-CL	lb	3	18	24	1	330	APPARENTLY CUTS CEMENT, CURVED, NARROW
123	SEM-CL	lb	2	18	120	2	48	APPARENTLY CUTS CEMENT, BORDER OF GRAIN, FILLED WITH SURROUNDING CEMENT, STRAIGHT TRACE, PARALLEL SET
124	SEM-CL	ld	2	19	60	2	52	INTRAGRANULAR, INSIDE GRAIN, APPARENTLY FILLED WITH SURROUNDING CEMENT, IRREGULAR TRACE, PARALLEL SET
125	SEM-CL	lc	2	19	118	3	59	ENDS WITHIN GRAIN, APPARENTLY FILLED WITH SURROUNDING CEMENT, IRREGULAR TRACE, PARALLEL SET

126	SEM-CL	lc	2	19	90	1	52	ENDS WITHIN GRAIN, APPARENTLY FILLED WITH SURROUNDING CEMENT, IRREGULAR TRACE, PARALLEL SET
127	SEM-CL	lb	2	19	108	1	63	APPARENTLY CUTS CEMENT, FILLED WITH SURROUNDING CEMENT, STRAIGHT TRACE, PARALLEL SET
128	SEM-CL	ld	3	19	33	3	35	INTRAGRANULAR, INSIDE GRAIN, APPARENTLY FILLED WITH SURROUNDING CEMENT, IRREGULAR TRACE
129	SEM-CL	lc	3	19	22	1	339	AMBIGUOUS RELATIONSHIP TO CEMENT, TIP OF GRAIN, SHORT, DIFFUSE
130	SEM-CL	lb	2	20	83	13	32	PROBABLY TRANS-CEMENT, VARIABLE APERTURE, PIECES OF GRIN WITHIN FRACTURE, ZIGZAGGING
131	SEM-CL	lc	3	20	100	1	356	NARROW, INTRAGRANULAR, STRAIGHT TRACE, AMBIGUOUS RELATIONSHIP TO CEMENT
132	SEM-CL	ld	4	20	50	0.5	356	INTRAGRANULAR, INSIDE GRAIN, DIFFUSE, STRAIGHT TRACE
133	SEM-CL	ld	4	20	63	0.5	4	INTRAGRANULAR, INSIDE GRAIN, DIFFUSE, STRAIGHT TRACE
134	SEM-CL	lc	4	21	102	0.5	15	NARROW, INTRAGRANULAR, STRAIGHT TRACE, AMBIGUOUS RELATIONSHIP TO CEMENT
135	SEM-CL	lc	2	21	42	1	324	AMBIGUOUS RELATIONSHIP TO CEMENT, ZIGZAGGING, PARALLEL SET, PARALLEL TO BORDER OF GRAIN
136	SEM-CL	lc	2	21	78	1	312	AMBIGUOUS RELATIONSHIP TO CEMENT, ZIGZAGGING, PARALLEL SET, PARALLEL TO BORDER OF GRAIN
137	SEM-CL	lb	2	21	122	2	305	PROBABLY CUTS CEMENT, STRAIGHT TRACE, PARALLEL SET
138	SEM-CL	lc	2	21	180	1	328	ZIGZAGGING, AMBIGUOUS RELATIONSHIP TO CEMENT, PARALLEL SET, DIFFUSE
139	SEM-CL	lb	2	21	132	3	313	STRAIGHT TRACE, PROBABLY CUTS CEMENT, PARALLEL TO BORDER OF GRAIN, PARALLEL SET

140	SEM-CL	lb	2	21	50	3	273	CURVED, PROBABLY CUTS CEMENT, TIP OF GRAIN, VARIABLE APERTURE
141	SEM-CL	lc	2	21	35	2	287	AMBIGUOUS RELATIONSHIP TO CEMENT, PARALLEL SET
142	SEM-CL	lc	2	21	45	2	273	AMBIGUOUS RELATIONSHIP TO CEMENT, PARALLEL SET
143	SEM-CL	lb	2	22	10	1	63	PROBABLY CUTS CEMENT, BORDER OF GRAIN, FILLED WITH SURROUNDING CEMENT
144	SEM-CL	lb	2	22	20	1	314	PROBABLY CUTS CEMENT, BORDER OF GRAIN, FILLED WITH SURROUNDING CEMENT
145	SEM-CL	lc	3	22	63	2	334	AMBIGUOUS RELATIONSHIP TO CEMENT, APPARENTLY FILLED WITH SURROUNDING CEMENT, DIFFUSE
146	SEM-CL	lc	3	22	25	2	345	AMBIGUOUS RELATIONSHIP TO CEMENT, APPARENTLY FILLED WITH SURROUNDING CEMENT, DIFFUSE
147	SEM-CL	lb	1	22	10	2	292	TIP OF GRAIN, PROBABLY CUTS CEMENT, SHORT, FILLED WITH SURROUNDING CEMENT
148	SEM-CL	la	1	23	178	5	274	CUTS CEMENT, STRAIGHT TRACE, FILLED WITH SURROUNDING CEMENT
149	SEM-CL	lb	1	23	30	2	63	BRANCHES FROM F-170, PROBABLY CUTS CEMENT, FILLED WITH SURROUNDING CEMENT
150	SEM-CL	lb	1	23	5	2	48	TIP OF GRAIN, PROBABLY CUTS CEMENT, FILLED WITH SURROUNDING CEMENT, SHORT
151	SEM-CL	lb	1	23	12	3	308	TIP OF GRAIN, PROBABLY CUTS CEMENT, FILLED WITH SURROUNDING CEMENT, SHORT
152	SEM-CL	lc	3	23	110	1	295	PARALLEL SET, AMBIGUOUS RELATIONSHIP TO CEMENT, STRAIGHT TRACE, CONTINUES OUTSIDE THE PICTURE
153	SEM-CL	lc	3	23	105	3	291	PARALLEL SET, AMBIGUOUS RELATIONSHIP TO CEMENT, CONTINUES OUTSIDE THE PICTURE, ZIGZAGGING

154	SEM-CL	lc	3	23	85	2	290	PARALLEL SET, AMBIGUOUS RELATIONSHIP TO CEMENT, STRAIGHT TRACE
155	SEM-CL	lc	3	23	55	2	272	AMBIGUOUS RELATIONSHIP TO CEMENT, STRAIGHT TRACE, ENDS WITHIN GRAIN
156	SEM-CL	lc	3	23	60	1	327	AMBIGUOUS RELATIONSHIP TO CEMENT, STRAIGHT TRACE, PARALLEL TO BORDER OF GRAIN
157	SEM-CL	lc	3	23	40	1	84	PARALLEL SET, AMBIGUOUS RELATIONSHIP TO CEMENT, STRAIGHT TRACE
158	SEM-CL	lc	3	23	49	1	88	PARALLEL SET, AMBIGUOUS RELATIONSHIP TO CEMENT, STRAIGHT TRACE
159	SEM-CL	lc	3	23	13	1	270	AMBIGUOUS RELATIONSHIP TO CEMENT, STRAIGHT TRACE, SHORT, LARGE APERTURE
160	SEM-CL	lc	2	23	49	3	290	PROBABLY TRANS-CEMENT, LARGE AND VARIABLE APERTURE, CURVE, TIP OF GRAIN

WELL: SAN JUAN 32-9

SAMPLE: 6008.1

DEPTH:6008.1

NOTCH AZIMUTH: 90

FRACTURE INVENTORY

FRACTURE NUMBER	DETECTION METHOD	Classification		PICTURE NUMBER	LENGTH (um)	APERTURE (um)	AZIMUTH (°)	OBSERVATIONS
		Laubach's (1997)	PREDICTIVE SUITABILITY					
1	PETROG. MIC.	la+	1	1			0	OBSERVED IN THE CORE, FILLED WITH CALCITE
2	SEM-CL	la+	1	3	450	15	340	OPEN
3	SEM-CL	la+	2	3	180	8	350	OPEN, TRANS-CEMENT
4	SEM-CL	lb	2	3	50	3	300	CLOSED, TRANS-CEMENT
5	SEM-CL	lb	2	3	40	5	40	CLOSED, PROBABLY TRANS-CEMENT
6	SEM-CL	lb	2	7	60	2	315	CURVED, PROBABLY TRANS-CEMENT, PROBABLY CRUSHING RELATED
7	SEM-CL	lb	3	7	20	2	10	PROBABLY TRANS-CEMENT, FILLED WITH QUARTZ, PROBABLY CRUSHING RELATED
8	SEM-CL	lb	3	7	20	2	10	PROBABLY TRANS-CEMENT, FILLED WITH QUARTZ, PROBABLY CRUSHING RELATED
9	SEM-CL	lc	3	7	40	1	290	INTRAGRANULAR, PROBABLY INHERITED
10	SEM-CL	lc	3	7	40	1	355	INTRAGRANULAR, PROBABLY INHERITED
11	SEM-CL	lc	3	7	40	4	10	TIP OF GRAIN
12	SEM-CL	lb	2	7	60	8	70	THICK, PIECES OF GRAIN INSIDE OF FRACTURE, PROBABLY TRANS-CEMENT
13	SEM-CL	lb	3	6	55	5	345	VARIABLE APERTURE, FILLED WITH QUARTZ

14	SEM-CL	ld	4	6	15	0.5	77	SMALL INTRAGRANULAR, UNKNOWN RELATIONSHIP WITH CEMENT
15	SEM-CL	lc	3	6	45	0.5	85	THIN, AMBIGUOUS RELATIONSHIP TO CEMENT
16	SEM-CL	lb	3	6	80	8	73	ODDLY SHAPED, VARIABLE APERTURE, TWO TYPES OF CEMENT (REACTIVATED?)
17	SEM-CL	lc	3	8	30	3	320	AMBIGUOUS RELATIONSHIP TO CEMENT, STRAIGHT TRACE
18	SEM-CL	lc	3	8	73	4	45	VARIABLE FRACTURE, AMBIGUOUS RELATIONSHIP TO CEMENT
19	SEM-CL	lc	3	8	15	2	57	TIP OF GRAIN, AMBIGUOUS RELATIONSHIP TO CEMENT, PARALLEL SET
20	SEM-CL	lc	4	8	30	2	45	INTRAGRANULAR, DOES NOT CUT ENTIRE GRAIN, PARALLEL SET
21	SEM-CL	lb	3	8	28	7	33	VARIABLE APERTURE, BORDER OF GRAIN, PROBABLY TRANS-CEMENT
22	SEM-CL	lc	3	8	25	3	45	INTRAGRANULAR, VARIABLE APERTURE, AMBIGUOUS RELATIONSHIP TO CEMENT
23	SEM-CL	la+	1	9	80	8	60	OPEN, ODDLY SHAPED, CONNECTS TO A PORE, SEEMS TO BE TRANSGRANULAR
24	SEM-CL	lc	3	9	18	3	70	VERY SMALL, INTRAGRANULAR, AMBIGUOUS RELATIONSHIP TO CEMENT
25	SEM-CL	lb	2	10	80	3	335	VARIABLE APERTURE, INTRAGRANULAR, PIECES OF GRAIN INSIDE OF FRACTURE
26	SEM-CL	lb	2	10	12	3	350	VERY SMALL, VARIABLE APERTURE, INTRAGRANULAR, PARALLEL SET
27	SEM-CL	lb	2	10	53	15	280	LARGE VARIABLE APERTURE, PROBABLY TRANS-CEMENT, FILLED WITH QUARTZ

28	SEM-CL	la+	1	11	80	10	0	CONTINUES OUT OF PHOTO, FILLED IN CALCITE, TRANSGRANULAR
29	SEM-CL	la+	1	11	290	11	350	TRANSGRANULAR, FILLED WITH CALCITE, Oval
30	SEM-CL	la+	1	11,12	310	7	355	BRANCHES FROM F31, TRANSGRANULAR, FILLED WITH CALCITE
31	SEM-CL	la+	1	11,12	575	9	353	SERPENTINE, FILLED WITH CALCITE, TRANSGRANULAR
32	SEM-CL	la	1	11	115	3	357	PARALLEL SET, TRANS-CEMENT, FILLED WITH CALCITE
33	SEM-CL	lc	1	11	50	2	20	BRANCHES FROM F32, FILLED WITH CALCITE, INTRAGRANULAR
34	SEM-CL	la	1	11	115	10	75	ODDLY SHAPED, PROBABLY TRANSGRANULAR, FILLED WITH CALCITE
35	SEM-CL	la+	1	12,13	510	9	353	PARTIALLY FILLED WITH CALCITE & QUARTZ, TRANSGRANULAR, PARALLEL SET
36	SEM-CL	la+	1	13	350	12	352	CONTINUES OUT OF PHOTO, PARTIALLY FILLED WITH CALCITE, TRANSGRANULAR, CONNECTS WITH F35
37	SEM-CL	la+	1	12,13	500	8	350	PARTIALLY FILLED WITH CALCITE & QUARTZ, TRANSGRANULAR, PARALLEL SET
38	SEM-CL	la	1	17	45	10	354	FILLED WITH QUARTZ, PARTIALLY DISPLACED, VARIABLE APERTURE
39	SEM-CL	la	1	17	20	8	0	ZIGZAGGING, PARTIALLY OPEN, PARTIALLY FILLED WITH QUARTZ, TIP OF THE GRAIN
40	SEM-CL	lc	2	17	12	0.5	0	VERY SMALL, PARALLEL SET, AMBIGUOUS RELATIONSHIP WITH THE CEMENT, INTRAGRANULAR
41	SEM-CL	lc	2	17	18	0.5	352	VERY SMALL, PARALLEL SET, AMBIGUOUS RELATIONSHIP WITH THE CEMENT, INTRAGRANULAR

42	SEM-CL	la	1	18	160	6	352	LARGE APERTURE, STRAIGHT TRACE, TRANS-CEMENT FILLED WITH CALCITE
43	SEM-CL	la	1	18	70	8	310	LARGE APERTURE, STRAIGHT TRACE, TRANS-CEMENT FILLED WITH CALCITE
44	SEM-CL	ld	4	18	82	0.5	55	NARROW, PROBABLY INHERITED, CUT BY F43, INTRAGRANULAR
45	SEM-CL	lc	3	18	105	1	12	INTRAGRANULAR, AMBIGUOUS RELATIONSHIP WITH CEMENT
46	SEM-CL	lc	3	18	42	1	0	TIP OF GRAIN, AMBIGUOUS RELATIONSHIP WITH CEMENT
47	SEM-CL	lc	3	18	110	1	303	ZIGZAG PATTERN, INTRAGRANULAR, AMBIGUOUS RELATIONSHIP WITH CEMENT
48	SEM-CL	3D	5	18	48	1	90	PROBABLY INHERITED, INTRAGRANULAR
49	SEM-CL	lc	2	18	80	3	5	INTRAGRANULAR, CRUSHED GRAIN, AMBIGUOUS RELATIONSHIP TO CEMENT
50	SEM-CL	la	1	18	43	5	58	CURVED, PROBABLY TRANS-CEMENT, PIECES OF GRAIN INSIDE FRACTURE, BORDER OF GRAIN
51	SEM-CL	ld	4	18	33	0.5	320	INTRAGRANULAR, PROBABLY INHERITED
52	SEM-CL	lc	3	18	43	1	50	INTRAGRANULAR, BORDER OF GRAIN, BRANCHES FROM F50
53	SEM-CL	ld	4	18	30	0.5	332	PROBABLY INHERITED, INTRAGRANULAR
54	SEM-CL	lc	3	18	22	1	338	AMBIGUOUS RELATIONSHIP WITH CEMENT, BRANCHES FROM F49
55	SEM-CL	lc	3	18	47	1	27	INTRAGRANULAR, AMBIGUOUS RELATIONSHIP WITH CEMENT, STRAIGHT TRACE
56	SEM-CL	lc	3	18	39	1	0	TIP OF GRAIN, ZIGZAG PATTERN, AMBIGUOUS RELATIONSHIP TO CEMENT

57	SEM-CL	lc	2	19	28	3	327	STRAIGHT TRACE, AMBIGUOUS RELATIONSHIP WITH CEMENT, INTRAGRANULAR
58	SEM-CL	lb	2	19	32	8	22	VARIABLE APERTURE, DISPLACED, PROBABLY TRANS-CEMENT
59	SEM-CL	lc	2	19	50	2	353	INTRAGRANULAR, VARIABLE APERTURE, AMBIGUOUS RELATIONSHIP WITH CEMENT
60	SEM-CL	lb	2	19	52	18	273	LARGE APERTURE, PROBABLY TRANS-CEMENT WITH PIECES OF GRAIN INSIDE FRACTURE
61	SEM-CL	lb	2	19	90	20	341	LARGE APERTURE, PROBABLY TRANS-CEMENT WITH PIECES OF GRAIN INSIDE FRACTURE
62	SEM-CL	lc	3	19	137	2	330	CUTS A GRAIN OF CHERT, AMBIGUOUS RELATIONSHIP WITH CEMENT
63	SEM-CL	lc	3	19	40	2	295	BRANCHES FROM F62, INTRAGRANULAR
64	SEM-CL	lc	3	19	40	2	46	ALSO BRANCHES FROM F62, INTRAGRANULAR
65	SEM-CL	la+	1	20	320	3	340	CONTINUES OUTSIDE PHOTO, PARTIALLY FILLED WITH CALCITE & QUARTZ, TRANSGRANULAR, PARALLEL SET
66	SEM-CL	la+	1	20	130	2	358	BRANCHES FROM F42, PARTIALLY OPEN, PARTIALLY FILLED WITH CALCITE & QUARTZ, TRANSGRANULAR
67	SEM-CL	lb	2	20	48	3	295	STRAIGHT TRACE, PROBABLY TRANS-CEMENT
68	SEM-CL	lc	3	21	40	8	46	STRAIGHT TRACE, AMBIGUOUS RELATIONSHIP TO CEMENT
69	SEM-CL	lb	2	21	38	7	80	VARIABLE APERTURE, TWO CEMENTATION EVENTS, PROBABLY CUTS CEMENT

70	SEM-CL	lc	3	21	40	1	86	ZIGZAGGING, PARTLY BORDER OF GRAIN, MIGHT BE INHERITED
71	SEM-CL	lb	2	21	73	3	67	PROBABLY CUTS CEMENT, VARIABLE APERTURE
72	SEM-CL	la+	3	21	150	2	300	OPEN, CUTS CALCITE CEMENTATION IN MACROFRACTURE, MIGHT BE INDUCED
73	SEM-CL	la	3	21	45	10	32	VARIABLE APERTURE, TRANS-CEMENT, DISPLACED, PROBABLY CRUSHING RELATED
74	SEM-CL	la	3	21	23	8	272	STRAIGHT TRACE, LARGE APERTURE, PIECES OF GRAIN INSIDE FRACTURE, PROBABLY CRUSHING RELATED
75	SEM-CL	la	3	21	29	7	88	STRAIGHT TRACE, PIECES OF GRAIN INSIDE FRACTURE, PROBABLY CRUSHING RELATED
76	SEM-CL	la	3	21	110	8	10	ODDLY SHAPED, VARIABLE APERTURE, TRANS-CEMENT, PROBABLY CRUSHING RELATED
77	SEM-CL	lc	3	21	25	1	321	INTRAGRANULAR, BRANCHES FROM F76, AMBIGUOUS RELATIONSHIP WITH CEMENT
78	SEM-CL	lc	3	21	18	0.5	321	CURVED, BRANCHES FROM F76, AMBIGUOUS RELATIONSHIP WITH CEMENT
79	SEM-CL	lb	3	21	47	3	30	PROBABLY TRANS-CEMENT, PROBABLY CRUSHING RELATED, VARIABLE APERTURE
80	SEM-CL	lc	3	22	72	2	38	INTRAGRANULAR, PROBABLY CRUSHING RELATED, AMBIGUOUS RELATIONSHIP TO CEMENT
81	SEM-CL	lc	3	22	75	2	352	INTRAGRANULAR, PROBABLY CRUSHING RELATED, AMBIGUOUS RELATIONSHIP TO CEMENT

82	SEM-CL	lc	3	22	90	2	300	INTRAGRANULAR, PROBABLY CRUSHING RELATED, AMBIGUOUS RELATIONSHIP TO CEMENT
83	SEM-CL	ld	4	22	28	1	76	NARROW, INTRAGRANULAR
84	SEM-CL	ld	4	22	27	1	290	NARROW, INTRAGRANULAR, TIP OF GRAIN
85	SEM-CL	ld	4	22	43	1	89	NARROW, INTRAGRANULAR
86	SEM-CL	lb	3	22	140	5	315	ILL-DEFINED, PROBABLY TRANS-CEMENT
87	SEM-CL	lb	3	22	98	4	321	ILL-DEFINED, PROBABLY TRANS-CEMENT
88	SEM-CL	ld	4	22	30	4	39	ILL-DEFINED
89	SEM-CL	ld	4	22	42	3	19	ILL-DEFINED
90	SEM-CL	lb	2	23	18	3	80	TIP OF GRAIN, PROBABLY TRANS-CEMENT, STRAIGHT TRACE
91	SEM-CL	lb	2	23	51	12	87	VARIABLE APERTURE, DISPLACED, PROBABLY CUTS CEMENT
92	SEM-CL	lb	2	23	65	3	310	INTRAGRANULAR, VARIABLE APERTURE, PROBABLY TRANS-CEMENT
93	SEM-CL	ld	4	23	12	0.5	346	VERY SMALL, TIP OF GRAIN, ODDLY SHAPED
94	SEM-CL	ld	4	23	11	0.5	352	VERY SMALL, TIP OF GRAIN, STRAIGHT TRACE
95	SEM-CL	la	1	23	55	8	340	TRANS-CEMENT, BORDER OF GRAIN, CURVED
96	SEM-CL	lc	3	23	80	1	21	INTRAGRANULAR, AMBIGUOUS RELATIONSHIP WITH CEMENT, SERPENTINE
97	SEM-CL	lc	3	23	28	0.5	348	INTRAGRANULAR, AMBIGUOUS RELATIONSHIP WITH CEMENT
98	SEM-CL	lc	3	24	63	5	39	INTRAGRANULAR, AMBIGUOUS RELATIONSHIP TO CEMENT, STRAIGHT TRACE
99	SEM-CL	ld	4	25	32	1	28	VERY DIFFUSE, ODDLY SHAPED, TIP OF GRAIN

100	SEM-CL	lc	2	25	127	9	5	INSIDE CHERT GRAIN, AMBIGUOUS RELATIONSHIP TO CEMENT
101	SEM-CL	lb	2	25	48	11	11	TIP OF GRAIN, INSIDE CHERT GRAIN
102	SEM-CL	lc	3	25	45	2	22	ILL-DEFINED, CURVED, AMBIGUOUS RELATIONSHIP TO CEMENT
103	SEM-CL	la	1	26	43	5	81	LARGE APERTURE, PIECES OF GRAIN INSIDE FRACTURE, TRANS-CEMENT
104	SEM-CL	lc	3	26	73	1	21	NARROW, INTRAGRANULAR, AMBIGUOUS RELATIONSHIP TO CEMENT
105	SEM-CL	ld	4	26	71	1	302	DIFFUSE, ILL-DEFINED, PROBABLY INHERITED

WESTWATER SPRINGS

SAMPLE: WS13

NOTCH AZIMUTH:

FRACTURE INVENTORY

FRACTURE NUMBER	DETECTION METHOD	Classification		PICTURE NUMBER	LENGTH (um)	APERTURE (um)	AZIMUTH (°)	OBSERVATIONS
		Laubach's (1997)	PREDICTIVE SUITABILITY					
1	SEM-CL	lc	2	1	37	2	48	AMBIGUOUS RELATIONSHIP TO CEMENT, BORDER OF GRAIN, APPARENTLY FILLED WITH SURROUNDING CEMENT
2	SEM-CL	lb	2	1	32	1	13	PROBABLY CUTS CEMENT, FILLED WITH SURROUNDING CEMENT, STRAIGHT TRACE
3	SEM-CL	ld	4	1	53	1	308	PROBABLY INHERITED, THIN, DIFFUSE, TIP OF GRAIN, PARALLEL SET
4	SEM-CL	ld	4	1	87	1	315	PROBABLY INHERITED, THIN, DIFFUSE, PARALLEL SET
5	SEM-CL	ld	4	1	72	1	312	PROBABLY INHERITED, THIN, DIFFUSE, PARALLEL SET
6	SEM-CL	ld	4	1	101	1	312	PROBABLY INHERITED, THIN, DIFFUSE, PARALLEL SET
7	SEM-CL	ld	4	1	99	1	310	PROBABLY INHERITED, THIN, DIFFUSE, PARALLEL SET
8	SEM-CL	ld	4	1	97	1	310	PROBABLY INHERITED, THIN, DIFFUSE, PARALLEL SET
9	SEM-CL	ld	4	1	21	1	328	PROBABLY INHERITED, THIN, DIFFUSE, TIP OF GRAIN, PARALLEL SET
10	SEM-CL	ld	4	1	39	1	323	PROBABLY INHERITED, THIN, DIFFUSE, PARALLEL SET
11	SEM-CL	ld	4	1	43	1	325	PROBABLY INHERITED, THIN, DIFFUSE, PARALLEL SET
12	SEM-CL	ld	4	1	29	1	323	PROBABLY INHERITED, THIN, DIFFUSE, PARALLEL SET
13	SEM-CL	lb	2	1	50	2	0	PROBABLY CUTS CEMENT, FILLED WITH SURROUNDING CEMENT, PARALLEL SET
14	SEM-CL	lb	2	1	6	3	14	PROBABLY CUTS CEMENT, FILLED WITH SURROUNDING CEMENT, PARALLEL SET, LARGE APERTURE, SMALL

15	SEM-CL	ld	4	1	33	1	32	PROBABLY INHERITED, THIN, DIFFUSE, PARALLEL SET
16	SEM-CL	ld	4	1	55	1	29	PROBABLY INHERITED, THIN, DIFFUSE, PARALLEL SET
17	SEM-CL	lb	2	1	70	3	288	PROBABLY CUTS CEMENT, FILLED WITH SURROUNDING CEMENT, TIP OF GRAIN, CURVED
18	SEM-CL	lb	2	1	119	6	302	PROBABLY CUTS CEMENT, FILLED WITH SURROUNDING CEMENT, VARIABLE APERTURE
19	SEM-CL	ld	4	1	49	0.5	84	PROBABLY INHERITED, THIN, DIFFUSE, PARALLEL SET, DISPLACED BY F-18
20	SEM-CL	ld	4	1	95	0.5	68	PROBABLY INHERITED, THIN, DIFFUSE, PARALLEL SET, DISPLACED BY F-18
21	SEM-CL	ld	4	1	42	0.5	64	PROBABLY INHERITED, THIN, DIFFUSE, PARALLEL SET, DISPLACED BY F-18
22	SEM-CL	ld	4	1	108	0.5	69	PROBABLY INHERITED, THIN, DIFFUSE, PARALLEL SET, DISPLACED BY F-18
23	SEM-CL	ld	4	1	128	1	295	PROBABLY INHERITED, THIN, DIFFUSE
24	SEM-CL	ld	4	1	112	1	77	PROBABLY INHERITED, THIN, DIFFUSE
25	SEM-CL	lc	2	1	70	1	71	AMBIGUOUS RELATIONSHIP TO CEMENT, PARALLEL SET, STRAIGHT TRACE
26	SEM-CL	lb	2	1	125	1	63	PROBABLY CUTS CEMENT, FILLED WITH SURROUNDING CEMENT, ZIGZAGGING, CUTS INHERITED FEATURES, PARALLEL SET
27	SEM-CL	lb	2	1	25	3	46	PROBABLY CUTS CEMENT, FILLED WITH SURROUNDING CEMENT, STRAIGHT TRACE, ENDS WITHIN GRAIN, PARALLEL SET
28	SEM-CL	lb	2	1	50	1	53	PROBABLY CUTS CEMENT, FILLED WITH SURROUNDING CEMENT, CURVED, CUTS INHERITED FEATURES, PARALLEL SET
29	SEM-CL	lb	2	2	130	1	25	PROBABLY CUTS CEMENT, FILLED WITH SURROUNDING CEMENT, ZIGZAGGING TRACE, PARALLEL TO BORDER OF GRAIN
30	SEM-CL	ld	4	2	35	8	338	DISSOLUTION FEATURE?, WITHIN GRAIN, PROBABLY FILLED WITH SURROUNDING CEMENT

31	SEM-CL	lb	2	2	163	1	47	PROBABLY CUTS CEMENT, FILLED WITH SURROUNDING CEMENT, ZIGZAGGING TRACE, CUTS INHERITED FEATURES WITHIN GRAIN
32	SEM-CL	ld	4	2	75	2	311	PROBABLY INHERITED, DIFFUSE, CURVED, WITHIN GRAIN
33	SEM-CL	lb	2	2	126	1	41	PROBABLY CUTS CEMENT, FILLED WITH SURROUNDING CEMENT, SLIGHTLY ZIGZAGGING TRACE, PARALLEL SET
34	SEM-CL	la	1	2	110	18	356	CUTS CEMENT, TWO CEMENTATION EVENTS, LARGE APERTURE, ENDS WITHIN GRAIN, STRAIGHT TRACE
35	SEM-CL	ld	4	3	30	0.5	39	PROBABLY INHERITED, THIN, STRAIGHT TRACE, AFFECTED BY DISSOLUTION ZONE AT BORDER OF GRAIN
36	SEM-CL	ld	4	3	62	0.5	57	PROBABLY INHERITED, THIN, STRAIGHT TRACE, AFFECTED BY DISSOLUTION ZONE AT BORDER OF GRAIN
37	SEM-CL	ld	4	3	35	0.5	56	PROBABLY INHERITED, THIN, STRAIGHT TRACE, AFFECTED BY DISSOLUTION ZONE AT BORDER OF GRAIN
38	SEM-CL	ld	4	3	134	0.5	334	PROBABLY INHERITED, THIN, STRAIGHT TRACE, ENDS WITHIN GRAIN
39	SEM-CL	lc	4	3	46	1	82	AMBIGUOUS RELATIONSHIP TO CEMENT, STRAIGHT TRACE
40	SEM-CL	ld	4	3	140	5	339	PROBABLY INHERITED, DISSOLUTION ZONE ALONG FRACTURE
41	SEM-CL	ld	4	3	28	4	51	PROBABLY INHERITED, ASSOCIATED DISSOLUTION ZONE, WITHIN GRAIN
42	SEM-CL	ld	4	3	142	1	58	PROBABLY INHERITED, THIN, STRAIGHT TRACE, PARALLEL SET
43	SEM-CL	ld	4	3	122	1	59	PROBABLY INHERITED, THIN, STRAIGHT TRACE, PARALLEL SET
44	SEM-CL	lc	2	4	110	6	27	CLOSE TO PRESSURE SOLUTION ZONE, AMBIGUOUS RELATIONSHIP TO CEMENT, ENDS WITHIN GRAIN
45	SEM-CL	lb	2	4	63	1	350	PROBABLY CUTS CEMENT, FILLED WITH SURROUNDING CEMENT, ZIGZAGGING TRACE, PARALLEL TO BORDER OF GRAIN

46	SEM-CL	lc	2	4	145	15	90	AMBIGUOUS RELATIONSHIP TO CEMENT, VARIABLE APERTURE, PROBABLY TWO CEMENTATION EVENTS, LARGE APERTURE
47	SEM-CL	lb	2	4	60	3	281	PROBABLY CUTS CEMENT, FILLED WITH SURROUNDING CEMENT, ZIGZAGGING TRACE, PARALLEL SET
48	SEM-CL	la	2	4	55	3	315	CUTS CEMENT, PROBABLY DISPLACED, STRAIGHT TRACE, ASSOCIATED DISSOLUTION ZONE, TIP OF GRAIN
49	SEM-CL	lc	4	5	20	2	285	AMBIGUOUS RELATIONSHIP TO CEMENT, PARALLEL SET, STRAIGHT TRACE, ENDS WITHIN GRAIN
50	SEM-CL	lc	4	5	40	2	277	AMBIGUOUS RELATIONSHIP TO CEMENT, PARALLEL SET, STRAIGHT TRACE, ENDS WITHIN GRAIN
51	SEM-CL	lb	2	5	18	4	28	PROBABLY CUTS CEMENT, SMALL, FILLED WITH SURROUNDING CEMENT, TIP OF GRAIN
52	SEM-CL	ld	4	5	152	1	280	PROBABLY INHERITED, THIN, DIFFUSE, STRAIGHT TRACE, PARALLEL SET
53	SEM-CL	ld	4	5	70	0.5	274	PROBABLY INHERITED, THIN, TIP OF GRAIN, CURVED TRACE, PARALLEL SET
54	SEM-CL	ld	4	5	142	1	273	PROBABLY INHERITED, THIN, CURVED TRACE, PARALLEL SET
55	SEM-CL	ld	4	5	178	0.5	279	PROBABLY INHERITED, THIN, CURVED TRACE, PARALLEL SET
56	SEM-CL	ld	4	5	168	0.5	299	PROBABLY INHERITED, THIN, STRAIGHT TRACE, PARALLEL SET
57	SEM-CL	ld	4	5,6	413	0.5	335	PROBABLY INHERITED, THIN, TIP OF GRAIN, STRAIGHT TRACE
58	SEM-CL	ld	4	6	160	1	63	PROBABLY INHERITED, THIN, STRAIGHT TRACE.
59	SEM-CL	ld	4	6	310	1	293	PROBABLY INHERITED, THIN, STRAIGHT TRACE, PARALLEL SET
60	SEM-CL	ld	4	6	335	1	300	PROBABLY INHERITED, THIN, STRAIGHT TRACE, PARALLEL SET
61	SEM-CL	la	1	6	310	21	293	CUTS CEMENT, PROBABLY TWO CEMENTATION EVENTS, PARALLEL SET, STRAIGHT, PIECES OF GRAIN IN FRACTURE

62	SEM-CL	ld	4	6	32	2	326	PROBABLY INHERITED, WITHIN GRAIN, ASSOCIATED DISSOLUTION ZONE?
63	SEM-CL	ld	4	6	93	1	2	PROBABLY INHERITED, THIN, STRAIGHT TRACE, PARALLEL SET, CUT BY F-61
64	SEM-CL	ld	4	6	72	1	15	PROBABLY INHERITED, THIN, STRAIGHT TRACE, PARALLEL SET, CUT BY F-61
65	SEM-CL	la	1	6	140	3	28	CUTS CEMENT, CURVED TRACE, PARALLEL SET, PIECES OF GRAIN IN FRACTURE
66	SEM-CL	la	1	6	82	2	15	CUTS CEMENT, CURVED TRACE, PARALLEL SET, PROBABLY AFFECTED BY PRESSURE SOLUTION ZONE
67	SEM-CL	la	1	6	75	4	30	CUTS CEMENT, CURVED TRACE, PARALLEL SET, AFFECTED BY PRESSURE SOLUTION ZONE, PIECES OF GRAIN IN FRACTURE
68	SEM-CL	la	1	6	50	4	17	CUTS CEMENT, CURVED TRACE, PARALLEL SET, PROBABLY AFFECTED BY PRESSURE SOLUTION ZONE
69	SEM-CL	la	1	6	118	10	39	CUTS CEMENT, CURVED TRACE, PARALLEL SET, AFFECTED BY PRESSURE SOLUTION ZONE, PIECES OF GRAIN IN FRACTURE
70	SEM-CL	lc	3	7,8	125	3	308	AMBIGUOUS RELATIONSHIP TO CEMENT, ENDS WITHIN GRAIN, CURVED TRACE
71	SEM-CL	lc	3	7	65	1	348	AMBIGUOUS RELATIONSHIP TO CEMENT, PROBABLY INHERITED, TIP OF GRAIN, IRREGULAR TRACE
72	SEM-CL	lb	3	7,8	48	1	336	PROBABLY CUTS CEMENT, FILLED WITH SURROUNDING CEMENT, SLIGHTLY ZIGZAGGING TRACE, SHORT
73	SEM-CL	ld	4	7,9	210	10	335	PROBABLY INHERITED, WIDE, PROBABLY ASSOCIATED DISSOLUTION ZONE
74	SEM-CL	lc	4	7,10	170	6	342	COMPLEX TRACE, AMBIGUOUS RELATIONSHIP TO CEMENT, BRANCHES IN DIFFERENT DIRECTIONS
75	SEM-CL	lb	2	8	32	2	319	PROBABLY CUTS CEMENT, FILLED WITH SURROUNDING CEMENT, TIP OF GRAIN
76	SEM-CL	lb	2	8,9	75	3	304	PROBABLY CUTS CEMENT, FILLED WITH SURROUNDING CEMENT, VARIABLE APERTURE, ENDS WITHIN GRAIN

77	SEM-CL	lb	2	8,9	98	4	289	PROBABLY CUTS CEMENT, FILLED WITH SURROUNDING CEMENT, VARIABLE APERTURE, ENDS WITHIN GRAIN
78	SEM-CL	la+	1	8,9	280	25	63	TRANSGRANULAR, CURVED TRACE, PARALLEL SET, TWO CEMENTATION
79	SEM-CL	lc	4	8A	70	10	321	AMBIGUOUS RELATIONSHIP TO CEMENT, SHORT, LARGE VARIABLE APERTURE, PARALLEL SET, PROBABLY INHERITED
80	SEM-CL	lc	4	8A	240	8	325	AMBIGUOUS RELATIONSHIP TO CEMENT, IRREGULAR TRACE, PARALLEL SET, PROBABLY INHERITED, ASSOCIATED DISSOLUTION ZONE
81	SEM-CL	lc	4	8A	57	11	318	AMBIGUOUS RELATIONSHIP TO CEMENT, SHORT, LARGE VARIABLE APERTURE, PARALLEL SET, PROBABLY INHERITED
82	SEM-CL	lc	4	8A	80	1	351	AMBIGUOUS RELATIONSHIP TO CEMENT, STRAIGHT TRACE, PARALLEL SET, PROBABLY INHERITED
83	SEM-CL	lc	4	8A	150	0.5	13	AMBIGUOUS RELATIONSHIP TO CEMENT, STRAIGHT TRACE, PARALLEL SET, PROBABLY INHERITED
84	SEM-CL	lb	2	8A	138	1	55	PROBABLY CUTS CEMENT, FILLED WITH SURROUNDING CEMENT, PARALLEL TO F-78, ENDS WITHIN GRAIN
85	SEM-CL	lb	2	8A,9,10	248	1	345	PROBABLY CUTS CEMENT, FILLED WITH SURROUNDING CEMENT, STRAIGHT, INTRAGRANULAR
86	SEM-CL	lb	2	8A	22	2	43	PROBABLY CUTS CEMENT, FILLED WITH SURROUNDING CEMENT, STRAIGHT TRACE, ENDS WITHIN GRAIN, SHORT
87	SEM-CL	lb	2	9,10	60	3	283	PROBABLY CUTS CEMENT, FILLED WITH SURROUNDING CEMENT, CURVED TRACE, PARALLEL TO BORDER OF GRAIN
88	SEM-CL	la	2	10	20	3	282	CUTS CEMENT, FILLED WITH SURROUNDING CEMENT, CURVED TRACE, AFFECTS BORDER OF GRAIN, SHORT
89	SEM-CL	lc	4	9,10	162	0.5	287	AMBIGUOUS RELATIONSHIP TO CEMENT, THIN, STRAIGHT TRACE, PARALLEL TO BORDER OF GRAIN, PROBABLY INHERITED

90	SEM-CL	ld	4	10	53	2	328	PROBABLY INHERITED, TIP OF GRAIN, CURVED TRACE, DIFFUSE, PARALLEL SET
91	SEM-CL	ld	4	9,10	85	2	347	PROBABLY INHERITED, STRAIGHT TRACE, DIFFUSE, PARALLEL SET
92	SEM-CL	ld	4	9,10	100	1	323	PROBABLY INHERITED, STRAIGHT TRACE, DIFFUSE, PARALLEL SET
93	SEM-CL	ld	4	9,10	110	3	323	PROBABLY INHERITED, STRAIGHT TRACE, DIFFUSE, PARALLEL SET
94	SEM-CL	la	1	10	200	30	27	PARTIALLY FILLED WITH QUARTZ CEMENT, IRREGULAR TRACE, PIECES OF GRAIN WITHIN FRACTURE,
95	SEM-CL	la	1	10	110	22	63	PARTIALLY FILLED WITH QUARTZ CEMENT, IRREGULAR TRACE, VARIABLE APERTURE, BRANCHES FROM F-95
96	SEM-CL	lb	2	11	265	4	21	PROBABLY CUTS CEMENT, FILLED WITH SURROUNDING CEMENT, ZIGZAGGING TRACE, CONTINUES OUT OF PHOTO
97	SEM-CL	lc	3	11,12	172	3	310	AMBIGUOUS RELATIONSHIP TO CEMENT, DIFFUSE, SLIGHTLY ZIGZAGGING TRACE, CONTINUES OUTSIDE PHOTO
98	SEM-CL	lc	3	11	180	3	282	AMBIGUOUS RELATIONSHIP TO CEMENT, DIFFUSE, SLIGHTLY ZIGZAGGING TRACE, CONTINUES OUTSIDE PHOTO
99	SEM-CL	lc	3	10	140	1	308	AMBIGUOUS RELATIONSHIP TO CEMENT, STRAIGHT TRACE, DIFFUSE
100	SEM-CL	lb	4	12	42	2	30	CUTS CEMENT, FILLED WITH SURROUNDING CEMENT, IRREGULAR, PROBABLY ASSOCIATED TO DISSOLUTION, INTRAGRANULAR
101	SEM-CL	lc	4	12	62	2	73	AMBIGUOUS RELATIONSHIP TO CEMENT, DIFFUSE, PROBABLY ASSOCIATED TO DISSOLUTION
102	SEM-CL	lc	4	12	145	1.5	16	AMBIGUOUS RELATIONSHIP TO CEMENT, STRAIGHT TRACE, PROBABLY INHERITED
103	SEM-CL	lc	4	12	152	1	308	AMBIGUOUS RELATIONSHIP TO CEMENT, ZIGZAGGING TRACE, PROBABLY ASSOCIATED TO DISSOLUTION, PROBABLY

104	SEM-CL	la	1	12	80	6	74	INTRACEMENT, FILLED WITH SURROUNDING CEMENT, STRAIGHT TRACE, PARALLEL TO BORDER OF GRAIN
105	SEM-CL	ld	4	13	65	18	312	PROBABLY INHERITED, LARGE APERTURE, SHORT, PROBABLY ASSOCIATED TO DISSOLUTION ZONE
106	SEM-CL	lb	2	16	160	8	287	PROBABLY CUTS CEMENT, FILLED WITH SURROUNDING CEMENT, PARALLEL SET, VARIABLE APERTURE, DISPLACED
107	SEM-CL	lc	2	16	21	1	21	FILLED WITH SURROUNDING CEMENT, INTRAGRANULAR, STRAIGHT, PARALLEL SET
108	SEM-CL	lc	2	16	15	6	13	PROBABLY FILLED WITH SURROUNDING CEMENT, WITHIN GRAIN, STRAIGHT, PARALLEL SET
109	SEM-CL	lc	2	16	28	3	346	PROBABLY FILLED WITH SURROUNDING CEMENT, WITHIN GRAIN, STRAIGHT PARALLEL SET
110	SEM-CL	lb	2	16	65	3	73	PROBABLY CUTS CEMENT, FILLED WITH SURROUNDING CEMENT, STRAIGHT TRACE, PARALLEL SET
111	SEM-CL	lb	2	16	85	4	66	PROBABLY CUTS CEMENT, FILLED WITH SURROUNDING CEMENT, ZIGZAGGING TRACE, PARALLEL SET, VARIABLE APERTURE, DISPLACED
112	SEM-CL	lc	2	16	38	1	349	AMBIGUOUS RELATIONSHIP TO CEMENT, FILLED WITH SURROUNDING CEMENT, STRAIGHT TRACE, PARALLEL SET
113	SEM-CL	lc	2	16	35	1	345	AMBIGUOUS RELATIONSHIP TO CEMENT, FILLED WITH SURROUNDING CEMENT, STRAIGHT TRACE, PARALLEL SET
114	SEM-CL	lb	2	16	49	3	25	PROBABLY CUTS CEMENT, FILLED WITH SURROUNDING CEMENT, STRAIGHT TRACE, PARALLEL SET, DISPLACED
115	SEM-CL	lb	2	16	180	3	312	PROBABLY CUTS CEMENT, FILLED WITH SURROUNDING CEMENT, ZIGZAGGING, PARALLEL SET, VARIABLE APERTURE, DISPLACED

116	SEM-CL	lc	2	16	72	1	84	PROBABLY CUTS CEMENT, FILLED WITH SURROUNDING CEMENT, PARALLEL SET, VARIABLE APERTURE, DISPLACED
117	SEM-CL	lc	3	14	280	1	89	AMBIGUOUS RELATIONSHIP TO CEMENT, ASSOCIATED DISSOLUTION ZONE, PARALLEL TO BORDER OF GRAIN, PROBABLY INHERITED
118	SEM-CL	lc	4	14,15	250	0.5	61	AMBIGUOUS RELATIONSHIP TO CEMENT, PARALLEL TO BORDER OF GRAIN, PROBABLY INHERITED, THIN
119	SEM-CL	lc	3	14	98	1	344	AMBIGUOUS RELATIONSHIP TO CEMENT, IRREGULAR TRACE, ENDS AGAINST F-120
120	SEM-CL	lc	3	14	235	1	289	AMBIGUOUS RELATIONSHIP TO CEMENT, STRAIGHT TRACE
121	SEM-CL	lc	3	14	78	1	307	AMBIGUOUS RELATIONSHIP TO CEMENT, STRAIGHT TRACE, ENDS AGAINST F-120
122	SEM-CL	lc	3	15	30	2	53	PROBABLY CUTS CEMENT, PROBABLY FILLED WITH SURROUNDING CEMENT, PARALLEL SET, SHORT, ENDS WITHIN GRAIN AGAINST F-123
123	SEM-CL	lb	2	15	102	8	311	PROBABLY CUTS CEMENT, FILLED WITH SURROUNDING CEMENT, PROBABLY ASSOCIATED DISSOLUTION ZONE
124	SEM-CL	lb	2	15	25	2	45	PROBABLY CUTS CEMENT, PROBABLY FILLED WITH SURROUNDING CEMENT, PARALLEL SET, SHORT, ENDS AGAINST F-123
125	SEM-CL	ld	4	15	113	20	320	PROBABLY INHERITED, LARGE APERTURE, CUT BY F-126, PROBABLY ASSOCIATED TO INHERITED DISSOLUTION ZONE
126	SEM-CL	lb	2	15	42	2	25	PROBABLY CUTS CEMENT, PROBABLY FILLED WITH SURROUNDING CEMENT, PARALLEL SET, SHORT, ENDS WITHIN GRAIN, STRAIGHT TRACE
127	SEM-CL	la	1	15	110	13	338	CUTS CEMENT, FILLED WITH SURROUNDING CEMENT, VARIABLE APERTURE, SLIGHTLY ZIGZAGGING, PIECES OF GRAIN IN FRACTURE

128	SEM-CL	la	1	15	73	15	54	CUTS CEMENT, FILLED WITH SURROUNDING CEMENT, VARIABLE APERTURE, ZIGZAGGING, PIECES OF GRAIN IN FRACTURE
129	SEM-CL	la	1	17	100	40	335	CUTS CEMENT, TWO CEMENTATION EVENTS, LARGE APERTURE, STRAIGHT TRACE, PIECES OF GRAIN WITHIN FRACTURE
130	SEM-CL	la	1	17	45	4	83	CUTS CEMENT, FILLED WITH SURROUNDING CEMENT, CURVED TRACE, AFFECTING BORDER OF GRAIN, DISPLACED
131	SEM-CL	la	1	17	31	10	12	CUTS CEMENT, FILLED WITH SURROUNDING CEMENT, CURVED TRACE, AFFECTING BORDER OF GRAIN, DISPLACED
132	SEM-CL	lc	2	18	39	1	35	AMBIGUOUS RELATIONSHIP TO CEMENT, SHORT, THIN, APPARENTLY FILLED WITH SURROUNDING CEMENT, DISPLACED
133	SEM-CL	la	1	18	170	5	53	CUTS CEMENT, FILLED WITH SURROUNDING CEMENT, STRAIGHT TRACE
134	SEM-CL	la	1	18	63	5	333	CUTS CEMENT, FILLED WITH SURROUNDING CEMENT, STRAIGHT TRACE, CONTINUES OUTSIDE PHOTO
135	SEM-CL	la	1	18	40	20	350	CUTS CEMENT, FILLED WITH SURROUNDING CEMENT, STRAIGHT TRACE, VARIABLE APERTURE, DISPLACED
136	SEM-CL	la	1	18	45	12	69	CUTS CEMENT, FILLED WITH SURROUNDING CEMENT, STRAIGHT TRACE, LARGE APERTURE, TWO CEMENTATION EVENTS
137	SEM-CL	la	1	21,22	118	10	83	CUTS CEMENT, FILLED WITH SURROUNDING CEMENT, SLIGHTLY ZIGZAGGING TRACE, TWO CEMENTATION EVENTS, PARALLEL SET
138	SEM-CL	lb	1	22	73	3	66	PROBABLY CUTS CEMENT, FILLED WITH SURROUNDING CEMENT, CURVED TRACE, BRANCHES FROM F-137
139	SEM-CL	lc	3	21,22	55	1	77	AMBIGUOUS RELATIONSHIP TO CEMENT, CURVED TRACE, DIFFUSE

140	SEM-CL	la	1	21,22	82	10	54	CUTS CEMENT, FILLED WITH SURROUNDING CEMENT, SLIGHTLY ZIGZAGGING TRACE, PIECES OF GRAIN WITHIN FRACTURE, PARALLEL SET
141	SEM-CL	lc	3	21	72	1	81	AMBIGUOUS RELATIONSHIP TO CEMENT, CURVED TRACE, DIFFUSE
142	SEM-CL	lb	1	21	32	3	88	PROBABLY CUTS CEMENT, FILLED WITH SURROUNDING CEMENT, STRAIGHT TRACE, BRANCHES FROM F-140
143	SEM-CL	la	1	21	56	2	71	CUTS CEMENT, FILLED WITH SURROUNDING CEMENT, AFFECTS BORDER OF GRAIN, PIECES OF GRAIN WITHIN FRACTURE
144	SEM-CL	lb	2	22	170	2	334	PROBABLY CUTS CEMENT, FILLED WITH SURROUNDING CEMENT, TIP OF GRAIN (PLAGIOCLASE)
145	SEM-CL	la	1	23	103	15	8	CUTS CEMENT, FILLED WITH SURROUNDING CEMENT, AFFECTS BORDER OF GRAIN, TWO CEMENTATION EVENTS
146	SEM-CL	lb	2	23	135	3	304	PROBABLY CUTS CEMENT, FILLED WITH SURROUNDING CEMENT, VARIABLE APERTURE, SLIGHTLY ZIGZAGGING TRACE
147	SEM-CL	lc	3	23	82	1	23	AMBIGUOUS RELATIONSHIP TO CEMENT, STRAIGHT TRACE, TIP OF GRAIN
148	SEM-CL	la	1	26,27	270	10	74	CUTS CEMENT, FILLED WITH SURROUNDING CEMENT, TWO CEMENTATION EVENTS, PIECES OF GRAIN WITHIN FRACTURE
149	SEM-CL	la	1	26	65	7	40	CUTS CEMENT, FILLED WITH SURROUNDING CEMENT, BRANCHES FROM F-148, VARIABLE APERTURE
150	SEM-CL	la	1	27	121	15	278	CUTS CEMENT, FILLED WITH SURROUNDING CEMENT, TWO CEMENTATION EVENTS, PIECES OF GRAIN WITHIN FRACTURE
151	SEM-CL	lb	2	27	183	3	25	PROBABLY CUTS CEMENT, FILLED WITH SURROUNDING CEMENT, CONTINUES OUTSIDE PHOTO, STRAIGHT TRACE

COTTONWOOD FLAT IRON

SAMPLE: FI-19

NOTCH AZIMUTH: 15

FRACTURE INVENTORY

FRACTURE NUMBER	DETECTION METHOD	Classification		PICTURE NUMBER	LENGTH (um)	APERTURE (um)	AZIMUTH (°)	OBSERVATIONS
		Laubach's (1997)	PREDICTIVE SUITABILITY					
1	SEM-CL	lb	2	1	60	2	65	PROBABLY CUTS CEMENT, FILLED WITH SURROUNDING CEMENT, STRAIGHT TRACE
2	SEM-CL	lb	2	1	23	3	338	PROBABLY CUTS CEMENT, FILLED WITH SURROUNDING CEMENT, STRAIGHT TRACE
3	SEM-CL	lb	2	1	35	2	328	PROBABLY CUTS CEMENT, STRAIGHT TRACE, ENDS WITHIN GRAIN
3A	SEM-CL	lb	2	1	43	2	49	PROBABLY CUTS CEMENT, STRAIGHT TRACE, FILLED BY SURROUNDING CEMENT, ZIGZAGGING
4	SEM-CL	ld	4	1	41	1	356	DIFFUSE, STRAIGHT TRACE, AMBIGUOUS RELATIONSHIP TO CEMENT, PROBABLY INHERITED
5	SEM-CL	lb	2	1	62	5	73	PROBABLY TRANS-CEMENT, FILLED WITH SURROUNDING CEMENT, ZIGZAGGING, LARGE APERTURE
6	SEM-CL	ld	4	1	48	1	337	DIFFUSE, STRAIGHT TRACE, AMBIGUOUS RELATIONSHIP TO CEMENT, PROBABLY INHERITED
6A	SEM-CL	ld	4	1	31	1	342	DIFFUSE, STRAIGHT TRACE, AMBIGUOUS RELATIONSHIP TO CEMENT, PROBABLY INHERITED
7	SEM-CL	lb	2	1	21	4	332	PROBABLY CUTS CEMENT, BORDER OF THE GRAIN, FILLED WITH SURROUNDING CEMENT
8	SEM-CL	lb	3	1	68	2	274	APPARENTLY FILLED WITH SURROUNDING CEMENT, STRAIGHT TRACE

9	SEM-CL	lb	3	1	68	1	320	APPARENTLY FILLED WITH SURROUNDING CEMENT, STRAIGHT TRACE
10	SEM-CL	lb	2	2	95	2	11	PROBABLY TRANS-CEMENT, FILLED WITH SURROUNDING CEMENT, NARROW
11	SEM-CL	lc	3	2	92	1	295	APPARENTLY FILLED WITH SURROUNDING CEMENT, STRAIGHT TRACE
12	SEM-CL	la	1	2	82	2	29	CUTS CEMENT, ORDER OF GRAIN, STRAIGHT TRACE
13	SEM-CL	lc	2	2	55	1	38	PARALLEL SET, APPARENTLY FILLED BY SURROUNDING CEMENT
14	SEM-CL	lc	3	2	50	1	0	STRAIGHT TRACE, AMBIGUOUS RELATIONSHIP TO CEMENT
15	SEM-CL	la+	1	3	115	1	87	TRANSGRANULAR, DISPLACE GRAINS, FILLED WITH SURROUNDING CEMENT
16	SEM-CL	lc	2	3	62	1	43	APPARENTLY WITH SURROUNDING CEMENT, NARROW, STRAIGHT TRACE
17	SEM-CL	lc	2	3	68	1	51	APPARENTLY WITH SURROUNDING CEMENT, NARROW, STRAIGHT TRACE
18	SEM-CL	lb	2	3	58	2	48	PROBABLY CUTS CEMENT, STRAIGHT TRACE, TIP OF GRAIN
19	SEM-CL	ld	3	3	79	2	311	PROBABLY INHERITED, BORDER OF GRAIN
20	SEM-CL	lb	2	3	91	2	347	PROBABLY TRANS-CEMENT, STRAIGHT TRACE, CUTS AN APPARENTLY INHERITED SYSTEM
21	SEM-CL	ld	3	3	45	1	321	PROBABLY INHERITED, CONTINUES OUTSIDE OF PHOTO
22	SEM-CL	lb	2	4	42	5	20	VARIABLE APERTURE, PROBABLY CUTS CEMENT, FILLED WITH SURROUNDING CEMENT
23	SEM-CL	lb	2	5	38	2	81	PROBABLY CUTS CEMENT, FILLED WITH SURROUNDING CEMENT, STRAIGHT TRACE, ENDS WITHIN GRAIN
24	SEM-CL	lb	4	5	62	1	57	INTRAGRANULAR, PROBABLY INHERITED, ODDLY SHAPED

25	SEM-CL	ld	4	5	21	8	287	VARIABLE APERTURE, PROBABLY INHERITED
26	SEM-CL	lc	3	6	98	1	30	AMBIGUOUS RELATIONSHIP TO CEMENT, NARROW, PROBABLY INHERITED
27	SEM-CL	ld	4	6	71	12	312	AMBIGUOUS RELATIONSHIP TO CEMENT, PROBABLY NOT PERPENDICULAR TO THE PLANE OF THE PHOTO
28	SEM-CL	ld	4	6	48	6	335	AMBIGUOUS RELATIONSHIP TO CEMENT, PROBABLY NOT PERPENDICULAR TO THE PLANE OF THE PHOTO
29	SEM-CL	lc	3	6	31	2	83	AMBIGUOUS RELATIONSHIP TO CEMENT, NARROW, STRAIGHT TRACE
30	SEM-CL	lc	3	6	18	1	88	AMBIGUOUS RELATIONSHIP TO CEMENT, PARALLEL SET, STRAIGHT TRACE
31	SEM-CL	lb	3	6	20	1	287	PROBABLY TRANS-CEMENT, PARALLEL SET
32	SEM-CL	lb	3	6	22	1	276	PROBABLY TRANS-CEMENT, ODDLY SHAPED DISSOLUTION ZONES
32A	SEM-CL	lb	2	6	31	4	299	VARIABLE APERTURE, PROBABLY FILLED WITH SURROUNDING CEMENT, TIP OF GRAIN
33	SEM-CL	lc	3	6	41	1	71	INTRAGRANULAR, AMBIGUOUS RELATIONSHIP TO CEMENT
34	SEM-CL	lb	3	6	53	1	318	PROBABLY TRANS-CEMENT, VERY NARROW
35	SEM-CL	ld	4	7	110	0.5	64	PROBABLY INHERITED, VERY NARROW
36	SEM-CL	lb	2	7	48	3	300	PROBABLY TRANS-CEMENT, ENDS WITHIN GRAIN, STRAIGHT TRACE, FILLED WITH SURROUNDING CEMENT
37	SEM-CL	ld	4	7	30	1	46	AMBIGUOUS RELATIONSHIP TO CEMENT, DIFFUSE, ENDS WITHIN GRAIN
38	SEM-CL	ld	4	7	22	3	295	INTRAGRANULAR, ENDS WITHIN GRAIN, VARIABLE APERTURE

39	SEM-CL	ld	4	7	25	3	272	INTRAGRANULAR, ENDS WITHIN GRAIN, VARIABLE APERTURE
40	SEM-CL	lb	2	7	61	1	342	PROBABLY TRANS-CEMENT, FILLED WITH SURROUNDING CEMENT, STRAIGHT TRACE
40A	SEM-CL	lb	2	7	31	2	352	PROBABLY TRANS-CEMENT, FILLED WITH SURROUNDING CEMENT, VARIABLE APERTURE
41	SEM-CL	lb	3	7	48	1	352	PROBABLY TRANS-CEMENT, FILLED WITH SURROUNDING CEMENT, STRAIGHT TRACE
42	SEM-CL	ld	3	7	95	1	0	AMBIGUOUS RELATIONSHIP TO CEMENT, NARROW, CURVED, PROBABLY INHERITED
43	SEM-CL	la	1	7	142	12	90	TRANS-CEMENT, VARIABLE APERTURE
44	SEM-CL	lb	2	7,10	52	5	11	PROBABLY TRANS-CEMENT, STRAIGHT TRACE, FILLED WITH SURROUNDING CEMENT
44A	SEM-CL	ld	3	8	24	2	307	TRANSGRANULAR, ENDS WITHIN GRAIN
45	SEM-CL	ld	4	7	80	1	50	AMBIGUOUS RELATIONSHIP TO CEMENT, CURVED, NARROW, PROBABLY INHERITED
45A	SEM-CL	lc	3	8	36	1	72	AMBIGUOUS RELATIONSHIP TO CEMENT, ENDS WITHIN GRAIN, NARROW
46	SEM-CL	ld	4	7	70	1	90	AMBIGUOUS RELATIONSHIP TO CEMENT, STRAIGHT TRACE, NARROW, PROBABLY INHERITED
46A	SEM-CL	lc	2	8	68	2	40	AMBIGUOUS RELATIONSHIP TO CEMENT, FILLED WITH SURROUNDING CEMENT, TIP OF GRAIN, STRAIGHT TRACE
47	SEM-CL	lb	2	8	28	3	295	PROBABLY TRANS-CEMENT, FILLED WITH SURROUNDING CEMENT, STRAIGHT TRACE, ENDS WITHIN GRAIN
47A	SEM-CL	lb	2	8	38	1	55	PROBABLY TRANS-CEMENT, NARROW, APPARENTLY FILLED WITH SURROUNDING CEMENT

48	SEM-CL	lb	2	9	55	2	38	PROBABLY TRANS-CEMENT, TIP OF GRAIN, CURVED
49	SEM-CL	lb	2	9	42	2	38	PROBABLY TRANS-CEMENT, TIP OF GRAIN, STRAIGHT TRACE
50	SEM-CL	lc	2	9	30	1	309	PARALLEL SET, STRAIGHT TRACE, APPARENTLY FILLED WITH SURROUNDING CEMENT
51	SEM-CL	lb	2	9	95	2	305	PARALLEL SET, STRAIGHT TRACE, FILLED WITH SURROUNDING CEMENT
52	SEM-CL	lb	2	9	29	2	305	PARALLEL SET, STRAIGHT TRACE, FILLED WITH SURROUNDING CEMENT, ENDS WITHIN GRAIN
53	SEM-CL	lb	2	9	106	2	304	PARALLEL SET, STRAIGHT TRACE, FILLED WITH SURROUNDING CEMENT, ODDLY SHAPED WALLS
54	SEM-CL	ld	2	9	33	2	304	PARALLEL SET, STRAIGHT TRACE, APPARENTLY FILLED WITH SURROUNDING CEMENT, ENDS WITHIN GRAIN
55	SEM-CL	lb	2	9	70	1	305	PARALLEL SET, STRAIGHT TRACE, FILLED WITH SURROUNDING CEMENT, ENDS WITHIN GRAIN
56	SEM-CL	lc	2	9	45	2	303	PARALLEL SET, STRAIGHT TRACE, APPARENTLY FILLED WITH SURROUNDING CEMENT
57	SEM-CL	lb	2	9	29	2	308	PARALLEL SET, STRAIGHT TRACE, FILLED WITH SURROUNDING CEMENT
58	SEM-CL	lb	2	9	110	4	25	STRAIGHT TRACE, FILLED WITH SURROUNDING CEMENT, ODDLY SHAPED WALLS
59	SEM-CL	lb	2	9	20	1	61	PROBABLY TRANS-CEMENT, SHORT, CURVED
60	SEM-CL	ld	3	9	75	2	358	INTRAGRANULAR; STRAIGHT TRACE, APPARENTLY FILLED WITH SURROUNDING CEMENT
61	SEM-CL	lc	3	9	60	1	39	AMBIGUOUS RELATIONSHIP TO CEMENT, ODDLY SHAPED, DIFFUSE

62	SEM-CL	lc	3	9	98	2	14	AMBIGUOUS RELATIONSHIP TO CEMENT, NARROW, ODDLY SHAPED
63	SEM-CL	lb	2	9	43	4	40	PROBABLY TRANS-CEMENT, TIP OF GRAIN, LARGE APERTURE, STRAIGHT TRACE
64	SEM-CL	lc	2	10	80	8	28	PROBABLY FILLED WITH SURROUNDING CEMENT, PIECES OF GRAIN IN FRACTURE, CRUSHING RELATED
64A	SEM-CL	lb	2	10	10	3	22	PROBABLY CUTS CEMENT, VARIABLE APERTURE, ENDS WITHIN GRAIN, TIP OF GRAIN
65	SEM-CL	lb	2	10	27	0.5	20	PROBABLY CUTS CEMENT, STRAIGHT TRACE, ENDS WITHIN GRAIN
65A	SEM-CL	lb	2	10	26	0.5	347	PROBABLY CUTS CEMENT, DISPLACED, TIP OF GRAIN
66	SEM-CL	la	1	10	18	11	80	CUTS CEMENT, LARGE APERTURE
66A	SEM-CL	lb	2	10	27	7	352	PROBABLY CUTS CEMENT, ODDLY SHAPED, VARIABLE APERTURE
67	SEM-CL	la	1	10	50	6	338	CUTS CEMENT, VARIABLE APERTURE
68	SEM-CL	lc	3	10	41	0.5	338	AMBIGUOUS RELATIONSHIP TO CEMENT, NARROW, DIFFUSE, STRAIGHT TRACE
69	SEM-CL	lc	3	10	52	2	0	AMBIGUOUS RELATIONSHIP TO CEMENT, ODDLY SHAPED, VARIABLE APERTURE
70	SEM-CL	la	1	10	19	7	303	CUTS CEMENT, STRAIGHT TRACE, ENDS WITHIN GRAIN
71	SEM-CL	lb	2	10	61	10	56	PROBABLY CUTS CEMENT, FILLED WITH SURROUNDING CEMENT, STRAIGHT TRACE
72	SEM-CL	lb	2	10	12	3	90	PROBABLY CUTS CEMENT, ENDS WITHIN GRAIN, STRAIGHT TRACE, SHORT
73	SEM-CL	lc	4	10	52	1	314	AMBIGUOUS RELATIONSHIP TO CEMENT, BORDER OF GRAIN, NARROW, PROBABLY INHERITED

74	SEM-CL	lb	2	10	16	1	32	PROBABLY CUTS CEMENT, SHORT, ENDS WITHIN GRAIN
75	SEM-CL	lc	3	10	14	0.5	12	AMBIGUOUS RELATIONSHIP TO CEMENT, SHORT, ENDS WITHIN GRAIN, STRAIGHT TRACE
76	SEM-CL	lc	3	10	12	0.5	7	AMBIGUOUS RELATIONSHIP TO CEMENT, SHORT, ENDS WITHIN GRAIN, STRAIGHT TRACE
77	SEM-CL	la	1	11	73	11	301	CUTS CEMENT, VARIABLE APERTURE, FILLED WITH SURROUNDING CEMENT, ODDLY SHAPED
78	SEM-CL	lb	2	11	29	2	275	PROBABLY CUTS CEMENT, VARIABLE APERTURE, FILLED WITH SURROUNDING CEMENT
79	SEM-CL	ld	4	11	54	1	2	PROBABLY INHERITED, ODDLY SHAPED WALLS, ENDS WITHIN GRAIN, CURVE
80	SEM-CL	ld	4	11	68	2	62	PROBABLY INHERITED, ODDLY SHAPED WALLS, ENDS WITHIN GRAIN, CURVE
81	SEM-CL	lb	2	11	75	1	337	PROBABLY CUTS CEMENT, FILLED WITH SURROUNDING CEMENT, BORDER OF GRAIN
82	SEM-CL	lb	2	11	170	2	284	PROBABLY CUTS CEMENT, FILLED WITH SURROUNDING CEMENT, STRAIGHT TRACE
83	SEM-CL	lb	2	11	120	0.5	305	PROBABLY CUTS CEMENT, FILLED WITH SURROUNDING CEMENT, STRAIGHT TRACE, NARROW
84	SEM-CL	lb	2	11	80	2	0	PROBABLY CUTS CEMENT, FILLED WITH SURROUNDING CEMENT, CURVED, NARROW, VARIABLE APERTURE

PART III. ENGINEERING APPLICATION OF RESULTS

INTRODUCTION TO PART III: INCORPORATING GEOLOGIC INFORMATION IN DUAL-POROSITY SIMULATORS

Numerical simulation of fluid flow in hydrocarbon-bearing reservoirs has evolved so that few significant decisions are made without it. Numerical simulation, as most commonly practiced, consists of dividing up the flow domain into many cells or grid blocks around which discretized forms of species-conservation equations are solved. The solutions change with time as each cell loads and unloads with fluids. Some of these cells can contain wells, and it is from these that we gain predictions on rates or pressures with which to make economic forecasts.

Even though simulations are quite large—10,000 cells is fairly common, and some types of simulators can reach 100,000 or more—the detail representable by simulators is still far less than what is known to exist in reservoirs. Even for a simple simulation, each cell must start off with three scalar components of permeability, a porosity component, a pressure component, and at least one saturation component. Pressure and saturation tend to be smoothed by physical effects, but porosity, and especially permeability, vary widely. Determining the scale on which these variations take place and how to represent them in simulators has been the subject of intense research over the past few years.

The difficulties imposed by disparities of scale are especially present in simulations of fractured reservoirs; in many cases, nearly all of the flow capacity in these reservoirs passes through features that are so small that they are difficult to detect. Yet fractured reservoirs compose a large (and ever-increasing) fraction of United States resources in both carbonate and sandstone facies.

There are two ways to model flow in fractured media. The first is the dual porosity approach. In this method, the pore space in each cell is divided into flowing and nonflowing

regions. The two regions can exchange mass with each other, but only the flowing region supports flow (that is, directly communicates to the wells). Some simulators assign a limited amount of flow to the second region as well. The second method is the explicit fracture method. In this, each fracture (its geometry, size and frequency of occurrence) is put into a simulator and the conservation laws solved along them allowing (usually) for varying degrees of mass transfer from the surrounding matrix.

Superficially, it would appear that the explicit method is the best approach because it directly accounts for the actual physical nature of fractures. In truth, neither method is entirely satisfactory. The detail required by the explicit method means that it is impossible to solve flow fields larger than a few square meters in extent, an area that is far smaller than even the smallest hydrocarbon reservoirs. The dual porosity models can model quite large areas, but their cell-by-cell representations are not based on the local fracture distributions. In fact, most of the parameters in dual porosity simulators are assigned through history matching in current practice. Our goal was to develop a procedure to assign the parameters of dual porosity simulators based on the actual local (that is, on the same scale as the cells) fracture patterns. The method combines the best features of the two approaches.

Figures 3 and 15 through 19 in Part I of this report schematically represent how this might be accomplished. We first imagine that the volume of a cell has been independently selected, usually a practical limit on time and/or expense. We further imagine that cumulative distribution functions (cdf) of fracture attributes (fig. 17 shows only the attributes of aperture width, length, and orientation) are known, as is a cdf that gives the frequency of occurrence of fractures in the volume.

We randomly select the number of fractures in the volume; figure 17 shows this as picking a random number RN uniformly distributed between zero and one and taking the inverse of the distribution cdf. This process would normally be repeated several times (fig. 17 shows only one sampling) until a target fracture porosity for the block is met. The next step is to spatially distribute the fractures within the cell. After this, we sample the appropriate cdf's for the

attributes of each fracture. In general, the fractures will intersect within the cells and this must be corrected for as indicated. Finally, the entire ensemble of fractures is converted into a single porosity, three permeabilities and, perhaps, a mass transfer coefficient for the cell. The entire process would be repeated for each cell. Since each of the attributes for a swarm of fractures is a random variable, the cell properties will be so also.

Such a laborious process as illustrated in figure 17 would be computationally intensive—maybe even rivaling the expense of the flow simulation. However, it seems equally clear that, if the cdfs are representative of the cell volume and the effective property generation algorithm is accurate, this procedure is the blend of the dual porosity and explicit approaches discussed above.

The key elements—and the ones focused upon in this report—are (1) insuring that the cdfs are consistent with the underlying state of stress in the medium, (2) seeing that measured cdfs have been adjusted so that the scale of the original measurements (the cdfs are normally taken from outcrop measurements but can be acquired from core measurements) agrees with the cell volume and (3) developing a scale-up procedure that lumps all of the aforementioned detail into a summary that is both useful and accurate.

Part II of this report describes results of a novel technique based on scanned CL observation that allows inference of fracture attributes at scales ranging over three orders of magnitude. The first part of Part III discusses the attempts to generate fracture distributions from solutions to the loading equations based on randomized initial conditions and a prespecified state of stress. This section shows that a variety of cdfs are possible, but that most of these are in reasonable agreement with those measured in outcrop. And, finally, the last part of Part III describes attempts to derive the actual population statistics from those measured in the previous section. This approach holds the key for the adjustment of the fracture statistics from one scale to another. This section also describes results in converting the fracture statistics on a particular scale to a cdf of permeability.

Geomechanical Modeling

Modeling Concepts

Natural fracture patterns are difficult to characterize in the subsurface and at the surface. In the subsurface, only limited information is available, typically acquired from wellbores. Fracture systematics are not well constrained from these data, thus it is challenging to generate a comprehensive fracture network that can be used for fluid flow modeling. Surface outcrops are more amenable to characterization but still represent significant challenges. If the outcrop is being examined to characterize near surface flow, joint traces may be evident, but a fracture's opening and its extent in three dimensions are still difficult to discern. If the outcrop is being used as an analog for a subsurface reservoir, another difficulty is extrapolating the surface fracture pattern to the subsurface, subtracting out any weathering or uplift-related features and accounting for subsurface stress conditions on fracture opening.

The Model

Ideally, a characterization model should be able to incorporate a priori information such as mechanical and fluid flow boundary conditions as well as be conditioned by observations. Thus, if observations are made at one locality (the surface), they can be applied to another locality with different "fracturing conditions" by the application of a transform. The advantage of a mechanically based model (Olson, 1993; Renshaw and Pollard, 1994) over stochastic realization techniques (Dershowitz and Einstein, 1988; Kulatilake and others, 1993) is that the mechanical model intrinsically includes relationships between fracture processes and boundary conditions. If surface data are to be applied to the subsurface, the modification of fracture parameters can be investigated by varying boundary conditions in the model. If insufficient data are available to characterize a fracture network, that data can be augmented with other parameters such as bed

thickness, stress state, and mechanical properties to be included as a priori information to obtain a more complete realization.

The model is based on two-dimensional, plane strain elasticity, using a displacement discontinuity technique (Crouch and Starfield, 1983) to represent the fractures. The conceptual framework for fracture propagation follows Segall (1984, 1984a) and its implementation is described in detail in Olson (1993). Briefly, propagation is controlled by linear elastic fracture mechanics assuming a subcritical fracture propagation law (Atkinson and Meredith, 1987), where propagation velocity, v , is given by

$$v = A (KI/KI_c)^n \quad (1)$$

where KI is the mode I stress intensity factor, KI_c is the fracture toughness of the material, n is the subcritical growth index of the material, and A is the maximum possible propagation velocity at critical propagation ($KI = KI_c$). Mixed-mode I-II fracture propagation is implemented using the maximum circumferential stress criterion of Erdogan and Sih (1963). Mixed-mode joint propagation results in curving crack paths which are sensitive to fracture spacing, in situ stress and bed thickness and fracture surface roughness (Pollard and others, 1982; Olson and Pollard, 1989; Renshaw and Pollard, 1994). Strain rate effects can also be significant in determining fracture network geometry (Segall, 1984a; Wu and Pollard, 1993).

Simulations were run on a finite-size body dimensioned 10 x 10 m. Propagation was limited to a slightly smaller area within this body that measured 8 x 8 m. A translational symmetry was employed to reduce the edge effects of the finite body (Renshaw and Pollard, 1994), incorporating the effects of equivalent fracture patterns immediately above and below the modeled pattern (about symmetry planes at $y=4$ m) and to either side in x (about symmetry planes at $x=4$ m). The x boundaries ($x=5$ m) were discretized into 10 boundary elements and were constrained to zero normal displacement and zero shear stress. The y boundaries ($y=5$ m) were discretized in the same manner and had a constant rate extensional strain applied. It is this extension that drives crack propagation. Simulations were run until fractures stopped propagating or until a pre-determined maximum strain was reached. The strain rate in all cases was

1×10^{-20} /s. The final strain at the end of the simulation, unless otherwise noted, was 1×10^{-4} , chosen based on a strain measurement on jointed granite by Segall and Pollard (1983).

Following Segall (1984), this loading can be generalized to other conditions by superposing an isotropic, compressive stress state. Crack propagation occurred incrementally with addition of constant length patches when required according to the fracture mechanics propagation criterion. Because of computational limitations, starter cracks that are randomly seeded into the model have a considerable length (0.3 m). Because all of the patches need to be of the same length (Crouch and Starfield, 1983), greater initial lengths reduce the total number of patches for a complete simulation.

Model Results

Several simulations were carried out to demonstrate the sensitivity of fracture propagation to various boundary conditions and material properties. Figure 1 demonstrates the impact of bed thickness on fracture spacing. Crack paths are straight, based on the assumption that the in situ stress anisotropy is great and prevents crack path curving (Olson and Pollard, 1989). Bed thickness was varied from 2 to 10 m, with the expected increase in spacing with increased bed thickness. This bed thickness/spacing effect is related to the stress shadow around the fractures. The same subcritical growth index of 40 was used for all bed thicknesses, with the unexpected result that spacing became more clustered with increased bed thickness. This is an interesting result in that previous work (Olson, 1993; Renshaw and Pollard, 1994) suggested that clustering was primarily controlled by the subcritical index (high values, greater than 3, resulted in clustering). This previous work also suggested that values of $n > 10$ would result in non-physical fracture patterns. The discrepancy here is probably due to the incorporation of bed thickness effects in this work, whereas the previous studies were strictly two dimensional.

Figure 2 is displayed alongside figure 1 and represents two changes in the simulation. The starter cracks for figure 6-1 are all parallel, whereas those in figure 2 have two possible

orientations that are orthogonal (either parallel to x or y). Secondly, mixed-mode propagation is allowed, and since the loading is a uniaxial extension in y with zero displacement in x (no other stress anisotropy present), there is significant crack path curving. However, as fracture stress perturbation scales with the shortest dimension of a 3d crack (Olson, 1993), there is less crack to crack interaction in the thinner bedded examples and thus straighter overall propagation. This suggests that thinner beds, in general, might be expected to have straighter cracks. This would be in addition to stress anisotropy (Olson and Pollard, 1989) and surface roughness effects (Renshaw and Pollard, 1994). Crack path curving increases as bed thickness increases, and general fracture density decreases similar to that shown in figure 1.

Figures 3 and 4 are meant to investigate the effects of the subcritical growth index. Both examples are loaded at the same rate (1×10^{-20} /s) and to the same final strain (1×10^{-4}). The only difference is that for figure 3 a large subcritical growth index was used, $n=40$, whereas for figure 4, $n=5$ was used. As a lower subcritical index minimizes the velocity contrast between fractures of different stress intensity (see equation 1), more fractures are able to grow prior to the crack inhibiting effect of stress relief of neighboring fractures with $n=5$. Atkinson and others (1987) reported a wide range of subcritical growth indices from 1 to over 100 (depending on fracture mechanism and rock type), so a wide variety of fracture patterns could result under similar loading conditions depending on this material property.

The simulation conditions to generate figures 5 (bed thickness = 5 m) and 6 (bed thickness = 2 m) were similar those for figure 2 except that 80 starter cracks were used instead of 40. The general relationship of lower fracture density for larger bed thickness holds, although the difference between bed thicknesses is stronger for high subcritical growth index (part B in each figure) than for low (part A in each figure). A single event uniaxial extension was imposed as loading, as with all the other cases, but the results imply all around extension on first glance because of the apparently chaotic fracture pattern. Upon closer examination, there is a sub-linear fabric that appears to have developed first in the simulated patterns but stress relief in the y direction favored stress rotation and local changes in the favored propagation direction. Figure 7

shows the sequential development of the pattern from figure 6A, and it is apparent that the advance of crack propagation in this example tends to divide the body up into smaller and smaller pieces, until all of the fracture initiation sites have been exhausted and all of the fracture tips intersected. This progressive division of rock into smaller pieces is similar to that observed in outcrop by Barton and Hsieh (1989).

Implications for Fracture Geometry

Results from the forward modeling indicate that there is a systematic relationship between boundary conditions and final fracture geometry that can be exploited for the purpose of fracture pattern inversion from observed data. For example, the generation of orthogonal fracture sets with a single, coaxial loading is demonstrated. Preexisting fracture sets remain open throughout the deformation history, and subsequent fracture generations divide the body into smaller and smaller domains. Multiple switches in fracture direction can result if stress relief due to fracturing overcomes any stress anisotropy that might otherwise restrict opening mode fractures to one orientation. Such patterns probably indicate near surface or uplift-related fracture propagation. Such guidelines based on mechanical modeling can help in the interpretation of outcrops and the extrapolation of their fracture patterns to the subsurface.

Also, results presented here potentially expand the range for the subcritical growth index that will generate physically reasonable fracture patterns. The probable reason for this difference from previous results is the incorporation of three dimensional effects in the modeling for this study. Further work is needed to explore this point more fully, and to examine other rate limiting effects such as fluid flow (Segall, 1984).

CHAPTER 1: INTRODUCTION

Significant oil and gas have been produced from the various types of fractured reservoirs across the world (Saidi, 1987). Fractured rocks, therefore, constitute an important type of reservoir rock.

The behavior of naturally fractured reservoirs is very different from that of conventional reservoirs (Aguilera 1980, van Golf-Racht 1982, Saidi 1987). The primary cause of this difference is the inherent character of naturally fractured reservoirs: most hydrocarbon resides in the pore space of the matrix whereas the flow of hydrocarbon towards wells is dominated by flow through networks of fractures. Consequently, the behavior of naturally fractured reservoirs is dominated by the properties of the individual fractures and the networks formed by the fractures.

One of the biggest difficulties in studying naturally fractured reservoirs is that available data are limited, usually to one spatial direction (i.e., along a wellbore). Furthermore most fractured-reservoir simulations are based on simplified idealized models (Saidi, 1987). The assumptions of these models are sometimes clearly different from the conditions of underground reservoirs. Therefore, it is desirable to find a more accurate, efficient, practicable simulation method based on actual data for the fractures in a given field.

Making use of the latest findings in structural geology, this study attempts to relate, through numerical simulation, certain properties of fractures and their statistical distributions to the flow properties of naturally fractured reservoirs. Thus, ultimately, the performance of commonly-used simulators for fractured reservoirs can be improved.

1.1 Characterization of Naturally Fractured Reservoirs

1.1.1 Basic Properties of Fractures

The spatial variation of fracture features, such as aperture, size, orientation and nature, are so complicated and irregular that characterization of a fractured reservoir is substantially more difficult than that of a conventional reservoir. Thus the characterization of a fracture reservoir should follow a certain pattern. First of all, the local characteristics of single fractures should be examined. Afterwards multi-fracture systems should then be evaluated.

Parameters for individual fractures include fracture aperture, size, nature and orientation. Fracture aperture is the gap between the fracture walls. Fracture size is related to the shape of fractures in space. When a fracture is defined as a disk in space, the radius of the disk quantifies the size of the fracture. The “nature” of fractures refers to the state of fractures, including open, filled with minerals and wall characteristics. Fracture orientation is the parameter relating the fracture to its environment. Fractures with similar orientation can be grouped together as a fracture set.

Parameters for a population of fractures include fracture property distributions (aperture, size, orientation), matrix block size and shape, and fracture density. Fracture density expresses the extent of rock fracturing. It can be quantified using either volumetric fracture density, i.e., the ratio of fracture area to bulk volume, or areal fracture density, i.e., the ratio of cumulative length of fractures to matrix bulk area in a flow cross-section.

1.1.2 Outcrop Study

Outcrop study is one important means to investigate fractured reservoirs. It involves the collection of various data along the face of the outcrop, including all single-fracture and fracture-population parameters, such as the orientation of fracture systems and layer strike, fracture

density, fracture aperture and size, lithological data, etc. The fracture scaling equations used in this research are the results of an outcrop study that is detailed in Section 1.3.2.

One of the disadvantages of this method is that surface outcrops may have experienced geological processes different from those of the underground reservoir, and the nature of the fracture system might have dramatically changed thereby. Although outcrop study is currently a very important means to study fracture systems and can provide some valuable information, it is not sufficient to obtain a complete description of underground fractured reservoirs.

1.1.3 Detection and Evaluation of Fractures

The characterization of naturally fractured reservoirs underground relies heavily on the detection and evaluation of fracture systems. The detection and evaluation of fracture systems is not a one-step task. It is a procedure that continues through the exploration and development of fractured reservoirs. It is the result of information obtained during various phases of field work, such as exploration, drilling, coring, logging, testing and production. Some of these results represent direct information, such as observations on outcrops, core analysis in the laboratory, and images obtained in borehole televiewer logging.

Drilling operation can sometimes provide useful information to describe the fracture system qualitatively (van Golf-Racht, 1982). Indications of fractured zones in drilling operation include unusually high drilling rates, loss of drilling fluids, very poor core recovery and significant increase of wellbore size.

In the past several decades, much effort has been made to make the detection of fractures easier and more accurate through well logging. However, the qualitative and quantitative evaluation of fracture systems was found to be much more complicated than expected, due mainly to the technical difficulties regarding the identification of fractures (Saidi, 1987). Generally, the various logging techniques are based on an anomaly in the normal tool response in a fractured zone. A log tool is usually sensitive to the presence of a high-permeability path

(formed by fractures) in a low permeability porous medium (rock matrix). From this sensitivity fracture systems can be evaluated. Available log options for evaluation of fracture systems include lithology logs (SP and gamma ray), caliper logs, temperature logs, resistivity logs, dipmeter logs, porosity logs (density, neutron and sonic), and their combinations.

1.1.4 Core Analysis

Core analysis can provide direct information on underground fracture systems (van Golf-Racht, 1982). Information expected from core analysis includes single-fracture parameters such as aperture, size, orientation and morphology (open, partially open, filled, closed, etc.), and fracture-population parameters. Unless the core is altered in the coring and recovery process, the information from core analysis reflects the actual state of the fractured reservoir.

Unfortunately, for macrofractures (those visible macroscopically), some parameters like size distributions and fracture density are not available or reliable through core analysis, because the core only samples a few macrofractures. These properties can be determined for a large population of microfractures (those visible only under magnification), however, from examination of thin sections as discussed in Section 1.3 below.

1.1.5 Definition of Dual Porosity

In general, the porosity of fractured reservoirs can be classified as matrix porosity ϕ_m and fracture porosity ϕ_f . The two porosities are expressed as

$$\begin{aligned}\phi_m &= \frac{\text{matrix void volume}}{\text{matrix bulk volume}} \\ \phi_f &= \frac{\text{fracture void volume}}{\text{total bulk volume}}\end{aligned}\tag{1.1}$$

As noted above, the prominent feature of fractured reservoirs is that (1) the fractures have a negligible storage capacity but extremely high permeability; and (2) the matrix has an important storage capacity, but a very small permeability.

Matrix porosity can be measured by using conventional techniques like core analysis. However, measurement of fracture porosity is complicated because of the very small fracture volume. In some fractured reservoirs, fracture porosity is of the order of 0.1% of the rock volume (Saidi, 1987). Such a value of porosity is less than the accuracy range of most methods available for measuring porosity. The main methods for measuring or estimating fracture porosity are well testing and history-matching of reservoir performance.

1.2 Simulation of Naturally Fractured Reservoirs

Current simulation technology for naturally fractured reservoirs is based on either continuum or discrete-fracture models. Discrete-fracture flow models represent each fracture individually and can incorporate many of the characteristics of real fracture systems (Wolff *et al.*, 1990; Dershowitz and Doe, 1988; Long *et al.*, 1985), such as complex fracture geometry. However, their use is limited by the large number of fractures that may be present and the capacity of simulators and computer resources. In a real fractured reservoir, there are numerous fractures in-situ connecting one another to form complicated fracture networks. On the other hand, most geological and engineering data available are limited in a single space direction (for instance, in a wellbore) or at scattered blocks (coring in different wells). Thus crucial information on the locations and properties of fractures is usually poorly known.

Therefore, continuum-fracture models (or dual-porosity models) are more commonly used. An advantage of this type of model is that it can simulate complex recovery mechanisms.

Warren and Root (1963) presented a dual-porosity model composed of cubic matrix blocks, each of which is surrounded by fractures in three orthogonal directions. The flow towards the

wellbore is considered to take place in the fractured network, while the matrix continuously feeds the system of fractures. The two media, fracture network and block, are considered to be an overlapping continuum. The fundamental fluid flow equations (continuity equation, flow equation and equation of state) are written independently for each medium, and transfer of fluid between the two media is taken into consideration by a transfer function in the continuity equations.

Naturally fractured reservoirs are extremely complex. Consequently, it is often difficult to have sufficient, reliable input data. The input data required for dual-porosity simulation of fractured reservoirs include matrix and fracture permeability, matrix and fracture porosity, matrix block size, initial saturation for each phase, initial pressure, matrix and fracture compressibility, fluid properties, relative-permeability functions for each phase in matrix and fractures. Each of these parameters or functions might vary with position through the reservoir. The better the input data, the more reliable and accurate will be the simulation results.

1.3 Advances in Characterization of Fracture Systems

Field observations and laboratory studies have revealed important aspects of natural fracture systems, described in this section.

1.3.1 Correlation between Microfractures and Macrofractures

Fracture properties are often poorly known because most macrofractures do not intersect the wellbore where they can be detected and characterized. Yet the numerous macrofractures not intersecting the wellbore play a critical role in overall behavior of fractured reservoirs. Most current fracture detection methods – when they yield any information at all – commonly do not provide statistically significant data sufficient to establish fracture abundance and porosity patterns. However, microfractures are more common and can be effectively sampled even in small volumes of rock (e.g., cores). This implies that a study of microfractures not only avoids

the fracture-sampling problem but also may provide useful information about critical attributes of macrofractures.

Recent technology development allows the easy and cost-efficient analysis of microfractures in cores. This technique, called photomultiplier-based imaging of electron beam-induced luminescence (scanned cathodoluminescence or scanned CL) (Milliken, 1994), can be used to image the microfractures by highlighting the cement that fills most microfractures.

In many cases, observations show that microfractures have a diagenetic history of mineralization similar to that of macrofractures (Laubach *et al.*, 1997). This result indicates that the relative timing of micro- and macrofractures is similar, and that their roles in conducting mineralizing fluids are analogous. Many data also show that microfractures share common orientation patterns with macrofractures. This suggests that the same differential stresses control the orientations of both very small and very large fractures.

Several studies have shown that the length and aperture of macrofractures in outcrops follow power-law distributions over various length scales (Odling, 1997; Laubach *et al.*, 1997, Marrett, 1997; Gross and Engelder, 1995). The power-law distributions for length and aperture observed in outcrops can be written as

$$N = ab^{-c} \quad (\text{aperture}) \quad (1.2)$$

$$N = mL^{-e} \quad (\text{length}) \quad (1.3)$$

where N is the cumulative number of fractures in a given outcrop with aperture equal to or greater than b (for Equation 1.2), or with length equal to or greater than L (for Equation 1.3); a , c , m , e are positive empirical factors, that depend on the particular formation. The power-law distribution is a straight line in a log-log plot. Figure 1.1 is a study of fracture length distribution in one outcrop (Laubach *et al.*, 1997). Figure 1.2 is another outcrop study of fracture length

distributions on various scales (Odling, 1997). Each curve in the figure represents a different scale in the same region. The fracture length distribution for all scales follows the same power-law distribution. Figure 1.3 shows the power-law distribution for aperture in various formations (Marrett, 1997). For most of these distributions, there are two deviations from the power-law (straight line), at the top and bottom portions of the distributions. Geologists (Marrett, 1997; Odling, 1997) argue that the upper deviation is due to truncation error of sampling, in other words, the inability to observe small fractures in outcrops, and the lower deviation (which we call falloff) is due to censoring error, i.e. infrequency of observation of large fractures in a finite sample.

Laboratory core analysis also reveals that microfractures follow the same power-law distribution as macrofractures observed in outcrops (Laubach *et al.*, 1997). Figure 1.4 shows the distribution relationship between microfractures and macrofractures in the Mesaverde formation, San Juan basin, New Mexico. This implies that microfractures and macrofractures are simply different size fractions of the same fracture sets. This insight offers the potential for using scaling relations to quantitatively link fracture size attributes across the gap between microfractures and macrofractures. In addition, microfracture data can be extrapolated by scaling to obtain macrofracture properties in cases where outcrops are unavailable for a particular formation.

This new microfracture analysis and scaling method is important for characterizing fractured reservoirs because a very small volume of rock is statistically sufficient to obtain microfracture data, which is related by scaling to the macrofractures which dominate the fluid flow in the rock. It is a more accurate and cost-efficient approach for getting information needed for simulation of fractured reservoirs.

1.3.2 An Outcrop Study

An outcrop study conducted by Laubach *et al.* (1997) further verifies the correlation between microfractures and macrofractures. The study focuses on the fractured sandstones of the

Mesaverde Group in the San Juan Basin, New Mexico. Large amounts of natural gas have been produced from these sandstones. Fractures represent a minor contribution to the storage capacity of the system but they provide the dominant flow conduits in production from the reservoirs. Laubach *et al.* performed both surface and subsurface investigations for this formation.

One large well-exposed pavement (the Westwater Springs Pavement) was selected to perform surface investigation. A smaller area within the pavement was also identified for a detailed survey of macrofracture properties. Data were collected for each fracture including fracture orientation, fracture length, fracture aperture (where possible), fracture termination type, angle of connection with other fractures, fracture cement type and other characteristics. Additional data were collected along scan lines in the Westwater pavement to test the relationship between the fracture distributions in one and two dimensions.

Figure 1.5 shows the power-law distribution for the length of microfractures and macrofractures in the Westwater pavement. Laubach *et al.* (1997) attribute the curvature in individual data clusters to a combination of truncation and censoring errors. Marrett (1996) shows that short and long fractures (shorter or longer than height of the mechanical layer) differ in their apparent power-law exponent based on outcrop sampling (cf. also Rossen (1998), reproduced in Appendix B). The exponents of the two distributions differ approximately by one.

1.4 Delineation of Research Motivations and Objectives

1.4.1 Research Motivations

In Figure 1.3, some curves exhibit falloff from the linear (power-law) trend at large fracture aperture, but some do not. Geologists believe that the falloff is due to censoring error of sampling (Marrett, 1997). One other explanation for falloff is that there might be a largest aperture existing in the population. In addition, a deviation above the straight line in the curve was almost never observed in outcrops, but should be just as common as falloff if falloff is the

result of random sampling. A Monte Carlo study was conducted to test these issues, as reported in Chapter 2.

Fracture aperture has a significant impact on the properties of fractured reservoirs. Based on various studies (Figure 1.3), the distribution of fracture aperture fits a power law, implying a great number of fractures with small apertures within the population. The capacity for fluid flow in fracture is proportional to cubic power of aperture (Bird *et al.*, 1960). Marrett (1996) shows that aperture scales roughly with fracture length. His study (1997) also suggests that few largest fractures in the population greatly affect the permeability anisotropy and porosity of fractured rock. It is desirable to test how the power-law distribution affects the permeability and porosity of fractured reservoirs. This motivates a Monte Carlo study on this issue also described in Chapter 2.

Fractures have significant impact on fluid flow primarily when fractures connect up to form a high-permeability conduit for flow. Therefore, the calculation of permeability of fractures is meaningful only when there are fractures interconnecting to form a flow path in the direction of flow. For a given distribution of fracture size, the interconnectivity of fractures must be determined before the permeability of the fracture system can be calculated. This is discussed in Chapter 3.

1.4.2 Research Objectives

The ultimate aim of this research program is to incorporate the results of new approaches for quantifying the occurrence of open natural fractures and fracture-controlled permeability anisotropy, outlined in the previous section, into commonly used dual-porosity simulators for naturally fractured reservoirs.

The goals of this report are more modest, however: (1) testing the effect of a power-law distribution for fracture aperture on the permeability and porosity of fractured reservoirs using a simplified model; and (2) testing the connectivity of fracture networks based on a power-law

distribution for fracture length using Monte Carlo study and numerical simulation. These efforts represent a first step toward relating statistical data for individual fractures to values for effective permeability and permeability anisotropy for grid blocks in dual-porosity simulation.

Frequency/Length plot. Westwater Paveme

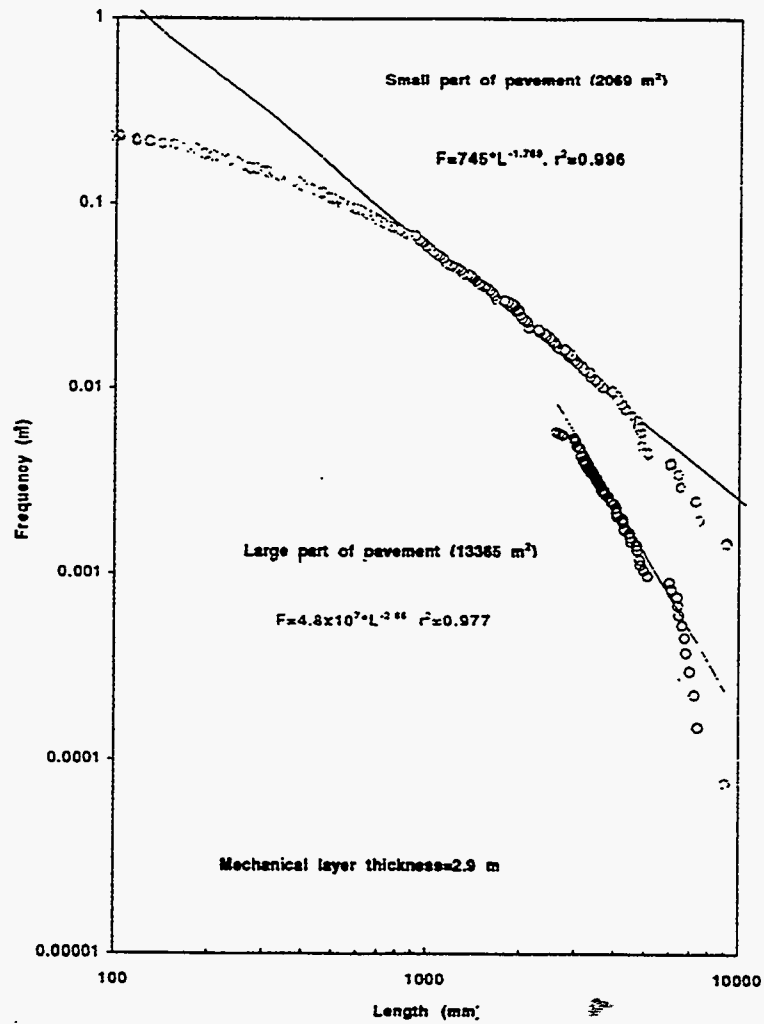


Figure 1.1. Power-law distribution for fracture length in the Westwater Pavement (Laubach *et al.*, 1997).

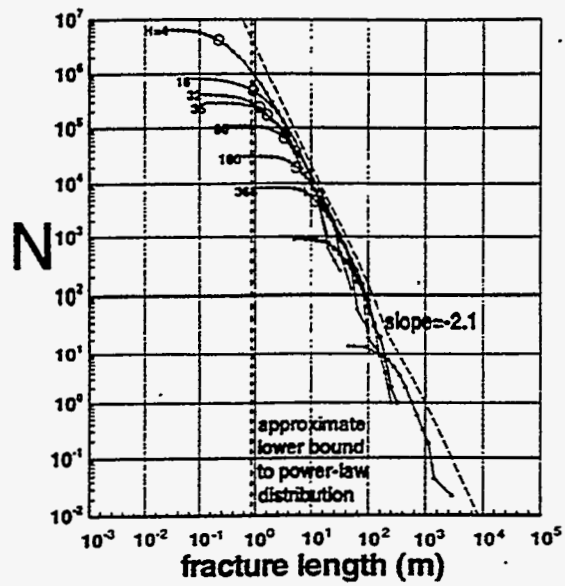


Figure 1.2. Power-law distribution for fracture length in the Devonian basin, western Norway (Odling, 1997).

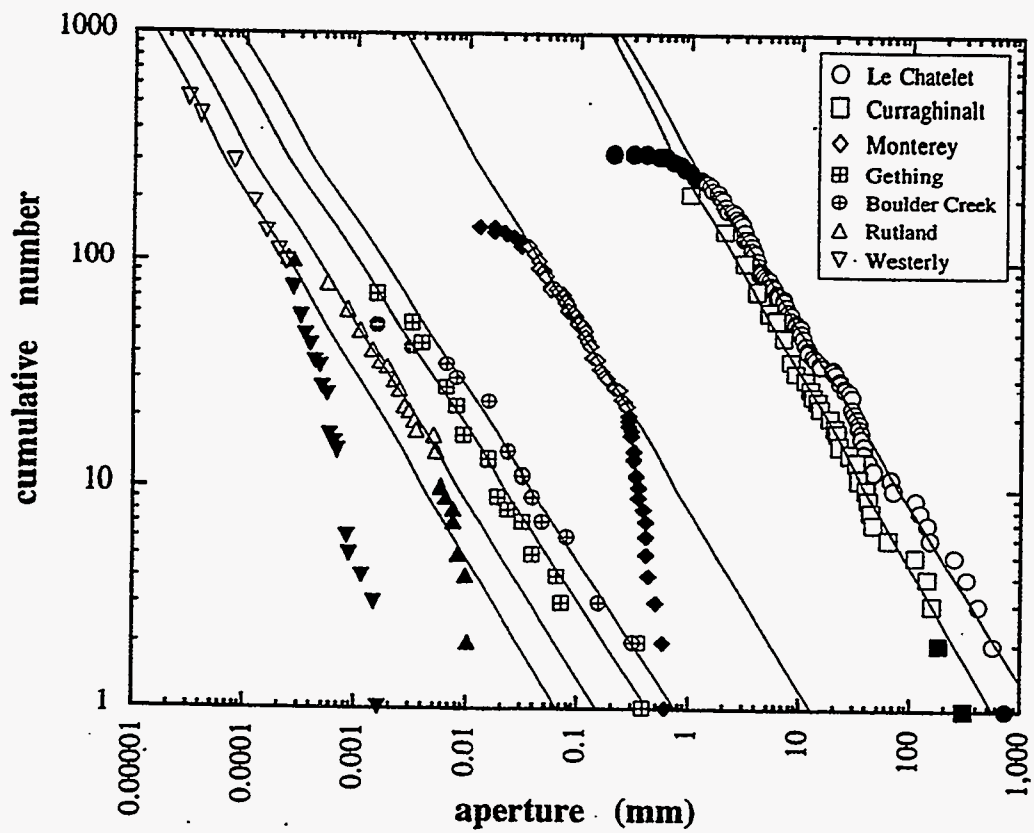


Figure 1.3. Power-law distribution for fracture aperture in various formations (Marrett, 1997).

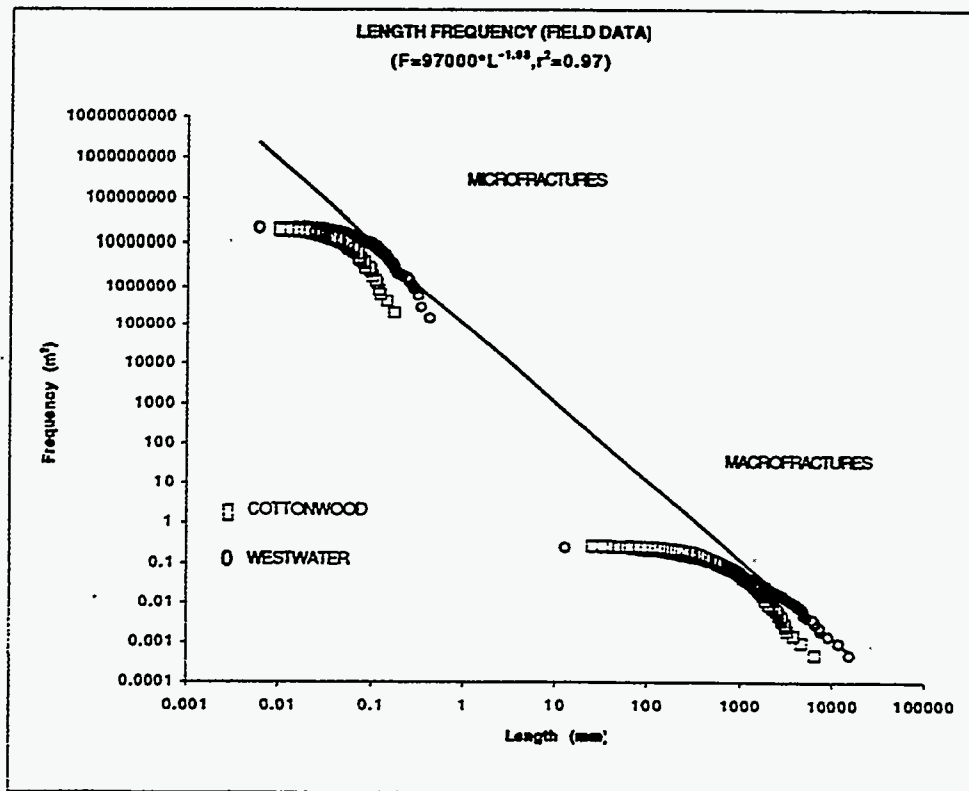
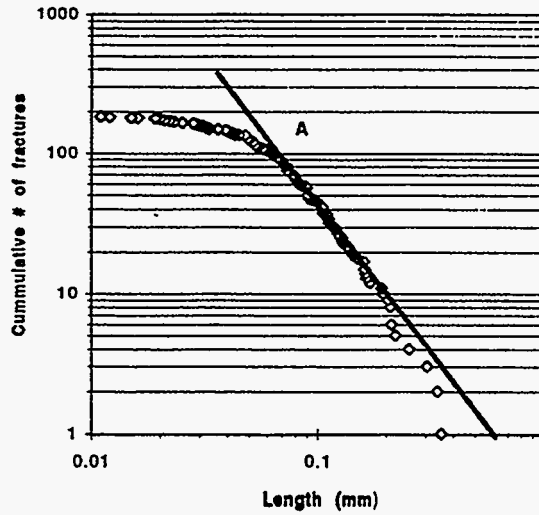
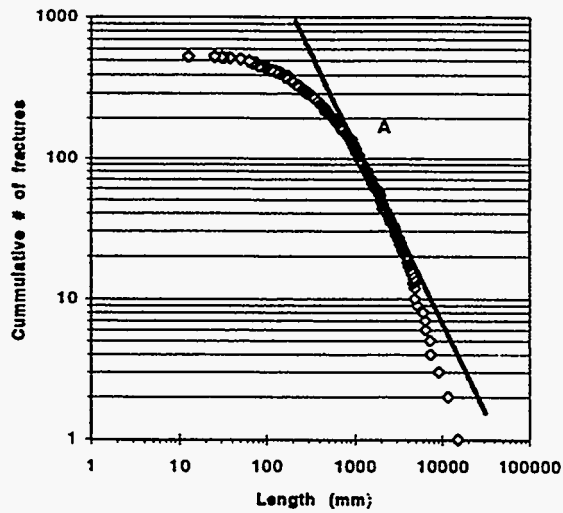


Figure 1.4. Relationship between the power-law distributions for the length of the microfractures and macrofractures in the Mesaverde formation, San Juan basin, New Mexico (Laubach *et al.*, 1997).



(a)



(b)

Figure 1.5. The power-law distributions for the lengths of micro and macrofractures in the Westwater pavement (Laubach *et al.*, 1997). (a) Power-law distribution for microfracture length; (b) Power-law distribution for macrofracture length.

CHAPTER 2: A SIMPLIFIED MONTE CARLO STUDY OF FRACTURE APERTURE AND PERMEABILITY DISTRIBUTIONS

Open fractures have significant impact on fluid flow in rock. Fracture aperture can be related to permeability by Darcy's law (Lake, 1989) and the equation for fluid flow in a slit (Bird *et al.*, 1960). The key characteristic of fractured reservoirs is that fluid flow in the reservoir is primarily in fractures, especially in the fractures of large aperture; the matrix and small fractures with most of the porosity contribute little to flow. Therefore, the distribution of fracture apertures in a fractured reservoir should have an important impact on distribution and anisotropy of effective permeability.

2.1 Fracture Aperture Distribution

A basic problem for theories of fluid flow in fractured rock has been that fracture systems comprise many individual fractures collectively ranging over many orders of magnitude in aperture and length. Many recent analyses have suggested that aperture and length distributions in populations of open fractures follow power-law scaling (Odling, 1997; Marrett, 1996; Clark *et al.*, 1995; Gross and Engelder, 1995). For those models that are based on average properties of fractures, meaningful averages can not be defined for phenomena that follow a power law. Small values compose most of the power-law distribution, but a few large values play a very important role in the overall properties of the population. Moreover, the variation in properties expected from one location to another (one grid block to another in dual-porosity simulation) is large.

The next several sections discuss a Monte Carlo study of the impact of fracture aperture distribution on the permeability and porosity of naturally fractured rock.

2.2 A Simplified Fractured Reservoir Model

2.2.1 Model Assumptions

Figure 2.1 shows a simplified fractured-reservoir model. The fractured reservoir is defined as rectangular, with height H , length in the direction of flow L , and width normal to these two directions W . All fractures are assumed open and parallel, and extend across the region. The fractures are shown as horizontal but could be vertical without altering the results below. We assume that the occurrence and properties of the fractures are uncorrelated, and, for simplicity, we assume that the matrix without fractures has zero permeability.

Based on this simplified model, Rossen (1997) has derived the probability distribution function for observed fracture aperture in a sub- interval of height h (for assumptions and derivation see Appendix A)

$$\begin{aligned} p(b) &= 1 - E(n)h \quad \text{for } b = 0 \\ p(b) &= hn(b) \quad \text{for } b > 0 \end{aligned} \quad (2.1)$$

where

h = a small interval in height; the total number of intervals in the selected region is H/h .

b = aperture of fracture; $b=0$ means no fracture is observed in the small interval of height h .

$n(b)$ = expected number of fractures with aperture b per unit length of scanline, given by

$$n(b) = \frac{ac}{H^*} b^{-c-1} \quad (2.2)$$

where a , c are empirical factors for power-law distribution; H^* is the length of the measured scanline. Equation 2.2 is derived from the cumulative number frequency function $N(b)$ observed in outcrops (e.g., Figure 1.3)

$$n(b) = \frac{1}{H^*} \frac{dN}{db} \quad (2.3)$$

where $N(b)$ has the form

$$N(b) = ab^{-c} \quad (2.4)$$

$E(n)$ = expected number of fractures of all apertures per unit length of scanline, is given by

$$E(n) = \int_{b_{min}}^{b_{max}} n(b) db \quad (2.5)$$

where b_{min} and b_{max} are the upper and lower limits on aperture b . In Figure 1.3, the data deviate from the power-law relation for very large and very small values of b . In the model, however, there are no values of b above b_{max} or below b_{min} . In principle, for a real power-law distribution, b_{max} is infinite and b_{min} is zero. One purpose of this study is to explore the relation between b_{min} , b_{max} and the sort of deviations from power-law behavior in data observed in Figure 1.3.

The cumulative distribution function $P(b)$ corresponding to Equation 2.1 is

$$\begin{aligned} P(b) &= (1 - E(n)h) + \int_{b_{min}}^b hn(b') db' \\ &= 1 - \int_{b_{min}}^{b_{max}} \frac{ac}{H^*} b^{-c-1} db + \int_{b_{min}}^b \frac{hac}{H^*} b'^{-c-1} db' \\ &= 1 + \frac{ah}{H^*} (b_{max}^{-c} - b^{-c}) \end{aligned} \quad (2.6)$$

2.2.2 Effective Permeability and Porosity

The fracture porosity ϕ_f for the region of the model is given by

$$\phi_f \equiv \frac{\sum_{i=1}^{H/h} b_i}{H} \quad (2.7)$$

The expected value of fracture porosity $E(\phi_f)$, derived from Equation 2.2 is

$$E(\phi_f) = \int_{b_{min}}^{b_{max}} bn(b)db = \frac{ac}{H^*} \left(\frac{b_{max}^{1-c} - b_{min}^{1-c}}{1-c} \right) \quad (2.8)$$

The effective permeability of the entire region is

$$\bar{k} = \frac{\sum_{i=1}^{H/h} \bar{k}_i}{H/h} \quad (2.9)$$

Where \bar{k}_i is the effective permeability of each interval, given by

$$\bar{k}_i = \frac{b_i^3}{12h} \quad (2.10)$$

The expected value of permeability for the region is

$$\begin{aligned}
 E(\bar{k}) &= \int_{b_{\min}}^{b_{\max}} p(b) \frac{b^3}{12h} db \\
 &= \frac{a}{12} \left(\frac{b_{\max}^{3-c} - b_{\min}^{3-c}}{3-c} \right)
 \end{aligned}
 \tag{2.11}$$

2.3 Monte Carlo Study of Fracture Aperture Sampling

2.3.1 Computational Approach

For a particular formation, we assume that Equation 2.2 applies and its parameters are known. $E(n)$ can then be calculated using Equation 2.5. One point should be noted here. For a real power-law distribution, b_{\min} is zero and b_{\max} is infinite. But the computer has limited capacity and can not represent an infinite number of fractures in the region; for $b_{\min} = 0$ it is impossible to find a finite sub-interval height h such that only one fracture appears in the region, as required by the model (Appendix A). Thus we use a finite b_{\min} corresponding to the minimum aperture observed in the outcrop on the power-law trend (Figure 1.3). We also use a finite b_{\max} to test how a finite b_{\max} value affects deviations from the power-law trend at large values of b . In the simulations, b_{\max} ranges from small values to very large values.

In our spreadsheet program, a random number generator generates a random value x between 0 and 1 for each interval. If x is less than the value of $(1-E(n)h)$ (Equation 2.1), there is no fracture in this interval. If x is greater than $(1-E(n)h)$, this implies that there is a fracture in the interval. In Equation 2.6, $P(b)$ is replaced by x and then the aperture of the fracture in this interval can be calculated by

$$b = \left[b_{max}^{-c} + \frac{(1-x)H^*}{ah} \right]^{-\frac{1}{c}} \quad (2.12)$$

This calculation is repeated for all (H/h) intervals. For each realization, the total number of fractures and the aperture of each fracture in the region of height H can thus be obtained. The aggregate properties (effective permeability and porosity) of the region can then be calculated by using Equations 2.7 and 2.9.

In this study, a power-law distribution of fracture aperture observed in the Boulder Creek sandstone formation (Laubach *et al.*, 1997) is used

$$N(b) = 0.851 b^{-0.758} \quad (2.13)$$

For this formation, $a = 0.851$, $c = 0.758$, $H^* = 90.5$ mm (Equations 2.3 and 2.4). In Figure 1.3, for the Boulder Creek formation, $b_{min} = 0.0067$ mm. Different b_{max} values are selected as part of the study.

2.3.2 Results and Analysis

A series of realizations for the Boulder Creek formation have been run. Figure 2.2 – 2.5 show the results for different values of b_{max} .

The aperture distributions resulting from these realizations have a great deal of variation in shape. The shapes (large b) can be grouped to three cases: (1) power-law (straight line in log-log plot); (2) falloff as observed in some of the outcrops (deviation below straight line at large b); (3) deviation above the power-law (straight line). For each case in Figures 2.2 to 2.5, a power-law straight line is drawn with slope -0.758 for this formation as in Equation 2.13. The straight line is fit to the upper portion of the curve. Because this study is very elementary, the three cases

are identified only qualitatively. The underlying rule for identification of the three cases is the trend of lower portion (large b) of the curve relative to the straight line. For illustration, the trends in Figures 2.2 – 2.5 are identified by type.

For small values of b_{\max} (0.3 mm), the simulated aperture distributions all deviate below the straight line trend of the power law as shown in Figure 2.2 (a) and (b). A similar deviation is seen in outcrop data (Figure 1.3).

In Figure 2.3 – 2.5, b_{\max} increases from 1000 to 10^8 mm, and the data follow the straight-line trend more closely, but there are still many realizations showing falloff or deviation-above in the lower portions of curves. From these results, we can conclude that whether or not a simulated aperture distribution is a straight line in a log-log plot is a stochastic event. The deviation of data from the straight-line trend in several of the cases in Figure 1.3 may reflect a finite b_{\max} , or may be a random result with an essentially infinite b_{\max} .

To further study the effect of b_{\max} on fracture aperture data, a Monte Carlo study was conducted over a range of b_{\max} values. For each value of b_{\max} , 30 realizations were run and the percentage of realizations following a straight-line distribution was calculated. Figure 2.6 shows the result of this Monte Carlo study. In the legend, “straight line” represents the percentage of realizations, out of 30, having a straight-line trend, as in Figure 2.3 (b). The “falloff” curve represents the percentage of realizations having “falloff” observed at large b as in Figure 2.3 (d). The “deviation above” curve indicates the percentage of realizations having a deviation above the straight-line trend at large b , as the one in Figure 2.3 (a). Note that the horizontal axis in Figure 2.6 is a log scale.

In Figure 2.6, with increasing of b_{\max} , the probability that one observes a power-law trend over the whole range of aperture values increases. The probability of having a falloff in the lower portion of the curve of aperture distribution dramatically decreases as b_{\max} increases to around 1000 mm and then levels off at around 20% as b_{\max} becomes larger. The probability of “deviation-above” the trend increases at low values of b_{\max} and then levels off.

2.4 Monte Carlo Study of Fractured-Reservoir Permeability

The purpose of this portion of the research is to determine the effective permeability distribution of a region of a fractured reservoir with a power-law distribution of fracture aperture, using the same simplified fractured-reservoir model as above.

2.4.1 Computational Approach

For each realization described in the section 2.3, we obtain the total number of fractures, effective permeability and porosity of the region. We can also find the largest aperture in the set of fractures. Repeating the realizations one thousand times gives results for all these parameters (number of fractures, largest aperture, permeability and porosity) that approach the true probability distributions for these random variables.

Rossen (1997) has derived an equation for predicting the probability of largest observed aperture b_1 (Appendix A)

$$\begin{aligned}
 P_{\max}(b_1) &\equiv [\text{probability that at least one aperture} > b_1] \\
 &= 1 - [\text{probability that all apertures} < b_1] \\
 &= 1 - [\text{probability that aperture} < b_1 \text{ in one interval } h]^{H/h} \\
 &= 1 - [1 - (\text{probability that aperture} > b_1 \text{ in one interval } h)]^{H/h} \\
 &= 1 - [1 - \int_{b_1}^{\infty} p(b') db']^{H/h} = 1 - [1 - h \int_{b_1}^{\infty} n(b') db']^{H/h} \\
 &= 1 - [1 + \frac{ach}{H} (\frac{b_{\max}^{-c} - b_1^{-c}}{c})]^{H/h} \tag{2.14}
 \end{aligned}$$

The permeability of the region can be calculated using Darcy's law (Lake, 1989) and Equation 2.10

$$\bar{k} \equiv \frac{Q}{A} \frac{\mu L}{\Delta \Phi} = \sum \bar{k}_i (h/H) \tag{2.15}$$

where Q is flow rate, A is cross sectional area of the region (HW in this case), μ is fluid viscosity, $\Delta\Phi$ is difference in total flow potential (pressure and hydrostatics) in the flow direction, and L is given in Figure 2.2. A simple estimate, k_1 , counting only the single fracture with the largest aperture, b_1 , is given by

$$k_1 = \frac{1}{HW} \left(\frac{1}{12} \frac{b_1^3 W \Delta\Phi}{\mu L} \right) \frac{\mu L}{\Delta\Phi} = \frac{1}{12} \frac{b_1^3}{H} \quad (2.16)$$

In the following Monte Carlo study, one thousand realizations were run for each case with different parameters (e.g. H , h , b_{\max} , etc.). For each case, results for fracture frequency, largest observed aperture, permeability and porosity are compared to Equations 2.14 – 2.16.

2.4.2 Results and Analysis

Figure 2.7 shows cumulative statistics for 1000 realizations, each like those in Figure 2.2 – 2.5 for one set of parameters. Each of these 1000 realizations represents one region of height H in which there are 1000 intervals of height h . The number of fractures observed in the 1000 realizations (Figure 2.7 (a)) is normally distributed, that is, the data for the number of fractures observed fall on a straight line in the probability plot. On average, about 418 fractures are observed in the 1 m height of the region.

These results violate the strict assumptions in the mathematical derivation of the model (Appendix A) in two ways. First, with nearly half of the intervals of height h containing a fracture, the odds of one interval containing two fractures is not virtually zero, as assumed. Second, individual fractures of aperture up to 1000 mm (Figure 2.7 (c)) are observed, albeit rarely. This clearly violates the assumption that interval height h is larger than any individual fractures. As a result, permeabilities and porosities calculated with those assumptions are enormous.

These occasional wide fractures have a large impact on permeability. Therefore, the shape of the distribution of permeabilities in Figure 2.7 (c) fits nearly exactly the shape of the distribution of largest fractures in Figure 2.7 (b). Figure 2.8 shows the correlation between the largest fracture aperture and permeability for the simulation results. They have a linear correlation in the log-log plot with the slope of 3 approximately, which is in agreement with Equation 2.16. This implies that the analytical formulae for the largest observed fracture, Equation 2.14, predicts effective permeability of the region as well. The single largest fracture controls effective permeability because it is much larger than the rest and permeability scales as the third power of aperture.

The value of b_{\max} has substantial impact on permeability. Figure 2.9 shows results for a larger value of b_{\max} . Most of the distribution is unchanged, but the single largest observed aperture increases as b_{\max} becomes larger. That is, no difference would be observed in most individual cases (realizations), but occasionally, large values of b are possible with larger values of b_{\max} . For relatively small b_{\max} , the largest observed aperture is sensitive to increasing b_{\max} . With b_{\max} approaching infinity (e.g., $b_{\max} > 100$ m), the largest observed aperture is no longer sensitive to increasing b_{\max} . The effective permeability and porosity change nearly exactly as the largest observed aperture does, but the fracture frequency does not change much. Equation 2.11 indicates that the expected value of effective permeability diverges to infinity as b_{\max} approaches infinity. That is, the bulk of the probability distribution for permeability is unaffected as b_{\max} approaches infinity, but the tail of this distribution with huge values increases, which causes the expected value of permeability to diverge.

Figure 2.10 is the same as Figure 2.9 except $h = 2$ mm; that is, there are 500 intervals in the region instead of 1000. Changing the value of h does not substantially change the results over most of the distribution, but extreme, unusually high values of permeability are higher with larger h . Figure 2.11 compares results for different values of h . Note a larger value of h gives less variation in fracture frequency. Since h is an artificial parameter of our computational model, this represents a numerical artifact in our technique.

Figure 2.12 shows how H affects the results. There are two groups of curves with different values of b_{\max} in the graphs. One group of results is for $H = 1$ m, the other for $H = 10$ m. For both, $h = 1$ mm. There are 10000 intervals for the case of $H = 10$ m, 10 times as for $H = 1$ m. Increasing the height of the region substantially increase the value of the largest observed aperture, and thus alters the distributions of effective permeability and porosity. For fixed h , increasing the height of the region means more intervals in the region, and thus there is an increasing chance of observing an extremely wide aperture. Figure 2.13 is the same as Figure 2.12 except $h = 2$ mm.

We also compare the distribution of largest observed aperture with that predicted by Equation 2.14. The results are shown in Figure 2.14 – 2.17. All cases show good fits. This implies that the Equation 2.14 can be used to predict the distribution of largest aperture, and therefore the distribution of permeabilities.

These results reflect the simplifying assumptions made in our model, especially that all fractures extend across the region of interest (Figure 2.1). In reality, fracture length is finite and flow is through interconnected *networks* of fractures. The next chapter introduces a model for these effects.

2.5 Conclusions

- (1) For small values of the upper limit to aperture size, b_{\max} , the simulated aperture distributions all deviate below the straight-line trend of the power law (Figures 2.2 (a) and (b) and 2.6). For large values of b_{\max} , that a simulated aperture distribution follows a power-law trend is a stochastic event. Therefore, a finite value of b_{\max} may exist and cause the falloff in occurrence of large aperture observed in three cases by Marrett (1997) (Figure 1.3); or the observed falloff may be a stochastic result.

- (2) The Monte Carlo study of fracture aperture distribution shows that with increasing of b_{\max} , the probability that one observes a power-law trend over the whole range of aperture values increases.
- (3) As Rossen (1997) predicted (Appendix A), the number of fractures observed in a given interval is a normally distributed random variable.
- (4) Simulation results for the Boulder Creek sandstone violate the initial assumptions (Appendix A) that h is larger than any fracture apertures observed and so small that the probability of two fractures in the interval h is virtually zero. As a result, permeabilities and porosities calculated with those assumptions are enormous.
- (5) For the Boulder Creek formation, with large b_{\max} , effective permeability is dominated by the single fracture with largest observed aperture. Increasing the value of b_{\max} does not change most of the aperture distribution, but increases the single largest observed aperture.
- (6) The simulated results fit the analytical equation for the largest observed aperture (Equation 2.14) very well. Thus, this equation can be used to predict the distribution of effective permeability.
- (7) Interval height h does affect the simulation results. In some cases (large values of b_{\max}), effective permeability is higher with larger h . Since h is an arbitrary parameter introduced in the model, this is a numerical artifact in the model.
- (8) As predicted (Equations 2.14 and 2.16), the expected value of permeability increases (approaching infinity) as the size of the porous medium H increases (Figure 2.12).

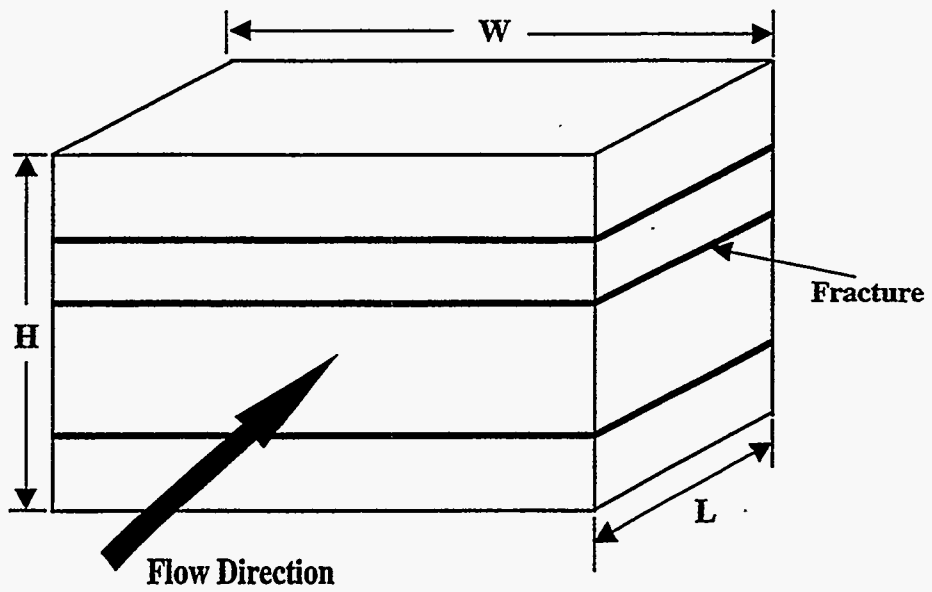
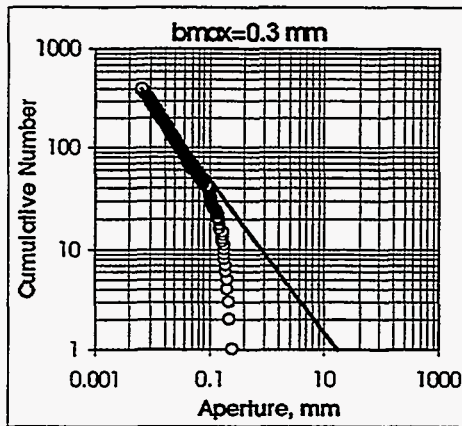
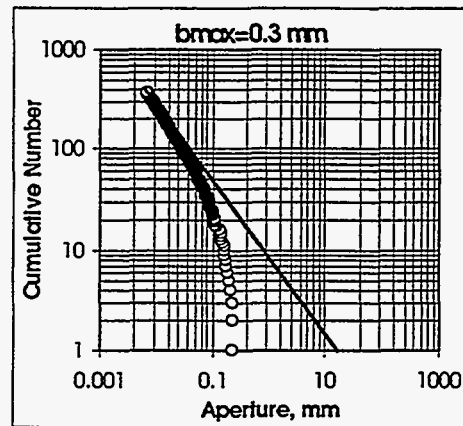


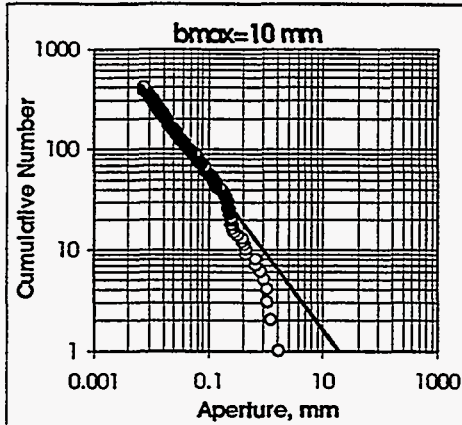
Figure 2.1. Schematic of a simplified fractured reservoir model



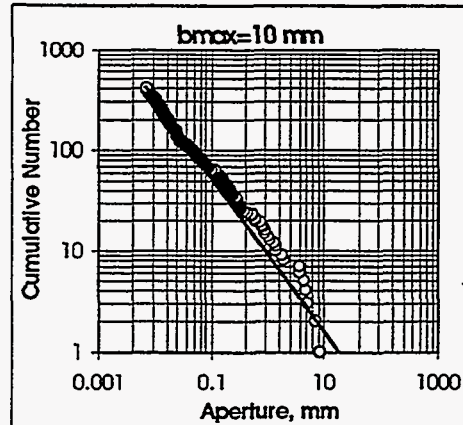
(a)



(b)

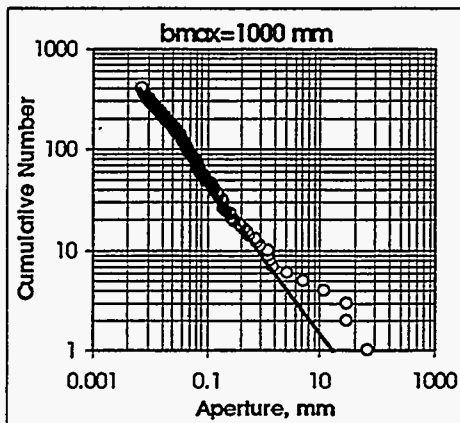


(c)

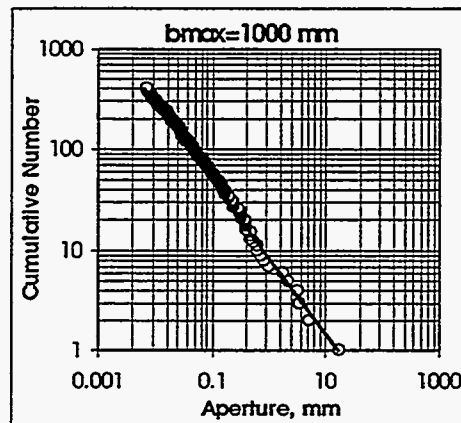


(d)

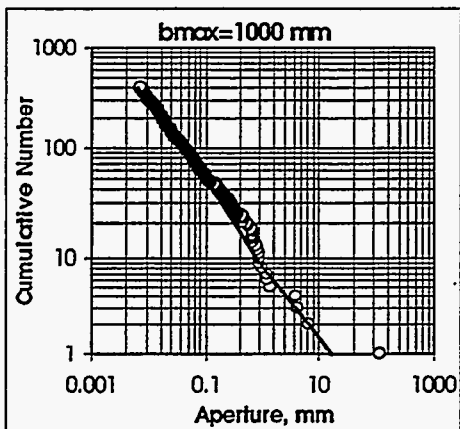
Figure 2.2. Realizations of power-law aperture distribution for the Boulder Creek formation with $b_{\max}=0.3$ (a, b) and 10 mm (c, d). Type of trend: (a) falloff; (b) falloff; (c) falloff; (d) falloff.



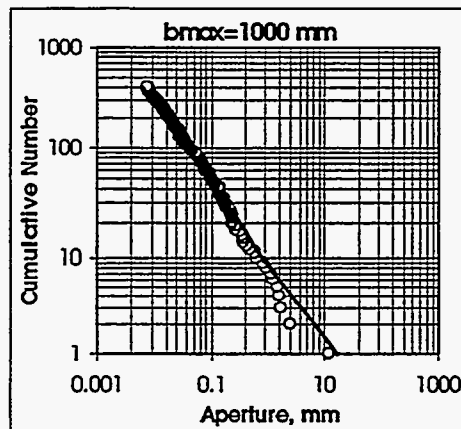
(a)



(b)

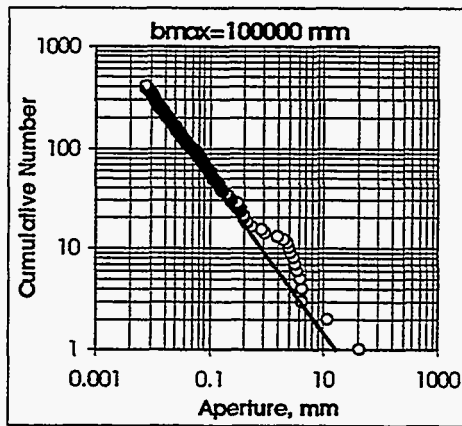


(c)

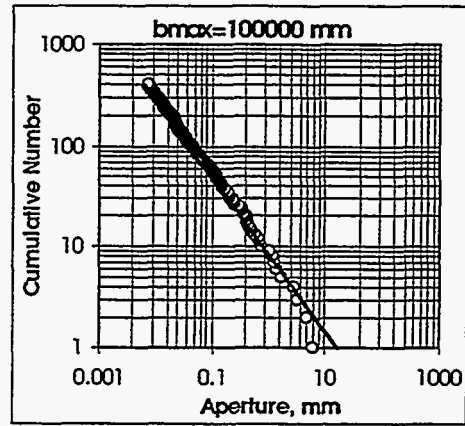


(d)

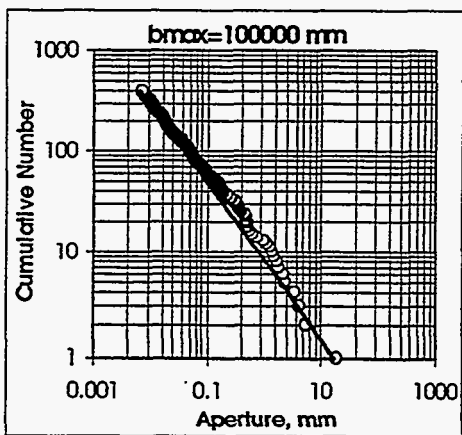
Figure 2.3. Realizations of power-law aperture distribution for the Boulder Creek formation with $b_{max} = 1000$ mm. Type of trend: (a) deviation above; (b) straight line; (c) deviation above; (d) falloff.



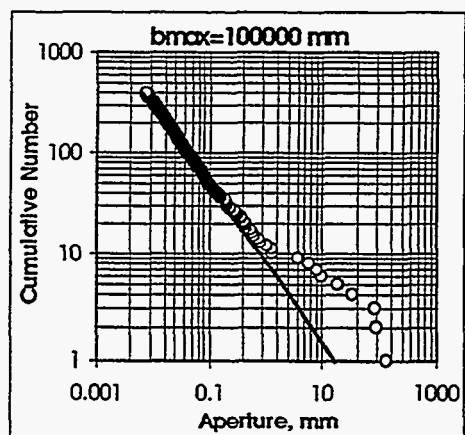
(a)



(b)

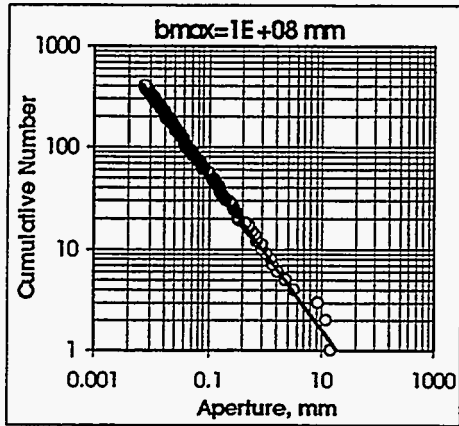


(c)

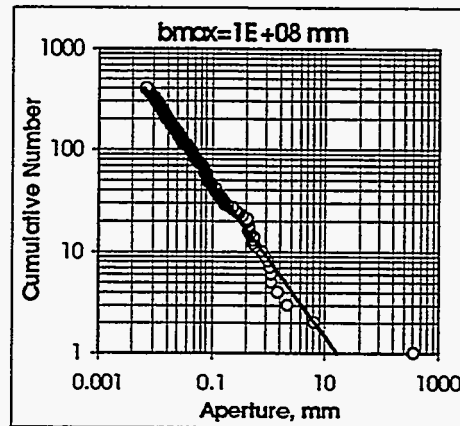


(d)

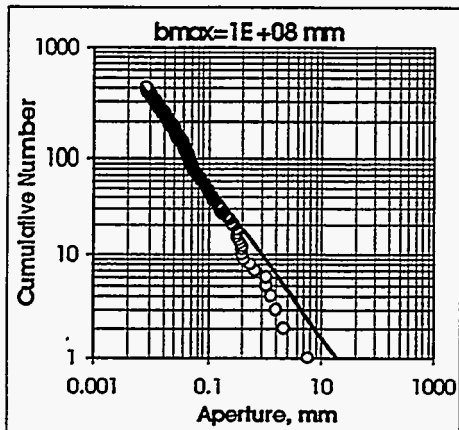
Figure 2.4. Realizations of power-law aperture distribution for the Boulder Creek formation with $b_{\max} = 100,000$ mm. Type of trend: (a) deviation above; (b) falloff; (c) straight line; (d) deviation above.



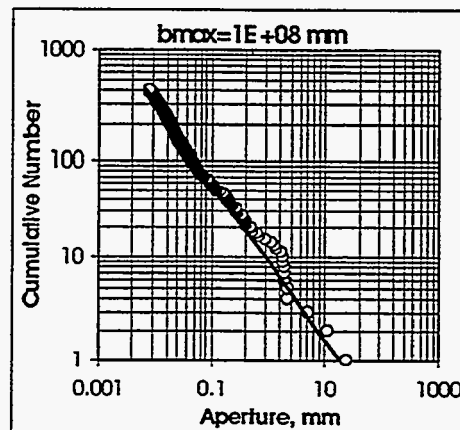
(a)



(b)



(c)



(d)

Figure 2.5. Realizations of power-law aperture distribution for the Boulder Creek formation with $b_{\max} = 10^{10}$ mm. Type of trend: (a) straight line; (b) deviation above; (c) falloff; (d) straight line.

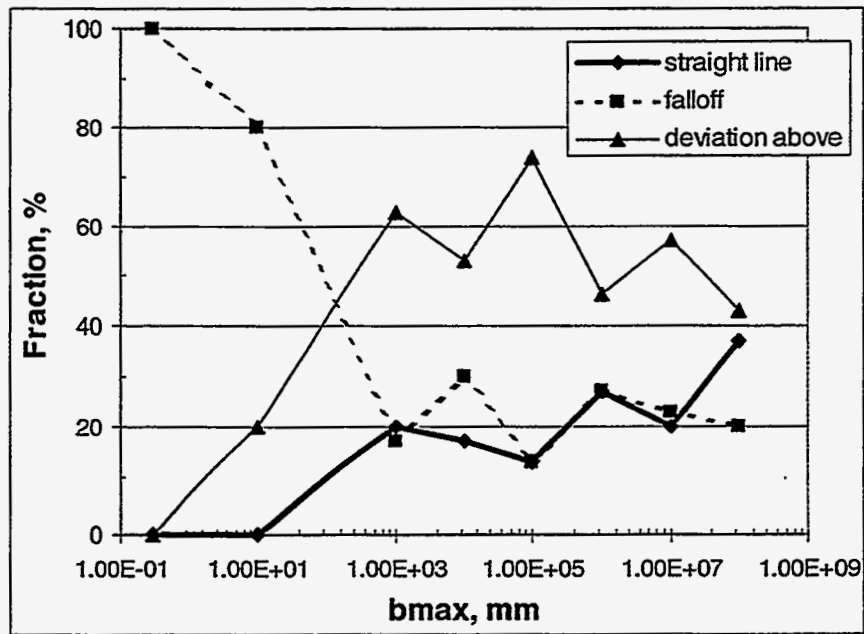


Figure 2.6. Effect of b_{max} on percentages of straight-line, falloff and deviation-above trends in fracture aperture. For each value of b_{max} , a total 30 realizations were run.

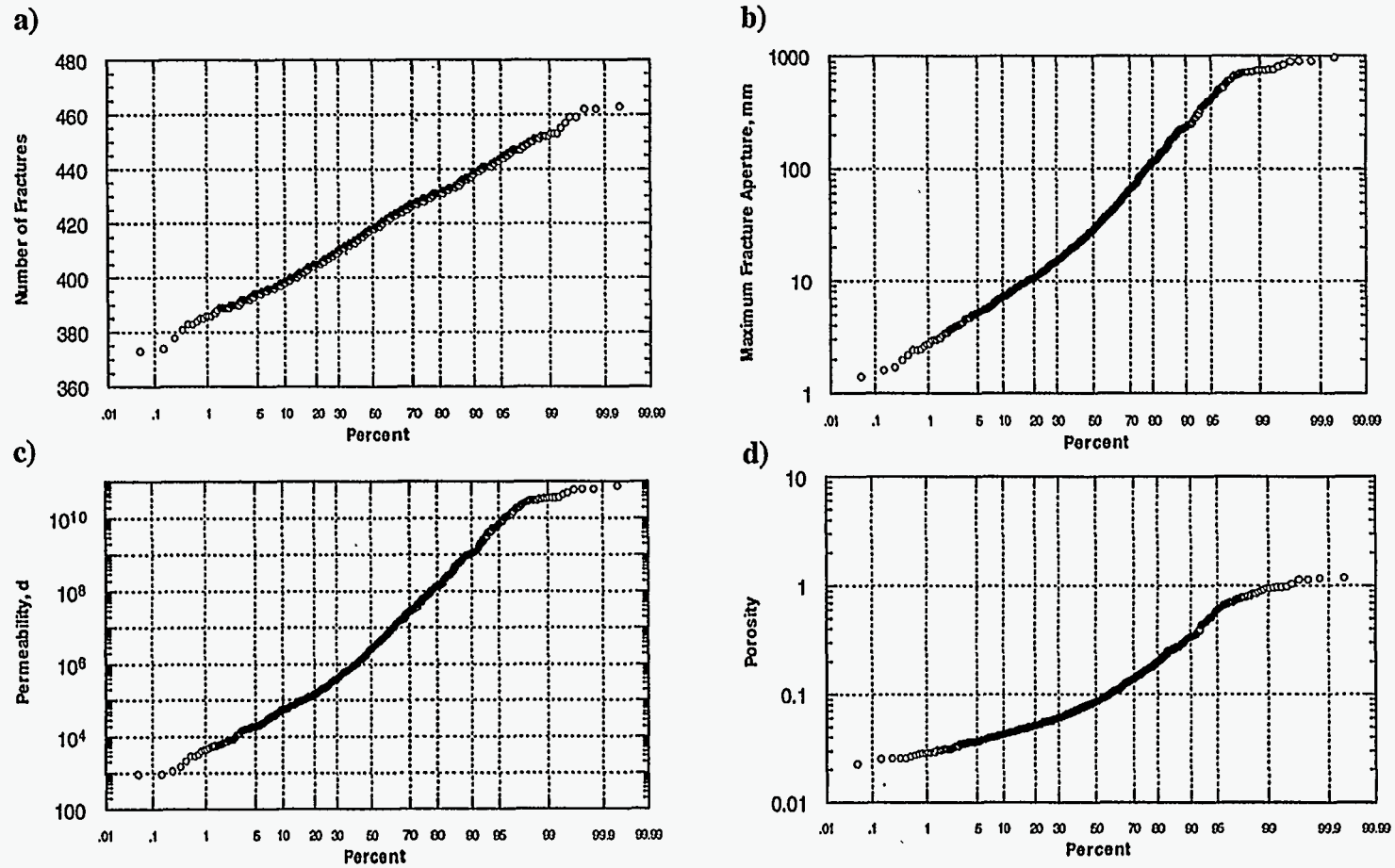


Figure 2.7. Results of 1000 realizations of fracture occurrence and apertures in a 1 m block, using parameters of Boulder Creek sandstone. $b_{\max} = 1$ m, $b_{\min} = 0.0067$ mm, $H = 1$ m, $h = 1$ mm.

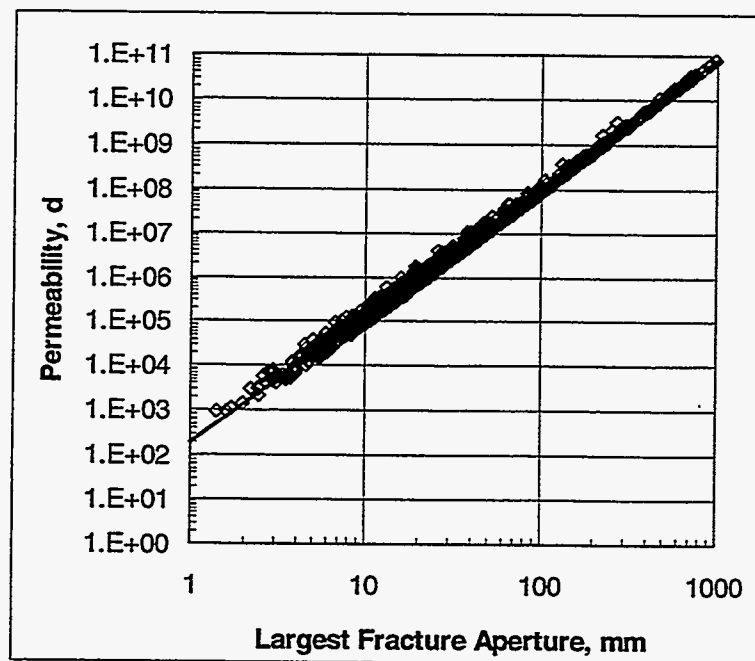


Figure 2.8. Correlation between the largest fracture aperture and permeability for the simulation results shown in Figure 2.7.

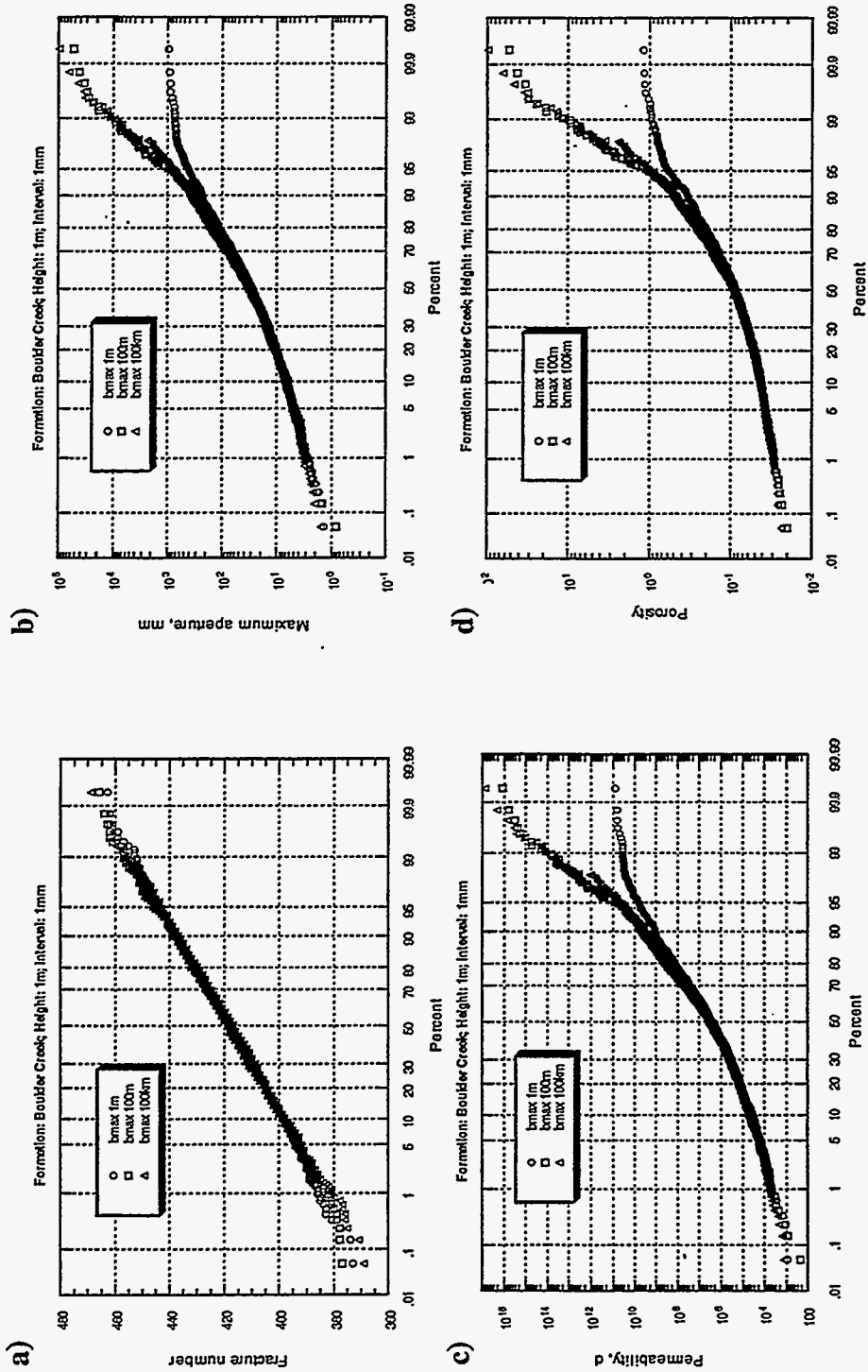


Figure 2.9. Comparison of results of 1000 realizations of fracture occurrence and apertures for three values of b_{\max} (1, 100, 100,000 m) in a 1 m block, using parameters of Boulder Creek sandstone. $b_{\min} = 0.0067$, $H = 1$ m, $h = 1$ mm.

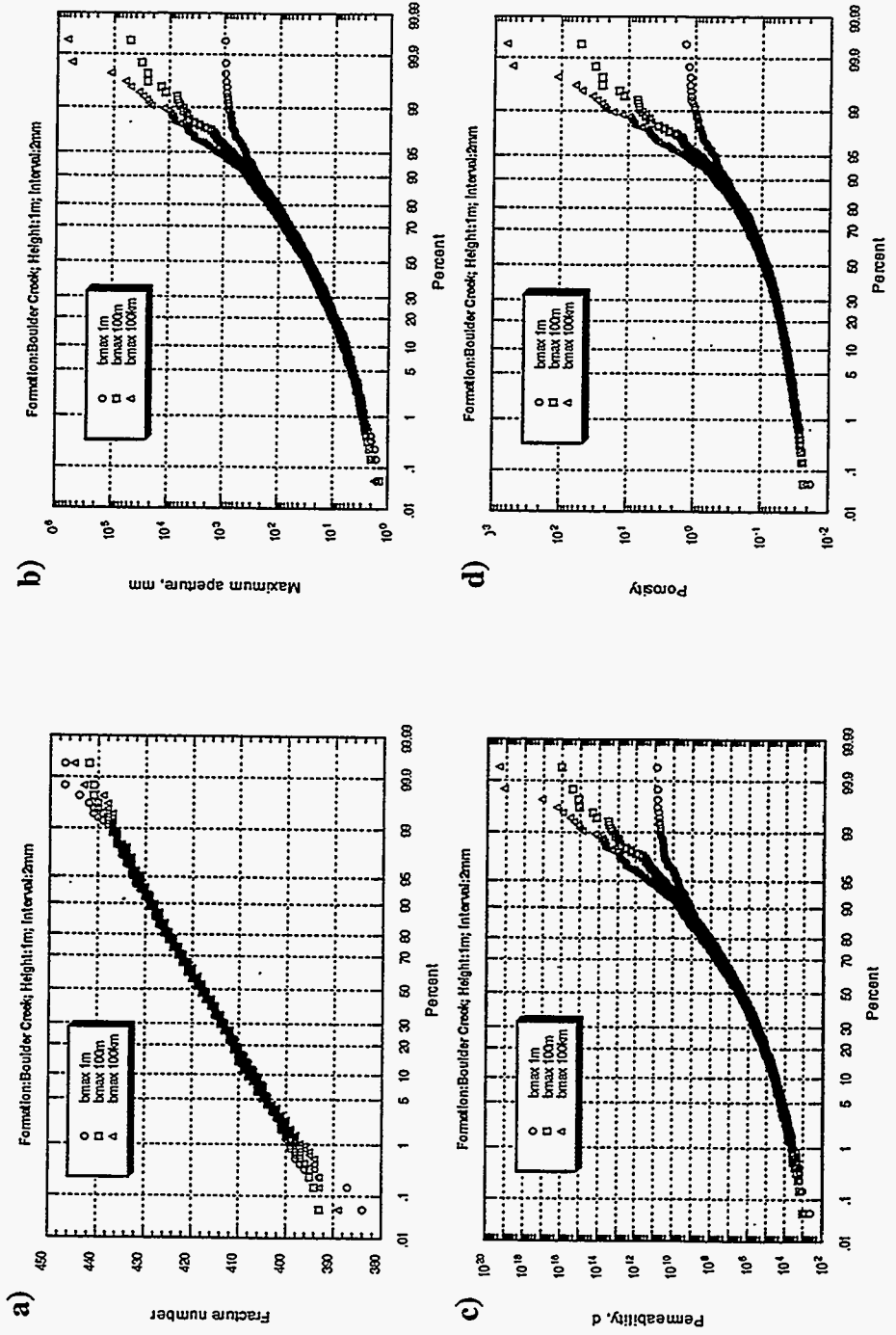


Figure 2.10. Comparison of results of 1000 realizations of fracture occurrence and apertures for three values of b_{max} (1, 100, 100,000 m) in a 1 m block, using parameters of Boulder Creek sandstone. $b_{min} = 0.0067$, $H = 1$ m, $h = 2$ mm.

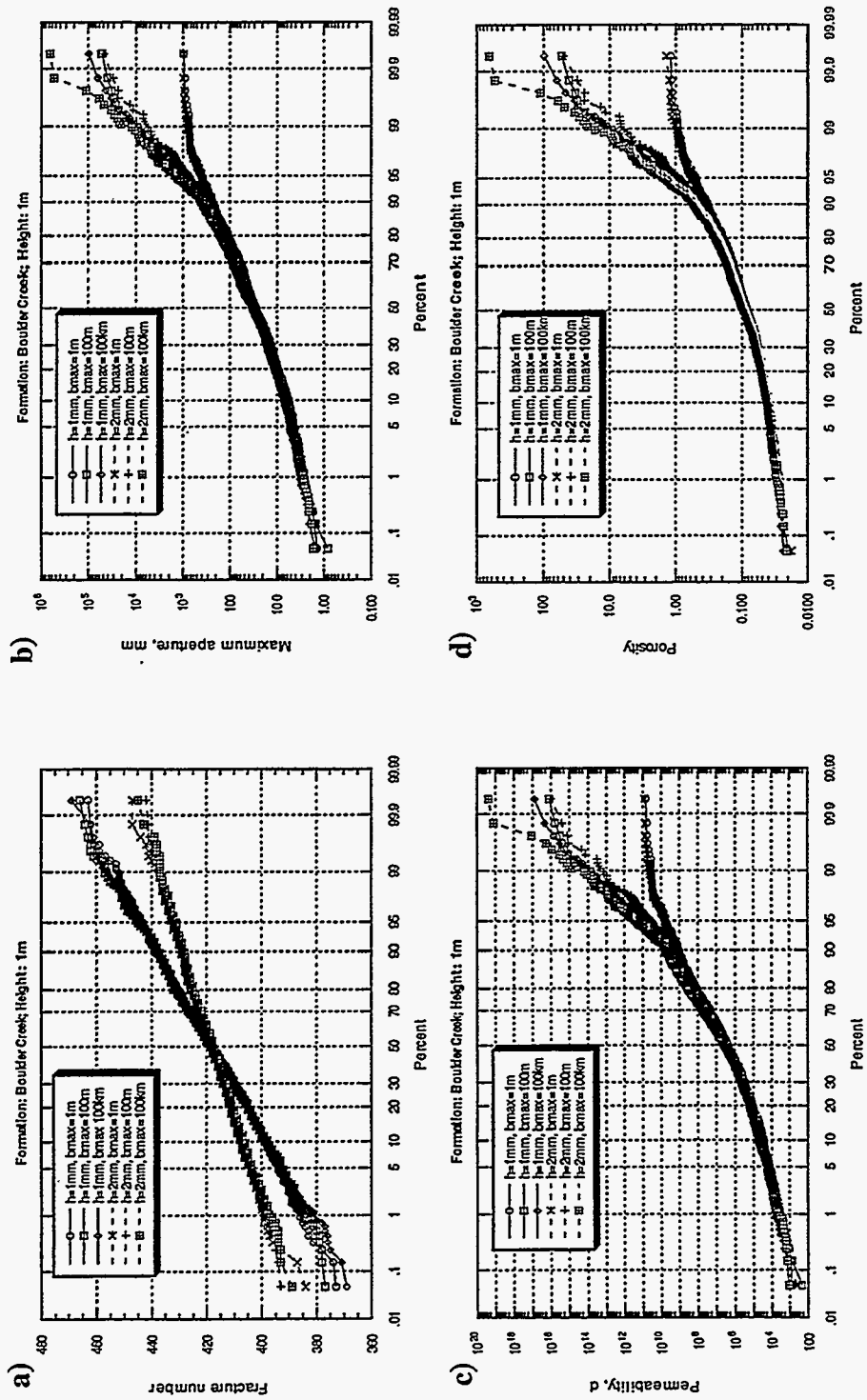


Figure 2.1.1. Comparison of results of different values of b_{max} (1, 100, 100,000 m) and h (1, 2 mm) in a 1 m block, using parameters of Boulder Creek sandstone. $b_{min} = 0.0067$, $H = 1$ m.

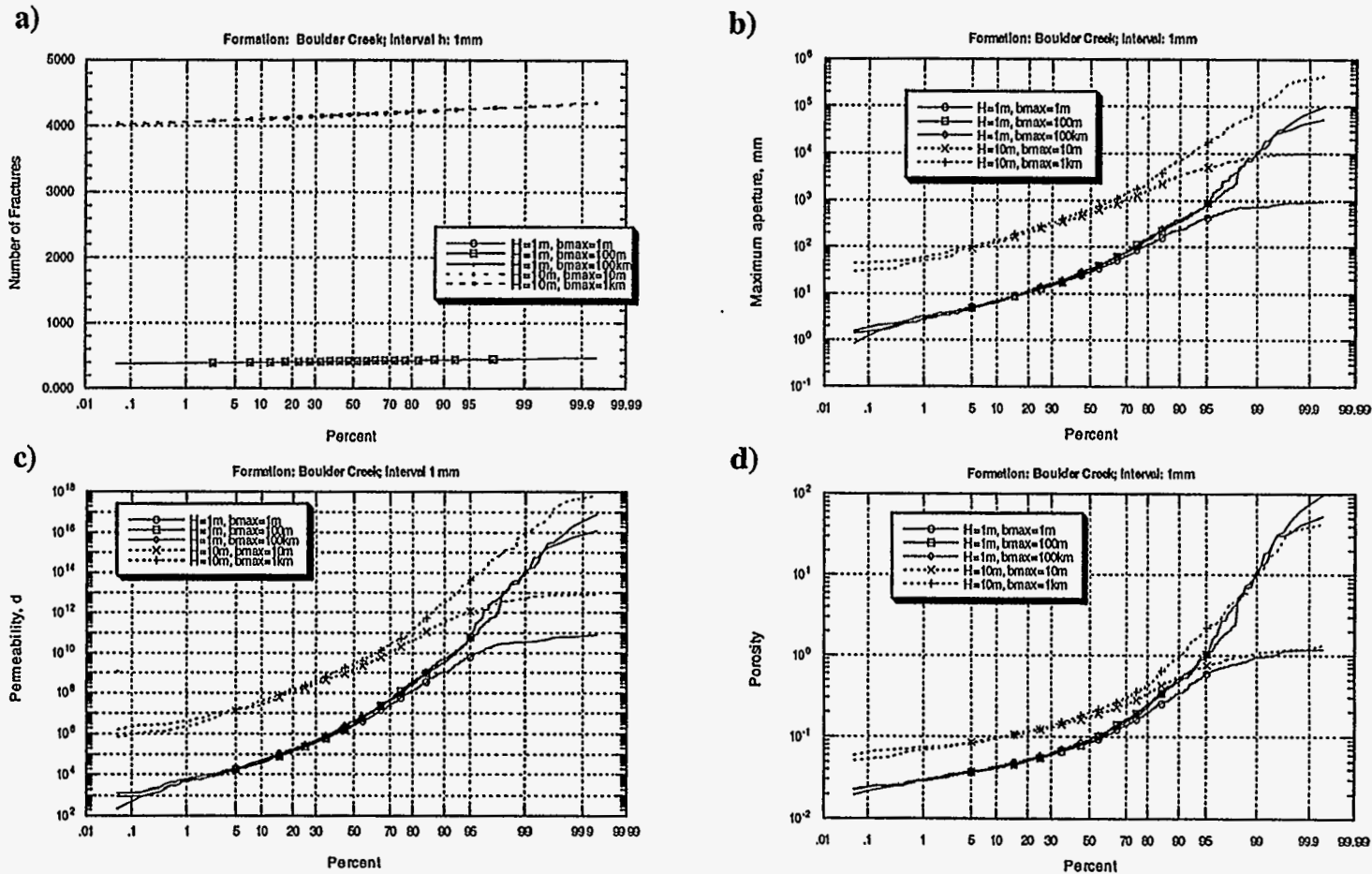
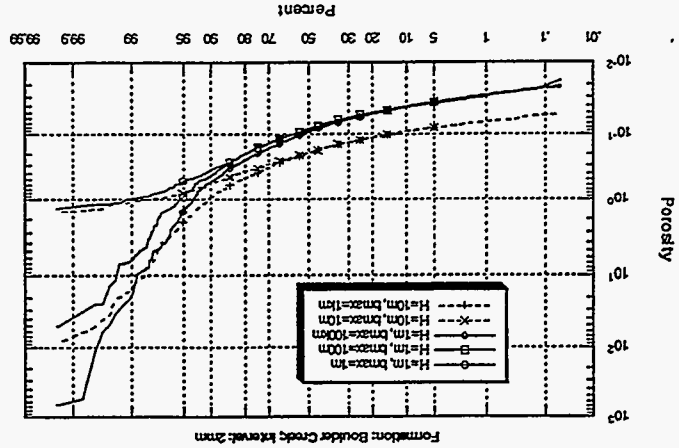
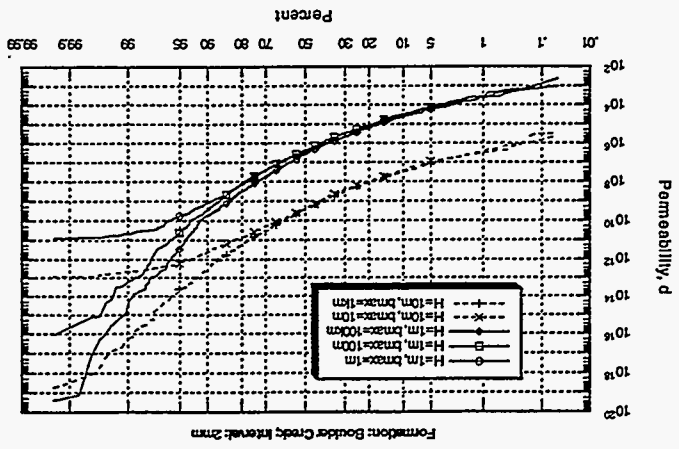


Figure 2.12. Comparison of results of different b_{max} and H , using parameters of Boulder Creek sandstone. $b_{min} = 0.0067$, $h = 1$ mm.

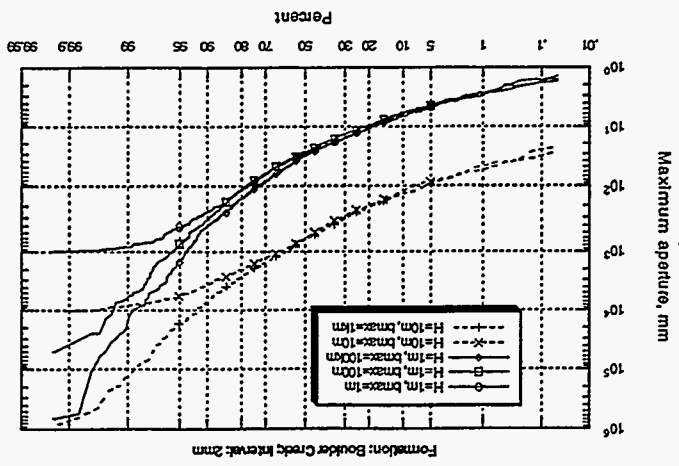
Figure 2.13. Comparison of results of different values of b_{max} (1, 100, 100000 m) and H (1, 10 m), using parameters of Boulder Creek sandstone. $b_{min} = 0.0067, h = 2$ m.



(a)



(b)



(c)

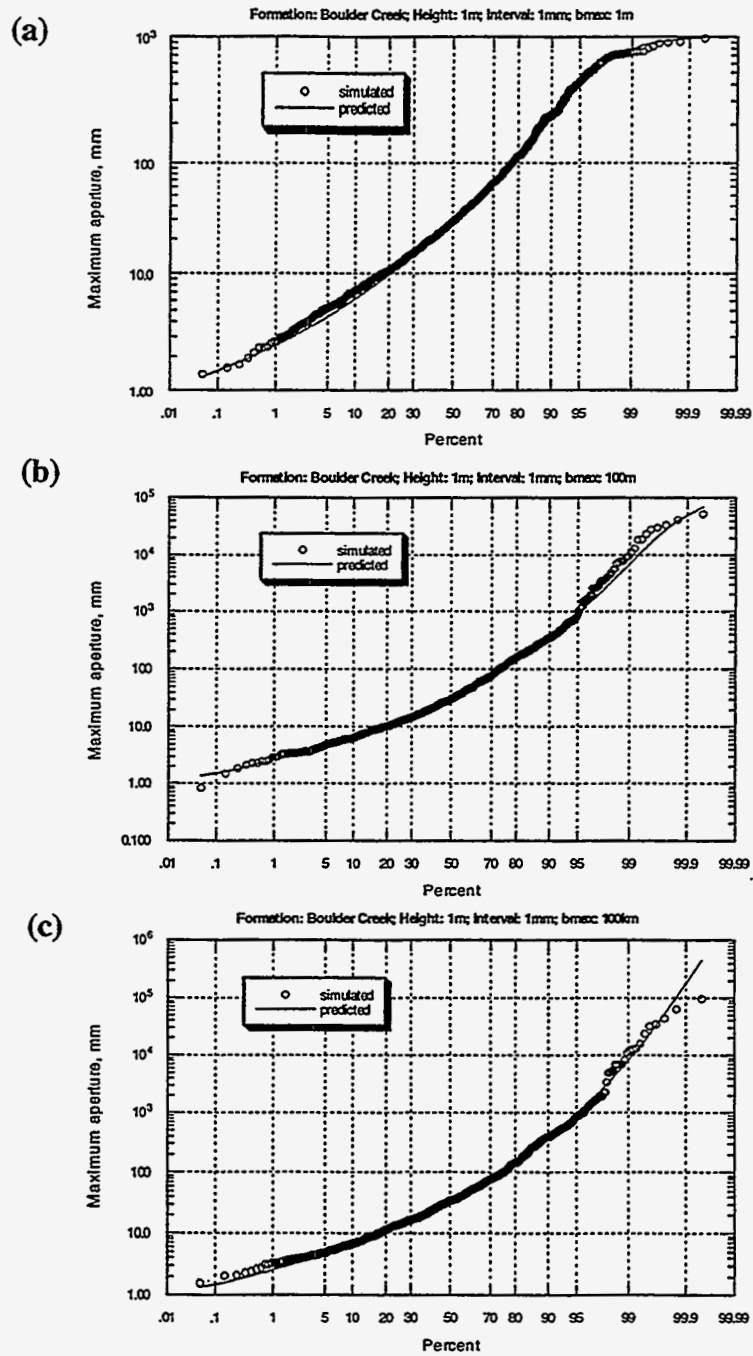


Figure 2.14. Comparison of simulated and predicted maximum aperture distribution for different values of b_{\max} . $H=1\text{m}$, $h=1\text{mm}$. (a) $b_{\max} = 1\text{ m}$; (b) $b_{\max} = 100\text{ m}$; (c) $b_{\max} = 100\text{ km}$.

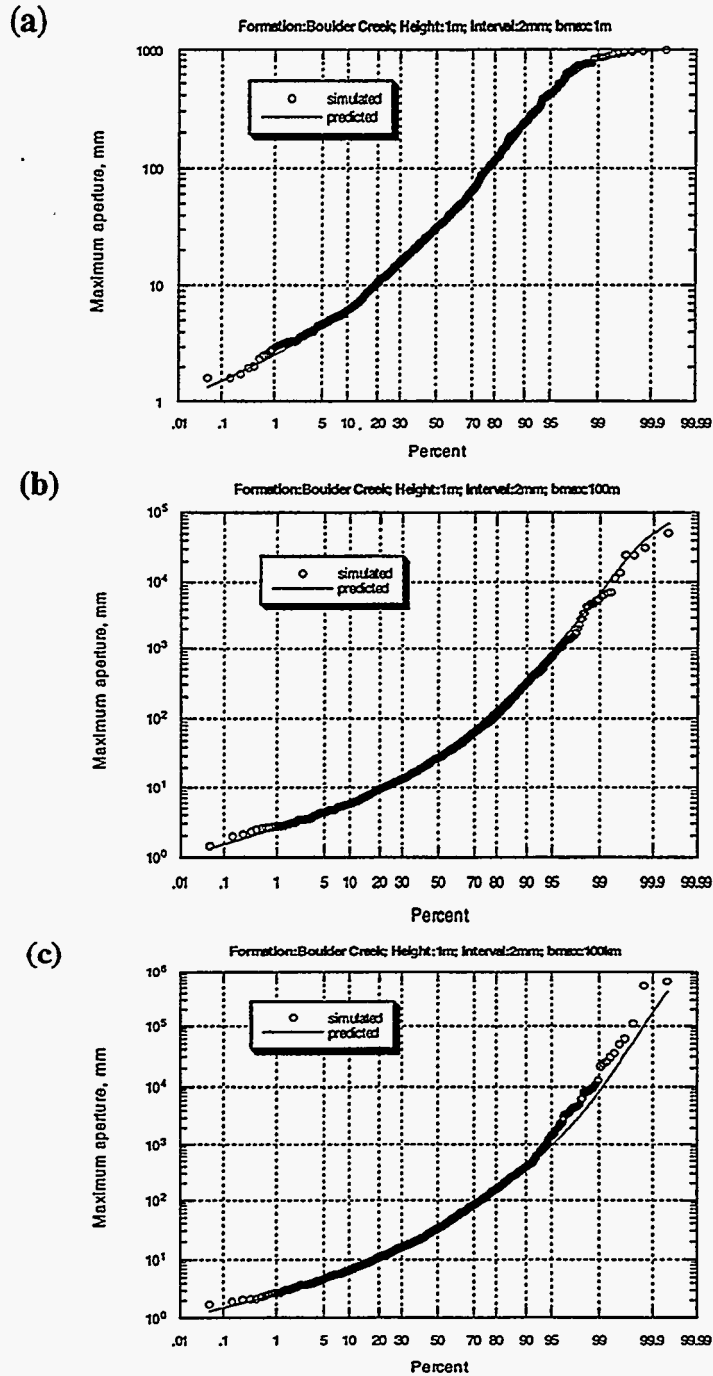
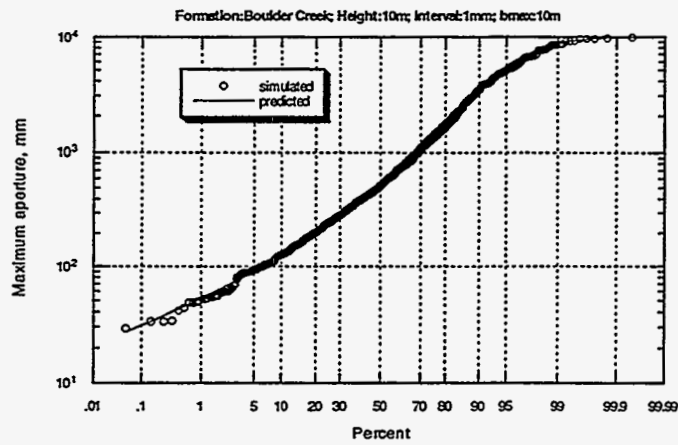
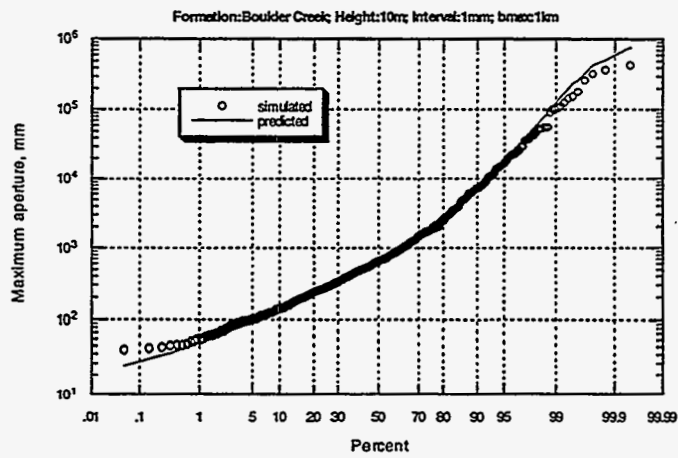


Figure 2.15. Comparison of simulated and predicted maximum aperture distribution for different values of b_{\max} . $H=1\text{m}$, $h=2\text{mm}$. (a) $b_{\max} = 1 \text{ m}$; (b) $b_{\max} = 100 \text{ m}$; (c) $b_{\max} = 100 \text{ km}$.

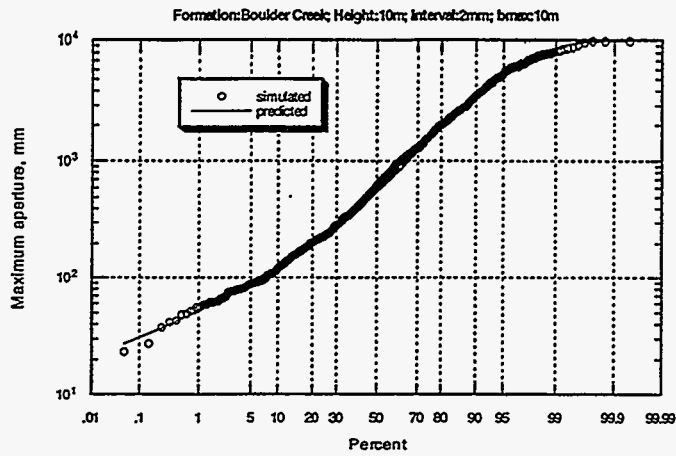


(a)

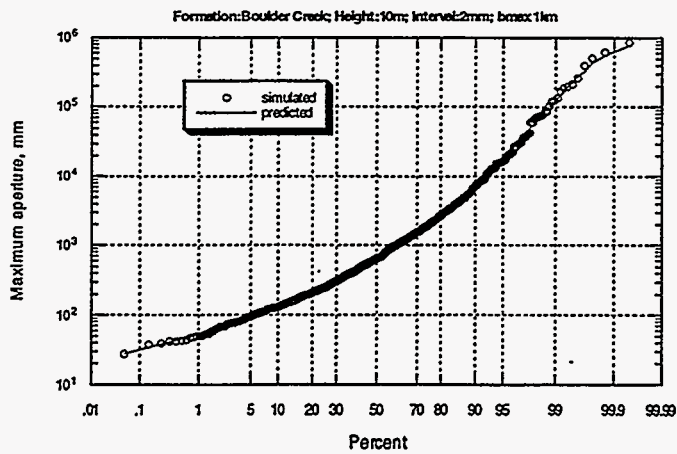


(b)

Figure 2.16. Comparison of simulated and predicted maximum aperture distribution for different values of b_{max} . $H=10m$, $h=1mm$. (a) $b_{max} = 10 m$; (b) $b_{max} = 1 km$.



(a)



(b)

Figure 2.17. Comparison of simulated and predicted maximum aperture distribution for different values of b_{\max} . $H=10\text{m}$, $h=2\text{mm}$. (a) $b_{\max} = 10\text{ m}$; (b) $b_{\max} = 1\text{ km}$.

CHAPTER 3: 3-D FRACTURE NETWORK INTERCONNECTIVITY

In reality, fractures of limited length are dispersed in a reservoir in 3D space. Fractures have significant impact on the fluid flow primarily when they connect up to form a high-permeable conduit for flow. Therefore, before the permeability and permeability anisotropy of grid blocks in dual-porosity simulation are calculated, the interconnectivity of fractures in 3D space must be determined.

3.1 Generation of 3-D Fracture Network

3.1.1 FracMan™ Program and Conceptual Geometry Models

A commercial fracture simulator called FracMan™ was selected to study the interconnectivity of the fracture system. FracMan™ is a software package developed by Golder Associates Inc. (Seattle, Washington) to model the geometry of discrete features. It provides functionalities such as raw data analysis, generation of fracture networks according to the given input parameters and conceptual geometry model, connectivity analysis for the fracture network generated, finite-element mesh generation and output post-processing to facilitate flow and transport modeling in networks of fractures using companion program Mafic™.

There are nine conceptual geometry models in the simulator that can be used to generate fracture networks. They are Enhanced Baecher, Nearest Neighbor, Levy-Lee Fractal, War Zone, Poisson Rectangle, Non-Planar Zone, Fractal POCS, Fractal Box and Geostatistical models. Several of these models are briefly described here. This description is not an exhaustive description of features in FracMan™, which can be found elsewhere (Dershowitz *et al.*, 1995).

The Baecher model was one of the first well-characterized discrete-fracture models. In this model, the fracture centers are located randomly and without autocorrelation in space using a Poisson process, and the fractures are generated as disks with a radius and orientation selected

randomly using statistical distributions chosen by the user. The Enhanced Baecher model (Dershowitz *et al.*, 1989) extends the Baecher model by providing a provision for fracture terminations. We did not use the fracture termination option in our study.

The Nearest Neighbor model is a simple, non-stationary model in which fracture intensity decreases exponentially with distance from “major features” identified by the user.

The Levy-Lee fractal model utilizes a process based upon “Levy flight” (Mandelbrot, 1985). The Levy-flight process is a type of random walk, for which the length L of each step is given by the probability function

$$P_{L_s} [L > L_s] = L_s^{-D} \quad (3.1)$$

where D is the fractal mass dimension of the point field of fracture centers, and L_s is the distance from one fracture to the next for the previous step in the generation sequence.

The War Zone model (Dershowitz, 1989) simulates regions of increased fracture intensity which cannot be represented by abstract statistical or mathematical processes such as fractals. In the War Zone model, regions with different geologic characteristics are classified as “war zones”. The boundaries of war zones are defined by large, sub-parallel fractures. These “war zones” have a higher fracture intensity, such that the “war-zone intensity factor” is the ratio of fracture intensity inside war zones to the intensity outside war zones.

3.1.2 Constraints on Modeling

For a given power-law distribution of fracture length in a particular region, whether or not the fractures link up is a stochastic event. In this sense, the connectivity of fractures is a percolation problem.

From Equation 1.3, a power-law distribution for fracture length can be expressed as

$$\frac{N}{V_0} = \frac{m}{V_0} L^{-e} = m' L^{-e} \quad (3.2)$$

where V_0 is the volume of the outcrop region in which Equation 1.3 is obtained; and m , m' and e are constants. Strictly, N in Equation 1.3 represents the cumulative number of fractures with exposed length greater than L in a given area of outcrop; in Equation 3.2 it is cumulative number in a given volume of reservoir.

In principle, the number of fractures N in a power-law distribution such as Equations 1.2, 1.3 or 3.2 is infinite, if the power-law extends to zero aperture or length. But, because the resources of the computer are limited, it is not possible for the computer to generate all the fractures in the region. Therefore, only fractures of length greater than some cut-off length L_{min} are represented. Thus, the total number of fractures represented in a region with volume of V can be expressed as

$$N = Vm'L_{min}^{-e} \quad (3.3)$$

where L_{min} is the minimum fracture length modeled in the region. The computer represents only the finite number of fractures in the Equation 3.3 with length greater than some given length L_{min} . In other words, there is a truncation error in the model because of excluding the smaller fractures. This implies that one has difficulty determining connectivity for sure at any given scale, because one cannot generate all the infinite number of fractures in that region. According to Equation 3.3, for given N , the smaller the region volume V , the smaller L_{min} can be and the smaller this truncation effect. Therefore one goal in this research was to study the fracture connectivity at the small scale and then attempt to upscale those results to larger scale.

However, the connectivity of fractures at one scale does not necessarily determine the connectivity of fractures at another scale. Figure 3.1 illustrates this physical restriction schematically. This restriction implies that one cannot necessarily scale-up results for small regions to larger regions. This conjecture is confirmed by simulation in Figure 3.2. The details of the simulation method and parameter values used are discussed below. In Figure 3.2 (b) each sub-region has a connected pathway but the region as whole has none. Figure 3.3 shows the trace

maps of fracture intersections with the trace plane located in the middle of the region in the two cases.

Rossen (Appendix B) has studied the scaling of fracture frequency and length with the volume of observation for power-law distributions of fracture length (Equation 3.2). There are three important cases:

- (1) For $e > 3$, the fractures appear to grow longer (relative to the size of region) as the size of a cubic region decreases. Thus, fractures are guaranteed to link up and/or cross the region individually if the size of region shrinks sufficiently. Interconnectivity of the fracture network is guaranteed on the microscopic scale.
- (2) For $e < 3$, the fractures appear more numerous and larger as the size of the cubic region increases. Thus fractures are guaranteed to link up on the megascopic scale as the size of the region increases sufficiently. The outcrop data for the Westwater pavement (Laubach *et al.*, 1997) used in much of this research reflects an exponent e of $2.85 < 3$.
- (3) For a region confined to a bed of fixed thickness, the height stays fixed as the cross-sectional area of the region increases. In this case, the fractures are not guaranteed to link up on either the microscopic scale or megascopic scale. This suggests that the search for connectivity focus on regions of size equal to the thickness of the layer, where the probability of connectivity among the finite number of fractures that can be modeled on a computer is greatest.

To verify these three conclusions, a series of realizations of fracture systems using FracMan™ have been generated. Figure 3.4 shows case (1), i.e. a power-law distribution with exponent $e > 3$. Both 3D cube and 2D horizontal intersection planes, one midway through and one at the top of the region, are shown in the figure. Fractures appear longer, relative to the size of the region, as the cube shrinks. Only the 50 largest fractures in the region are shown in Figure 3.4, but the whole distribution scales as illustrated here.

Figure 3.5 shows case (2), i.e. with exponent $e < 3$. Fractures in the cube appear longer, relative to the size of the region, as the size of the region grows. This case corresponds to the Westwater pavement data, for which $e = 2.85$.

Figure 3.6 shows case (3), a region of fixed thickness of 2.9 m. In Figure 3.6, a layer with fixed thickness of 2.9m is defined in the middle of the cube. The exponent e of power-law fracture size distribution is 2.85, as in the Westwater pavement data. The fractures appear shorter as the size of the region increases. Thus it is not guaranteed that fractures link up at the megascopic scale for finite-width regions with $e < 3$. (This is clearest from comparing Figure 3.6 (a) and (b) (10 km and 100 m). For Figure 3.6 (c) (10 m), the fractures appear longer, but not all of them intersect the horizontal planes at the middle and top of the region.) As the size of the region shrinks below the thickness of the layer, the region becomes cubic in shape. This corresponds to case (2); i.e., the fractures do not link up in the microscopic scale either.

Table 3.1 shows the fracture cutoff length L_{min} (Equation 3.3) relative to the size of the region for the various cases. Table 3.1 includes also a fourth case, a system of fixed thickness with $e > 3$. For this case fractures appear longer as the size of the region increases, and therefore fractures link up on the megascopic scale. According to Equation 3.3, for a cubical medium, the total number of fractures in the system can be expressed as

$$\begin{aligned}
 N &= L_R^3 m' L_{min}^{-b} \\
 &= m' L_R^{3-b} \left(\frac{L_{min}}{L_R} \right)^{-b}
 \end{aligned}
 \tag{3.4}$$

where L_R is the size of the cube; then the volume of the cube is L_R^3 . For a medium with fixed thickness H , the number of fractures is

$$\begin{aligned}
 N &= HL_R^2 m' L_{min}^{-b} \\
 &= m' HL_R^{2-b} \left(\frac{L_{min}}{L_R} \right)^{-b} \quad (3.5)
 \end{aligned}$$

In the table, each entry represents the dimensionless fracture cutoff length L_{min}/L_R , the ratio of minimum fracture length in the system to the size of the block. This is a measure of the fracture length relative to the size of the region.

3.2 Simulation Study of Fracture Interconnectivity

As mentioned above, the calculation of effective permeability of a fracture system is meaningful primarily when the fractures connect up across the region of interest to form a conduit for the fluid flow. There are many factors affecting the interconnectivity of fracture systems following power-law size distributions. A simulation study using the FracMan™ fracture simulator has been conducted and some primary results obtained. The parameters used here are taken from field data for the Westwater pavement as described in Chapter 1.

3.2.1 Input Parameters for FracMan™

FracMan™ includes a module called FracWorks™ with which users can generate a population of discrete fractures from stochastic descriptions and view this population on the computer screen. Fracture realizations can be saved in a variety of formats for use in simulation, pathway analysis, and finite-element flow modeling.

In FracWorks™, users specify a random seed and the size of the cubical generation region (Figure 3.7). To generate fracture networks, users also provide fracture input parameters, including conceptual geometry model, intensity (number of fractures in the region, fracture area/region volume, or fracture volume/region volume), dimension of the region, mean

orientation of fractures in pole notation, orientation distribution, fracture length distribution, elongation direction and distribution, aspect ratio, termination percentage, etc.

There are 7 types of fracture-orientation distributions in FracWorks™: Fisher, Bivariate Fisher, Bivariate Bingham, Bivariate Normal, Bootstrap, MultiBootstrap and constant. Users provide the mean orientation for the fracture orientation distribution. The pole notation is usually used to represent the orientation of a fracture plane. The pole direction of a plane is the normal direction of that plane, i.e. the direction perpendicular to the plane. Directions in FracWorks™ are stated in terms of their trend and plunge, where trend is the positive angle (clockwise) from North (-x direction) as shown in Figure 3.7, and plunge is measured downward from horizontal (upward directions are stated as having a negative plunge.). All angles are measured in degrees. For example, a fracture plane with direction of Pole (90, 0) in Figure 3.7 is a vertical fracture and parallel to x-z plane.

According to data from the Westwater pavement (Laubach *et al.*, 1997), almost all fractures there are perpendicular to the layer, i.e., vertical. Therefore, in this study, the Bivariate Fisher orientation distribution is selected. The Bivariate Fisher distribution is defined by the probability density function

$$f(\phi, \theta) = C^{-1} \sin \phi \exp\left[\left(\kappa_1 \sin^2 \theta + \kappa_2 \cos^2 \theta\right) \cos \phi\right] \quad (3.6)$$

where c is the normalizing constant and κ_1, κ_2 are dispersion coefficients. θ and ϕ are variant angles from the mean orientation, as defined in Figure 3.8. We set the dispersion coefficient κ_1 to zero; then all generated fractures are vertical ($\phi=0$). The second dispersion coefficient κ_2 can be changed to adjust the variation of fracture orientation in the horizontal plane.

Fracture length distribution type can be chosen among constant, Exponential, Truncated Exponential, Log Normal, Truncated Log Normal, Truncated Normal, Power Law, Truncated

Power Law, Uniform, Bootstrap and MultiBootstrap distributions. We use a power-law distribution in agreement with the observations of Laubach *et al.* (1997) and Odling (1997).

The primary input data used in this study, intended to reflect the Westwater field data, are listed in Table 3.2.

For the Westwater pavement data, the number of fractures with length L per unit volume is given by (Appendix B)

$$n' = 0.275 L^{-3.85} \quad (3.7)$$

Then the cumulative number of fractures of length greater than L_{min} in region of volume V is

$$\begin{aligned} N &= V \int_{L_{min}}^{\infty} 0.275 L^{-3.85} dL \\ &= 0.0965 V L_{min}^{-2.85} \end{aligned} \quad (3.8)$$

Thus, for the Westwater formation (Equation 3.3), $m' = 0.0965$, $e = 2.85 < 3$.

In FracWorks™, the user specifies the number of fractures and the size of the region, i.e. N and V in equation 3.8; we then set L_{min} for the power-law fracture length distribution to satisfy

$$L_{min} = \left(\frac{N}{0.0965 V} \right)^{-\frac{1}{2.85}} \quad (3.9)$$

Because a fracture is defined as a disk in the simulator, FracWorks™ uses the radius, rather than the diameter, of the disk to quantify the length of the fracture. The minimum radius R_{min} is then simply $L_{min}/2$.

FracWorks™ allows users to define trace planes or wellbores within the region to test or sample the generated fracture networks. In this study, to test the connectivity of the generated

fracture networks, two parallel trace planes, one defined as the source and the other as the sink, were defined: the source trace plane on the surface of the front of the region (defined as the South side of the region), the sink trace plane on the surface of the back side (North side) of the region, as shown in Figure 3.7. The “Pathways Analysis” function in FracWorks™ checks whether fractures in the region connect the two trace planes. It can calculate out how many pathways there are in the fracture population connecting the two trace planes and how many fractures are in the backbone of each pathway.

3.2.2 Simulation Results

The first phase of this simulation study is to simulate the original Westwater data by using various conceptual geometry models and to study the connectivity of the fracture systems.

3.2.2.1 Realizations Using The Original Westwater Data and The Enhanced Baecher Model

Some realizations were generated using the original Westwater data (Equation 3.9 and Table 3.2). Figure 3.9 shows some results. Connection of the fractures in 3D space may be difficult to see in 3D (cf. Figure 3.9 (c)). Therefore, for each case in Figure 3.9, a trace plane located in the middle of the region has been used to get the trace map of the fractures to illustrate the degree of connectivity of the fractures. For quantitative accuracy, however, we used the “Pathways Analysis” function in FracWork™ to test whether the fractures connect up in 3D space. Unfortunately, not a single case we examined with these parameters shows connectivity across the 100×130 m region.

3.2.2.2 Realizations Using The Original Westwater Data and Other Models

It is possible that fracture connectivity depends on autocorrelation or clustering of fractures into coherent, long-range paths. The Enhanced Baecher model assumes fractures are placed

randomly with no correlation in their positions. Limited attempts to find long-range connectivity with other models proved fruitless, however.

Figure 3.10 represents only two cases out of a number of realizations using two other models, Levy-Lee and War Zone models, with various parameters. Similarly, no single realization obtains connectivity. For the War Zone model (Figure 3.10 (b)), the trace map on the right is very similar to that in Figure 3.9 (c) using Enhanced Baecher model. This is due to the lack of very large fractures in the population of fractures, which is required for this model to form the war zones. Therefore, the lack of clustering in the trace map reflects the fact that no War Zone exists in the region.

One simple way to represent clustering of fractures into regions of greater density is to increase the pre-exponential factor in the power-law distribution, Equation 3.7. It is also possible that the lack of connectivity reflects the inability to represent the large number of small fractures with a finite computer. The remainder of this chapter examines these two issues.

3.2.2.3 Effect of Pre-Exponential Factor

To test the effect of the pre-exponential factor in a power-law distribution, Equation 3.7 is rewritten as

$$N = (0.0965)CVL_{min}^{-2.85} \quad (3.10)$$

where C is pre-exponential factor. By increasing C in equation 3.10, the total number of fractures of each length increases, including long fractures. Thus, the greater the pre-exponential factor C is, the more likely fractures are to connect up. Whether the fractures connect up in any given realization is a stochastic event. Thus, as the pre-exponential factor increases from zero to infinity, the probability that fractures link up in any given realization in a given region increases from zero to one.

However, a computer has limited resources. It can deal with only a finite population of fractures in any given region. In principle, for the infinite population of fractures specified by a power-law distribution, increasing the pre-exponential factor increases the number of large fractures as well as small ones. But the fracture population that can be modeled in a finite computer is finite. Thus, for a fixed number of fractures to be modeled, increasing the pre-exponential factor means modeling more large fractures and raising L_{min} . Equation 3.9 becomes

$$L_{min} = \left(\frac{N}{0.0965CV} \right)^{\frac{1}{2.85}} \quad (3.11)$$

Numerous runs have been performed to explore the issues raised above. For a given pre-exponential factor C , total number of fractures N and region volume V , the connectivity of the generated fracture networks is a stochastic event. Therefore, in the simulation study, five realizations were run using FracMan™ for each set of the parameters and then the percentage of realizations having connectivity out of the total five realizations was calculated. This relatively small number of realizations is insufficient for precise statistical analysis, but is sufficient to draw qualitative correlations.

Figure 3.11 shows the simulation results for a region with size of $3 \times 3 \times 2.9$ m. The vertical axis is the percentage of connectivity observed in five runs for each parameter value in the figure. The horizontal axis is C , the multiplier of the pre-exponential factor (Equation 3.10) used in the simulation. The number in the legend gives the total number of fractures N generated in the region. In Figure 3.11, a distinct transition zone is observed in which the fractures may or may not connect up. The transition zones for different number of fractures overlap, but may shrink in width as the number of fractures increases.

After analyzing the data from the Westwater pavement, Mace (1998) estimated that the fracture density in a highly-fractured zone within the pavement is about 10 times that averaged over the whole pavement (represented by Equation 3.8). The simulation results (Figure 3.11)

show that the fractures get connectivity with the multiplier of the pre-exponential factor C around 5 – 10. This indicates that the fractures in the highly-fractured zone in the Westwater pavement may link up.

Figure 3.12 is for a region with size of $10 \times 10 \times 2.9$ m. Two points should be noticed. All curves are moved to right compared to Figure 3.11, which implies that for a larger region it is more difficult for fractures to link up. The other is that the transition zone is wider, at least for simulations with fewer fractures represented (smaller N).

Figure 3.13 shows the results for a region with size of $130 \times 100 \times 2.9$ m which is the actual size of the Westwater pavement. Although the transition zones shrink with increasing fracture number N , they do not overlap.

Figure 3.14 summarizes the results shown in Figure 3.11 – 3.13. The number below each set of data indicates the number of fracture N used in each simulation for the given region size. The data for the regions of $3 \times 3 \times 2.9$ m and $10 \times 10 \times 2.9$ m are clustered in a narrow portion of this figure. The data for these two regions are shown also in Figure 3.15.

One expects that the multiplier of pre-exponential factor C affects connectivity, since it alters the underlying fracture distribution (Equation 3.7). One expects also some scatter in results, since fracture placement and connectivity are stochastic events. Any systematic effect of L_{\min} , however, is a numerical artifact. The underlying fracture distribution has no cutoff length (at least on this scale): L_{\min} is introduced to accommodate finite computer resources (Equation 3.3). In Figure 3.14, for the region of $130 \times 100 \times 2.9$ m, it is clear that the fracture connectivity is related not only to pre-exponential factor C but also to L_{\min} . In other words, these results are strongly affected by the artifact of truncating the fracture population at the fracture length cutoff, L_{\min} .

In Figure 3.15, for the region of $3 \times 3 \times 2.9$ m, fracture connectivity appears to be independent of L_{\min} . There is some scatter in results, but no systematic trend with L_{\min} . Thus it appears one can safely truncate the fracture population at a cutoff of from 0.1 to 0.3 m without altering the connectivity. Results for the region of $10 \times 10 \times 2.9$ m show some correlation with L_{\min} , especially

for obtaining 60% or greater chance of connectivity, though the case is not as clear-cut as that for the region of $130 \times 100 \times 2.9$ m as shown in Figure 3.15. The case with 6000 fractures in a $10 \times 10 \times 2.9$ m region overlaps those for 500 fractures in a $3 \times 3 \times 2.9$ m region in Figure 3.15. The results differ strongly, however. A value of $C = 7$ gives a 60% chance of connectivity for the $3 \times 3 \times 2.9$ m region but no connectivity for the larger region, even for the same value of L_{\min} (about 0.3 m). This difference between connectivity at different length scales mirrors that in Figure 3.1 (a), and reflects the finding in Appendix B, that connectivity is harder to achieve in larger regions of fixed height with $e < 3$. Indeed, Figure 3.15 guided the choice of parameters for Figure 3.2 (b). There, $L_{\min} = 0.3053$ m and $C = 9$ give a high probability of connectivity in a $3 \times 3 \times 2.9$ m region, but a much lower probability of connectivity in a $10 \times 10 \times 2.9$ m region.

3.2.2.4 Effect of Fracture Orientation

To test the effect of variation of fracture orientation on connectivity, some simulations were repeated with a larger (second) dispersion coefficient ($\kappa_2=80$) in the Bivariate Fisher fracture orientation distribution (Equation 3.6). This increase from 40 to 80 in this coefficient implies greater variation of fracture orientation in the horizontal direction (trend) as shown in Figure 3.16. In Figure 3.16, all points (each point represents a pole direction) are distributed on or very near to the circle, meaning that all fractures are vertical or nearly vertical (plunge angle equals zero). Because the mean orientation is set to Pole (90, 0), i.e. W-E direction in the figure, the angle between a point and W-E direction represents the variation of the pole direction from the mean direction (W-E). (Note that if the pole (normal) direction points to W-E, the fracture is N-S.) The results are shown in Figures 3.17 to 3.19. They are roughly similar to the results in Figures 3.11 to 3.13. There is no marked effect of increasing the variation of fracture orientation in this case.

3.3 Conclusions

- (1) For a given power-law distribution of fracture size in a particular region, the connectivity of fractures is stochastic event.
- (2) The number of fractures in a power-law distribution is infinite if the power-law extends to zero length. But a computer has limited resources; thus it can not simulate all fractures present in a finite region. A fracture length cut-off L_{\min} is introduced to represent a finite population of fractures. Therefore, it is difficult to determine connectivity for sure at any given scale because of excluding the large number of smaller fractures.
- (3) Connectivity of fractures at one scale does not necessarily determine the connectivity of fractures at another scale. Thus results for small regions cannot be up-scaled simply to larger regions.
- (4) For the original study data from the Westwater pavement, no connectivity is observed using various conceptual fracture geometry models in FracMan™, a commercial fracture simulator. The lack of connectivity may reflect the inability to include the large number of small fractures with a finite computer; or lack of connectivity in the outcrop, or connectivity only in the highly-fractured zones.
- (5) By increasing the pre-exponential factor in a power-law distribution, the total number of fractures of each length increases, including long fractures. Thus, the fractures are more likely to link up. As the pre-exponential factor increases from zero to infinity, the probability that fractures connect up in any given region increases from zero to one. For a fixed number of fractures to be modeled using FracMan™, increasing the pre-exponential factor means modeling more large fractures and raising the fracture length cut-off L_{\min} . Changing the pre-exponential factor alters the original underlying distribution. Based on the simulation results and Mace's (1998) estimate, one could observe connectivity in the highly-fractured subzone in the Westwater pavement.

- (6) Three sizes of region ($3 \times 3 \times 2.9$ m, $10 \times 10 \times 2.9$ m and $130 \times 100 \times 2.9$ m) were investigated. Five realizations were run for each set of the parameters and then the percentage of having connectivity was calculated. Fracture connectivity for the region of $3 \times 3 \times 2.9$ m is independent of L_{\min} , implying that one can safely truncate the fracture population within the range investigated without altering the connectivity. But results for the regions of $10 \times 10 \times 2.9$ m and $130 \times 100 \times 2.9$ m show that the connectivity has relatively strong correlation with L_{\min} . These results show that truncation of fracture population affects the connectivity of fractures.
- (7) The simulation study for the regions with different sizes verify that the connectivity of fractures in a small region does not necessarily determine the connectivity of fractures at a larger region.
- (8) There is no marked effect of increasing the variation of fracture orientation on the connectivity of fractures for the case studied.

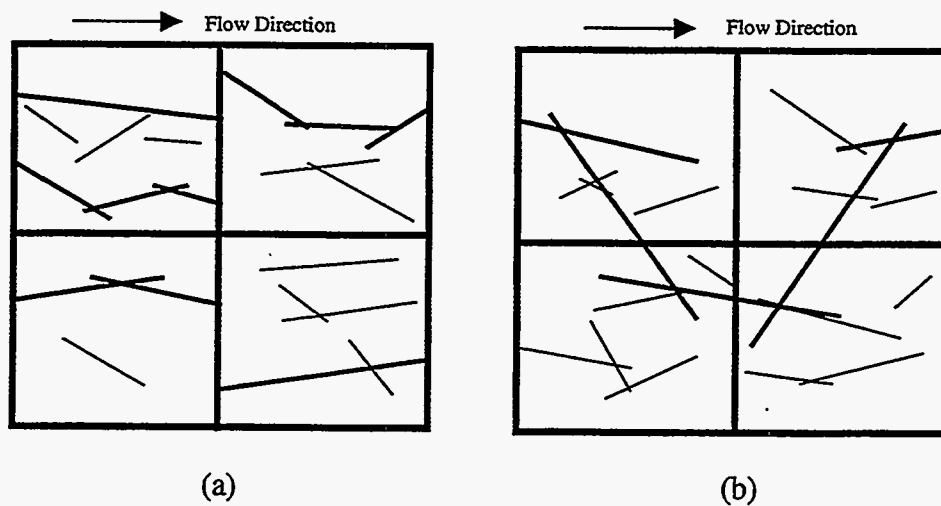
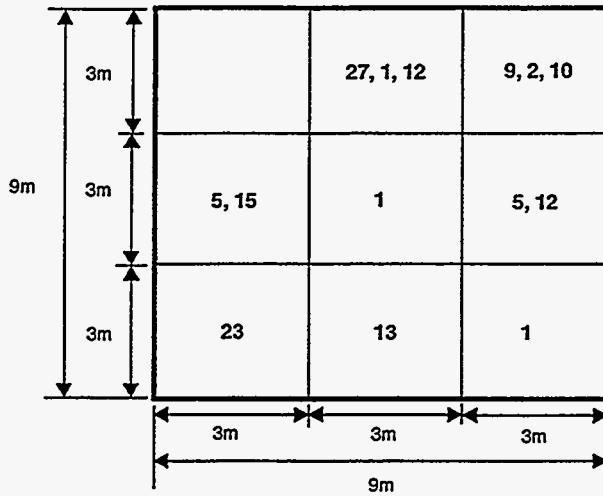
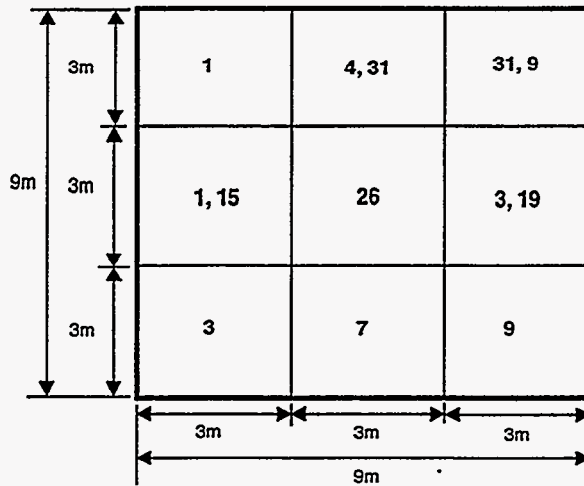


Figure 3.1. A schematic illustration of the difficulty in relating fracture connectivity at different scales. (a) All four small regions have at least one path of connected fractures across the region but the large region does not have any connected path of fractures across it. (b) The large region has one path of connected fractures, but none of the small regions has a connected path across it in the direction of flow.

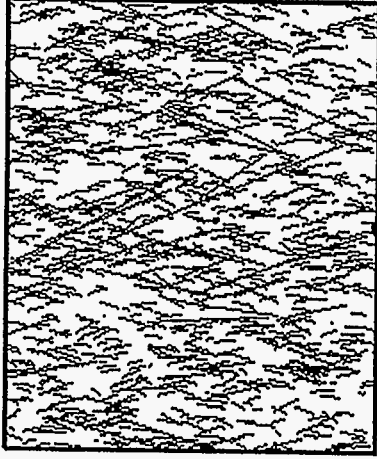


(a)

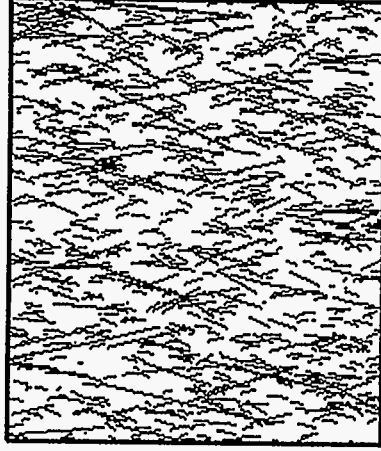


(b)

Figure 3.2. Two simulation cases verifying the physical restriction shown in Figure 3.1. In both cases, the large region has dimension of 9 m by 9 m by 2.9 m and the 9 sub-regions have dimension of 3 m by 3 m by 2.9 m; there are a total of 6000 fractures in the large region. Each number printed in the sub-regions represents one path across that sub-region and the number of fractures in the backbone of that path. (a) There are two pathways that cross the large region from the bottom to the top; one has 39 fractures; the other has 17 fractures. But there is one sub-region without connectivity (upper left). (b) There is no single pathway in the large region. But every sub-region has connectivity.



(a)



(b)

Figure 3.3. The trace maps of the middle trace planes of two simulations cases shown in Figure 3.2.

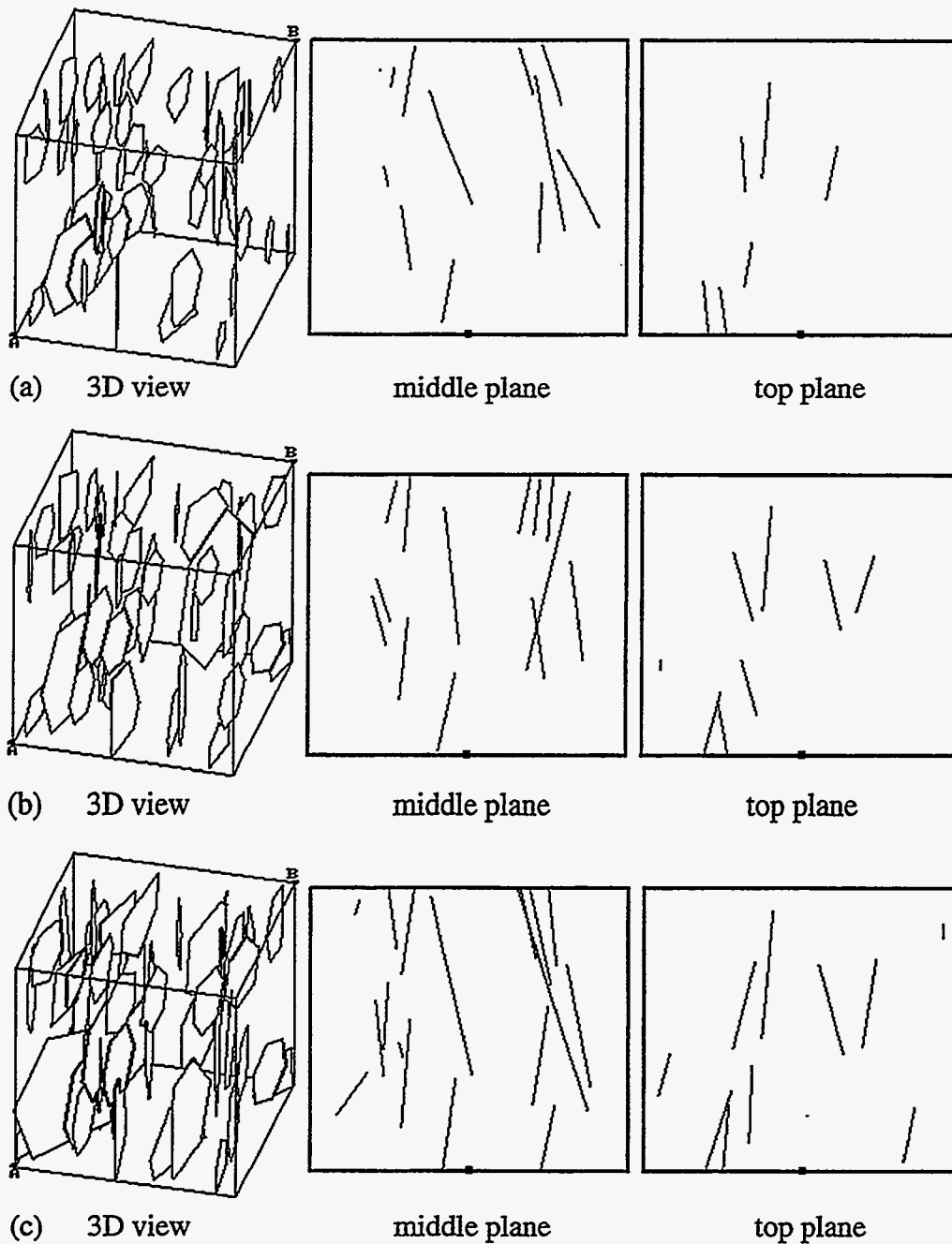


Figure 3.4. Scaling of fractures length with size of cubical regions with $e=3.15 > 3$. Cubes are (a)10km (b)100m (c)1m on a side. In each case, the 50 largest fractures in the region are shown. The second and third plot in each case shows intersections of fractures with horizontal planes at the middle and top of the region.

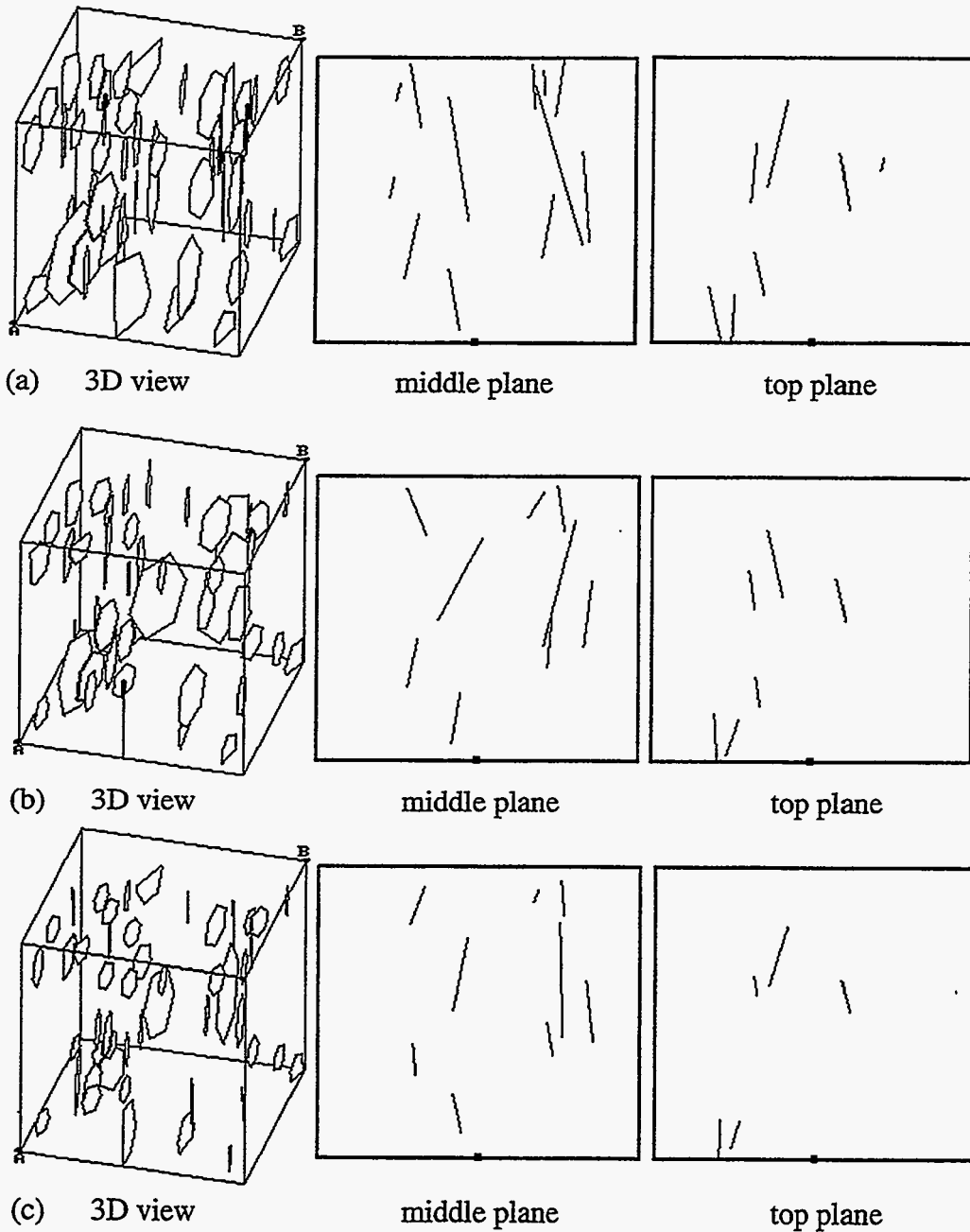


Figure 3.5. Scaling of fractures length with size of cubical regions with $e=2.85 < 3$. Cubes are (a) 10km (b) 100m (c) 1m on a side. In each case, the 50 largest fractures in the region are shown. The second and third plot in each case shows intersections of fractures with horizontal planes at the middle and top of the region.

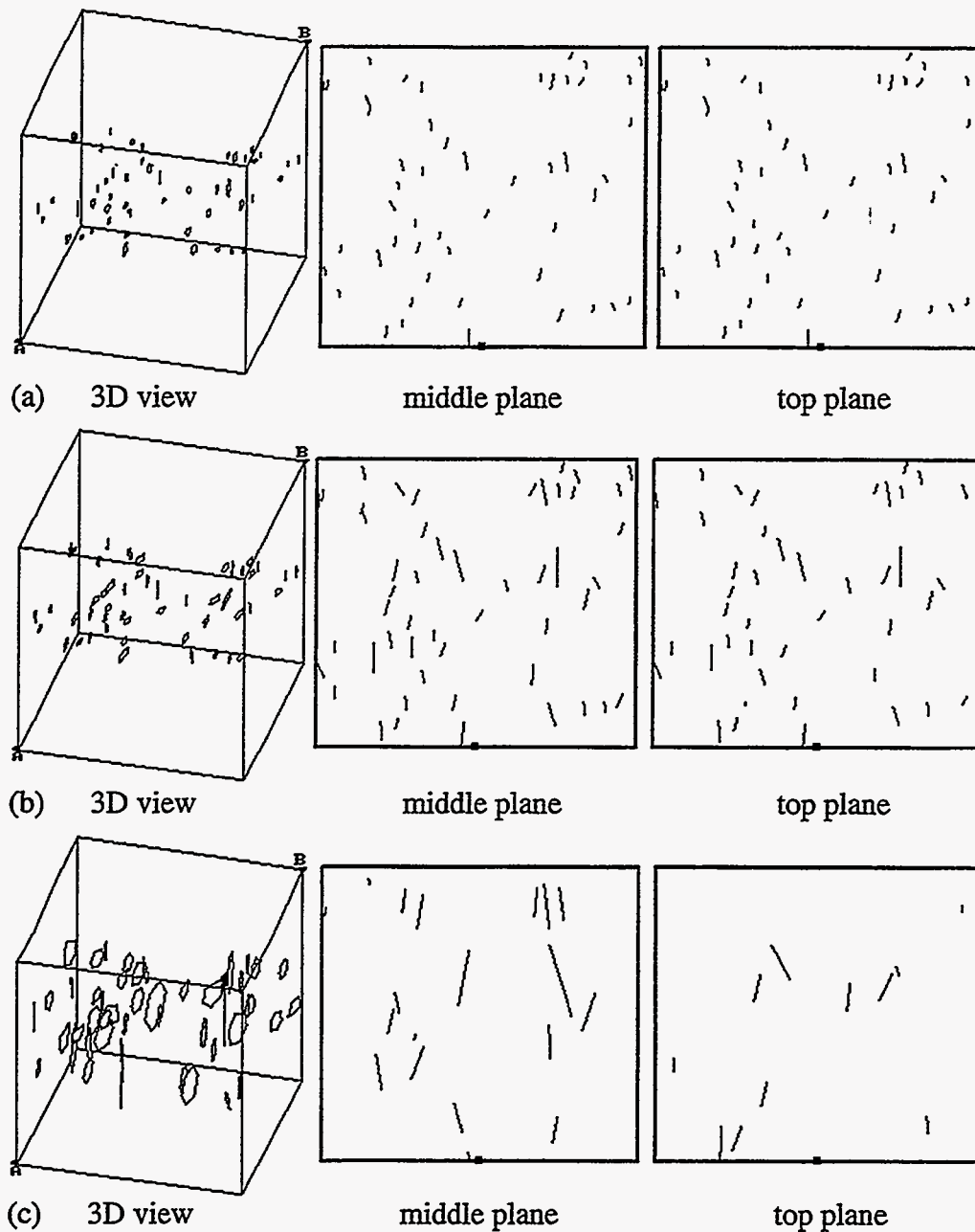


Figure 3.6. Scaling of fractures length with lateral extent of region of fixed thickness $H=2.9\text{m}$ with $e=2.85 < 3$. Lateral extent of region is (a)10km (b)100m (c)10m on a side. In each case, the 50 largest fractures in the region are shown. The second and third plot in each case shows intersections of fractures with horizontal planes at the middle and top of the fractured region. Although a cubical region is shown on the left diagram in each case, all fractures are confined to a zone of fixed thickness (2.9m) in the middle of the cube.

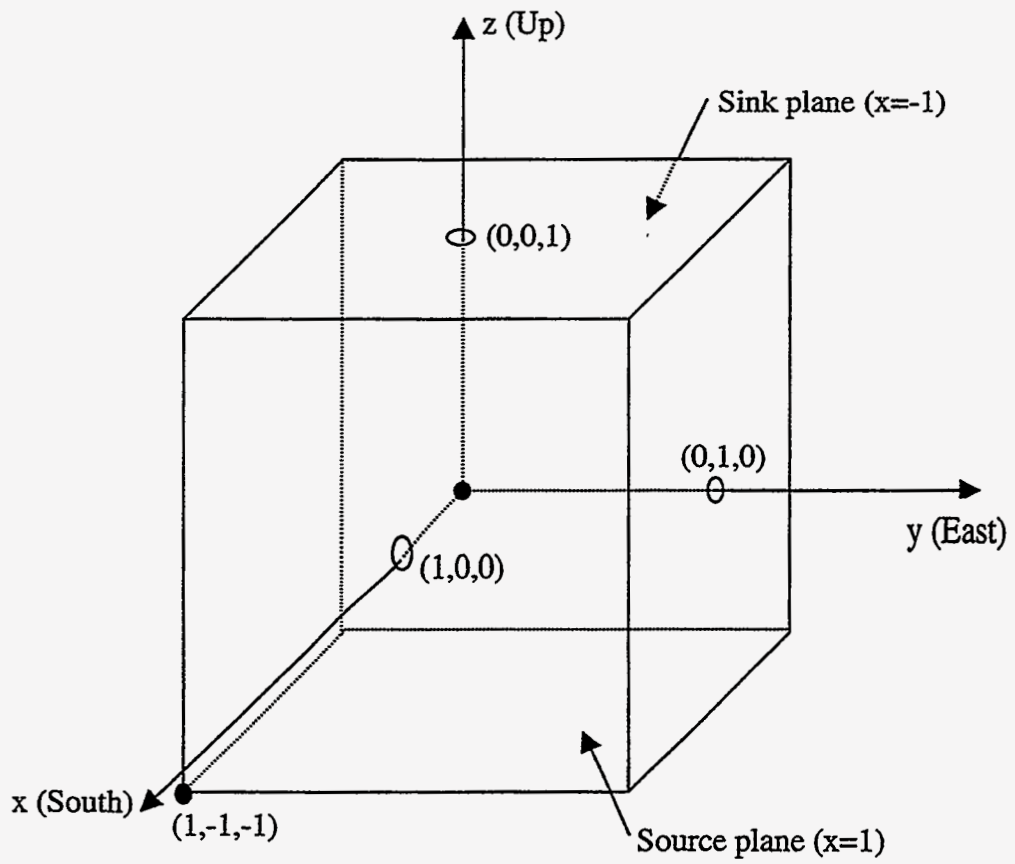


Figure 3.7. FracMan™ generation region.

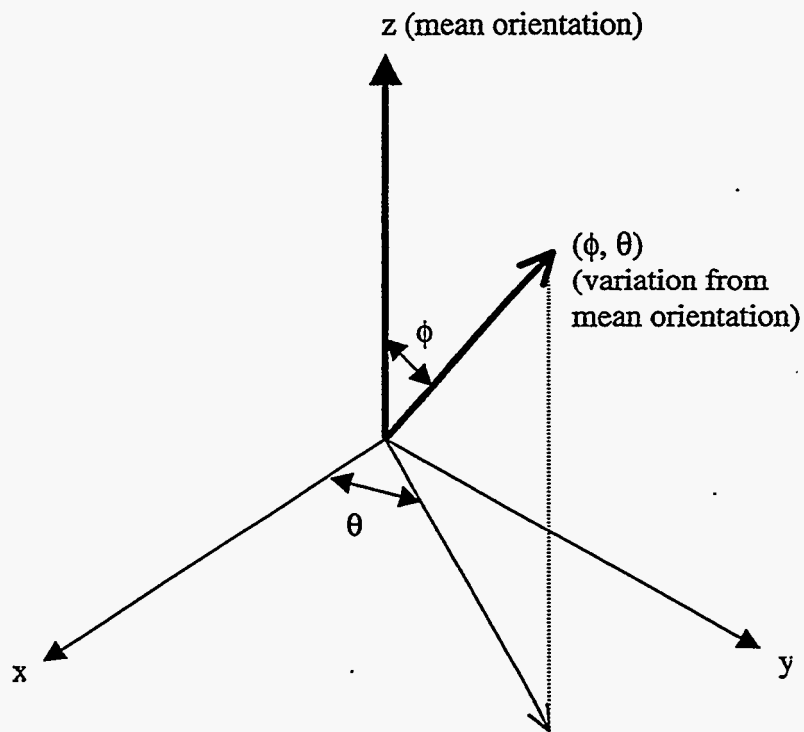


Figure 3.8. Coordinate of fracture orientation distribution function in FracMan™

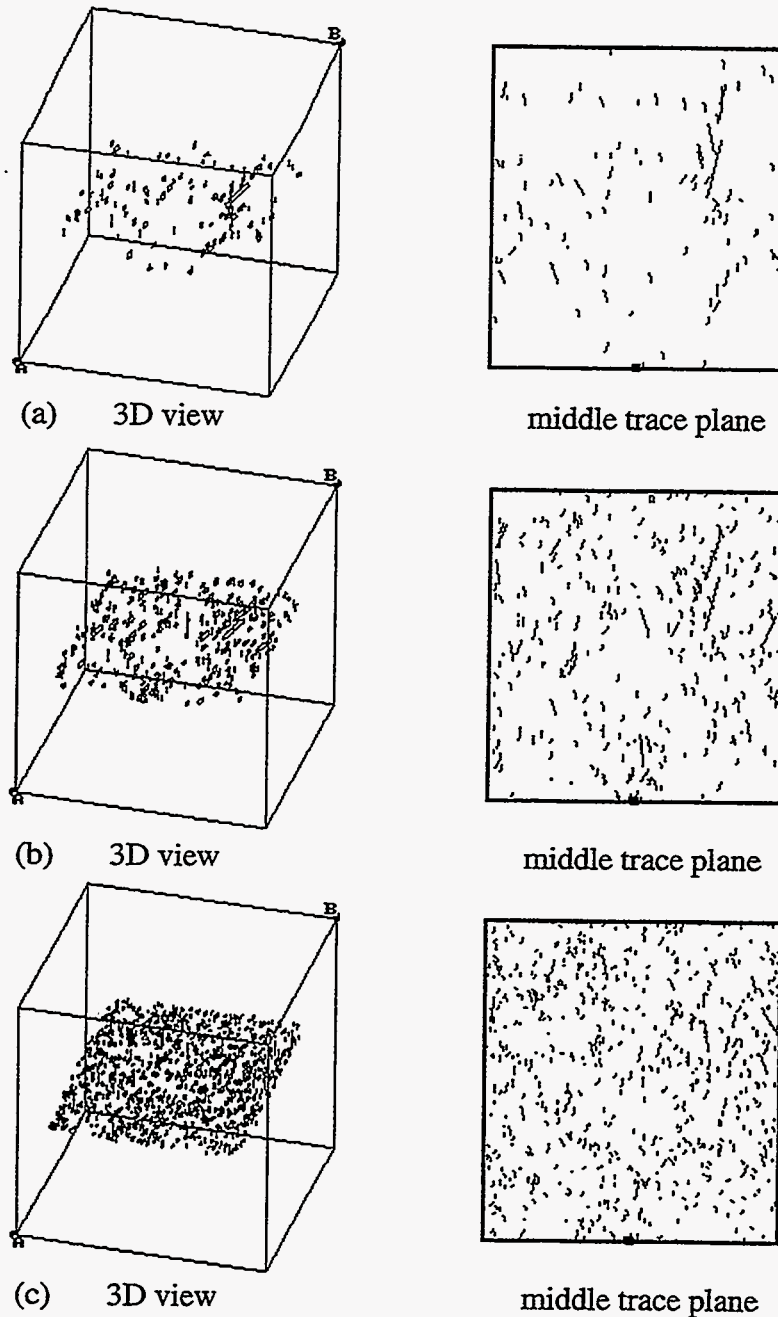
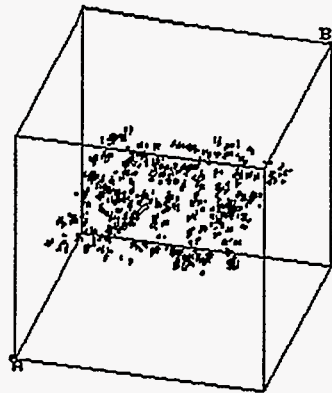
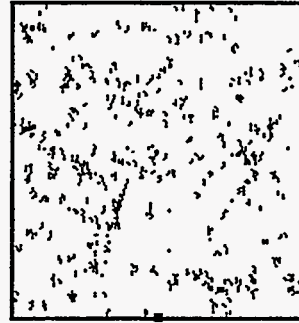


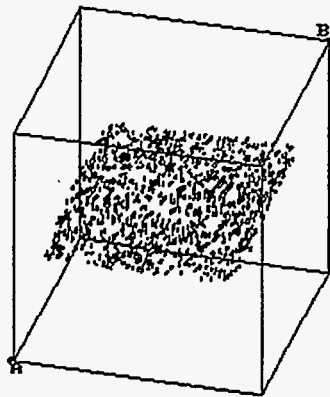
Figure 3.9. Three realizations of fracture population with parameters intended to represent the Westwater pavement using the Enhanced Baecher model. The size of the layer is 130m by 100m by 2.9m. The right-hand plot in each case shows intersections of fractures with a horizontal plane in the middle of the layer. (a) 100 fractures, $L_{min} = 2.65\text{m}$; (b) 300 fractures, $L_{min} = 2.18\text{m}$; (c) 1000 fractures, $L_{min} = 1.18\text{m}$.



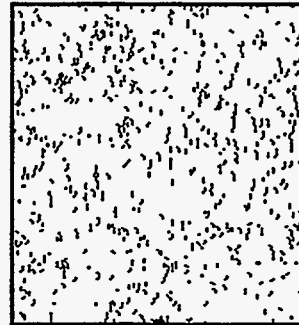
(a) 3D view



middle trace plane



(b) 3D view



middle trace plane

Figure 3.10. Two realizations with parameters taken from the Westwater pavement using Levy-Lee and War Zone models. The size of the layer is 130m by 100m by 2.9m. The number of fractures in the layer is 1000 and $L_{\min}=1.18\text{m}$. The right-hand plot in each case shows intersections of fractures with a horizontal plane in the middle of the layer. (a) Levy-Lee model; (b) War Zone model.

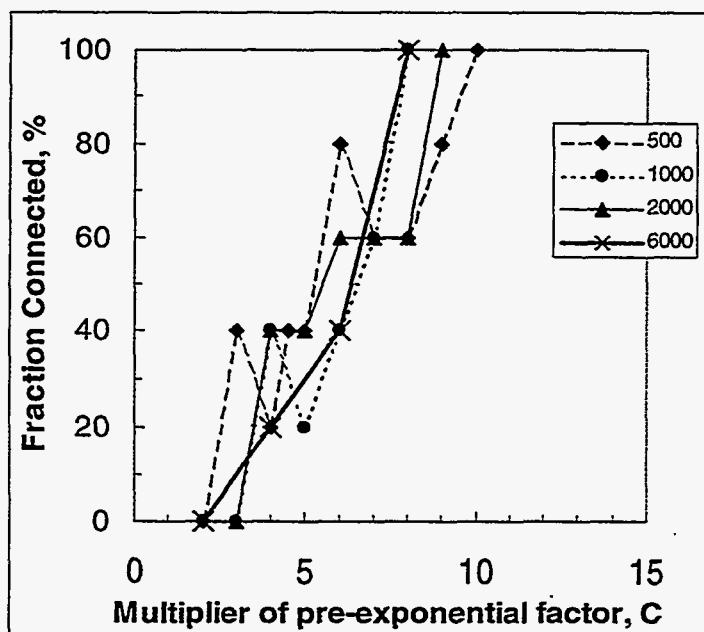


Figure 3.11. Connectivity of fractures for varying pre-exponential factors. The size of the region is $3 \times 3 \times 2.9$ m. Mean orientation: Pole(90, 0); orientation distribution: Bivariate Fisher with dispersion coefficients $\kappa_1=0$, $\kappa_2=40$.

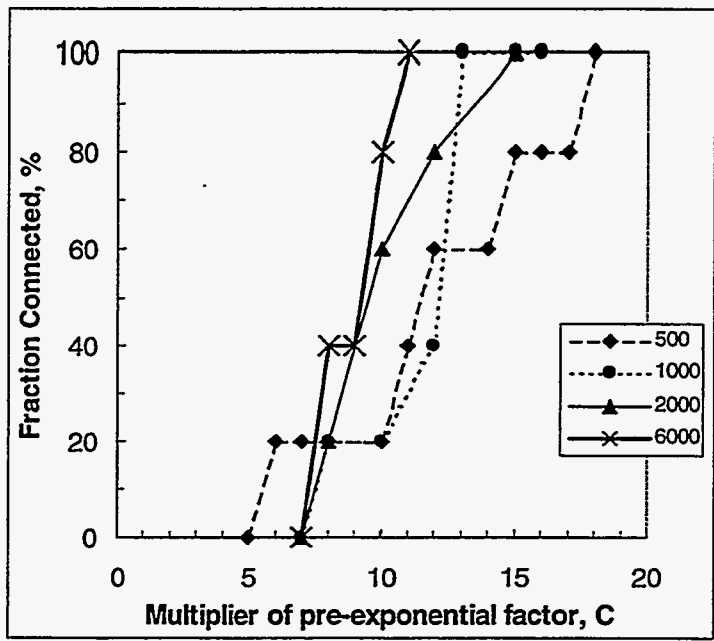


Figure 3.12. Connectivity of fractures for varying pre-exponential factors. The size of the region is $10 \times 10 \times 2.9$ m. Mean orientation: Pole(90, 0); orientation distribution: Bivariate Fisher with dispersion coefficients $\kappa_1=0$, $\kappa_2=40$.

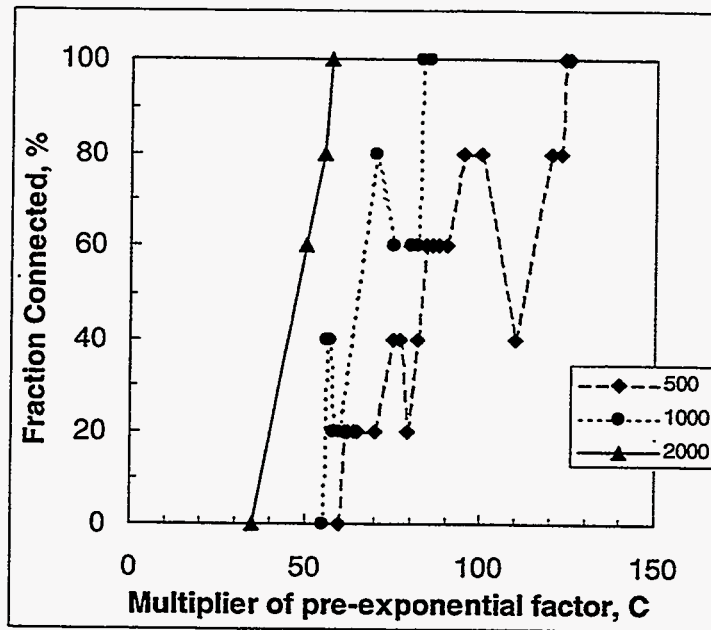


Figure 3.13. Connectivity of fractures for varying pre-exponential factors. The size of the region is $130 \times 100 \times 2.9$ m. Mean orientation: Pole(90, 0); orientation distribution: Bivariate Fisher with dispersion coefficients $\kappa_1=0$, $\kappa_2=40$.

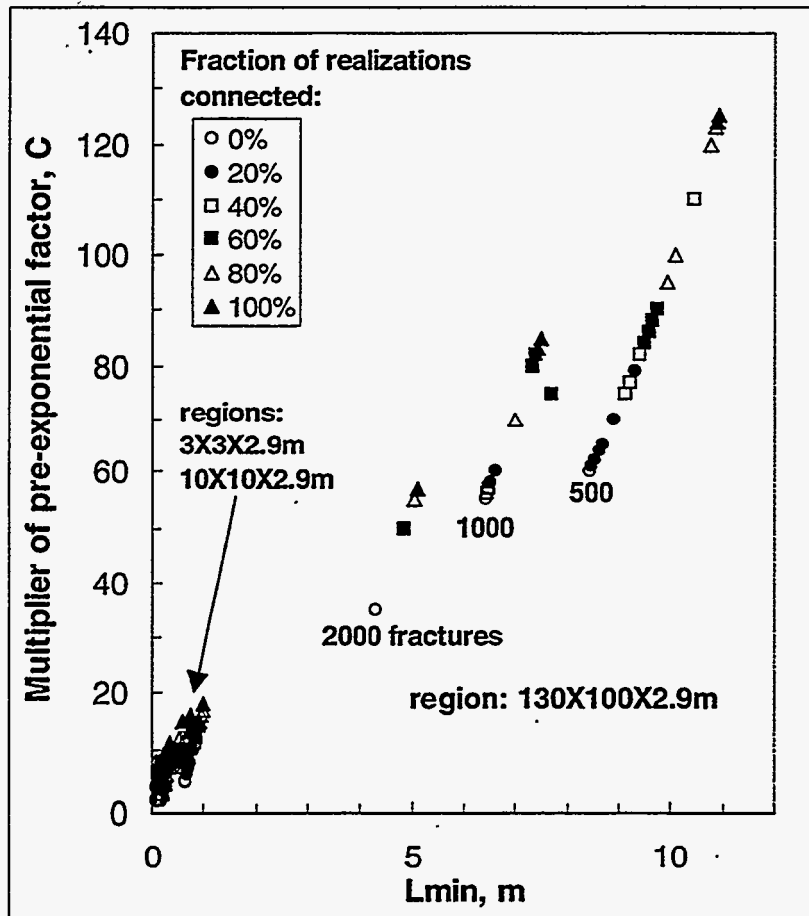


Figure 3.14. Fracture connectivity results for three regions. The number below each set of results indicates the number of fractures in the region.

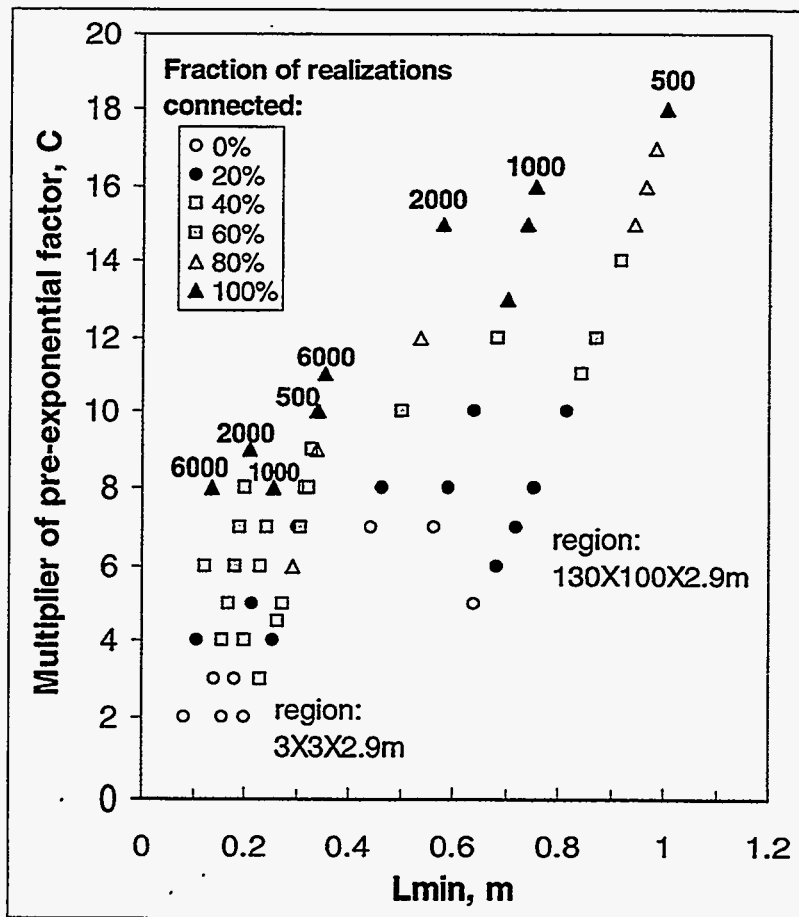
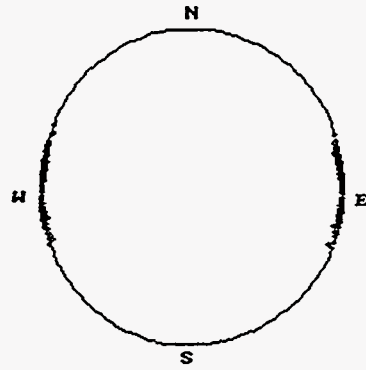
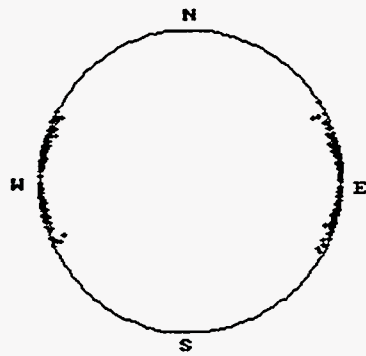


Figure 3.15. Fracture connectivity results for two regions. The number above each set of results indicates the number of fractures in the region.



(a)



(b)

Figure 3.16. Rose diagrams for the Bivariate Fisher fracture orientation distribution. (a) dispersion coefficients $\kappa_1=0$, $\kappa_2=40$; (b) dispersion coefficients $\kappa_1=0$, $\kappa_2=80$. Mean orientation is Pole (90, 0) (W-E). The wider range of point distribution represents greater variation of fracture orientation in the horizontal direction. Note that all fractures are nearly vertical.

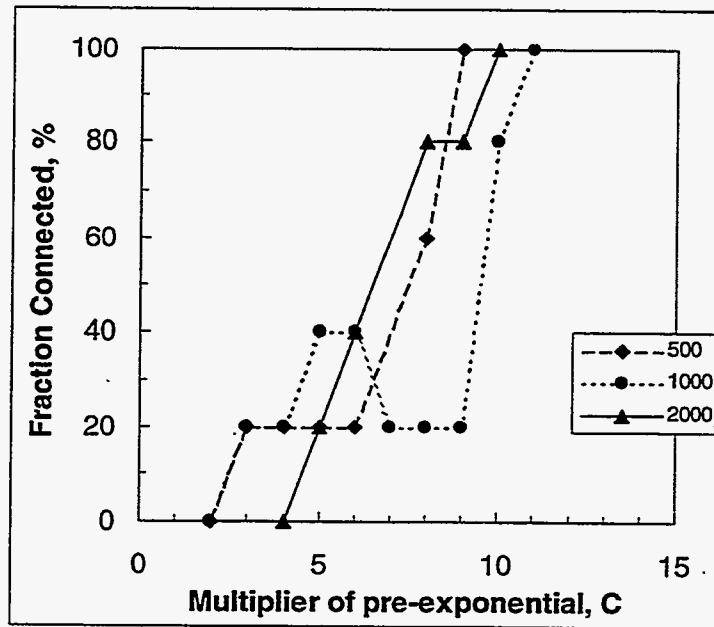


Figure 3.17. Connectivity of fractures for varying pre-exponential factor, C. The size of the region is $3 \times 3 \times 2.9$ m. Mean orientation: Pole(90, 0); orientation distribution: Bivariate Fisher with dispersion coefficients $\kappa_1=0$, $\kappa_2=80$.

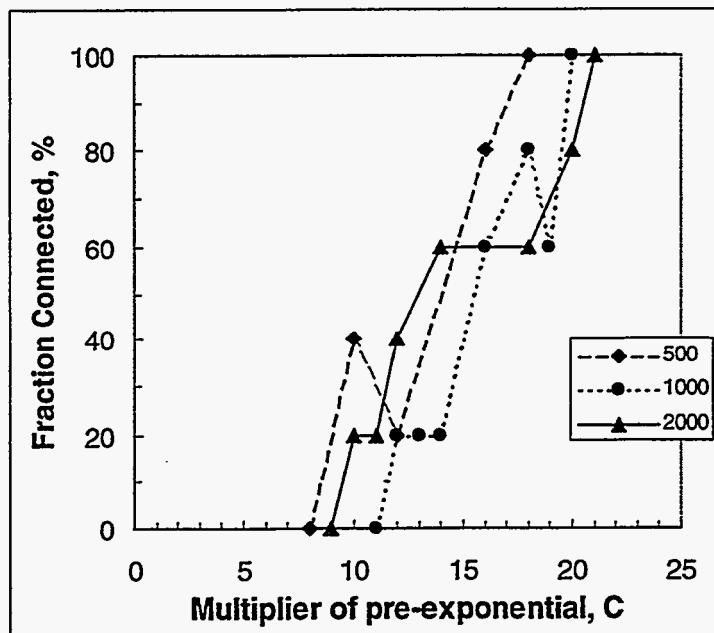


Figure 3.18. Connectivity of fractures for varying pre-exponential factor, C. The size of the region is $10 \times 10 \times 2.9$ m. Mean orientation: Pole(90, 0); orientation distribution: Bivariate Fisher with dispersion coefficients $\kappa_1=0$, $\kappa_2=80$.

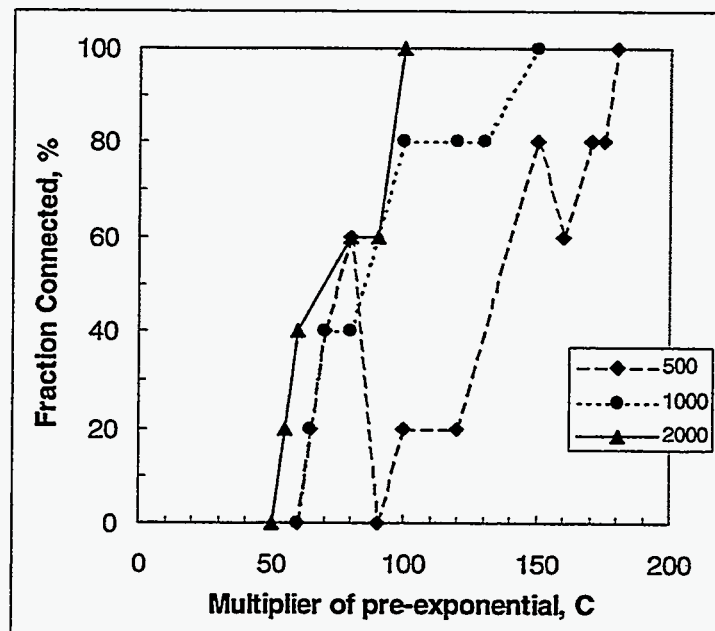


Figure 3.19. Connectivity of fractures for varying pre-exponential factor, C. The size of the region is 130×100×2.9 m. Mean orientation: Pole(90, 0); orientation distribution: Bivariate Fisher with dispersion coefficients $\kappa_1=0$, $\kappa_2=80$.

Table 3.1. The fracture relative length for various cases of power-law exponents

L_{min}/L_b Case	Block Size, m					
	10	50	100	200	500	1000
1	0.221538	0.241121577	0.25008046	0.259372	0.2721872	0.2823003
2	0.2830245	0.262143927	0.25363258	0.245398	0.2349204	0.227293
3	0.1434881	0.088787364	0.0722055	0.05872	0.0446792	0.036335
4	0.1910543	0.106163997	0.0824285	0.064	0.0458034	0.035563

Case 1: $b < 3$; Case 2: $b > 3$; Case 3: $b < 3$ with fixed thickness 2.9m; Case 4: $b > 3$ with fixed thickness 2.9m

Total number of fractures in the system is 10.

Table 3.2. Input data for connectivity simulation study in FracMan™

Generation Options		Generation Region	
Geometric Model	<i>Enhanced Baecher</i>	Shape	<i>Box</i>
Generation Mode	<i>Centers</i>	Region	<i>Inside</i>
Truncation Mode	<i>By Region</i>	Region Dim.(L,W,H), m	<i>[varying]</i>
Orientation	<i>Pole</i>	Center (x,y,z)	<i>0,0,0</i>
Intensity	<i>Number of Fractures</i>		
Number of Sides	<i>6</i>		
Geometric Properties			
Pole(tr, pl)	<i>90, 0</i>	Aspect Ratio	<i>1</i>
Distribution	<i>Bivariate Fisher</i>	Distribution	<i>[constant]</i>
Dispersion	κ_r, κ_z	Termination %	<i>0</i>
Size (Min. radius)		Number of Fractures	
Distribution	<i>Power-law Exponent 3.85</i>	Correlation	<i>[constant]</i>
Dir. of Elong (tr, pl)	<i>0, 0</i>		
Distribution	<i>[constant]</i>		

CHAPTER 4: CONCLUDING REMARKS AND FUTURE WORK

4.1 Conclusions

In this study two Monte Carlo studies were conducted to investigate characteristics of the power-law distribution for fracture aperture and its effects on the properties of naturally fractured reservoirs based on a simplified fractured reservoir model. Comparisons were made between analytical and simulated results. The 3D connectivity of fractures following a power-law distribution for fracture length was examined using Monte Carlo techniques.

The following important conclusions can be made based on the work presented in this report.

- (1) A simplified fractured reservoir model has been developed. The Fracture aperture distribution function and other functions for calculating the properties of the fracture reservoir based on this model have been derived. The field data from the Boulder Creek sandstone were realized using the derived equations. The simulation results show that whether or not the simulated aperture follows a power law is a stochastic event, and a physical finite value of the upper limit to aperture size, b_{\max} , may exist actually. This may explain the falloff in occurrence of large aperture observed in the three cases presented by Marrett (1997) (Figure 1.3).
- (2) A Monte Carlo study was then conducted to investigate how the value of b_{\max} affects the aperture distribution in the simulation. The results show that with increasing of b_{\max} , the probability that one observes a power-law trend over the whole range of aperture values increases.
- (3) Using the same model, another Monte Carlo study was performed. The purpose of this study is to determine how the power-law distribution for fracture aperture affects the aggregate properties (permeability and porosity) of fractured-reservoirs. The

simulated fracture number, largest observed aperture, permeability and porosity are plotted in the probability graph. As predicted, the number of fractures observed in a given region is a normally distributed random variable.

- (4) Simulation results for the field data violate the initial assumptions made for the model. As a result, permeabilities and porosities calculated with those assumptions are enormous, especially for the large value of b_{\max} . A numerical artifact in the model is that the height of intervals, h , an arbitrary parameter introduced in the model, affects the simulation results.
- (5) Increasing the value of b_{\max} does not change most of the simulated fracture aperture distribution, but increases the single largest observed aperture. With a large b_{\max} , the effective permeability is dominated by the single largest observed aperture. The distribution of simulated largest observed aperture fits well the analytical equation derived with the model (Equation 2.14). Therefore, the distribution of effective permeability can be predicted using the analytical equations of the model (Equations 2.14 and 2.16).
- (6) The simulation results show that the expected value of permeability increases as the size of the porous medium increases, which is consistent with the prediction of the model. The model predicts that the expected value of permeability approaches infinity for the power-law distribution for fracture aperture as the size of the porous medium increases to infinity.
- (7) To study the 3D connectivity of fracture populations following a power-law distribution for fracture length, a commercial fracture simulator FracMan™ was used. An attempt to obtain connectivity for the field data from the Westwater pavement using various built-in fracture geometry models was made, but failed. This may reflect the inability to include a large number of small fractures with a finite computer, or lack of connectivity in the outcrop, or connectivity only in the highly-fractured zones.

- (8) Connectivity of fractures at one scale does not necessarily determine the connectivity of fractures at another scale. This is proved by the simulation and Monte Carlo study. This makes scale-up of results from one scale to a larger one difficult.
- (9) Connectivity of fractures can be achieved by increasing the pre-exponential factor in the power-law distribution for fracture length. Increasing the pre-exponential factor increases the total number of fractures of a given length and thus the fractures are more likely to link up. This implies a change in the underlying distribution. As the pre-exponential factor increases from zero to infinity, the probability that fractures connect up in any given region increases from zero to one. The distribution based on data from the Westwater pavement must be increased by about a factor of 5 to 10 (Figure 3.15) to obtain connectivity, which is in agreement with Mace's (1998) analysis. This also implies that the fractures in the highly-fractured zone in the Westwater pavement could link up.
- (10) A Monte Carlo study was conducted to investigate the effect of pre-exponential factor and fracture length cutoff L_{min} on connectivity at different scales. For the region of $3 \times 3 \times 2.9$ m, with the Westwater data, connectivity is independent of L_{min} in the simulated range of L_{min} . For larger regions (with the thickness fixed at 2.9 m), the results show the relative strong correlation with L_{min} . The study results verify the physical restriction stated in (8).

4.2 Future Work

There is a great deal of work that should be done to better characterize and simulate naturally fractured reservoirs that follow power-law distributions for fracture aperture and length. Some of the important aspects of the problem that should be addressed are listed here.

- (1) The ultimate aim of this research program was to incorporate the new findings in fracture scaling into commonly used dual-porosity simulators for naturally fractured

reservoirs. In other words, based on the fracture scaling correlation, find out, using a statistic process, the most reasonable input data (e.g., effective permeability and porosity) of each grid for the dual-porosity model. This study investigates the effect of the power-law distribution for fracture aperture on permeability and porosity based on a simplified model. The directional permeability and its anisotropy should be determined eventually. Then the fluid flow through the fracture networks should be simulated using a finite-element method, such as that in Mafic™, by which directional permeability can be calculated. The permeability calculated using the above procedure should be a random variable. Through a Monte Carlo study, its distribution can be obtained, corresponding to the input power-law distributions for fracture aperture and length.

- (2) The 3D connectivity of fractures is an important issue to address before estimating permeability. This study suggests that the data from the Westwater pavement do not indicate fracture connectivity unless fractures are clustered spatially. Other field data may be tested.
- (3) Based on thorough analysis of the field data, other fracture geometry models should be explored as well.

REFERENCES

- Aguilera, R., 1980: *Naturally Fractured Reservoirs*, PennWell Publishing Company, Tulsa, OK.
- Bird, R. B., W. E. Stewart, E. N. Lightfoot, 1960: *Transport Phenomena*, John Wiley & Sons, Inc., New York.
- Clark, M. B., S. L. Brantley, D. M. Fisher, 1995: "Power-law Vein-thickness Distributions and Positive Feedback in Vein Growth", *Geology*, v.23, p.975-978.
- Dershowitz, W., G. Lee, J. Geier, T. Foxford, P. Lapointe, A. Thomas, 1995: *User Documentation for FracMan™*, Golder Associates Inc., Seattle, Washington.
- Dershowitz, W., J. Geier, K. Lee, 1989: "Field Validation of Conceptual Models for Fracture Geometry", submitted to *Rock Mechanics and Rock Engineering*.
- Dershowitz, W., T. W. Doe, 1988: "Practical Applications of Discrete Fracture Approaches in Hydrology, Mining and Petroleum Extraction", *Proceedings of the International Conference on Fluid Flow in Fractured Rocks*, Atlanta, Georgia, p.381.
- Gross, M. R. and T. Engelder, 1995: "Strain Accommodated by Brittle Failure in Adjacent Units of the Monterey Formation, U.S.A.: Scale Effects and Evidence for Uniform Displacement Boundary Conditions", *Journal of Structural Geology*, v.17, p.1301-1318.
- Jensen, J. L., L. W. Lake, P. M. W. Corbett, and D. J. Goggin, 1997: *Statistics for Petroleum Engineers and Geoscientists*, Prentice Hall, Englewood Cliffs, NJ.
- Kazemi, H., 1969: "Pressure Transient Analysis of Naturally Fractured Reservoir with Uniform Fracture Distribution", *Society of Petroleum Engineers Journal*, December, p.451-462.
- Lake, L. W., 1989: *Enhanced Oil Recovery*, Prentice Hall, Englewood Cliffs, NJ.
- Laubach, S. E., R. Marrett, W. R. Rossen, L. W. Lake, O. Ortega, and Y. Gu, 1997: *Using Microstructure Observations to Quantify Fracture Properties and Improve Reservoir Simulations*, Annual report submitted to BDM-Oklahoma, Inc., Bureau of Economic Geology, University of Texas at Austin, Austin, TX.
- Long, J. C. S., P. Gilmour, and P. A. Witherspoon, 1985: "A Model for Steady Fluid Flow in Random Three-Dimensional Networks of Disc-Shaped Fractures", *Water Resources Research*, v.21, p.1105.
- Mace, R., 1998: personal communication, Bureau of Economic Geology, University of Texas at Austin.
- Mandelbort, B. B., 1985: "Self-Affine Fractals and Fractal Dimension", *Physica Scripta*, v.32, p.257-260.

- Marrett, R., 1997: "Permeability, Porosity and Shear Wave Anisotropy from Scaling of Open Fracture Populations, in Hoak, T. E., Blomquist, P. K., and Klawitter, A. (Editors), *Fractured Reservoirs: Descriptions, Predictions and Applications*, Rocky Mountain Association of Geologists Guidebook.
- Marrett, R., 1996: "Aggregate Properties of Fracture Populations", *Journal of Structural Geology*, v.18, p.169-178.
- Milliken, K. L., 1994: "The Widespread Occurrence of Healed Microfractures in Siliciclastic Rocks: Evidence from Scanned Cathodoluminescence Imaging", *The proceedings of North American Rock Mechanics Symposium*, Rotterdam, Balkema, v.1, p.825-832.
- Odling, N. E., 1997: "Scaling and Connectivity of Joint Systems in Sandstones from Western Norway", *Journal of Structural Geology*, v.19, p.1257-1271.
- Pollard, T., 1959: "Evaluation of Acid Treatments from Pressure Buildup Analysis", *Transactions AIME* 216, p.38-43.
- Saidi, A. M., 1987: *Reservoir Engineering of Fractured Reservoirs (Fundamental and Practical Aspects)*, Total Edition Press, Paris.
- van Golf-Racht, T. D., 1982: *Fundamentals of Fractured Reservoir Engineering*, Elsevier Scientific Publishing Company, the Netherlands.
- Warren, J. E., and P. J. Root, 1963: "The Behavior of Naturally Fractured Reservoirs", *Society of Petroleum Engineers Journal*, September, p.245-255.
- Wolff, M., M. A. Miller and L. W. Lake, 1990: "Oil Recovery from Geologically Based Fracture Networks", *In Situ*, v.14, p.407-427.

APPENDIX A. PROBABILITY ANALYSIS OF PROPERTIES OF A SIMPLIFIED FRACTURED RESERVOIR (FROM ROSSEN, 1997)

A lot of work that has been done in this research is essentially based on Rossen's research (1997, 1998). For the purpose of a thorough understanding and reference, it is necessary to present his work in Appendix A and B.

Model Assumptions and Derivations

The initial assumptions are extremely simple, as illustrated in Figure 2.1. The region of interest in the reservoir is rectangular, with height H , length in the direction of flow L , and width normal to these two directions W . All fractures are assumed parallel (shown horizontal in Figure 2.1, but they could be vertical with no change in what follows) and extend across the region. The probability distribution for fracture apertures is assumed to be known:

$$\frac{n(b) db}{\text{length of transect}} \equiv \text{number of fractures with aperture between } b \text{ and } (b+db) \text{ per unit} \quad (\text{A.1})$$

The *transect* is a line drawn perpendicular to the plane of all the fractures; thus a transect would be a vertical line in Figure 2.1. We assume that the occurrence and properties of the fractures are uncorrelated, and, for simplicity, we assume that a matrix without fractures has zero permeability.

Let $E(n)$ be the expected value of the number of fractures of all apertures per unit length of transect; then

$$E(n) = \int_0^{\infty} n(b) db . \quad (\text{A.2})$$

This distribution $n(b)$ is related to that of Marrett (1997). Marrett counted the number of fractures observed in a transect of length H^* and noted their apertures, and derived $N(b)$, the cumulative number of fractures observed with aperture greater than or equal to b . We assume that this function describes the true aperture distribution, not just one realization of it; then

$$N(b) = H^* \int_b^{\infty} n(b') db'. \quad (\text{A.3})$$

Let N_t be the total number of fractures observed in this transect, then

$$N_t \equiv N(0). \quad (\text{A.4})$$

Marrett determined that between cutoffs b_{\min} and b_{\max} $N(b)$ has the form

(A.5)

$$N(b) = ab^{-c} \text{ for } b_{\min} < b < b_{\max}.$$

He argues that in reality Equation A.5 applies for $0 < b < \infty$; that difficulties in observing small apertures explain the lower limit b_{\min} ; and that the relative infrequency of fractures with large aperture, together with statistical variation, explains the deviation from Equation A.5 for large b .

Combining Equations A.3 and A.5, one can show that $n(b)$ has the same basic form as $N(b)$:

$$n(b) = -\frac{ac}{H^*} b^{-(c-1)} \equiv a' b^{-c'} \text{ for } b_{\min} < b < b_{\max} \quad (\text{A.6})$$

with

$$a' \equiv -\frac{ac}{H^*}$$

$$c' \equiv -c - 1$$

The expected value of the fracture porosity ϕ_f , $E(\phi_f)$, derived from Equation A.6 is

$$E(\phi_f) = \int_0^{\infty} bn(b)db = a' \left(\frac{b_{\max}^{c'+2} - b_{\min}^{c'+2}}{c'+2} \right). \quad (A.7)$$

For all values of c' other than -2 , this integral diverges if $b_{\max} \rightarrow \infty$ and $b_{\min} = 0$. For $c' < -2$, the integral diverges at the lower limit; for $c' > -2$, as reported by Marrett, the integral diverges at the upper limit. This does not mean that observed porosities are infinite, but that extraordinarily large porosities are observed frequently enough that the expected value of porosity is infinite.

Derived Functions

The number of fractures in any portion of a reservoir is itself a random number. Probability theorems are most straight-forward when the number of random events (e.g., the number of rolls of the dice, or number of times colored balls are removed from a bag) is set in advance. The following formalism allows one to incorporate the fracture aperture distribution of Equation A6 into such a conceptual framework. In the process, one makes simplifying assumptions that are not strictly followed by this aperture distribution. We believe the errors caused by these deviations do not fundamentally alter the conclusions of this analysis.

We assume that there exists a length scale h that has two properties. First, there are no fractures with aperture greater than h :

$$\int_h^{\infty} n(b)db \cong 0. \quad (A.8)$$

Second, the probability that two fractures occur within a single interval of length h is essentially zero. The probability of one fracture in such an interval is $(E(n)h)$; therefore, we assume,

$$(E(n)h)^2 \cong 0. \quad (A.9)$$

We then divide the interval H in Figure 2.1 into (H/h) sub-intervals of thickness h and ask whether there is a fracture in each sub-interval and, if so, what is its aperture. (We assume that h is chosen so that (H/h) is an integer.) The actual set of fractures in the interval is then the result of (H/h) independent samplings from a probability distribution $p(b)$ given by

$$\begin{aligned}
 p(0) &= 1 - E(n) h \text{ for } b = 0 \\
 p(b) &= h n(b) \text{ for } b > 0 .
 \end{aligned}
 \tag{A.10}$$

Here an aperture $b = 0$ means no fracture is observed in this interval. The cumulative distribution function (cdf) corresponding to Equation A10 is

$$P(b) \equiv \int_0^b p(b) db
 \tag{A.11}$$

$$P(0) = 1 - E(n)h
 \tag{A.12}$$

$$P(b) = (1 - E(n) h) + \int_0^b h n(b) db \quad \text{for } b > 0 .$$

This cdf is helpful in carrying out the Monte Carlo studies on aperture distribution. Note that while Marrett's cumulate distribution $N(b)$ (Equation A.3) represents fractures with apertures greater than or equal to b , this represents fractures with aperture less than or equal to b .

Widest Observed Fracture

Just as the number of fractures observed in any interval is a random variable, so is the widest aperture observed in any interval. The probability distribution for the widest observed aperture can be derived as follows.

Let $P_{>}(b) \equiv$ [probability that at least one observed aperture $> b$] (A.13)

$$= 1 - [\text{probability that all observed apertures} < b] \quad (\text{A.14})$$

The probability of the event in brackets is the probability that in all (H/h) sub-intervals, apertures are less than b (where zero aperture means no fracture is observed in the sub-interval). The apertures in each sub-interval are assumed independent and uncorrelated, so

$$P_{>}(b) = 1 - [\text{probability that the aperture in any given sub-interval} < b]^{(H/h)} \quad (\text{A.15})$$

$$= 1 - \left(1 - \int_b^{\infty} p(b') db' \right)^{(H/h)} \quad (\text{A.16})$$

$$= 1 - \left(1 - h \int_b^{\infty} n(b') db' \right)^{(H/h)} \quad (\text{A.17})$$

For large (H/h) , the expression subtracted from 1 inside the brackets in Equation A17 must be small, except for $P_{>}(b)$ very near 1. As interval H increases, $P_{>}(b)$ shifts to larger values of b , since, as H increases, only with smaller values of the integral can the expression inside the brackets be sufficiently small that $P_{>}(b)$ is significantly less than 1. For the aperture distribution of Equation A.6,

$$P_{>}(b) = 1 - \left(1 - a'h \left(\frac{b_{\max}^{c'+1} - b^{c'+1}}{c'+1} \right) \right)^{(H/h)} \quad (\text{A.18})$$

Number of Fractures Observed

The number of fractures observed in interval H is the number of nonzero values of b observed in the (H/h) sub-intervals, each sampling the distribution $p(b)$ (Equation A.10). The central limit theorem of probability theory (Jensen *et al.*, 1997) states that for a population of realizations, each comprising a large number of samplings from a probability distribution with finite mean μ and variance σ^2 , the mean of the population is distributed normally about μ , with variance σ^2/\sqrt{n} , regardless of the nature of the original distribution. The probability distribution for observing a fracture in a given sub-interval is simply

$$p_f(0) = 1 - E(n) h \quad (A.19)$$

$$p_f(1) = \langle n \rangle h$$

where $p_f(0)$ is the probability of finding no fracture in sub-interval h , and $p_f(1)$ is the probability of finding a fracture there. Note that p_f has finite mean and variance whatever the aperture distribution $p(b)$ (Equation A.10). Therefore the actual number of fractures observed in a given interval H is normally distributed about the expected value, $(H E(n))$.

Effective Permeability for Interval

The central limit theorem can also predict the probability distribution of effective permeability, but the assumption of finite mean and variance, and requirement of a "large" sample population, is more restrictive. Given a fracture of aperture b_i in sub-interval i , the effective permeability k_i of that sub-interval is given by Darcy's law (Lake, 1989)

$$k_i \equiv \frac{Q_i \mu L}{A \Delta \Phi} \quad (A.20)$$

where Q_i is flow rate, A is cross sectional area of the interval (hW in this case), m is fluid viscosity, $\Delta\Phi$ is difference in total flow potential (pressure + hydrostatics) in the flow direction, and L is given in Figure 2.1. The flow rate Q_i is given by that through a rectangular slit of aperture b_i (where $b_i = 0$ if there is no fracture present) (Bird *et al.*, 1960):

$$k_i = \frac{1}{hW} \left(\frac{1}{12} \frac{b_i^3 W \Delta\Phi}{\mu L} \right) \frac{\mu L}{\Delta\Phi} = \frac{1}{12} \frac{b_i^3}{h} \quad (\text{A.21})$$

The effective permeability of the entire interval is based on the flow through all fractures and the total cross-sectional area of the interval:

$$k_{\text{eff}} = \left(\frac{\sum_{i=1}^{H/h} Q_i}{HW} \right) \frac{\mu L}{\Delta\Phi} = \frac{\sum_{i=1}^{H/h} \left(\frac{1}{12} \frac{b_i^3 W \Delta\Phi}{mL} \right)}{HW} \frac{\mu L}{\Delta\Phi}$$

$$\left(\frac{\sum_{i=1}^{H/h} k_i}{H/h} \right) = \quad (\text{A.22})$$

In other words, the effective permeability of the overall interval is the arithmetic average of the effective permeabilities of all the (H/h) sub-intervals.

According to the central limit theorem, the expected value of this average is just the mean of the probability distribution for k_i , and the probability distribution for k_{eff} is normally distributed around this value. For the probability distribution of Equation A6, this expected value is

$$E(k_{\text{eff}}) \equiv \int_0^{\infty} p(b) \frac{b^3}{12h} db$$

$$= \frac{a'}{12} \left(\frac{b_{\text{max}}^{c'+4} - b_{\text{min}}^{c'+4}}{c'+4} \right) \quad (\text{A.23})$$

If $b_{\max} \rightarrow \infty$, and $c' > -4$ as reported by Marrett, $E(k_{\text{eff}})$ is infinite. As with porosity (Equation A.7), this does not mean that actually observed effective permeabilities are infinite, but that extraordinarily large permeabilities are observed frequently enough that the expected value of k_{eff} is infinite.

Even for finite b_{\max} , the probability distribution for $k_{\text{eff},i}$, with its factor b_i^3 (Equation A.21), has potentially an even longer tail extending toward large values of k_{eff} than does the distribution for aperture b itself (Equation A.6). Therefore, with large upper limit b_{\max} on the aperture distribution, the central limit theorem may apply only for extremely large populations of fractures, and effective permeabilities may not be normally distributed.

APPENDIX B. FRACTURE FREQUENCY IN OUTCROPS AND SCALING OF FRACTURE
FREQUENCY WITH VOLUME OF OBSERVATION (FROM ROSSEN, 1998)

Fracture Frequency in Outcrops

The frequency of observation of fractures in two-dimensional (2D) outcrops differs from the spatial frequency of fractures in a 3D rock layer, and this relationship depends on fracture size. In this section we derive the relationship between these two frequency functions analytically, given certain assumptions.

We assume initially that each fracture is a vertical, circular disk of diameter D as shown in Figure B1; the strike of the fracture is irrelevant to the discussion that follows here. The centers of these disk-shaped fractures are assumed to be randomly distributed in the given layer. Any portion of a fracture disk that extends outside the layer is truncated at the layer boundary. The frequency of occurrence of fractures (number of fracture centers per unit volume of layer) as a function of fracture diameter is assumed to obey a power law as described more fully below.

Consider a layer of thickness H that is sampled at a horizontal plane at a vertical location z^* as shown in Figure B1. In this terminology, H is the thickness of the layer at the time of fracturing. Values of $z^* < H$ would correspond to an outcrop thinned by erosion so that the plane at z^* is later exposed; z^* is then the *apparent* thickness of the layer at the time of observation of the outcrop. The distinction between $z^* = H$ and $z^* < H$ is potentially important. If $z^* = H$, then no fractures centered above this level can intersect the plane of the outcrop, as shown in Figure B1, because no fractures from other layers extend into the layer of interest. If $z^* < H$, however, fractures centered above the eventual plane of the outcrop could pass into the plane of the outcrop. Note (Figure B1) that although the diameter of the disk-shaped fracture is D , its apparent length L in the outcrop is less than D unless the fracture is centered on the outcrop plane.

Let the following functions be defined for fracture frequencies in the 3D layer volume (subscripted 3) and in the 2D outcrop (subscripted 2):

$$N_3(D) \equiv \text{number of fractures of diameter } D \text{ or greater per unit volume of layer} \quad (\text{B.1})$$

$n_3(D) dD \equiv$ number of fractures with diameter between D and $(D+dD)$ per unit volume of reservoir; i.e.,

$$n_3(D) = - (dN_3/dD) ; N_3(D) \equiv \int_D^{\infty} n_3(D') dD' . \quad (\text{B.2})$$

N_3 is the cumulative probability distribution (cdf) for fracture diameter, and n_3 is the corresponding probability distribution function (pdf). N_3 is the function N discussed in Appendix A.

For a 2D outcrop, the corresponding frequency functions are

$$N_2(L) \equiv \text{number of fractures of length } L \text{ or greater per unit area of outcrop} \quad (\text{B.3})$$

$n_2(L) dL \equiv$ number of fractures with length between L and $(L+dL)$ per unit are of outcrop;

i.e.,

$$n_2(L) = - (dN_2/dL) ; N_2(L) \equiv \int_L^{\infty} n_2(L') dL' . \quad (\text{B.4})$$

A fracture appears in the outcrop only if its center at z is within a distance less than $(D/2)$ of the outcrop at z^* (cf. Figure B1). If it is seen within the outcrop, its apparent length L in the outcrop is given by

$$\left(\frac{L}{2}\right)^2 + (z - z^*)^2 = \left(\frac{D}{2}\right)^2 . \quad (\text{B.5})$$

The diameter D of a fracture centered at z that appears in the outcrop with length L is given by

$$D = \sqrt{(L^2 + 4(z - z^*)^2)} . \quad (\text{B.6})$$

The total number of fractures of length L found in the given layer is obtained by summing over all positions z the number of fractures centered at that position that have length L in the outcrop:

$$n_2(L) = \int_0^H n_3(\sqrt{(L^2 + 4(z - z^*)^2)}) dz \quad (B.7)$$

To avoid having to carry out this integration for each new field case, it is helpful to define dimensionless variables as follows:

$$z_D \equiv z/H \quad (B.8)$$

$$z_D^* \equiv z^*/H \quad (B.9)$$

$$L_D \equiv L/H \quad (B.10)$$

$$n_2(L) = H \int_0^1 n_3\left(H\sqrt{(L_D^2 + 4(z_D - z_D^*)^2)}\right) dz_D \quad (B.11)$$

The cumulative distribution function N_2 is then

$$N_2(L) = \int_L^\infty n_2(L') dL' = \int_L^\infty \int_0^H n_3\left(\sqrt{(L')^2 + 4(z' - z^*)^2}\right) dz' dL' \quad (B.12)$$

$$= H^2 \int_L^\infty \left(\int_0^1 n_3\left(H\sqrt{(L_D')^2 + 4(z_D' - z_D^*)^2}\right) dz_D' \right) dL_D' \quad (B.13)$$

If the pdf for fracture diameter D in the layer, $n_3(D)$, is a power law of the form

$$n_3(D) = A_3 D^{-B_3} \quad (B.14)$$

with pre-exponential factor A_3 and exponent B_3 , then

$$n_3\left(H\sqrt{(L_D')^2 + 4(z_D' - z_D^*)^2}\right) = H^{-B_3} n_3\left(\sqrt{(L_D')^2 + 4(z_D' - z_D^*)^2}\right)$$

(B.15)

and

$$N_2(L) = H^{2-B_3} \int_{L_D}^{\infty} \left(\int_0^1 n_3 \left(\sqrt{(L_D')^2 + 4(z_D' - z^* D)^2} \right) dz_D' \right) dL_D' \quad (B.16)$$

where

$$n_3 \left(\sqrt{(L_D')^2 + 4(z_D' - z_D^*)^2} \right) = A_3 \left((L_D')^2 + 4(z_D' - z_D^*)^2 \right)^{-B_3/2} \quad (B.17)$$

Therefore

$$N_2(L) = A_3 H^{2-B_3} I(z^*, B_3) \quad (B.18)$$

where

$$I(z^*, B_3) \equiv \int_{L_D}^{\infty} \left(\int_0^1 \left((L_D')^2 + 4(z_D' - z^* D)^2 \right)^{-B_3/2} dz_D' \right) dL_D' \quad (B.19)$$

The double integral I in Equation B.19 is a function of only the dimensionless position of the outcrop surface z^* and the exponent B_3 . Therefore, for a given value of z^* (for instance, $z^* = 1$, corresponding to outcrop at the top of the layer), a single numerical integration applies to all power-law distributions with the given value of the exponent B_3 , independent of the pre-exponential factor A_3 and layer thickness H .

Figures B.2 and B.3 shows the value of this double integral for $z^* = 1$ and 0.5 (outcrop at top or middle of original layer), respectively, and exponent $B_3 = 3.85$ as in the Westwater pavement, Mesaverde sandstone, San Juan basin. The two cases are roughly similar in their behavior, except that the number of small fractures is about twice as large for $z^* = 0.5$ as for $z^* = 1$. (This difference is expected, since for $z^* = 0.5$ fractures centered both above and below the plane of observation can enter the plane (Figure B.1).) In both cases, the

cumulative frequency function shows a power-law dependence on length, with exponent 2.85 for large fractures and 1.85 for small fractures. The transition between these two scaling regimes, highlighted in Figures B.4 and B.5, occurs for fractures between about 0.2 and 2 times the layer thickness for $z^* = 0.5$ and between 0.5 and 5 times the layer thickness for $z^* = 1$.

These figures reproduce the behavior seen in the outcrop: a different scaling of fracture frequency for short and long fractures in outcrops, differing by one in their exponents. It also confirms that the volumetric frequency exponent B_3 equals the apparent scaling exponent for large fractures minus one (in this case, 2.85 (Figure B.3) $+ 1 = 3.85 = B_3$).

The value of the integral in Equation B19 for a dimensionless fracture length L_D of 1 corresponds to the number of fractures of length equal to or greater than the thickness of the layer. Marrett and Ortega (1997) reported approximately 90 fractures of length greater than or equal to 2.9 m (the thickness of the mechanical layer) in the Westwater pavement, which has exposed area 130×100 m. This corresponds to $L_D = 1$ in Figure B.4 (assuming $z^* = H$), for which the value of the double integral is 0.18. That in turn suggests that (cf. Equation B.18)

$$90 / (130 \times 100) = A_3 (2.9)^{(2-3.85)} (0.18)$$

$$A_3 = 0.275 \tag{B.20}$$

which is the pre-exponential factor to use in modeling the fractures in the Westwater pavement.

Scaling of Fracture Frequency with Volume of Observation

Fractures affect flow in a reservoir most profoundly when they link up to form an interconnected network of fractures throughout the reservoir. Whether fractures do link up, and at what length scale they do so, depends on the value of the exponent B_3 in Equation B14. In particular, whether small fractures link up on the microscopic scale or large fractures link up on the megascopic scale depends on the value of B_3 , as discussed in this section.

Suppose the fractures in a porous medium follow a scaling law between fracture frequency and fracture-disk diameter D of the form

$$N_3(D) = a D^{-e} . \quad (\text{B.21})$$

Here $N_3(D)$ is the cumulative number of fractures of diameter D or greater per unit volume of reservoir (Equation B.2), and a and e are constants related to A_3 and B_3 (Equation B.14) as follows:

$$N_3(D) \equiv \int_D^{\infty} n_3(D') dD' = \int_D^{\infty} A_3 D'^{-(B_3)} dD' = \left(\frac{A_3}{B_3-1} \right) D^{-(B_3-1)} \quad (\text{B.22})$$

$$a = \left(\frac{A_3}{B_3-1} \right) ; e = B_3 - 1 . \quad (\text{B.23})$$

Based on outcrop studies of the Westwater pavement of the Mesaverde sandstone, San Juan basin, e has a value for that fractured layer of approximately $(3.85 - 1) = 2.85$.

Consider a region "R" of the reservoir that is cubic in shape, of volume L_R^3 (cf. Figure B.6). The total number of fractures of diameter D or greater, $N_R(D)$, within this region is

$$N_R(D) = L_R^3 N_3(D) = a L_R^3 D^{-e} . \quad (\text{B.24})$$

Suppose one limits consideration to some fixed number of the largest fractures within R as L_R varies. For instance, to save computation time, we often limit consideration to the 1,000 largest fractures in a given region of interest as we vary L_R . Let D_D be the (dimensionless) diameter of a fracture relative to the size of the region

$$D_D \equiv D/L_R . \quad (\text{B.25})$$

For instance, if a fracture is 5 m in diameter and resides within a cubical region 10 m on a side, then $D_D = 5/10 = 0.5$. Then the dimensionless fracture-diameter distribution in a cubical region of size L_R is given by

$$N_{RD}(D_D) = a L_R^{3-e} D_D^{-e}. \quad (B.26)$$

Equation B.26 gives the distribution of fracture diameters measured, in effect, with a ruler that grows or shrinks with the size of the region of interest - it gives the distribution of fractures larger than some given fraction or multiple of the region size.

According to Equation B26, how the dimensionless fracture-diameter distribution scales with region size L_R depends on the sign of $(3-e)$. There are three important cases.

- (1) For power-law exponent $e > 3$, the number of fractures that are relatively long compared to L_R (i.e., with large D_D) *increases* as L_R *decreases*, because the factor (L_R^{3-e}) increases as L_R decreases. That means that as one scales down in region size, the fractures appear to grow longer as the size of the region decreases. These longer fractures (relative to the region size) are guaranteed to link up and/or cross the region individually if L_R shrinks sufficiently. Thus, interconnectivity of the fracture network is guaranteed on the microscopic scale. On the other hand, as one scales up in region size, the large fractures (compared to the region of interest) appear relatively less numerous and smaller. Individual large fractures might have large local impacts on permeability, but the large fractures would not link up by themselves to give interconnectivity.
- (2) For power-law exponent $e < 3$, the number of fractures that are relatively long compared to L_R (i.e., with large D_D) increases as L_R *increases*, because the factor (L_R^{3-e}) increases as L_R decreases. That means that as one scales *up* in region size, fractures appear more numerous and larger as the size of the region increases. The fractures are guaranteed to link up on the *megascopic* scale as L_R increases sufficiently. The implications of this behavior are profound. First, long fractures (presumably with wide apertures) have enormous effective permeabilities, giving high effective permeabilities for the fracture population. Moreover, at whatever scale one attempts to model fracture permeability, larger, longer fractures, with enormous diameter, aperture

and permeability, would link up at the next higher length scale, with even greater effects on permeability than those modeled at the given scale.

- (3) It is thought, however, that most fractures are confined to regions of finite thickness H . For instance, the mechanical thickness of the outcrop of the Westwater pavement is 2.9 m. This means that the scaling of cubical regions envisioned in case (2) above cannot continue indefinitely; regions larger than H are square, flat rectangular regions of lateral dimension L_R and fixed thickness H (Figure 2.7). For length scale $L_R >$ layer thickness H , volume scales not as in Equation B.24, but as $(L_R^2 H)$, and Equations B.25 and B.26 become

$$N_R(D) = L_R^2 H N_3(D) = a H L_R^2 D^{-e} \quad (\text{B.27})$$

$$N_{RD}(D_D) = a H L_R^{2-e} D_D^{-e} \quad (\text{B.28})$$

where constants a and H do not vary as region size increases. This means that for $e > 2$, as for the Westwater pavement with $e = 2.85$, the number of fractures that are relatively long compared to L_R (i.e., with large D_D) *decreases* as L_R increases. In turn, that means that as one scales up in region size beyond the layer thickness, fractures appear to grow less numerous and shorter as the size of the region increases. These fractures are less likely to link up on the macroscopic scale as L_R increases.

Thus, for scaling-law exponents $2 < e < 3$, as with the Westwater pavement ($B_3 = 3.85$, $e = 2.85$), fractures are not guaranteed to link up at either the microscopic or the megascopic scale. Whether they link up at all, and give any effective permeability independent of the matrix, must be determined by Monte Carlo simulation.

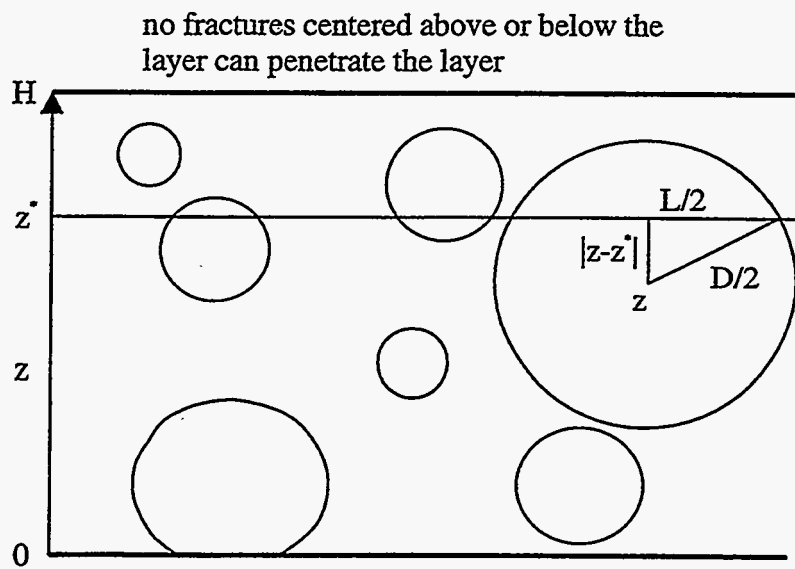


Figure B.1. Model for circular disk-shaped fractures in layer of thickness H , sampled at plane at z^* .

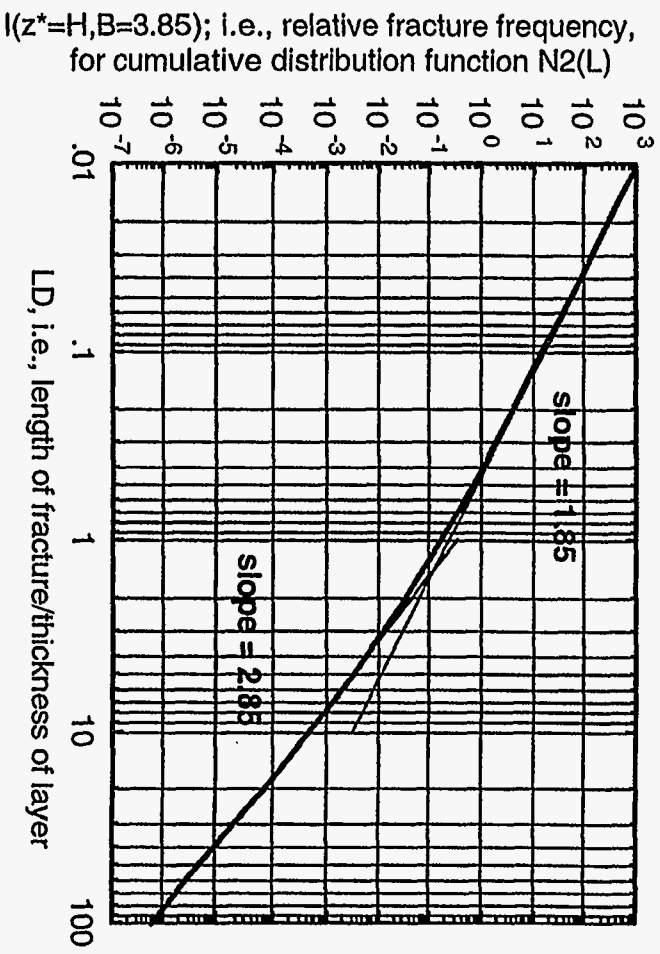


Figure B.2. Value of double integral I (Equation B.19) for $B_3 = 3.85$ and $z^* = H$ (outcrop at top of layer).

$I(z^* = H/2, B=3.85)$; i.e., relative fracture frequency,
for cumulative distribution function $N_2(L)$

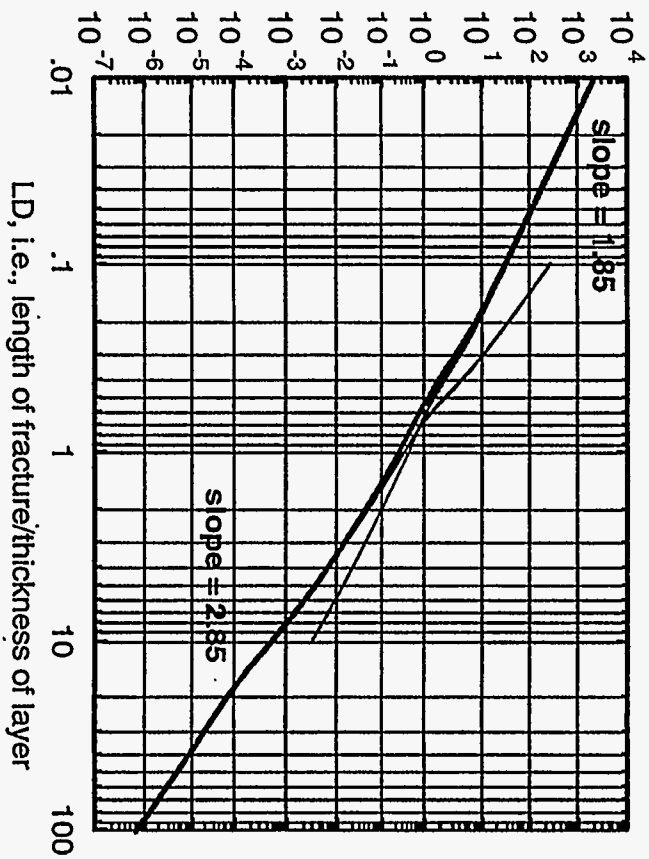


Figure B.3. Value of double integral I (Equation B.19) for $B_3 = 3.85$ and $z^* = H/2$ (outcrop at middle of layer).

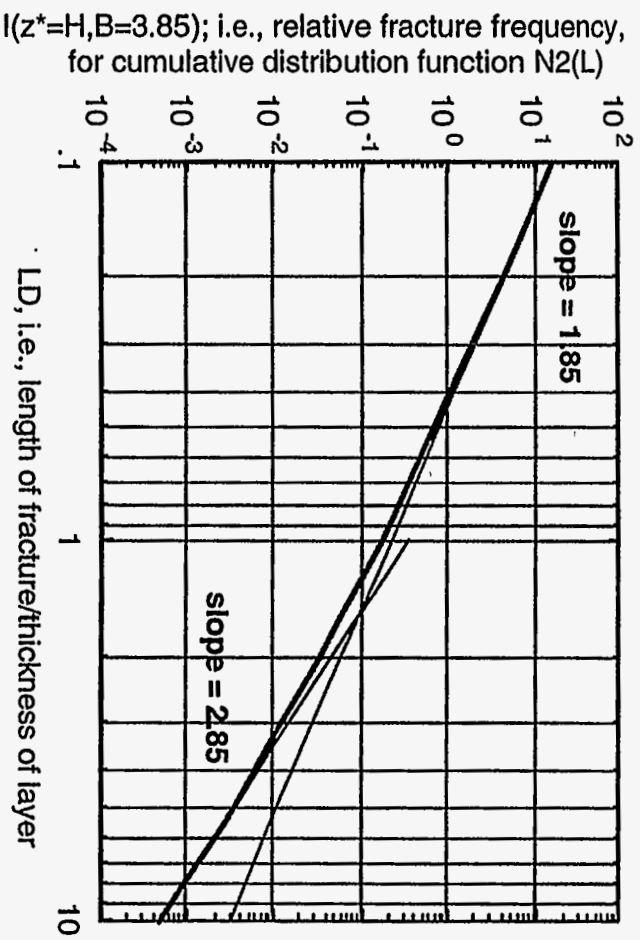


Figure B.4. Enlargement of Figure B.2 near transition in scaling regimes.

$I(z^* = H/2, B=3.85)$; i.e., relative fracture frequency,
for cumulative distribution function $N_2(L)$

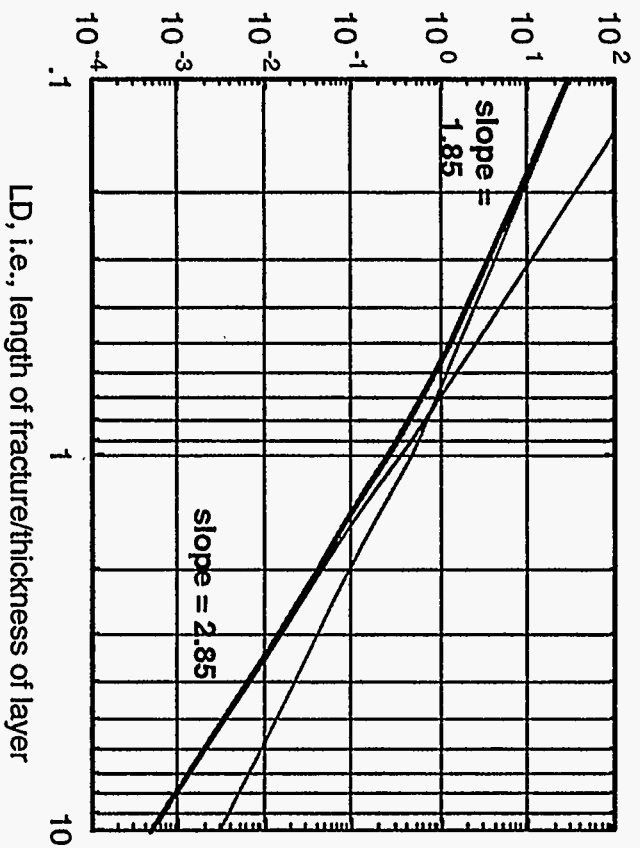


Figure B.5. Enlargement of Figure B.3 near transition in scaling regimes.

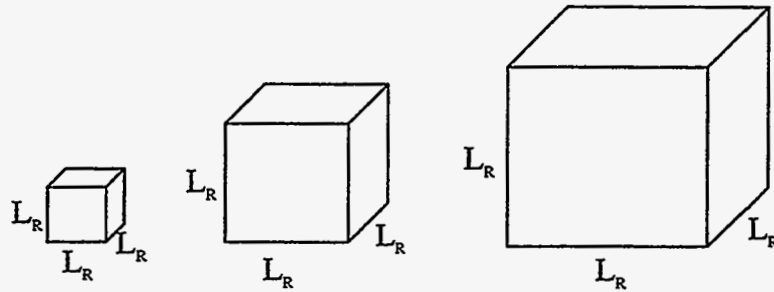


Figure B.6. Scaling up region size for cubical shaped region.

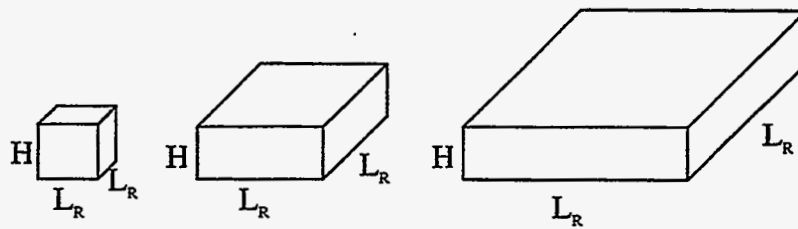


Figure B.7. Scaling up region size with fixed thickness H .

APPENDIX C. NOMENCLATURE

a	empirical factor in the power-law distribution for fracture aperture
A	cross-sectional area of the region
b	fracture aperture
b_1	the largest fracture aperture in the region
b_i	fracture aperture in the i th interval
b_{\min}	minimum fracture aperture
b_{\max}	maximum fracture aperture
c	exponent of the power-law distribution for fracture aperture
C	pre-exponential factor of the power-law distribution for fracture length
D	fractal mass dimension in the Levy-flight process
e	exponent of the power-law distribution for fracture length
$E(\phi_f)$	expected value of fracture porosity
$E(\bar{k})$	expected value of permeability of the region
$E(n)$	expected number of fractures of all apertures per unit length of scanline
h	height of the intervals
H	thickness of the region
H^*	length of the scanline measured in outcrops
k_1	permeability of the region based only on the single fracture with the largest aperture b_1
\bar{k}	effective permeability of the entire region
\bar{k}_i	effective permeability of the i th interval
L	fracture length
L_R	length of the region

L_s	step length in the Levy-flight process
L_{\min}	minimum fracture length
m	empirical factor in the power-law distribution for fracture length
m'	$= m/V_0$
$n(b)$	number of fractures with aperture b per unit length of scanline
n'	number of fractures with length L per unit volume
N	cumulative number of fractures observed in outcrops
$p(b)$	probability distribution function for fracture aperture
$P(b)$	cumulative distribution function for fracture aperture
P_{L_s}	probability function for the Levy-flight process
$P_{\max}(b_1)$	probability function of the largest observed aperture b_1
Q	flow rate
R_{\min}	minimum radius of the disc-shaped fracture
V_0	volume of the original outcrop region
V	volume of the region
W	width of the region
x	random number generated by computer

Greek Symbols

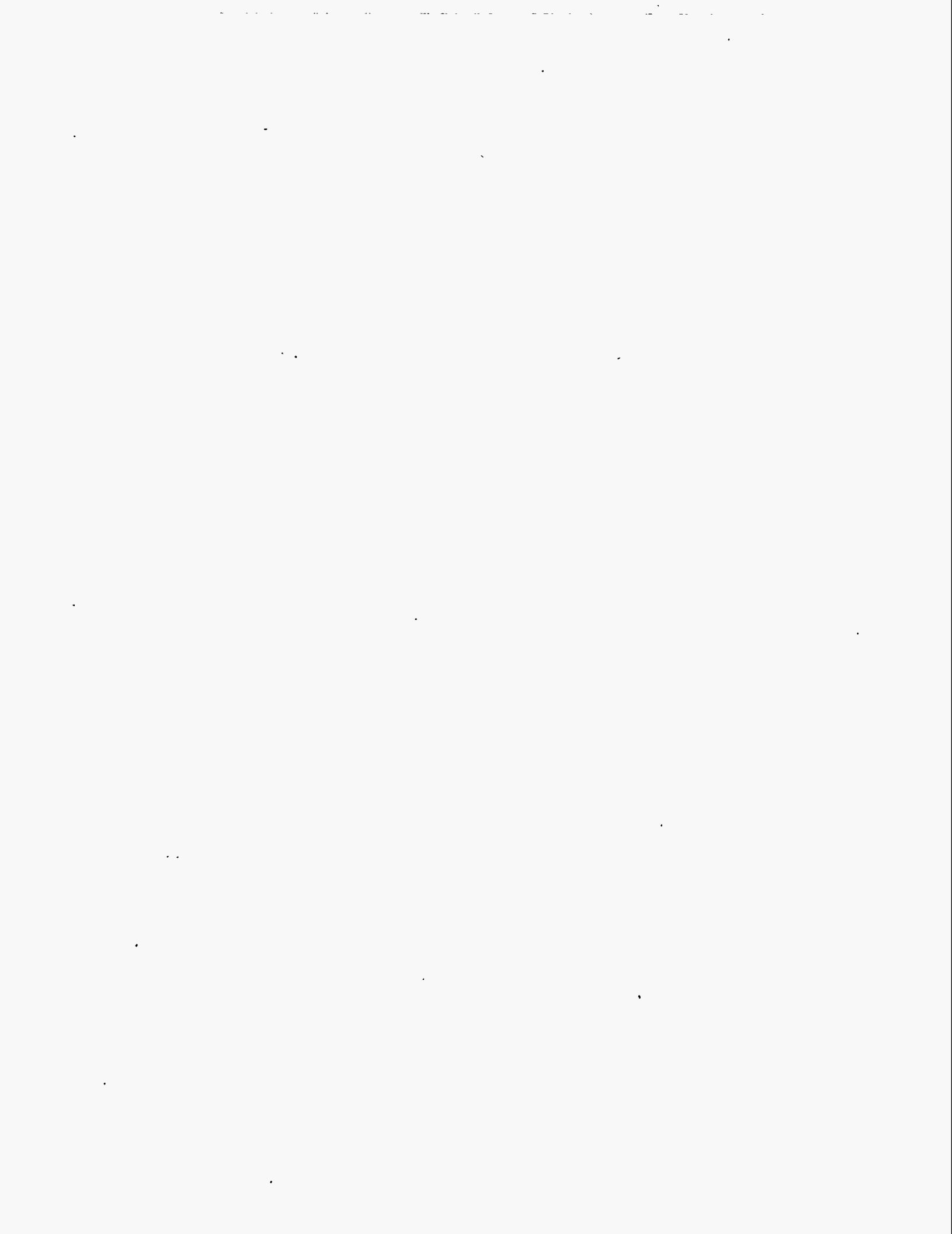
Δ	difference
ϕ	variant angle from the mean orientation
ϕ_f	fracture porosity
ϕ_m	matrix porosity

Φ	fluid potential
κ_1	dispersion coefficient in bivariate Fisher orientation distribution function
κ_2	dispersion coefficient in bivariate Fisher orientation distribution function
μ	fluid viscosity

Subscripts

0	original (outcrops)
1	largest observed aperture in the region; the first dispersion coefficient
2	the second dispersion coefficient

f	fracture
i	the <i>i</i> th interval
m	matrix
min	minimum
max	maximum
R	simulated region



PART IV: TECHNOLOGY TRANSFER

A multifaceted technology transfer effort is under way. The centerpiece of the effort is the ongoing dialog we have established with leading scientists from a group of eight companies in the petroleum industry. In the context of technology transfer, this influential group is exposed to our ongoing research and our preliminary results throughout the course of the project. This has resulted in several abstracts and papers on technical results that are coauthored by members of the university research team and the industry group. In addition to the research collaboration and guidance they provide, this industry group is a conduit for technology transfer to their respective companies, and through their professional contacts (as well as our own), a technology transfer link to the industry as a whole. As listed below, this link is maintained through regular, formal group meetings, E-mail alerts, a dedicated project Web site, informal written reports, and site visits by our research group to industry and vice versa.

Technology is also being accomplished through lectures to other companies and to University audiences, presentations at professional meetings, technical publications, and the public project Web site described in this report.

INDUSTRY GROUP

Two formal meetings have been held with the industry sponsors group and another meeting is scheduled for 1998. These formal meetings have been supplemented by numerous informal meetings and by the use of the project Web site and E-mail communications. Details of these meetings were presented in quarterly reports and previous annual reports:

- Initial planning and concept presentation meeting, Austin, July 1996;
- Progress meeting no. 1, Austin, May 1997;
- Progress meeting no. 2, Austin, August 1998;
- Workshop, fall 1998.

In addition, we have issued informal reports on aspects of our research to industry representatives for their review and have made sets of illustrations available to industry research partners to facilitate technology transfer to their companies.

Publications and Presentations

Published Papers

Although research is ongoing and most of the formal publications to result from this work have yet to be written, several preliminary results from this project have already appeared in the technical literature.

Marrett , R., and Laubach, S. E., 1997, "Diagenetic controls on fracture permeability and sealing": *Int. J. Rock Mech. & Min. Sci.*, v. 34, no. 3-4 (June 1997).

Marrett, R., 1997, "Permeability, porosity, and shear wave anisotropy from scaling of open fracture populations": in *Fractured Reservoirs: Characterization and Modeling*, Rocky Mountain Association of Geologists Guidebook (September 1997), p. 217-226.

Laubach, S. E., Marrett, R., and Lake, L., 1997, Progress report on new methods of natural fracture characterization and simulation: The University of Texas at Austin, Bureau of Economic Geology, research progress report prepared for industry sponsors of the natural fracture project and the Department of Energy, 22 p. + attachments.

Burns, S. L., and Laubach, S. E., 1998, Virtual Collaboratory *Frac City* facilitates geoscientific collaboration and technology transfer: *Geoscience Information Society*, v. 28, p. 111-116.

Published Abstracts

- Marrett, R., Laubach, S. E., Rossen, W., Olson, J., Lake, L., 1998, Integration of new fracture observation, characterization, and fluid-flow modeling technology (abs.): American Association of Petroleum Geologists Annual Convention Official Program, v. 7.
- Ortega, O., Marrett, R., Hamlin, S., Clift, S., and Reed, R., 1998, Quantitative macrofracture prediction using microfracture observations: a successful case study in the Ozona Gas Field, West Texas (abs.): American Association of Petroleum Geologists Annual Convention Official Program, v. 7.
- Reed, R., and Laubach, S. E., 1998, Density and distribution of microfractures in sandstone: importance to diagenesis (extended abs.): American Association of Petroleum Geologists Annual Convention Official Program, v. 7.
- Clift, S. J., Laubach, S. E., Abegg, F. E., Aslesen, K. S., Laroche, T. M., and Stanley, R. G., 1998, New core analysis methods applied to Permian sandstone, Pakenham (Wolfcamp) field, Terrell County, Texas (abs.): Southwest section, American Association of Petroleum Geologists.
- Marrett, R., Rossen, W., and Laubach, S. E., 1998, Integration of new technologies for fracture observation, characterization, and fluid-flow modeling (abs.): Fractured Reservoirs: Practical Exploration and Development Strategies, Rocky Mountain Association of Geologists symposium proceedings, p. 319.
- Laubach, S. E., 1998, Fractured reservoir predictive case histories: domestic and international examples: Fractured Reservoirs (abs.): Practical Exploration and Development Strategies, Rocky Mountain Association of Geologists symposium proceedings, p. 319.

- Laubach, S. E., and Clift, S., 1998, New core analysis methods applied to Permian sandstone, Pakenham field, Terrell County, Texas: Fractured Reservoirs (abs.): Practical Exploration and Development Strategies, Rocky Mountain Association of Geologists symposium proceedings, p. 359.
- Laubach, S. E., and Marrett, R., 1997, Inferring fracture permeability from rock microstructure (abs.): American Association of Petroleum Geologists Bulletin, v. 81, no. 8, p. 1393-1394.
- Laubach, S. E., 1997, Recent advances in core-based structural analysis (abs.): American Association of Petroleum Geologists Hedberg Research Conference, meeting notes, unpaginated, Bryce, Utah, June.
- Marrett, R., and Laubach, S. E., 1997, Diagenetic controls on fracture permeability and sealing (abs.): International Journal of Rock Mechanics and Mining Science, v. 34, nos. 3-4, p. 409.
- Clift, S. J., Abegg, F. E., Aslesen, K. S., Laroche, T. M., Stanley, R. G., and Laubach, S. E., 1997, Predicting fracture cementation in Permian sandstone, Pakenham (Wolfcamp) Field, Terrell County, Texas (abs.): W. D. DeMis, ed., Permian Basin Oil and Gas Fields: Turning Ideas into Production, West Texas Geological Society Publication No. 97-102.
- Laubach, S. E., 1997, New core analysis methods for fractured siliciclastic reservoirs (abs.): American Association of Petroleum Geologists Annual Convention Official Program, v. 6, A67.
- Johns, M. K., Laubach, S. E., and Milliken, K. L., 1997, Syncementation crack-tip and crack-seal microtextures and their implications for fracture connectivity and porosity interpretation (abs.): American Association of Petroleum Geologists Annual Convention Official Program, v. 6, A56.

- Marrett, R., Ortega, O., Reed, R., and Laubach, S. E., 1997, Predicting macrofracture permeability from microfractures (abs.): American Association of Petroleum Geologists Annual Convention Official Program, v. 6, A76.
- Laubach, S. E., and Marrett, R., 1997, Controls on fracture permeability (abs.): in Kim, K., ed., Proceedings, 36th U.S. Rock Mechanics Symposium, Columbia University, New York, June, 1997.
- Laubach, S. E., 1996, Fracturing and diagenesis as coupled processes (abs.): GSA Abstracts with programs, v. 28, no. 7, p. A-136–A-137.
- Ortega, O. J., and Marrett, R., 1997, Use of microscopic information for macrofracture characterization in Mesaverde Group Sandstones from the surface and subsurface of the San Juan Basin (abs.), *in* Natural Fracture Systems in the Southern Rockies, Four Corners Geological Society, Durango, Colorado, June 13 and 14, 1997.
- Marrett, R., 1996, Scale dependence of fractures and fracture permeability (abs.): GSA Abstracts with programs, v. 28, no. 7.
- Ortega, O., and Marrett, R., 1996, Significance of finite layer thickness on scaling of fractures (abs.): GSA Abstracts with programs, v. 28, no. 7.
- Reed, R. M., and Laubach, S. E., 1996, The role of microfractures in the development of quartz overgrowth cements in sandstones: new evidence from cathodoluminescence studies (abs.): GSA Abstracts with programs, v. 28, no. 7, p. A-280.

Completed Thesis

Ortega, O. J., 1997, Prediction of macrofracture properties using microfracture information, Mesaverde Group sandstones, San Juan Basin, New Mexico, The University of Texas at Austin, Thesis, 278 p.

Gu, Y., 1998, Fracture simulation, The University of Texas at Austin, Thesis, 300 p.

Papers in Press

The following papers have been accepted for publication. In addition to these papers, several manuscripts not listed here are in preparation for publication. These reports are available on the project Web site.

Milliken, K. L., and Laubach, S. E., 1998, Brittle deformation in sandstone diagenesis as revealed by scanned cathodoluminescence imaging with application to characterization of fractured reservoirs: Springer-Verlag.

Lectures

In addition to presentations associated with direct industry contacts and sponsor group meetings, the research group has made several invited presentations to industry and academic audiences. In general, the travel costs for these presentations have been borne by the group or University issuing the invitation rather than by our project budget. The number of presentations of this type will increase as the research moves closer to completion.

“The challenges of reservoir structure in the 21st Century”: presented to American Association of Petroleum Geologists Reservoir Deformation Research Group annual meeting, Salt Lake City, May.

“Incorporation of microstructural and statistical fracture data into a reservoir model”:
Fractured Reservoirs: Practical Exploration and Development Strategies, Rocky Mountain
Association of Geologists symposium.

“Origin of reservoir fractures”: Invited keynote speaker, The Woodworth Conference of the
Geological Society of London, marking 100 years in the evolution of fracture analysis,
Coleraine, Northern Ireland, April.

“Fractured reservoir analysis: implications for the petroleum engineer”: presented to
Departmental Seminar, Petroleum and Geosystems Engineering, The University of Texas at
Austin, Austin, Texas, February.

“Current research on reservoir fractures”: presented to Bureau of Economic Geology, The
University of Texas at Austin, Austin, Texas, February.

“Strategies for reservoir structural analysis”: lecture presented to PDVSA (Maraven),
Caracas, Venezuela, February.

“Research on structural geology and reservoir engineering”: briefing presented to the
Chairman, The University of Texas Board of Regents, Austin, Texas, January.

“Practical tools for fractured reservoirs”: Fractured Reservoirs: Practical Exploration and
Development Strategies, Rocky Mountain Association of Geologists symposium, Denver,
Colorado, January.

“The new paradigm in core analysis”: presented to Department of Geology, New Mexico
Tech University, Socorro, New Mexico, January. Invited.

“Structural geology in support of reservoir engineering in modern reservoir management”:
presented to graduate class in reservoir engineering (PGSE 360), Department of Petroleum and
Geosystems Engineering, The University of Texas at Austin, November.

“Métodos revolucionarios de análisis de muestras de testigos para yacimientos fracturados
(Revolutionary core analysis methods for fractured reservoirs)”: keynote address presentado para
la celebración del 32dcmo aniversario de la fundación del Instituto Mexicano del Petróleo,
Mexico City, Mexico, October. Invited.

“Inferring fracture permeability from rock microstructure”, presented to American Association of Petroleum Geologists International Conference, Vienna, Austria, September. Invited.

“Diagenetic controls on fracture permeability”: presented to 36th U.S. Rock Mechanics Symposium, Columbia University, New York, July. Invited.

“Fracture properties from rock microstructure”: presented to American Association of Petroleum Geologists Hedberg Research Conference, Bryce, Utah, June. Invited.

“Using core analysis to characterize fractures and calibrate seismic data”: presented to GRI technical advisory group, Denver, Colorado, June.

“Current progress in fracture evaluation”: presented to New Methods of Fracture Characterization and Simulation workshop, Austin, Texas, May.

“Fracture orientation and fracture quality prediction case studies: lessons for practical application”: presented to New Methods of Fracture Characterization and Simulation workshop, Austin, Texas, May.

“Diagenesis from a different perspective”: presented to SEPM Clastic Diagenesis Group discussion meeting, Dallas, Texas, April. Invited. Best Presentation Award.

“Uncovering fractures”: keynote address presented to imaging systems dinner, American Association of Petroleum Geologists convention, Dallas, Texas, April. Invited.

“Diagenetic controls on fracture permeability”: presented to 36th U.S. Rock Mechanics Symposium, Columbia University, New York, July.

“Current progress in fracture evaluation”: presented to industry sponsors of BEG fracture research, Austin, Texas, May.

“Diagenesis from a different perspective”: presented to SEPM Clastic Diagenesis Group discussion meeting, Dallas, Texas, April. Invited.

“Uncovering fractures”: keynote address presented to imaging systems dinner, American Association of Petroleum Geologists convention, Dallas, Texas, April.

“New methods of fractured reservoir characterization: examples from the Val Verde basin”: presented to SIPES convention, Austin, Texas, March.

“Results of tests on horizontal core”: presented to Parker & Parsley, Inc., Austin, Texas, March.

“Recent breakthroughs in analysis of natural fractures”: presented to Department of Geology, Tulsa University, Tulsa, Oklahoma, February.

“Fracture analysis methods and applications” and “Application of new structural petrology methods to Chevron’s Wolfcamp sandstone core, Pakenham field”: presented to Chevron, Midland, Texas, January.

“Quantification and prediction of reservoir fracture attributes”: presented to PEMEX, Tampico, Mexico, January.

“Using petrology to unlock gas resources in West Texas”: presented to Chevron, Houston, Texas, August.

“Future of outcrop-based studies of natural fractures” and “Advanced subsurface fracture and stress characterization methods”: presented to Mobil Corp. strategy meeting for fracture and stress research, Dallas, Texas, August.

“Overview of reservoir simulation project”, “Summary of fractured reservoir analyses completed to date”, “New fracture characterization methods”, and “Inferring fracture conductivity from sidewall core samples”: presented to industry/DOE workshop on fractured reservoir simulation, Austin, Texas, July.

“Field and core seminar on fracture systems in carbonate rocks”: lectures and field trip presented to Amoco Production geophysics team, Austin, Texas, July.

“New fracture characterization methods for siliciclastic rocks”: presented to North American Rock Mechanics Symposium, Montreal, Canada, June.

“Geochemical controls on the evolution of porosity and implications of new microstructural observations for kinetics of crack growth at subcritical tensile stresses”: presented to Exxon Production Research, Houston, Texas, June.

“Synthesis of petrologic and structural approaches for solving reservoir characterization challenges”: presented to Union Pacific Resources, Fort Worth, Texas, May.

Awards

Best presentation award, structural diagenesis, SEPM Clastic Diagenesis Research Group, Dallas, Texas, April 1997.

ACKNOWLEDGMENTS

This project was funded by the U.S. Department of Energy under contract number DE-AC22-94PC91008 through BDM-Oklahoma, Inc., under subcontract number G4S51732. This project was also supported by Chevron U.S.A. Production Company; Conoco, Inc.; Exxon Production Research Company; Mobil Technology Company; Sanchez Oil & Gas Company; Tom Brown, Inc.; and Union Pacific Resources, with in-kind support from Oxford Instruments.